

Ignacio Rojas  
Gonzalo Joya  
Joan Cabestany (Eds.)

LNCS 7903

# Advances in Computational Intelligence

12th International Work-Conference  
on Artificial Neural Networks, IWANN 2013  
Puerto de la Cruz, Tenerife, Spain, June 2013  
Proceedings, Part II

2  
Part II



Springer

*Commenced Publication in 1973*

Founding and Former Series Editors:

Gerhard Goos, Juris Hartmanis, and Jan van Leeuwen

## Editorial Board

David Hutchison

*Lancaster University, UK*

Takeo Kanade

*Carnegie Mellon University, Pittsburgh, PA, USA*

Josef Kittler

*University of Surrey, Guildford, UK*

Jon M. Kleinberg

*Cornell University, Ithaca, NY, USA*

Alfred Kobsa

*University of California, Irvine, CA, USA*

Friedemann Mattern

*ETH Zurich, Switzerland*

John C. Mitchell

*Stanford University, CA, USA*

Moni Naor

*Weizmann Institute of Science, Rehovot, Israel*

Oscar Nierstrasz

*University of Bern, Switzerland*

C. Pandu Rangan

*Indian Institute of Technology, Madras, India*

Bernhard Steffen

*TU Dortmund University, Germany*

Madhu Sudan

*Microsoft Research, Cambridge, MA, USA*

Demetri Terzopoulos

*University of California, Los Angeles, CA, USA*

Doug Tygar

*University of California, Berkeley, CA, USA*

Gerhard Weikum

*Max Planck Institute for Informatics, Saarbruecken, Germany*

Ignacio Rojas Gonzalo Joya  
Joan Cabestany (Eds.)

# Advances in Computational Intelligence

12th International Work-Conference  
on Artificial Neural Networks, IWANN 2013  
Puerto de la Cruz, Tenerife, Spain, June 12-14, 2013  
Proceedings, Part II



Springer

## Volume Editors

Ignacio Rojas  
University of Granada  
Department of Computer Architecture  
and Computer Technology  
18071 Granada, Spain  
E-mail: irojas@ugr.es

Gonzalo Joya  
University of Malaga  
Department of Electronics Technology  
29071 Malaga, Spain  
E-mail: gjoya@uma.es

Joan Cabestany  
Universitat Politecnica de Catalunya  
Department of Electronics Engineering  
08034 Barcelona, Spain  
E-mail: cabestany@aha-dee.upc.edu

ISSN 0302-9743  
ISBN 978-3-642-38681-7  
DOI 10.1007/978-3-642-38682-4  
Springer Heidelberg Dordrecht London New York

e-ISSN 1611-3349  
e-ISBN 978-3-642-38682-4

Library of Congress Control Number: 2013938983

CR Subject Classification (1998): J.3, I.2, I.5, C.2.4, H.3.4, D.1, D.2

LNCS Sublibrary: SL 1 – Theoretical Computer Science and General Issues

© Springer-Verlag Berlin Heidelberg 2013

This work is subject to copyright. All rights are reserved, whether the whole or part of the material is concerned, specifically the rights of translation, reprinting, re-use of illustrations, recitation, broadcasting, reproduction on microfilms or in any other way, and storage in data banks. Duplication of this publication or parts thereof is permitted only under the provisions of the German Copyright Law of September 9, 1965, in its current version, and permission for use must always be obtained from Springer. Violations are liable to prosecution under the German Copyright Law.

The use of general descriptive names, registered names, trademarks, etc. in this publication does not imply, even in the absence of a specific statement, that such names are exempt from the relevant protective laws and regulations and therefore free for general use.

*Typesetting:* Camera-ready by author, data conversion by Scientific Publishing Services, Chennai, India

Printed on acid-free paper

Springer is part of Springer Science+Business Media (www.springer.com)

# Preface

We are proud to present the set of final accepted papers of the 12th edition of the IWANN conference—International Work-Conference on Artificial Neural Networks—held in Puerto de la Cruz, Tenerife (Spain), during June 12–14, 2013.

IWANN is a biennial conference that seeks to provide a discussion forum for scientists, engineers, educators, and students on the latest ideas and realizations in the foundations, theory, models, and applications of hybrid systems inspired on nature (neural networks, fuzzy logic and evolutionary systems) as well as in emerging areas related to the above items. It also aims to create a friendly environment that could lead to the establishment of scientific collaborations and exchanges among attendees. The proceedings include all the presented communications at the conference. The publication of an extended version of selected papers in a special issue of several specialized journals (such as *Neurocomputing*, *Soft Computing* and *Neural Processing Letters*) is also foreseen. Since the first edition in Granada (LNCS 540, 1991), the conference has evolved and matured. The list of topics in the successive Call for Papers has also evolved, resulting in the following list for the present edition:

1. **Mathematical and theoretical methods in computational intelligence.** Mathematics for neural networks. RBF structures. Self-organizing networks and methods. Support vector machines and kernel methods. Fuzzy logic. Evolutionary and genetic algorithms.
2. **Neurocomputational formulations.** Single-neuron modelling. Perceptual modelling. System-level neural modelling. Spiking neurons. Models of biological learning.
3. **Learning and adaptation.** Adaptive systems. Imitation learning. Reconfigurable systems. Supervised, non-supervised, reinforcement and statistical algorithms.
4. **Emulation of cognitive functions.** Decision making. Multi-agent systems. Sensor mesh. Natural language. Pattern recognition. Perceptual and motor functions (visual, auditory, tactile, virtual reality, etc.). Robotics. Planning motor control.
5. **Bio-inspired systems and neuro-engineering.** Embedded intelligent systems. Evolvable computing. Evolving hardware. Microelectronics for neural, fuzzy and bioinspired systems. Neural prostheses. Retinomorph systems. Brain-computer interfaces (BCI). Nanosystems. Nanocognitive systems.
6. **Advanced topics in computational intelligence.** Intelligent networks. Knowledge-intensive problem-solving techniques. Multi-sensor data fusion using computational intelligence. Search and meta-heuristics. Soft computing. Neuro-fuzzy systems. Neuro-evolutionary systems. Neuro-swarm. Hybridization with novel computing paradigms.

7. **Applications.** Expert Systems. Image and Signal Processing. Ambient intelligence. Biomimetic applications. System identification, process control, and manufacturing. Computational Biology and bioinformatics. Parallel and distributed computing. Human-computer Interaction, Internet modeling, communication and networking. Intelligent systems in education. Human-robot interaction. Multi-agent Systems. Time series analysis and prediction. Data mining and knowledge discovery.

At the end of the submission process, and after a careful peer review and evaluation process (each submission was reviewed by at least 2, and on average 2.9, Program Committee members or additional reviewers), 116 papers were accepted for oral or poster presentation, according to the recommendations of reviewers and the authors' preferences.

It is important to note, that for the sake of consistency and readability of the book, the presented papers are not organized as they were presented in the IWANN 2013 sessions, but are classified into 16 chapters. The organization of the papers is in two volumes arranged following the topics list included in the call for papers. The first volume (LNCS 7902), entitled *Advances in Computational Intelligence. Part I* is divided into nine main parts and includes the contributions on:

1. Invited Talks to IWANN 2013
2. Applications of Computational Intelligence
3. Hybrid Intelligent Systems
4. Kernel Methods and SVM
5. Learning and Adaptation
6. Mathematical and Theoretical Methods in Computational Intelligence
7. Data Mining with Evolutionary Computation and ANN
8. Self-Organizing Network
9. Advances in Computational intelligence

In the second volume (LNCS 7903), entitled *Advances in Computational Intelligence. Part II* is divided into seven main parts and includes the contributions on:

1. Metaheuristics
2. Bioinformatics/Biomedicine in Computational Intelligence
3. Fuzzy Logic and Soft Computing Applications
4. Artificial Intelligence and Games
5. Biological and Bio-inspired Dynamical Systems for Computational Intelligence
6. Brain-Computer Interfaces and Neurotechnologies
7. Video and Image Processing

The 12th edition of the IWANN conference was organized by the University of Granada, University of Malaga, Polytechnical University of Catalonia, and University of La Laguna, together with the Spanish Chapter of the IEEE Computational Intelligence Society. We wish to thank to the Spanish Ministerio de

Ciencia e Innovacion and the University of La Laguna for their support and grants.

We would also like to express our gratitude to the members of the different committees for their support, collaboration, and good work. We especially thank the Local Committee, Program Committee, the reviewers, and special session organizers. Finally, we want to thank Springer, and especially Alfred Hoffman and Anna Kramer for their continuous support and cooperation.

June 2013

Ignacio Rojas  
Gonzalo Joya  
Joan Cabestany

# Organization

## Program Committee

Leopoldo Acosta	
Vanessa Aguiar-Pulido	University of Coruña
Arnulfo Alanis Garza	Instituto Tecnológico de Tijuana
Ali Fuat Alkaya	
Amparo Alonso-Betanzos	University of A Coruña
Juan Antonio Alvarez-García	University of Seville
Jhon Edgar Amaya	University of Tachira (UNET)
Gabriela Andrejkova	
Cesar Andres	Universidad Complutense de Madrid
Miguel Angel Lopez	
Anastassia Angelopoulou	University of Westminster
Plamen Angelov	Lancaster University
Davide Anguita	University of Genoa
Cecilio Angulo	Universitat Politcnica de Catalunya
Angelo Arleo	CNRS - University Pierre and Marie Curie Paris VI
Corneliu Arsene	SC IPA SA
Miguel Atencia	
Jorge Azorín-López	University of Alicante
Davide Bacciu	University of Pisa
Javier Bajo	Universidad Politécnica de Madrid
Juan Pedro Bandera Rubio	ISIS Group, University of Malaga
Cristian Barrué	Technical University of Catalunya
Andrzej Bartoszewicz	Technical University of Lodz
Bruno Baruque	University of Burgos
David Becerra Alonso	University of the West of Scotland
Lluís Belanche	UPC
Sergio Bermejo	UPC
Julio Brito	
Joan Cabestany	Universitat Politcnica de Catalunya
Inma P. Cabrera	University of Malaga
Tomas Calvo	Universidad de Alcalá
Jose Luis Calvo Rolle	Universidad de A Coruña
Francesco Camastra	University of Naples Parthenope
Carlos Carrascosa	GTI-IA DSIC Universidad Politecnica de Valencia
Luis Castedo	Universidad de A Coruña
Pedro Castillo	UGR



Andreu Catalá	
Ana Cavalli	GET/INT
Miguel Cazorla	University of Alicante
Iwann Chair	University of Granada, Spain
Jesus Cid-Sueiro	Universidad Carlos III de Madrid
Maximo Cobos	Universidad de Valencia
Valentina Colla	Scuola Superiore S. Anna
Pablo Cordero	Universidad de Málaga
Oscar Cordon	University of Granada
Francesco Corona	TKK
Ulises Cortes	UPC
Carlos Cotta	University of Malaga
Marie Cottrell	SAMM Université Paris 1 Panthéon-Sorbonne
Raúl Cruz-Barbosa	Universidad Tecnológica de la Mixteca
Manuel Cruz-Ramírez	University of Córdoba
Erzsébet Csuha-j-Varjú	Eötvös Loránd University
Daniela Danciu	University of Craiova
Suash Deb	C.V. Raman College of Engineering
Angel Pascual Del Pobil	Universitat Jaume I
Enrique Dominguez	University of Malaga
Julian Dorado	Universidade da Coruña
Abrahan Duarte	
Richard Duro	Universidade da Coruna
Gregorio Díaz	University of Castilla - La Mancha
Emil Eirola	Aalto University
Patrik Eklund	Umea University
Javier Fernandez De Canete	University of Malaga
Francisco Fernandez De Vega	Universidad de Extremadura
Alberto Fernandez Gil	University Rey Juan Carlos
Enrique Fernandez-Blanco	University of A Coruña
Manuel Fernández Carmona	Universidad de Málaga
Antonio J. Fernández Leiva	Universidad de Málaga
Francisco Fernández Navarro	University of Córdoba
Carlos Fernández-Lozano	Universidade da Coruña
Jose Manuel Ferrandez	Universidad Politecnica de Cartagena
Ricardo Ferreira	Nove de Julho University
Aníbal R. Figueiras-Vidal	Universidad Carlos III de Madrid
Oscar Fontenla-Romero	University of A Coruña
Colin Fyfe	University of the West of Scotland
Rodolfo Garcia Bermudez	
Carlos Garcia Puntonet	Granada University
Juan M Garcia-Gomez	UPV
Francisco Garcia-Lagos	Universidad de Malaga
Jose Garcia-Rodriguez	University of Alicante
Patricio García Báez	Universidad de La Laguna

Pablo García Sánchez	University of Granada
Maribel García-Arenas	Universidad de Granada
Patrick Garda	Université Pierre et Marie Curie - Paris 6
Peter Gloesekoetter	Muenster University of Applied Sciences
Juan Gomez Romero	Universidad Carlos III de Madrid
Juan Gorriz	University of Granada
Karl Goser	Technical University Dortmund
Bernard Gosselin	University of Mons
Manuel Grana	University of Basque Country
Bertha Guijarro-Berdiñas	University of A Coruña
Nicolás Guil Mata	University of Málaga
Alberto Guillen	University of Granada
Barbara Hammer	Barbara Hammer
Yadira Hernandez	
Francisco Herrera	University of Granada
Álvaro Herrero	University of Burgos
Cesar Hervas	
Tom Heskes	Radboud University Nijmegen
Wei-Chiang Hong	Oriental Institute of Technology
Pedro Isasi	University Carlos III of Madrid
Jose M. Jerez	Universidad de Málaga
M. Dolores Jimenez-Lopez	Rovira i Virgili University
Juan Luis Jiménez Laredo	University of Granada
Gonzalo Joya	
Vicente Julian	GTI-IA DSIC UPV
Christian Jutten	University of Grenoble
Paul Keether	
Fernando L. Pelayo	University of Castilla - La Mancha
Alberto Labarga	University of Granada
Raul Lara Cabrera	
Nuno Lau	Universidade de Aveiro
Amaury Lendasse	Aalto University
Miguel Lopez	University of Granada
Otoniel Lopez Granado	Miguel Hernandez University
Rafael Marcos Luque Baena	University of Málaga, Spain
Ezequiel López-Rubio	University of Málaga
Kurosh Madani	LISSI / Université PARIS-EST Creteil (UPEC)
Mario Martin	Universitat Politecnica de Catalunya
Bonifacio Martin Del Brio	University of Zaragoza
Jose D. Martin-Guerrero	University of Valencia
Luis Martí	Universidad Carlos III de Madrid
Francisco Martínez Estudillo	ETEA
José Luis Martínez Martínez	Universty of Castilla-La Mancha
José Fco. Martínez-Trinidad	INAOE

Francesco Masulli	University of Genova
Montserrat Mateos	Universidad Pontificia de Salamanca
Jesús Medina-Moreno	University of Cadiz
Maria Belen Melian Batista	
Mercedes Merayo	Universidad Complutense de Madrid
Jj Merelo	Universidad de Granada
Gustavo Meschino	Universidad Nacional de Mar del Plata
Jose M. Molina	Universidad Carlos III de Madrid
Jose Muñoz	University of Malaga
Augusto Montisci	University of Cagliari
Antonio Mora	University of Granada
Angel Mora Bonilla	University of Malaga
Claudio Moraga	European Centre for Soft Computing
Gines Moreno	University of Castilla-La Mancha
Jose Andres Moreno	
Juan Moreno Garcia	Universidad de Castilla-La Mancha
J. Marcos Moreno Vega	
Susana Muñoz Hernández	Technical University of Madrid
Nadia Nedjah	State University of Rio de Janeiro
Manuel Nuñez	UCM
Erkk Oja	Aalto University
Manuel Ojeda-Aciego	University of Malaga
Sorin Olaru	Suplec
Iván Olier	The University of Manchester
Madalina Olteanu	SAMM, Université Paris 1
Julio Ortega	Universidad de Granada
Alfonso Ortega de La Puente	
Emilio Ortiz-García	Universidad de Alcala
Oswaldo Pacheco	Universidade de Aveiro
Esteban José Palomo	University of Málaga, Spain
Diego Pardo	Barcelona Tech
Miguel Angel Patricio	Universidad Carlos III de Madrid
Alejandro Pazos Sierra	
Francisco J. Pelayo	University of Granada
Jose Manuel Perez Lorenzo	Universidad de Jaen
Vincenzo Piuri	University of Milan
Hector Pomares	University of Granada
Alberto Prieto	Universidad de Granada
Alexandra Psarrou	University of Westminster
Francisco A. Pujol	University of Alicante
Pablo Rabanal	Universidad Complutense de Madrid
Juan Rabuñal	University of A Coruña
Vladimir Rasvan	
Leonardo Reyneri	Politecnico di Torino

Ismael Rodriguez	Universidad Complutense de Madrid
Juan A. Rodriguez	Universidad de Malaga
Sara Rodríguez	University of Salamanca
Ignacio Rojas	University of Granada
Samuel Romero-Garcia	University of Granada
Ricardo Ron-Angevin	University of Málaga
Eduardo Ros	
Fabrice Rossi	SAMM - Université Paris 1
Fernando Rubio	Universidad Complutense de Madrid
Ulrich Rueckert	University of Paderborn
Addisson Salazar	Universidad Politecnica Valencia
Sancho Salcedo-Sanz	Universidad de Alcalá
Albert Samà	Universitat Politècnica de Catalunya
Francisco Sandoval	Universidad de Málaga
Jose Santos	University of A Coruña
Jose A. Seoane	University of Bristol
Eduardo Serrano	UAM
Olli Simula	Helsinki University of Technology
Evgeny Skvortsov	
Jordi Solé-Casals	Universitat de Vic
Shiliang Sun	
Carmen Paz Suárez Araujo	
Peter Szolgay	Pazmany Peter Catholic University
Javier Sánchez-Monedero	
Ricardo Tellez	Pal Robotics
Ana Maria Tome	Universidade Aveiro
Carme Torras	IRI (CSIC-UPC)
Claude Touzet	University of Provence
Olga Valenzuela	University of Granada
Miguel Ángel Veganzones	Universidad del País Vasco (UPV/EHU)
Francisco Velasco-Alvarez	Universidad de Málaga
Sergio Velastin	Kingston University
Marley Vellasco	PUC-Rio
Alfredo Vellido	Universitat Politecnica de Catalunya
Francisco J Veredas	Universidad de Málaga
Michel Verleysen	Universite catholique de Louvain
Thomas Villman	University of Applied Sciences Mittweida
Changjiu Zhou	Singapore Polytechnic
Ahmed Zobia	University of Exeter
Pedro Zufiria	Universidad Politécnica de Madrid

## Additional Reviewers

Acosta, Leopoldo  
Affenzeller, Michael  
Alonso, Concepcion  
Angulo, Cecilio  
Azorín-López, Jorge  
Calabuig, Daniel  
Cazorla, Miguel  
Chaczko, Zenon  
Comas, Diego Sebastián  
Contreras, Roxana  
Danciu, Daniela  
Estévez, José Ignacio  
Gabadinho, Alexis  
Garcia-Rodriguez, Jose  
Luque Baena, Rafael Marcos

López-Rubio, Ezequiel  
Marichal, Graciliano Nicolas  
Moreno, Jose Andres  
Orts Escolano, Sergio  
Palomo, Esteban José  
Perez-Suay, Adrian  
Prochazka, Ales  
Ruiz de Angulo, Vicente  
Selisteanu, Dan  
Stoica, Cristina  
Takac, Boris  
Toledo, Pedro A.  
Veredas, Francisco J.  
Zhou, Yang

# Table of Contents – Part II

## Metaheuristics

Model Probability in Self-organising Maps . . . . .	1
<i>Anastassia Angelopoulou, Alexandra Psarrou, José Garcia-Rodríguez, Markos Mentzelopoulos, and Gaurav Gupta</i>	
Topological Effects on the Performance of Island Model of Parallel Genetic Algorithm . . . . .	11
<i>Guan Wang and Kwok Yip Szeto</i>	
Artificial Bee Clustering Search . . . . .	20
<i>Tarcísio Souza Costa and Alexandre César Muniz de Oliveira</i>	
A Metaheuristic Approach for the Seaside Operations in Maritime Container Terminals . . . . .	28
<i>Eduardo Lalla Ruiz, Christopher Expósito Izquierdo, Belén Melián Batista, and José Marcos Moreno-Vega</i>	
Restricted Dynamic Heterogeneous Fleet Vehicle Routing Problem with Time Windows . . . . .	36
<i>Jesica de Armas, Belén Melián-Batista, and José A. Moreno-Pérez</i>	
Effect of the Initial Solutions to Balance Routes in Vehicle Routing Problem with Time Windows . . . . .	46
<i>Alondra De Santiago, Belén Melián-Batista, Ada Álvarez, and Francisco AngelBello</i>	
An Ant System Algorithm for the Neutralization Problem . . . . .	53
<i>Ramazan Algin, Ali Fuat Alkaya, Vural Aksakalli, and Dindar Öz</i>	
Solving Credit Card Fraud Detection Problem by the New Metaheuristics Migrating Birds Optimization . . . . .	62
<i>Ekrem Duman and Ilker Elikucuk</i>	

## Bioinformatics/Biomedicine in Computational Intelligence

Parametric and Non-parametric Feature Selection for Kidney Transplants . . . . .	72
<i>Raimundo Garcia-del-Moral, Alberto Guillén, Luis Javier Herrera, Antonio Cañas, and Ignacio Rojas</i>	

Acute Lymphoblastic Leukemia Identification Using Blood Smear Images and a Neural Classifier . . . . .	80
<i>Adnan Khashman and Hayder Hassan Abbas</i>	
Modeling of Survival Curves in Food Microbiology Using Fuzzy Wavelet Neural Networks . . . . .	88
<i>Vassilis S. Kodogiannis and Ilias Petrounias</i>	
Modeling Tissue Temperature Dynamics during Laser Exposure . . . . .	96
<i>Loris Fichera, Diego Pardo, and Leonardo S. Mattos</i>	
An Ensemble of Classifiers Guided by the AAL Brain Atlas for Alzheimer’s Disease Detection . . . . .	107
<i>Alexandre Savio and Manuel Graña</i>	
Saccadic Points Classification Using Multilayer Perceptron and Random Forest Classifiers in EOG Recordings of Patients with Ataxia SCA2 . . . . .	115
<i>Roberto Antonio Becerra García, Gonzalo Joya Caparrós, Rodolfo Valentín García Bermúdez, Luis Velázquez Pérez, Roberto Rodríguez Labrada, and Carmen Pino Ávila</i>	
Phonocardiography Signal Segmentation for Telemedicine Environments . . . . .	124
<i>Santiago Murillo Rendón, Cristian Castro Hoyos, Carlos M. Travieso-González, and Germán Castellanos-Domínguez</i>	
Selection of Wavelet Decomposition Level for Electro-Oculographic Saccadic De-noising . . . . .	135
<i>Rodolfo Valentín García-Bermúdez, Fernando Rojas, Roberto Antonio Becerra García, Luis Velázquez Pérez, and Roberto Rodríguez</i>	
Identification of Postural Transitions Using a Waist-Located Inertial Sensor . . . . .	142
<i>Daniel Rodríguez Martín, Albert Samà, Carlos Pérez López, Andreu Català, Joan Cabestany, and Alejandro Rodríguez Molinero</i>	
Evaluating Multiple Sequence Alignments Using a LS-SVM Approach with a Heterogeneous Set of Biological Features . . . . .	150
<i>Francisco Ortuño, Olga Valenzuela, Héctor Pomares, and Ignacio Rojas</i>	
Animal Vibrissae: Modeling and Adaptive Control of Bio-inspired Sensors . . . . .	159
<i>Carsten Behn, Tonia Schmitz, Hartmut Witte, and Klaus Zimmermann</i>	

Brain Signal Based Continuous Authentication: Functional NIRS Approach . . . . .	171
<i>Michitaro Shozawa, Ryota Yokote, Seira Hidano, Chi-Hua Wu, and Yasuo Matsuyama</i>	
Risk Prediction of Femoral Neck Osteoporosis Using Machine Learning and Conventional Methods . . . . .	181
<i>Tae Keun Yoo, Sung Kean Kim, Ein Oh, and Deok Won Kim</i>	
Out of Core Computation of HSPs for Large Biological Sequences . . . . .	189
<i>Andrés Rodríguez Moreno, Óscar Torreño Tirado, and Oswaldo Trelles Salazar</i>	
Bio-Cirrus: A Framework for Running Legacy Bioinformatics Applications with Cloud Computing Resources . . . . .	200
<i>Tor Johan Mikael Karlsson, Óscar Torreño Tirado, Daniel Ramet, Juan Lago, Juan Falgueras Cano, Noura Chelbat, and Oswaldo Trelles</i>	
Activity Recognition Based on a Multi-sensor Meta-classifier . . . . .	208
<i>Oresti Baños, Miguel Damas, Héctor Pomares, and Ignacio Rojas</i>	
Indoor Activity Recognition by Combining One-vs.-All Neural Network Classifiers Exploiting Wearable and Depth Sensors . . . . .	216
<i>Benoît Delachaux, Julien Rebetz, Andres Perez-Uribe, and Héctor Fabio Satizábal Mejía</i>	
<b>Fuzzy Logic and Soft Computing Applications</b>	
On Galois Connections and Soft Computing . . . . .	224
<i>F. García-Pardo, I.P. Cabrera, Pablo Cordero, and Manuel Ojeda-Aciego</i>	
A Proximity-Based Method for Discovery of Generalized Knowledge and Its Incorporation to the Bousi~Prolog System . . . . .	236
<i>Pascual Julián-Iranzo and Clemente Rubio-Manzano</i>	
Fuzzy Property-Oriented Concept Lattices in Morphological Image and Signal Processing . . . . .	246
<i>Cristina Alcalde, Ana Burusco, Juan Carlos Díaz, Ramón Fuentes-González, and Jesús Medina-Moreno</i>	
Automated Inference with Fuzzy Functional Dependencies over Graded Data . . . . .	254
<i>José Manuel Rodríguez-Jiménez, Pablo Cordero, Manuel Enciso, and Angel Mora</i>	



On the Classification of Fuzzy-Attributes in Multi-adjoint Concept Lattices . . . . .	266
<i>Maria Eugenia Cornejo, Jesús Medina-Moreno, and Eloisa Ramírez</i>	
Can Machine Learning Techniques Help to Improve the Common Fisheries Policy? . . . . .	278
<i>María Pérez-Ortiz, Rosa Colmenarejo, Juan Carlos Fernández Caballero, and César Hervás-Martínez</i>	
Integration of Fuzzy Systems and Genetic Algorithm in Permeability Prediction . . . . .	287
<i>Ahmad Ja'fari and Rasoul Hamidzadeh Moghadam</i>	
Annotating “Fuzzy Chance Degrees” When Debugging XPath Queries . . . . .	300
<i>Jesús M. Almendros-Jiménez, Alejandro Luna Tedesqui, and Ginés Moreno</i>	

**Artificial Intelligence and Games**

Designing and Evolving an Unreal Tournament™ 2004 Expert Bot . . . . .	312
<i>Antonio M. Mora, Francisco Aisa, Ricardo Caballero, Pablo García-Sánchez, Juan Julián Merelo, Pedro A. Castillo, and Raúl Lara-Cabrera</i>	
Evolving the Strategies of Agents for the ANTS Game . . . . .	324
<i>José Carpio, Pablo García-Sánchez, Antonio M. Mora, Juan Julián Merelo, Jesús Caraballo, Fermín Vaz, and Carlos Cotta</i>	
Interactive Techniques for Entertainment Applications Using Mobile Devices . . . . .	334
<i>José Luis Gutiérrez Rivas, Pedro Cano Olivares, and Javier Díaz Alonso</i>	
Car Setup Optimization via Evolutionary Algorithms . . . . .	346
<i>Carlos Cotta, Antonio J. Fernández-Leiva, Alberto Fuentes Sánchez, and Raúl Lara-Cabrera</i>	

**Biological and Bio-inspired Dynamical Systems for Computational Intelligence**

Numerical Implementation of Gradient Algorithms . . . . .	355
<i>Miguel Atencia, Yadira Hernández, Gonzalo Joya, and Francisco Sandoval</i>	

A CNN Based Approach for Solving a Hyperbolic PDE Arising from a System of Conservation Laws - the Case of the Overhead Crane .....	365
<i>Daniela Danciu</i>	
Reflections on Neural Networks as Repetitive Structures with Several Equilibria and Stable Behavior .....	375
<i>Vladimir Răsvan</i>	
A Retina-Inspired Neurocomputing Circuit for Image Representation ...	386
<i>Hui Wei, Qing-song Zuo, and Bo Lang</i>	
Evolutionary Approach in Inventory Routing Problem .....	395
<i>Dragan Simić and Svetlana Simić</i>	

## Brain-Computer Interfaces and Neurotechnologies

BCI-Based Navigation in Virtual and Real Environments .....	404
<i>Francisco Velasco-Alvarez, Ricardo Ron-Angevin, and Miguel Angel Lopez-Gordo</i>	
A Motor Imagery Based Brain-Computer Interface Speller .....	413
<i>Bin Xia, Jing Yang, Conghui Cheng, and Hong Xie</i>	
A New Method for BCI Spelling Using a 7 Segments Display .....	422
<i>N. Galea-Sevilla, Miriam España, Alberto Guillén, and Ignacio Rojas</i>	
Motor Imagery EEG-Based Person Verification .....	430
<i>Phuoc Nguyen, Dat Tran, Xu Huang, and Wanli Ma</i>	

## Video and Image Processing

Computer-Aided Diagnosis in Wound Images with Neural Networks ....	439
<i>María Navas, Rafael M. Luque-Baena, Laura Morente, David Coronado, Rafael Rodríguez, and Francisco J. Veredas</i>	
Hierarchical Self-Organizing Networks for Multispectral Data Visualization .....	449
<i>Esteban José Palomo, Ezequiel López-Rubio, Enrique Domínguez, and Rafael Marcos Luque-Baena</i>	
A Self-organizing Map for Traffic Flow Monitoring .....	458
<i>Rafael Marcos Luque-Baena, Ezequiel López-Rubio, Enrique Domínguez, Esteban José Palomo, and José Manuel Jerez</i>	

Image Noise Detection in Global Illumination Methods Based on Fast Relevance Vector Machine . . . . .	467
<i>Joseph Constantin, André Bigand, Ibtissam Constantin, and Denis Hamad</i>	
Improving 3D Keypoint Detection from Noisy Data Using Growing Neural Gas . . . . .	480
<i>José García-Rodríguez, Miguel Cazorla, Sergio Orts-Escolano, and Vicente Morell</i>	
Football Video Annotation Based on Player Motion Recognition Using Enhanced Entropy . . . . .	488
<i>Markos Mentzelopoulos, Alexandra Psarrou, Anastassia Angelopoulou, and José García-Rodríguez</i>	
Model-Based Multi-view Registration for RGB-D Sensors . . . . .	496
<i>Marcelo Saval-Calvo, Jorge Azorín-López, and Andrés Fuster-Guilló</i>	
3D Hand Pose Estimation with Neural Networks . . . . .	504
<i>Jose Antonio Serra, José García-Rodríguez, Sergio Orts-Escolano, Juan Manuel García-Chamizo, Anastassia Angelopoulou, Alexandra Psarrou, Markos Mentzelopoulos, Javier Montoyo-Bojo, and Enrique Domínguez</i>	
<b>Author Index . . . . .</b>	<b>513</b>

# Table of Contents – Part I

## Invited Talks to IWANN 2013

It's as Easy as ABC: Introducing Anthropology-Based Computing . . . . .	1
<i>John N.A. Brown</i>	
Extreme Learning Machine: A Robust Modeling Technique? Yes! . . . . .	17
<i>Amaury Lendasse, Anton Akusok, Olli Simula, Francesco Corona, Mark van Heeswijk, Emil Eirola, and Yoan Miche</i>	
A Novel Framework to Design Fuzzy Rule-Based Ensembles Using Diversity Induction and Evolutionary Algorithms-Based Classifier Selection and Fusion . . . . .	36
<i>Oscar Cordón and Krzysztof Trawiński</i>	

## Applications of Computational Intelligence

Using Nonlinear Dimensionality Reduction to Visualize Classifiers . . . . .	59
<i>Alexander Schulz, Andrej Gisbrecht, and Barbara Hammer</i>	
Which Dissimilarity Is to Be Used When Extracting Typologies in Sequence Analysis? A Comparative Study . . . . .	69
<i>Sébastien Massoni, Madalina Olteanu, and Nathalie Villa-Vialaneix</i>	
Implementation of the C-Mantec Neural Network Constructive Algorithm in an Arduino Uno Microcontroller . . . . .	80
<i>Francisco Ortega-Zamorano, José Luis Subirats, José Manuel Jerez, Ignacio Molina, and Leonardo Franco</i>	
A Constructive Neural Network to Predict Pitting Corrosion Status of Stainless Steel . . . . .	88
<i>Daniel Urda, Rafael Marcos Luque, Maria Jesus Jiménez, Ignacio Turias, Leonardo Franco, and José Manuel Jerez</i>	
Robust Sensor and Actuator Fault Diagnosis with GMDH Neural Networks . . . . .	96
<i>Marcin Witczak, Marcin Mrugalski, and Józef Korbicz</i>	
Diffusion Methods for Wind Power Ramp Detection . . . . .	106
<i>Ángela Fernández, Carlos M. Alaíz, Ana M. González, Julia Díaz, and José R. Dorronsoro</i>	

Computational Study Based on Supervised Neural Architectures for Fluorescence Detection of Fungicides . . . . .	114
<i>Yeray Álvarez Romero, Patricio García Báez, and Carmen Paz Suárez Araujo</i>	
Study of Alternative Strategies to Selection of Peer in P2P Wireless Mesh Networks . . . . .	124
<i>Lisette Valdés, Alfonso Ariza, Sira M. Allende, Rubén Parada, and Gonzalo Joya</i>	
A Cloud-Based Neural Network Simulation Environment . . . . .	133
<i>Erich Schikuta and Erwin Mann</i>	
Performance Evaluation over Indoor Channels of an Unsupervised Decision-Aided Method for OSTBC Systems . . . . .	144
<i>Paula M. Castro, Ismael Rozas-Ramallal, José A. García-Naya, and Adriana Dapena</i>	
A Decision-Making Model for Environmental Behavior in Agent-Based Modeling . . . . .	152
<i>Noelia Sánchez-Marroño, Amparo Alonso-Betanzos, Óscar Fontenla-Romero, Miguel Rodríguez-García, Gary Polhill, and Tony Craig</i>	
Version of the New SHA Standard Applied to Manage Certificate Revocation in VANETs . . . . .	161
<i>Francisco Martín-Fernández and Pino Caballero-Gil</i>	
System Identification of High Impact Resistant Structures . . . . .	169
<i>Yeesock Kim, K. Sarp Arsava, and Tahar El-Korchi</i>	
Spikes Monitors for FPGAs, an Experimental Comparative Study . . . . .	179
<i>Elena Cerezueta-Escudero, Manuel Jesus Domínguez-Morales, Ángel Jiménez-Fernández, Rafael Paz-Vicente, Alejandro Linares-Barranco, and Gabriel Jiménez-Moreno</i>	
On Second Language Tutoring through Womb Grammars . . . . .	189
<i>Leonor Becerra Bonache, Veronica Dahl, and J. Emilio Miralles</i>	

## Hybrid Intelligent Systems

Simulated Annealing for Real-Time Vertical-Handoff in Wireless Networks . . . . .	198
<i>María D. Jaráiz-Simon, Juan A. Gómez-Pulido, Miguel A. Vega-Rodríguez, and Juan M. Sánchez-Pérez</i>	
A Fuzzy Tabu Search Approach to Solve a Vehicle Routing Problem . . . . .	210
<i>Kaj-Mikael Björk and József Mezei</i>	

Improved Particle Swarm Optimization Method in Inverse Design Problems . . . . .	218
<i>Y. Volkan Pehlivanoglu</i>	
Solving the Unknown Complexity Formula Problem with Genetic Programming . . . . .	232
<i>Rayco Batista, Eduardo Segredo, Carlos Segura, Coromoto León, and Casiano Rodríguez</i>	
Three Alternatives for Parallel GPU-Based Implementations of High Performance Particle Swarm Optimization . . . . .	241
<i>Rogério M. Calazan, Nadia Nedjah, and Luiza de Macedo Mourelle</i>	
A Particle-Swarm-Optimized Fuzzy Classifier Used for Investment Decision Support . . . . .	253
<i>Lars Krueger and Matthias Walter</i>	
Ant Colony Optimization Inspired Algorithm for 3D Object Segmentation . . . . .	262
<i>Rafael Arnay and Leopoldo Acosta</i>	

## Kernel Methods and SVM

Kernelizing the Proportional Odds Model through the Empirical Kernel Mapping . . . . .	270
<i>María Pérez-Ortiz, Pedro Antonio Gutiérrez, Manuel Cruz-Ramírez, Javier Sánchez-Monedero, and César Hervás-Martínez</i>	
Parallel Support Vector Data Description . . . . .	280
<i>Phuoc Nguyen, Dat Tran, Xu Huang, and Wanli Ma</i>	
Antinoise Texture Retrieval Based on PCNN and One-Class SVM . . . . .	291
<i>Le Tian, Yi-De Ma, Li Liu, and Kun Zhan</i>	

## Learning and Adaptation

A FPGA Spike-Based Robot Controlled with Neuro-inspired VITE . . . . .	299
<i>Fernando Perez-Peña, Arturo Morgado-Estevez, Alejandro Linares-Barranco, Angel Jiménez-Fernández, Juan Lopez-Coronado, and Jose Luis Muñoz-Lozano</i>	
A Cognitive Approach for Robots' Autonomous Learning . . . . .	309
<i>Dominik M. Ramík, Kurosh Madani, and Christophe Sabourin</i>	
Self-Organizing Incremental Neural Network (SOINN) as a Mechanism for Motor Babbling and Sensory-Motor Learning in Developmental Robotics . . . . .	321
<i>Tarek Najjar and Osamu Hasegawa</i>	

Alternative OVA Proposals for Cooperative Competitive RBFN Design in Classification Tasks . . . . .	331
<i>Francisco Charte Ojeda, Antonio Jesús Rivera Rivas, María Dolores Pérez-Godoy, and María Jose del Jesus</i>	
Committee C-Mantec: A Probabilistic Constructive Neural Network . . . .	339
<i>José Luis Subirats, Rafael Marcos Luque-Baena, Daniel Urda, Francisco Ortega-Zamorano, José Manuel Jerez, and Leonardo Franco</i>	

## Mathematical and Theoretical Methods in Computational Intelligence

Secure Semi-supervised Vector Quantization for Dissimilarity Data . . . .	347
<i>Xibin Zhu, Frank-Michael Schleif, and Barbara Hammer</i>	
Border-Sensitive Learning in Kernelized Learning Vector Quantization . . . . .	357
<i>Marika Kästner, Martin Riedel, Marc Strickert, Wieland Hermann, and Thomas Villmann</i>	
Smoothed Emphasis for Boosting Ensembles . . . . .	367
<i>Anas Ahachad, Adil Omari, and Aníbal R. Figueiras-Vidal</i>	
F-Measure as the Error Function to Train Neural Networks . . . . .	376
<i>Joan Pastor-Pellicer, Francisco Zamora-Martínez, Salvador España-Boquera, and María José Castro-Bleda</i>	
Isomorphisms of Fuzzy Sets and Cut Systems . . . . .	385
<i>Jiří Močkoř</i>	
Hierarchical Modified Regularized Least Squares Fuzzy Support Vector Regression through Multiscale Approach . . . . .	393
<i>Arindam Chaudhuri</i>	
Minimal Learning Machine: A New Distance-Based Method for Supervised Learning . . . . .	408
<i>Amauri Holanda de Souza Junior, Francesco Corona, Yoan Miche, Amaury Lendasse, Guilherme A. Barreto, and Olli Simula</i>	
Extending Extreme Learning Machine with Combination Layer . . . . .	417
<i>Dušan Sovilj, Amaury Lendasse, and Olli Simula</i>	

## Data Mining with Evolutionary Computation and ANN

Texture Classification Using Kernel-Based Techniques . . . . .	427
<i>Carlos Fernandez-Lozano, Jose A. Seoane, Marcos Gestal, Tom R. Gaunt, and Colin Campbell</i>	

A Genetic Algorithms-Based Approach for Optimizing Similarity Aggregation in Ontology Matching . . . . .	435
<i>Marcos Martínez-Romero, José Manuel Vázquez-Naya, Francisco Javier Nóvoa, Guillermo Vázquez, and Javier Pereira</i>	
Automatic Fish Segmentation on Vertical Slot Fishways Using SOM Neural Networks . . . . .	445
<i>Álvaro Rodríguez, Juan R. Rabuñal, María Bermúdez, and Alejandro Pazos</i>	
Clustering of Gene Expression Profiles Applied to Marine Research . . . . .	453
<i>Vanessa Aguiar-Pulido, Victoria Suárez-Ulloa, Daniel Rivero, José M. Eirín-López, and Julián Dorado</i>	
Genetic Programming to Improvement FIB Model: Bond and Anchorage of Reinforcing Steel in Structural Concrete . . . . .	463
<i>Juan Luis Pérez, Ismael Vieito, Juan Rabuñal, and Fernando Martínez-Abella</i>	
Rainfall Forecasting Based on Ensemble Empirical Mode Decomposition and Neural Networks . . . . .	471
<i>Juan Beltrán-Castro, Juliana Valencia-Aguirre, Mauricio Orozco-Alzate, Germán Castellanos-Domínguez, and Carlos M. Travieso-González</i>	
<b>Self Organizing Network</b>	
Self-regulating Neurons in the Sensorimotor Loop . . . . .	481
<i>Frank Pasemann</i>	
Comparison of Two Memristor Based Neural Network Learning Schemes for Crossbar Architecture . . . . .	492
<i>Janusz A. Starzyk and Basawaraj</i>	
Geometrical Complexity of Data Approximators . . . . .	500
<i>Evgeny M. Mirkes, Andrei Zinovyev, and Alexander N. Gorban</i>	
Self-Organization Process in Large Spiking Neural Networks Leading to Formation of Working Memory Mechanism . . . . .	510
<i>Mikhail Kiselev</i>	
Self-organized Learning by Self-Enforcing Networks . . . . .	518
<i>Christina Klüver and Jürgen Klüver</i>	
Network Anomaly Detection with Bayesian Self-Organizing Maps . . . . .	530
<i>Emiro de la Hoz Franco, Andrés Ortiz García, Julio Ortega Lopera, Eduardo de la Hoz Correa, and Alberto Prieto Espinosa</i>	



## Advances in Computational Intelligence

A Novel Neural Network Parallel Adder . . . . .	538
<i>Fangyue Chen, Guangyi Wang, Guanrong Chen, and Qinbin He</i>	
Improved Swap Heuristic for the Multiple Knapsack Problem . . . . .	547
<i>Yacine Laalaoui</i>	
Maximum Margin Clustering for State Decomposition of Metastable Systems . . . . .	556
<i>Hao Wu</i>	
Hybrid Approach for 2D Strip Packing Problem Using Genetic Algorithm . . . . .	566
<i>Jaya Thomas and Narendra S. Chaudhari</i>	
Sea Clutter Neural Network Classifier: Feature Selection and MLP Design . . . . .	575
<i>Jose Luis Bárcena-Humanes, David Mata-Moya, María Pilar Jarabo-Amores, Nerea del-Rey-Maestre, and Jaime Martín-de-Nicolás</i>	
SONN and MLP Based Solutions for Detecting Fluctuating Targets with Unknown Doppler Shift in Gaussian Interference . . . . .	584
<i>David Mata-Moya, María Pilar Jarabo-Amores, Nerea del-Rey-Maestre, Jose Luis Bárcena-Humanes, and Jaime Martín-de-Nicolás</i>	
An Ensemble of Computational Intelligence Models for Software Maintenance Effort Prediction . . . . .	592
<i>Hamoud Aljamaan, Mahmoud O. Elish, and Irfan Ahmad</i>	
Sleep Stage Classification Using Advanced Intelligent Methods . . . . .	604
<i>José Manuel Sánchez Pascualvaca, Carlos Fernandes, Alberto Guillén, Antonio M. Mora, Rogerio Largo, Agostinho C. Rosa, and Luis Javier Herrera</i>	
An $n$ -Spheres Based Synthetic Data Generator for Supervised Classification . . . . .	613
<i>Javier Sánchez-Monedero, Pedro Antonio Gutiérrez, María Pérez-Ortiz, and César Hervás-Martínez</i>	
Improving the Classification Performance of Optimal Linear Associative Memory in the Presence of Outliers . . . . .	622
<i>Ana Luíza Bessa de Paula Barros and Guilherme A. Barreto</i>	
SMBSRP: A Search Mechanism Based on Interest Similarity, Query Relevance and Distance Prediction . . . . .	633
<i>Fen Wang, Changsheng Xie, Hong Liang, and Xiaotao Huang</i>	

An Unfolding-Based Preprocess for Reinforcing Thresholds in Fuzzy  
 Tabulation ..... 647  
*Pascual Julián-Iranzo, Jesús Medina-Moreno, P.J. Morcillo,  
 Ginés Moreno, and Manuel Ojeda-Aciego*

**Author Index** ..... 657

# Model Probability in Self-organising Maps

Anastassia Angelopoulou<sup>1</sup>, Alexandra Psarrou<sup>1</sup>, José García-Rodríguez<sup>2</sup>,  
Markos Mentzelopoulos<sup>1</sup>, and Gaurav Gupta<sup>1</sup>

<sup>1</sup> Department of Computer Science and Software Engineering,  
University of Westminster, UK

{agelopa,psarroa,mentzem,G.Gupta3}@wmin.ac.uk

<sup>2</sup> Department of Computing Technology, University of Alicante, Spain  
jgarcia@dtic.ua.es

**Abstract.** Growing models have been widely used for clustering or topology learning. Traditionally these models work on stationary environments, grow incrementally and adapt their nodes to a given distribution based on global parameters. In this paper, we present an enhanced unsupervised self-organising network for the modelling of visual objects. We first develop a framework for building non-rigid shapes using the growth mechanism of the self-organising maps, and then we define an optimal number of nodes without overfitting or underfitting the network based on the knowledge obtained from information-theoretic considerations. We present experimental results for hands and we quantitatively evaluate the matching capabilities of the proposed method with the topographic product.

**Keywords:** Minimum Description Length, Self-organising networks, Shape Modelling.

## 1 Introduction

In any learning framework, it is very crucial the initialisation of the object. The main task is to find a suitable segmentation that separates the object of interest from the background. Segmentation is a pre-processing step in many computer vision applications. These applications include visual surveillance [2,5,9,11], and object tracking [1,7,8,16]. While a lot of research has been focused on efficient detectors and classifiers, little attention has been paid to efficiently labeling and acquiring suitable training data. Existing approaches to minimise the labeling effort [10,12,15,18] use a classifier which is trained in a small number of examples. Then the classifier is applied on a training sequence and the detected patches are added to the previous set of examples. Levin *et al.* [12] start with a small set of hand labeled data and generate additional labeled examples by applying co-training of two classifiers. Nair and Clark [15] use motion detection to obtain the initial training set. Lee *et al.* [12] use a variant of eigentracking to obtain the training sequence for face recognition and tracking. Sivic *et al.* [18] use boosting orientation-based features to obtain training samples for their face detector.

A disadvantage of these approaches is that either a manual initialization [10] or a pre-trained classifier is needed to initialise the learning process. Having a sequence of images this can be avoided by using an incremental model. One of the most important characteristics of the GNG is that it does not require the restarting of the initialisation of the network for every image in a sequence of  $k$  frames.

In this paper, we are interested in the minimisation of the user intervention in the learning process of the network by utilising an automatic criterion for maximum node growth in the GNG network based on different parameters. We achieve that by taking into consideration that human skin has a relatively unique colour and the complexity or simplicity of the proposed model is decided by information-theoretic measures. The remainder of the paper is organised as follows. Section 2 introduces the framework for object modelling using topological relations. Section 3 proposes an approach to minimise the user intervention in the termination of the network using knowledge obtained from information-theoretic considerations. In Section 4 our method is applied to real and artificial shapes before conclusions are drawn in Section 5.

## 2 Characterising 2D Objects Using GNG

GNG [4] is an unsupervised incremental self-organising network independent of the topology of the input distribution or space. It uses a growth mechanism inherited from the Growth Cell Structure [3] together with the Competitive Hebbian Learning (CHL) rule [13] to construct a network of the input data set. In GNG, the growing process starts with two nodes, and new nodes are incrementally inserted until a predefined condition is satisfied, such as the maximum number of nodes or available time. During the learning process local error measures are gathered to determine where to insert new nodes. New nodes are inserted near the node with the highest accumulated error and new connections between the winner node and its topological neighbours are created.

Identifying the points of the image that belong to objects allows the GNG network to obtain an induced Delaunay triangulation of the objects. In other words, to obtain an approximation of the geometric appearance of the object. Let an object  $O = [O_G, O_A]$  be defined by its geometry and its appearance. The geometry provides a mathematical description of the object's shape, size, and parameters such as translation, rotation, and scale. The appearance defines a set of object's characteristics such as colour, texture, and other attributes.

Given a domain  $\mathbf{S} \subseteq \mathbb{R}^2$ , an image intensity function  $\mathbf{I}(x, y) \in \mathbb{R}$  such that  $\mathbf{I} : \mathbf{S} \rightarrow [0, \mathbf{I}_{max}]$ , and an object  $O$ , its standard potential field  $\Psi_T(x, y) = f_T(I(x, y))$  is the transformation  $\Psi_T : \mathbf{S} \rightarrow [0, 1]$  which associates to each point  $(x, y) \in \mathbf{S}$  the degree of compliance with the visual property  $T$  of the object  $O$  by its associated intensity  $\mathbf{I}(x, y)$ .

Considering:

- The input distribution as the set of points in the image:

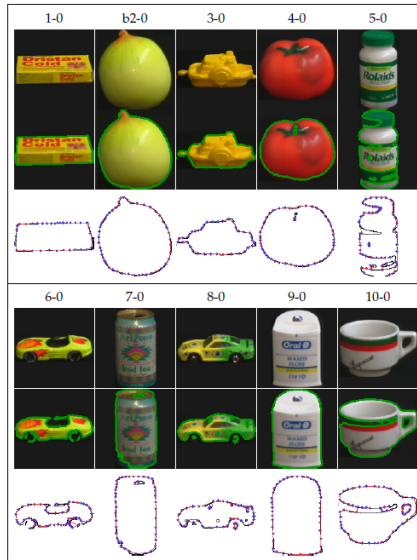
$$\mathbf{A} = \mathbf{S} \tag{1}$$

$$\xi_w = (x, y) \in \mathbf{S} \quad (2)$$

- The probability density function according to the standard potential field obtained for each point of the image:

$$p(\xi_w) = p(x, y) = \Psi_T(x, y) \quad (3)$$

During this learning process, the neural network is obtained which preserves the topology of the object  $O$  from a certain feature  $T$ . Therefore, from the visual appearance  $O_A$  of the object is obtained an approximation to its geometric appearance  $O_G$ . To speed up the learning we used the faster Manhattan distance [6,14] compared to the Euclidean distance in the original algorithm. Figure 1 shows shapes extracted from the Columbia Object Image Library (coil-100) dataset and their corresponding modified GNG networks. The 100 object coil-100 dataset consists of colour images of 72 different poses for each object. The poses correspond to  $5^\circ$  rotation intervals.



**Fig. 1.** First shape of each of the first 10 objects in coil-100, showing the original image, the thresholded region, and the modified GNG contour representation

### 3 Adaptive Learning

The determination of accurate topology preservation, requires the determination of best similarity threshold and best network map without overfitting. Let  $\Omega(x)$  denote the set of pixels in the objects of interest based on the configuration of

$x$  (e.g. colour, texture, etc.) and  $\mathcal{Y}$  the set of all image pixels. The likelihood of the required number of nodes to describe the topology of an image  $y$  is:

$$p(y|x) = \left\{ \prod_{u \in \Omega(x)} p_{skin}(u) \prod_{v \in \mathcal{Y} \setminus \Omega(x)} p_{bkgd}(v) \right. \\ \left. \propto \prod_{u \in \Omega(x)} \frac{p_{skin}(u)}{p_{bkgd}(u) + p_{skin}(u)} \right\} * e_T \quad (4)$$

and  $e_T \leq \prod_{u \in \Omega(x)} p_{skin}(u) + \prod_{v \in \mathcal{Y} \setminus \Omega(x)} p_{bkgd}(v)$ .  $e_T$  is a similarity threshold and defines the accuracy of the map. If  $e_T$  is low the topology preservation is lost and more nodes need to be added. On the contrary, if  $e_T$  is too big then nodes have to be removed so that Voronoï cells become wider. We can describe the optimum number of similarity thresholds, required for the accuracy of the map for different objects, as the unknown clusters  $K$ , and the network parameters as the mixture coefficients  $W_K$ , with  $d$ -dimensional means and covariances  $\Theta_K$ . To do that, we use a heuristic criterion from statistics known as the Minimum Description Length (MDL) [17]. Such criteria take the general form of a prediction error, which consists of the difference of two terms:

$$E = model\_likelihood - complexity\_term \quad (5)$$

a likelihood term that measures the model fit and increases with the number of clusters, and a complexity term, used as penalty, that grows with the number of free parameters in the model. Thus, if the number of cluster is small we get a low value for the criterion because the model fit is low, while if the number of cluster is large we get a low value because the complexity term is large.

The information-criterion MDL of Rissanen [17], is defined as:

$$MDL(K) = -\ln[L(X|W_K, \Theta_K)] + \frac{1}{2}M \ln(N) \quad (6)$$

where

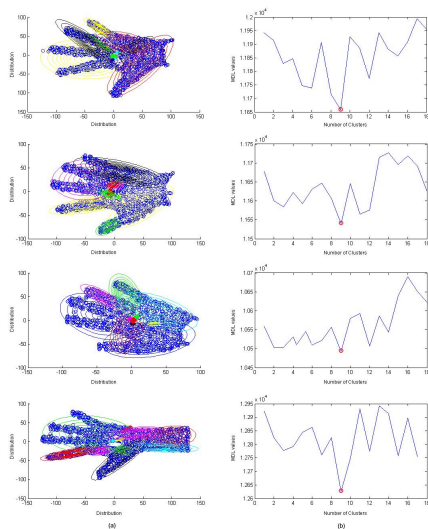
$$L(X|W_K, \Theta_K) = \max \prod_{i=1}^N p(x_i|W_K, \Theta_K) \quad (7)$$

The first term  $-\ln[L(X|W_K, \Theta_K)]$  measures the model probability with respect to the model parameter  $W_K, \Theta_K$  defined for a Gaussian mixture by the mixture coefficients  $W_K$  and  $d$ -dimensional means and covariances  $\Theta_K$ . The second term  $\frac{1}{2}M \ln(N)$  measures the number of free parameters needed to encode the model and serves as a penalty for models that are too complex.  $M$  describes the number of free parameters and is given for a Gaussian mixture by  $M = 2dK + (K - 1)$  for  $(K - 1)$  adjustable mixture weights and  $2d$  parameters for  $d$ -dimensional means and diagonal covariance matrices. The optimal number of similarity thresholds can be determined by applying the following iterative procedure:

- For all  $K$ , ( $K_{min} < K < K_{max}$ )
  - (a) Maximize the likelihood  $L(X|W_K, \Theta_K)$  using the EM algorithm to cluster the nodes based on the similarity thresholds applied to the data set.
  - (b) Calculate the value of MDL(K) according to Equations 6 and 7.

- Select the model parameters ( $W_K, \Theta_K$ ) that corresponds to minimisation of the MDL(K) value.

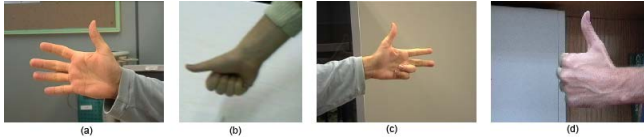
Figure 2 shows the value of MDL(K) for clusters within the range of ( $1 < K < 18$ ). We have doubled the range in the MDL(K) minimum and maximum values so we can represent the extreme cases of 1 cluster which represents the whole data set, and 18 clusters which over classify the distribution and corresponds to the overfitting of the network with similarity threshold  $e_T = 900$ . A global minimum and therefore optimal number of clusters can be determined for  $K = 9$  which indicates that the best similarity threshold that defines the accuracy of the map without overfitting or underfitting the data set is  $e_T = 500$ . To account for susceptibility for the *EM* cluster centres as part of the MDL(K) initialisation of the mixture coefficients the measure is averaged over 10 runs and the minimal value for each configuration is selected.



**Fig. 2.** (a) Plot of hand distributions. (b) Plot of the MDL values versus the number of cluster centres. The Minimum Description Length MDL(K) is calculated for all cluster configurations with ( $1 < K < 18$ ) clusters, and a global minimum is determined at 9 (circled point).

## 4 Experiments

We tested our method on a data set of hand images recorded from 5 participants each performing a set of different gestures (Figure 3). To create this data set we have recorded images over several days and a simple webcam was used with image resolution  $800 \times 600$ . In total, we have recorded over 75000 frames,



**Fig. 3.** (a) to (d) represent some of the most common gestures used in sign language

and for computational efficiency, we have resized the images from each set to  $300 \times 225$ ,  $200 \times 160$ ,  $198 \times 234$ , and  $124 \times 123$  pixels. We obtained the data set from the University of Alicante, Spain and the University of Westminster, UK. Also, we tested our method with 49 images from Mikkel B. Stegmann<sup>1</sup> online data set. In total we have run the experiments on a data set of 174 images. Since the background is unambiguous the network adapts without occlusion reasoning. For our experiments only complete gesture sequences are included. There are no gestures with partial or complete occluded regions, which means that we do not model multiple objects that interact with the background. Table 1 shows topology preservation, execution time, and number of nodes when different variants in the  $\lambda$  and the  $K$  are applied in a hand as the input space. Faster variants get worse topology preservation but the network converges quickly. However, the representation is sufficient and can be used in situations where minimum time is required like online learning for detecting obstacles in robotics where you can obtain a rough representation of the object of interest in a given time and with minimum quality.

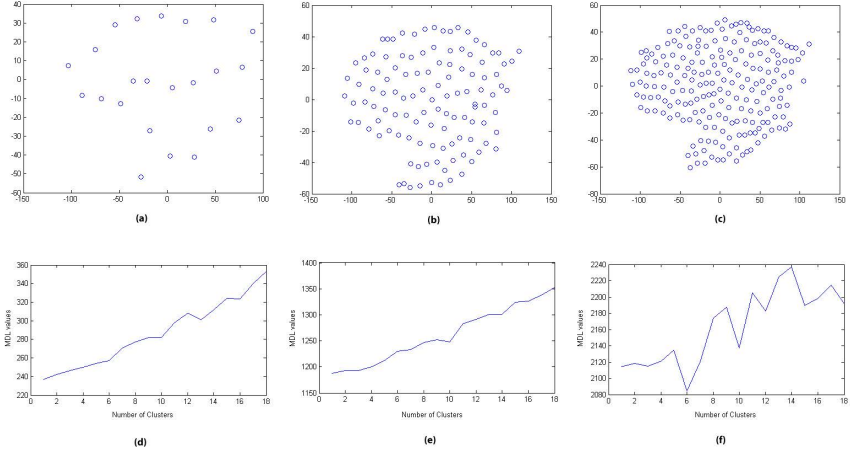
**Table 1.** Topology Preservation and Processing Time Using the Quantisation Error and the Topographic Product for Different Variants

Variant	Number of Nodes	Time (sec)	QE	TP
$\text{GNG}_{\lambda=100, K=1}$	23	0.22	8.932453	0.4349
$\text{GNG}_{\lambda=100, K=9}$	122	0.50	5.393949	-0.3502
$\text{GNG}_{\lambda=100, K=18}$	168	0.84	5.916987	-0.0303
$\text{GNG}_{\lambda=300, K=1}$	23	0.90	8.024549	0.5402
$\text{GNG}_{\lambda=300, K=9}$	122	2.16	5.398938	0.1493
$\text{GNG}_{\lambda=300, K=18}$	168	4.25	4.610572	0.1940
$\text{GNG}_{\lambda=600, K=1}$	23	1.13	0.182912	-0.0022
$\text{GNG}_{\lambda=600, K=9}$	122	2.22	0.172442	0.3031
$\text{GNG}_{\lambda=600, K=18}$	168	8.30	0.169140	-0.0007
$\text{GNG}_{\lambda=1000, K=1}$	23	1.00	0.188439	0.0750
$\text{GNG}_{\lambda=1000, K=9}$	122	12.02	0.155153	0.0319
$\text{GNG}_{\lambda=1000, K=18}$	168	40.98	0.161717	0.0111

<sup>1</sup> <http://www2.imm.dtu.dk/~aam/>



Figure 4 shows the plots of the MDL(K) values versus the number of clusters for minimum, maximum and approximate match similarity threshold ( $e_T = 100$ ,  $e_T = 900$ , and  $e_T = 500$ ). As the similarity threshold increases the optimum number for the MDL(K) values increases as well with an optimum growth at  $K = 9$ . Table 2 shows the topographic product for a number of nodes. We can see that the insertion of more nodes makes no difference to the object's topology. Based on the maximum size of the network an optimum result is achieved when at least half of the network is developed. Table 2 shows that for the different type of gestures this optimum number is in the range  $> 90$  and  $< 130$ .



**Fig. 4.** (a), (b), and (c) Plot of data set for similarity thresholds  $e_T = 100$ ,  $e_T = 900$ , and  $e_T = 500$ . (d), (e), and (f) Plot of the MDL(K) values versus the number of clusters centres generated by the similarity thresholds during the growth process of the GNG.

**Table 2.** The Topographic product for various data sets

Image (a) Nodes	TP	Image (b) Nodes	TP	Image (c) Nodes	TP	Image (d) Nodes	TP
26	-0.0301623	26	-0.021127	24	-0.017626	19	-0.006573
51	-0.030553	51	-0.021127	47	-0.047098	37	-0.007731
77	0.04862	77	0.044698	71	0.046636	56	0.027792
102	0.048256	102	0.021688	95	0.017768	75	0.017573
<b>128</b>	<b>0.031592</b>	<b>128</b>	<b>0.011657</b>	<b>119</b>	<b>0.014589</b>	<b>94</b>	<b>0.018789</b>
153	0.038033	153	0.021783	142	0.018929	112	0.016604
179	0.047636	179	0.017223	166	0.017465	131	0.017755
205	0.038104	205	-0.013525	190	0.017718	150	0.007332
230	0.037321	230	0.017496	214	-0.007543	168	0.007575

Our modified GNG network has been compared to the methodology of the active snake model that adheres only to global shape transformations. The parameters for the snake are summarised in Table 3. The execution time for modified GNG is approximately 4 times less compared to the snake. The computational and convergence results are summarised in Table 4.

In all our experiments, the parameters of the network are as follows:  $\lambda = 100$  to 1000,  $\epsilon_x = 0.1$ ,  $\epsilon_n = 0.005$ ,  $\Delta x_{s_1} = 0.5$ ,  $\Delta x_i = 0.0005$ ,  $\alpha_{max} = 125$ . For the MDL(K) value we have experimented with cluster centres within the range of  $1 < K < 18$ .

**Table 3.** Parameters and Performance for Snake

Hand	Constants	Iterations	Time (sec)
Sequence (a)	$\alpha = 4$ $\beta = 1$ $\gamma = 2$ $\kappa = 0.6$ $D_{min} = 0.5$ $D_{max} = 2$	50	15.29
Sequence (b)	$\alpha = 4$ $\beta = 1$ $\gamma = 2$ $\kappa = 0.6$ $D_{min} = 0.5$ $D_{max} = 2$	40	15.20
Sequence (c)	$\alpha = 4$ $\beta = 1$ $\gamma = 3$ $\kappa = 0.6$ $D_{min} = 0.5$ $D_{max} = 2$	40	12.01
Sequence (d)	$\alpha = 4$ $\beta = 1$ $\gamma = 3$ $\kappa = 0.6$ $D_{min} = 0.5$ $D_{max} = 2$	20	5.60

**Table 4.** Convergence and Execution Time Results of modified GNG and snake

Method	Convergence (Iteration times)	Time (sec)
snake	50	15.29
	40	15.20
	40	12.01
	20	5.60
modified GNG	5	4.88
	3	2.17
	2	1.22
	2	0.73

## 5 Conclusions and Future Work

Based on the capabilities of GNG to readjust to new input patterns without restarting the learning process, we developed an approach to minimise the user

intervention by utilising an automatic criterion for maximum node growth. This automatic criterion for GNG is based on the object's distribution and the similarity threshold ( $e_T$ ) which determines the preservation of the topology. The model is then used to the representation of motion in image sequences by initialising a suitable segmentation. During testing we found that for different shapes there exists an optimum number that maximises topology learning versus adaptation time and MSE. This optimal number uses knowledge obtained from information-theoretic considerations.

## References

1. Angelopoulou, A., García, J., Psarrou, A., Gupta, G.: Tracking gestures using a probabilistic self-organising network. In: Proc. of the International Joint Conference on Neural Networks, IJCNN 2010, pp. 1–7 (2010)
2. Dalal, N., Triggs, B.: Histograms of Oriented Gradients for Human Detection. In: Proc. of the IEEE Conference on Computer Vision and Pattern Recognition, vol. I, pp. 886–893 (2005)
3. Fritzke, B.: Growing Cell Structures - a self-organising network for Unsupervised and supervised Learning. *The Journal of Neural Networks* 7(9), 1441–1460 (1994)
4. Fritzke, B.: A growing Neural Gas Network Learns Topologies. In: *Advances in Neural Information Processing Systems* 7 (NIPS 1994), pp. 625–632 (1995)
5. García-Rodríguez, J., Angelopoulou, A., García-Chamizo, J.M., Psarrou, A., Escolano, S.O., Giménez, V.M.: Autonomous Growing Neural Gas for applications with time constraint: Optimal parameter estimation. *Neural Networks* 32, 196–208 (2012)
6. Gupta, G., Psarrou, A., Angelopoulou, A., García, J.: Region analysis through close contour transformation using growing neural gas. In: Proc. of the International Joint Conference on Neural Networks, IJCNN 2012, pp. 1–8 (2012)
7. Kakumanu, P., Makrogiannis, S., Bourbakis, N.: A survey of skin-color modeling and detection methods. *Pattern Recognition* 40(3), 1106–1122 (2007)
8. Kruppa, H.: Object Detection using Scale-specific Boosted Parts and a Bayesian Combiner. PhD Thesis, ETH Zrich (2004)
9. Kruppa, H., Santana, C., Sciele, B.: Fast and Robust Face Finding via Local Context. In: Proc. of the IEEE International Workshop on Visual Surveillance and Performance Evaluation of Tracking and Surveillance, pp. 157–164 (2003)
10. Lee, M., Nevatia, R.: Integrating Component Cues for Human Pose Estimation. In: Proc. of the IEEE International Workshop on Visual Surveillance and Performance Evaluation of Tracking and Surveillance, pp. 41–48 (2005)
11. Leibe, B., Seemann, E., Sciele, B.: Pedestrian Detection in Crowded Scenes. In: Proc. of the IEEE Conference on Computer Vision and Pattern Recognition, vol. I, pp. 878–885 (2005)
12. Levin, A., Viola, P., Freund, Y.: Unsupervised improvement of visual detectors using co-training. In: Proc. of the IEEE International Conference on Computer Vision, vol. I, pp. 626–633 (2003)
13. Martinez, T., Schulten, K.: Topology Representing Networks. *The Journal of Neural Networks* 7(3), 507–522 (1994)
14. Mignotte, M.: Segmentation by fusion of histogram-based k-means clusters in different color spaces. *IEEE Trans. on Image Processing* 5(17), 780–787 (2008)

15. Nair, V., Clark, J.: An Unsupervised, Online Learning Framework for Moving Object Detection. In: Proc. of the IEEE Conference on Computer Vision and Pattern Recognition, vol. II, pp. 317–324 (2004)
16. Papageorgiou, C., Oren, M., Poggio, T.: A General Framework for Object Detection. In: Proc. of the IEEE International Conference on Computer Vision, pp. 555–562 (1998)
17. Rissanen, J.: Modelling by shortest data description. *Automatica* 14, 465–471 (1978)
18. Sivic, J., Everingham, M., Zisserman, A.: Person Spotting: Video Shot Retrieval for Face Sets. In: Leow, W.-K., Lew, M., Chua, T.-S., Ma, W.-Y., Chaisorn, L., Bakker, E.M. (eds.) CIVR 2005. LNCS, vol. 3568, pp. 226–236. Springer, Heidelberg (2005)

# Topological Effects on the Performance of Island Model of Parallel Genetic Algorithm

Wang Guan and Kwok Yip Szeto\*

Department of Physics,  
The Hong Kong University of Science and Technology  
phszeto@ust.hk

**Abstract.** The topological features of the communication network between computing nodes in Parallel Genetic Algorithms, under the framework of the island model, is discussed in the context of both the local rate of information exchange between nodes, and the global exchange rate that measures the level of information flow in the entire network. For optimal performance of parallel genetic algorithm for a set of benchmark functions, the connectivity of the network can be found, corresponding to a global information exchange rate between 40-70%. This range is obtained by statistical analysis on the search for solutions of four benchmark problems: the 0-1 knapsack, the Weierstrass's function, the Ackley's function, and the Modified Shekel's foxholes function. Our method is based on the cutting of links of a fully connected network to gradually decrease the connectivity, and compare the performance of the genetic algorithm on each network. Suggestions for the protocol in applying this general guideline in the design of a good communication network for parallel genetic algorithms are made, where the islands are connected with 40% of links of a fully connected network before fine tuning the parameters of the island model to enhance performance in a specific problem.

**Keywords:** Parallel Genetic Algorithms, Island Model, Network, Information, Exchange, Connectivity, Non-separable Function Optimization, Knapsack.

## 1 Introduction

Genetic algorithm (GA) is based on Darwinian ideas on biological evolution, where the survival of the fittest will eliminate poor members of the population and the fit ones will evolve towards ever increasing, or at least non-decreasing fitness [1,2]. For computer science, genetic algorithm is a type of evolutionary algorithms that implements this Darwinian idea for selecting the best candidate solutions to a problem, such as the search for the global minimum of a function. Genetic algorithms have been successfully applied to many areas, such as in solving the crypto-arithmetic problem [3], time series forecasting [4], traveling salesman problem [5], function optimization [5], adaptive agents in stock markets [7], and airport scheduling [8].

---

\* Corresponding author.

The intrinsic parallelism in the population of candidate solutions can be extended to a higher level where the entire population is divided into a group of sub-populations so that the single population genetic algorithm becomes a parallel genetic algorithm with many sub-populations. This generalization for genetic algorithm from one population to many populations is inspired by the idea of “divide and conquer”, and is a natural implementation of parallel computing [9,10].

One of the standard models used in dividing a population into sub-population is the island model [11-14]. The simplest realization of this model is to have equal sized sub-population, or demes which evolve independently according to the original algorithm and, interchange information by exchanging a set of individuals at regular interval. Each sub-population has its specific residency in an island and the performance of the island model depends on several parameters: (1) the number of island, which in real application is constrained by the available hardware, (2) the percentage of migrating individuals (3) the frequency of migrations. In this paper, we focus on the effect of the percentage of migrating individual, with fixed number of island and fixed number of generations elapsed between migration processes.

When we have a fixed number  $N$  of islands or sub-populations, and perform information exchange between subpopulations, we have to introduce a network of communication between islands. The network is defined by a graph with  $N$  nodes and  $L$  links. This then raises the question of the effects of the topology on the performance of the island model. In this paper, we will start with a fully connected network of  $N$  nodes so that the number of links is  $L_{\max} = N(N-1)/2$ . We will introduce two definitions on the information exchange rates: a local exchange rate that describes the information exchanged through the migration of individuals between two islands, and a global exchange rate that describes the total number of individuals migrating in the network. Through numerical experiments on a set of benchmark functions, we arrive at a general protocol on how to design the network and information exchange to optimize the performance of the parallel genetic algorithm in the island model.

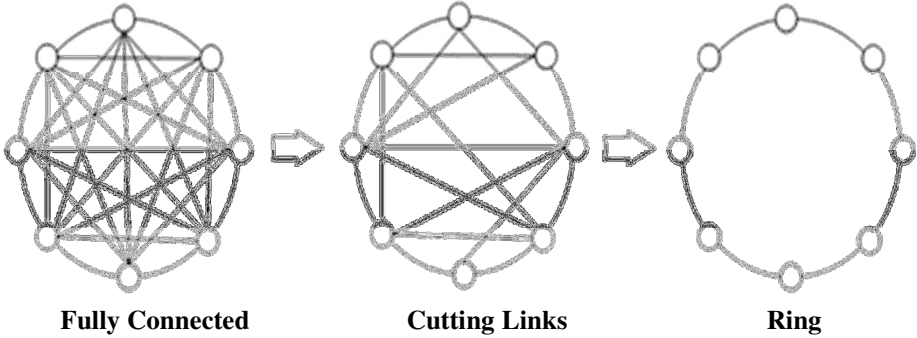
Since the number of benchmark tests can only be finite, our conclusion on how to select good topologies for parallel search is not universal. Nevertheless, we like to illustrate certain general properties of the network that should be exploited in designing parallel genetic algorithm. For specific problems, there must be fine tuning of various parameters which will enhance performance, but our goal is to find a general guideline or protocol in the construction of a network of communication in the island model so that we have in general a good starting point. Since many important features of a network can affect the performance, we further focus on the connectivity of the network. We thus investigate only the effect of the number ( $L$ ) of links, given the size ( $N$ ) of the network. We address this mathematical problem by means of cutting edges from a fully connected topology ( $L = L_{\max}$ ), until we reach a ring, which is the least connected topology of  $N$  nodes and  $L = N$  links. (We treat each island with equal importance so that the tree structure is excluded in our topological analysis). This is a continuation of the previous research in discussing different topologies and exchange rates for parallel genetic algorithm [15,16].

## 2 Rate of Information Exchange

We start with the island model with  $N$  islands, each occupied by a subpopulation of  $N_C$  chromosomes. Each subpopulation  $i$  gets the best  $M$  chromosomes from each of its  $K_i$  neighbors in the communication network (in total  $M \cdot K_i$  chromosomes) to replace its worst  $M \cdot K_i$  chromosomes. The Exchange Rate ( $X$ ) for individual population  $i$  is defined as  $X_i = M \cdot K_i / N_C$ . We define the Global Exchange Rate as  $X_G = 2M \cdot L / (N \cdot N_C)$ , where  $2M \cdot L$  is the total number of exchange chromosomes, and  $N \cdot N_C$  is the total number of chromosomes for all the subpopulations. The total number of chromosomes involved in communication in the host sub-population is  $M + M \cdot K_i$ . Since it is reasonable that the exchanged-in chromosomes do not interfere with the exchanged-out chromosomes, we have the limit  $M + M \cdot K_i \leq N_C$ .

While the local information exchange rate is defined by the number  $M$  of exchanged chromosomes between subpopulations, the global exchange rate is affected by many other factors besides the local rate. In particular, the global exchange rate depends on  $L$ , therefore a topological change of the network will change the global rate significantly. For a fully connected communication network of  $N$  nodes, we have the maximum global exchange rate. The degree for each node is  $K_{\max} = K_{Full} = N - 1$ . If we fix the number of chromosome exchanged to be  $M=1$  (only sending the best chromosome to the neighbors), then the number of chromosomes in each sub-population is at least as large as the number of chromosomes in the sub-population residing in a node in the fully connected network. Here we have assumed that the total number of chromosomes used in our parallel genetic algorithm is fixed and is divided equally among all  $N$  nodes. In our experiment we have  $N=16$  and  $M=1$ , so we easily get a maximum  $X_{GMax} = 0.9375$  for the fully connected network, and a minimum  $X_{GMin} = 0.125$  for the ring. When we evaluate the performance of island model on benchmark functions, our scheme of varying  $L$  is based on the following model. We start from a fully connected network, so that  $L$  is at maximum. We then randomly cut links until the network becomes a ring, which is the topology of a connected network with minimum  $L$ . This is shown in Fig.1. We perform independent non-communicating genetic algorithm for three generations before communication and undergo chromosome exchange. For each fixed topology before link cutting, we run for 15 generations with 5 times of communication.

In order to use parallel genetic algorithm, we need to choose a basic genetic algorithm for the individual sub-population. In this paper, we use the Mutation Only



**Fig. 1.** Randomly cut links from a fully connected network until it becomes a ring

Genetic Algorithm (MOGA) which is a generalization of traditional genetic algorithm in the framework of Mutation matrix, (not to be confused with Multi-Objective Genetic Algorithm). We have shown that MOGA is more adaptive and efficient than simple genetic algorithm and interested readers can find more details of MOGA in Ref.[17-19]. We will not discuss the various ways MOGA can be generalized here, as various methods have been designed to compute the mutation matrix adaptively to achieve optimal performance, including the variation that crossover is implemented [19]. The important point here is that our general discussion of the island model does not depend on the details of the genetic algorithm used in each sub-population, as long as they are the same type of algorithm. We use MOGA since it can be more efficient, and can also be reduced to traditional genetic algorithm easily [17].

### 3 Benchmark Functions and MOGA

We test the performance of our Quasi-Parallel genetic algorithms under different parameter settings on the optimization problems using four benchmark functions:

1. The Knapsack problem is described as the following. The knapsack has a maximum weight capacity  $C$ , which is called the optimal number. We consider the allocation of  $n$  items in the knapsack. When item  $i$  is in the knapsack, its loading is given by the weight  $w_i$  while the profit for carrying it is  $p_i$ .

$$\text{Given } (w_1, w_2, \dots, w_n) \text{ and } (p_1, p_2, \dots, p_n), \text{ our goal is to}$$

$$\text{maximize } \sum_{i=1}^n p_i x_i \text{ subject to the constraint } \sum_{i=1}^n w_i x_i \leq C \cdot$$

In our experiment we have  $n=16$  items with weight  $w_i = 2^{i-1}$  and profit  $p_i = 1$  for  $i=0,1,\dots,15$ . Our goal is to find a configuration of item occupancy  $\{x_i\}$  so that we get as close to the knapsack weight capacity as possible. Here  $x_i$  is a



binary variable which is 1 if item  $i$  is in the knapsack, and 0 otherwise. We use the string of  $\{x_i\}$  to denote a chromosome.

2. The Weierstrass's Function is a simplified version of F11 (Shifted Rotated Weierstrass's Function) from CEC2005 benchmark suite [20]. The definition of Weierstrass's Function is:

$$f(x_1, \dots, x_D) = \sum_{i=1}^D \left\{ \sum_{k=0}^{k_{\max}} [a^k \cdot \cos(2\pi b^k (x_i + 0.5))] \right\} - D \sum_{k=0}^{k_{\max}} [a^k \cdot \cos(2\pi b^k \cdot 0.5)]$$

where  $a = 0.5$ ,  $b = 3$ ,  $k_{\max} = 20$ ,  $x_i \in [-0.5, 0.5]$ .  $D$  is the dimension of the function. The global minimum of the function is obtained when all  $x_i = 0$ , and  $f_{\min} = 0$ . This problem is different from the Knapsack Problem because its variables are continuous. Therefore, we do not expect to find the global optima exactly using discrete encoding. Here we employ a binary string to encode each  $\{x_i\}$ . Hence the binary string can represent an integer  $I$  whose value ranges from 0 to  $I_{\max}$  in decimal notation. For a chromosome  $s$ , its value after encoding is  $C_s = \frac{I_s}{I_{\max}} - 0.5$ ,  $I_{\max} = 2^H - 1$  where  $I_s$  is the integer represented by chromosome  $s$ . We use  $H=15$ . Because the Weierstrass's Function have  $D$  variables, the total length of the chromosome is  $L = D \times H$ .

3. The 2D Ackley's is from reference [21]. The function is defines as following:

$$f(x, y) = 20 + e - 20 \exp \left( -0.2 \sqrt{\frac{(x^2 + y^2)}{2}} \right) - \exp \left( \frac{1}{2} (\cos(2\pi x) + \cos(2\pi y)) \right)$$

where  $x, y \in [-5, 5]$ . The function with  $x, y$  in the range indicated has 121 local minima. The landscape of both Weierstrass Function and 2D Ackley's Function is symmetric.

4. The 2D Modified Shekel's Foxholes function is from reference [22] and the landscape now is non-symmetric:

$$f(x, y) = - \sum_{i=1}^{30} \frac{1}{(x - a_i)^2 + (y - b_i)^2 + c_i}$$

where  $x, y \in [-10, 10]$ , and  $a_i, b_i, c_i$  are taken from Ref.[22] There are 17 local minima in this range.

## 4 Results

We use parallel genetic algorithm in the island model connected in a network shown in Fig.1 to find optimal solution for the above four different benchmark functions. Our network has  $N=16$  nodes, each with 16 chromosomes. For the experiment on the Knapsack Problem, the optimal number is fixed to be 10050. For each point we run our program 100 times and take the average (see Fig.2). We also run the program for topologies with increasing links from a ring to a fully connected network. The results are basically the same for the Weierstrass Function with  $D = 1$ . For each point we run

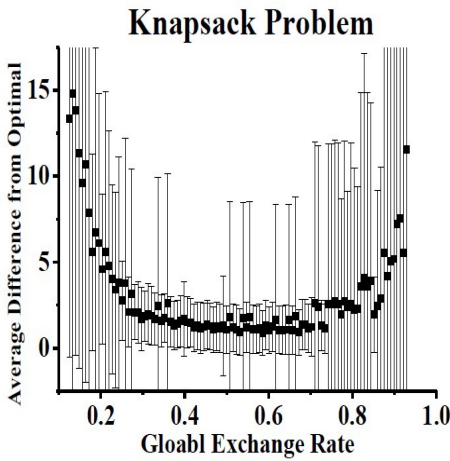


Fig. 2. Knapsack Problem

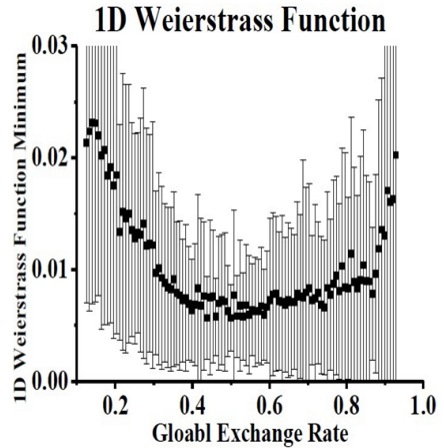


Fig. 3. 1D Weierstrass Function

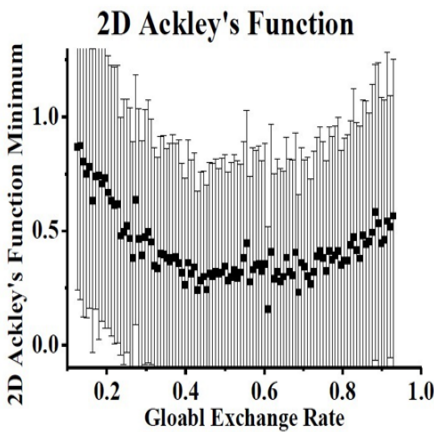


Fig. 4. 2D Ackley's Function

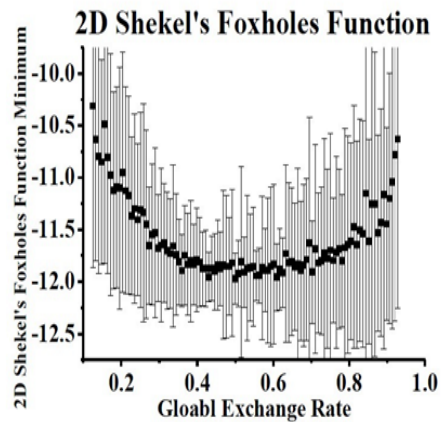


Fig. 5. Shekel's Foxholes Function

for 30 times and take average, (see Fig.3). For the 2D Ackley's Function, we aim at finding the global minimum of this function. Each chromosome has 14 bits. The first 7 bits represent  $x \in [-5,5]$  and the next 7 bits represent  $y \in [-5,5]$ . Thus, the precision is  $102^7 = 0.078$ . We do the problem on topologies with decreasing links from a fully connected network to a ring (See Fig.4). For the 2D Shekel's Foxholes function, we aim at finding the global minimum of this function. Each chromosome has 16 bits. The first 8 bits represent  $x \in [-10,10]$  and the next 8 bits represent  $y \in [-10,10]$ . Thus, the precision is also  $202^8 = 0.078$ . We do the problem on topologies with decreasing links from a fully connected network to a ring. The results are shown in Fig. 5.

From the results on these four benchmark functions, we observe a best performance basin of global exchange rate. The performance is best when the exchange rate is neither too low nor too high, with exchange rate in the range from 0.4 to 0.7. We can understand this feature heuristically. When the exchange rate is too low, each node is running almost independently so there is little exploitation of the good chromosomes from other populations. The effect is that we divide the solution space and search for a good solution without helping each other. When the exchange rate is too high, each node exploits too many chromosomes and the populations tend to become very similar. This then defeats the purpose of parallel genetic algorithm for now the sub-populations do not explore and essentially run as one identical population. In practical application, we have to consider both the hardware cost and algorithm complexity for making communications. Thus, we may use a network that achieves a global exchange rate at 0.4, since this is the beginning of best performance basin, but at the same time utilizes the least number of links, thereby minimizing the communication cost.

## 5 Discussion

We have tested the island model of parallel genetic algorithm defined on a network for solving the optimization problem in four benchmark functions. Our focus is on the topology of the communication network that the parallel algorithm uses, when the local information exchange is fixed. The single parameter we use to parameterize the topology of the network is the number of links, when the number of nodes or sub-populations is given. This simplification of the description of the topology is achieved through link cutting process of a fully connected network. For the four benchmark problems, which are the knapsack problem, the Weierstrass's function, the Ackley's function, and the Modified Shekel's foxholes function, we obtain some general conclusion on the number of links used, which correspond to the global exchange rate in the range of 0.4 to 0.7. Although this is never meant to be a universal range for optimization, and the range in fact is rather large, we nevertheless can make some general remarks on the application of our investigation. For an optimization problem where there is no prior information about the nature of the solution space, we suggest that we can start with a network with global exchange rate equal to 0.4 when we decide to use parallel genetic algorithm under the framework of the island model. This choice will give the least number of links used, thereby reducing cost in the case

of implementation in hard ware and also time delay in communication. When we have only 40% of links of a fully connected network, we have a small, yet sufficient number of links that can give good performance of the search process before any fine tuning. One can always gradually increase the number of links to see if the improvement in performance is worthwhile to the extra cost for the additional connection. Within the confine of the four benchmark functions tested, our guideline on the range of the number of links used is valid.

In this work, we focus on varying the number of links while in a separate work we discuss the importance of local exchange rate for a given topology of network: i.e., we fix  $L$  and the topology, but vary  $M$ . For this case, our conclusion is that the performance can be improved with increasing local exchange rate (i.e., increasing  $M$ ). In the context of the present work, it is therefore a good idea to use a global exchange rate equal to 0.4, or equivalently starting with a network resulted from cutting 60% of the links of a fully connected network and then use the maximum allowed number of local exchanged chromosomes. As mentioned in the introduction, our work on the topology of the communication network only addresses the number of links used, and there are much more complex problems such as the way these links are organized in the network that may improve the performance of our algorithm. For future work, we will investigate the importance of connectivity, shortest path length, etc, in other class of networks, such as the small world or hierarchical networks. Our goal is to find general guidelines for starting a search using parallel genetic algorithm when prior knowledge of the problem is absent.

**Acknowledgement.** We acknowledge the discussion with Wu Degang. K.Y. Szeto acknowledges the support of grant FSGRF13SC25.

## References

1. Holland, J.H.: *Adaptation in Natural and Artificial Systems*. University of Michigan Press, Ann Arbor (1975)
2. Goldberg, D.E.: *Genetic Algorithms in Search, Optimization, and Machine Learning*. Addison-Wesley, Reading (1989)
3. Li, S.P., Szeto, K.Y.: Cryptoarithmetic problem using parallel Genetic Algorithms. In: Mendl 1999 (1999)
4. Szeto, K.Y., Cheung, K.H.: Multiple time series prediction using genetic algorithms optimizer. In: IDEAL 1998, pp. 127–133 (1998)
5. Jiang, R., Szeto, K.Y., Luo, Y.P., Hu, D.C.: Distributed parallel genetic algorithm with path splitting scheme for the large traveling salesman problems. In: WCC 2000, pp. 478–485 (2000)
6. Szeto, K.Y., Cheung, K.H., Li, S.P.: Effects of dimensionality on parallel genetic algorithms. In: *Proceedings of the 4th ISAS Conference*, vol. 2, pp. 322–325 (1998)
7. Fong, A.L.Y., Szeto, K.Y.: Rule Extraction in Short Memory Time Series using Genetic Algorithms. *European Physical Journal B* 20, 569–572 (2001)

8. Shiu, K.L., Szeto, K.Y.: Self-adaptive Mutation Only Genetic Algorithm: An Application on the Optimization of Airport Capacity Utilization. In: Fyfe, C., Kim, D., Lee, S.-Y., Yin, H. (eds.) IDEAL 2008. LNCS, vol. 5326, pp. 428–435. Springer, Heidelberg (2008)
9. Bondi, A.B.: Characteristics of scalability and their impact on performance. In: Proceedings of the 2nd International Workshop on Software and Performance, pp. 195–203 (2000)
10. Cantú-Paz, E.: Efficient and accurate parallel genetic algorithms, pp. 16, 17, 22. Kluwer Academic, USA (2000)
11. Gustafson, S., Burke, E.K.: The Speciating Island Model: An alternative parallel evolutionary algorithm. *Journal of Parallel and Distributed Computing* 66, 1025–1036 (2006)
12. Scheutz, M., Schermerhorn, P.: Adaptive algorithms for the dynamic distribution and parallel execution of agent-based models. *Journal of Parallel and Distributed Computing* 66, 1037–1051 (2006)
13. Melab, N., Cahon, S., Talbi, E.-G.: Grid computing for parallel bio-inspired algorithms. *Journal of Parallel and Distributed Computing* 66, 1052–1061 (2006)
14. Delaossa, L., Gámez, J.A., Puerta, J.M.: Initial approaches to the application of islands-based parallel EDAs in continuous domains. *Journal of Parallel and Distributed Computing* 66, 991–1001 (2006)
15. Wang, C.G., Szeto, K.Y.: Sales Potential Optimization on Directed Social Networks: A Quasi-Parallel Genetic Algorithm Approach. In: Di Chio, C., et al. (eds.) *EvoApplications 2012*. LNCS, vol. 7248, pp. 114–123. Springer, Heidelberg (2012)
16. Wang, G., Wu, D., Chen, W., Szeto, K.Y.: Importance of Information Exchange in Quasi-Parallel Genetic Algorithms. In: *GECCO 2011*, pp. 127–128 (2011)
17. Szeto, K.Y., Zhang, J.: Adaptive Genetic Algorithm and Quasi-parallel Genetic Algorithm: Application to Knapsack Problem. In: Lirkov, I., Margenov, S., Waśniewski, J. (eds.) *LSSC 2005*. LNCS, vol. 3743, pp. 189–196. Springer, Heidelberg (2006)
18. Ma, C.W., Szeto, K.Y.: Locus Oriented Adaptive Genetic Algorithm: Application to the Zero/One Knapsack Problem. In: *RASC 2004*, pp. 410–415 (2004)
19. Law, N.L., Szeto, K.Y.: Adaptive Genetic Algorithm with Mutation and Crossover Matrices. In: *IJCAI 2007*, pp. 2330–2333 (2007)
20. Suganthan, P.N., Hansen, N., Liang, J.J., Deb, K., Chen, Y.P., Auger, A., Tiwari, S.: Problem Definitions and Evaluation Criteria for the CEC 2005 Special Session on Real-Parameter Optimization (2005)
21. Ackley, D.H.: *A connectionist machine for genetic hill climbing*. Kluwer Academic Publishers, Boston (1987)
22. Bersini, H., Dorigo, M., Langerman, S., Seront, G., Gambardella, L.: Results of the first international contest on evolutionary optimisation (1st icoe), CEC 1996, pp. 611–615 (1996)

# Artificial Bee Clustering Search

Tarcísio Souza Costa and Alexandre César Muniz de Oliveira

Universidade Federal do Maranhão, UFMA - Departamento de Informática,  
65.085-580 – Campus do Bacanga, São Luís - MA, Brasil  
priestcp@gmail.com, acmo@deinf.ufma.br

**Abstract.** Clustering Search (\*CS) has been proposed as a generic way of combining search metaheuristics with clustering to detect promising search areas before applying local search procedures. The clustering process may keep representative solutions associated to different search subspaces (search areas). In this work, a new approach is proposed, based on Artificial Bee Colony (ABC), observing the inherent characteristics of detecting promising food sources employed by that metaheuristic. The proposed hybrid algorithm, performing a Hooke & Jeeves based local, is compared against other versions of ABC: a pure ABC and another hybrid ABC, exploring an elitist criteria.

## 1 Introduction

Modern metaheuristics attempt to balance exploration and exploitation movements explicitly by employing global and local search strategies. The global algorithm plays the role of generator of reference points to diversified search areas, which are more intensively inspected by problem-specific components further. Early hybrid algorithms have demonstrated concern about rationally employing local search. Instead of always applying local search procedures over entire population, the global algorithm runs normally until a promising area is detected, according to a specific criteria, for example, when a new best individual is found (elitist criteria). In a general way, the following action must be better to exploit the expected promising area, in a reduced search domain, by a local search procedure.

Clustering Search (\*CS) has been proposed as a generic way of combining search metaheuristics with clustering, aiming to detect promising search areas before applying local search procedures [4]. Its generalized nature is achieved both by the possibility of employing any metaheuristic and by also applying to combinatorial and continuous optimisation problems. Clusters of mutually close solutions provide reference points to relevant areas of attraction in the most of search metaheuristics. Relevant search areas can be treated by problem-specific local search procedures. Furthermore, the cluster center itself is always updated by a procedure involving inner solutions, called assimilation [4].

Artificial Bee Colony (ABC) is a recently proposed optimisation algorithm [1] that simulates the intelligent behavior of honey bees, providing a population-based search procedure in which individuals called foods positions are modified

by the artificial bees, aiming to discover promising food sources and, finally, the one with the optimal amount of nectar [1].

This paper is devoted to propose a new \*CS approach, called Artificial Bee Clustering Search (ABCS), applied to unconstrained continuous optimisation, in which promising search areas are associated to promising food sources and the bee movement is performed by the intrinsic \*CS operation known as assimilation [4]. The remainder of this paper is organized as follows. Section 2 describes the concepts behind \*CS and ABC. ABCS is described in section 3 and computational results are presented in 4. The findings and conclusions are summarized in section 5.

## 2 Algorithms Foundations

A challenge in hybrid metaheuristic is to employ efficient strategies to cover all the search space, applying local search only in actually promising search areas. The inspiration in nature has been pursued to design flexible, coherent and efficient computational models. In this section, the Clustering Search (\*CS) and ABC are briefly described, introducing concepts needed to further explain how to combine them to allow detecting promising search areas before applying the Hooke & Jeeves local search procedure [3].

### 2.1 Clustering Search

\*CS attempts to locate promising search areas by framing them by clusters. A cluster is defined by a *center*,  $c$ , that is generally, initialized at random and, posteriorly, it tends to progressively slip along really promising points in the search space. The number of clusters  $\mathcal{NC}$  can be fixed a priori [5] or dynamically determined according to the width of the search areas being explored by the metaheuristic [4]. In the later case, clusters can be created in a way that all candidate solutions are covered by, at least, a cluster. By the other hand, inactive clusters, i.e., clusters not covering any solutions may be eliminated.

The coverage is determined by a *distance metric* that computes the similarity between a given solution and the cluster center and must consider the problem nature. For example, in unconstrained continuous optimization, the similarity has been defined regarding the Euclidean distance [4]. \*CS can be splitted off in four conceptually independent parts: a) the search metaheuristic (SM), b) the iterative clustering (IC) component, c) the analyzer module (AM), and d) the local searcher (LS).

The SM component can be implemented by any optimization algorithm that generates diversified solutions of the search space. It must work as a full-time solution generator, exploring the search space by manipulating a set of solutions, according to its specific search strategy. IC component aims to gather similar solutions into groups, maintaining a representative cluster center for them. A *distance metric*,  $\Delta$ , must be defined, *a priori*, allowing a similarity measure for the clustering process.

AM component examines each cluster, in regular intervals, indicating a probable promising cluster. A *cluster density*, also named *volume*,  $\delta_j$ , is a measure that indicates the activity level inside the cluster  $j$ . For simplicity,  $\delta_j$  can count the number of solutions generated by SM and grouped into  $c_j$ . Whenever  $\delta_j$  reaches a certain *threshold*  $\lambda$ , meaning that some information template becomes predominantly generated by SM, such cluster must be better investigated to accelerate the convergence process on it. Clusters with lower  $\delta_j$  can be eliminated or perturbed, as part of a mechanism that allows creating posteriorly other clusters, keeping framed the most active of them.

At last, the LS component is an internal searcher module that provides the exploitation of a supposed promising search area, framed by a cluster. In unconstrained continuous optimisation, the component LS has been commonly implemented by a Hooke-Jeeves direct search [3].

## 2.2 Artificial Bee Colony

In the ABC algorithm, the colony of artificial bees contains three groups of bees: employed bees, onlookers and scouts. A bee waiting on the dance area for making decision to choose a food source, is called an onlooker and a bee going to the food source visited by itself previously is named an employed bee. A bee carrying out random search is called a scout. In the ABC algorithm, first half of the colony consists of employed artificial bees and the second half constitutes the onlookers. For every food source, there is only one employed bee. In other words, the number of employed bees is equal to the number of food sources around the hive. The employed bee whose food source is exhausted by the employed and onlooker bees becomes a scout.

At each cycle ABC perform three basic operations: place employed bees on their food sources and evaluate their nectar amounts; after sharing the nectar information of food sources, onlookers select food source depending on their nectar amounts; send scout bees to explore new sources randomly on the search space. These main steps are repeated through a predetermined Maximum Cycle Number ( $M\mathcal{C}\mathcal{N}$ ) or until a termination criterion is satisfied.

Employed bees share the nectar amount of food sources on the dance area that will be used by onlooker bees as parameter to decide which source is better to be explored. The decision to be done by onlooker bees is governed by Equation 1:

$$p_i = \frac{fit_i}{\sum_{n=1}^{\mathcal{SN}} fit_n} \quad (1)$$

where  $p_i$  is the probability associated with food source  $i$ ,  $fit_i$  is the fitness value of solution  $i$  and  $\mathcal{SN}$  is the total number of food sources which is equal to the number of employed bees or onlooker bees. Both employed and onlooker bees modify their food sources, if the modification increase nectar amounts of those sources, onlooker and employed bees memorize the best source and forget



previous one. Thus, to produce a candidate food position from the old one in memory is done by following equation:

$$v_{ij} = x_{ij} + \phi_{ij}(x_{ij} - x_{kj}) \quad (2)$$

where  $k \in \{1, 2, \dots, SN\}$  and  $j \in \{1, 2, \dots, D\}$  are randomly chosen indexes, and  $D$  is the dimension of variables.

A food source is assumed to be abandoned if its fitness cannot be improved through certain number of cycles. The value of pre-determined number of cycles is called “limit” for abandonment [2].

### 3 Artificial Bee Clustering Search

The Artificial Bee Clustering Search (ABCS) algorithm is based on potential characteristic of detecting promising areas presented by ABC algorithm. Such potential characteristic can be seen on basic operations of ABC, such as the exploration and abandonment of a food source. An onlooker bee can be compared with a solution that must be assimilated by a cluster on a \*CS-based algorithms, because this bee will increase a source’s fitness after it has explored and found a better position to this food source. ABCS is proposed to represent all food sources as central regions of clusters and onlooker bees are solutions that can be or cannot be assimilated by these clusters.

```

program ABCS
  begin
    Initialize Population;
    repeat
      Place the employed bees on their food sources;
      Place the onlooker bees on the food sources depending on
      their nectar amounts;
      Memorize the quantity of activations (accounting of
      density) of each source;
      Perform Local Search in promising areas (top activated
      food sources);
      Send the scouts to the search area for discovering new
      food sources;
      Memorize the best food source found so far;
    until requirements are met
  end;
end.

```

(Pseudo-code adapted from [2])

The accounting of density of a food source  $i$  ( $\delta_i$ ) is a parameter to perform local search. This parameter is another metric of a food source, that will inform which food sources are most promising, to detect these promising areas  $\delta_i$  increases whenever an onlooker bee access the food source and gets a new better

position. If a food source reach a certain threshold there is a time to perform local search in such source to find better solutions. This threshold is known in \*CS as cluster density(Section 2).

$$\delta_i \geq \mathcal{PD} \cdot \frac{\mathcal{NP}}{|\mathcal{SN}|} \quad (3)$$

where  $\mathcal{PD}$  is a pressure of density,  $\mathcal{NP}$  is the colony size and  $\mathcal{SN}$  is the total number of food sources. Pressure of density is a well known metric of \*CS based algorithms that allows controlling the sensibility of the component AM.

ABCS is proposed to add to ABC some clustering elements without modifying the main structure of original algorithm. This work proposes to add two elements in ABCS: the amount of activations of each food source and local search routines. The algorithm used to perform local search in ABCS is the Hooke & Jeeves' algorithm [3].

## 4 Computational Experiments

Some functions were minimized to test the competitiveness of ABCS with others: A pure ABC, HABC (Hybrid Artificial Bee Colony) and ECS (Evolutionary Clustering Search [4]). The results in tables 3 and 4 were obtained allowing all algorithms to perform up to Maximum Function Evaluations (*Max FE*) (Table 1) in each one of 30 trials. The list of parameters of all algorithms are summarized in Table 1, where the value 80 of  $\mathcal{NP}$  was used based on [2], the other values were empirically tested.

**Table 1.** Parameters of all algorithms

	Parameters					
Algorithm	$\mathcal{NP}$	<i>Limit</i>	$\mathcal{MCN}$	<i>Error Rate</i>	<i>Max FE</i>	$\mathcal{PD}$
ABC	80	200	10000	0.0001	$2 * 10^6$	
HABC						
ABCS						10
	<i>PopSize</i>	<i>MaxGen</i>	$\mathcal{NC}$			
ECS	200	8000	40			2.5

Table 2 shows the total benchmark test functions used in experiments, where  $D$  is the number of variables (Dimension), *Min* is the optimal solution and *Range* is the known upper and lower bounds of the domain of functions's variables. HABC algorithm was not designed to detect promissing areas, it only activate the Hooke & Jeeves Local Search whenever the better current solution has been improved (elitist strategy). The variables Mean, Standard Deviation (StdDev), H/A (Hits/Attempts) and FE (Function Evaluations) are necessary to analyze the performance of algorithms. FE is a mean between total function calls in 30 executions  $\mathcal{N}$  for each function.

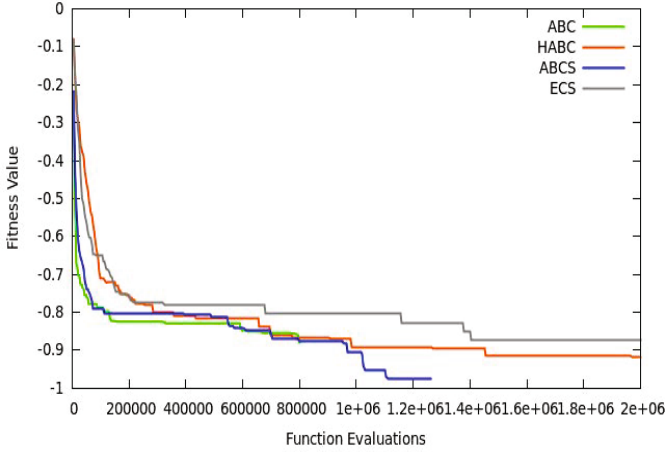
**Table 2.** 11 Test Functions used in the experiments

Function	Range	D	Min
Michalewicz	$[0, \pi]$	10	-9.6601
Rosenbrock	$[-30,30]$	30	0
Rastrigin	$[-5.12,5.12]$	30	0
<i>Schweffel</i> <sub>7</sub>	$[-500,500]$	30	0
Langerman	$[0,10]$	10	-1.4999
Zakarov	$[-5,10]$	30	0
Ridge	$[-64,64]$	30	0
Colville	$[-10,10]$	4	0
Sphere	$[-5.12,5.12]$	30	0
Griewank	$[-600,600]$	30	0
Ackley	$[-15,30]$	30	0

**Table 3.** First set of functions

Function		ABC	HABC	ABCS	ECS
Michalewicz	Mean	-9.6600	-9.6600	-9.6600	-9.6355
	StdDev	6.8215E-005	6.9391E-005	5.8031E-005	0.0214
	H/A	30/30	30/30	30/30	6/30
	FE	35874.48	911211.31	97753.20	1745612.73
Rosenbrock	Mean	0.0343	0.0001	0.0001	6.4467E-005
	StdDev	0.0499	0.00002	2.5765E-005	4.8001E-005
	H/A	0/30	30/30	30/30	30/30
	FE	800081.10	185090.24	171625.75	508843.9
Rastrigin	Mean	0.0001	0.0001	0.0001	1.9567
	StdDev	7.1006E-005	1.1056E-005	3.0449E-005	0.8046
	H/A	30/30	30/30	30/30	2/30
	FE	70597.24	43929.13	30982.41	1928062.2
<i>Schweffel</i> <sub>7</sub>	Mean	7.8033E-005	1295.28	0.0001	1075.82
	StdDev	6.2561E-005	252.88	6.1813E-005	416.58
	H/A	30/30	0/30	30/30	0/30
	FE	109758.65	2000000	733098	2000000
Langerman	Mean	-0.9551	-0.8450	-1.0715099	-0.8445
	StdDev	0.2802	0.1331	0.2954	0.1781
	H/A	4/30	1/30	7/30	2/30
	FE	733114.20	1952654.20	1001020.17	1918115.96

The ABCS algorithm presented better results with fewer calls for most minimized functions. HABC got bad performance at *Schweffel*<sub>7</sub>, because this function is extremely multimodal and HABC performs many calls to Hooke & Jeeves, without information about which food sources are promising, getting parked in local minimum points. ECS get better results to *Schweffel*<sub>7</sub> when the parameter  $\mathcal{PD}$  is less than 2.5, 2.5 was used because is the best one to overall functions.



**Fig. 1.** Convergence history comparison of all algorithms at Langerman

**Table 4.** Second set of functions

Zakarov	Mean	136.45	0.023	0.014	2.5389
	StdDev	23.76	0.025	0.0172	1.555
	H/A	0/30	0/30	0/30	0/30
	FE	800040.58	2000000	2000000	2000000
Ridge	Mean	417.33	0.0003	0.0002	0.766
	StdDev	170.63	0.00007	1.98E-005	0.538
	H/A	0/30	2/30	25/30	0/30
	FE	800040.10	1938631.93	1447802.55	2000000
Colville	Mean	0.17965	0.0001	0.0001	0.00006
	StdDev	0.13612	2.86E-005	2.96E-005	5.5197E-005
	H/A	0/30	30/30	30/30	30/30
	FE	800218.517	22002.65	15069.03	3123.6
Sphere	Mean	100.000	100.000	100.000	100.000
	StdDev	3.67E-005	8.66E-006	3.08E-005	2.2968E-006
	H/A	30/30	30/30	30/30	30/30
	FE	30326.89	57343.65	11508.96	3274.2
Griewank	Mean	0.0001	0.0001	0.0001	0.0001
	StdDev	4.82E-005	9.07E-006	0.00002	3.574E-005
	H/A	30/30	30/30	30/30	30/30
	FE	55186.20	39759	11105.58	4943
Ackley	Mean	0.0001	0.0001	0.0001	8.646E-005
	StdDev	3.33E-005	1.46E-005	2.38E-005	7.1095E-005
	H/A	30/30	30/30	30/30	30/30
	FE	61055.17	40015.55	32731.55	366911.866

Figure 1 illustrates the progress of all algorithms minimizing Langerman function. The mean of objective function (known as fitness value in the chart) was calculated between 30 trials at intervals of 5000 function evaluations.

## 5 Conclusion

In this work a new approach is proposed combining Clustering Search with Artificial Bee Colony. The proposal is called Artificial Bee Clustering Search (ABCS) and two elements of \*CS are added to ABCS aiming to improve inherent characteristics of detecting promising food sources by ABC: Quantity of activations of each food source and the Local Search component. Some unconstrained continuous optimisation functions are minimized and ABCS presented competitive results compared to other algorithms: Pure ABC, HABC and ECS.

Future work consist of testing some \*CS components as the *distance metric* and different types of bee assimilation by food sources.

## References

1. Karaboga, D.: An Idea Based On Honey Bee Swarm for Numerical Optimization, Technical Report TR06, Erciyes University, Engineering Faculty, Computer Engineering Department (2005)
2. Karaboga, D., Akay, B.: A comparative study of Artificial Bee Colony Algorithm. *Applied Mathematics and Computation* 214, 108–132 (2009)
3. Hooke, R., Jeeves, T.A.: Direct search solution of numerical and statistical problems. *J. Assoc. Comput. Mach.* 8, 212–229 (1961)
4. Oliveira, A.C.M., Lorena, L.A.N.: Detecting promising areas by evolutionary clustering search. In: Bazzan, A.L.C., Labidi, S. (eds.) SBIA 2004. LNCS (LNAI), vol. 3171, pp. 385–394. Springer, Heidelberg (2004)
5. Chaves, A.A., Correa, F.A., Lorena, L.A.N.: Clustering Search Heuristic for the Capacitated p-median Problem. *Springer Advances in Software Computing Series* 44, 136–143 (2007)
6. Costa, T.S., Oliveira, A.C.M., Lorena, L.A.N.: Advances in Clustering Search. *Advances in Soft Computing* 73, 227–235 (2010)

# A Metaheuristic Approach for the Seaside Operations in Maritime Container Terminals

Eduardo Lalla Ruiz, Christopher Expósito Izquierdo, Belén Melián Batista,  
and José Marcos Moreno-Vega

Departamento de Estadística, Investigación Operativa y Computación  
Universidad de La Laguna  
38271 La Laguna, Spain  
{elalla,cexposit,mbmelian,jmmoreno}@ull.es

**Abstract.** The service time of the container vessels is the main indicator of the competitiveness of a maritime container terminal. This work proposes two Variable Neighbourhood Searches (VNS) in order to tackle the Tactical Berth Allocation Problem and the Quay Crane Scheduling Problem, which are the main operational problems in the seaside. These metaheuristics are integrated into a framework that provides an overall planning for the vessels arrived to port within a given time horizon. The performance of the proposed VNSs is compared with the most highlighted solution methods published in the related literature. In addition, the effectiveness of the framework is assessed in real size environments.

**Keywords:** Metaheuristic, Container Terminal, Seaside Operations.

## 1 Introduction

The maritime container terminals are core elements within the international sea freight trade (Vis and de Koster [10]). These facilities are open systems dedicated to the exchange of containers in multimodal transportation networks. In general terms, a container terminal is split into three different functional areas (Petering [7]). Firstly, the quay area is the part of the port in which the container vessels are berthed in order to load and unload containers to/from them. Secondly, the yard area is aimed at storing the containers until their later retrieval. Lastly, the mainland interface connects the terminal with the road transportation.

The most widespread indicator concerning the competitiveness of a maritime container terminal is the service time required to serve the container vessels arrived to the port (Yeo [4]). The seaside operations are those arising in the quay area of a maritime container terminal and directly related to the service of container vessels. The operational decisions stemming from the service of container vessels can be modeled through a well-defined sequence of steps. Once the container vessel arrives to the port, a berthing position in the quay is assigned to it on the basis of its particular characteristics (dimensions, stowage plan, etc.). A subset of the available quay cranes at the terminal is allocated to the vessel. These quay cranes perform the loading and unloading operations associated

with the containers of the vessel. An in-depth survey on the seaside operations is conducted by Meisel [6].

The Tactical Berth Allocation Problem (TBAP) pursues to determine the berthing position, berthing time and allocation of quay cranes for the container vessels arrived to the port over a well-defined time horizon. In the TBAP, we are given a set of incoming container vessels  $V$ , a set of berths  $B$  and a maximum number of available quay cranes  $Q$ . Each container vessel  $v \in V$  must be assigned to an empty berth  $b \in B$  within its time window  $[t_v, t'_v]$ . The berthing position of a vessel should be close to the departure position of its containers. In this regard, the housekeeping cost,  $h_{ss'}$ , represents the effort associated with moving a given container between the berthing positions  $s$  and  $s'$  of the quay (Giallombardo et al. [2]). For each container vessel  $v \in V$ , the service time,  $s_v$ , is defined according to the containers included into its stowage plan. That is, the number of containers to be loaded and unloaded to/from the vessel at hand. A quay crane profile determines the distribution of quay cranes used during the service time of a given container vessel. The set of available quay crane profiles is denoted by  $P$ . The usage cost of each profile  $p \in P$  is denoted by  $c_p$ . The main goal of the TBAP is to maximize the usage cost of the quay crane profiles used to serve the vessels and minimize the housekeeping costs derived from the transshipment of containers among container vessels. A comprehensive description of the TBAP is provided by Vacca et al. [9].

The Quay Crane Scheduling Problem (QCSP) is aimed at scheduling the loading and unloading operations of containers to/from a given container vessel. We are given a set of tasks,  $\Omega = \{1, \dots, n\}$ , and the quay cranes with similar technical characteristics allocated to the vessel,  $Q' = \{1, \dots, q\}$ , where  $Q' \subseteq Q$ . Each task  $t \in \Omega$  represents the loading or unloading operations of a group of containers located in the same bay of the vessel,  $l_t$ . The time required by a quay crane in order to perform the task  $t$  is denoted by  $w_t$ . Furthermore, each quay crane  $q \in Q'$  is ready after time  $r_q$  and is initially located in the bay  $l_q$ . All the quay cranes can move between two adjacent bays at speed  $\dot{l}$ . The QCSP introduces particular constraints concerning its application scope. The quay cranes move on rails and, therefore, they cannot cross each other. In addition, they have to keep a safety distance,  $\delta$  (expressed as a number of bays), between them in order to minimize potential collisions. This fact avoids that the quay cranes perform at the same time tasks located at a distance lower than  $\delta$  bays. Lastly, there are precedence relationships among tasks located in the same bay (Kim and Park [5]). For instance, unloading tasks have to be performed before loading operations. The objective of the QCSP is to determine the processing time of each task in such a way that the finishing time of the last performed task (makespan) is minimized. The makespan of a given schedule is the service time of the associated vessel. A mathematical formulation for the QCSP is proposed by Meisel. [6].

In spite of the great deal of attention gathered by these operational problems over the last years (Steenken et. al [8]), there is a lack of integration approaches in which the interactions between them are considered. In this work we address

the integration of the seaside operations in a maritime container terminal. In this context, we propose two VNS algorithms in order to individually tackle the TBAP and the QCSP, respectively. These metaheuristics are integrated into an effective framework with the goal of providing an overall planning for serving incoming container vessels within a given time horizon.

The remainder of this work is structured as follows. Section 2 introduces a framework based on metaheuristics aimed at tackling the main seaside operations and the interactions between them. Finally, Section 3 analyzes the performance of the proposed metaheuristics compared to other approaches from the related literature and assesses the effectiveness of the integration strategy. In addition, some general guidelines for further research are presented.

## 2 Metaheuristic Approach

A Variable Neighbourhood Search (VNS) is a metaheuristic that has demonstrated to be competitive in a large number of practical scopes. It is based upon the systematic change of several neighbourhood structures (Hansen and Mladenović [3]). In this work we develop two VNSs in order to address the TBAP and the QCSP, respectively. Later, these metaheuristics are integrated into a framework.

### 2.1 VNS Algorithm for Solving the TBAP

Algorithm 1 depicts the pseudocode of the proposed VNS aimed at solving the TBAP. The VNS uses two neighbourhood structures based upon the reinsertion movement  $N_a(\gamma, \lambda)$ , namely,  $\lambda$  vessels and their assigned profiles are removed from the berth  $b \in B$  and reinserted in another berth  $b'$ , where  $b \neq b'$ , and the interchange movement  $N_b(\gamma)$ , which consists in exchanging a vessel  $v \in V$  assigned to berth  $b \in B$  with another vessel  $v'$  assigned to berth  $b'$ , where  $b \neq b'$ .

The starting solution of the VNS,  $\gamma$ , is generated by assigning the profile  $p \in P$  with the highest usage cost to each vessel. The berthing position of each vessel is selected at random, whereas the starting of its service time is selected as the earliest possible within its time window (line 1). The value of the parameter  $k$  is set to 1 (line 2). The shaking process (line 4) allows to escape from those local optima found along the search by using the neighbourhood structure  $N_a$ . The solution exploitation phase of the VNS algorithm is based on a Variable Descent Neighbourhood Search (VND) (lines 5 – 14). Given a solution  $\gamma'$ , it explores one neighbourhood at time until a local optimum with respect to the neighbourhood structures  $N_a$  and  $N_b$  is found. The application of the neighbourhoods structures in the VND is carried out according to the value of the parameter  $k_1$ , initially set to 1 (line 6). The first neighbourhood structure explored is  $N_a$  and later  $N_b$ . The best solution found by means of the VND is denoted by  $\gamma'$ . The objective function value of  $\gamma'$  allows to update the best solution found along the search (denoted by  $\gamma$ ) and restart  $k$  (lines 15 – 17). Otherwise, the value of  $k$  is increased (line 19). These steps are carried out until  $k = k_{max}$  (line 21).



```

1:  $\gamma \leftarrow$  Generate initial solution
2:  $k \leftarrow 1$ 
3: repeat
4:    $\gamma' \leftarrow$  Shake( $\gamma, k$ )
5:   repeat
6:      $k_1 \leftarrow 1$ 
7:      $\gamma'' \leftarrow$  Local Search( $\gamma, k_1$ )
8:     if  $f(\gamma'') > f(\gamma')$  then
9:        $\gamma' \leftarrow \gamma''$ 
10:       $k_1 \leftarrow 1$ 
11:     else
12:        $k_1 \leftarrow k_1 + 1$ 
13:     end if
14:   until  $k_1 = k_{1max}$ 
15:   if  $f(\gamma') > f(\gamma)$  then
16:      $\gamma \leftarrow \gamma'$ 
17:      $k \leftarrow 1$ 
18:   else
19:      $k \leftarrow k + 1$ 
20:   end if
21: until  $k = k_{max}$ 

```

**Algorithm 1.** VNS for the TBAP

```

1:  $\sigma \leftarrow$  Generate initial solution
2:  $ES \leftarrow \emptyset$ 
3: repeat
4:    $k \leftarrow 1$ 
5:   repeat
6:      $\sigma' \leftarrow$  Shake( $\sigma, k$ )
7:      $\sigma'' \leftarrow$  Local Search( $\sigma'$ )
8:     Update  $ES$ 
9:     if  $f(\sigma'') < f(\sigma)$  then
10:       $\sigma \leftarrow \sigma''$ 
11:     else
12:        $k \leftarrow 1$ 
13:     end if
14:   until  $k = k_{max}$ 
15:    $\sigma', \sigma'' \leftarrow$  Select schedules from  $ES$ 
16:    $\sigma \leftarrow$  Combine( $\sigma', \sigma''$ )
17:   until Stopping Criteria

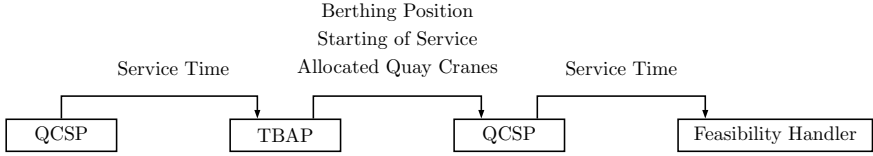
```

**Algorithm 2.** VNS for the QCSP

## 2.2 VNS Algorithm for Solving the QCSP

The pseudocode of the proposed VNS for the QCSP is depicted in Algorithm 2. It is based upon two neighbourhood structures, namely, reassignment ( $N_1$ ) and interchange of tasks ( $N_2$ ). The search starts generating an initial schedule,  $\sigma$ , by assigning each task  $t \in \Omega$  to its nearest quay crane (line 1). The value of the parameter  $k$  is also set to 1 (line 4). A shaking procedure allows to reach unexplored regions of the search space by means of the reassignment of  $k$  tasks to another quay crane. The reassigned tasks are selected on the basis of a frequency memory. In this way, at each step, a neighbour schedule,  $\sigma'$ , is generated at random from  $\sigma$  within the neighbourhood structure  $N_k$  (line 6). A local optimum,  $\sigma''$ , is reached through a local search based on the proposed neighbourhood structures (line 7). An improvement in the value of  $\sigma''$  allows to update  $\sigma$  and restart  $k$  (lines 9, 10 and 11). Otherwise, the value of  $k$  is increased (line 13). These steps are carried out until  $k = k_{max}$  (line 15).

An elite set,  $ES$ , is included into the VNS with the goal of collecting the promising schedules found along the search. It is composed of the fittest schedules and those local optima with the highest diversity in  $ES$ . The diversity of two schedules is measured as the number of tasks performed by different quay cranes. At each step,  $ES$  provides a pair of schedules  $\sigma$  and  $\sigma'$  selected at random (line 16) in order to be combined (line 17) and restart the search. The combination process keeps those tasks performed by the same quay crane, whereas the remaining tasks are randomly assigned to one quay crane.



**Fig 1.** Structure of the metaheuristic-based framework for the seaside operations

### 2.3 Integrated Approach

The service time of a given vessel is directly derived from the number and schedule of its allocated quay cranes. As indicated in the introduction, the TBAP assumes an estimation of this time in order to determine the berthing position and the starting of the service time of each vessel. However, the real service time is only known during the schedule of its tasks, which is defined by the QCSP.

In this work we propose a functional integration approach aimed at providing an overall service planning for container vessels arrived to port. The TBAP and the QCSP are integrated into a framework that allows to tackle the dependencies between both. The structure of the proposed framework is depicted in Figure 1. Firstly, an estimation of the service time for each vessel within the time horizon is pursued. In this regard, the QCSP is solved for each vessel by means of some domain-specific solver for it, for example, the proposed VNS. In all the cases, the number of considered quay cranes is the maximum allowed according to the dimensions of the vessel at hand. Short computational times should be used in this step due to the fact that it is intended to get an estimation of the service time. Once the service time of each vessel is estimated, the TBAP is solved through some optimization technique. The TBAP provides the berthing position, berthing time and the subset of quay cranes allocated to each vessel. However, the service time is estimated so far. Hence, the QCSP is solved for each vessel using the real subset of allocated quay cranes. It is worth mentioning that the real service time can be different to the estimated one and, therefore, it can produce overlap in the service of the vessels. In order to avoid this fact, the last stage of the framework (denoted by *Feasibility Handler*) adjusts the berthing time of the involved vessels.

## 3 Discussion and Further Research

This section is devoted to individually assess the performance of the VNSs proposed in order to solve the TBAP and the QCSP, respectively. In addition, the effectiveness of the developed framework is analyzed in real size instances. All the computational experiments reported in this work have been carried out on a computer equipped with a CPU Intel 3.16 GHz and 4 GB of RAM.

Table 1 presents a comparison among CPLEX, the Tabu Search combined with Branch and Price (TS-BP) developed by Giallombardo et al. [2] and the

**Table 1.** Comparison between VNS and TS-B&P (Giallombardo et al. [2]) for the TBAP

<i>Instance</i>				<i>CPLEX</i>	<i>TS-BP</i>		<i>VNS</i>	
<i>Name</i>	<i>V</i>	<i>B</i>	<i>P</i>	$UB_{CPLEX}$	$f_{BP-TS}$	t. (s)	$f_{VNS}$	t. (s)
$A_{p10}$	20	5	10	1383614	97.26	81	97.25	4.86
$A_{p20}$	20	5	20	1384765	97.19	172	96.99	10.49
$A_{p30}$	20	5	30	1385119	97.37	259	96.94	12.23
$B_{p10}$	30	5	10	1613252	95.68	308	96.66	12.46
$B_{p20}$	30	5	20	1613769	95.12	614	96.20	26.55
$B_{p30}$	30	5	30	1613805	—	920	96.33	59.71
$C_{p10}$	40	5	10	2289660	97.41	1382	97.50	68.47
$C_{p20}$	40	5	20	2290662	97.37	3144	97.62	99.04
$C_{p30}$	40	5	30	2291301	96.60	4352	96.72	223.1

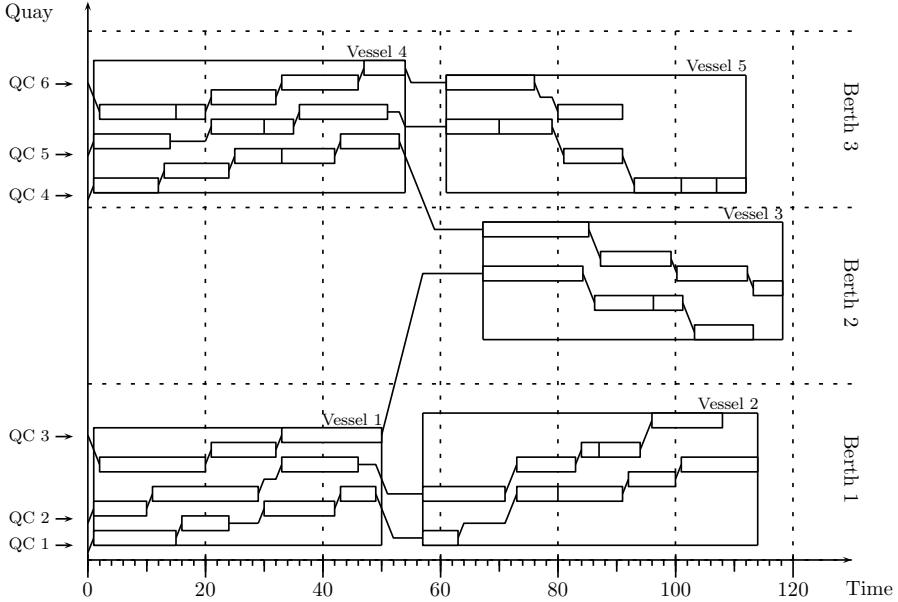
proposed VNS. The first column (*Instance*) shows the instances to solve. For each instance, the name (*Name*), the vessels (*V*), the berths (*B*) and the profiles (*P*) are presented. Column *CPLEX* shows the results obtained by CPLEX with a maximum computational time of 2 hours. The next columns (*TS-BP* and *VNS*) show the results obtained by TS-BP and VNS with  $k_{max} = 5$  and  $k_{1max} = 2$ , respectively. In each case, the objective function value scaled up to 100 with respect to  $UB_{CPLEX}$  and the computational time (in seconds) are reported, respectively.

The computational results illustrated in Table 1 indicate that the proposed VNS is highly competitive for the wide range of problem instances at hand. It reports the best-known solutions by means of short computational times, less than 225 seconds in the worst case. This fact motivates its use within integration strategies such as that proposed in Section 2.3. Furthermore, it is worth pointing out that TS-BP requires larger times to provide solutions with similar quality.

Table 2 shows a comparison for the QCSP between the proposed VNS and the exact technique called UDS proposed by Bierwirth and Meisel [1]. The execution

**Table 2.** Comparison between VNS and UDS (Bierwirth and Meisel [1]) for the QCSP

<i>Instance</i>				<i>UDS</i>		<i>VNS</i>	
<i>Set</i>	<i>n</i>	<i>q</i>	$f_{UDS}$	t. (m)	$f_{VNS}$	t. (m)	Gap (%)
A	10	2	459.9	1.12 E-5	459.9	0.001	0.00
B	15	2	666.6	3.68 E-5	666.6	0.017	0.00
C	20	3	604.8	6.26 E-4	604.8	0.096	0.00
D	25	3	804.6	3.43 E-3	804.6	0.254	0.00
E	30	4	730.2	0.10	730.2	0.570	0.00
F	35	4	863.7	1.08	865.5	1.140	0.24
G	40	5	753.0	2.37	759.0	1.930	0.89
H	45	5	889.8	19.16	891.0	3.240	0.15
I	50	6	817.8	23.97	818.1	4.780	0.07



**Fig 2.** Example of solution reported by the metaheuristic-based framework

of the VNS is stopped when 20 iterations are performed. In addition, we set  $k_{max} = 5$  and an elite set with 10 solutions (5 by quality and 5 by dispersion). Column *Instance* shows the name of the group of instances (*Set*), number of tasks ( $n$ ) and number of quay cranes ( $q$ ) to solve. There are 10 instances in each group. Next columns (*UDS* and *VNS*) present the average objective function value and the average computational time (in minutes) required by both methods. In the case of VNS, the gap between both solution methods is also reported.

There are no differences in the quality of the solutions found by both methods in small instances. The time used by the VNS is slightly larger than the UDS. However, there are relevant differences between the times for large instances. In those cases, the VNS is also high effective. The reported solutions are optimal or near-optimal in all the cases (with a gap below 1%).

We illustrate in Figure 2 a complete example of the solution reported by the developed metaheuristic-based framework. We have  $V = 5$  vessels,  $B = 3$  berths and  $Q = 6$  quay cranes. In this case, the berthing position and berthing time of each vessel is defined within its time window by means of the VNS for the TBAP. The tasks of each vessel (represented as small rectangles) are performed by one quay crane (defined by the VNS for the QCSP). It is worth pointing out that the interferences between quay cranes give rise to waiting times within each vessel. In addition, the quay cranes have to wait for some vessel because it is not already berthed, see vessel 3. Finally, as indicated in Subsection 2.3, after knowing the real service time of each vessel, overlaps between vessels can appear,

for instance, between vessels 4 and 5. In those cases, the *Feasibility Handler* is devoted to appropriately delay the berthing time of the vessel 5.

The proposed metaheuristic-based framework is able to tackle high-dimension instances. Its effectiveness is directly founded on the performance of the domain-specific methods used to solve the TBAP and the QCSP. However, some directions can be followed for further research. First, container terminal managers are highly interested on having a suitable management of the vehicles used to transport the loaded and unloaded containers to/from the vessels. Our framework will be extended for this purpose. Future works must address the dynamic nature of the environment. For instance, the quay cranes are subject to breakdowns.

**Acknowledgments.** This work has been partially funded by the Spanish Ministry of Economy and Competitiveness (project TIN2012-32608). Eduardo Lalla Ruiz and Christopher Expósito Izquierdo thank Canary Government and Caja-Canarias the financial support they receive through their post-graduate grants, respectively.

## References

1. Bierwirth, C., Meisel, F.: A fast heuristic for quay crane scheduling with interference constraints. *Journal of Scheduling* 12, 345–360 (2009)
2. Giallombardo, G., Moccia, L., Salani, M., Vacca, I.: Modeling and solving the tactical berth allocation problem. *Transportation Research Part B: Methodological* 44(2), 232–245 (2010)
3. Hansen, P., Mladenović, N.: Variable neighborhood search. In: Burke, E.K., Kendall, G. (eds.) *Search Methodologies*, pp. 211–238. Springer, US (2005)
4. Yeo, H.J.: Competitiveness of asian container terminals. *The Asian Journal of Shipping and Logistics* 26(2), 225–246 (2010)
5. Kim, K.H., Park, Y.-M.: A crane scheduling method for port container terminals. *European Journal of Operational Research* 156(3), 752–768 (2004)
6. Meisel, F.: *Seaside Operations Planning in Container Terminals*. Contributions to Management Science. Physica-Verlag HD (2010)
7. Petering, M.E.H.: Decision support for yard capacity, fleet composition, truck substitutability, and scalability issues at seaport container terminals. *Transportation Research Part E: Logistics and Transportation Review* 47(1), 85 (2011)
8. Steenken, D., Voß, S., Stahlbock, R.: Container terminal operation and operations research - a classification and literature review. In: Günther, H.-O., Kim, K.H. (eds.) *Container Terminals and Automated Transport Systems*, pp. 3–49. Springer, Heidelberg (2005)
9. Vacca, I., Salani, M., Bierlaire, M.: An exact algorithm for the integrated planning of berth allocation and quay crane assignment. *Transportation Science* (2012)
10. Vis, I.F.A., de Koster, R.: Transshipment of containers at a container terminal: An overview. *European Journal of Operational Research* 147(1), 1–16 (2003)

# Restricted Dynamic Heterogeneous Fleet Vehicle Routing Problem with Time Windows\*

Jesica de Armas, Belén Melián-Batista, and José A. Moreno-Pérez

Dpto. de Estadística, I.O. y Computación  
Escuela Técnica Superior de Ingeniería Informática  
Universidad de La Laguna  
38271 La Laguna, Spain  
{jdearmas,mbmelian,jamoreno}@ull.es

**Abstract.** This paper tackles a Restricted Dynamic Heterogeneous Fleet Vehicle Routing Problem with Time Windows as a real-world application of a courier service company in the Canary Islands, Spain. In this particular application of the Vehicle Routing Problem with Time Windows (VRPTW), customer requests can be either known at the beginning of the planning horizon or dynamically revealed over the day. Moreover, a heterogeneous fleet of vehicles has to be routed in real time. In addition, some other constraints required by the company, such as the allowance of extra hours for the vehicles, as well as, the use of several objective functions, are taken into account. This paper proposes a metaheuristic procedure to solve this particular problem. It has already been installed in the fleet management system of the company. The computational experiments indicate that the proposed method is both feasible to solve this real-world problem and competitive with the literature.

**Keywords:** Dynamic vehicle routing, Time windows, Heterogeneous fleet, Metaheuristics.

## 1 Introduction

Contrary to the classical static vehicle routing problems, real-world applications often include evolution, as introduced by Psaraftis in 1980 [9], which takes into consideration the fact that the problem data might change over the planning horizon. Latest developments in fleet management systems and communication technology have enabled people to quickly access and process real-time data. Therefore, dynamic vehicle routing problems have been lately given more attention. Last decade has been characterized by an increasing interest for dynamic routing problems, with solution methods ranging from mathematical programming to metaheuristics (see Pillac et al, 2013 [8] for a comprehensive review of dynamic vehicle routing problems).

---

\* This work has been partially funded by the Spanish Ministry of Economy and Competitiveness (project TIN2012-32608) and the Spanish Ministry of Industry, Tourism and Trade (project TSI-020100-2011-298).

The main goal of the Restricted Dynamic Heterogeneous Fleet VRPTW (RD-HFVRPTW) tackled in this paper is to dynamically route couriers taking into account not only the requests known at the beginning of the planning horizon, but also new service requests that arrive over it. In the particular real-world application posed to the authors by a company in the Canary Islands, all delivery and about the 60% of the pick-up requests are known in advance, whereas the remaining pick-up requests arrive over the planning horizon. Moreover, companies offering courier services often have a heterogeneous fleet of vehicles, which represents an additional difficulty in the resolution of the problem. Using exact methods is not a suitable solution for this kind of problems, since the arrival of a new request has to be followed by a quick re-optimization phase to include it into the solution at hand. Therefore, most dynamic problems rely on the use of metaheuristics.

Solution approaches for Dynamic Vehicle Routing Problems (DVRP) can be divided into two main classes: those applied to dynamic and deterministic routing problems without any stochastic information, and those applied to dynamic and stochastic routing problems, in which additional stochastic information regarding the new requests is known. Given the fact that in the real-world application tackled in this paper, the information is dynamically given by the company fleet management system, we will focus on the first class of dynamic problems. In this case, solution methods can be based on either periodic or continuous re-optimization. Periodic optimization approaches firstly generate an initial solution consisting of a set of routes that contain all the static customers. Then, a re-optimization method periodically solves a static routing problem, either when new requests arrive or at fixed time slots [1]. On the other hand, continuous re-optimization approaches carry out the optimization over the day by keeping high quality solutions in an adaptive memory. In this case, vehicles do not know the next customer to be visited until they finish the service of a request.

The following literature references regarding periodic optimization approaches to solve the DVRP with Time Windows (DVRPTW) are worth mentioning. Chen and Xu [1] proposed a dynamic column generation algorithm for solving the DVRPTW based on their notion of decision epochs over the planning horizon, which indicate the moments of the day when the re-optimization process is executed. Some other papers that make also use of time slices and solve static VRPs are due to Montemani et al. [7], Rizzoli et al. [10] and Khouadjia et al. [4]. In these last papers, requests are never urgent and can be postponed since time windows are not handled. On the other hand, the work by Hong [3] does consider time windows and therefore, some request can be urgent. Hong proposes a Large Neighborhood Search algorithm for real-time vehicle routing problem with time windows, in which each time a new request arrives, it is immediately considered to be included in the current solution. In our work, the same consideration is taken into account given the urgency of some requests. The main differences of the problem tackled in this paper and the one proposed by Hong are on one hand, the fact that we consider a heterogeneous fleet of vehicles, and on the other hand, the fact that we consider a restricted version of dynamism.

Furthermore, in our real-world problem customers and vehicles can have more than one time window in the same planning horizon. In addition, customers can be postponed according to their assigned priorities. There also exist constraints that do not allow certain customers to be visited by some of the vehicles due to road restrictions. Extra hours for the vehicles may also be allowed in our problem, which incur in additional costs. Finally, several objective functions are considered and hierarchically evaluated. Hierarchic evaluation means that the functions are considered in a certain order, so that if two selected solutions have equal objective function values for a function, then the next one in the order is considered to break ties. The objective functions considered in this work are total traveled distance, time balance, that is defined as the longest minus the shortest route in time required, and cost, which includes fuel consumption and other salaries.

The main contributions of this paper are the following. This work tackles a variant of a Dynamic VRPTW, which handles all the real-world constraints required by a courier service company. The problem combines constraints, which have not been managed all together in the literature as far as we know. A meta-heuristic solution approach is proposed. Furthermore, this optimization tool has been inserted into the fleet management system of the company. Computational experiments over instances based on the real ones are carried out in this paper. Moreover, some preliminary experiments performed with the fleet management system are quite promising. The static part of the problem has already been successfully tested with other companies. The current state of this real-world application is the on-line communication between the fleet management system and the courier service company. Therefore, the last phase of the whole system is the combination of the solver proposed in this paper with the rest of the system, which will be performed in future works.

The rest of the paper is organized as follows. Section 2 is devoted to thoroughly describe the real-world problem posed to the authors by the company. Section 3 summarizes the metaheuristic procedure developed to solve the problem at hand. Section 4 reports the computational experiments performed in this work. Finally, the conclusions are given in Section 5.

## 2 Problem Description

The real-world VRPTW tackled in this paper is defined by means of a network that contains the depot and a set of  $N$  customer nodes,  $C$ , which represent the requests characterized by their type (static or dynamic), demand, location, arrival time,  $at_i$  and time window,  $[e_i, l_i]$ , which might not be unique. As indicated above customers can have several time windows during the day. The depot has an associated time window,  $[e_0, l_0]$ , and a set of  $K$  heterogeneous vehicles  $V = \{v_1, \dots, v_K\}$  with different capacities  $VC = \{vc_1, \dots, vc_K\}$ , driving to a Heterogeneous Fleet VRPTW (HFVRPTW). Moreover, associated with each vehicle,  $k$ , there are one or more time windows  $[ev_k, lv_k]$  that represent its working shift and that can be different from one vehicle to another.



As mentioned in the introduction, in the particular application of the courier service company considered in this paper, all delivery requests and a percentage of the pick-up requests are known at the beginning of the planning horizon. Therefore, these customers are considered to be static. The remaining pick-up requests, which are known over the day, are considered to be dynamic and an arrival time  $at_i \in [e_0, l_0]$  is associated to the dynamic customer  $i$ . Thus, a Dynamic HFVRPTW is being taken into consideration. At this point, it is worth mentioning that the company does not allow exchanging delivery packages between vehicles due to operational purposes. If it were permitted, vehicles would have to meet in some intermediate point and devote time to carry out the exchange. Therefore, the static customers (deliveries and pick-ups) that are routed at the beginning of the planning horizon do not change their assigned route. Finally, the dynamic customers have then to be assigned to any of the existing routes while guaranteeing feasibility. The so obtained problem is referred to as Restricted Dynamic HFVRPTW (RDHFVRPTW) in this paper.

The objective function associated to the problem has not yet been established. An additional feature required by the company is the presence of multiple objective functions that have to be taken into consideration in the optimization phase. The total traveled distance, time balance, infeasibility and cost are used as it will be explained in the next section. The first objective function measures the total distance traveled by all the vehicles involved in the solution. The time balance function is stated as the time difference between the largest route and the shortest route regarding time. The infeasibility function reports the sum of time infeasibilities at each customer, i.e., the sum of the differences between the arrival time which exceeds the time window of a customer, and the upper limit of this customer's time window. Finally, the cost function indicates the fuel consumption.

In order to measure the dynamism of a given problem instance, Lund et al. [6] defined the *degree of dynamism* of the system as follows:

$$\delta = \frac{|C_D|}{N} \times 100,$$

where  $|C_D|$  indicates the number of dynamic customers. Moreover, since the disclosure time of requests is also important, Larsen [5] defined the *reaction time* of customer  $i$ , that measures the difference between the arrival time,  $at_i$ , and the end of the corresponding time window,  $l_i$ . Notice that longer reaction times indicate that there is more flexibility to insert any new request into the existing routes. Therefore, the effective degree of dynamism provided by Larsen is stated as follows:

$$\delta_{TW}^e = \frac{1}{N} \sum_{i \in C} \left( 1 - \frac{l_i - at_i}{T} \right),$$

where  $T$  is the length of the planning horizon. These measures will be used in the computational experience section to generate the set of problem instances used in this work.

### 3 Metaheuristic Solution Approach

The solution method proposed in this work to solve the RDHFVRPTW is summarized in Algorithm 1, which will be now thoroughly described. First of all, an initial solution consisting of all the static customers is generated by using the Solomon Heuristic [11]. The obtained solution is then improved running a Variable Neighborhood Search algorithm proposed in [2] to solve the static problem with all the constraints required by the company for which this dynamic problem has also to be solved. This process (lines 3 – 4) is iterated for a certain number of iterations and the best reached solution is selected to be implemented by the company. In this step, all the requests known at the beginning of the planning horizon are already inserted in a route. As indicated above, these requests are not allowed to change their route assignments.

---

#### Algorithm 1. General Algorithm

---

```

// Create solution  $S^*$  containing all static customers
1 Initialize solution  $S^*$ ;
2 while (a maximum number of iterations is not reached) do
3    $S \leftarrow$  Run Solomon Heuristic;
4    $S' \leftarrow$  Apply the VNS proposed by De Armas et al. [2] to  $S$ ;
5   if ( $S'$  is better than  $S^*$ ) then
6      $S^* \leftarrow S'$ ;

// Insert dynamic customers at their arrival times
7 while (a new dynamic customer,  $i$ , appears) do
8   Try to insert  $i$  in the closest feasible existing route,  $r$  if it exists;
9   if (route  $r$  does not exist) then
10    if (extra hours are allowed) then
11      Insert customer  $i$  in a route without any accumulated infeasibility
12      taking into account the different objective functions;
13    else
14      if (the priority of customer  $i$  allows it) then
15        Postpone customer  $i$  until the next day;
16      else if (there is an alternative permitted customer  $j$  that let the
17      insertion of  $i$ ) then
18        Postpone customer  $j$ ;
19      else
20        Insert customer  $i$  in the route that supposes the smallest
21        infeasibility (if it coincides among routes, consider the remaining
22        objective functions);
23  Report infeasibility to the company;

```

---

Once the selected initial solution is being implemented, new dynamic customers might be revealed over the planning horizon, which have to be inserted

in any existing route. Let us suppose that the dynamic customer  $i$  arrives at time  $at_i$ . As reported in line 8, the algorithm first tries to insert  $i$  in the closest possible feasible existing route. For each of these routes, from the last visited customer to the last customer in the route, it is searched the feasible insertion point either with the least distance or time balance increment. The company is interested in either minimizing the total distance and the number of routes or minimizing the time balance if all the available vehicles are used (stopping available vehicles is not desirable). If there were ties, the remaining objective functions are hierarchically evaluated. In this case, after the distance objective or time balance and cost are considered.

If the previous option is not feasible and no feasible alternative is available for customer  $i$ , then there are two options. On one hand, in case that extra hours are allowed for the vehicles (lines 10 – 11), violating their time window constraints, customer  $i$  is tried to be inserted in a route using time window infeasibility as the objective function guiding the search. If there were ties, distance, time balance and cost, are hierarchically taken into consideration. On the other hand, if extra hours are not permitted by the company, then the notion of request priority shows up. If customer  $i$  has a low priority, then it can be postponed until the following day (lines 13 – 14). If it is not possible, but there is a customer  $j$  that can be postponed allowing the insertion of  $i$  (lines 13 – 14), then customer  $j$  is postponed, while  $i$  is inserted. In order to select customer  $i$ , the objective functions are hierarchically evaluated in the following order: number of postponed requests, extra hours, distance or time balance and cost.

If all the previous attempts have failed, customer  $i$  is inserted in the route with the least increment of the following objective functions (lines 17 – 18): infeasibility, distance or time balance and cost. Finally, there are two cases in which customer  $i$  cannot be inserted in the current solution: vehicle capacities are violated or there is not any vehicle with a working shift long enough to insert the new customer. In these two cases, the corresponding infeasibility is reported to the company (line 19).

## 4 Discussion and Future Research

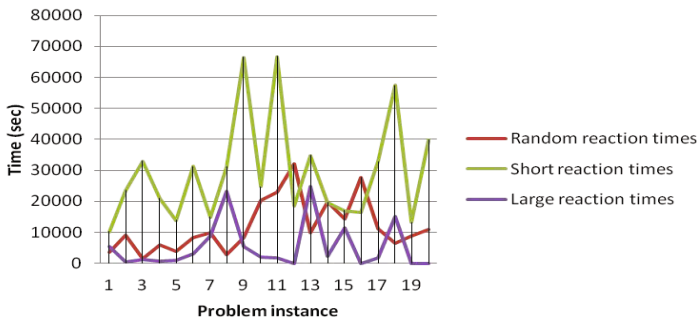
This section is devoted to analyze the performance of the algorithm proposed in this work. Despite the fact that experiments within the real system have to be carried out, the goals of the reported experiments are both to corroborate the good behavior of the method and discuss the effect of the input data over the total reached infeasibility. With these goals in mind, it has been created a set of instances based on the real data provided by a company in the Canary Islands, taking into account the features of the courier service company. A total of 20 different instances consisting of 100 customers, from which the 20% are dynamic, have been generated. In order to obtain instances with a wide range of effective dynamism degrees, random, short and large reaction times have been considered. Moreover, the standard Solomon instances are used to compare the results given by our algorithm with the best known solutions from the literature.

The first experiment reported in this section corresponds to the comparison over the standard Solomon instances. Note that the algorithm proposed in this work is thought to solve dynamic problems with the inclusion of all the real-world constraints explained in previous section. Therefore, the method is not supposed to be the most competitive over these instances, particularly due to the fact that real instances have different features. Table 1 summarizes the comparative, in which average values of number of vehicles ( $NV$ ) and traveled distance ( $TD$ ) are reported. The first column of the table shows the instance categories corresponding to the Solomon instances. Note that in the worst case, the deviation is about 5%.

**Table 1.** Computational results of the standard static Solomon instances

	$NV$	$TD$	$BestNV$	$BestTD$
$C1$	10.00	835.88	10.00	828.38
$C2$	3.12	621.01	3.00	589.90
$R1$	14.08	1252.41	11.91	1203.16
$R2$	5.00	988.26	3.00	941.87
$RC1$	13.62	1402.50	12.00	1345.56
$RC2$	6.00	1127.62	3.62	1111.99

The second experiment reported in this work is summarized in Figure 1. It shows, for each problem instance, the total infeasibility accumulated at the end of the execution when random, short and large reaction times are considered. It is noticeable that there is a clear difference between short and large reaction times. Let us remind that the reaction time of a customer provides the difference between the end of its time window and its arrival time. Longer reaction times lead to a more insertion flexibility and therefore to less infeasibility. As indicated in Figure 1, this expected behavior is obtained by our solution method.



**Fig. 1.** Total infeasibility for different reaction times

**Table 2.** Dynamic customers

Dynamic Request	81	82	83	84	85	86	87	88	89	90
Arrival Time	14105	27790	19617	14111	9494	21474	31747	19119	17287	30821
Dynamic Request	91	92	93	94	95	96	97	98	99	100
Arrival Time	21811	21064	14527	15419	19106	20479	7725	25892	12850	15807

**Table 3.** Solution example. Insertion of dynamic requests

	<i>R1</i>	<i>R2</i>	<i>R3</i>	<i>R4</i>	<i>R5</i>	<i>R6</i>	<i>R1</i>	<i>R2</i>	<i>R3</i>	<i>R4</i>	<i>R5</i>	<i>R6</i>
Last visited customer	4	5	4	5	4	3	5	6	5	6	5	3
Accumulated infeasibility	0	0	0	0	0	0	0	0	0	0	0	0
	<i>(C97,R5,5,0)</i>						<i>(C85,R3,8,2060)</i>					
Last visited customer	7	8	6	9	7	3	8	9	7	9	8	3
Accumulated infeasibility	0	0	2060	0	0	0	0	0	2060	0	1751	0
	<i>(C99,R5,10,1751)</i>						<i>(C81,R4,16,0)</i>					
Last visited customer	8	9	7	9	8	3	8	9	7	10	8	3
Accumulated infeasibility	0	0	2060	0	1751	0	0	0	2060	0	1751	0
	<i>(C84,R7,17,0)</i>						<i>(C93,R4,13,3103)</i>					
Last visited customer	8	9	7	10	8	3	9	9	7	10	8	3
Accumulated infeasibility	0	0	2060	3103	1751	0	1475	0	2060	3103	1751	0
	<i>(C94,R1,11,1475)</i>						<i>(C100,R3,11,5425)</i>					
Last visited customer	10	11	8	11	9	3	11	12	9	12	10	3
Accumulated infeasibility	1475	0	5425	3103	1751	0	1475	0	5425	3103	1751	0
	<i>(C89,R5,12,1751)</i>						<i>(C95,R2,19,2211)</i>					
Last visited customer	11	12	9	12	10	3	12	13	9	12	10	3
Accumulated infeasibility	1475	2211	5425	3103	1751	0	1475	2211	5425	3103	3592	0
	<i>(C88,R5,13,3592)</i>						<i>(C83,R5,13,1751)</i>					
Last visited customer	13	13	10	12	11	3	14	13	10	13	11	3
Accumulated infeasibility	1475	2211	5425	3103	1751	0	1475	2211	5425	3103	3153	0
	<i>(C96,R5,14,3153)</i>						<i>(C92,R1,20,2945)</i>					
Last visited customer	14	13	11	13	11	3	14	13	11	13	11	3
Accumulated infeasibility	2945	2211	5425	3103	3153	0	3776	2211	5425	3103	3153	0
	<i>(C86,R1,21,3776)</i>						<i>(C91,R3,12,5425)</i>					
Last visited customer	17	16	11	13	14	3	19	17	12	14	14	3
Accumulated infeasibility	3776	2211	5425	3103	3153	0	3776	4814	5425	3103	3153	0
	<i>(C98,R2,20,4814)</i>						<i>(C82,R4,15,8586)</i>					
Last visited customer	21	18	12	15	16	3	22	19	13	15	16	3
Accumulated infeasibility	3776	4814	5425	8586	3153	0	3776	4814	5425	8586	8332	0
	<i>(C90,R5,17,8332)</i>						<i>(C87,R5,17,8612)</i>					

### 4.1 Example Solution

In this section, a solution example corresponding to a problem instance with short reaction times is provided. The initial static solution is 0 – 15 – 73 – 17 – 16 – 40 – 5 – 72 – 51 – 67 – 37 – 47 – 78 – 68 – 25 – 9 – 13 – 27 – 45 – 8 – 39 –

53 – 34 – 0 – 11 – 54 – 29 – 70 – 55 – 22 – 42 – 38 – 36 – 79 – 43 – 10 – 57 – 48 – 1 – 75 – 74 – 26 – 18 – 65 – 0 – 32 – 71 – 21 – 76 – 60 – 44 – 80 – 56 – 61 – 0 – 52 – 64 – 23 – 58 – 12 – 7 – 49 – 31 – 20 – 28 – 69 – 33 – 3 – 19 – 62 – 0 – 46 – 14 – 4 – 24 – 77 – 35 – 66 – 6 – 30 – 59 – 41 – 2 – 0 – 63 – 50 – 0, where routes  $R1$  to  $R6$  are separated by zeros. The dynamic customers go from  $C81$  up to  $C100$ , and their arrival times in seconds are shown in Table 2. Table 3 reports how the dynamic customers are inserted indicating if they incur in any infeasibility. In this table, as an example, vector  $(C85, R3, 8, 2060)$  indicates that customer  $C85$  is inserted into route  $R3$  in position 8 leading to an infeasibility value in time equal to 2060. The dynamic customers are selected according to their arrival times to be inserted into the current solution. Firstly, customer  $C97$  is taken into consideration and the best position into every route is calculated. In this case,  $C97$  is inserted in position 5 of route  $R5$  because it produces the least traveled distance increment. Then, customer  $C85$  arrives and has to be served in any of the routes. The best option corresponds to position 8 of route  $R3$ , reaching a total infeasibility value of 2060. The remainder customers are then selected and inserted as indicated in Table 3. For those readers interested in replicating the experiment, the instance used in this section can be downloaded from <https://sites.google.com/site/gciports/vrptw/dynamic-vrptw>.

## 5 Conclusions

This work tackles a variant of a Dynamic VRPTW, which handles all the real-world constraints required by a courier service company. The problem combines constraints, which have not been managed all together in the literature, as far as we know. A metaheuristic solution approach is proposed for solving the problem at hand. It is worth mentioning that this optimization tool has been inserted into the fleet management system owned by the company, who is the technical support of the previous one and the nexus with our research. The computational experience carried out in this work over a set of generated instances based on the real ones, has a twofold goal, corroborating the good behavior of the method and discussing the effect of the input data over the total reached infeasibility. Moreover, preliminary experiments that have been performed with the fleet management system are quite promising. The current state of this real-world application is to set up the on-line communication between the fleet management system and the courier service company, which is being correct. Therefore, the last phase of the whole system is the combination of the solver proposed in this paper with the rest of the system, which constitutes future research.

## References

1. Chen, Z.L., Xu, H.: Dynamic column generation for dynamic vehicle routing with time windows. *Transportation Science* 40(1), 74–88 (2006)
2. De Armas, J., Melián-Batista, B., Moreno-Pérez, J.A., Brito, J.: Real-World Heterogeneous Fleet Vehicle Routing Problem with Soft Time Windows. Under review (2013)

3. Hong, L.: An improved LNS algorithm for real-time vehicle routing problem with time windows. *Computers & Operations Research* 39(2), 151–163 (2012)
4. Khouadjia, M.R., Sarasola, B., Alba, E., Jourdan, L., Talbi, E.G.: A comparative study between dynamic adapted PSO and VNS for the vehicle routing problem with dynamic requests. *Applied Soft Computing* 12(4), 1426–1439 (2012)
5. Larsen, A.: *The Dynamic Vehicle Routing Problem*, PhD Thesis (2001)
6. Lund, K., Madsen, O.B.G., Rygaard, J.M.: Vehicle routing problems with varying degrees of dynamism. Technical Report. IMM Institute of Mathematical Modelling (1996)
7. Montemanni, R., Gambardella, L.M., Rizzoli, A.E., Donati, A.: Ant colony system for a dynamic vehicle routing problem. *Journal of Combinatorial Optimization* 10(4), 327–343 (2005)
8. Pillac, V., Gendreau, M., Gueret, C., Medaglia, A.L.: A review of dynamic vehicle routing problems. *European Journal of Operational Research* 225(1), 1–11 (2013)
9. Psaraftis, H.N.: A Dynamic-programming solution to the single vehicle many-to-many immediate request dial-a-ride problem. *Transportation Science* 14(2), 130–154 (1980)
10. Rizzoli, A.E., Montemanni, R., Lucibello, E., Gambardella, L.M.: Ant colony optimization for real-world vehicle routing problems. *Swarm Intelligence* 1, 135–151 (2007)
11. Solomon, M.M.: Algorithms for the Vehicle-Routing and Scheduling Problems with Time Window Constraints. *Operations Research* 35(2), 254–265 (1987)

# Effect of the Initial Solutions to Balance Routes in Vehicle Routing Problem with Time Windows

Alondra De Santiago, Belén Melián-Batista<sup>1</sup>,  
Ada Álvarez<sup>2</sup>, and Francisco AngelBello<sup>3</sup>

<sup>1</sup> ETS de Ingeniería Informática  
Universidad de La Laguna, España  
alondra.de.santiago.19@ull.edu.es, bmelian@ull.es

<sup>2</sup> Universidad Autónoma de Nuevo León, México  
Facultad de Ingeniería Mecánica y Eléctrica  
ada.alvarezs@uanl.mx

<sup>3</sup> Tecnológico de Monterrey  
Campus Monterrey, México  
fangel@itesm.mx

**Abstract.** This work is motivated by a real problem posed to the authors by a company in Tenerife, Spain. Given a set of service orders, daily routes have to be designed in order to minimize the total traveled distance while balancing the workload of drivers in terms of required time. A bi-objective mixed-integer linear model for the problem is formulated and a solution approach, based on metaheuristics, is proposed. One of the main handicaps associated to this approach is the fact that it is very time consuming for non-standard literature instances, mainly due to the initial solution generation method. Therefore, the goal of this work is to study the performance of three different ways to build the initial solutions and observe what is their impact on the approximations of the Pareto Front for Solomon instances of 100 customers. Results obtained on a real instance are also discussed.

**Keywords:** VRP with time windows, metaheuristics, bi-objective problem, initial solutions.

## 1 Introduction

We study a bi-objective Vehicle Routing Problem with Time Windows (VRPTW) motivated by a real problem in the Canary Islands, Spain. It involves the design of daily routes from a central depot to a set of several geographically dispersed customers with known demands and predefined time windows, using a fleet of identical vehicles of known capacity. The service-time windows indicate the earliest and latest times for starting the service at each customer. Economic and social viewpoints stated by the company trigger the following two conflicting objectives: to minimize the total traveled distance and minimize the difference between the maximal and minimal route lengths regarding time. Recent approaches recognize the VRPTW as a multi-objective optimization problem.



For an overview, see [3], [4]. The main difficulty involved in solving this type of problems is the large computational cost, so that the last two decades have been characterized by the development of approximate solution methods. To the best of our knowledge, the two objectives tackled in this work have not been previously considered.

We provide an integer linear program to model the problem and an algorithm based on metaheuristics to solve it, both developed by the authors in [9]. Computational results obtained with this tools showed that the proposed method produces good approximations of the Pareto frontiers and yields significantly better results than those obtained by the tools currently applied by the company, both in quality and in the expended time for obtaining them. The goal of this paper is to analyze the effect of the initial solutions generated using three different algorithms in the final Pareto fronts.

## 2 Mathematical Formulation

In order to make this paper self-contained we briefly report the mathematical model used in the paper to obtain the Pareto fronts for small instances of 25 customers. The bi-objective VRPTW tackled in this paper can be modeled on a complete graph, whose nodes are the  $n$  customers plus the depot (denoted by 0). In the following,  $V = 0, 1, \dots, n$  denotes the set of indexes of the nodes and subset  $I$  denotes the set of indexes for the customers;  $d_i$  indicates the demand of customer  $i$ ;  $c_{ij}$  represents the cost for using arc  $(i, j)$ ;  $Q$  is the capacity of each vehicle;  $t_{ij}$  is the travel time from node  $i$  to node  $j$  using arc  $(i, j)$ ;  $s_i$  denotes the service time at customer  $i$ ; and  $a_i(b_i)$  denotes the earliest (latest) time instant for starting the service at customer  $i$ .

In the case of the depot,  $s_0 = 0$ ,  $a_0 = 0$ ,  $b_0 = T$ . Decision variables  $x_{ij}$  are binary. They are equal to 1 if arc  $(i, j)$  is used in any route, and 0 otherwise. Auxiliary variables  $e_i$  denote the instant at which the service starts at customer  $i$ ;  $u_i$  represents the accumulated demand serviced along a route after visiting customer  $i$ .

Mathematical models for classical VRPTW, which include constraints (1)–(6) below, may be found in the literature. Constraints (1) ensure that each customer is served by exactly one vehicle; (2) are the flow conservation equations; (3) and (4) concern to sub-tour elimination and vehicles capacity; (5) and (6) are time-windows constraints.

$$\sum_{\forall i \in V, i \neq j} x_{ij} = 1, \quad \forall j \in I \quad (1)$$

$$\sum_{\forall j \in V, j \neq i} x_{ij} - \sum_{\forall i \in V, i \neq j} x_{ji} = 0, \quad \forall i \in V \quad (2)$$

$$u_i - u_j + Qx_{ij} \leq Q - d_j, \quad \forall i, j \in I, i \neq j \quad (3)$$

$$d_i \leq u_i \leq Q, \quad \forall i \in I \quad (4)$$

$$a_i \leq e_i \leq b_i, \quad \forall i \in I \quad (5)$$

$$e_i - e_j + (b_i + s_i + t_{ij} - a_i)x_{ij} \leq b_i - a_j, \quad \forall i, j \in I, i \neq j \quad (6)$$

This set is completed with the following constraints:

$$x_{ij} \in \{0, 1\}, \forall i, j \in V, j \neq i \quad (7)$$

$$u_i \geq 0, e_i \geq 0, \quad \forall i \in I \quad (8)$$

They focus on minimizing the total traveled distance or number of routes. However, we are interested in the total length of the routes as well as in their balance regarding time. When time balance is also considered, constraints (6) do not guarantee that service starts as soon as possible, artificially lengthening routes. Let  $v_i$  denote the instant at which a vehicle arrives at customer  $i$ ;  $w_i$  the time a vehicle must wait before starting the service at customer  $i$  and  $r_{ij} = w_j$  if arc  $(i, j)$  is used, and 0 otherwise. Binary variables  $y_i$  will be equal to 1 if the vehicle arrives before the beginning of the time window for customer  $i$ , and 0 otherwise. Then, constraints (9) to (11) are required to compute the instant at which service starts at customer  $j$ , while constraints (12) to (15) are added to enforce the service to start as soon as possible.

$$e_i - e_j + (b_i + s_i + t_{ij} - a_j)x_{ij} + (b_i - s_j - t_{ji} - a_j)x_{ji} + r_{ij} - r_{ji} \leq b_i - a_j, \forall i, j \in I, j \neq i \quad (9)$$

$$e_i = v_i + \sum_{\forall j \in V, j \neq i} r_{ji}, \quad \forall i \in I \quad (10)$$

$$0 \leq r_{ij} \leq b_0 x_{ij}, \quad \forall i \in V, \forall j \in I \quad (11)$$

$$v_i + b_0 y_i \leq a_i + b_0, \quad \forall i \in I \quad (12)$$

$$v_i + b_0 y_i \geq a_i, \quad \forall i \in I \quad (13)$$

$$\sum_{\forall j \in V, j \neq i} r_{ji} - b_0 y_i \leq 0, \quad \forall i \in I \quad (14)$$

$$e_i - (b_i - a_i)y_i \leq b_i, \quad \forall i \in I \quad (15)$$

Constraints (16) and (17) ensure that service starts as soon as possible at the first customer visited in any route and (18) relate the time a vehicle reaches a customer with the time the vehicle leaves the preceding customer.

$$v_i \geq t_{0i}x_{0i}, \quad \forall i \in I \quad (16)$$

$$e_i \leq (t_{0i} - b_i)x_{0i} + r_{0i} + b_i, \quad \forall i \in I \quad (17)$$

$$e_i - v_j + (b_0 + s_i + t_{ij})x_{ij} \leq b_0, \forall i, j \in I, i \neq j \quad (18)$$

To compute the longest (shortest) route, (19) and (20) are required.

$$L_{max} \geq e_i + s_i + t_{i0}x_{i0}, \forall i \in I \quad (19)$$

$$L_{min} \leq e_i + s_i + t_{i0}x_{i0} + (1 - x_{i0})b_0, \forall i \in I \quad (20)$$

Then, the mathematical model[9] proposed in this paper is stated as follows:

$$\begin{aligned} & \min(z_1, z_2), \\ \text{where } z_1 &= \sum_{i \in V} \sum_{j \in V, j \neq i} c_{ij}x_{ij} \text{ and } z_2 = L_{max} - L_{min}, \\ & \text{s.t. (1) to (20)} \end{aligned}$$

### 3 Solution Approach

Multi-objective programming techniques focus on finding the set of efficient points or, in the case of heuristic procedures, an approximation of the efficient set. In order to solve the combinatorial optimization problem tackled in this paper, we propose a Scatter Search (*SS*) based metaheuristic algorithm that borrows ideas proposed by Molina et al. [5] for non-linear multi-objective optimization. *SS* is a population based method that uses a set of high quality and disperse solutions (*RefSet*) to create new ones. The neighborhood structure used in the local searches is defined by removing a customer from one route and re-inserting it in a different one. The objective functions guiding the search are the total traveled distance (*Distance*), the time balance (*TimeBalance*) and a combination of both objectives (*Compromise*). An outline of the algorithm is shown in Algorithm 1.

---

#### Algorithm 1. General *SS* Algorithm

---

```

while ( $|Pop| < PopSize$  or  $iter < Max\_Iter$ ) do
   $S \leftarrow$  Feasible solution created by the H1_Solomon, Beasley or Potvin
  algorithm;
   $S^1 \leftarrow LocalSearchDistance(S)$ ;
   $S^2 \leftarrow LocalSearchTimeBalance(S^1)$ ;
   $S^3 \leftarrow LocalSearchDistance(S^2)$ ;
   $S^4 \leftarrow LocalSearchCompromise(S^3)$ ;
  while (no new solutions in EfficientSet or  $iter2 < Max\_iter2$ ) do
    Generate or Update the EfficientSet;
    Generate RefSet, such that  $|RefSet| = 20$ ;
    Apply the combination process;
    Run LocalSearchCompromise over the obtained solutions;
    Update RefSet;

```

---

Where *Max\_iter* and *Max\_iter2* are given parameters.

#### 3.1 Create Initial Solutions

In this step we create an initial population (*Pop*) with *PopSize* solutions using three different algorithms: the Solomon sequential heuristic I1 [7], the Route–first cluster–second algorithm proposed by Beasley[1] and the parallel route building algorithm proposed by Potvin and Rousseau [8] with some modifications. Since the resolution of the VRPTW is very time consuming, the rationale behind this contribution is finding the fastest initial algorithm that does not deteriorate the solution quality.

In the Solomon Heuristic I1, routes are created one at a time. A route is initialized with a seed customer, using two criteria, the farthest unrouted customer,

**Table 1.** Coverage Measures comparing the Real Solution and *PR*

	<i>NofPoints PR</i>	
<i>PF</i>	4.89	0.94
	1.69	0.09
<i>PR</i>	12.25	0.93
	7.9	0.09

	<i>PF PR</i>	
<i>PF</i>	0	0.42
<i>PR</i>	0.23	0

Coverage of two sets

and the unrouted customer with the earliest deadline. The remaining unrouted customers are added to this route until the time windows and/or capacity constraint is reached. If unrouted customers remain, the initialization and insertion procedures are then repeated until all customers are serviced.

In the route–first cluster–second algorithm, as the name suggests, we first need to construct a TSP tour over all customers and then choose an arbitrary orientation of the TSP, partition the tour according to capacity and time windows constraints, finally solve a shortest path problem.

The third algorithm by Potvin and Rousseau, builds routes in parallel rather than one at a time, selecting the next customer to be inserted based on a generalized regret measure over all routes. In the initialization phase of this procedure, a set of  $n_r$  routes is initialized at once, and the remaining customers are then inserted into any of those routes. One difficulty with this parallel strategy is to decide what the initial number of routes,  $n_r$ , should be. Potvin and Rousseau [8] estimate  $n_r$  by applying the sequential algorithm of Solomon [7] only once, and select as customers seed for each parallel route, the farthest customer from the depot in each one of the routes generated by the sequential algorithm of Solomon.

## 4 Computational Experiments

Computational tests were conducted on a processor Intel Core with a 3.404 GHz and 4 GB RAM, under Ubuntu. We used instances with 50 and 100 customers from the standard Solomon VRPTW benchmark. To assess the quality of the approximate fronts produced by our method, they were compared with optimal fronts obtained by the developed model and the weighted-sum method [2]. Eleven combinations of the objective functions  $z_1$  (distance) and  $z_2$  (time balance) were considered:  $z = \alpha_1 z_1 + \alpha_2 z_2$ , where  $\alpha_1$  and  $\alpha_2$  range from 0 up to 1 with increments of 0.1. Optimal solutions were found using the Cplex 11.1 with a maximum time of 2 hours each combination. We used instances with 25 customers from the standard Solomon VRPTW benchmark for this purpose and Table 1 summarizes the obtained results, and show for example that *PR* finds efficient fronts with a larger number of points and coverage measure shows that this algorithm dominates the exact model.

Due to space restrictions, results are averaged over all instances. Table 2 shows the comparison between the three algorithms for generating the initial solutions,

**Table 2.** Average of *Nofpoints* and *SSC*

	50customers		100customers	
	<i>NofPoints</i>	<i>SSC</i>	<i>NofPoints</i>	<i>SSC</i>
<i>SolH</i>	15.982	0.909	20.304	0.897
	5.061	0.049	6.548	0.050
<i>Beasley</i>	23.929	0.879	23.929	0.879
	8.596	0.091	8.596	0.091
<i>PR</i>	16.196	0.903	16.804	0.868
	6.895	0.060	8.737	0.102

**Table 3.** Coverage measure for all test problems

	50customers			100customers		
	<i>SolH</i>	<i>Beasley</i>	<i>PR</i>	<i>SolH</i>	<i>Beasley</i>	<i>PR</i>
<i>SolH</i>	0.00	0.62	0.48	0	0.498	0.492
<i>Beasley</i>	0.28	0.00	0.31	0.44	0	0.439
<i>PR</i>	0.39	0.60	0.00	0.351	0.45	0

**Table 4.** Average of Best Distance Solution comparing *SolH1*, *Beasley* and *PR*

	50customers		100customers	
	<i>D</i>	<i>CPU</i>	<i>D</i>	<i>CPU(time)</i>
<i>SolH1</i>	628.79	58.14	1088.63	380.26
<i>Beasley</i>	655.34	545.90	1087.68	1329.05
<i>PR</i>	628.55	248.86	1084.77	358.8

**Table 5.** Real instance results

<i>SolH</i>		<i>Beasley</i>		<i>Potvin</i>		Company solution	
<i>D</i>	<i>TB</i>	<i>D</i>	<i>TB</i>	<i>D</i>	<i>TB</i>	<i>D</i>	<i>TB</i>
838.6	10320	820.4	7260	818.3	8160	1247.3	14040

Solomon Heuristic [7], *SolH1*, route–first cluster–second [1], *FRSC*, and Potvin and Rosseau [8], *PR*, using the metrics [2] *number of points* (*NofPoints*), *size of the space covered* (*SSC*) and Table 3 shows the *coverage of two sets*. Table 4 reports the average of the best distance values (*D*) and *CPU* times yielded by solutions of the approximate fronts obtained by each methodology. The results show that *SolH* is capable of finding a larger number of points of the approximation of the efficient front and the  $C(SolH, *)$  metric, confirms that *SolH* obtains efficient fronts with better non-dominated solutions and the *CPU* time required is one of the smaller.

Table 5 shows the value of each objective obtained by the proposed methodology and the company solution.

To conclude, the experimental results suggest that the best alternative to construct the initial solutions for the scatter search algorithm is applying the Solomon sequential heuristic II[7].

## 5 Conclusions

The VRPTW is a highly constrained problem. Time windows constraints make it difficult to solve, requiring a meticulous design of heuristics to obtain high quality solutions. This situation becomes more critical when more than one criterion is involved, leading to time consuming algorithms. This is particularly problematic when a real-world problem has to be solved. The goal of this work is to analyze the effect of the initial solution generation method in the final Pareto fronts and in the computational times. The algorithm used to solve the problem is based on the scatter search metaheuristic, which was tested using the three considered initial solutions. In order to make the paper self-contained, a mathematical model for the bi-objective VRPTW motivated by a real problem is also shown. Computational experiments show the influence that we have when applying different methods for constructing the initial solutions. Finally, our results outperform the company solution for the real data.

**Acknowledgments.** This work has been partially funded by the Spanish Ministry of Economy and Competitiveness (project TIN2012-32608) and the Spanish Ministry of Industry, Tourism and Trade (project TSI-020100-2011-298). Alondra De Santiago thanks Conacyt the financial support for her post-graduate grant.

## References

1. Beasley, J.E.: Route First-Cluster Second Methods for Vehicle Routing. *Omega* 1, 403–408 (1983)
2. Coello Coello, C., Van Veldhuizen, D.A., Lamont, G.B.: *Evolutionary algorithms for solving multiobjective problems*. Kluwer, New York (2002)
3. Jozefowicz, N., Semet, F., Talbi, E.G.: Multi-objective vehicle routing problems. *European Journal of Operational Research* 189(2), 293–309 (2008)
4. Kumar, S.N., Panneerselvam, R.: A Survey on the Vehicle Routing Problem and Its Variants. *Intelligent Information Management* 4(3), 66–74 (2012)
5. Molina, J., Laguna, M., Mart, R., Caballero, R.: SSPMO: A Scatter Tabu Search Procedure for Non-linear Multiobjective Optimization. *INFORMS Journal on Computing* 19(1), 91–100 (2007)
6. Ngueveu, S.U., Prins, C., Wolfler-Calvo, R.: An effective memetic algorithm for the cumulative capacitated vehicle routing problem. *Computers & Operations Research* 37, 1877–1885 (2010)
7. Solomon, M.M.: Algorithms for the Vehicle-Routing and Scheduling Problems with Time Window Constraints. *Operations Research* 35(2), 254–265 (1987)
8. Potvin, J.Y., Rousseau, J.M.: A Parallel Route Building Algorithm for the Vehicle-Routing and Scheduling Problem with Time Windows. *European Journal of Operational Research* 66(3), 331–340 (1993)
9. Melián, B., De Santiago, A., AngelBello, F., Álvarez, A.: A Bi-objective Vehicle Routing Problem with Time Windows: a real case in Tenerife. *Under Second Review in a Journal* (2012)

# An Ant System Algorithm for the Neutralization Problem<sup>\*</sup>

Ramazan Algin<sup>1</sup>, Ali Fuat Alkaya<sup>1</sup>, Vural Aksakalli<sup>2</sup>, and Dindar Öz<sup>1</sup>

<sup>1</sup> Marmara University, Department of Computer Engineering, Istanbul, Turkey

<sup>2</sup> Istanbul Sehir University, Department of Industrial Engineering, Istanbul, Turkey  
{algin.ramazan,ozdindar}@gmail.com, falkaya@marmara.edu.tr,  
aksakalli@sehir.edu.tr

**Abstract.** We consider a path planning problem wherein an agent needs to safely and swiftly navigate from a given source location to a destination through an arrangement of disk-shaped obstacles. The agent possesses a limited neutralization capability in the sense that it can neutralize a certain number of obstacles enroute and pass through them safely upon neutralization. Optimal utilization of such a capability is called the neutralization problem. This problem is essentially a shortest path problem with resource constraints, which has been shown to be NP-Hard except for some trivial variants. In this study, we propose an ant system algorithm for the neutralization problem. In the proposed algorithm, the state transition rule makes use of certain problem-specific information to guide the ants. We show how the parameters of the algorithm can be fine-tuned for enhanced performance and we present limited computational experiments including a real-world naval minefield dataset. Our experiments suggest that the proposed algorithm finds high quality solutions in general with reasonable computational resources.

**Keywords:** ant system, path planning, metaheuristics, optimization.

## 1 Introduction

In this study, we tackle a path planning problem where the goal is to safely and swiftly navigate an agent from a given source location to a destination through an arrangement of disk-shaped obstacles in the plane. The agent is given a neutralization capability with which the agent can safely traverse through the disc after neutralizing it for a cost added to its traversal length. However, number of allowed neutralizations is limited, say by  $K$ , due to a particular reason such as the payload capacity of the agent or vehicle. The central issue here is how to direct the agent to optimally utilize this neutralization capability. This problem is called as the neutralization problem [1] which is NP-Hard.

Ant colony optimization (ACO) [2] is one of the most commonly used metaheuristics to solve path planning problems. The ACO is an umbrella concept that

---

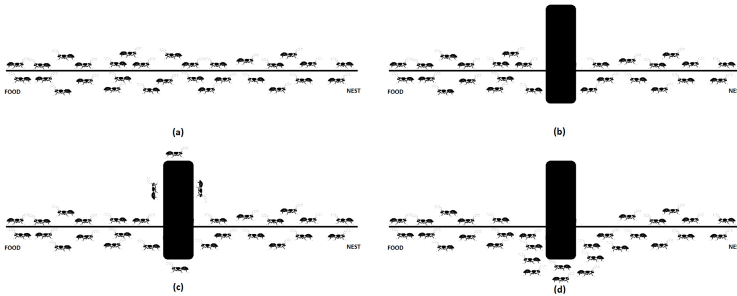
<sup>\*</sup> This work is supported by Marmara University Scientific Research Committee under the project ID FEN-D-100413-0135.

has some variations including ant system (AS) [3], ant colony system (ACS) [3], elitist ant system [4], max-min ant system (MMAS) [5] and some more [2]. The neutralization problem is also a path planning problem and the purpose of this study is to utilize the AS to solve this problem.

The rest of this paper is organized as follows. Section 2 presents an overview of the AS. Section 3 gives the definition of the neutralization problem. In Section 4, we describe our AS algorithm and how it is applied to solve the neutralization problem. Section 5 reports the results of experiments and their discussion. Section 6 concludes the paper with some future work.

## 2 Ant System

Ant system (AS) algorithm was first introduced by Marco Dorigo in 1992 and applied for solving the Travelling Salesman Problem (TSP) [4,6]. The AS is inspired by real ants life. In real life, ants can find the shortest path between their nest and food with the help of the pheromone [3]. Pheromone is a kind of chemical that is used by some kind of animals in different ways. Ants use it to communicate each other while finding the shortest path between the nest and the food. When an ant passes from a path, it lays some pheromone on this path which causes this path to become more desirable by other ants. At the same time, there is pheromone evaporation on all paths. Then paths which are not selected by ants become less desirable because of the pheromone evaporation. For a better understanding, consider the example given in Fig. 1.



**Fig. 1.** (a) Ants are walking between food and nest without any obstacles on their path. (b) An obstacle occurs. (c) About half of the ants choose the upper path, the other half chooses the lower path. (d) Since ants walking on the shorter lower path reach the other side more quickly, more pheromone accumulates on the shorter path. Consequently, more and more ants start to choose this lower path over time.

The AS algorithm can easily be explained by considering the TSP as the tackled problem. Consider a graph  $(V, E)$  where  $V$  represents the set of cities and  $E$  is the set of edges between cities. In this graph, edges have travelling



costs ( $\delta$ ). In addition to the travelling costs of edges, the AS algorithm needs to use the desirability value ( $\tau$ ) for each edge. The desirability in the algorithm is analogous to the pheromone in the real life and they will be used interchangeably through this manuscript. Different from the constant travelling costs of edges, the level of pheromone on each edge changes during execution of the algorithm based on the ants edge preferences. The goal of the TSP is finding the minimum closed tour length by visiting the each city only once [4].

In the implementation of the AS algorithm for TSP, each ant is initialized and then placed on the cities randomly (there must be at least one ant at each city). The edges are initialized to a predetermined initial pheromone level ( $\tau_0$ ). Then, the ants start their tours. Each ant tries to complete its tour by choosing the next city, if it is not visited before, according to the state transition rule. The state transition rule assigns probabilities based on the pheromone level and travelling cost to the edges. When all ants complete their tours global update rule is applied to all edges. By applying the global update rule, the level of pheromone on edge which is selected by ants increases and also at the same time pheromone evaporation occurs on all edges. The edges which are not selected by ants lose pheromone quickly and have less desirability, which means that the probability for being selected by other ants decrease.

State transition rule is applied according to the formula given by (1). This formula gives the probability of ant  $k$  that wants to go from city  $a$  to city  $b$ .

$$p_k(a, b) = \begin{cases} \frac{[\tau(a, b)] \cdot [1/\delta(a, b)]^\beta}{\sum_{u \in J_k(a)} [\tau(a, u)] \cdot [1/\delta(a, u)]^\beta} & \text{if } b \in J_k(a) \\ 0, & \text{otherwise} \end{cases} \quad (1)$$

where  $\tau$  is the pheromone,  $\delta(a, b)$  is the cost of edge that is between city  $a$  and city  $b$ .  $\beta$  is a parameter which determines the relative importance of pheromone versus distance ( $\beta > 0$ ).  $J_k(a)$  is a set that keeps the unvisited cities. In (1), by multiplying the  $\tau(a, b)$  and the heuristic value  $1/\delta(a, b)$ , the edges which have shorter length get higher pheromone.

When all ants complete their tours, global update rule is applied to all edges according to the formula given in (2).

$$\tau(a, b) = (1 - \alpha) \cdot \tau(a, b) + \sum_{k=1}^m \Delta\tau_k(a, b) \quad (2)$$

$$\text{where} \quad \Delta\tau_k = \begin{cases} \frac{1}{L_k}, & \text{if } (a, b) \in \text{tour done by ant } k \\ 0, & \text{otherwise} \end{cases}$$

$\alpha$  is pheromone decay parameter between 0 and 1,  $m$  is the number of ants and  $L_k$  is tour length performed by ant  $k$ .

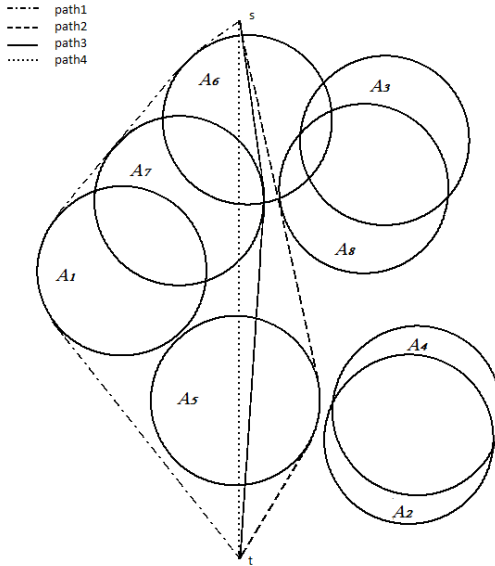
In the next section, definition of the neutralization problem will be given.

### 3 The Neutralization Problem

Neutralization problem instance is a tuple  $(s, t, \mathcal{A}, c, K)$ , where  $s$  is start point and  $t$  is terminal point in  $\mathbb{R}^2$ ,  $\mathcal{A}$  is a finite set of open discs in  $\mathbb{R}^2$ ,  $c$  is a cost

function  $\mathbb{R}_{\geq 0}$ , and  $K$  is a given constant in  $\mathbb{R}_{\geq 0}$ . In this problem we have an agent that wants to go from  $s$  to  $t$ . This agent cannot enter the discs unless he/she has an option to neutralize discs that can be considered as obstacle or threat like mine. The agent has neutralization capability that is limited with  $K$  number of discs where  $K \leq |A|$ . When discs are neutralized their neutralization cost is added to the cost of the path. In this problem our aim is taking the agent from  $s$  to  $t$  safely and using the shortest path.

An example for the neutralization problem is given in Fig. 2. In this figure, each disc has radius of 3 and neutralization cost of 0.8. As seen in figure, when our agent has  $K = 0$  neutralization, (s)he chooses path 1. Similarly, when  $K = 1, 2, 3$ , paths 2, 3 and 4 are our optimum paths, respectively. For  $K = 1$ , only  $A_6$  neutralized, for  $K = 2$ ,  $A_5$  and  $A_6$  are neutralized and for  $K = 3$ ,  $A_5, A_6$  and  $A_7$  are neutralized.



**Fig. 2.** An example to the neutralization problem and optimal paths for  $K=0, 1, 2$  and  $3$

Similar to the TSP setting, an instance of the neutralization problem is represented by graph  $(V, E)$ . In this graph there is also a set of discs and the edges intersecting these discs have additional travelling cost which is calculated proportionally by the number of discs intersected. Actually, these additional costs represent the neutralization cost of the discs. Another property of the edges is their weight values. Simply, weight of an edge represents the intersection status with a disc. So, the number of intersecting discs determines the weight value for an edge. Cost and weight of a path on the graph are sum of costs and weight of the edges on the path. Therefore the weight property of a path is used for

checking its feasibility, i.e. satisfying the maximum number of neutralization ( $K$ ) constraint.

To our knowledge, the neutralization problem defined above is studied in [1] where the authors develop a two phase algorithm for solving the neutralization problem. However, their proposed algorithm is based on the assumption that every disc has the same radius and same neutralization cost. In this paper, that constraint is released and we provide a solution method for more realistic scenarios. On the other hand, neutralization problem is closely related to the problems undertaken in real world applications in diverse fields such as telecommunications routing [7], curve approximations [8], scheduling and minimum-risk routing of military vehicles and aircraft [9]. Therefore, the techniques developed in this study may also be applied to other application domains.

In the next section, we provide the details of the ant system algorithm proposed for solving the neutralization problem.

#### 4 Ant System Algorithm Proposed for Solving the Neutralization Problem

In the neutralization problem, we have an agent and this agent wants to go from the start point ( $s$ ) to the target ( $t$ ) point. From now on ants are our agents and our aim is still the same, we want to take these agents from  $s$  to  $t$  safely using the shortest path algorithm.

In our AS design, we made use of costs of the shortest paths from each node to destination. The cost of shortest path on each vertex guides the ants on their decisions. However the shortest path information is not enough to guide an ant, because a shortest path may be infeasible due to its weight. Therefore, the ant should also be aware of the weight information of the shortest paths. The pheromone level on each edge is definitely another guiding tool for the ants. With all these information at hand, the ant will choose the vertex to go next at each step. Our AS algorithm developed for the neutralization problem is given in Fig. 3.

We modified the original state transition rule (1) to apply to our problem. The probability of ant  $k$  that wants to go from vertex  $a$  to vertex  $b$ , in state transition rule is found according to the formula given in (3).

$$p_k(a, b) = \begin{cases} \frac{[\tau(a, b)] \cdot [1/(\omega(a, b, t) \cdot \delta(b, t))]^\beta}{\sum_{u \in J_k(a)} [\tau(a, u)] \cdot [1/(\omega(a, u, t) \cdot \delta(u, t))]^\beta} & \text{if } b \in J_k(a) \\ 0, & \text{otherwise} \end{cases} \quad (3)$$

where  $\tau(a, b)$  is the pheromone level of edge which is between vertex  $a$  and vertex  $b$ ,  $t$  is our terminal or destination point,  $\delta(b, t)$  is total cost of path that is between vertex  $b$  and vertex  $t$  (terminal).  $\beta$  is a parameter which determines the relative importance of pheromone versus distance ( $\beta > 0$ ).  $J_k(a)$  is a set that keeps possible vertex to go.  $\omega$  is the weight function which is found by

---

```

1. for each edge  $(a, b)$ 
2.      $\tau(a, b) = \tau_0$ 
3. end for
4. /*Main loop*/
5. for  $n$  iterations
6.     for each ant  $k$ 
7.          $\mu(k) = K$ 
8.         place ant  $k$  on  $s$ 
9.     end for
10.    repeat
11.        for each ant  $k$ 
12.            /*suppose that ant  $k$  is at vertex  $v^*$ */
13.            if  $(\mu(k) \leq \eta(\lambda(v)))$ 
14.                return the shortest path found by Dijkstra's algorithm
15.            end if
16.            ant  $k$  chooses next vertex according to (3)
17.            if next vertex == null /*this means ant is jammed*/
18.                restart ant  $k$  by placing it at  $s$  and setting  $\mu(k) = K$ 
19.            end if
20.        end for
21.    until all ants reach  $t$ 
22.    for each edge  $(a, b)$ 
23.        apply global update rule given in (2)
24.    end for
25. end for
26. return best path found

```

---

**Fig. 3.** Ant system algorithm proposed for solving the neutralization problem

$$\omega(a, b, t) = \eta(\lambda(a)) - \mu(k) + \vartheta(a, b) + 1 \quad (4)$$

where  $\lambda(a)$  is the shortest path from vertex  $a$  to  $t$ ,  $\eta(\lambda(a))$  is weight of shortest path from vertex  $a$  to  $t$ ,  $\mu(k)$  is the number of remaining neutralizations for ant  $k$ ,  $\vartheta(a, b)$  is weight of edge which is between vertex  $a$  and vertex  $b$ . In this formulation, we favor the edges which have greater amount of pheromone, and which have smaller cost and smaller weight on the shortest path to  $t$ . Global update rule that we use in our problem is exactly same as in (2).

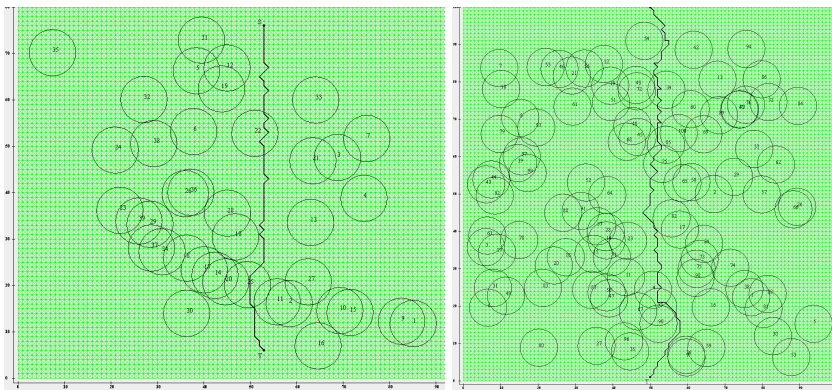
In the next section there will be some computational experiments on real and synthetic data.

## 5 Experimental Work and Discussion

After designing the ant system algorithm for solving the neutralization problem, computational tests are carried out to assess its performance. The computational

tests are conducted both on real and random discrete minefields. The real minefield has 39 discs on a  $[0, 92] \times [0, 80]$  rectangle [10]. On the other hand there are seven random minefields each having 100 discs on  $[0, 100] \times [0, 100]$  rectangles. The real minefield and one of the random minefields are given in Fig. 4.

The performance of AS is compared with the exact solutions that are obtained by an exact algorithm having a high order of run-time complexity. The exact method used in this study is a novel approach which is currently being developed and based on applying  $k$ - $th$  shortest path algorithm starting from a lower bound solution. On the average, our proposed AS obtains the solution in 290 seconds for ten ants and ten iterations whereas the exact algorithm requires 69 hours.



**Fig. 4.** Real minefield (left) and a random minefield (right)

For the AS proposed in this study, we followed the following work plan to find out the best performing parameter values from the set given in Table 1. Before that, we should note that when the modified AS is run with a parameter set, the best path of the ants is recorded as the output of that run.

To find out the best parameter values for a parameter of modified AS, say  $\beta$ , the parameter is fixed to a value, say 2, and all results taken with various combinations of  $m$ ,  $\alpha$  and  $n$  are averaged to find out average results for that value of the parameter. In this way, the average performance of the parameter value on all circumstances is presented. This analysis is repeated on all minefields. AS has four parameters and their values make a total of 270 different combinations. The performance analysis for the parameters is given in Table 1 where both cost of best path and its percentage deviation from the exact solution are displayed.

We may reach the following conclusions after analyzing Table 1. We firstly observe that increasing the value of the  $\beta$  parameter gives better paths. Based on the state transition rule, we can say that the increase for  $\beta$  means the ants are guided to the shortest but feasible paths. It is interesting to note that the value of the  $\alpha$  parameter does not have any significant effect on the performance. On the other hand, increasing the number of ants ( $m$ ) and number of iterations

**Table 1.** Performance analysis of parameter values

	parameter values	real minefield		random minefield(avg)	
		tc	dev	tc	dev
$m$	5	78,38	5,2%	117,85	8%
	10	76,97	3,3%	117,45	7%
	<b>20</b>	<b>76,97</b>	<b>3,3%</b>	<b>116,50</b>	<b>6%</b>
$\beta$	1	113,88	52,9%	150,18	37%
	2	101,40	36,1%	136,50	25%
	5	95,36	28,0%	132,20	21%
	10	87,60	17,6%	128,27	17%
	20	81,11	8,9%	120,16	10%
	<b>100</b>	<b>76,97</b>	<b>3,3%</b>	<b>116,42</b>	<b>6%</b>
$\alpha$	0,01	77,80	4,4%	117,36	7%
	0,02	76,97	3,3%	117,21	7%
	0,05	76,97	3,3%	117,57	7%
	<b>0,10</b>	<b>76,97</b>	<b>3,3%</b>	<b>116,77</b>	<b>7%</b>
	0,20	76,97	3,3%	117,34	7%
$n$	10	76,97	3,3%	117,58	7%
	50	76,97	3,3%	117,02	7%
	<b>100</b>	<b>76,97</b>	<b>3,3%</b>	<b>116,89</b>	<b>7%</b>

**Table 2.** Detailed performance analysis of the  $\beta$  parameter

$\beta$	avg	avg dev
50	124,87	14,1%
60	122,48	11,9%
70	121,17	10,7%
80	120,73	10,3%
90	120,49	10,1%
100	120,26	9,9%
<b>110</b>	<b>118,89</b>	<b>8,6%</b>
120	119,95	9,6%
130	126,71	15,8%
140	125,58	14,7%
150	124,61	13,9%

( $n$ ) bring better paths which is expected due to pheromone update. When more ants pass from a path with more iterations, pheromone level on this path is increased. We should note that the best parameter set shows a performance about %6 away from the optimum. Most of this gap is due to the zigzag patterns of the paths that is a result of the stochastic decisions of ants (see Fig. 4).

One wonders about the limit of  $\beta$  where the performance increase stops. To reveal this, we ran the modified AS algorithm with a mesh of  $\beta$  values where  $\alpha$ ,  $m$  and  $n$  were set to 0.1, 10 and 100, respectively. The results are given in Table 2. It can be easily observed that the performance with respect to various  $\beta$  values, shows a  $U$  shape result. That is, the performance gets better for increasing values of  $\beta$  from 1 up to 110 and the best performance is obtained when  $\beta = 110$ . The reason why the performance deteriorates after  $\beta = 110$  is due to the probability values converging to zero.

## 6 Summary, Conclusions and Future Work

In this study, an ant system algorithm is developed and tested for solving the neutralization problem. Proposed ant system algorithm differs from the

original AS in the state transition rule. In our state transition rule, we favor the edges which have greater amount of pheromone, and which have smaller cost and smaller weight on the shortest path to the destination. The performance of the proposed AS algorithm is compared with exact solution both on real and synthetic data and the results are promising. As a future work, the algorithm can be improved by applying some postprocessing or by trying some other state transition rule rules. In addition, other ACO algorithms may be exploited to solve neutralization problem.

## References

1. Alkaya, A.F., Aksakalli, V., Periebe, C.E.: Heuristics for Optimal Neutralization in a Mapped Hazard Field (submitted for publication)
2. Dorigo, M., Stutzle, T.: *Ant Colony Optimization*. MIT Press Cambridge (2004)
3. Dorigo, M., Gambardella, L.M.: Ant Colony system: A Cooperative learning approach to the Travelling Salesman Problem. *IEEE Transaction on Evolutionary Computation* 1(1) (1997)
4. Dorigo, M., Maniezzo, V., Colorni, A.: The ant system: Optimization by a colony of cooperating agents. *IEEE Trans. Syst., Man, Cybern. B* 26(2), 29–41 (1996)
5. Stutzle, T., Hoos, H.: Improvements on the ant system, introducing the MAX-MIN ant system. In: *Proc. ICANNGA97–Third Int. Conf. Artificial Neural Networks and Genetic Algorithms*. Springer, Wien (1997)
6. Lawler, E.L., Lenstra, J.K., Rinnooy-Kan, A.H.G., Shmoys, D.B.: *The Travelling Salesman Problem*. Wiley, New York (1985)
7. Kuipers, F., Korkmaz, T., Krunz, M., Van Mieghem, P.: Performance evaluation of constraintbased path selection algorithms. *IEEE Network* 18, 16–23 (2004)
8. Dahl, G., Realfsen, B.: Curve approximation and constrained shortest path problems. In: *International Symposium on Mathematical Programming, ISMP 1997* (1997)
9. Zabaranin, M., Uryasev, S., Pardalos, P.: Optimal Risk Path Algorithms. In: Murphey, R., Pardalos, P. (eds.) *Cooperative Control and Optimization*, vol. 66, pp. 271–303. Kluwer Academic, Dordrecht (2002)
10. Fishkind, D.E., Priebe, C.E., Giles, K., Smith, L.N., Aksakalli, V.: Disambiguation protocols based on risk simulation. *IEEE Trans Syst. Man Cybernet Part A* 37, 814–823 (2007)

# Solving Credit Card Fraud Detection Problem by the New Metaheuristics Migrating Birds Optimization

Ekrem Duman<sup>1</sup> and Ilker Elikucuk<sup>2</sup>

<sup>1</sup> Özyeğin University, Faculty of Engineering,  
Industrial Engineering Department, Istanbul, Turkey  
ekrem.duman@ozyegin.edu.tr

<sup>2</sup> Intertech, Decision Support Systems Department, Istanbul Turkey  
Ilker.elikucuk@intertech.com.tr

**Abstract.** Statistical fraud detection problem is a very difficult problem in that there are very few examples of fraud. The great majority of transactions are legitimate. On the other hand, for this binary classification problem the costs of the two types of classification errors (FP=false positive and FN=false negative) are not the same. Thus, the classical data mining algorithms do not fit to the problem exactly. Departing from this fact, we have solved this problem by genetic algorithms and scatter search. Now, we apply the recently developed new metaheuristics algorithm namely the migrating birds optimization algorithm (MBO) to this problem. Results show that it outperforms the former approach. The performance of standard MBO is further increased by the help of some modified benefit mechanisms.

**Keywords:** migrating birds optimization algorithm, fraud, credit cards, genetic algorithms.

## 1 Introduction

When a credit card is copied or stolen, the transactions made by them are labeled as fraudulent. These fraudulent transactions should be prevented or detected in a timely manner otherwise the resulting losses can be huge. Banks typically use two layers of fraud prevention/detection systems; rule based layer and statistical analysis layer. Here we are concerned with the statistical layer only where an incoming transaction is compared to card usage behavior of the card holder and if there is a considerable deviation, a high suspicion score is returned.

Statistical fraud detection is not an easy problem at all due to several reasons. First, fraud data sets are extremely skewed; out of 100.000 transactions only a few turn out to be fraud [1]. Secondly, the techniques used by fraudsters change in time gradually [2-4]. Thus, a model developed now may not be effective enough in future. In addition to these the idea exchanges between the banks are very limited because of the privacy issues; no one wants other banks know how many frauds they were faced with and no bank shares details of their solution if they think they have a good one. In this regard, our study differentiates from many in literature and although we will not



be able to share all details, we will be talking about a fraud detection solution developed using real data and implemented in real life.

Due to its importance it is possible to find a lot of studies on fraud detection in literature. The most commonly used fraud detection methods are rule-induction techniques, decision trees, neural networks, Support Vector Machines (SVM), logistic regression, and meta-heuristics such as genetic algorithms [5-12]. These techniques can be used alone or in collaboration using ensemble or meta-learning techniques to build classifiers. Quah and Sriganesh [13], suggest a framework which can be applied real time where first an outlier analysis is made separately for each customer using self organizing maps and then a predictive algorithm is utilized to classify the abnormal looking transactions. Panigrahi et al. [14] suggest a four component fraud detection solution which is connected in a serial manner. The main idea is first to determine a set of suspicious transactions and then run a Bayesian learning algorithm on this list to predict the frauds. Sanchez et al. [15] presented a different approach and used association rule mining to define the patterns for normal card usage and indicating the ones not fitting to these patterns as suspicious. The study of Bolton and Hand [2] provides a very good summary of literature on fraud detection problems.

In most of the studies listed above the classical accuracy based model performance measures are used. Among these the accuracy ratio, the capture rate, the hit rate, the gini index and the lift are the most popular ones [16-17]. However, since the fraudsters use all available limit on the card they captured, an algorithm which is more successful in detecting the cards with higher available limits is more prominent. In this case the cost of making a false positive error and a false negative error will not be the same and actually false negative error (labeling a fraudulent transaction as legitimate) will be a variable. We will take this cost function here similar to few studies in literature [18-19]. A rather more detailed review of these two studies will be given in the next section.

The contributions of this study to the literature are three fold. First, we are talking on models built with real data and implemented in real life. Second, the new metaheuristic MBO is used to solve a credit card detection problem for the first time and this will be one of the very few studies where any member of the metaheuristic algorithms family is used. Third, the performance of MBO is improved further through the use of modified benefit mechanisms.

The rest of the paper is organized as follows. In the next section, the fraud detection problem we were faced is described in detail together with the explanation of closely related previous work. In the third section we describe the MBO algorithm as it is used to solve the quadratic assignment problem in [1]. Implementation of MBO on the credit card fraud detection problem and the modifications made on it to improve its performance are detailed in section four. The paper is finalized in section five by giving a summary of the study and the major conclusions.

## **2 Problem Definition and Previous Work**

There has been a growing amount of financial losses due to credit card frauds as the usage of the credit cards become more and more common. As such, many papers reported huge amounts of losses in different countries [2, 20].

Credit card frauds can be made in many ways such as simple theft, application fraud, counterfeit cards, never received issue (NRI) and online fraud (where the card holder is not present). In online fraud, the transaction is made remotely and only the card's details are needed. A manual signature, a PIN or a card imprint are not required at the time of purchase. Though prevention mechanisms like CHIP&PIN decrease the fraudulent activities through simple theft, counterfeit cards and NRI; online frauds (internet and mail order frauds) are still increasing in both amount and number of transactions. According to Visa reports about European countries, approximately 50% of the whole credit card fraud losses in 2008 are due to online frauds [21].

When the fraudsters obtain a card, they usually use (spend) all of its available (unused) limit. According to the statistics, they do this in four - five transactions, on the average [18]. Thus, for the fraud detection problem, although the typical prediction modeling performance measures are quite relevant, as indicated by the bank authorities, a performance criterion, measuring the loss that can be saved on the cards whose transactions are identified as fraud is more prominent. In other words, detecting a fraud on a card having a larger available limit is more valuable than detecting a fraud on a card having a smaller available limit.

As a result, what we are faced with is a classification problem with variable misclassification costs. Each false negative has a different misclassification cost and the performance of the model should be evaluated over the total amount of saved available usable limits instead of the total number of frauds detected.

If we define;

TP = the number of correctly classified alerts

TN = the number of correctly classified legitimates

FP = the number of false alerts

FN = the number of transactions classified as legitimate but are in fact fraudulent

c = the cost of monitoring an alert

TFL = the total amount of losses due to fraudulent transactions

S = savings in TFL with the use of fraud detection system

$\rho$  = savings ratio

Then,

TFL = sum of the available limits of the cards whose transactions are labeled as TP or FN

c = cost of monitoring including staff wages, SMSs, phone calls. On the average, it is a small figure (less than a dollar)

$S = (\text{available limits of the cards of TP transactions}) - c(\text{FP} + \text{TP})$

$\rho = S/\text{TFL}$

where the maximum value S can take is TFL and  $\rho$  can take is 1. A good predictor will be the one having a high  $\rho$ .

Duman and Ozcelik [18] tackled the same problem for another bank in Turkey. After putting the problem in the same way and pointing out the classical DM algorithms may not perform well for the objective of maximizing savings ratio they implemented a metaheuristic approach which is a hybrid of genetic algorithms and scatter search (the GASS algorithm). In GASS, the number of parent solutions was taken as 50 and

child solutions were generated by the recombination operator. Each parent is recombined by every other parent so that the number of children was 1225 in each generation. One of the child solutions is selected randomly and one of its genes is mutated. As the fitness function the savings ratio is used. In the selection process, besides the fittest members which are determined by roulette selection, the most diverse solutions are also inherited to the next generation in [18]. GASS improved the savings ratio by more than 200% with a cost of 35% increase in the number of alerts. However, it had some limitations in that the authors were allowed to improve the score generated by some groups of variables only and the variables about MCCs (merchant category codes) and out of country expenditures were left out of the scope of the study. The problem was that a second score was being generated with these left out variables and the authors had no control on how these two scores were interfering.

The study of Duman and Sahin [19] gives a summary of previous results obtained in another bank where this study is carried out also. The results obtained by classical decision trees (C5.0, CART, CHAID), artificial neural networks, SVM, logistic regression and GASS are compared. The results obtained by a special cost sensitive decision tree where in splitting a node the savings ratios of the resulting leaf nodes are considered, is also given. It was shown that the GASS and the newly proposed cost sensitive decision trees were the two best performing methods.

The studies [22-24] are the other studies that tackle cost sensitive decision trees in literature.

### 3 The MBO Algorithm

The MBO algorithm is a neighborhood search technique [1]. It starts with a number of initial solutions corresponding to birds in a V formation. Starting with the first solution (corresponding to the leader bird), and progressing on the lines towards the tails, each solution is tried to be improved by its neighbor solutions (for the implementation of QAP (quadratic assignment problem), a neighbor solution is obtained by pairwise exchange of any two locations). If the best neighbor solution brings an improvement, the current solution is replaced by that one. There is also a benefit mechanism for the solutions (birds) from the solutions in front of them. Here we define this benefit mechanism as sharing the best unused neighbors with the solutions that follow (here “unused” means a neighbor solution which is not used to replace the existing solution). In other words, a solution evaluates a number of its own neighbors and a number of best neighbors of the previous solution and considered to be replaced by the best of them. Once all solutions are improved (or tried to be improved) by neighbor solutions, this procedure is repeated a number of times (tours) after which the first solution becomes the last, and one of the second solutions becomes first and another loop starts. The algorithm is stopped after a specified number of iterations.

Below, first the notation used and then the pseudo-code of the MBO algorithm are given. Let,

$n$  = the number of initial solutions (birds)

$k$  = the number of neighbor solutions to be considered

$x$  = the number of neighbor solutions to be shared with the next solution

$m$  = number of tours

$K$  = iteration limit

Pseudocode of MBO:

1. Generate  $n$  initial solutions in a random manner and place them on an hypothetical V formation arbitrarily.
2.  $i=0$
3. while( $i < K$ )
4.     for ( $j=0; j < m; j++$ )
5.         Try to improve the leading solution by generating and evaluating  $k$  neighbors of it.
6.          $i=i+k$
7.         for each solution  $s_r$  in the flock (except leader)
8.             Try to improve  $s_r$  by evaluating  $(k-x)$  neighbors of it and  $x$  unused best neighbors from the solution in the front.
9.              $i=i+(k-x)$
10.         endfor
11.     endfor
12.     Move the leader solution to the end and forward one of the solutions following it to the leader position.
13. endwhile
14. return the best solution in the flock

As should already be noticed, the MBO algorithm has great similarities with the migrating birds' story. First it treats the solutions as birds aligned on a V formation. The number of neighbors generated ( $k$ ) can be interpreted as the induced power required which is inversely proportional to the speed (recall the discussion above). With a larger  $k$  we would assume that birds are flying at a low speed where we can also make the analogy that while traveling at a low speed, one can explore the surrounding in more detail. The benefit mechanism between the birds is respected and by generating fewer neighbors for the solutions at the back, it was made possible that they get tired less and save energy by using the neighbors of the solutions in the front. The parameter  $x$  is seen as the WTS where an optimum value can be sought for. Its optimum value could be interpreted as the optimum overlap amount of the wingtips. In line 4, the parameter  $m$  can be regarded as the number of wing flaps or the profile power needed where we can assume that, as each bird travels the same distance, they all spend the same profiling energy. In line 12, similar to the real birds' story, the bird who spent the most energy and thus got tired moves back to get some rest and another bird fills its position.

For the MBO to perform better, it is necessary to determine the best values of some parameters. These are the number of birds to have in the flock ( $n$ ), the speed of the flight ( $k$ ), the WTS ( $x$ ) and the number of wing flaps before a change in the order of the birds or the profiling energy spent ( $m$ ). Similar to birds' story, one could expect some certain values of these parameters and their combinations might increase the

performance of the algorithm. For the printed circuit board assembly originated quadratic assignment problem the best parameter values were obtained to be  $n = 51$ ,  $m = 10$ ,  $k = 11$  and  $x = 1$  in [1].

The philosophy of the MBO is that, by starting with a number of solutions, it is aimed to explore more areas of the feasible solution space. The exploration is made possible by looking at the neighbor solutions. Each time one of the solutions (the one in the front) is explored in more detail. When one of the solutions fails to improve itself by its own neighbors and if the solution in the front is more promising, it is replaced by one of the neighbors of the solution in the front. This way the neighborhood around the more promising solution will be explored in a greater detail (by the combined forces of two birds or solutions). Still after a few iterations these solutions may go to different directions as long as they find improvements along their ways. However, after some time we might expect most of the solutions converge to one or several neighborhoods where local optima or even the global optimum are contained. The convergence can be faster with larger values of  $x$  but in that case the termination could take place before the feasible region is thoroughly explored and thus the results obtained might not be good.

## 4 Results and Discussion

In the following subsections first the details of the experimental setting are given. Then, the results obtained by standard MBO and GASS are displayed together with their parameter fine tuning experiments. This is followed by some improvement attempts on MBO by employing different neighborhood functions.

### 4.1 Details of Experimental Setting

The original data of the time period used to form the training set have about 22 million transactions. The distribution of this data with respect to being normal or fraudulent is highly skewed so that only 978 transactions were fraudulent in this set. So, to enable the models to learn both types of profiles, some under sampling or oversampling techniques should be used. Instead of oversampling the fraudulent records by making multiple copies of them, we use stratified sampling to under sample the legitimate records to a meaningful number. Firstly, we identify the variables which show the most different distributions w.r.t. being fraudulent or normal. Then, we use these variables as the key variables in stratified sampling so that the characteristics of their distributions w.r.t. being fraudulent or not remains the same. For stratified sampling, we use those five variables which show the most different distributions to form a stratified sample with a ratio of nine legitimate transactions to one fraudulent transaction.

### 4.2 Results Obtained by MBO

The total number of variables in the data mart was 139 (all binary). Starting with the full set of variables, a variable reduction is made first. Each time the variables having

coefficients close to zero (in the trained model) are eliminated and a new model is generated. This resulted in 15 variables where the coefficients of the variables were significantly different than zero. During these runs the MBO parameter values are used same as the best set obtained in [1].

Then a set of parameter fine tuning experiments are made on MBO. According to this analysis the best set of parameters is determined to be:

**Table 1.** MBO versus GASS

	<b>MBO</b>			<b>GASS</b>	
<b>RUN</b>	$\rho$	<b>TPR</b>		$\rho$	<b>TPR</b>
1	94,74	91,94		90,92	79,34
2	95,13	91,94		85,64	77,69
3	94,21	91,53		90,89	78,1
4	94,74	91,94		90,63	77,89
5	94,26	91,74		90,94	79,34
6	91,3	77,89		94,78	91,32
7	94,91	91,74		91,22	79,75
8	94,91	91,74		93,78	89,26
9	94,71	91,94		94,26	91,74
10	91,04	78,1		91,41	79,96
<b>AVG</b>	<b>93,98</b>	<b>88,91</b>		<b>91,45</b>	<b>82,78</b>

- Number of Birds: 15
- Number of Neighbors : 7
- Number of Flaps: 3
- Number of Overlaps: 2

The parameter values of the GASS algorithm implemented here are determined in accordance with the study [18], namely:

- Number of variables (genes): 15
- Number of initial solutions: 15
- Maximum number of tested solutions: 15000

Mutation procedure: One of the 15 genes is selected randomly and a uniform number between 0 and 1 (U(0,1)) is added to its value. If the result is greater than the upper bound (1.0), the final value is obtained by subtracting the upper bound from the new value.

Mutation rate: 8% of the intermediate solutions are selected for mutation.

Selection procedure: Roulette wheel

The results obtained by GASS and MBO are compared in Table 1 where TPR stands for true positive rate.

The results in Table 2 indicate that the MBO algorithm performs significantly better than the GASS algorithm (about three per cent higher limit saving and about five per cent higher TPR is obtained). This superiority is also validated by an independent t-test where the p-values turn out to be 2.3 per cent and 2.6 per cent for the limit savings and TPR, respectively.

**Table 2.** MBO when two genes are shared

RUN	Standard MBO			Gene Sharing	
	$\rho$	TPR		$\rho$	TPR
1	94,74	91,94		94,71	91,94
2	95,13	91,94		95,13	91,94
3	94,21	91,53		94,96	91,94
4	94,74	91,94		95,13	91,94
5	94,26	91,74		94,74	91,94
6	91,3	77,89		94,27	91,74
7	94,91	91,74		94,26	91,74
8	94,91	91,74		90,33	85,74
9	94,71	91,94		94,74	91,94
10	91,04	78,1		95,19	92,15
<b>AVG</b>	<b>93,98</b>	<b>88,91</b>		<b>94,35</b>	<b>91,3</b>

### 4.3 Modifications on MBO

After finding out that the MBO algorithm is a good solver in fraud detection, we continued with testing a different mechanism in MBO. For this purpose instead of sharing some neighbor solutions with the followers, inspired by the genetic algorithms, we wanted to see the effects of sharing some genes (coefficient values). A neighbor solution of a current solution is generated by getting a number of genes (say,  $y$ ) from the front solution (the selection of which  $y$  genes is determined randomly) and the rest of the genes are copied from the current solution where one of them is mutated like in the standard MBO. For the value of  $y$  (the number of genes shared), values from 1 to 5 are tested. We saw that two genes sharing happened to bring the most improvement. To test the significance of this improvement, we tabulated the results of 10 runs in Table 2 and applied t-test. According to t-test, the differences on the performances of the two are not significant with p-values of 29.2% and 11.5% for  $\rho$  and TPR, respectively.

To conclude, we can say that when the standard MBO of Duman et al. [1] is coupled with a good benefit mechanism with gene sharing between solutions, its performance can slightly be increased.

## 5 Summary and Conclusions

In this study we solved the credit card fraud detection problem by the new metaheuristics migrating birds optimization algorithm. This study is one of the few studies where a metaheuristic algorithm is utilized in fraud detection and it performed better than a previous implementation of a combination of genetic algorithms and scatter search. The standard MBO is further improved by testing alternative benefit mechanisms.

As future work, alternative settings of V formation (like more than two tails etc) can be tested.

## References

1. Duman, E., Uysal, M., Alkaya, A.F.: Migrating Birds Optimization: A new metaheuristic approach and its performance on quadratic assignment problem. *Information Sciences* 217, 65–77 (2012)
2. Bolton, R.J., Hand, D.J.: Statistical fraud detection: A review. *Statistical Science* 28(3), 235–255 (2002)
3. Kou, Y., et al.: Survey of fraud detection techniques. In: *Proceedings of the 2004 IEEE International Conference on Networking, Sensing and Control*, Taipei, Taiwan, March 21–23 (2004)
4. Phua, C., et al.: A comprehensive survey of data mining-based fraud detection research. *Artificial Intelligence Review* (2005)
5. Sahin, Y., Duman, E.: An overview of business domains where fraud can take place, and a survey of various fraud detection techniques
6. Brause, R., Langsdorf, T., Hepp, M.: Neural data mining for credit card fraud detection. In: *Proceedings of the 11th IEEE International Conference on Tools with Artificial Intelligence* (1999)
7. Hanagandi, V., Dhar, A., Buescher, K.: Density-Based Clustering and Radial Basis Function Modeling to Generate Credit Card Fraud Scores. In: *Proceedings of the IEEE/IAFE, Conference* (1996)
8. Juszczak, P., Adams, N.M., Hand, D.J., Whitrow, C., Weston, D.J.: Off-the-peg and bespoke classifiers for fraud detection. *Computational Statistics & Data Analysis* 52(9) (2008)
9. Quah, J.T., Sriganesh, M.: Real-time credit card fraud detection using computational intelligence. *Expert Systems with Applications* 35(4) (2008)
10. Shen, A., Tong, R., Deng, Y.: Application of classification models on credit card fraud detection. In: *International Conference on Service Systems and Service Management*, Chengdu, China (June 2007)
11. Wheeler, R., Aitken, S.: Multiple algorithms for fraud detection. *Knowledge-Based Systems* 13(2/3) (2000)
12. Chen, R.-C., Chiu, M.-L., Huang, Y.-L., Chen, L.-T.: Detecting credit card fraud by using questionnaire-responded transaction model based on support vector machines. In: Yang, Z.R., Yin, H., Everson, R.M. (eds.) *IDEAL 2004*. LNCS, vol. 3177, pp. 800–806. Springer, Heidelberg (2004)
13. Han, J., Camber, M.: *Data mining concepts and techniques*. Morgan Kaufman, San Diego (2000)



14. Quah, J.T.S., Srinagesh, M.: Real-time credit fraud detection using computational intelligence. *Expert Systems with Applications* 35, 1721–1732 (2008)
15. Panigrahi, S., Kundu, A., Sural, S., Majumdar, A.: Credit Card Fraud Detection: A Fusion Approach Using Dempster-Shafer Theory and Bayesian Learning. *Information Fusion*, 354–363 (2009)
16. Sanchez, D., Vila, M.A., Cerda, L., Serrano, J.M.: Association rules applied to credit card fraud detection. *Expert Systems with Applications* 36, 3630–3640 (2009)
17. Kim, M., Han, I.: The Discovery of Experts' Decision Rules from Qualitative Bankruptcy Data Using Genetic Algorithms. *Expert Systems with Applications* 25, 637–646 (2003)
18. Gadi, M.F.A., Wang, X., do Lago, A.P.: Credit Card Fraud Detection with Artificial Immune System. In: Bentley, P.J., Lee, D., Jung, S. (eds.) *ICARIS 2008*. LNCS, vol. 5132, pp. 119–131. Springer, Heidelberg (2008)
19. Duman, E., Ozcelik, M.H.: Detecting credit card fraud by genetic algorithm and scatter search. *Expert Systems with Applications* 38, 13057–13063 (2011)
20. Duman, E., Sahin, Y.: A Comparison of Classification Models on Credit Card Fraud Detection with respect to Cost-Based Performance Metrics. In: Duman, E., Atiya, A. (eds.) *Use of Risk Analysis in Computer-Aided Persuasion*. NATO Science for Peace and Security Series E: Human and Societal Dynamics, vol. 88, pp. 88–99. IOS Press (2011)
21. Gartner Reports, from the World Wide Web (May 10, 2010),  
<http://www.gartner.com>
22. Mena, J.: *Investigate Data Mining for Security and Criminal Detection*. Butterworth-Heinemann, Amsterdam (2003)
23. Ling, C.X., Sheng, V.S.: Test Strategies for Cost-Sensitive Decision Trees. *IEEE Transactions on Knowledge and Data Engineering* 18(8) (2006)
24. Liu, X.: A Benefit-Cost Based Method for Cost-Sensitive Decision Trees. In: 2009 WRI Global Congress on Intelligent Systems, pp. 463–467 (2009)

# Parametric and Non-parametric Feature Selection for Kidney Transplants

Raimundo Garcia-del-Moral<sup>1</sup>, Alberto Guillén<sup>2</sup>,  
Luis Javier Herrera<sup>2</sup>, Antonio Cañas<sup>2</sup>, and Ignacio Rojas<sup>2</sup>

<sup>1</sup> Intensive Care Unit. Santa Ana Hospital  
Motril, Granada Spain

<sup>2</sup> Department of Computer Architecture and Computer Technology  
Universidad de Granada Spain

**Abstract.** This paper presents a comparison of several methods of measuring the quality of a subset of features that characterise kidney's graft so they can be evaluated to be transplanted. First, two non-parametric methods, Delta Test and Mutual Information, are used isolated and in a multiobjective manner using a genetic algorithm and comparing the solutions will all the possible solutions obtained by brute force. Afterwards, LSSVM are used to approximate the score of the graft so, for smaller approximation errors, the subset of features is considered better. The results obtained are confirmed from the clinical perspective by an expert.

## 1 Introduction

Since the first kidney transplant in 1954 [8], this type of surgery have become an usual practice in more than 80 countries allowing patience with terminal kidney insufficiency to increase their life expectancy and improve their life quality [2,1,9]. The advances in immunodepresor therapies, organ preservation and receptor selection have optimised the survival of the implant. This is translated into an 80%-90% of success for the first year and 50%-70% for five years.

Although the total number of donors has increased in the last ten years, the donation rate kept a constant value between 30 and 35 donors per million of inhabitants due to the simultaneous increase of the spanish population. Because of this, the National Transplant Organisation (Organizacin Nacional de Transplantes, ONT) has been working on an strategic plan (Plan 40) which aims to increase donation rate by transplantation for asystolic donors, living donors and expanded criteria donors.

The 89% of the transplants accomplished in Spain use organs from brain death donors although there has been a raise in the number of transplant from living people in the last two years. The decrease of fatalities in traffic accidents has changed the donor profile. Nowadays, both, hemorrhagic and ischemic, cerebrovascular accidents (CVA) have become the most frequent type of death among donors, representing the 65.1% meanwhile only the 5.7% came from a Traumatic brain injury (TBI) in the year 2010.

Another consequence of the new profile of donor is an increase in the donor's mean age which changed from 34.5 years in 1992 to 57.5 in year 2010. Over the 79% of donors are older than 45 and the 46.6% older than 60. Considering these data, nowadays, more than the 50% of the donors in Spain are considered expanded criteria donors using the international definition (UNOS definition) [3], therefore, it is required a biopsy before implanting the organ to analyse its viability.

Several scores for the validity of the implant have been developed in the latest years. The scores also predict the final evolution of the transplant. However, these scores were not developed considering elder donors for kidney transplants.

The final aim of the research is to develop a model that could predict the viability of the kidney graft following clinical criteria and donor's analytics. The gold standard is the result of the biopsy carried out using the andalusian protocol for biopsies of expanded criteria donors.

In machine learning, this problem can be tackled from several perspectives. First of all, it is necessary to study the data and see which features seem the most important by the time of giving a score. On the other hand, a model that, for given values of the analytics is able to compute a value, is also requested.

The work presented in this paper will focus mostly in selecting the features that could be the most relevant. Afterwards, models to predict the validity of an implant will be designed with the hope that the selected set of variables lead to obtain smaller test errors.

The main novelty that it is presented in this paper is that we propose to consider Test Delta minimisation and Mutual Information maximization as a multiobjective problem.

## 2 Material and Methodologies

### 2.1 Material

**Patients.** The patients considered in this study included all donors with expanded criteria that were treated between January 1998 and December 2010 in Granada-Jaen transplantation unit. For all patients, a pre-implant biopsy was done before kidney transplantation. All biopsies were evaluated following the andalusian protocol for pre-implant biopsy valoration. This protocol analyse glomerular sclerosis, tubular atrophy, hyaline arterioloopathy and interstitial fibrosis. A sample is considered adequate when it contains, at least, 25 glomeruli and two small arterioles. A score smaller or equal than seven determines a favourable histology for transplantation.

**Geographic Area of Analysis.** The provinces of Jaen and Granada provided the data for the analysis. More concretely the Hospitals San Cecilio y Virgen de las Nieves in Granada, Hospital de Jaén, Hospital San Juan de la Cruz of Úbeda, Hospital Comarcal San Agustin of Linares, Hospital Comarcal Santa Ana of Motril and Hospital General Básico of Baza.

The waiting list in this area is unique for its population. For the study, all donors considering the expanded criteria considering 4 cases from the province of Huelva. Other 18 organs included in the study come from other provinces according to the optimization policy of the regional government.

The list of variables considered in the study are:

1. Time at Intensive Care Unit
2. Kidney donor risk index DRIS
3. United Kingdom risk index
4. Creatinine lightening by MDRD 4
5. MDRD4 IDMS lightening
6. Lightening by Cockcroft-Gault
7. Donor's age
8. Categorized donor's age
9. Donor's sex
10. Donor's size
11. Donor's weight
12. Donor's IMC
13. Donor's classification according to IMC
14. Diabetes in donor
15. Donor's HTA
16. Atherosclerosis in donor
17. Death cause
18. Proteinuria when extracted
19. Urea when extracted
20. Creatinine when extracted
21. Type of Catecholamines used
22. Use of Catecholamines

## 2.2 Methods

This subsection describes briefly the methods applied to analyse the data and how a model that is able to predict the score was designed.

**Feature Selection.** The problem of feature selection consists on finding the most representative variables of a data set. The main issue is how to determine if a subset of features is adequate or not. As it is supposed that the subset should represent the non-linear relationship between the inputs and the outputs so, if we design a model, this could fit better the target function.

Therefore, it could be quite obvious that the best criterion to perform variable selection is to build a model for each possible combination. Unfortunately, training algorithms are quite computationally expensive and the number of possible solutions increases exponentially.

To overcome the first problem and get rid of the setting of the numerous parameters that a model can have, non-parametric methods were proposed as

criteria for feature selection. More concretely Gamma and Delta Test [10] and Mutual Information [4].

To ameliorate the second one, this is, the evaluation of all possible subsets, several heuristics like Genetic Algorithms, Tabu Search, Forward-Backward Search and the hybridization of them have been proposed [7].

Furthermore, some works propose the combination of evaluating the subsets and designing the model in parallel [6].

In the real data set that we have, there are 22 variables, which is translated into 4,194,303 of possible solutions (no variables selected is not a solution). It is not feasible to build a model for each combination, however, it is possible to compute the non-parametric fitnesses for each solution. This is known as brute force approach and will be used in the experiments.

**Model Design.** Among the wide variety of models, Least Square Support Vector Machines [12] have been used due to the high quality solutions they provide.

LS-SVMs are reformulations to standard SVMs, closely related to regularization networks and Gaussian processes but additionally emphasize and exploit primal-dual interpretations from optimization theory. LS-SVMs are a paradigm specially well suited for function approximation problems.

The LS-SVM model is defined in its primal weight space by

$$\hat{y} = W^T \phi(X) + b, \quad (1)$$

where  $W^T$  and  $b$  are the parameters of the model,  $\phi(X)$  is a function that maps the input space into a higher-dimensional feature space and  $X$  is the  $n$ -dimensional vector of inputs  $x_i$ . In Least Squares Support Vector Machines for function approximation, the following optimization problem is formulated,

$$\min_{W,b,e} J(W, e) = \frac{1}{2} W^T W + \gamma \frac{1}{2} \sum_{i=1}^N e_i^2, \quad (2)$$

subject to the equality constraints (inequality constraints in the case of SVMs)

$$e_i = y_i - \hat{y}_i(X_i), i = 1 \dots N. \quad (3)$$

Solving this optimization problem in dual space leads to finding the  $\lambda_i$  and  $b$  coefficients in the following solution

$$\hat{y}_i = \sum_{i=1}^N \lambda_i K(X, X_i) + b, \quad (4)$$

where the function  $K(X, X_i)$  is the kernel function defined as the dot product between the  $\phi(X)$  and  $\phi(X_i)$  mappings. If we consider Gaussian kernels, the width of the kernel  $\sigma_i$  together with the regularization parameter  $\gamma$ , are the hyper-parameters of the problem. Note that in the case of Gaussian kernels, the obtained model resembles Radial Basis Function Networks (RBFN), with the particularities that there is an RBF node per data point, and that

overfitting is controlled by a regularization parameter instead of by reducing the number of kernels [11]. In LS-SVM, the hyper-parameters of the model are usually optimized by cross-validation.

The main flaw of these methods is that they become more complex as the number of samples in the training data increases. As the dataset only contains 201 donors, we have chosen this model as the approximator.

### 3 Experiments

In this section we have performed several considering several ways of selecting a subset of variables.

On first place, a popular multiobjective genetic algorithm (NSGA-II [5]) was tested using as functions to be optimised the Delta Test value of the individual that codes a solution and its Mutual Information.

Afterwards, instead of using any other heuristic, we explored the whole solution space in order to find the minimum Delta Test value and the maximum value for the Mutual Information.

After the selection was made, LSSVMs were designed and tested their outputs with the real outputs, computing the root mean squared error.

After all this process, we are able to determine which subset of variables could be better in terms of minimization of approximation error and considering the opinion of an expert in kidney transplants.

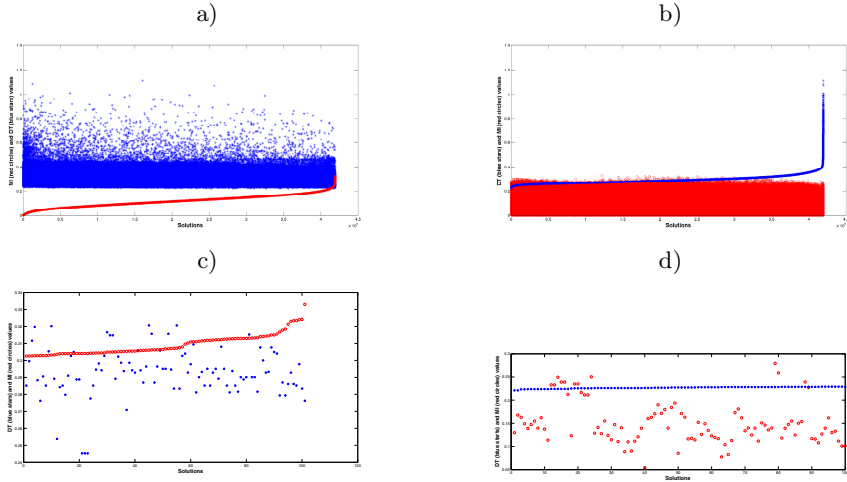
**NSGA-II Results.** The stopping criterium to stop the algorithm was a fixed number of iterations (150) after observing that this number was enough for the population to converge. The results obtained using different population sizes are shown in Table 1. The algorithm was executed ten times and the variables selected were the ones that appeared in the Pareto Front more that the 60% of the times.

**Table 1.** Results obtained for the execution of the NSGA-II with the objective of minimising the DT and maximising the MI

pop size	vars selected	DT	MI
30	3 6 7 9 12 18 19 22	0.2399	0.2479
60	3 7 9 12 13 18 19 22	0.2605	0.2757
120	3 7 9 12 18 19 22	0.2604	0.2660

As we can see, the algorithm has a robust behaviour providing nearly the same results for all the runs.

**Brute-force Results.** Table 2 shows some of the results chosen from all the 4,194,303 solutions. The critria were to obtain the solution providing the maximum MI the solution that provided the minimum DT. As we know the whole



**Fig. 1.** Plots of the complete solution set sorted by the (a) MI value (red circles) and (b), the DT value (blue stars). c) and d) are a zoom of the area we are interested in.

solution space, it is easy to find out which solutions satisfy more the two objectives: minimum DT with a reasonable large MI and vice-versa. These two selections are shown in the first two rows of the Table. In order to select the subsets, a plot of the near min/max solutions was made. Figures included 1 represent a) the solutions sorted according to the MI, b) the solutions sorted according to the DT and c) and d) are a zoom of the areas we are interested in.

**Table 2.** Results obtained for the execution of the brute force algorithm computing the DT and the MI

type of selection	vars selected	DT	MI
min(DT)	8 9 14 15 19 21 22	0.2211	0.1296
max(MI)	3 4 9 12 18 19 22	0.2762	0.3330
near min(DT)	3 4 8 9 11 18 22	0.2453	0.2794
near max(MI)	1 3 4 6 7 9 12 18 19 20 22	0.2453	0.3041

**Table 3.** Results obtained for the execution of the brute force algorithm computing the DT and the MI

subset	RMSE Train (std)	RMSE Test (std)
GA-pop30	0.7402 (0.0189)	0.7704 (0.1067)
GA-pop60	0.7419 (0.0185)	0.7656 (0.1186)
GA-pop120	0.7442 (0.0185)	0.7638 (0.1172)
BF-minDT	0.6763 (0.0160)	0.6891 (0.1194)
BF-maxMI	0.7386(0.0166)	0.7590(0.1228)
BF-nearMinDT	0.7346 (0.0213)	0.7493(0.1089)
BF-nearMaxMI	0.7216 (0.0194)	0.7280 (0.1163)

**Approximation Errors Using LS-SVMs.** Once there are several subsets of variables that are supposed to be representative, it is possible to build the LS-SVMs that will approximate the generated output with the real one. Table 3 shows the results in terms of the root mean squared error for the four subsets (1 from the GA and 3 from the brute force).

## 4 Discussion

With all results exposed, it is possible to discuss about which criterium (DT or MI) seems better or if it is better to optimise them simultaneously in order to have a compromise.

As the results showed, the smallest approximation error achieved was using the selection provided by the minimum value of the DT selecting variables 8 9 14 15 19 21 22.

From the clinical perspective, these variables are included in previous works in the literature as well as new ones that should be studied on a higher cohort of patients. However, this selection excludes two variables that are widely used to evaluate the renal function as are the lightening of creatinine and seric creatinine concentration.

The selection includes seven variables that have been analysed in the literature and that could be taken into account in the clinical practice introducing novelties in the area.

## 5 Conclusions

Machine learning can be applied to a wide variety of problems, in this paper, the identification of the features that characterised the validity of a kidney graft has been tackled. Two widely used non-parametric methods were used separately and in a multiobjective way. Then, a model was used as well to measure how accurate could be the approximation of the score. The results showed a better behaviour of the Delta Test providing a subset of variables validated by an expert and providing the smallest approximation errors when using LSSVMs.

## References

1. Tajima, A., Ueda, D., Hirai, M., Morinaga, S., Sudoko, H., Yamaguchi, Y., Mitsuhashi, T., Nakano, M., Kanbayashi, T., Ushiyama, T.: Dialysis versus renal transplantation; a comparative study on medical cost and quality of life in patients with chronic renal failure. *Hinyokika Kyo* 33(10), 1536–1541 (1987)
2. Ojo, A.O., Hanson, J.A., Meier-Kriesche, H., et al.: Survival in recipients of marginal cadaveric donor kidneys compared with other recipients and wait-listed transplant candidates. *J. Am. Soc. Nephrol.* 12(589) (2001)
3. Rosengard, B.R., Feng, S., Alfrey, E.J., Zaroff, J.G., Emond, J.C., Henry, M.L., et al.: Report of the Crystal City meeting to maximize the use of organs recovered from the cadaver donor. *Am. J. Transplant.* 2(8), 701–711 (2002)



4. Bonnländer, B.V., Weigend, A.S.: Selecting input variables using mutual information and nonparametric density estimation. In: Proc. of the ISANN, Taiwan (2004)
5. Deb, K., Agrawal, S., Pratap, A., Meyarivan, T.: A fast and elitist multiobjective genetic algorithm: NSGA-II. *IEEE Trans. Evolutionary Computation* 6(2), 182–197 (2002)
6. Guillén, A., Pomares, H., González, J., Rojas, I., Valenzuela, O., Prieto, B.: Parallel multiobjective memetic rbfns design and feature selection for function approximation problems. *Neurocomputing* 72(16-18), 3541–3555 (2009)
7. Guillén, A., Sovilj, D., Lendasse, A., Mateo, F., Rojas, I.: Minimising the delta test for variable selection in regression problems. *IJHPSA* 1(4), 269–281 (2008)
8. Harrison, J.H., Merrill, J.P., Murray, J.E.: Renal homotransplantation in identical twins. *Surg. Forum* 6(432) (1956)
9. Schnuelle, P., Lorenz, D., Trede, M., Van Der Woude, F.J.: Impact of renal cadaveric transplantation on survival in end-stage renal failure: evidence for reduced mortality risk compared with hemodialysis during long-term follow-up. *J. Am. Soc. Nephrol.* 9(11), 2135–2141 (1998)
10. Pi, H., Peterson, C.: Finding the embedding dimension and variable dependencies in time series. *Neural Comput.* 6(3), 509–520 (1994)
11. Rossi, F., Lendasse, A., Franois, D., Wertz, V., Verleysen, M.: Mutual information for the selection of relevant variables in spectrometric nonlinear modelling. *Chem. and Int. Lab. Syst.* 80, 215–226 (2006)
12. Suykens, J.A.K., Van Gestel, T., De Brabanter, J., De Moor, J., Vandewalle, B.: *Least Squares Support Vector Machines*. World Scientific, Singapore (2002)

# Acute Lymphoblastic Leukemia Identification Using Blood Smear Images and a Neural Classifier

Adnan Khashman<sup>1</sup> and Hayder Hassan Abbas<sup>1,2</sup>

<sup>1</sup> Intelligent Systems Research Centre (ISRC)

<sup>2</sup> Department of Electrical and Electronic Engineering,  
Near East University, Lefkosa, Mersin 10, Turkey  
{khashman, hayder.hassan}@ieee.org

**Abstract.** There is a need for fast and cost-effective leukemia identification methods, because early identification could increase the likelihood of recovery. Currently, diagnostic methods require sophisticated expensive laboratories such as immune-phenotype and cytogenetic abnormality. Therefore, we propose an identification method based on using blood smear images of normal and cancerous cells, in addition to a neural network classifier. We focus in this paper on identifying Acute Lymphoblastic Leukemia (ALL) cases, and implement our experiments following three learning schemes for a neural model. The neural classifiers distinguish between normal blood cells and ALL-infected cells. The experimental results show that the proposed novel leukemia identification system can be effectively used for such a task, and thus could be implemented for identifying other leukemia types in real life applications.

**Keywords:** Acute lymphoblastic leukemia (ALL), Blood cell identification, Neural networks, Medical image processing.

## 1 Introduction

Leukemia is a type of blood disease or so-called cancer of the blood that begins in the bone marrow; and usually caused by an excessive alterations in the production of malignant and immature white blood cells [1]. There are four common types of leukemia; namely, Acute Myelogenous Leukemia (AML), Acute Lymphoblastic Leukemia (ALL), Chronic Myelogenous Leukemia (CML), and Chronic Lymphocytic Leukemia (CLL) [2].

This paper focuses on the ALL type because this blood cancer has been occurring most commonly in children in Iraq as a result of prolonged exposure to radiation and other chemical pollution. The rate of childhood leukemia in Iraq has doubled over a 15-year period; a rate that is compared unfavorably with neighboring countries, “It is known that the Basrah/Iraq region was exposed to environmental insults including chemical weapons agents such as pyrophoric depleted uranium and leukemogen benzene, as well as water and air pollution” [3].

The word acute in ALL comes from the fact that the disease progresses rapidly and it can be fatal within weeks to months if left untreated [2]. Leukemia is treatable if it

is diagnosed and treated in at early stage [1]. The early identification of the leukemia type can greatly increase the likelihood of recovery. In fact several diagnostic methods are available to identify leukemia type on basis of immune phenotype, cytogenetic abnormality, morphology, cytochemistry, and molecular genetic abnormalities. However, these diagnostic methods vary in the level of complexity, speed of the process, and the accuracy of leukemia classification [2].

In general, various recent studies suggested different methods for leukemia blood cell identification. Some works considered also the use of neural networks as classifiers for identification purposes. For instance, in [4] the authors focused on acute leukemia samples and used a flow cytometer instrument to analysis the images of normal and abnormal blood cells. The obtained data was then used as input for a neural network classifier. In [2] the authors presented the first phase of an automated leukemia form identification system, which was the segmentation of infected cell images. The segmentation process provided two enhanced images for each blood cell containing the cytoplasm and the nuclei regions of the cell. In [1], a neural network classifier was suggested for the screening task, basing its decision on features extracted from cell images. In [5], the authors used six morphological features which were extracted from acute leukemia blood cell images together with a neural network for classifying and distinguishing the blasts from acute leukemia blood samples. More recently, in [6] the authors suggested the use of an ensemble particle swarm model selection (EPSMS) to classify acute leukemia cases. In [7], the researchers used 12 manually extracted features from leukemia blood cell images together with the K-nearest neighbor (k-NN) classifier to identify leukemic cases.

All these recent works aimed identifying leukemia cases based on using single blood cell images and a classifier. Despite their successful outcome, we believe that their results can be improved by eliminating some elements which may hinder the results in one way or another. For example, the works in [1], [2], [5], and [7] based their identification systems on cell image features which to have to be manually extracted; this approach requires more time and complex calculations. While, in [4] the researchers used special equipment, namely; a flow cytometer instrument which is costly and may not be available in troubled countries such in Iraq.

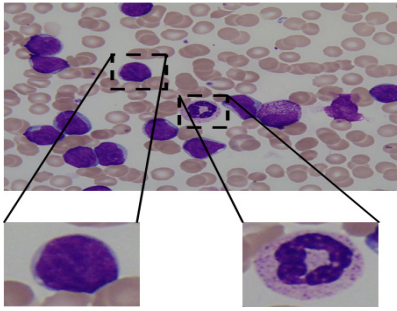
Therefore, we propose in this paper a fast and automated Leukemia-infected blood cell identification using pattern averaging of whole cell images and neural network classifiers. The proposed system is implemented to identify ALL-infected abnormal cells from normal blood cells; however, it can also be trained to identify the other types of leukemia.

Our approach in this paper comprises two phases: firstly, the image processing phase where data is extracted from whole cell images (thus avoiding the segmentation process and reducing time costs), and secondly, the identification phase where three neural models are implemented to associate the extracted image data from the first phase with the decision of 'normal' or 'abnormal' blood cell, i.e. ALL-infected. The three neural classifiers differ in their learning schemes based on using different training-to-validation data ratios. A comparison between their performances will be applied to select the optimal classifier for this task.

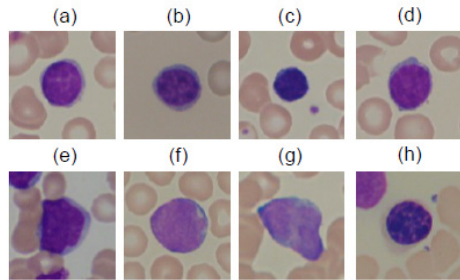
## 2 Blood Cell Image Database

The blood cell images that are used in this work are obtained from the freely available online ALL-IDB databases [8]. These images are microscopic images which had been labeled by expert oncologists as lymphocytes healthy and lymphoblast blood cells. Fig.1 shows an example image from this database, where the left-side cell image was labeled as abnormal (blast), while the right-side cell image was labeled as normal blood cell.

Our proposed identification system uses single blood cells in its implementation; therefore, we have constructed a second database (ALL-DB2) by cropping single cell images from the blood smear images in the ALL-IDB database. Our single cell image database contains both normal and abnormal blood cells, as shown in examples in Fig. 2. For the purpose of developing our identification system, 80 single-cell images are used; representing 40 normal blood cells and 40 abnormal blood cells that are infected by ALL-Leukemia. These images are color images of size 60×60 pixels.



**Fig. 1.** Example of cell images from blood sample. Left: lymphoblasts, and Right: lymph-ocytes [8].

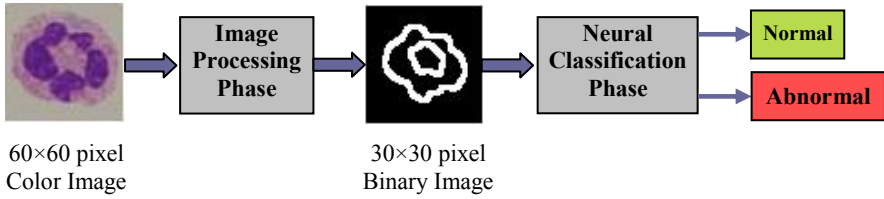


**Fig. 2.** Example images contained in the ALL-IDB: healthy cells (a-d), probable lymphoblasts from ALL patients (e-h). Cropped from [8].

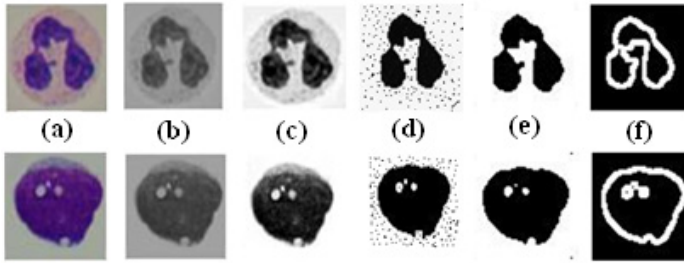
## 3 The Identification System

The best definition of a practical ANN is that it is a set of interconnected neurons that incrementally learn from given set of data to mimic the human brain in linear and nonlinear trends in complex data; so that it has capability to predict and adapt to new situations containing partial information [9]. We opt to use neural networks with whole images rather than selected features within the images, because neural networks have the capability to arbitrate fuzzy patterns more successfully than crisp patterns [10],[11],[12].

The proposed system comprises two phases: image processing phase where single-cell images undergo enhancement by use of a spatial filter and automatic edge detection yielding the input data for the second phase, which is neural network identification; as illustrated in Fig. 3.



**Fig. 3.** The two phases of the ALL-infected cell identification system



**Fig. 4.** Examples of normal blood cells (top) and abnormal ALL-infected blood cells (bottom) throughout the image processing phase. (a) Original image (b) Gray scale image (c) Binary image (d) Median filtered image (e) Smoothed image (f) Edge-detected image.

### 3.1 Image Processing Phase

During this phase all 80 single cell images from our database (ALL-DB2) undergo conversion from RGB colour to grey images. The grey scale images are then binarized using Otsu's thresholding method which chooses the threshold to minimize the interclass variance of the black and white pixels [13]. The binary images are then filtered using median filter for noise reduction. The filtered binary images undergo edge detection using Canny operator. Finally, we apply pattern averaging using  $2 \times 2$  kernel in order to 'fuzzify' the images and reduce their size from  $60 \times 60$  to  $30 \times 30$  pixels. The obtained  $30 \times 30$  image representation is then used as the input data to the neural networks during training and generalization in the second phase. Fig. 4 shows examples of abnormal and normal blood cells throughout the image processing phase.

### 3.2 Neural Classification Phase

In this phase a neural network based on the back propagation learning algorithm is utilized due to its implementation simplicity and the availability of sufficient database for training this supervised learner. The neural network has an input layer with 900 neurons receiving the processed  $30 \times 30$  pixel cell images on a pixel-per-node basis. One hidden layer is used with 72 hidden neurons which assures meaningful training while keeping the time cost to a minimum. The output layer has two neurons relaying the decision of the identification system regarding whether the blood cell is normal

[1 0] or abnormal [0 1]. A threshold value of 0.5 is applied to each output value resetting the output to binary ‘1’ or ‘0’. Fig. 5 shows the topology of the neural network.

The arbitration of supervised neural networks involves training the testing stages. During training input data samples are repeatedly presented to the neural model while dictating to the learning what the desired or target output should be. Once converged to a minimum value of error which the user sets, the model is considered as trained, and thus, ready to be tested with data samples that were not ‘seen’ before by the neural classifier. The performance of the trained neural model during testing or validation reflects how good it learnt and how intelligent it could be considered.

In this work we have a total of 80 blood cell images containing 40 normal and 40 abnormal or ALL-infected cells. The approach adopted in this work to train the neural model, is based on investigating different neural network learning schemes as suggested in [14]. The reason for trying different learning scheme is to optimize the neural model training and performance. Thus, we adopted three learning schemes where the data training-to-validation ratios are as follows:

- **Learning Scheme I – [75%:25%]:** 75% of the blood cells images, i.e. 60 images (30 normal and 30 abnormal) were used for training, while 25%, i.e. remaining 20 images (10 normal and 10 abnormal) were used for testing or validation.
- **Learning Scheme II – [50%:50%]:** 50% of the blood cells images, i.e. 40 images (20 normal and 20 abnormal) were used for training, while 25%, i.e. remaining 40 images (20 normal and 20 abnormal) were used for testing or validation.
- **Learning Scheme III – [25%:75%]:** 25% of the blood cells images, i.e. 20 images (10 normal and 10 abnormal) were used for training, while 75%, i.e. remaining 60 images (30 normal and 30 abnormal) were used for testing or validation.

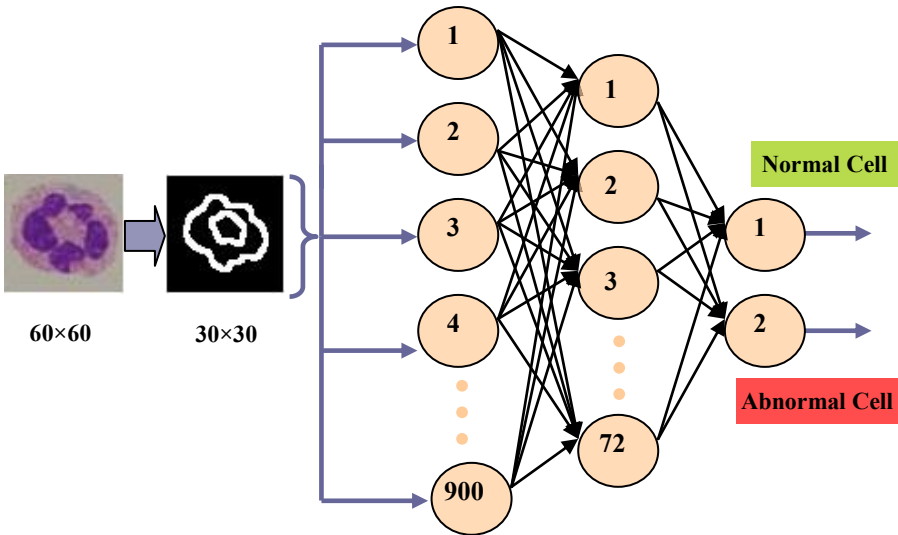


Fig. 5. ALL-infected cell identification system and neural network topology

## 4 Implementation Results

The implementation of our proposed identification system; including the image processing phase and the neural network arbitration phase, was realized using the MATLAB software tool. Several experiments were carried out to train and test the neural network under the three learning schemes *LS-I*, *LS-II*, and *LS-III*.

The evaluation of the performance of the three neural classifiers was based upon three factors; namely, the obtained error value, the identification overall accuracy rate, and the identification run time. Table 1 lists the finalized training parameters of the neural network under the three learning schemes. The obtained error values and time cost when implementing the three schemes are listed in Table 2, whereas the obtained identification accuracy rates are listed in Table 3. Fig. 6 shows the learning curves of the three neural classifiers during training.

**Table 1.** Neural network final training parameters

Parameters	Final Value
Input layer neurons	900
Hidden layer neurons	62
Output layer neurons	2
Random initial weight range	-0.1 to 0.1
Learning rate	0.09
Momentum factor	0.45
Minimum required error	0.001
Maximum permitted iterations	5000

**Table 2.** The three learning schemes and implementation results of ALL-Leukemia identification system model

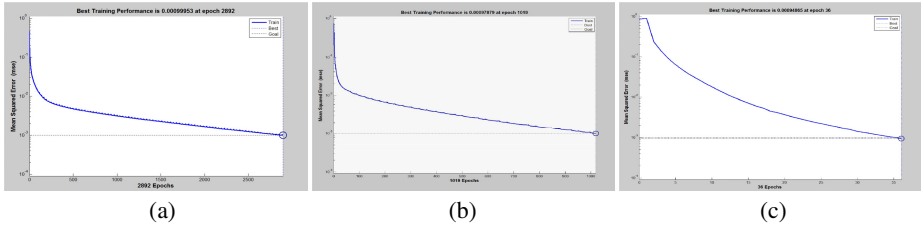
Learn- ing Scheme	Learning Ratio (%)	Obtained Error	Training Time (s)	Run Time (s)	Number of Iterations
<b>LS-I</b>	<b>(75:25)</b>	<b>0.0175</b>	<b>38.08</b>	<b>0.721</b>	<b>62</b>
LS-II	(50:50)	0.01798	21.308	1.73	68
LS-III	(25:75)	0.01768	8.01	2.29	34

Upon inspecting the results in Table 2 and Table 3, we could deduce that implementing the neural network under LS-I outperforms implementations under LS-II and LS-III. Following LS-I, the highest overall accuracy rate of 90% correct identification was achieved together with the least error value of 0.0175 and the fastest run time of 0.721 second. This indicates that the neural classifier training under LS-I provides the most optimal results for this application.

**Table 3.** Correct cell identification accuracy rates

Learning Scheme	Training Accuracy Rate (%)		Testing Accuracy Rate (%)		Overall Accuracy Rate (%)	
	NBC <sup>a</sup>	ABC <sup>b</sup>	NBC	ABC	Training	Testing
LS-I	(30/30) 100	(30/30) 100	(9/10) 90	(9/10) 90	(60/60) 100	(18/20) 90
LS-II	(20/20) 100	(20/20) 100	(15/20) 75	(17/20) 85	(40/40) 100	(32/40) 80
LS-III	(10/10) 100	(10/10) 100	(22/30) 73.3	(23/30) 76.6	(20/20) 100	(45/60) 75.1

<sup>a</sup> Normal Blood Cells. <sup>b</sup> Abnormal Blood Cells

**Fig. 6.** Learning curves (error convergence) in (a) Scheme I (b) Scheme II, and (c) Scheme III.

## 5 Conclusions

A novel approach to acute lymphoblastic leukemia (ALL) blood cell identification was presented. The novelty in this work is not only in using a neural model as a classifier, but also in considering normal and abnormal (leukemic) blood cells as a whole without the need to extract local features. This in turn reduces the computational and time costs by avoiding segmentation and local feature extraction from the blood cell images.

The motivation behind this work and the reason for focusing on the ALL blood cancer is its increasing occurrence amongst children in conflict zones such as in Iraq. Our database contains single blood cell images of both normal healthy cells and abnormal ALL-infected cells. The source of our database is a freely available online database that contains blood smear microscopic images labeled by expert oncologists as normal or abnormal.

The neural network within this identification system was trained and tested following three different learning schemes. These schemes differ in the ratio of the number of cells images used for training, against those used for testing or validation. The aim of employing different learning schemes is to seek an optimal neural classifier considering the available data and the application.

The experimental results indicate that such an approach to identifying infected blood cells can be successfully employed in real life applications, thus avoiding the use of expensive and often unavailable cytometer instruments; in particular in conflict



zones. The obtained results under learning scheme LS-I are very encouraging with an identification accuracy of 90%, error value of 0.0175, and cell identification run time of 0.721 seconds. Further work will focus on developing a model to identify the other three common types of leukemia following the same approach.

## References

1. Francis, E.U., Mashor, M., Hassan, Y.R., Abdullah, A.A.: Screening of Bone Marrow slide Images for Leukaemia using Multilayer Perceptron (MLP). In: IEEE Symposium on Industrial and Applications (ISIEA 2011), pp. 25–28 (2011)
2. Khashman, A., Al-Zgoul, E.: Image Segmentation of Blood Cells in Leukemia Patients. In: Recent Advances in Computer Engineering and Application, pp. 104–109 (2010)
3. Hagopian, A., Lafta, R., Hassan, J., Davis, S., Mirick, D., Takaro, T.: Trends in Childhood Leukemia in Basrah, Iraq, 1993–2007. *American Journal of Public Health* 100(6), 1081–1087 (2010)
4. Adjouadi, M., Ayala, M., Cabrerizo, M., Zonic, N., Lizarraga, G., Rossman, M.: Classification of Leukemia Blood Samples Using Neural Networks. *Annals of Biomedical Engineering* 38(4), 1473–1482 (2009)
5. Harun, N.H., Mashor, M.Y., Abdul Nasir, A.S., Rosline, H.: Automated Classification of Blasts in Acute Leukemia Samples Using HMLP Networks. In: Proceedings of the 3rd International Conference on Computing and Informatics (ICOCI), pp. 55–60 (2011)
6. Escalante, H., Montes-y-Gómez, B., Jesús, C., González, A., Gómez-Gila, P., Altamirano, L., Reyesa, C.A., Retaa, C., Rosalesa, A.: Acute Leukemia Classification by Ensemble Particle Swarm Model Selection. *Artificial Intelligence in Medicine* (2012), doi:10.1016/j.artmed.2012.03.005
7. Supardi, N.Z., Harun, N.H., Mashor, M.Y., Bakri, F.A., Hassan, R.: Classification of Blasts in Acute Leukemia Blood Samples Using *K*-Nearest Neighbour. In: IEEE 8th International Colloquium on Signal Processing and its Applications, pp. 461–465 (2012)
8. Donida Labati, R., Piuri, V., Scotti, F.: ALL-IDB web site, Università degli Studi di Milano. Department of Information Technology, <http://www.dti.unimi.it/fscotti/all>
9. Duda, R.O., Hart, P.E., Stork, D.G.: *Pattern Classification*, 2nd edn. Thomson Learning, New York (2010)
10. Khashman, A., Buruncuk, K., Jabr, S.: Intelligent Detection of Voltage Instability in Power Distribution Systems. In: Sandoval, F., Prieto, A.G., Cabestany, J., Graña, M. (eds.) IWANN 2007. LNCS, vol. 4507, pp. 870–877. Springer, Heidelberg (2007)
11. Khashman, A.: A Modified Back Propagation Learning Algorithm with Added Emotional Coefficients. *IEEE Transactions on Neural Networks* 19(11), 1896–1909 (2008)
12. Theodoridis, S., Koutroubas, K.: *Pattern Classification*, 4th edn. Elsevier Inc., London (2009)
13. Otsu, N.: A threshold selection method from gray level histograms. *IEEE Transactions on Systems, Man and Cybernetics* 9, 62–66 (1979)
14. Khashman, A.: Neural networks for credit risk evaluation: Investigation of different neural models and learning schemes. *Expert Systems with Applications* 37(9), 6233–6239 (2010)

# Modeling of Survival Curves in Food Microbiology Using Fuzzy Wavelet Neural Networks

Vassilis S. Kodogiannis<sup>1</sup> and Ilias Petrounias<sup>2</sup>

<sup>1</sup> School of Electronics and Computer Science, University of Westminster,  
London, United Kingdom

V.Kodogiannis@westminster.ac.uk

<sup>2</sup> Manchester Business School, University of Manchester, Manchester, United Kingdom

Ilias.petrounias@manchester.ac.uk

**Abstract.** The development of accurate models to describe and predict pressure inactivation kinetics of microorganisms is very beneficial to the food industry for optimization of process conditions. The need for methods to model highly nonlinear systems is long established. The architecture of a novel clustering-based fuzzy wavelet neural network (CB-FWNN) model is proposed. The objective of this research is to investigate the capabilities of the proposed scheme, in predicting the survival curves of *Listeria monocytogenes* inactivated by high hydrostatic pressure in UHT whole milk. The proposed model is obtained from the Takagi–Sugeno–Kang fuzzy system by replacing the THEN part of fuzzy rules with a “multiplication” wavelet neural network. Multidimensional Gaussian type of activation functions have been used in the IF part of the fuzzy rules. The performance of the proposed scheme has been compared against neural networks and partial least squares models usually used in food microbiology.

**Keywords:** predictive modeling, fuzzy-wavelet neural networks, partial least squares regression, clustering.

## 1 Introduction

There has been continued interest in the food industry in using high hydrostatic pressure processing as a non-thermal preservation technique. Its primary advantage is that it can inactivate microorganisms and certain enzymes at ambient temperature, thus avoiding the detrimental effects of cooking temperatures on various food quality attributes, such as nutritional value, flavor and taste. However, as foods are frequently implicated as carriers of foodborne pathogens, it is important to provide information on the effect of high-pressure processing on these micro-organisms. The inactivation of micro-organisms by high pressure is well documented; typically, vegetative pathogens can be inactivated at a pressure range of 200–700 MPa [1]. The exact mechanism of high pressure inactivation has been fully elucidated, but it is generally accepted that high pressure results in morphological, genetic and biochemical alterations causing cell death due to accumulated damage [2]. *Listeria monocytogenes* is a ubiquitous

foodborne pathogen associated with outbreaks of listeriosis from consumption of various food commodities, such as vegetables, dairy products, seafood and meat [3]. The pathogen is of great health concern for the food industry, because it is characterized by high mortality rates, especially in pregnant women, neonates, elderly and immune-compromised. It is a very hardy micro-organism that can grow over a wide range of pH values (4.3 to 9.1) and temperature ranges from 0 to 45°C. The inactivation of micro-organisms by heat and other processing methods has been traditionally assumed to follow first-order kinetics. However, significant deviations from linearity have frequently been reported [4]. A number of models have been proposed to describe these nonlinear survival curves, such as the Weibull model [5].

The aim of the current research study is to investigate the feasibility of utilizing a hybrid fuzzy-wavelet-neural network (FWNN) methodology as an alternative to classical neural networks in the area of food microbiology. In the proposed clustering-based fuzzy wavelet neural network (CB-FWNN) a fuzzy subtractive clustering (FSC) has been utilized as a “first-stage” process to find out the initial set and adequate number of clusters, fuzzy rules and ultimately define the structure in the incorporated in the design wavelet neural network (WNN), while multivariate fuzzy sets are utilized in the premise part of the CB-FWNN structure. Once the number of clusters is defined via the FSC scheme, candidate models representing possible states of the structure are clustered using a modified Expectation-Maximization (EM) technique during the training. The proposed EM version which is responsible for partitioning the data as well as finding the cluster parameters enables a feedback link from output error into the clustering process. The obtained clusters are multivariate Gaussians (Gaussian Mixture Models - GMM) each with different size and orientation from the other. The outputs of the clustering block are the firing strengths multiplied by the consequence part of the CB-FWNN structure. CB-FWNN scheme utilizes WNNs in the consequent part of each rule, similarly to existing FWNN schemes. However in the proposed structure a novel WNN that incorporates an extra multiplication layer as well as a linear combination of weights (MWNN-LCW) has been applied [6].

The overall objective of this study is to design one-step ahead predictive schemes to model the survival of *Listeria monocytogenes* in ultra high-temperature (UHT) whole milk during high pressure treatment using the proposed CB-FWNN structure. Its performance will be judged against PLS and NN models and an evaluation will be made to compare the goodness-of-fit of these model.

## 2 Experimental Case

### 2.1 Bacterium and Preparation and Pressurization

*Listeria monocytogenes* NCTC 10527 from the collection of the Laboratory of Microbiology and Biotechnology of Foods, Agricultural University of Athens was used throughout this study [7]. The culture was revived by inoculation in 9ml of tryptic soy broth supplemented with 0.6% yeast extract and incubation at 30°C for 24 h. Aliquots of 3.0ml of sample containing 0.3 ml of cell suspension and 2.7 ml of UHT whole milk were transferred in polyethylene pouches and heat-sealed taking care to expel most of the air. The pouches were placed in duplicate in each of the six small vessels of the

high pressure unit and the system was pressurized at 350, 450, 550 and 600 MPa, respectively. The come-up rate was approximately 100 MPa per 7s and the pressure release time was less than 3s. Each experiment was repeated twice and duplicate pouches were used for each pressure/time combination.

### 2.2 Enumeration of Survivors

Immediately after treatment, pressurized pouches were removed from the vessels and their contents were aseptically diluted in ¼ sterile Ringer’s solution. One hundred microlitres (100 µl) of at least three serial dilutions were spread-plated in triplicate on the non selective Tryptic Soy Agar (TSA) medium supplemented with 0.6% yeast extract for the enumeration of *L. monocytogenes*. The data from the plate counts were transformed to log10 values prior to further analysis.

## 3 Modeling Using CB-FWNN

This paper presents a clustering based FWNN that follows an “ANFIS structure” and its details are illustrated in Fig. 1. However significant differences against ANFIS have been considered in the proposed modeling structure. In the proposed structure instead of a linear function, a novel Linear Combination Multiplication Weight Wavelet Neural Network (MWNN-LCW) has been utilized [6]. The specific model integrated two learning schemes; Weighted Least Square as well as the classic gradient descent (GD) learning algorithms.

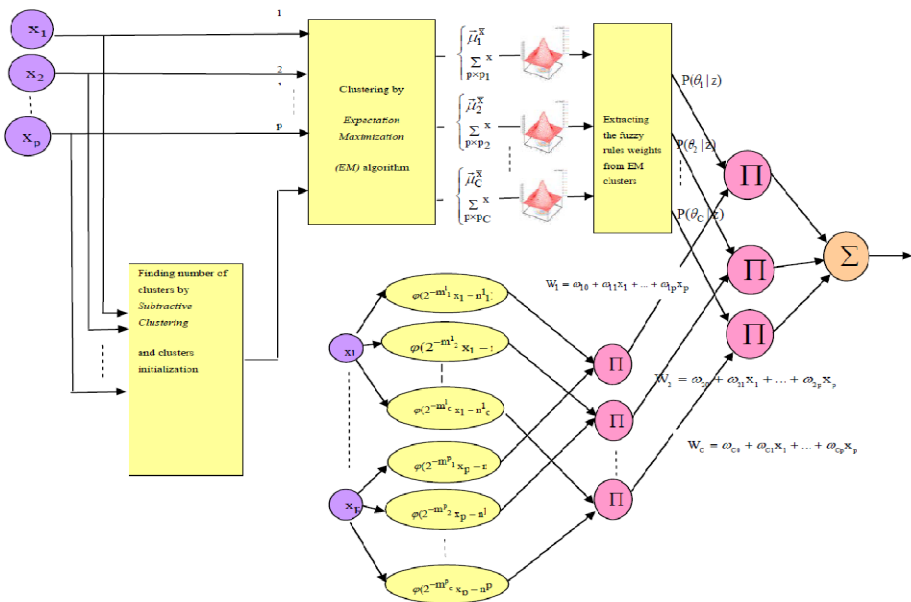


Fig. 1. CB-FWNN proposed structure

However, GD scheme is characterized by slow convergence training speed. Hence, in this study, the scale and translation parameters and local linear model parameters which have been randomly initialized at the beginning are optimized by using the Extended Kalman Filter (EKF) algorithm. In order to design the CB-FWNN structure, we assume initially, that one cluster in the input-output space corresponds to one potential fuzzy logic rule. Then the first step in structure learning is the determination of the number of fuzzy sets in the universal of discourse of each input variable [8]. In this research, the number of clusters are determined by subtractive clustering based on the training data as described earlier and remain constant throughout. Once the number of clusters defined, then the layout of the desired CB-FWNN can be sketched. At the consequence section, different scales of wavelet-neurons  $\varphi_{x^p}(m_i^p, n_i^p)$  assigned for every dimension of the input. Knowing the optimum number of clusters, the number of different scales which each input dimension is going to be decomposed then can be determined, while the known number of clusters could assist in the determination of the number of fuzzy rules  $c$  as well as to the number of unknown parameters at the antecedent section. CB-FWNN's output is formulated as,

$$\begin{aligned} \hat{y}_j &= \sum_{i=1}^C \gamma_i(X_j) W_i(X_j) \phi_i(X_j) \\ &= \sum_{i=1}^C \gamma_i(X_j) W_i(X_j) \prod_{p=1}^P \varphi_{m_i^p, n_i^p}(x_j) \\ &= \sum_{i=1}^C W_i(X_j) \gamma_i(X_j) \left( \prod_{p=1}^P \cos\left(2\pi\beta \left(\frac{x_j^p - n_i^p}{m_i^p}\right)\right) e^{-\frac{\left(\frac{x_j^p - n_i^p}{m_i^p}\right)^2}{v}} \right) \end{aligned} \tag{1}$$

The conditional density  $p(y | x)$  is a mixture of Gaussians functions at the output of clustering sub-unit therefore the regression problem is re-formulated also as

$$\begin{aligned} \hat{y}_j &= f(x) = E[y_j | x_j] \\ &= \int_y y_j p(y_j | x_j) dy = \frac{\int y_j p(x_j, y_j) dy}{p(x_j)} \\ &= \sum_{i=1}^c \frac{[W_i \phi_i(x_j)] p(x_j | \theta_i) p(\theta_i)}{p(x_j)} = \sum_{i=1}^c W_i \times P(\theta_i | x_j) [\phi_i(x_j)] \end{aligned} \tag{2}$$

where  $\phi_i(x_j)$  is related to the  $i^{th}$  from  $c$  MWNN-LCW outputs, and the  $j^{th}$  input vector.  $W_i(X_j)$  is the linear combination weight and  $P(\theta_i | X_j)$  is the probability that the  $i^{th}$  Gaussian component is generated by the input vector  $X_j$  as depicted in the following equation, which replaces  $\gamma$  in eq. 1.

$$P(\theta_i | x_j) = \frac{\frac{P(\theta_i)}{(2\pi)^{p/2} \sqrt{|\Sigma_i|}} \exp\left(-\frac{1}{2}(x_j - \mu_i)^T (\Sigma_i)^{-1} (x_j - \mu_i)\right)}{\sum_{i=1}^c \frac{P(\theta_i)}{(2\pi)^{p/2} \sqrt{|\Sigma_i|}} \exp\left(-\frac{1}{2}(x_j - \mu_i)^T (\Sigma_i)^{-1} (x_j - \mu_i)\right)} \tag{3}$$

The final output based on dynamics of the proposed structure is derived by merging Eqs. 1 and 2 and have the following form

$$\hat{y}_j = \sum_{i=1}^C W_i(X_j) \times P(\theta_i | X_j) \left( \prod_{p=1}^P \cos(2\pi\beta \left( \frac{x_j^p - n_i^p}{m_i^p} \right)) \right) e^{-\frac{(x_j^p - n_i^p)^2}{m_i^p}} \quad (4)$$

The cluster parameters in this proposed scheme are estimated with the use of Expectation Maximization algorithm, while the Wavelet Neural Network parameters have been modified by Extended Kalman Filter and Weighted Least Square. The choice of EM algorithm is justified by the fact that this approach avoids numerical instabilities encountered in Gradient Decent algorithm and presents an improved learning convergence.

### 4 Discussion of Results

For identification we consider the case where the plant is observable and where input-output measurements are available. Dependent on the kind of inputs used, either parallel or series-parallel models can be utilized [9]. The objective of this study is to investigate the feasibility of using a CB-FWNN scheme for the development a series-parallel model of survival curves of *Listeria monocytogenes* under high pressure in whole milk.

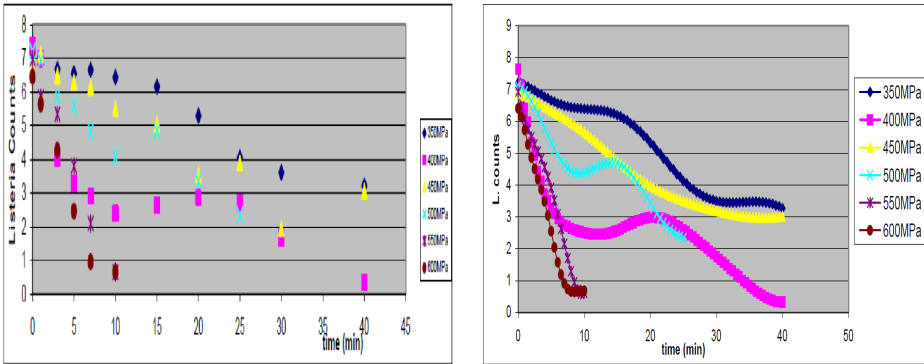
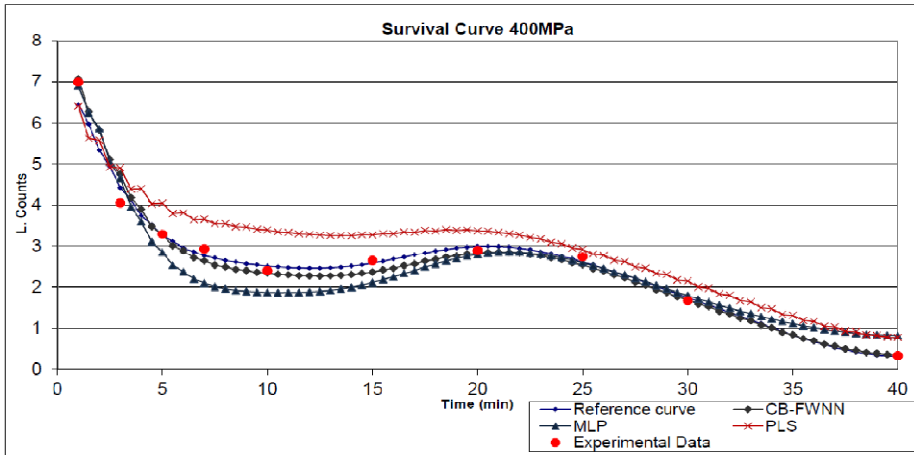


Fig. 2. Illustration of the experimental data and survival curves

The survival curves of *Listeria monocytogenes* inactivated by high hydrostatic pressure were obtained at seven pressure levels (350, 400, 450, 500, 550 and 600 MPa) in UHT whole milk, as shown in Fig. 2. Interestingly, the shapes of the survival curves that follow those experimental data change considerably depending on the treatment pressure levels. Small data set conditions exist in many fields, including food analysis. It is hard to catch the pattern of high order non-linear functions by a standard feed-forward neural network-like scheme with small sample sets, since they have shown weakness in providing sufficient information for forming population patterns. Inspired by the way the RBF network approximates a nonlinear function through

Gaussian local-basis functions, we have employed such a network to each “survival curve” defined from the experimental data. Hence, for each pressure level case, an RBF network has been associated with. Each “continuous survival curve” has been verified against the real experimental samples. Based on these continuous datasets, the capabilities of the proposed CB-FWNN architecture has been verified as a one-step-ahead prediction system. Comparative studies have been conducted with the utilization of Multilayer NN (MLP) and PLS models. Pressure levels of 400 MPa and 500 MPa have been used as testing datasets, while the remaining levels as training ones. The performance against the unknown 400MPa and 500MPa curves is illustrated in Figs. 3 and 4 respectively.



**Fig. 3.** CB-FWNN’s performance in the 400 MPa

Results showed that the CB-FWNN was very effective in predicting the response of the pathogen, implying that although the CB-FWNN has been trained on different survival curves, it has managed to learn the underlying process with high accuracy.

In a similar way, an MLP neural network using the classic back-propagation learning algorithm was constructed with the same input structure as CB-FWNN. Through trial and error, eventually two hidden layers with 12 and 8 nodes respectively have been employed. The learning algorithm was responsible for the network’s slow convergence, which took approximately 30,000 epochs. Figs. 3 and 4 illustrate the MLP performance for both testing survival curves.

Like CB-FWNN and MLP, the PLS regression model was constructed to anticipate the dynamic nature of the specific problem, by including past values of the *Listeria* counts as inputs. The calculated by XLSTAT software, equation has the following form

$$\begin{aligned}
 Y_1 = & 0.1646857 - 0.000172X_1 - 0.0055X_2 \\
 & - 0.0055X_3 - 0.0055X_4 - 0.955X_5 + 1.9412X_6
 \end{aligned}
 \quad (5)$$

Figs. 3 and 4 illustrate the PLS performance for both testing survival curves. With regard to the assessment of the quality of the overall model predictions various statistical criteria were calculated at all the tested validation experiments.

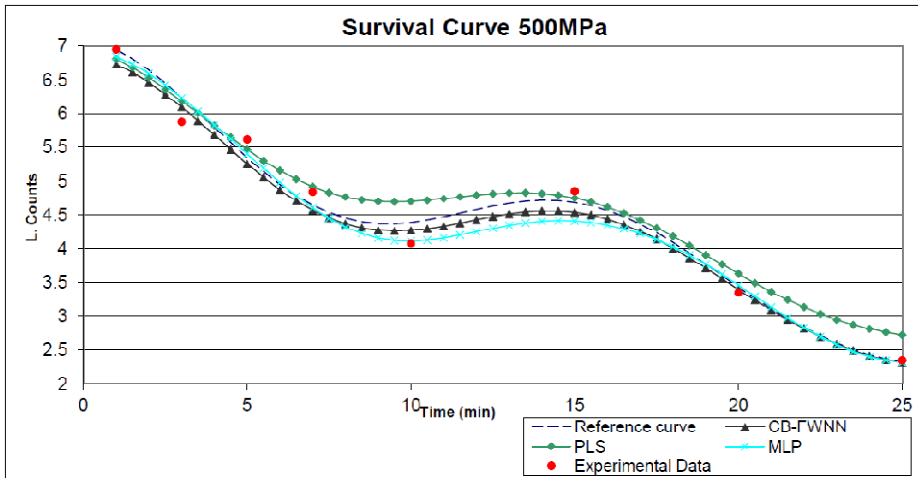


Fig. 4. CB-FWNN's performance in the 500 MPa

## 5 Conclusions

In conclusion, the survival curves of *L. monocytogenes* in UHT whole milk could have different shapes depending on the treatment pressure levels. The development of accurate mathematical models to describe and predict pressure inactivation kinetics of microorganisms, such *L. monocytogenes* should be very beneficial to the food industry for optimization of process conditions and improved dependability of HACCP programs. In this research study we have applied a fuzzy-wavelet neural network, and validated it in a series-parallel identification scheme for the modeling of the *Listeria monocytogenes* survival/death curves. Results and comparison with other methods have revealed a very good accuracy which was accompanied with a high speed training process. Future research will investigate the possibility of engaging the proposed scheme in a parallel-mode architecture, while it would interesting to consider the modeling of the combined effect of high hydrostatic pressure and mild heat on the inactivation kinetics of *Listeria*.

## References

1. Tholozan, J.L., Ritz, M., Jugiau, F., Federighi, M., Tissier, J.P.: Physiological effects of high hydrostatic pressure on *Listeria monocytogenes* and *Salmonella Typhimurium*. *J. Appl. Microbiology* 88, 202–212 (2000)
2. Patterson, M.F., Kilpatrick, D.J.: The combined effect of high hydrostatic pressure and mild heat on inactivation of pathogens in milk and poultry. *J. Food Prot.* 61, 432–436 (1998)



3. Ryser, E.T., Marth, E.H.: *Listeria, Listeriosis and Food Safety*. Marcel Dekker Inc., New York (1999)
4. Hajmeera, M., Basheer, I., Cliver, D.O.: Survival curves of *Listeria monocytogenes* in chorizos modeled with artificial neural networks. *Food Microbiology* 23, 561–570 (2006)
5. Van Boekel Martinus, A.J.S.: On the use of the Weibull model to describe thermal inactivation of microbial vegetative cells. *International journal of food microbiology* 74(1-2), 139–159 (2002)
6. Amina, M., Kodogiannis, V.S., Petrounias, I., Lygouras, J.N., Nychas, G.-J.E.: Identification of the *Listeria Monocytogenes* survival curves in UHT whole milk utilising Local Linear Wavelet Neural Networks. *Expert Systems and Applications* 39(1), 1435–1450 (2012)
7. Amina, M., Panagou, E.Z., Kodogiannis, V.S., Nychas, G.-J.E.: Wavelet Neural Networks for modeling high pressure inactivation kinetics of *Listeria monocytogenes* in UHT whole milk. *Chemometrics and Intelligent Laboratory Systems* 103(2), 170–183 (2010)
8. Amina, M., Kodogiannis, V.S., Petrounias, I., Tomtsis, D.: A hybrid intelligent approach for the prediction of electricity consumption. *International Journal of Electrical Power & Energy Systems* 43(1), 99–108 (2012)
9. Nelles, O.: *Nonlinear system identification*. Springer (2000)

# Modeling Tissue Temperature Dynamics during Laser Exposure<sup>\*</sup>

Loris Fichera, Diego Pardo, and Leonardo S. Mattos

Department of Advanced Robotics, Istituto Italiano di Tecnologia  
Via Morego 30, 16163 Genova, Italy  
{loris.fichera,diego.pardo,leonardo.demattos}@iit.it

**Abstract.** This paper presents the simulation and learning of soft tissue temperature dynamics when exposed to laser radiation. Monte Carlo simulation is used to represent the photon distribution in the tissue while machine learning techniques are used to obtain the mapping from controllable laser inputs (power, pulse rate and exposure time) to the correspondent changes in temperature. This model is required to predict the effects of laser-tissue interaction during surgery, i.e., tissue incision depth and carbonization.

**Keywords:** Laser-tissue interaction, Temperature dynamics, Nonlinear regression

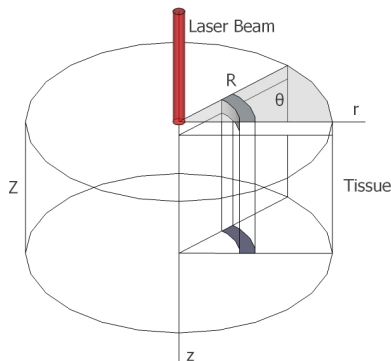
## 1 Introduction

Lasers are employed in a number of surgical specialties as cutting tools. Their use has gained popularity in those procedures where high-quality incisions are needed, e.g., in surgery of the vocal folds [1]. The quality of an incision encompasses the accuracy for both, depth and length of the cut executed by the surgeon. With respect to traditional surgery, where such a quality relies mainly on the surgeon's ability to handle the scalpel and on his/her delicate sense of touch, laser surgery requires a different type of dexterity. Improper use of the laser may result in harmful and undesired effects, such as *carbonization* [2]. In order to automatically supervise such effects, the interaction between laser and tissue must be modeled.

When tissue is irradiated with a laser beam molecules are promoted to an excited state due to the absorption of photons. Excited molecules collide with some partner in the surrounding medium and these collisions lead to both, the deactivation of the excited molecules and the increasing of the kinetic energy in the partners [2]. Tissue temperature rises microscopically because of the transfer of energy, in the form of heat, from photons to tissue. As tissue is composed mostly of water, at 100°C water molecules start to vaporize and the resulting ablation is

---

<sup>\*</sup> The research leading to these results has received funding from the European Union Seventh Framework Programme FP7/2007-2013 – Challenge 2 – Cognitive Systems, Interaction, Robotics – under grant agreement  $\mu$ RALP N°288233.



**Fig. 1.** Tissue Geometrical Model

called *thermal decomposition* [2]. Thus, cutting tissue can be roughly described as boiling water. Change in local temperature is the significant parameter during ablation by vaporization [2].

Here we propose to create a model of temperature dynamics in order to predict the consequences of laser radiation on soft-tissue. Despite analytical models have been extensively studied [2], the use of such models to predict the effects of laser radiation during real surgery seems inadequate. We envisioned a model similar to the internal mapping done by surgeons. Certainly, surgeons do not solve the very complex differential equations that govern the dynamics of tissue temperature, instead they use a different set of input variables, extracted from visual information, allowing them to interpret the state of the laser-tissue interaction and predicting the outcome of their actions. The experience and skills of the surgeons allow them to intrinsically establish how likely carbonization is and to supervise incision depth and thereby to decide the actions to perform.

In order to obtain this mapping, a regression between high level actions and changes in temperature is proposed. The behavior of temperature when tissue is being exposed to a laser can be simulated using numerical methods and therefore providing sufficient data to complete the regression. This paper describes the simulation process and the use of the output data to learn the tissue temperature dynamics.

## 2 Tissue Temperature Model

### 2.1 Analytic Model

A cylindrical reference system  $(r, z, \theta)$  is used to describe the tissue geometry. As shown in Fig.1, the longitudinal axis  $z$  is coincident with the direction of propagation of the laser and the origin is the intersection between such axis and the tissue surface. A circular laser beam is applied onto the top of the tissue.

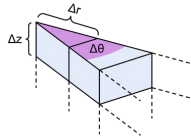
The analytic model of the tissue temperature dynamics [2] is given by,

$$\dot{T}(r, z, t) = \beta \left( \frac{\partial^2}{\partial r^2} + \frac{\partial^2}{r \partial r} + \frac{\partial^2}{\partial z^2} \right) T + \frac{1}{\rho \gamma} Q, \quad (1)$$

where  $\beta$  is the tissue temperature conductivity,  $\rho$  is the tissue density and  $\gamma$  is the tissue heat capacity. The rate of heat generation  $Q$  represents the source of heat provided by the laser. Unfortunately, exact solution of Eq. (1) is complex [2] and it involves several approximations and assumptions.

## 2.2 Discrete Representation

The tissue volume is discretized using a grid with constant increments ( $\Delta r = 0.025 \text{ mm}$ ,  $\Delta z = 0.025 \text{ mm}$  and  $\Delta \theta = 1/30 \text{ rad}$ ). A single volume element is shown in Fig 2.



**Fig. 2.** Detail of volume elements

*Definition I* Let us define  $\mathcal{T}$  as the set representing the temperature of a certain tissue volume, composed by  $N$  elemental volumes such that,

$$\mathcal{T} = \bigcup_{n \in \{1, \dots, N\}} T^n, \quad (2)$$

where  $T^n$  represents the temperature of a single elemental volume centered at a given radius ( $r$ ), angle ( $\theta$ ) and depth ( $z$ ).

Given that, as already suggested by Eq. (3), temperature dynamics is independent of the angular dimension, angular symmetry can be assumed. Tissue temperature is completely described given a single sample of the angular grid.

*Definition II* Let us define  $\mathbf{T} \in \mathbb{R}^{I \times J}$  as the temperature matrix that completely describes  $\mathcal{T}$ . Where  $I = Z/\Delta z$ ,  $J = R/\Delta r$  and  $N = I \times J \times (2\pi/\Delta \theta)$

The goal is to find a discrete model for the time evolution of the tissue temperature (i.e., temperature dynamics), which is given by

$$\mathbf{T}_{k+1} = f(\mathbf{T}_k, \mathbf{u}_k), \quad (3)$$

where  $\mathbf{T}_k$  is the temperature at time  $t = k \cdot \Delta t$  and  $\mathbf{u}$  is a vector representing the independent variables affecting the state of the system. The output of the model is the estimated variable, i.e., the temperature in the next sample time, ( $\mathbf{T}_{k+1}$ ). Input variables must include enough information to predict the output.

Therefore, the state of the variable being supervised has been included ( $\mathbf{T}_k$ ). Moreover, based on the mathematical relations revised in previous sections, we can assume that, given a certain type of tissue and a set of laser properties like laser type and beam size and profile, changes in temperature are driven by the laser power ( $P$ ) and length of the pulse duration ( $\tau$ ), i.e.,

$$\mathbf{u}_k = [P \quad \tau]^T. \quad (4)$$

Known and constant sample time ( $\Delta t$ ) is also assumed in Eq. (3). We hypothesize that a single function can be used to map the inputs to the prediction of the temperature in any point ( $r, z$ ) of the tissue volume.

*Hypothesis.* There exists a unique function,  $h$ , such that,

$$T_{k+1}^{i,j} = h(\mathbf{T}_k, \mathbf{u}_k, i, j) \square \quad (5)$$

The mapping proposed in Eq. (5) is clearly nonlinear, as the influence of  $\mathbf{u}$  is not proportional with respect to the location of the volume element. Moreover, as suggested in Eq. (1), the proportion of the changes in temperature due to heat transportation, i.e., those that take into account temperature in the surroundings of the elemental volume of interest, also vary with respect to the position of it.

The assumptions presented in the description of Eq.(3), together with the required approximation for the initial temperature  $\mathbf{T}_0$ , restrict the use of the model only to similar types of laser and tissues as well as similar environmental conditions. Despite more complex models may be envisioned, this model will allow to validate the proposed methodology and will orient more ambitious objectives. Besides, note that for this model no motion of the laser is considered and the laser application point is assumed to remain constant with respect to the tissue volume.

Nonlinear function approximation methods can be used to find the hypothesized function from data. A set of samples of the input and output variables,  $\left\{ \mathbf{T}_{k+1}^l, [\mathbf{T}, \mathbf{u}]_k^l \right\}_{l=1}^m$  is used to approximate such relation using a Statistical based nonlinear function approximation method known as Locally Weighted Projection Regression (LWPR)[3,4].

LWPR was selected as supervised learning algorithm as it is considered the state of the art in statistical nonlinear regression. This algorithm allows to learn nonlinear functions where there are large amounts of training data and high dimensional input spaces, it is also incremental, therefore new data can be included, allowing the model to adapt to changing circumstances [3].

### 3 Simulated Laser Tissue Thermal Interaction

This section describes the simulation of the dynamics of temperature across a given tissue volume while it is exposed to a laser beam. Simulation of temperature dynamics is obtained through a two-step process, as suggested in [5,6]. First a statistical model describing how the power delivered by the laser is spatially

distributed across the tissue volume is required. Next, such distribution is used to solve Eq. (1) in order to obtain a model of temperature dynamics. The spatial distribution of power is represented in terms of a probability distribution function named *Photon Absorption Probability* (PAP), which is computed by means of a *Monte Carlo Method* [5]. Temperature dynamics is obtained expressing the rate of heat generation  $Q$  in terms of the PAP and solving equation Eq. (1) using a *Finite Difference Method* [5].

### 3.1 Monte Carlo Photon Propagation

A Monte Carlo method is used as implemented in [5,7]. The laser beam is assumed to be made up of a large number  $N_p$  of photons, each propagating independently of one another. The motion pattern of photons is described by means of three random variables, namely a *step size* ( $s$ ), a *rotation angle*  $\varphi$  and a *deflection angle*  $\theta$  [5]. The step size is defined as

$$s = \frac{-\ln(\zeta)}{\mu_a + \mu_s}, \quad (6)$$

where  $\zeta$  is a random variable uniformly distributed in the interval  $(0, 1)$  the rotation angle  $\varphi$  is also a random variable uniformly distributed in the interval  $(0, 2\pi)$  the deflection angle  $\theta$  is characterized by the probability distribution of the direction cosine  $\cos \theta$

$$p(\cos \theta) = \frac{1 - g^2}{2(1 + g^2 - 2g \cos \theta)^{\frac{3}{2}}}, \quad (7)$$

where the *anisotropy factor*  $g$  represents the expected value of  $\cos \theta$ . Values for the direction cosine are obtained through *inverse transform sampling*. Such a technique allows to express a random variable  $\chi$ , of given probability distribution  $p(\chi)$ , in terms of another random variable  $\xi$ , uniformly distributed between 0 and 1. Thus, solving for  $\chi$  given its cumulative distribution function, i.e.,

$$\int_{-\infty}^x p(\chi) d\chi = \xi. \quad (8)$$

Applying inverse transform sampling to Eq. (7) results in

$$\cos \theta = \begin{cases} \frac{1}{2g} \left[ 1 + g^2 - \left( \frac{1-g^2}{1-g+2g\xi} \right) \right], & \text{if } g \neq 0 \\ 2\xi - 1, & \text{if } g = 0 \end{cases}. \quad (9)$$

The simulation proceeds as follows. Each photon crosses the tissue surface and propagates a certain step size  $s$ , with a rotational angle  $\varphi$  and a deflection angle  $\theta$ , reaching an *interaction site* within the tissue volume. Every time a photon reaches an interaction site, it drops part of its energy represented by its weight,  $w$ , according to the relation

$$\Delta w = \frac{\mu_a}{\mu_a + \mu_s} w, \quad (10)$$

where  $\mu_a$  and  $\mu_s$  are the tissue absorption and scattering coefficients respectively [5]. The weight loss is absorbed by the discrete volume of tissue where the interaction site is located. A photon propagates a certain number of steps, progressively decreasing its weight, until one of the following conditions occur, leading to its termination:

- **reflection:** the photon escapes out of the tissue volume
- **low weight:** the photon's weight falls below a certain threshold  $w_t$ , thus any further propagation step will bring little additional information; in this case, a variance reduction technique, named *Russian Roulette* [7], is used: the photon is given a chance in  $m$  to survive; if it does, its weight is multiplied by  $m$ , otherwise it is terminated

Once all photons have been terminated, the PAP is computed out of the tissue geometry. Cylindrical symmetry is assumed, i.e. the amount of energy absorbed by a specific volume element is assumed to be dependent just on its depth within the tissue and its radial distance from the point of application of the laser. For this reason, the PAP is computed as a 2D matrix, out of a single cylindrical sector, representing the distribution of power density across the tissue volume as a function of depth  $z$  and radius  $r$ , i.e.  $PAP(r, z)$ .

### 3.2 Finite Difference Method

Eq. (1) can be rewritten as

$$\Delta T(r, z, t) + \frac{Q}{\beta} = \frac{\rho\gamma}{\beta} \frac{\partial T(r, z, t)}{\partial t} \quad (11)$$

where  $\Delta$  represents the Laplacian operator. The rate of heat generation  $Q$  can be estimated using the following [5],

$$Q = PAP(r, z) * P \quad (12)$$

where  $P$  is the *laser power*.

A Finite Difference Method, *Forward Euler Integration*, is used to find a numerical solution to Eq. (11). The method discretizes time into regular intervals  $\Delta t$  solving the matrix  $\mathbf{T}_k \in \mathbb{R}^{I \times J}$ , for each discrete time step  $k$ . Given the initial temperature  $T^0$ , all the successive values of  $T^k$  are computed using the following relation

$$\frac{T_{i-1,j}^k - 2T_{i,j}^k + T_{i+1,j}^k}{(\Delta r)^2} + \frac{1}{i\Delta r} \frac{T_{i+1,j}^k - T_{i-1,j}^k}{2\Delta r} + \frac{T_{i,j-1}^k - 2T_{i,j}^k + T_{i,j+1}^k}{(\Delta z)^2} + \frac{Q_{i,j}^k}{\beta} = \frac{\rho\gamma}{\beta} \frac{T_{i,j}^{k+1} - T_{i,j}^k}{\Delta t} \quad (13)$$

which is the same as Eq. (11), where all the derivatives have been replaced by their difference quotients. Here,  $T_{i,j}^k$  denotes the element of the  $i$ -th row and the  $j$ -th column of matrix  $\mathbf{T}^k$ , i.e. the value of temperature for the discrete volume element located at radius  $i$  and at depth  $j$  at time  $k \cdot \Delta t$ .

Eq. (13) cannot be used for volume elements lying on the boundaries, as some of the terms would account for contributions from non-existing neighbours. Such terms must be replaced in order to take into account temperature variation due to heat exchange with the external environment. According to [5], a *Neumann boundary condition* can be used to this purpose, e.g. for a volume element lying on the top surface of the cylinder, the spatial contribution for the temperature variation is modeled as

$$\frac{\partial T}{\partial z} = -h \frac{(T_{i,j} - T_\infty)}{\rho\gamma\beta} \quad (14)$$

where  $h$  is a convection constant. Similar conditions apply to the other boundaries.

Finally, solving Eq. 13 requires to choose the values of the initial temperature  $T^0$ , the temperature of the environment  $T_\infty$  and the time step  $\Delta t$ . For the sake of simplicity, both initial temperature of tissue and environmental temperature are assumed to be  $37^\circ\text{C}$ . Care must be taken in the choice of  $\Delta t$ , to ensure convergence of the integration method. The range of acceptable values is limited by the following relation [5]:

$$\Delta t \leq \frac{1}{4} \frac{(\Delta r)^2}{\beta}. \quad (15)$$

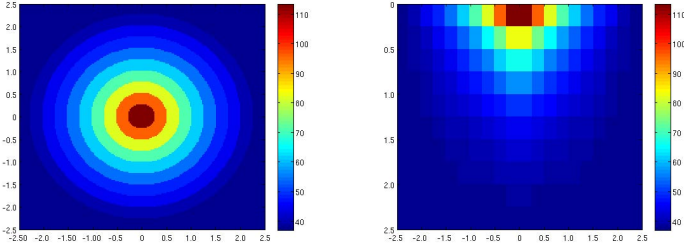
### 3.3 Simulation of Temperature Dynamics

Here we present the simulation involving a piece of tissue 0.25 mm high and 0.5 mm wide, being irradiated by a  $\text{CO}_2$  surgical laser [2]. The full set of parameters used for the simulation model is reported in Table 2. Input variables are summarized in Table 1. Within the beam, photons have been arranged in concentric circles, in order to obtain a flat beam profile [5]. Fig. 3 shows an example of the simulation, it shows the distribution of temperature across the tissue volume after 4 seconds of laser exposure, using a power of 0.5W and a pulse time of 0.2s. The temperature of the top of the tissue reaches  $110^\circ\text{C}$ . Fig. 4, shows the simulated temperature dynamics, recorded at various depths into the tissue: temperature on the surface has risen more rapidly compared to the rest of the tissue, due to the strong heat contribution from the laser beam. Temperature increase in deeper tissue volumes has been dominated by heat exchange phenomena, thus leading to a slower dynamics.

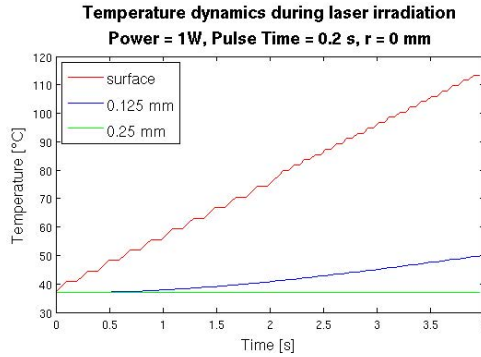
## 4 Learning Temperature Nonlinear Dynamics

A total of 200 laser interactions were simulated for the generation of the training data set. Each simulation has a randomly selected duration of laser exposure





**Fig. 3.** Top and section view of temperature distribution



**Fig. 4.** Temperature at various depths during laser irradiation

and equal amount of time for temperature evolution without the presence of the laser ( $P=0W$ ), i.e., the process of cooling down was also simulated. The training data was generated using diverse pulse rate given a fixed power ( $P=2W$ ), i.e., diverse effective fluence rate. Four types of pulse rates were considered ( $\tau = 0.0, 0.1, 0.2, 0.5$ ), 50 experiments were simulated for each pulse rate.

Each experiment consists of a sequence of  $K$  matrices (as the one shown in Fig. 3), representing the time evolution of the temperature ( $\mathbf{T}_k$ ) in a slice (lateral view) of the tissue cylindrical model. These sequences of tissue temperatures are used to generate the input ( $\mathbf{x}$ ) and output ( $\mathbf{y}$ ) vectors required for the supervised learning method. Here we describe its components in more detail, that is,

$$\mathbf{x} = [T_{i,j}^k \quad T_{i+1,j}^k \quad T_{i-1,j}^k \quad T_{i,j+1}^k \quad T_{i,j-1}^k \quad i \quad j \quad F^k]^T$$

$$\mathbf{y} = T_{i,j}^{k+1}$$
(16)

where  $F$  represents the fluence rate at instant  $k$ . Such fluence incorporates the power and pulse rate information, which are the independent variables ( $\mathbf{u}_k$ ) proposed in previous sections. Note that the information of the current state of the tissue temperature, required for the estimation of the change, has been reduced to the temperature of the volume of interest  $T_{i,j}$  and the one of its

**Table 1.** Input Variables

Symbol	Name of Parameter	Allowed Values
$P$	Power	1 to 5 W
$\tau$	Pulse Time	0.1, 0.2 or 0.5 s
$t$	Exposure time	0 to 5 s

**Table 2.** Parameters used in the simulation

Symbol	Name of Parameter	Value
$\mu_a$	Absorption Coefficient	714.6 cm <sup>-1</sup>
$\mu_s$	Scattering Coefficient	10 cm <sup>-1</sup>
$g$	Anisotropy factor	0.9
$\rho$	Density	1.07 g/cm <sup>3</sup>
$\beta$	Temperature Conductivity	0.0015 cm <sup>2</sup> / s
$\gamma$	Specific Heat Capacity	3.4 J / (g °C)
$h$	Heat Transfer Coefficient	0.000433 W / (cm <sup>2</sup> °C)
$\Delta r$	Radius of a Volume Element	0.025 mm
$\Delta z$	Depth of a Volume Element	0.025 mm
$\Delta \theta$	Amplitude of a Volume Element	1/30 rad
$br$	Beam Radius	0.25 mm
$N$	Number of Photons	50000
$w_t$	Weight Threshold	0.0001
$m$	Chance to survive the <i>Russian Roulette 2</i>	

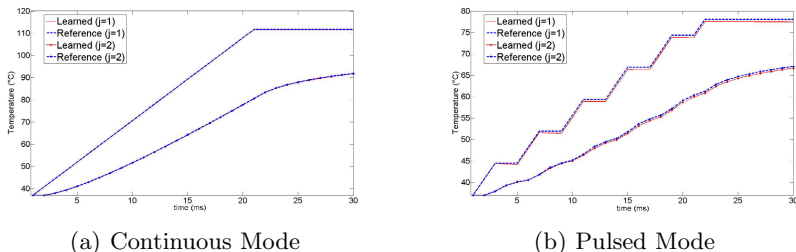
surroundings. This is in order to avoid unnecessary information that it is known to be less relevant or redundant.

The learning process uses a total of 627120 samples and the obtained model presents a normalized mean square error (nMSE) of 3.7% against the learning data set. The validation data set, with 176880 samples, presents a nMSE of 4.3%.

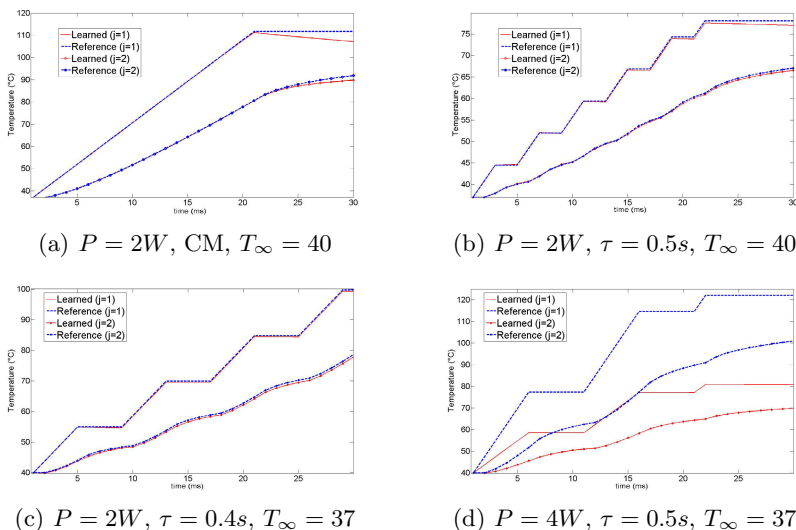
These results demonstrate that given a temperature of a volume element together with the temperature of its surroundings and the fluence rate being transferred from the laser, the learned model is able to estimate the temperature for such volume in the next time step.

#### 4.1 Analyzing Model Response

Besides verifying standard learning and validation errors, further tests and analysis are necessary in order to verify the quality of the model. The consistence of the model, as a dynamical system, must be tested recursively using its prediction as input for the next estimation. Convergence of the predicted temperature with respect to laser-tissue simulations is expected. Fig. 5 presents a comparison of the temporal response of the learned system with respect to the reference dynamics for diverse inputs. For the case of continuous laser mode (CM) (see Fig. 5(a)), the learned model accumulate a nMSE = 4.2% while for the case of pulsed laser mode (see Fig. 5(b)) the nMSE = 3.74%.



**Fig. 5.** Temperature dynamics at the center of the tissue at the surface ( $T_{1,1}$ ), and at  $z = 0.025\text{mm}$ , ( $T_{1,2}$ ) for continuous/pulsed type of laser modes. Time response of the reference (blue) and learned (red) models are shown.



**Fig. 6.** Temperature dynamics against diverse tests

Moreover, besides analyzing the response to new input vectors, we take the test of the system to an application level, and verify its behavior to diverse surgical situations. Fig. 6(a) and 6(b) present the time response of tissue temperature given a different initial and room temperature ( $T_\infty = 40$ ), which had been assumed to be constant for the learning process. It can be seen that the model is robust to this change with  $nMSE = 4.4\%$  for the continuous laser mode, while  $nMSE = 4.0\%$  for the pulsed laser mode. It can be observed that the tissue at the surface ( $j = 1$ ) gets more affected by the change in room temperature than tissue at ( $z = 0.025\text{mm}$ ,  $j = 2$ ). Another interesting test is to apply a different pulse rate for laser modulation. As presented in Fig. 6(c), no significant changes

occur. Finally, the model is tested with a different power, Fig. 6(d) shows that the model is not able to reproduce the behavior of the system of reference. Despite the dynamics is similar, the absolute values of temperature are not correctly followed. This clearly establish the need of improve the model in order to allow the estimation given diverse input power.

## 5 Conclusion

These results demonstrate that given a temperature of a volume element together with the temperature of its surroundings and the fluence rate being transferred from the laser, the learned model is able to estimate the temperature for such volume in the next time step.

The assumptions presented in this work restrict the use of the model only to similar types of laser and tissues as well as similar environmental conditions. Despite more complex models may be envisioned, this model will allow to validate the proposed methodology and will orient more ambitious objectives.

## References

1. Steiner, W., Ambrosch, P.: Endoscopic laser surgery of the upper aerodigestive tract: with special emphasis on cancer surgery. Thieme (2000)
2. Niemz, M.: Laser-tissue Interactions. Springer, Heidelberg (2003)
3. Vijayakumar, S., D'Souza, A., Schaal, S.: Incremental online learning in high dimensions. *Neural Computation* 17, 2602–2634 (2005)
4. Klanke, S., Vijayakumar, S., Schaal, S.: A library for locally weighted projection regression. *J. Mach. Learn. Res.* 9, 623–626 (2008)
5. Crochet, J.J., Gnyawali, S.C., Chen, Y., Lemley, E.C., Wang, L.V., Chen, W.R.: Temperature distribution in selective laser-tissue. *Journal of Biomedical Optics* 11(3), 1–10 (2006)
6. London, R.A., Glinsky, M.E., Zimmerman, G.B., Bailey, D.S., Eder, D.C., Jacques, S.L.: Laser-tissue interaction modeling with latis. *Appl. Opt.* 36(34), 9068–9074 (1997)
7. Wang, L., Jacques, S.L., Zheng, L.: Monte carlo modeling of light transport in multi-layered tissues. *Computer Methods and Programs in Biomedicine* 47(2), 131–146 (1995)

# An Ensemble of Classifiers Guided by the AAL Brain Atlas for Alzheimer's Disease Detection

Alexandre Savio\* and Manuel Graña

Grupo de Inteligencia Computacional (GIC), Universidad del País Vasco  
(UPV/EHU), San Sebastián, Spain

**Abstract.** Detection of Alzheimer's disease based on Magnetic Resonance Imaging (MRI) still is one of the most sought goals in the neuroscientific community. Here, we evaluate an ensemble of classifiers each independently trained with disjoint data extracted from a partition of the brain data volumes performed according to the 116 regions of the Anatomical Automatic Labeling (AAL) brain atlas. Grey-matter probability values from 416 subjects (316 controls and 100 patients) of the OASIS database are estimated, partitioned into AAL regions, and summary statistics *per* region are computed to create the feature sets. Our objective is to discriminate between control subjects and Alzheimer's disease patients. For validation we performed a leave-one-out process. Elementary classifiers are linear Support Vector Machines (SVM) with model parameter estimated by grid search. The ensemble is composed of one SVM per AAL region, and we test 6 different methods to make the collective decision. The best performance achieved with this approach is 83.6% accuracy, 91.0% sensitivity, 81.3% specificity and 0.86 of area under the ROC curve. Most discriminant regions for some of the collective decision methods are also provided.

## 1 Introduction

Alzheimer's Disease (AD) is one of the most important causes of disability in the elderly and with the increasing proportion of elderly in many populations, the number of dementia patients will rise also. Due to the socioeconomic importance of the disease in occidental countries there is a strong international effort focus in AD. In the early stages of AD brain atrophy may be subtle and spatially distributed over many brain regions, including the entorhinal cortex, the hippocampus, lateral and inferior temporal structures, as well as the anterior and posterior cingulate.

Machine learning methods have become very popular to classify functional or structural brain images to discriminate them into two classes: normal or a specific neurodegenerative disorder [1]. The development of automated detection procedures based in Magnetic Resonance Imaging (MRI) and other medical

---

\* This work has been partially supported by the "Ayudas para la Formación de Personal Investigador" fellowship from the Gobierno del País Vasco.

imaging techniques [2] is of high interest in clinical medicine. It is important to note that these techniques are aimed to help clinicians with more statistical evidence for the diagnosis, it is not intended to substitute any other existing diagnosis procedure.

Most published classification methods working on MRI data train a single classifier. However, it is challenging to train only a global classifier that can be robust enough to achieve good classification performance, mostly due to noise and small sample size of neuroimaging data. Other studies using ensemble of classifiers on brain anatomical MRI can be found in the literature. In [3] they propose a classification method via aggregation of regression algorithms fed with histograms of deformations generated from the Open Access Series of Imaging Studies (OASIS) database obtaining a 0.04 test error rate. Another study shows a local patch-based subspace ensemble method which builds multiple individual classifiers based on different subsets of local patches with the sparse representation-based classifier obtaining an accuracy of 90.8% on the ADNI database [4]. In [5] subsets of ranked features from neuroimaging data are used to in an ensemble of linear Support Vector Machine (SVM) classifiers obtaining 0.94 of Area Under the Receiver Operating Characteristic (ROC) Curve (AUC) when detecting a AD patients vs. control subjects.

In this paper we use modulated Grey-Matter (GM) maps partitioned according to the regions from the Automatic Anatomical Labeling (AAL) atlas to create datasets of statistical features of these GM maps within each of these regions for each subject. These datasets are put into a leave-one-out with grid search process for classifier validation. After that, an ensemble collective decision is made in order to obtain a classification result. We report the results of an ensemble of linear Support Vector Machine (SVM) classifiers.

Section 2 gives a description of the subjects selected for the study, the image processing, feature extraction details, cross-validation and classifier algorithms. Section 3 gives the classification performance results and in section 4 we provide conclusions of this work and further research suggestions.

## 2 Materials and Methods

In summary the procedure we have followed in this work was: (1) segment the subjects in 3 tissue volume estimation maps, (2) nonlinearly register each subject to the MNI template, (3) calculate the Jacobian determinant of the corresponding displacement fields, with this, (4) modulate the GM partial volume estimation maps. (5) Extract from the GM voxels inside each region of interest (ROI) in the AAL atlas a set of statistical values and finally, (6) use the feature set of each ROI in a leave-one-out classification procedure with parameter grid search. In figure 1 we show a pipeline of the experiment procedure.

The implementation of the feature extraction, classification and result measures have been done in Python with scikit-learn [6]. The source code and preprocessing scripts are freely available for download in <http://www.ehu.es/ccwintco/index.php/Usuario:Alexsavio>. The data can also be shared through an email to the corresponding author.

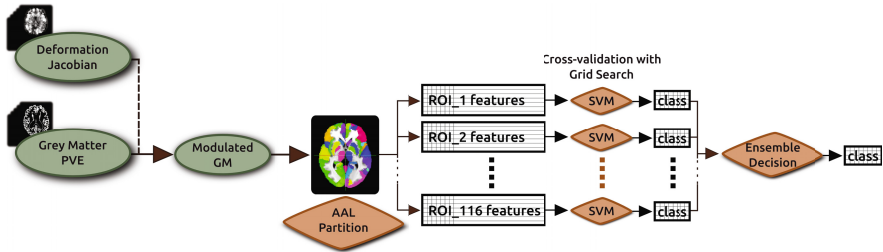


Fig. 1. Flow diagram of the feature extraction and ensemble of classifiers

## 2.1 Data

In this study we use all the subjects of a public available brain MRI database, the first Open Access Series of Imaging Studies (OASIS) [7]. These subjects were selected from a larger database of individuals who had participated in MRI studies at Washington University, they were all right-handed and older adults had a recent clinical evaluation. Older subjects with and without dementia were obtained from the longitudinal pool of the Washington University Alzheimer Disease Research Center (ADRC). This release of OASIS consists of a cross-sectional collection of 416 male (119 controls and 41 patients) and female (197 controls and 59 patients) subjects aged 18 to 96 years (218 aged 18 to 59 years and 198 subjects aged 60 to 96 years). Further demographic and image acquisition details can be found in [7].

This database includes at least 3 raw anatomical MP-RAGE images from each subject as well as post-processed images: (a) corrected for inter-scan head movement and rigidly aligned to the Talairach and Tournoux space [8], (b) transformed to a template with a 12-parameter affine registration and merged into a 1-mm isotropic image, (c) skull-stripped and corrected for intensity inhomogeneity and (d) segmented by tissue type. To carry out our experiment we have started with the volumes from (c).

## 2.2 Preprocessing

The spatial normalization of each subject of the database is performed with the FMRIB Software Library (FSL) FNIRT [9]. A four step registration process with increasing resolution and a scaled conjugate gradient minimization method has been performed using the default parameters, nearest neighbour interpolation and the standard Montreal National Institute (MNI) brain template.

In this registration process the subject  $S$  is nonlinearly registered to a template  $T$ , and a displacement vector  $\vec{u}(\vec{r})$  is obtained such that  $S(\vec{r} - \vec{u})$  corresponds with  $T(\vec{r})$ , where  $\vec{r}$  denotes the voxel location. The Jacobian matrix in this case describes the velocity of the deformation procedure in the neighboring area of each voxel and it is defined by

$$\mathbf{J}_i = \begin{pmatrix} \partial(x-u_x)/\partial x & \partial(x-u_x)/\partial y & \partial(x-u_x)/\partial z \\ \partial(y-u_y)/\partial x & \partial(y-u_y)/\partial y & \partial(y-u_y)/\partial z \\ \partial(z-u_z)/\partial x & \partial(z-u_z)/\partial y & \partial(z-u_z)/\partial z \end{pmatrix}. \quad (1)$$

The determinant of the Jacobian matrix is the most commonly used scalar measure of deformation for tensor-based brain morphometry analyses (TBM) [10]. The determinant of the Jacobian matrix  $\mathbf{J}_i$  is commonly used to analyze the distortion necessary to deform the images into agreement. A value  $\det(\mathbf{J}_i) > 1$  implies that the neighborhood adjacent to the displacement vector in voxel  $i$  was stretched to match the template (i.e., local volumetric expansion), while  $\det(\mathbf{J}_i) < 1$  is associated with local shrinkage.

Apart, we segment the subjects with FSL FAST [11] into 3 volumes with estimation maps of brain tissues: grey (GM) and white (WM) matter and cerebral-spinal fluid (CSF). In this case we are interested in the GM maps, which we multiply by the Jacobians from the non-linear registration in order to get a modulated GM map in the standard MNI space. Subsequently these maps are smoothed with a 2mm Full-Width Half-Maximum (FWHM) Gaussian filter and used for feature extraction. A visual check has been performed for all images in every processing step carried out in this experiment.

### 2.3 Feature Extraction

The Automatic Anatomical Labeling (AAL) atlas [12] is used to partition the GM maps into 116 brain anatomical regions. In this study we extract of each AAL anatomical region from each subject GM map 7 statistical measures: the maximum voxel value, the minimum, the mean, the variance, the median, the kurtosis and the skewness. Resulting in 116 sub-datasets of 416 subjects with 7 features each. One classifier for each of these, together, perform as an ensemble.

### 2.4 Support Vector Machines

The Support Vector Machine (SVM) [13] algorithm used for this study is included in the libSVM software package [14][6]. Given training vectors  $\mathbf{x}_i \in \mathbb{R}^n, i = 1, \dots, l$  of the subject features of the two classes, and a vector  $\mathbf{y} \in \mathbb{R}^l$  such that  $y_i \in \{-1, 1\}$  labels each subject with its class, in our case, for example, patients were labeled as -1 and control subject as 1. To construct a classifier, the SVM algorithm tries to maximize the classification margin. To this end it solves the following optimization problem:

$$\min_{w,b,\xi} \frac{1}{2} \mathbf{w}^T \mathbf{w} + C \sum_{i=1}^l \xi_i \quad (2)$$

subject to  $y_i(\mathbf{w}^T \phi(\mathbf{x}_i) + b) \geq (1 - \xi_i), \xi_i \geq 0, i = 1, 2, \dots, n$ . The dual optimization problem is

$$\min_{\alpha} \frac{1}{2} \boldsymbol{\alpha}^T \mathbf{Q} \boldsymbol{\alpha} - \mathbf{e}^T \boldsymbol{\alpha},$$



subject to  $\mathbf{y}^T \boldsymbol{\alpha} = 0$ ,  $0 \leq \alpha_i \leq C$ ,  $i = 1, \dots, l$ , where  $\mathbf{e}$  is the vector of all ones,  $C > 0$  is the upper bound on the error,  $\mathbf{Q}$  is an  $l \times l$  positive semi-definite matrix,  $Q_{ij} \equiv y_i y_j K(\mathbf{x}_i, \mathbf{x}_j)$ , and  $K(\mathbf{x}_i, \mathbf{x}_j) \equiv \phi(\mathbf{x}_i)^T \phi(\mathbf{x}_j)$  is the kernel function that describes the behavior of the support vectors. Here, the training vectors  $\mathbf{x}_i$  are mapped into a higher (maybe infinite) dimensional space by the function  $\phi(\mathbf{x}_i)$ .  $C$  is a regularization parameter used to balance the model complexity and the training error.

The option we choose to address the problem with the optimization function when unbalanced datasets are present is to adjust a weight for each class with a value inversely proportional to class frequencies. This converts the optimization equation 2 into:

$$\min_{w, b, \xi} \frac{1}{2} \mathbf{w}^T \mathbf{w} + u_y C \sum_{i=1}^l \xi_i, \quad (3)$$

where  $u_y$  is the weight value for a given class  $y$ .

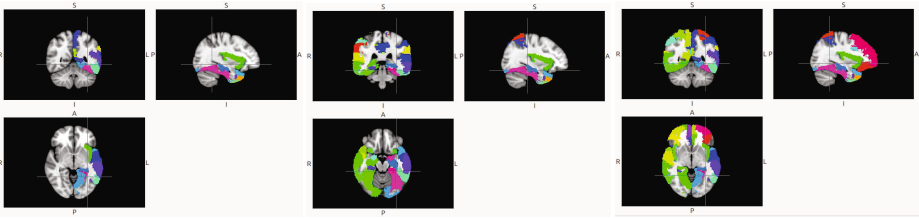
The chosen kernel function results in different kinds of SVM with different performance levels and the choice of the appropriate kernel for a specific application is a difficult task. In this study we only tested for a linear kernel, another kernel type and its parameter values in the grid search increased exponentially the experiment computation time.

## 2.5 Cross-Validation and Parameter Grid Search

A leave-one-out cross-validation is carried out to calculate the results. In each validation fold, one subject is kept out, a grid search through classifiers parameters is performed against the training set and the kept out subject is then tested against the previously trained classifier with best performance in the grid search. In this grid search we perform a 3-fold cross-validation against the training set using each possible combination of parameter values. The parameter value grid for SVM was  $C$  in  $[1e - 3, 1e - 2, 1e - 1, 1, 1e1, 1e2, 1e3]$ .

## 2.6 Ensemble Decisions

After obtaining the result from all the classifiers in the ensemble we have to make an aggregate decision to have only one class decision. Here we test 6 ensemble majority voting decision criteria using (1) all of the ROI classifiers, the 20 with best average (2) training AUC and (3) training F1-score, (4) an *a priori* set of temporal brain regions and hippocampus only in the left hemisphere known to be affected by AD, (5) another set of brain regions which include temporal and parietal areas of the brain, cingulum, insula and hippocampus from both hemispheres and (6) the same previous set of regions plus frontal lobe regions. In figure 2 we show the regions included in each of these *a priori* ROI maps.



**Fig. 2.** Slices of the MNI standard template showing the *a priori* maps of affected regions in the left temporal area (left), corresponding to mild AD (middle) and to normal AD (right) used for ensemble decision.

### 3 Results

In this section we present the linear kernel SVMs performance using the leave-one-out cross-validation. We report accuracy  $((TP + TN)/N)$ , sensitivity  $(TP/(TP + FN))$ , specificity  $(TN/(FP + TN))$  and area under the ROC curve (AUC) [15] for each ensemble decision. In table 1 we show the classification performance of the ensemble with linear SVMs.

**Table 1.** Support Vector Machine accuracy, sensitivity, specificity and ROC area of the leave-one-out cross-validation classification results.

	<b>Accuracy</b>	<b>Sensitivity</b>	<b>Specificity</b>	<b>AUC</b>
Majority Voting	83.6	75.0	86.4	80.7
<b>Best 20 Training AUC</b>	<b>83.6</b>	<b>91.0</b>	<b>81.3</b>	<b>86.2</b>
<b>Best 20 Training F1-score</b>	83.2	90.0	81.0	85.5
<b>Left Hem. AD ROIs</b>	82.4	81.0	82.9	81.9
<b>Mild AD ROIs</b>	82.0	74.0	84.5	79.9
<b>Normal AD ROIs</b>	83.2	79.0	84.5	81.7

The best classification performance is obtained using the majority voting of the 20 highest training AUC classifiers.

We performed the same experiments using Decision Trees (CART) [16] and Random Forests [17], and also against other deformation measures as the Jacobian determinant and trace, displacement vector magnitude and geodesic anisotropy, more detailed in [18]. Nevertheless we did not obtain in any of them a sensitivity measure  $> 70\%$ , which led us to discard those results. The parameter grid search values used for CART was criterion Gini or Entropy and maximum depth [None, 10, 20, 30], and for the RF we tested for number of estimators in [3, 5, 10, 30, 50, 100] and maximum number of feature to consider for best split  $[N, \sqrt{N}, \log_2(N), \text{automatic}, 1, 3, 5, 7]$ , where  $N$  is the number of features.

### 3.1 Discriminant ROIs

In figure 3 we show the 20 regions that have obtained best training AUC and F1-score during the leave-one-out. Most of the ROIs coincide with the manually selected ROIs, mainly with left hemisphere ROIs and frontal lobes.



**Fig. 3.** Slices of the MNI standard template where the 20 best training AUC (left) and F1-score (right) ROIs are colored.

## 4 Conclusions

In this paper we report classification results of an ensemble of SVM classifiers against GM data partitioned with the AAL atlas. The sample is the complete cross-sectional OASIS database. For each subject, the modulated GM data is partitioned into 116 regions and 7 statistical values from each are used as feature vectors. The results are in agreement with most of our previous classification experiments [1,18,19]. Although classification approaches using whole-brain features showed better performance.

It was of our interest to see the performance of the experiments which used *a priori* knowledge ROI maps against those experiments with supervised methods of feature selection. Unsupervised feature selection methods will most probably show worse classification performance than those which are supervised, but lead to more generalized systems and less fitted to the experimental database. We are aware that registration and segmentation errors can lead to biases in the accuracy of the classifiers. In addition, atrophy in brain structures can be interpreted as a late stage of AD and functional MRI could be used instead to detect previous stages of the disease. As future work we will be trying to successfully apply ensembles to deformation features, but we could also find more interesting approaches including functional MRI data.

**Acknowledgments.** We thank the Washington University ADRC for making MRI data available. This work has been supported by the MICINN grant TIN2011-23823.

## References

1. Chyzhyk, D., Graña, M., et al.: Hybrid dendritic computing with kernel-LICA applied to Alzheimer's disease detection in MRI. *Neurocomputing* 75(1), 72–77 (2012)
2. Davatzikos, C., Fan, Y., et al.: Detection of prodromal alzheimer's disease via pattern classification of MRI. *Neurobiology of Aging* 29(4), 514–523 (2008)
3. Chen, T., Rangarajan, A., et al.: CAVIAR: Classification via aggregated regression and its application in classifying OASIS brain database. In: *Proceedings / IEEE International Symposium on Biomedical Imaging: From Nano to Macro*, pp. 1337–1340 (April 2010)
4. Liu, M., Zhang, D., et al.: Ensemble sparse classification of alzheimer's disease. *NeuroImage* 60(2), 1106–1116 (2012)
5. Varol, E., Gaonkar, B., et al.: Feature ranking based nested support vector machine ensemble for medical image classification. In: *2012 9th IEEE International Symposium on Biomedical Imaging (ISBI)*, pp. 146–149 (May 2012)
6. Pedregosa, F., Varoquaux, G., et al.: Scikit-learn: Machine learning in python. *Journal of Machine Learning Research* 12, 2825–2830 (2011)
7. Marcus, D.S., Wang, T.H., et al.: Open access series of imaging studies (OASIS): cross-sectional MRI data in young, middle aged, nondemented, and demented older adults. *Journal of Cognitive Neuroscience* 19(9), 1498–1507 (2007)
8. Talairach, J., Tournoux, P.: *Co-Planar Stereotaxic Atlas of the Human Brain: 3-D Proportional System: An Approach to Cerebral Imaging*. Thieme (January 1988)
9. Smith, S.M., Jenkinson, M., et al.: Advances in functional and structural MR image analysis and implementation as FSL. *NeuroImage* 23(suppl. 1), 1–2 (2004) PMID: 15501092
10. Lepore, N., Brun, C., et al.: Generalized tensor-based morphometry of HIV/AIDS using multivariate statistics on deformation tensors. *IEEE Transactions on Medical Imaging* 27(1), 129–141 (2008) PMID: 18270068
11. Zhang, Y., Brady, M., et al.: Segmentation of brain MR images through a hidden markov random field model and the expectation-maximization algorithm. *IEEE Transactions on Medical Imaging* 20(1), 45–57 (2001) PMID: 11293691
12. Tzourio-Mazoyer, N., Landeau, B., et al.: Automated anatomical labeling of activations in SPM using a macroscopic anatomical parcellation of the MNI MRI single-subject brain. *NeuroImage* 15(1), 273–289 (1995) PMID: 11771995
13. Vapnik, V.N.: *Statistical Learning Theory*. Wiley-Interscience (September 1998)
14. Chang, C.-C., Lin, C.-J.: LIBSVM: a library for support vector machines (2001), Software available at <http://www.csie.ntu.edu.tw/~cjlin/libsvm>
15. Faraggi, D., Reiser, B.: Estimation of the area under the ROC curve. *Statistics in Medicine* 21(20), 3093–3106 (2002)
16. Quinlan, J.R.: Induction of decision trees. *Mach. Learn.* 1(1), 81–106 (1986)
17. Breiman, L.: Random forests. *Machine Learning* 45(1), 5–32 (2001)
18. Savio, A., Graña, M.: Deformation based feature selection for computer aided diagnosis of alzheimer's disease. *Expert Systems with Applications* 40(5), 1619–1628 (2013)
19. Savio, A., García-Sebastián, M.T., et al.: Neurocognitive disorder detection based on feature vectors extracted from VBM analysis of structural MRI. *Computers in Biology and Medicine* 41(8), 600–610 (2011)

# Saccadic Points Classification Using Multilayer Perceptron and Random Forest Classifiers in EOG Recordings of Patients with Ataxia SCA2

Roberto Becerra<sup>1</sup>, Gonzalo Joya<sup>2</sup>,  
Rodolfo Valentin García Bermúdez<sup>1</sup>, Luis Velázquez<sup>3</sup>,  
Roberto Rodríguez<sup>3</sup>, and Carmen Pino<sup>1</sup>

<sup>1</sup> Facultad de Informática y Matemática, Universidad de Holguín, Cuba  
{idertator,rodolfo,cpino}@facinf.uho.edu.cu

<sup>2</sup> Facultad de Matemática y Computación, Universidad de la Havana, Cuba  
Departamento de Tecnología Electrónica, Universidad de Málaga, España  
gjoya@uma.es

<sup>3</sup> Centre for Research and Rehabilitation of Hereditary Ataxias (CIRAH),  
Holguín, Cuba

**Abstract.** In this paper, we compare the performance of two different methods for the task of electrooculogram saccadic points classification in patients with Ataxia SCA2: *Multilayer Perceptrons* (MLP) and *Random Forest*. First we segment the recordings of 6 subjects into ranges of saccadic and non-saccadic points as the basis of supervised learning. Then, we randomly select a set of cases based on the velocity profile near each selected point for training and validation purposes using percent split scheme. Obtained results show that both methods have similar performance in classification matter, and seems to be suitable to solve the problem of saccadic point classification in electrooculographic records from subjects with Ataxia SCA2.

**Keywords:** eog signals, multilayer perceptron, random forest, saccades, ataxia sca2.

## 1 Introduction

Electrooculography is a common technique for measuring eye movements due its affordability and its accuracy. In the Centre for Research and Rehabilitation of Hereditary Ataxias (CIRAH) of Cuba, this technique is used for monitoring of patients with hereditary ataxias. Specifically, saccadic eye movements have an special interest for the researchers of this disease. This is because many parameters calculated from eye movements are affected by the evolution of this disease [1].

*Saccades* are a kind of eye movements, according [2] are rapid jerk-like movements of the eyes that direct the gaze to a new location, and ballistic movements in the sense of their duration. Saccadic points are those where the saccade begins and ends, but there is no unified criterium about where exactly begins or ends

a saccade. Currently the identification of these points is performed by manual means by experts in the area or automatically by computational algorithms.

Identification by manual means have drawbacks such as the subjectivity introduced by the expert which makes the points selection. This subjectivity generates variability between the identification performed by various of these experts. In the case of signals recorded to sick subjects, the difficulties of manual identification rises due the presence of noises and conditions inherent of the disease.

The way of detecting saccadic points by computational methods is very varied and somehow formalized by the taxonomy of Salvucci-Goldberg [3]. Among the methods described by the taxonomy the most common ones are those based on velocity thresholds. These methods have as main drawback that for subjects affected severely by neurological diseases such as Ataxia SCA2, the identification of saccadic points is very inaccurate. Besides there is no consensus in the literature about what value should take the velocity threshold used by these methods. There is a serious lack of research about the other methods proposed in the taxonomy, but presumably there is a notable difference in the results yielded by them and those yielded by velocity thresholds based methods.

From saccadic points and the corresponding signal channel, is possible to calculate saccadic features such as maximum velocity, latency, duration and the amplitude. These features have proven to be useful in the research of many neurological diseases due the contrast of the behaviour of these features between patients and healthy individuals, as well as between patients of different diseases. For instance, saccadic velocity is significantly slower in subjects with SCA2 than in control subjects or subjects with other ataxias like SCA1 or SCA3 [4]. Also, the calculation of these features supports drug clinical trials and other kind of efforts to improve living conditions of subjects suffering this disease [1].

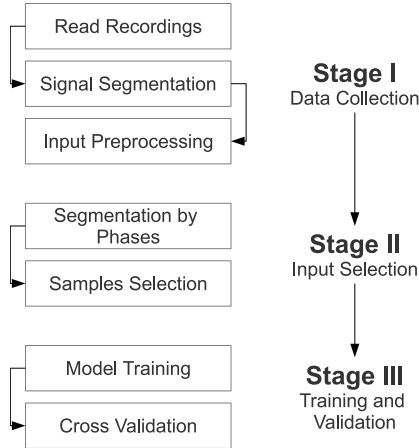
Latency, duration and amplitude are features very susceptible to the position of the saccadic points. So, the variability obtained by the methods currently employed have a negative impact on the utility of final data. On the other hand, the variability caused by the currently employed methods has a negative consequence on the interpretation of these features by experts, leading to misdiagnosis.

Form this considerations, new methods have to be explored to solve the problem of identification of saccadic points. Here we propose two methods based on computational intelligence, capable of learning from a set of examples. Machine Learning, specifically the supervised learning is a branch of Artificial Intelligence often used to solve classification problems. Also these techniques are used in the task of classifying EOG signal patterns [5,6,7]. In this paper we apply two different techniques of supervised learning to attack the problem of the saccadic and non-saccadic point classification in subjects with Ataxia SCA2, and analyze their performance. We aim to obtain results with high accuracy without the drawbacks present in traditional identification mechanisms.

The rest of this paper is organized as follows: In section 2 we describe the designed experiments and available data. Section 3 is devoted to analyze and comment the results. Finally, section 4 summarizes the main conclusions and future work lines.

## 2 Material and Methods

An experiment was designed to apply two machine learning techniques: Multilayer Perceptron (MLP) and Random Forest, to classify a velocity saccadic pattern dataset. The experiment was separated in several stages as shown in Figure 1. The work performed in each stage is described more deeply in the followings sections.



**Fig. 1.** Experiment main flow. Each stage are separated in a sequence of ordered steps.

In summary, each stage describes:

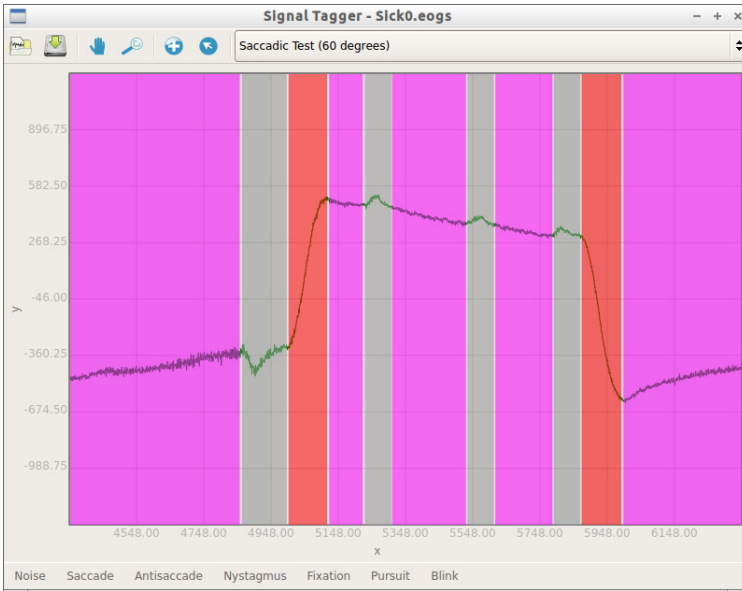
**Stage I:** Provide a set of cases that will conform the population used by the next stage. This population is built based of EOG segmented data (saccadic or non-saccadic) created in this stage.

**Stage II:** Selection of training and validation data taking into account to balance the most typical cases.

**Stage III:** Training and validation of both classifiers, using percentage split scheme to separate training data and validation data.

### 2.1 Data Collection

The data was recorded using the Otoscreen electronystamograph at a sampling rate of 204.8 Hz with a bandwidth of 0.02 to 70 Hz (analogic filtering). Specifically, 60 degrees saccadic signals were selected due to it's difference between healthy and sick subjects. Researchers from the *Centre of Research and Rehabilitation of Hereditary Ataxias* (CIRAH in spanish) provide us about 30 records of sick subjects, many of them in very bad shape. After the analysis of these records, only six of them meets good quality requirements to train classifiers.



**Fig. 2.** Signal editor main window. Pink segments mean *fixations*, gray segments mean *noise* and red segments mean *saccades*.

For signal segmentation purposes, a desktop application was developed capable to mark different types of segments as shown in Figure 2.

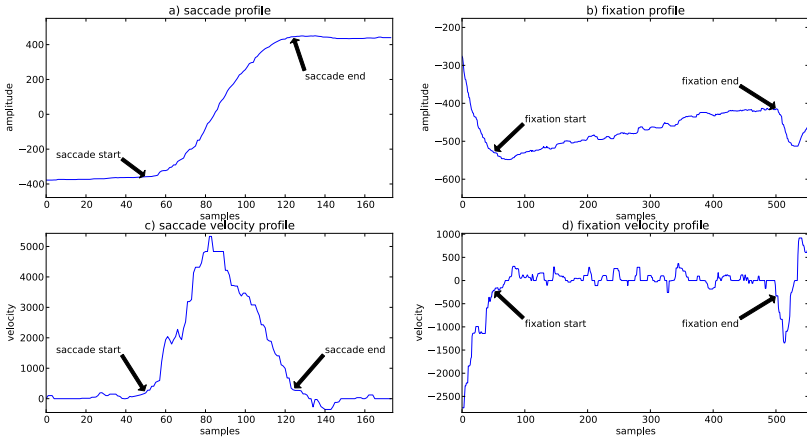
All the programming was done in Python language using NumPy and SciPy open source libraries for numerical calculations, and PySide Qt bindings for graphical user interface. The application uses **python-eog** for reading and writing the data managed by the user interface, developed by the authors too.

Even when the application is capable to tag many ocular events, in selected test only saccades, fixations and noise are relevant. For practical reasons we only need to discriminate saccades and non-saccades, thus, our task becomes a binary classification problem.

Many classical algorithms used to detect saccadic eye movements use a velocity threshold to set the initial and ending points of a single saccade. Even when they not agreed in a threshold value, there is a consensus about that the main criterion is the velocity. Thus, it seems reasonable to think that the pattern of velocities preceding and after a certain point in the signal determines if they are inside or outside of a certain event as shown in Figure 3.

The idea for input variables of a single case, was get the pattern of velocities before and after the target point, in a window fashion way. To build the cases population, an sliding window runs through each tagged point in selected records, using this tag as the classification class. If this tag is a saccade we mark the sample as a saccadic point, if the tag is fixation or noise we mark the sample as non-saccadic point.





**Fig. 3.** a) Time signal of a sample saccade, b) Time signal of a sample fixation, c) Velocity profile of a), d) Velocity profile of b)

Filtering is, very often, the preprocessing part of signal analysis. For velocity profile calculations the input signal is first filtered using a median filter with a window size of 53.71 ms. After filtering, the velocity profile is calculated using a central difference by eight points method, which has proven to be adequate to signal sampled by 200 Hz [8]. Finally, new filtering is carried out to eliminate differentiation noise.

This aggressive filtering is possible because we are interested only in the relationship between the samples in velocity profile, not the waveform itself.

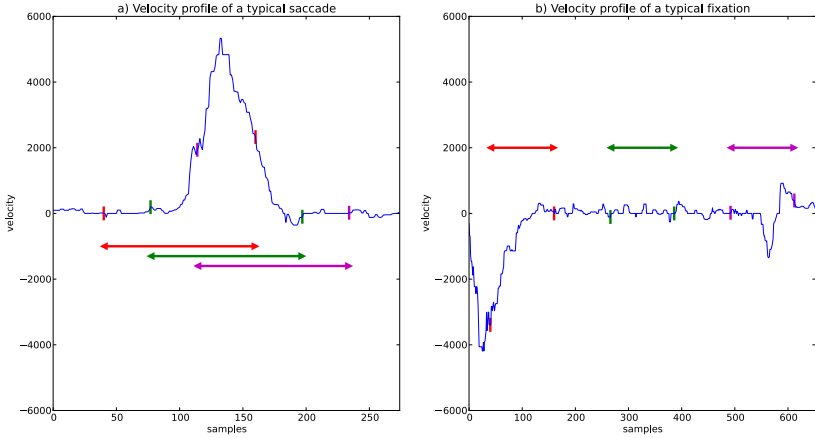
## 2.2 Input Selection

Once gathered instances population, we proceed to select the samples used for training and validation purposes. Is very important to provide a balanced set of input cases to the classifier in order to achieve better classification performance.

First, the number of cases used for training and validation process selected was 5000. The first half of them was devoted to saccade points and the another half to non saccadic points. The set of non-saccadic points was divided in fixation and noise points in equal proportions.

In Figure 4 is showed how different points belonging to the same saccade have a significative different window of velocities. That's mean that a point at beginning of the saccade usually have different window pattern than a point at the end of the saccade.

To get even more balanced set of data, was selected the same proportion of beginning, middle and end points of each class. As results of this input selection strategy, the samples count per class lays out in Table 1.



**Fig. 4.** Example of windows of points at beginning, middle and ending of an event. *Red* range means a window of a point at beginning of the saccade in a) and fixation in b). *Green* range means a window of a point at middle of the saccade in a) and fixation in b). *Magenta* range means a window of a point at ending of the saccade in a) and fixation in b).

**Table 1.** Distribution of input samples per zone in the event and per event itself

	Saccade	Non-Saccade	Total	
		Fixation	Noise	
<b>Start</b>	833	417	417	1667
<b>Middle</b>	834	416	416	1666
<b>End</b>	833	417	417	1667
<b>Total</b>	2500	1250	1250	5000

## 2.3 Training and Validation

Weka [9] is the software package used for training and validate the selected data.

Previous experiments carried out by the authors indicate that the optimum input features count for the MLP and RF input is of 121 components.

**Multilayer Perceptron.** MLPs are a kind of feedforward artificial neural network which consists in multiples layers of nodes in a directed graph, where each layer is fully connected to the next. Except for the input nodes, each node is a processing element with a nonlinear activation function.

The MLP classifier was trained with a topology of 121 nodes in input layer, 61 sigmoid nodes in the hidden layer and 1 linear node in the output layer. The network use backpropagation as training algorithm with a learning rate of 0.3 and a momentum of 0.2. 500 epochs were used to train this model.

**Random Forests.** RF is an ensemble of decision trees proposed by Leo Breiman [10]. The idea is based on building a forest of  $N$  decision trees, where in each tree we select  $M$  input cases in a random way using the same statistical distribution. Breiman in his paper proposes the use of Random Trees in the ensemble. In this type of trees, the split of features in each node is selected randomly from the  $K$  best splits.

Weka uses the algorithm proposed by Breiman. In our case we used the default values used in the package. This means that our model will generate an ensemble of 10 Random Tree. For each tree the random split has 8 features.

The classification is made by the vote of each tree in the ensemble and selecting the most popular class among them.

The speed and accuracy of RFs make them a very good choice for problems related to computer vision. So we expect very good results from them, because the problem we are treating is in some extent a computer vision problem.

The training process uses 5000 examples distributed as shown in Table 1. The training was evaluated using cross-validation with 5 folds. Finally we test the trained model against 5000 new examples not present in training data.

### 3 Results

The validation process performed by weka states the following results:

In Table 2 *Training Cross-validation* stands for the results obtained in the training process, and *Real Validation* stands for the results obtained in the test process (patterns not presented in the training process).

It is a common practice in comparison of several classifiers to use metrics like sensitivity, specificity and accuracy. These metrics are derived from results shown in Table 2 and describe proportions between right and wrong predicted cases.

*Sensitivity* yields how good the model can predict positive examples described by equation 1, in this case saccade points.

$$Sensitivity = \frac{TP}{FN + TP} * 100 \quad (1)$$

*Specificity* is the proportion on correct prediction on negative cases described by equation 2, in this case non-saccade points.

$$Specificity = \frac{TN}{TN + FP} * 100 \quad (2)$$

**Table 2.** Validation results for both classifiers, in training and validation data. **TP** are True Positive cases, **FP** are False Positive cases, **TN** are True Negative cases and **FN** are False Negative cases.

Classifier	TP	FP	TN	FN
<i>MLP Training Cross-validation</i>	2325	175	2323	177
<i>MLP Real Validation</i>	2291	209	2318	182
<i>RF Training Cross-validation</i>	2375	125	2334	166
<i>RF Real Validation</i>	2387	113	2318	182

*Accuracy* is the proportion of right predicted cases, described by equation 3.

$$Accuracy = \frac{TN + TP}{TN + FP + FN + TP} * 100 \quad (3)$$

Table 3 shows that both methods perform very well and very similar for the proposed task. However, these results also shows that the Random Forest performs slightly better than the Multilayer Perceptron.

**Table 3.** Performance metrics comparison between Multilayer Perceptron and Random Forest classifiers in training and validation data

Classifier	Sensitivity	Specificity	Accuracy
<b>MLP Training Cross-validation</b>	92.93 %	92.99 %	92.96 %
<b>MLP Real Validation</b>	92.64 %	91.73 %	92.18 %
<b>RF Training Cross-validation</b>	93.47 %	94.92 %	94.18 %
<b>RF Real Validation</b>	92.92 %	95.35 %	94.10 %

## 4 Conclusions

This paper presented a comparative between two machine learning techniques (Multilayer Perceptron and Random Forest) to solve saccade and non-saccade point classification problem of EOG signals measured to subjects with Ataxia SCA2.

The results obtained by the validation of both methods shown an accuracy above 92 percent. So, they are suitable to solve the proposed task without the drawbacks present in traditional methods. Also, this results stated a slightly better performance for Random Forest than Multilayer Perceptron.

The Random Forest classifier could be used to build a pseudo-realtime identification system due its performance in relation to training speed, and for its accuracy.

**Acknowledgements.** This work has been partially supported by AECID (Spanish Agency for International Cooperation and Development, Ministry of Foreign Affairs of Government of Spain) project A2/038418/11.

## References

1. Velázquez-Pérez, L., Rodríguez-Chanfrau, J., García-Rodríguez, J., Sánchez-Cruz, G., Aguilera-Rodríguez, R., Rodríguez-Labrada, R., Rodríguez-Díaz, J., Canales-Ochoa, N., Gotay, D., Almaguer Mederos, L., Laffita Mesa, J., Porto-Verdecia, M., Triana, C., Pupo, N., Batista, I., López-Hernandez, O., Polanco, I., Novas, A.: Oral zinc sulphate supplementation for six months in sca2 patients: A randomized, double-blind, placebo-controlled trial. *Neurochemical Research* 36, 1793–1800 (2011)

2. Findlay, J.M., Walker, R.: How are saccades generated? *Behavioral and Brain Sciences* 22, 706–713 (1999)
3. Salvucci, D.D., Goldberg, J.H.: Identifying fixations and saccades in eye-tracking protocols. In: *Proceedings of the 2000 Symposium on Eye Tracking Research & Applications, ETRA 2000*, pp. 71–78. ACM, New York (2000)
4. Birk, K., Fetter, M., Abele, M., Laccone, F., Brice, A., Dichgans, J., Klockgether, T.: Autosomal dominant cerebellar ataxia type i: oculomotor abnormalities in families with sca1, sca2, and sca3. *Journal of Neurology* 246, 789–797 (1999)
5. Tagluk, M., Sezgin, N., Akin, M.: Estimation of sleep stages by an artificial neural network employing eeg, emg and eog. *Journal of Medical Systems* 34, 717–725 (2010)
6. Özşen, S.: Classification of sleep stages using class-dependent sequential feature selection and artificial neural network. *Neural Computing and Applications*, 1–12 (2012)
7. Jesús Rubio, J., Ortiz-Rodriguez, F., Mariaca-Gaspar, C., Tovar, J.: A method for online pattern recognition of abnormal eye movements. *Neural Computing and Applications*, 1–9 (2011)
8. Inchingolo, P., Spanio, M.: On the identification and analysis of saccadic eye movements-A quantitative study of the processing procedures. *IEEE Transactions on ... Engineering* 9, 683–695 (1985)
9. Hall, M., Frank, E., Holmes, G.: The WEKA data mining software: an update. *ACM SIGKDD ...* 11(1), 10–18 (2009)
10. Breiman, L.: Random Forests. *Machine Learning* 45(1), 5–32 (2001)

# Phonocardiography Signal Segmentation for Telemedicine Environments

Santiago Murillo Rendón<sup>1</sup>, Cristian Castro Hoyos<sup>1</sup>,  
Carlos M. Travieso-Gonzales<sup>2</sup>, and Germán Castellanos-Domínguez<sup>1</sup>

<sup>1</sup> Universidad Nacional de Colombia, Manizales, Colombia

<sup>2</sup> Universidad de Las Palmas de Gran Canaria, España

**Abstract.** In this paper, phonocardiography (PCG) segmentation methodology based on envelope detection is developed by using a time-scale representation and a synthetic electrocardiogram signal (EKG). The heart cycle duration is calculated by autocorrelation of S1-S2 sounds that are synchronized with the synthetic EKG. Two algorithms for noisy signal removal are implemented to ensure the detection of signals with low signal to noise ratio. Approach is tested in a PCG database holding 232 recordings. Results show an achieved accuracy up of 90%, thus, overperforming three state-of-the-art PCG segmentation techniques used to compare the proposed approach. Additionally, the synthetic EKG is built by estimation of heart rate length, thus it does not use a patient recording EKG, reducing the computational cost and the amount of required devices.

**Keywords:** Heart Sound Segmentation, Phonocardiogram, Telemedicine, Autocorrelation.

## 1 Introduction

Auscultation is the basic diagnostic tool for every medical physician, because of its simplicity, associated low-cost, and its non-invasive nature. The heart sound recorded by auscultation or phonocardiography (PCG) is the primary mechanical analysis tool for the heart function. Other recent techniques, as echocardiography, suggest more sensible methods to estimate the cardiac mechanics. Nevertheless, their associated high cost and the elaborated medical knowledge needed for their evaluation make them unsuitable for uncontrolled environment applications, such as *telemedicine*.

In cardiac auscultation, the physician finds natural heart sounds originated by the opening and closing valves, named S1 and S2 sounds, respectively. The systolic interval starts at the beginning of S1 and extends until the beginning of S2, while the diastolic interval starts at the beginning of S2 and extends until the next S1. Occurrence of additional sounds in the periods, called little and big silences (intervals between S1 and S2), are clear evidence of myocardium mechanical failures. Each period composed by these systolic and diastolic periods is known as cardiac cycle and it is the basic unit for the sound heart analysis. Identification of those additional sounds requires a higher medical ability and their recognition can vary because of the inherent limitations in the listener and the limited sensibility of the human ear in the low-frequency range [1].

Hence, there is a need for development of automatic aided diagnosis tools, providing a more objective mechanism for identification of heart sounds.

To this end, several segmentation techniques are found in the literature that, however, commonly need for additional information extracted from signals as the electrocardiogram (EKG) or the carotid pulse [2]. That is, techniques must have more sources and thus increase the complexity and cost of the acquisition system, making its usage prohibitive in telemedicine applications. Particularly, a comparison of envelope-based segmentation methods is given in [3], where most of them make use of feature extraction techniques such as Shannon's energy envelope, Hilbert transform and other cardiac features. Other approaches use the energy estimated from the Short Time Fourier Transform spectrogram or the scalogram computed with the continuous wavelet transform [4, 5]. Afterwards, peak detection and time/amplitude thresholding are used in [6] for locating the S1 and S2 sounds. Nonetheless, energy is not always constant in the components of the PCG, since the auscultation focuses, pathologies, breathing and, in general, some other artifacts produce changes in the time-energy distribution, which in turn induce changes in the amplitude peaks of the signal. Moreover, the time threshold or window for locating sounds assumes a priori their length duration, leading to bartered segmentation, i. e., diastolic-systolic segments instead of the normal systolic-diastolic heart cycle. In [7], noisy signals are evaluated for a noise-robust detection method by repeating the signal recording when heart sound characteristics are masked by noise. However, the heart cycle estimation method implies a high computational cost that can not be accomplished in near real-time application.

In this paper, a PCG segmentation methodology based on envelope detection is discussed. The approach takes into consideration the changes in the Heart Rate as a mitigating factor, aiming to adapt the cardiac cycle length to each segment length. In the approach, the PCG envelope is computed from the signal time-scale representation. Then, the cardiac cycle length is estimated from the autocorrelation of 3-second windowed envelope signal. Lastly, the beginning of the QRS segment and the T-wave termination, on EKG, are synchronized to the beginning of S1 and S2 sounds, on PCG, respectively. Since the approach does not required any time or amplitude thresholding, issues related to the parameter tuning are avoided. Hence, the location and synchronization of the synthetic EKG signal ensures a segment-by-segment detection without bartering of the detected locations. Also two noise detection stages are implemented: one based on predetection of noisy signals, and other by evaluating the time-frequency periodicity similar to [7]. All the used methods are especially chosen to work efficiently in telemedicine applications. The performance is measured in terms of segmentation accuracy, that is, expert observation on whether the heart sound segment is properly located against the EKG. The paper is then organized as follows, the next section presents a theoretical background information. Afterwards, the proposed scheme for segmentation of PCG signals and state all the parametrization in the methodology is presented. In the fourth section, results of accuracy segmentation are shown. Finally some conclusions and future work are given as a summary of the research.

## 2 Method

### 2.1 Noise Predetection

The basic idea behind this stage is to estimate the energy variation along the PSG signal,  $x(t)$ ,  $t \in T_a$ . To this end, the Shannon energy is calculated, as follows [8]:

$$\eta(t) = -x(t)^2 \log x(t)^2 \quad (1)$$

So, if the signal is corrupted by noise within a given estimation segment,  $T_a$ , its energy should increase, being noticeably higher than the average energy value, and thus allowing to infer the presence of noise. Signals with strong noise indicators should be either rejected or recorded again. With this in mind, the average Shannon energy is calculated as:

$$\hat{\eta} = \mathcal{E} \{ \eta(t) : \forall t \in T_a \} \quad (2)$$

where  $\mathcal{E} \{ \cdot \}$  stands for expectation operator.

### 2.2 Time-Frequency Enhancement of PCG Signal

*Continuous Wavelet Transform:* Wavelet analysis that comes from the basic definition of Fourier theory is based on the representation of a time-varying signal via a space domain transformation, that is, to the time-frequency domain, as follows:

$$X(\tau, w) = \int_{T_a} [x(t) w^*(t - \tau)] e^{-j\omega t} dt \quad (3)$$

where  $w$  is a window function segmenting the signal in portions that are assumed to be stationary and  $\tau$  is a time offset. The window function gives the main feature of the STFT, i.e., the width of the window (called support) that provides the capability of managing the resolution of the representation. Nonetheless, the use of basis functions as well as the window components in transformation enables to analyze the signal at different frequency bands with different resolutions, in other words, every spectral component is not analyzed equally as for the STFT; this approach is then called Wavelet Transform (WT) that maps a one-dimensional signal into a two-dimensional representation, time and scale, allowing to give local (at a given resolution) information about the frequencies occurrences. The CWT is then defined as:

$$W(a, b) = \int_{T_a} x(t) \Psi_{a,b}^*(t) dt \quad (4)$$

where  $*$  denotes complex conjugation; variables  $a$  and  $b$  are the scale and translation, respectively, and compose the new dimension of the WT. The set of Wavelets is then generated by translations and dilations of a single Wavelet function called the mother Wavelet, i.e.,  $\Psi_{a,b}(t) = a^{-1/2} \Psi((t - b)/a)$ .



*Time-Scale Representation of PCG Signal:* After obtaining the time-scale signal representation, its energy must be computed. To get a smoother energy estimation, instead of Shannon operator in Eq. (2), the scalogram is used that is defined as follows:

$$W_{SCAL}(t, a) = \frac{1}{ca^2} |W(t, a)|^2 \quad (5)$$

where  $c$  is a energy normalization parameter such as the averaged energy of the signal and the averaged energy of the scalogram becomes equal.

Scalogram then provides with the temporal localization of the energy foci, which are expected to belong to the fundamental components of the signal. Thus, an envelope of the PCG signal can be obtained with more accuracy, if the PCG is portioned into short duration frames, when adding the energy concentration over time instants. Therefore, the following marginal estimation is accomplished:

$$\varepsilon(t) = \sum_{\forall a} |W_{SCAL}(t, a)|^2 \quad (6)$$

Since all short time duration segments of a long-term PCG signal can be assumed to be quasi-stationary, the autocorrelation of the envelope of such segments should provide with information about the periodicity of the PCG signal. Particularly, for a given PSG signal segment that lasts  $T_a$  holding several S1 and S2 events, the autocorrelation that should show the averaged duration of the heart sound cycle is estimated as follows:

$$r_{\varepsilon, \varepsilon}(t) = \begin{cases} \sum_{m=1}^{T_a - m - 1} \varepsilon(n + m) \varepsilon(m), & m \geq 0 \\ \varepsilon(-m), & m < 0 \end{cases} \quad (7)$$

Taking into account that for the autocorrelation function both properties hold: periodicity, i.e.  $r(\tau) = r(\tau + T)$ ,  $\forall t \in T$ , and maximum value,  $\max_{\forall \tau \in T} \{r(\tau)\} = r(0)$ , then one can infer that  $r(0) = r(T)$ , being  $T$  the period of the PCG signal that includes both S1 and S2 events. Since analysis frame in Eq. (7) lasts more than  $T$ , that is,  $T_a > kT$ , with  $k \approx 3 \dots 4$ , then the estimated correlation function will hold  $2k$  equally located peaks. The peak sequence relates the following matching events: (S1 coincides with S1)  $\rightarrow$  (S1-S2)  $\rightarrow$  (S1-S1)  $\rightarrow$  (S1-S2)  $\rightarrow$  ... Therefore, the distance between odd peaks is the estimated value of  $T$ .

It must be quoted that the obtained in Eq. (7) estimation of the segment duration  $T$  directly from the PCG signal avoids the usage of additional information, like the EKG or the carotid pulse recording.

### 2.3 Refined Time-Frequency Periodicity Analysis

Estimation of duration  $T$ , so far, assumes a high value of signal-to-noise ratio. However, regularity of peaks is strongly affected by the presence of noise. To cope with this issue, a refined periodicity estimation is provided based on the frequency band analysis of time-frequency plane.

In general, the spectrogram, given in (4), is linearly divided in  $F$  sub-bands, from each one of which the corresponding energy envelopes is accomplished by Eq. (6). Assuming a moderate signal-to-noise ratio, the same peak sequence relating the before considered matching events takes place, but for each one of the split bands. This paper considers  $F = 15$ . Afterwards, a matrix is constructed with sets of the autocorrelation envelopes gathering 5 neighboring sub-bands at the same time, where for each matrix the following periodicity value is introduced:  $\rho_i = (\lambda_{i2}/\lambda_{i1})^2$ , (being  $\lambda_{i1}$  the first and  $\lambda_{i2}$  - the second singular value). In case of strong periodicity, either relationship should hold:  $\rho_1 > \rho_2 > \rho_3$  or  $\rho_1 < \rho_2 < \rho_3$ , otherwise, one can infer the persistent noise in signal [7].

## 2.4 Synchronism for Segmentation

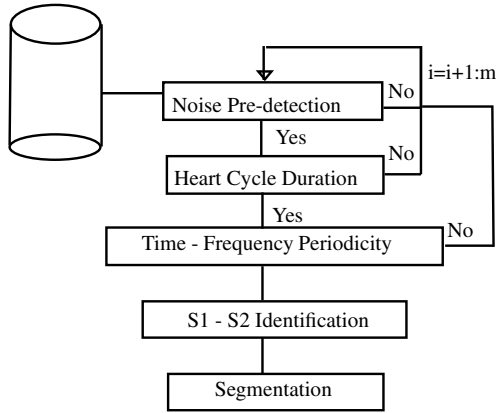
The intrinsic relationship among heart sounds and EKG provides us a tool for detecting or better determining whether an event in the envelope of the PCG signal is systolic or not, however, the simultaneous EKG is not always available. Having define the length of the heart cycle, we generate a synthetic EKG signal of the same length using the nonlinear model proposed in [9]. The EKG signal starts on the onset of the QRS (that is the associated beginning of a systolic sound) and has a duration of  $T$ . Synchronization refers then to identification of the first systolic sound over each analyzed PCG part. This is done when comparing the distance between the R-peaks and the T-wave end in the synthetic EKG signal with the first and second local maximums of the envelope, that is, the distance between the R-peak and the first local maxima of  $\varepsilon$  is minimum when compared with  $T$  if the signal starts some close at systolic sound, if not, we compare the second local maxima of  $\varepsilon$  with the end of the T-wave with a tolerance parameter and determine if it is a diastolic sound, in that case the segmentation is done from the next local maxima which is supposed to be a systolic sound. The  $T$  value is recalculated for each new heart cycle (the synthetic EKG adopts the new  $T$  value), that allows to adapt the segmentation to the heart rate variability, and therefore, a better segmentation performance can be achieved.

## 3 Experimental Setup

The methodology presented in this work is displayed in Fig. 1.

### 3.1 Database

In this work, the heart sound (Phonocardiogram, PCG) database for murmur detection of Control and Signal Processing Group at the Universidad Nacional de Colombia - Manizales is used. This database is composed of 29 patients, each one with 8 recordings, namely 4 recordings in the traditional auscultation focuses(aortic, pulmonary, mitral and tricuspid) in diaphragm and bell modes. All recordings have a duration of 20 seconds and present between 10 and 35 heart cycles according to heart rate of each patient. An electronic stethoscope and the meditron software were used. Signals were recorded in .wav at sampling frequency  $44.1kHz$  and resolution 16 bit. A labeling

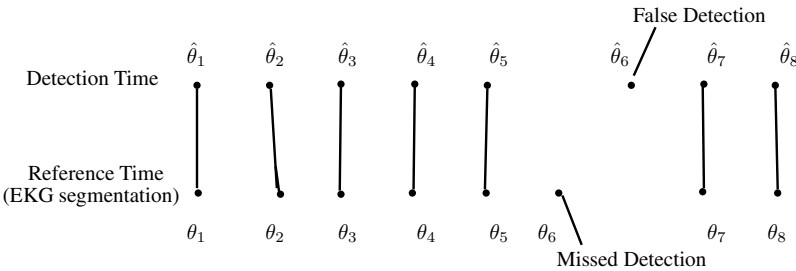


**Fig. 1.** Algorithm of the proposed methodology

process was made by a medical team, normal or pathological are the possible classes. The pathological state corresponds to the existence of abnormal sounds, especially the appearance of murmurs. Murmur intensity depends on auscultation focus, that is the principal reason to make the recording over all the 4 foci.

**3.2 Measurements**

For performance estimation, we use a traditional pan and Tompkins EKG segmentation algorithm, this is to know the start and end of each heart cycle, given the EKG and PCG correlation. To validate the method segmentation, the PCG segmentation should coincide with pan-tompkins results in at least 10%, in other case the part of signal is considered incorrectly segmented. We use this information to measure the method true and false detection, as a made in [10]:  $\hat{P}_F = N_F / (N_D + N_F)$  and  $\hat{P}_D = N_D / (N_D + N_M)$ , where  $N_D$  is the number true positives,  $N_F$  false negatives, and  $N_m$  false negatives. Thus,  $\hat{P}_F$  corresponds with the probability of false detection and  $\hat{P}_D$  the probability of detection. Fig. 2 explains the procedure.



**Fig. 2.** Explanation of measurements

### 3.3 Experiments

Signals are evaluated to identify a strong presence of noise as in Sec.2.1. It is important because the presence of noise in signals affects the time-frequency behavior. Then,  $T$  is estimated for each signal. The  $T$  in some signals might not be calculated, this occurs in signals with noise even after pre-detection stage. After that, we probe the signals with other noise detection method, here the periodicity in both frequency and time as in Sec. 2.3 is measured. Signals without periodicity are identified as noisy instances. The last stage consists in segmenting the clean signals, the measurements described in Sec. 3.2 are calculated with the idea of evaluating the method performance.

## 4 Results and Discussion

### 4.1 Predetection Stage

All 232 recorded signals were evaluated, in total 18 signals was detected as noisy signals for the bell mode and for the Diaphragm mode a total of 20 signals result noisy, the focus procedence source of noisy signals for each mode are showed in table 1. Note that several signals from pulmonary focus has been detected as noisy in relation with the other focuses, this is because of the presence of respiratory sounds. In this focus the proximity with the lung structures causes masking in heart sounds. In other words, this experiment shows the high presence of internal noise sources. In noise terms, this focus is followed by the mitral focus, here exist perturbations associated to lung structure too, due to the focus localization in the intercostal space. The other focuses are affected by different noise sources i.e., digestive sounds or human voice. It is important to emphasize that owing to the data acquisition conditions all the recordings are affected by external noise, this can justify the detection of some signals in this stage.

Note that noisy segments show a high energy with respect of the average energy, Fig. 3 exhibit a signal with noisy segments, here is evident the strong noise presence and its influence in energy values.

### 4.2 Heart Cycle Duration

For the rest of signals, after noise pre-detection, the heart cycle duration is estimated as in Sec. 2. For comparison purposes the EKG signal is used to identify the real heart frequency. In these terms, the estimated heart cycle duration is considered good if it matches at least in  $\pm 10\%$  the real value. As a result of this comparison we find 10

**Table 1.** Noise Pre-Detection

Focuses of Auscultation							
Bell Mode				Diaphragm Mode			
A	M	P	T	A	M	P	T
1	6	8	3	5	5	5	5

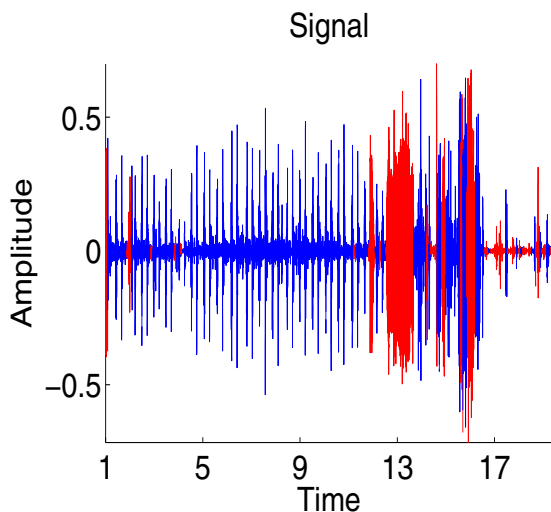


Fig. 3. Noisy Signal

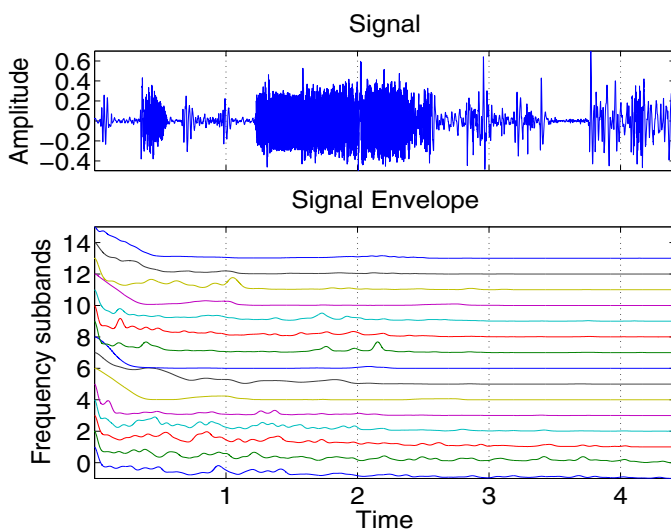


Fig. 4. Noisy signal

signals where  $T$  can not be calculated, this is only a 4.3% of the signals in the original dataset. The estimation problems occur because of the noise present in these signals that can not be detected in the predetection stage; the periodicity analysis is an additional method to identify this kind of noisy signals.

### 4.3 Refined Procedure of Computing Time-Frequency Periodicity

After this analysis, 15 signals were identified with periodicity problems. Fig.4 is an example of noisy signal and its frequency problems, the low homogeneity between the autocorrelations obtained of the 15 frequency subbands shows it. Nonetheless, in Fig. 5, it is showed a signal with periodic morphology, note the uniform dynamic along the signal through all the subbands, namely the peaks appear at the same time.

### 4.4 Achieved Segmentation

Lastly, after segmenting a total of 1741 heart cycles, according to the EKG reference, the present method identified 1516 of these heart cycles. It represents a sensibility of 90.88% and false detection rate of 9.11%, these values are calculated as explained in Sec.2. These results show the high efficiency of the exposed method and present that a good detection of noisy signals is a necessary stage for PCG signal segmentation. The present work shows the goodness of noise detection as a stage in automatic phonocardiography segmentation, and secondly, the use of segmentation methodologies based on envelope detection together with the synthetic EKG can improve the good segmentation rates.

Compared with other works, the present method has superior performance, for instance in [3], segmentation results for some kinds of envelope extraction methods are shown i.e., Shannon envelope shows segmentation efficiency for abnormal cases between 75.5% and 89.4%, and for normal cases from 65.9% to 78.2%), while Hilbert envelope shows low segmentation rates. Also this work say that CSCW shows segmentation efficiency between 96.2% and 100% for normal cases and between 72.7% and 88.2% for abnormal cases. In [11], discussed approach gives an accuracy from 88.29%

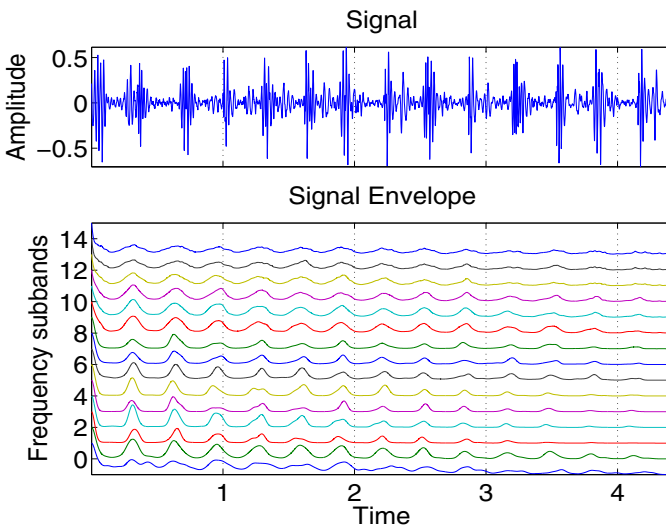


Fig. 5. Noisy signal

to 66.77% for Morlet envelope and Hilbert envelope, respectively. In [8] it is showed an accuracy of about 95.51%, but taking into account that they use a-priori information as the average heart rate and it is supposed a continuous hear rate. The presented method is robust to heart rate variability and even talking about patients with some arrhythmia it is possible to carry out a proper segmentation.

## 5 Conclusions and Future Work

An efficient segmentation methodology for PCG signals is presented that allows segmentation accuracy of up to 90% in most of the database registers. Method performance show that cycle heart length estimation by autocorrelation and synchronization with the synthetic EKG provides a good segmentation strategy with the joint analysis of the envelope of the original signal, it is important to note that the proposed method is chosen to work in telemedicine environments. This can enhance the traditional methods of PCG segmentation ensuring a correct length calculation and S1-S2 detection.

As regards the telemedicine application, it is important to note that the noise conditions for heart sound acquisition can not be adequate, for that reason it is necessary to implement strategies that contribute to identify the quality of recorded signals, for instance, the periodicity and energy methodologies used in the present work are a good response to this problem. The use of an adaptive synthetic EKG from a  $T$  estimation in each heart cycle segment, allows the segmentation even in patients with a large heart rate variability.

The low accuracy rates presented along the state of the art are understood, because the noisy signals diminish the methodologies performance, that as a result of the envelope distortions. Nevertheless, it is important to work in segmentation methods based on envelope, because its simplicity enables it to work in telemedicine applications. Despite the noise analysis, it is important to use a refined acquisition protocol, that allows to identify if it exists acceptable conditions for recording signals, that is, an environment free of noise and to get the lowest quantity of excluded signals.

Finally as a future work, we propose to find better methods to estimate the heart cycle duration, because a better evaluation of time-frequency signal periodicity is highly dependant on this, furthermore, it can improve the segmentation performance by decreasing the false detection rate. Also it is important to improve the synchronization methodology, that because there exist signals with attenuated sounds, that produce losses of peaks, which also decreases the accuracy rates.

**Acknowledgments.** This work is supported by the “*Aprendizaje de máquina a partir de múltiples expertos en clasificación multiclase de señales de voz*” project associated with “*Jóvenes Investigadores*” program by COLCIENCIAS and Universidad Nacional de Colombia - Manizales, the project “*Servicio de Monitoreo Remoto de Actividad Cardíaca para el Tamizaje Clínico en la red de Telemedicina del Departamento de Caldas*” and the “*Grupo de Control y Procesamiento Digital de Señales Código 20501007205*”

## References

1. Ari, S., Kumar, P., Saha, G.: A robust heart sound segmentation algorithm for commonly occurring heart valve diseases. *Journal of Medical Engineering and Technology* 32(6), 456–465 (2008)
2. Wang, P., Kim, Y., Ling, L.H., Soh, C.B.: First heart sound detection for phonocardiogram segmentation. In: 27th Annual International Conference of the Engineering in Medicine and Biology Society, IEEE-EMBS 2005, pp. 5519–5522 (January 2005)
3. Choi, S., Jiang, Z.: Comparison of envelope extraction algorithms for cardiac sound signal segmentation. *Expert Systems with Applications* 34(2), 1056–1069 (2008)
4. Malarvili, M.B., Kamarulafizam, I., Hussain, S., Helmi, D.: Heart sound segmentation algorithm based on instantaneous energy of electrocardiogram. In: *Computers in Cardiology*, pp. 327–330 (September 2003)
5. Yuenyong, S., Nishihara, A., Kongprawechnon, W., Tungpimolrut, K.: A framework for automatic heart sound analysis without segmentation. *BioMedical Engineering OnLine* 10, 13+ (2011)
6. Tseng, Y.-L., Ko, P.-Y., Jaw, F.-S.: JawDetection of the third and fourth heart sounds using Hilbert-Huang transform. *BioMedical Engineering OnLine* 8 (February 2012)
7. Kumar, D., Carvalho, P., Antunes, M., Paiva, R.P., Henriques, J.: Noise detection during heart sound recording using periodicity signatures. *Physiological Measurement* 32(5), 599 (2011)
8. Ari, S., Saha, G.: On a robust algorithm for heart sound segmentation. *Journal of Mechanics in Medicine and Biology* 7(2), 129–150 (2007)
9. Clifford, G.D., McSharry, P.E.: Generating 24-hour ECG, BP and respiratory signals with realistic linear and nonlinear clinical characteristics using a nonlinear model. In: *Computers in Cardiology*, pp. 709–712. IEEE (2004)
10. Sörnmo, L., Laguna, P.: *Bioelectrical Signal Processing in Cardiac and Neurological Applications*. Elsevier Academic Press (June 2005)
11. Zhong, L., Guo, X., Ji, A., Ding, X.: A robust envelope extraction algorithm for cardiac sound signal segmentation. In: 2011 5th International Conference on Bioinformatics and Biomedical Engineering, iCBBE, pp. 1–5 (2011)



# Selection of Wavelet Decomposition Level for Electro-Oculographic Saccadic De-noising

Rodolfo Garcá-Bermúdez<sup>1</sup>, Fernando Rojas<sup>2</sup>,  
Roberto Antonio Becerra García<sup>1</sup>,  
Luis Velázquez Pérez<sup>3</sup>, and Roberto Rodríguez<sup>3</sup>

<sup>1</sup> Facultad de Informática y Matemática, Universidad de Holguín, Cuba

{rodolfo, idertator}@facinf.uho.edu.cu

<sup>2</sup> Dept. of Computer Architecture and Technology, University of Granada, Spain

frojas@atc.ugr.es

<sup>3</sup> Centre for Research and Rehabilitation of Hereditary Ataxias (CIRAH),  
Holguín, Cuba

**Abstract.** Ataxia SCA2 is a neurological disorder among a group of inherited diseases of the central nervous system. In SCA2, genetic defects lead to impairment of specific nerve fibers, resulting in degeneration of the cerebellum and its afferent connections. As anomalies in the oculomotor system are well known symptoms in SCA2, electro-oculographic records become a useful technique for SCA2 diagnosis. This work presents a novel technique for determining how many decomposition levels are necessary to perform signal de-noising, based on the evaluation of the shape correspondence between the wavelet approximation coefficients and the EOG record, focusing in noise cancellation in order to obtain a clean velocity profile. Experimental results show the validity of the approach.

**Keywords:** Spino cerebellar ataxia type 2, electro-oculography, wavelet, de-noising, signal processing.

## 1 Introduction

The oculomotor system is substantially affected by ataxia SCA2, a dominantly inherited neurological disorder with an unusually high prevalence in northeastern Cuba. The effect of this disease on the latency, amplitude, duration and maximum velocity of the saccadic ocular movements has been shown in previous studies [1,2,3,4,5]. Also, electro-oculographic (EOG) records are substantially contaminated by the presence of biological noise and artifacts caused by the disease, amongst them permanent tremor and involuntary body and ocular movements, besides of the noise generated by skin electrodes and the electromyographic (EMG) activity of the extra-ocular muscles in healthy subjects.

Most of the clinical studies of ocular movements in ataxia patients use the velocity instead of ocular position directly measured by skin electrodes placed surrounding the eyes, thus causing the need to compute the first derivative of

this signal. In healthy subjects the ocular position signal is relatively easy to be differentiated using digital filters to remove noise [6], precedent researches recommend median filter and central difference algorithms in order to clean and differentiate the observed signal [7,6,8,9].

Inchingolo and Spanio [6], demonstrated that a sampling rate of 200 samples per second gave an appropriate evaluation of saccade characteristics for saccades higher than  $5^\circ$ , and the suitability of eight-points central difference derivative algorithm to compute the velocity profile.

However, our own experience with saccadic EOG records from ataxia patients reveals that the application of the eight-points central difference derivative algorithm has not been accurate enough to obtain an useful velocity profile, even if a median filter with different windows sizes was applied in order to clean the

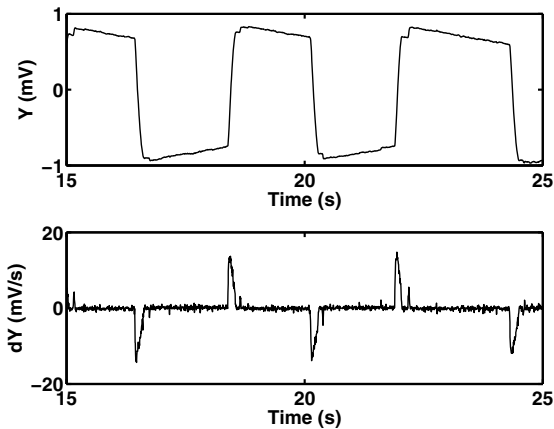


Fig. 1. Position (top) and velocity profiles (bottom) of a healthy subject

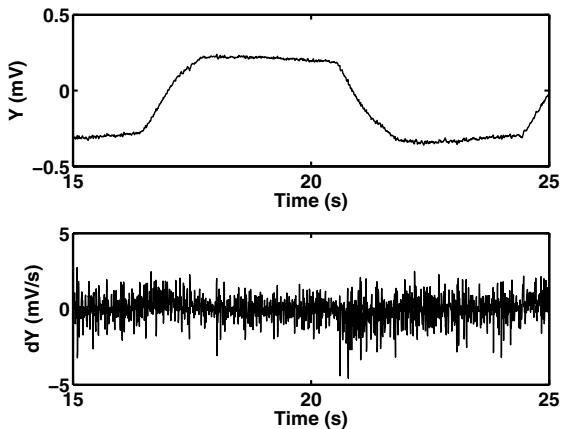


Fig. 2. Position (top) and velocity profiles (bottom) of an ataxia patient

position signal. Figures 1 and 2 show the position profile and the corresponding velocity profiles for a healthy subject and an ataxia patient whose values were calculated using the eight points central difference of the median filtered signal with a window size of 25 ms.

## 2 Wavelet De-noising

Currently we are working in a promissory approach using a wavelet transform to de-noise the ocular saccadic signal by means of the application of thresholds to the wavelet coefficients. Wavelet transform is a well known tool in biomedical variables, covering the processing of many different biological signals as electroencephalography, electromyography and electrocardiography amongst others [10,11,12]. A known problem related to the application of wavelet is to establish how many decomposition levels are necessary to perform signal de-noising. This problem has been solved by several researchers accordingly the characteristics of the signal and the goal of the application of wavelet analysis [13,14]. Our work covers a novel approach for the automatic selection of the decomposition level of EOG records from ataxia patients, focusing in noise cancellation in order to obtain a clean velocity profile.

The proposed algorithm consists of the following steps:

1. Apply a median filter to the EOG signal with a window width of 25 ms.
2. Compute the first derivative of the EOG signal using eight-points central difference method
3. Apply wavelet transform to the velocity profile
4. Compute the integration of wavelet approximation coefficient at every level
5. Compute the root total medium square error (RMSE) between the median filtered EOG signal and the integrated wavelet coefficient
6. Select each level until the RMSE growing rate changes abruptly

## 3 Material and Methods

### 3.1 Data Collection

The electro-oculogram recordings of 10 patients with severe ataxia and 10 healthy subjects diagnosed and classified in the “Centre for the Research and Rehabilitation of Hereditary Ataxias (CIRAH)” were used in order to perform the analysis of repeated ocular saccadic movement tests for 60° divergence stimuli. All the recordings were carried out by the medical staff of CIRAH. Each individual was placed in a chair, with a head fixation device to avoid head movements, the variables were collected by a two channel electronystagmograph (Otoscreen, Jaeger-Toennies). Recording conditions were set as follows: electrodes of silver chloride placed in the external borders of right eye (active electrode) and left eye (reference electrode) with sampling frequency 200 Hz. For stimulus generation a black screen CRT display showing a white circular target with an angular size of 0.7° was used. The stimulus and patient response data are automatically stored in ASCII files by Otoscreen electronystagmograph.

### 3.2 Wavelet Decomposition Level Selection

Data processing was accomplished using the Wavelet Toolbox and other functions of Matlab 7.11. The first step is EOG signal preprocessing applying a median filter with a time window of 25 ms, in order to reduce higher frequencies of noise, beyond the significant spectrum for saccadic features extraction. The first derivative is accomplished by an eight-points central difference algorithm appropriate for the sampling frequency of 200 Hz, defined by the following equation [6]:

$$V_y(i) = f_s \sum_{n=1}^m a_n (y(i+n) - y(i-n)) \quad (1)$$

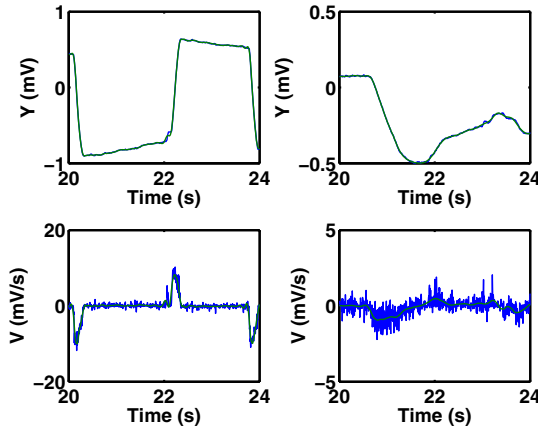
where:

$m = 4$ ;  $a_1 = 0.8024$ ;  $a_2 = -0.2022$ ;  $a_3 = 0.03904$ ;  $a_4 = -0.003732$ .

$f_s$ : sampling frequency

A discrete Daubechies wavelet transform (db5) is applied to the velocity signal up to level 8. This level is higher than the maximum level of interest, according to the previous visual check that it was performed. At that point, the approximation coefficient at every level is integrated by means of Matlab function `cumptrapz`, translation coefficients of the integral results were adjusted using a Nelder-Mead simplex direct search implemented in Matlab function `fminsearch`.

Root mean square error was computed by direct subtraction of every integrated approximation and the original position signal. Figure 3 shows the velocity profile and the wavelet approximation at two different levels for a healthy subject and an ataxia patient.



**Fig. 3.** Position (blue) and integration of wavelet approximation coefficient (green) for level 4 (top), healthy subject (left) and level 5 ataxia patient (right). Corresponding velocity and approximation coefficient (bottom).

### 4 Results and Discussion

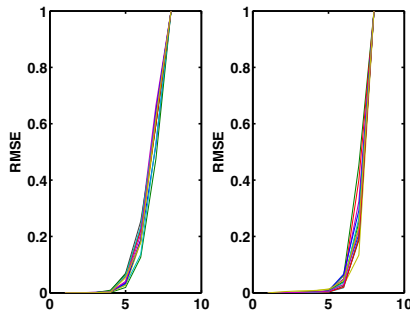
Visual inspection of the approximation coefficients for every record showed an uniform and consistent result: the maximum decomposition level for all healthy subjects was set at level 5, and for ataxia patient it was set at level 6. This difference is caused by the sharper behavior of saccades in healthy subjects, which are better shaped and show higher velocities than ataxia patients (Table 1).

**Table 1.** Maximum decomposition level labeled by visual inspection

<b>Healthy subject</b>	5	5	5	5	5	5	5	5	5	5	5	5	5	5
<b>Ataxia patient</b>	6	6	6	6	6	6	6	6	6	6	6	6	6	6

The shape of the growing rate of the RMSE was very similar for all the processed records which is illustrated in Figure 4 showing the normalized RMSE results for a healthy subject and an ataxia patient.

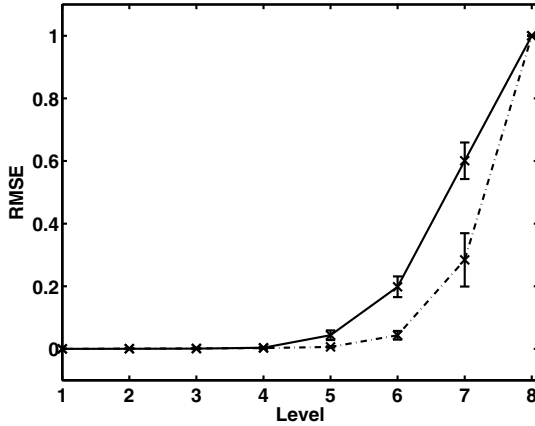
Table 2 an Figure 5 show the mean and standard deviation of RMSE for each decomposition level. An analysis of the values and the visual inspection of the graphic reveals a significant gap between the levels in the boundary of the maximum decomposition level, with no overlapped standard deviation. Therefore, it



**Fig. 4.** Normalized RMSE for a healthy subject (left) and an ataxia patient (right)

**Table 2.** Mean and standard deviation of RMSE for each level

Healthy subjects								
	1	2	3	4	5	6	7	8
<b>mean</b>	0.0000	0.0003	0.0008	0.0039	0.0438	0.1984	0.6009	1.0000
<b>standard dev.</b>	0.0000	0.0003	0.0005	0.0021	0.0154	0.0330	0.0583	0.0000
Ataxia Patients								
	1	2	3	4	5	6	7	8
<b>mean</b>	0.0000	0.0009	0.0015	0.0027	0.0063	0.0436	0.2844	1.0000
<b>standard dev.</b>	0.0000	0.0012	0.0019	0.0020	0.0021	0.0139	0.0852	0.0000



**Fig. 5.** RMSE mean and standard deviation for each level in healthy subjects (continue) and ataxia patients (dot)

is relatively simple to define the adequate threshold to establish the criterion for decomposition level selection.

## 5 Conclusions

The presence of very high noise levels in EOG recordings of ataxia patients constitutes a significant challenge for the extraction of the relevant features for the diagnosis and evaluation of their neurological condition. The application of a median filter, which it is the most popular filter for saccadic signals, does not achieve to obtain a position signal which could be differentiated, so other methods need to be evaluated to solve this problem.

Precedent works indicate the validity of wavelet transform to de-noise biological signals, including records of neurological system. Nevertheless, it is necessary to develop an algorithm which helps researchers to select the correct level of decomposition. The present work presents a simple approach to the decomposition level selection based in the specific characteristics of the saccadic EOG records. There exists a remarkable coincidence between the evaluation of the records by visual inspection of the original data and wavelet coefficients when compared with the shape of the plot of the RMSE computed between the data and the integral of the wavelet approximation coefficients of the velocity profile. The presence of a well defined knee in this plot, with a relevant gap in mean values and a relatively low standard deviation simplifies the task of threshold definition in order to perform level selection.

Future research will focus on the acquisition and processing of a higher number of recordings, including patients in different conditions, which it is necessary in order to assure the statistical consistency of these results.

## References

1. Bürk, K., Fetter, M., Abele, M., Laccone, F., Brice, A., Dichgans, J., Klockgether, T.: Autosomal dominant cerebellar ataxia type i: oculomotor abnormalities in families with SCA1, SCA2, and SCA3. *Journal of Neurology* 246(9), 789–797 (1999)
2. Hutton, J., Albrecht, J., Kuskowski, M., Schut, L.: Abnormal ocular motor function predicts clinical diagnosis of familial ataxia. *Neurology* 37(4), 698–701 (1987)
3. Schöls, L., Linnemann, C., Globas, C.: Electrophysiology in spinocerebellar ataxias: Spread of disease and characteristic findings. *The Cerebellum* 7(2), 198–203 (2008)
4. Velázquez Pérez, L., Sánchez Cruz, G., Canales Ochoa, N., Rodríguez Labrada, R., Rodríguez Díaz, J., Almaguer Mederos, L., Laffita Mesa, J.: Electrophysiological features in patients and presymptomatic relatives with spinocerebellar ataxia type 2. *Journal of the Neurological Sciences* 263(1-2), 158–164 (2007)
5. Velázquez-Pérez, L., Rodríguez-Labrada, R., Freund, H.J., Auburger, G.: Spinocerebellar ataxia type 2. In: Gazulla, J. (ed.) *Spinocerebellar Ataxia*, InTech (April 2012)
6. Inchingolo, P., Spanio, M.: On the identification and analysis of saccadic eye movements. a quantitative study of the processing procedures. *IEEE Transactions on Biomedical Engineering* 32(9), 683–695 (1985)
7. Enderle, J., Hallowell, M.: Saccade derivative filters and their clinical implications. *Biomedical Sciences Instrumentation* 34, 206–211 (1997)
8. Juhola, M.: Median filtering is appropriate to signals of saccadic eye movements. *Computers in Biology and Medicine* 21(1-2), 43–49 (1991)
9. Martínez, M., Soria, E., Magdalena, R., Serrano, A.J., Martín, J.D., Vila, J.: Comparative study of several fir median hybrid filters for blink noise removal in electrooculograms. *WSEAS Trans. Sig. Proc.* 4(3), 53–59 (2008)
10. Rui, G., Yiqin, W., Jianjun, Y., Fufeng, L., Haixia, Y.: Wavelet based de-noising of pulse signal. In: *Proceedings of 2008 IEEE International Symposium on IT in Medicine and Education, ITME 2008*, pp. 617–620 (2008)
11. Taelman, J., Van Huffel, S., Spaepen, A.: Wavelet-independent component analysis to remove electrocardiography contamination in surface electromyography. In: *29th Annual International Conference of the IEEE Engineering in Medicine and Biology Society, EMBS 2007*, pp. 682–685 (2007)
12. Poornachandra, S.: Wavelet-based denoising using subband dependent threshold for ECG signals. *Digital Signal Processing* 18(1), 49–55 (2008)
13. Salwani, M., Jasmy, Y.: Relative wavelet energy as a tool to select suitable wavelet for artifact removal in EEG. In: *2005 1st International Conference on Computers, Communications and Signal Processing with Special Track on Biomedical Engineering, CCSP 2005*, pp. 282–287 (2005)
14. Xu, L., Zhang, D., Wang, K., Li, N., Wang, X.: Baseline wander correction in pulse waveforms using wavelet-based cascaded adaptive filter. *Computers in Biology and Medicine* 37(5), 716–731 (2007)

# Identification of Postural Transitions Using a Waist-Located Inertial Sensor

Daniel Rodríguez Martín<sup>1</sup>, Albert Samà<sup>1</sup>, Carlos Pérez López<sup>1</sup>, Andreu Catalá<sup>1</sup>,  
Joan Cabestany<sup>1</sup>, and Alejandro Rodríguez Molinero<sup>2</sup>

<sup>1</sup> Technical Research Centre for Dependency Care and Autonomous Living (CETpD),  
Universitat Politècnica de Catalunya – BarcelonaTech (UPC), Spain  
{daniel.rodriguez-martin, albert.sama, carlos.perez-lopez,  
andreu.catala, joan.cabestany}@upc.edu

<sup>2</sup> Electrical & Electronic Engineering Department, NUI Galway (NUIG), Ireland  
alejandro.rodriguez@nuigalway.ie

**Abstract.** Analysis of human movement is an important research area, specially for health applications. In order to assess the quality of life of people with mobility problems like Parkinson's disease (PD) or stroke patients, it is crucial to monitor their daily life activities. The main goal of this work is to characterize basic activities and their transitions using a single sensor located at the waist. This paper presents a novel postural detection algorithm which is able to detect and identify 6 different postural transitions, sit to stand, stand to sit, bending up/down and lying to sit and sit to lying transitions with a sensitivity of 86.5% and specificity of 95%. The algorithm has been tested on 31 healthy volunteers and 8 PD patients who performed a total of 545 and 176 transitions respectively. The proposed algorithm is suitable to be implemented in real-time systems for on-line monitoring applications.

**Keywords:** Postural transitions, Accelerometers, Inertial Systems.

## 1 Introduction

Motion tracking and identification of daily life activities by inertial systems are useful in the evaluation of the quality of life in the elderly or patients with mobility problems [1], for example stroke patients or those with Parkinson's disease (PD). Among daily life activities, postural transitions (PT), mainly sit-to-stand (SiSt) and stand-to-sit (StSi), are very important since they are the most mechanically demanding activities and are considered as a prerequisite of walking [2]. For dependency care area, analyzing these transitions could be crucial for fall prevention [3] [4].

There are different methods to study and analyze human movements such as electromyography [5], photography and video [6], stereograph [7] and electrogoniometry with a pressure platform [1]. However, these systems are cumbersome and uncomfortable. Therefore, these systems cannot be used in an ambulatory monitoring.



Nowadays, Micro-Electro-Mechanical-Systems (MEMS) technology allows smaller and lighter sensors, such as miniaturized accelerometers and gyroscopes. The small size and low energy consumption enables the embedding of the sensors in devices that can be worn easily and can operate for a long time running on a small battery. MEMS have already been widely used to study human motion, and particularly in PT. For example, Bidargaggi et al. analyzed the waveform of a previously detected transition by reconstructing the accelerometer signals in the waist using wavelets in order to determine whether a SiSt or StSi transition occurred [8]. Najafi et al. used a gyroscope to obtain the chest tilt and consequently, detect postures [9]. By means of the frequency response of the gyroscope signal, they discovered a frequency band below 0.68Hz in which a significant peak appears when a PT has occurred. Najafi et al. combined this approach with other methods and constraints to generate a complete algorithm that recognizes basic activities in daily life [1]. Another interesting study used a mobile phone situated in a trouser pocket in a fixed position [10]. Through the correlation of the signal obtained with a signal template, a SiSt or StSi transition was identified. Static positions, like standing, sitting or lying can be identified by analyzing the accelerometer values in window sequences [11]. However, a sit position can be confused by a standing position depending on the tilt of the body. Thus, a dynamic and a change in the stationary movement analysis are proposed in this work.

This paper presents a novel postural transition detection algorithm using a unique triaxial accelerometer located at the waist, which is considered a comfortable location to carry an inertial sensor. The algorithm is suitable to be inserted in a microcontroller, since there are no complex calculations that require large memory usage or long time periods to calculate parameters for the algorithm. This algorithm presented has been tested in a database of 31 healthy patients and 8 PD patients. The final goal of this algorithm is to enable the evaluation of the quality of life in PD patients and enhance movement disorder detection algorithms for PD that are being developed under REMPARK project by means of the same inertial sensor located in the same place [12] [13].

## 2 Posture Transition Algorithm

A static position is characterized by the absence of movement and, then, only gravity ( $G$ ) is measured by means of the module of the accelerometer axis ( $a_x$ ,  $a_y$ ,  $a_z$ ), as shown in Eq. (1). Thus, when the sensor is located in the waist as shown in Figure 1, similar measurements may be obtained from different static positions, e.g. sitting and standing postures. Consequently, in order to discriminate between sit and stand postures it is needed to identify postural transitions. However, when a person is lying, the weight of the gravity may fall in the anterior axis ( $a_x$ ) or lateral axis ( $a_z$ ).

$$\sqrt{a_x^2 + a_y^2 + a_z^2} \Big|_{static} = G = 9.81 \text{ m/s}^2 \quad (1)$$

In dynamic postures, Eq. (1) is not valid, since accelerations applied to the inertial sensor makes vary value of Eq. (1), therefore, another features must be analyzed in order to study posture transitions, for example frequency response. According to Najafi et al., frequency response below 0.68Hz corresponds to postural transitions [9]. In this work, a Short Time Fourier Transform (STFT) is used to detect transitions. Formally:

$$X(f, t) = \int_{-\infty}^{\infty} w(t, \tau)x(t)e^{-i2\pi f t} dt \quad (2)$$

where  $x(t)$  is the accelerometer signal to be transformed,  $w(t, \tau)$  is the window function to be analyzed. The power spectral density of the window analyzed is composed by the amplitude of the signal and its frequency. A harmonic in the band below 0.68Hz which overpasses a certain threshold ( $Th_1$ ) is considered to lead to a postural transition event. This threshold will be set as the value that maximizes the minimum of sensitivity and specificity of a posture transition detection training dataset.

Once any postural transition is detected, it should be then identified. A simple approach which takes advantage of how gravity changes between axes in a PT is proposed. More concretely, the following condition differentiates the SiSt and bending down (BD) from StSi and bending up (BU) transitions:

$$\Delta(W_x - W_z) = \begin{cases} StSi, BU & < -Th_2 \\ SiSt, BD & > Th_2 \\ other & \end{cases} \quad (3)$$

$$W_x = \frac{\sum_{i=1}^n a_x(i)}{n} \quad (4)$$

$$W_z = \frac{\sum_{i=1}^n a_z(i)}{n} \quad (5)$$

where  $a_x$  and  $a_z$  in Eq. (4) and Eq. (5), are the anterior and lateral acceleration vectors of  $n$  samples, respectively.  $Th_2$  value has been set by maximizing the minimum specificity and sensitivity on the identification of the StSi and SiSt.



**Fig. 1.** Inertial Sensor

Assuming that the sensor is located according to Figure 1, the explanation of Eq. (3) is based on the effect of gravity on the axes. Overcoming the negative threshold on Eq. (3) means that the person has made a StSi or BU transition since Z axis tends to point the superior direction, then Z axis value is increased due to gravity and makes left part of Eq. (3) more negative when sitting. On the other hand, Eq. (3) might not vary and remains close to zero when the subject realizes stationary movements, for example walking, running, standing, sitting or lying. Furthermore, a decreasing value in Z axis is obtained because of the bending forward movement when a SiSt transition begins. The X axis is directed against gravity and tends to become positive when standing up. Note that anatomy and belt mounting has a very strong effect on the data captured and, consequently, only one axis might change instead of both X and Z axis. In order to overcome this problem, a relation among X and Z axis is used in Eq. (3).

The state machine shown in Figure 2 has been developed in order to establish the complete PT classifier. In this state machine it is very important to know the initial conditions since the triggering of the indicator given by Eq. (3) results in 2 possible posture transitions, which are distinguished through the initial conditions.

Furthermore, a Lying postural transition is detected whether the Y axis changes, if Y is under 0.5G it is understood that the person is in a prone position.

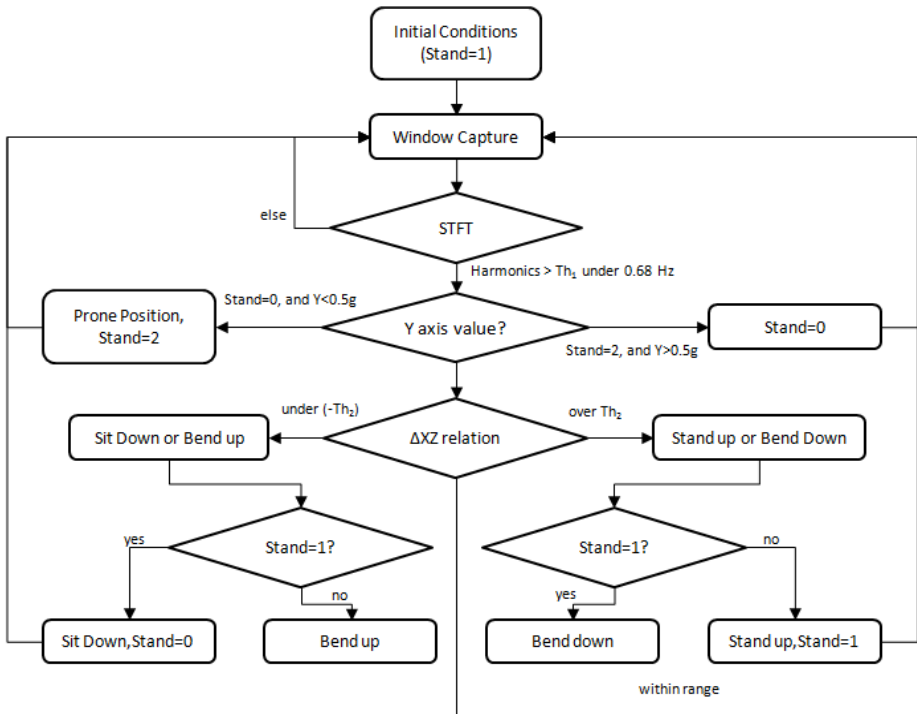


Fig. 2. Activity Recognition Algorithm

### 3 Experiments

The experiments have been performed using an inertial data-acquisition device developed at the Research Centre for Dependency Care and Autonomous Living of the Technical University of Catalonia (CETpD-UPC). This device has been already used in other research works [14]. With a size of 77x37x21 mm<sup>3</sup>, it is smaller than a mobile phone. The accelerometer used is LIS3LV02DQ, which is 3-axial and has a full scale of  $\pm 6G$  ( $1G=9.81 \text{ m/s}^2$ ) and has the data information conditioned and digitalized. The inertial data is stored in a  $\mu$ SD card.

Two test protocols have been performed. The first test protocol, which includes different daily life activities, was performed by 36 volunteers (22 men and 14 women, ages from 21 to 56 years old, mean age of 35.77 and standard deviation of  $\pm 9.58$ ). 5 randomly chosen volunteers have been used to set thresholds, and the rest have been used to test the classifier. Six transitions have been taken into account in this work: Bending up/down (BU/BD), Sitting from Lying (SL), Lying from Sitting (LS), Stand-to-Sit (StSi), Sit to Stand (SiSt). The participants wore an inertial sensor at the waist, fixed as shown in Figure 1. Every subject performed the test twice, removing his belt and relocating it again between tests. Each test lasted 3-4 minutes approximately.

Participants were video recorded in order to have a visual gold-standard. A total of 625 transitions have been analyzed, 80 of them were used to set thresholds  $Th_1$  and  $Th_2$ , among which 40 transitions belong to Sit-to-Stand and Stand-to-Sit transitions, 20 belong to Lying transitions and the other 20 to Bending transitions. The other 545 transitions were used to test the classifier, among which 311 transitions belong to Sit-to-Stand and Stand-to-Sit transitions, 124 belong to Lying transitions and the other 110 to Bending transitions. The second test protocol was performed by 8 patients with PD, who formed part of MOMOPA project database [15]. The entire tests were also video-recorded, and the thresholds achieved with the 5 randomly healthy volunteers were not changed in order to validate the algorithm in both data bases. A total of 176 transitions have been analyzed, 88 of them were SiSt and 88 were StSi. The signal has been sampled at 40Hz in both tests, which is enough to measure human motion [16]. Signal was divided into 128 samples windows, which have a duration of 3.2 seconds. This window length is enough since, according to Kralj's et al., the maximum time of a transition is 3.3 seconds [1]. However Kerr et al. confirmed that transitions may last up to 2 seconds in elderly people [7]. Windows are 50% overlapped to prevent possible loss of information.

### 4 Results and Discussion

A total of 80 transitions belonging to 5 purely random chosen healthy volunteers have been used to set  $Th_1$  and  $Th_2$ , which are the detector and identifier thresholds of SiSt, StSi BU and BD transitions.  $Th_1$  has been set to 2 having maximized the minimum sensitivity and specificity of detecting a transition among the 80 training set transitions.  $Th_2$  has been set to 1.5 through the same approach.

A total of 545 transitions have been evaluated (311 SiSt and StSi, 110 Bending and 124 Lying transitions). Results of sensitivity and specificity on healthy volunteers are shown in Table 1. Note that TN,TP,FP and FN mean True Negative cases, True Positive cases, False Negative cases and False Positive cases respectively, while Sensitivity= $\frac{TP}{TP+FN}$ , and Specificity =  $\frac{TN}{TN+FP}$ .

**Table 1.** Sensitivity and Specificity from different postural transitions on healthy volunteers

Activity	Predictions	N. Transitions	Result
SIT TO STAND	TN	359	Sensitivity 0,865
	TP	135	
	FN	21	Specificity 0,992
	FP	3	
STAND TO SIT	TN	359	Sensitivity 0,871
	TP	135	
	FN	20	Specificity 0,986
	FP	5	
BEND UP	TN	442	Sensitivity 0,946
	TP	52	
	FN	3	Specificity 0,996
	FP	2	
BEND DOWN	TN	446	Sensitivity 0,873
	TP	48	
	FN	7	Specificity 0,996
	FP	2	
LYING FROM SIT	TN	432	Sensitivity 1,000
	TP	62	
	FN	0	Specificity 1,000
	FP	0	
SIT FROM LYING	TN	432	Sensitivity 1,000
	TP	62	
	FN	0	Specificity 1,000
	FP	0	

Table 2 shows the results of the algorithm applied to 8 PD patients using the same parameters used with healthy people.

**Table 2.** Sensitivity and Specificity from different postural transitions on PD patients

Activity	Predictions	N. Transitions	Result
SIT TO STAND	TN	214	Sensitivity 0,932
	TP	82	
	FN	6	Specificity 0,963
	FP	8	
STAND TO SIT	TN	214	Sensitivity 0,92
	TP	81	
	FN	7	Specificity 0,955
	FP	10	

The method detects SiSt, StSi, BU and BD transitions with a specificity over 0.98. However, sensitivity measurements decrease especially at Bend Down, StSi and SiSt transitions, which have sensitivity around 0.90. In these cases volunteers tend to Bend down more slowly than when they Bend up, consequently  $Th_1$  is not enough to detect a transition so an adaptive threshold is proposed for future work in order to enhance these results. The StSi and SiSt transitions drawbacks come when volunteers sit at the bed. It has been found that some people have sat dropping, similarly to a fall, provoking deep rebounds in the signal. However, calculating the mean of the X axis and Z axis in a window of data neglects this effect by acting as a low-pass filter.

The postural transition algorithm described uses a single accelerometer located at the waist, and is based on the effect of gravity on the accelerometer axis. The sensor location is very important because it maximizes the difference between frontal acceleration or X axis and lateral or Z axis as considered in Eq. (2). For instance, if the sensor is located at a lateral side of the waist, then the lateral axis would be orthogonal to the rotations performed during postural transitions, thus gravity effect would be negligible and Eq. (2) would remain constant to postural changes. One of the main features of the system is the windowing-based analysis. On the one hand it allows reducing latency time, in other words, a result of the algorithm can be given in each window. On the other hand it permits the microcontroller to lighten the load of memory used to analyze the signal since it analyzes only a window instead of the whole signal.

As part of future work, it is proposed to enhance the correct identification of the PT by detecting some other activities, for example walking, running or activities that a person can only execute when she/he is stand. On the other hand this algorithm has to be validated in a larger database which is currently being performed with real PD patients which have to execute PT in their daily life in a home-environment situation.

## 5 Conclusions

Postural transitions are an important activity of daily life, and measuring them can be useful to evaluate quality of life. The postural transition detector presented in this work detects and identifies 6 different postures and uses a single accelerometer in a very comfortable position. The method has been shown to detect PT with specificity over 0.98 and sensitivity 0.865. It has also been tested in real PD patients, where the results achieved are 0.92 on sensitivity and 0.95 on specificity. The algorithm is suitable to be implemented in real-time for online monitoring as the algorithm as it is based in windowing analysis.

**Acknowledgements.** This work has been performed within the framework of the FP7 project REMPARK ICT-287677, which is funded by the European Community. The authors would like to acknowledge the contributions of their colleagues from REMPARK Consortium (<http://www.rempark.eu>)

## References

1. Najafi, B., Aminian, K., Paraschiv-Ionescu, A., Loew, F., Büla, C., Robert, P.: Ambulatory System for Human Motion Analysis Using a Kinematic Sensor: Monitoring of Daily Physical Activity in the Elderly. *IEEE Transactions on Biomedical Engineering* 50, 711–723 (2003)
2. Kralj, A., Jaeger, R.J., Muni, M.: Analysis of standing up and sitting down in humans: Definitions and Normative Data Representation. *Journal of Biomechanics* 23(11), 1123–1138 (1990)
3. Cheng, P.T., Liaw, M.Y., Wong, M.K., Tang, F.T., Lee, M.Y., Lin, P.S.: The sit-to-stand movement in stroke patients and its correlation with falling. *Archives of Physical Medicine and Rehabilitation* 79(9), 1043–1046 (1998)
4. Nyberg, L., Gustafson, Y.: Patient falls in stroke rehabilitation. A challenge to rehabilitation strategies. *Stroke* 26(5), 838–842 (1995)
5. Wheeler, J., Woodward, C., Ucovich, R.L., Perry, J., Walker, J.M.: Rising from a chair. Influence of age and chair design. *Physical Therapy* 65(1), 22–26 (1985)
6. Guzmán, R.A., Prado, H.E., Porcel, H., Cordier, B.: Differences in the momentum development during transfers sit to stand between fall and no fall elderly. *Geriatr. Gerontol.* 44(4), 200–204 (2009)
7. Kerr, K.M., White, J.A., Barr, D.A., Mollan, R.A.B.: Analysis of the sit-stand-sit movement cycle: development of a measure system. *Gait & Posture* 2(3), 173–181 (1994)
8. Bidargaggi, N., Klingbeil, L., Sarela, A., Boyle, J., Cheung, V., Yelland, C., Karunanithi, M., Gray, L.: Wavelet based approach for posture transition estimation using a waist worn accelerometer. In: *Proceedings of the 29th Annual International Conference of the IEEE EMBS*, pp. 1884–1887 (2007)
9. Najafi, B., Aminian, K., Loew, F., Blanc, Y., Robert, P.: Measurement of Stand-Sit and Sit-Stand Transitions Using a Miniature Gyroscope and Its Application in Fall Risk Evaluation in the Elderly. *IEEE Transactions on Biomedical Engineering* 49(8), 843–851 (2002)
10. Bieber, G., Koldrack, P., Sablowski, C., Peter, C., Urban, B.: Mobile physical activity recognition of Stand-up and Sit-down Transitions for user behavior analysis. In: *Proceedings of the 3rd International Conference on Pervasive Technologies Related to Assistive Environments*, article n. 50 (2010)
11. Karantonis, D.M., Narayanan, M.R., Mathie, M., Nigell, H.L., Celler, B.G.: Implementation of a Real-Time Human Movement Classifier Using a Triaxial Accelerometer for Ambulatory Monitoring. *IEEE Transactions on Information Technology in Biomedicine* 70(1), 156–167 (2006)
12. Samà, A., Perez, C., Rodríguez-Martín, D., Cabestany, J., Moreno Aróstegui, J.M., Rodríguez-Molinero, A.: A Heterogeneous Database for Movement Knowledge Extraction in Parkinson's Disease. In: *European Symposium on Artificial Neural Networks, Computational Intelligence and Machine Learning* (2013)
13. REMPARK—Personal Health Device for the Remote and Autonomous Management of Parkinson's Disease FP7-ICT-2011-7-287677
14. Samà, A., Angulo, C., Pardo, D., Català, A., Cabestany, J.: Analyzing human gait and posture by combining feature selection and kernel methods. *Neurocomputing* 74(16), 2665–2674 (2011)
15. MOMOPA—Monitoring the Mobility of Parkinson's Patients for Therapeutic Purposes FIS. ISCIH. 2009-2010
16. Zhou, S., Shan, Q., Fei, F., Li, W.J., Pin Kwong, C., Wu, P.C.K., Meng, B., Chan, C.K.H., Liou, J.Y.J.: Gesture Recognition for Interactive Controllers Using MEMS Motion Sensors. In: *Proceedings of the 2009 4th IEEE International Conference on Nano/Micro Engineered and Molecular Systems*, pp. 935–940 (2009)

# Evaluating Multiple Sequence Alignments Using a LS-SVM Approach with a Heterogeneous Set of Biological Features

Francisco Ortuño<sup>1,\*</sup>, Olga Valenzuela<sup>2</sup>, Héctor Pomares<sup>1</sup>, and Ignacio Rojas<sup>1</sup>

<sup>1</sup> Department of Computer Architecture and Computer Technology  
CITIC-UGR, University of Granada

<sup>2</sup> Department of Applied Mathematics, University of Granada  
fortuno@ugr.es

**Abstract.** Multiple sequence alignment (MSA) is an essential approach to apply in other outstanding bioinformatics tasks such as structural predictions, biological function analyses or phylogenetic modeling. However, current MSA methodologies do not reach a consensus about how sequences must be accurately aligned. Moreover, these tools usually provide partially optimal alignments, as each one is focused on specific features. Thus, the same set of sequences can provide quite different alignments, overall when sequences are less related. Consequently, researchers and biologists do not agree on how the quality of MSAs should be evaluated in order to decide the most adequate methodology. Therefore, recent evaluations tend to use more complex scores including supplementary biological features. In this work, we address the evaluation of MSAs by using a novel supervised learning approach based on Least Square Support Vector Machine (LS-SVM). This algorithm will include a set of heterogeneous features and scores in order to determine the alignment accuracies. It is assessed by means of the benchmark BALiBASE.

**Keywords:** multiple sequence alignments (MSAs), feature selection, supervised learning, least squares support vector machines (LS-SVM).

## 1 Introduction

Multiple sequence alignment (MSA) is one of the most useful tool for other biological and biomedical tasks. MSA strategies have been applied in a huge number of applications such as phylogenetic analyses, structural modelling, functional predictions or sequence database searching [20]. These methodologies also take advantage of high-throughput experiments or next-generation sequencing (NGS), which provide functional, structural and genomic information to obtain more accurate alignments in a reasonable time [13]. Therefore, MSAs are becoming one of the most powerful tools for analyses in bioinformatics [16].

Currently, one of the main challenges in MSA is to provide an evaluation method in order to efficiently calculate the quality of the alignment. Sequence

---

\* Corresponding author.



alignments have been traditionally evaluated by using well-known weighted matrices, such as Point Accepted Mutation (PAM) [5] or BLOSUM [11]. However, these matrices only consider the nucleotide or amino acid information provided by the sequences to evaluate each pair of aligned residues. Other MSA evaluations are also addressed by comparing with reference alignments. Several benchmarks, e.g. BALiBASE [26], provide a set of alignments which are considered as a gold standard because they were accurately obtained. Then, alignments provided by other tools are usually evaluated according to their similarity with these gold standard references. This evaluation is usually the most accurate to measure the quality of the alignment. However, these references are not available for all possible sequences and they cannot be used when novel sequences are compared. In these cases, the evaluation of alignments could result hard as there are not previously know references. For this reason, current scores are increasingly improving their evaluations by using additional biological features, such as protein structures or homologies. For instance, both Contact Accepted Mutation (CAO) [17] and STRIKE scores [14] included molecular contact information from protein structures to estimate the alignment quality.

In this work, a new supervised learning approach, based on Least Square Support Vector Machine (LS-SVM), is proposed in order to provide an alignment evaluation. This algorithm takes advantage of the integration of several biological features. These features are selected from resources and databases related to protein structures, homologies, chemical properties, etc. Additionally, other evaluations or scores calculated from alignments are also included in the data integration. The proposed method is assessed by the 218 alignments provided by BALiBASE.

## 2 Methods

### 2.1 The BALiBASE Benchmark

BALiBASE [26] defines several groups of sequences that are specifically prepared to be aligned by standard algorithms. This dataset includes a total of 218 manually extracted sets of sequences, usually provided by Protein Data Bank (PDB) [2]. These sets of sequences are organized in six subsets of sequences according to their families and similarities, namely RV11, RV12, RV20, RV30, RV40 and RV50. For example, the RV11 subset includes the set of less similar sequences ( $> 20\%$  of similarity). BALiBASE also provides a set of handmade reference alignments (*gold standard*) in order to compare them with alignments obtained by other tools. Thus, BALiBASE calculates a Sum-of-Pairs (SP) score, called BALIScore, to evaluate such alignments. These SP scores are used to assess the proposed evaluation scheme.

### 2.2 Input MSA Methodologies

Traditionally, several strategies have been applied in order to align multiple sequences, mainly classified as progressive algorithms or consistency-based methods. Recently, more sophisticated tools in MSA have also added further data to

**Table 1.** Summary of features and scores extracted for each alignment. 14 features/scores were retrieved. The ranking of relevance was also measured according to the NMIFS procedure. <sup>(1)</sup> These matches refer to percentage of aligned amino acids with the same feature.

	MEASUREMENT	Type	RANK		MEASUREMENT	Type	RANK
$f_1$	# of sequences	Feature	22	$f_{12}$	Domain Matches <sup>(1)</sup>	Feature	6
$f_2$	Average length	Feature	20	$f_{13}$	Number of Domains	Feature	16
$f_3$	Variance length	Feature	21	$f_{14}$	Shared Domains (%)	Feature	18
$f_4$	Shared 3D struct	Feature	2	$f_{15}$	Shared GO Terms (%)	Feature	17
$f_5$	Seqs. with 3D struct (%)	Feature	9	$f_{16}$	Gaps (%)	Feature	12
$f_6$	# of 3D struct.	Feature	13	$f_{17}$	Identities (%)	Feature	15
$f_7$	AAs Types Matches <sup>(1)</sup>	Feature	5	$f_{18}$	STRIKE	Score	1
$f_8$	Transmembrane AAs (%)	Feature	11	$f_{19}$	PAM250	Score	3
$f_9$	AAs in Strand (%)	Feature	14	$f_{20}$	BLOSUM62	Score	4
$f_{10}$	AAs in Helix (%)	Feature	19	$f_{21}$	RBLOSUM62	Score	10
$f_{11}$	Second. Struct. Matches <sup>(1)</sup>	Feature	7	$f_{22}$	GONNET	Score	8

align sequences, such as domains, secondary/tertiary structures or homologies. In this work, ten representative MSA tools were selected to evaluate the quality of their alignments. Among progressive algorithms, ClustalW [25], Muscle [8], Kalign [15], Mafft [12] and RetAlign [24] were chosen in the proposed optimization. Three additional algorithms based on consistency were also included in the optimization, namely T-Coffee [18], FSA [3] and ProbCons [7]. Finally, other two MSA tools using additional biological features (3DCoffee [19] and Promals [21]) were added.

Therefore, as BALiBASE is composed by 218 sets of sequences, these methods will provide a total of 2180 alignments to evaluate. In addition, the gold standard alignments from BALiBASE will also be included. The proposed algorithm will consequently be assessed by a set of 2398 alignments.

### 2.3 Feature Extraction and Feature Selection

The goal of this evaluation algorithm is to provide a set of biological features to enrich current MSA evaluations. Features related to the BALiBASE sequences and their alignments were extracted from well-known biological databases: Pfam [10], PDB [2], Uniprot [1] and Gene Ontology (GO) [4]. Such databases were consulted to obtain useful data which enrich the sequence information, building a complete set of features. For instance, we added information about the number and length of sequences, secondary and tertiary structures in proteins, chemical properties of amino acids (AAs), protein domains or percentage of identities. This algorithm also included some of the most known evaluation systems, such as BLOSUM62 [11], PAM250 [5], RBLOSUM62 [22] or STRIKE [14]. The final dataset was composed by 22 features (See summary in Table 1).

Additionally, the importance of these features to evaluate alignments was analysed by a feature selection approach. The feature selection allows reducing the number of features, trying to avoid the redundant or less relevant information. In this case, this procedure was performed by using the Normalized Mutual

Information Feature Selection (NMIFS) approach [9]. This approach is based on mutual information (MI) in order to measure the quality of each feature. The MI indicator is able to detect the relationship between features and it is totally independent of the space transformation. Therefore, the most relevant biological features according to the NMIFS procedure were chosen to be included in the subsequent LS-SVM algorithm.

## 2.4 LS-SVM Approach

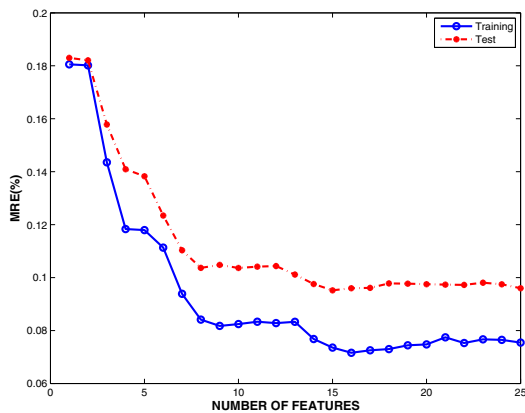
The proposed alignment evaluation was designed by a Least-Square Support Vector Machine (LS-SVM) model in terms of the previously extracted biological features. LS-SVMs are redesigned from standard support vector machines (SVMs), but applying a cost function based on least squares [23]. LS-SVMs can be used for prediction algorithms, but they have proved to be specially effective for regression problems. Since this algorithm aims to determine the accuracy of each alignment similar to the BALIScore provided by BALiBASE, a regression problem is being formulated. Therefore, the application of a LS-SVM was a suitable and faithful solution.

In addition, the proposed algorithm included a kernel based on the Radial Basis Function (RBF). Two hyper-parameters were then optimized in this approach: the kernel width and the regulation parameter. Such hyper-parameters' optimization was performed by using cross-validation. The LS-SVM algorithm was developed with the Matlab toolbox found in [6]. Finally, the LS-SVM evaluation algorithm was assessed by another 10-fold cross-validation procedure.

## 3 Results and Discussion

The proposed algorithm aims to obtain an accurate evaluation of alignments, trying to be similar to the BALIScore provided by BALiBASE, but without using gold standard references. As described above, the ten selected methodologies were firstly run for the 218 sets of BALiBASE in order to obtain a total dataset of 2398 alignments (10 alignments and the BALiBASE reference for each set of sequences). Subsequently, the 22 biological features related to the alignments and their sequences were retrieved from databases such as PDB, PFam, Uniprot and GO.

In order to select a subset of highly related features, the NMIFS procedure provided a ranking according to the feature significance with respect to the BALIScore (see 'Rank' column in Table 1). As shown by this ranking, the most significant features were usually scores (STRIKE, PAM and BLOSUM), but also some matches (similarities between sequences) of biological features such as domains, 3D structures or amino acid (AAs) types. Taking this ranking into consideration, an additional feature was progressively included in the LS-SVM evaluation algorithm to determine the optimal subset of features. As shown in Figure 1, the mean relative error (MRE) in the proposed evaluation decreases till reaching a subset of 16 features, where the error value is minimal. Therefore,



**Fig. 1.** Error evolution according to the number of features included in the LS-SVM algorithm. Both training and test errors by using a 10-fold cross-validation are shown. This error, called Mean Relative Error (MRE), is an average of the relative error in percentage.

it is not necessary to include the full dataset of features, as the minimal error can be accomplished with the 16 most relevant features. Then, this subset of 16 features was chosen to be included in the evaluation algorithm.

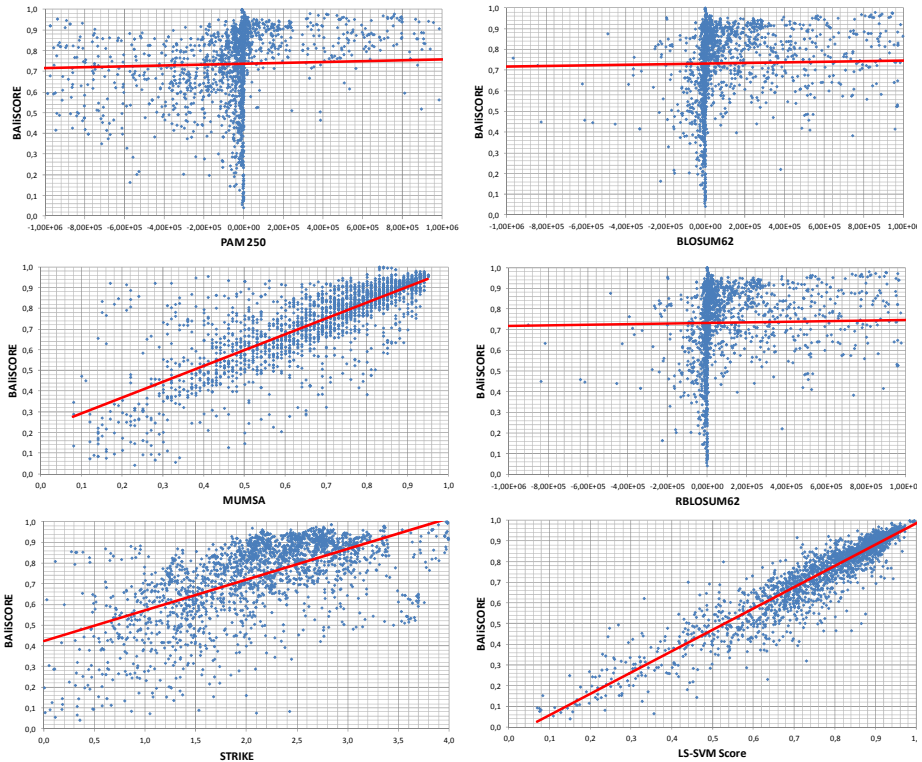
Subsequently, the LS-SVM approach was trained by using these 16 features and applying a 10-fold cross-validation procedure for the dataset of 2398 problems. That is, this dataset was randomly divided into 10 subsets and the LS-SVM was progressively trained using nine of them. The remaining subset was used to assess the trained evaluation algorithm. Thus, as this procedure was repeated 10 times for each different subset, an evaluation for each alignment in the full dataset was retrieved. These obtained evaluations were compared against the other scores in order to determine if the proposed evaluation had improved the previously designed scores.

This comparison against other evaluation scores was performed in terms of two different measures. Firstly, as BALIScore provides an accurate score with regard to the reference alignments, the correlation between different scores and the BALIScore was calculated. As shown in the Figure 2 and the Table 2, the alignment scores provided by LS-SVM significantly increased the correlation with respect to BALIScore. As can be seen, the PAM, BLOSUM and RBLOSUM scores did not provide any correlation with BALIScore. This could be a relevant disadvantage to those MSA methods which build their alignments by using such scores. Otherwise, MUMSA and STRIKE scores showed a quite better correlation but they do not reach the correlation obtained by our LS-SVM approach. This correlation measure is an useful issue because it could provide an interesting score to be considered in the building and optimization of alignments.

Additionally, since several alignments were provided for the same set of sequences (11 different alignments), a pairwise comparison of alignments was

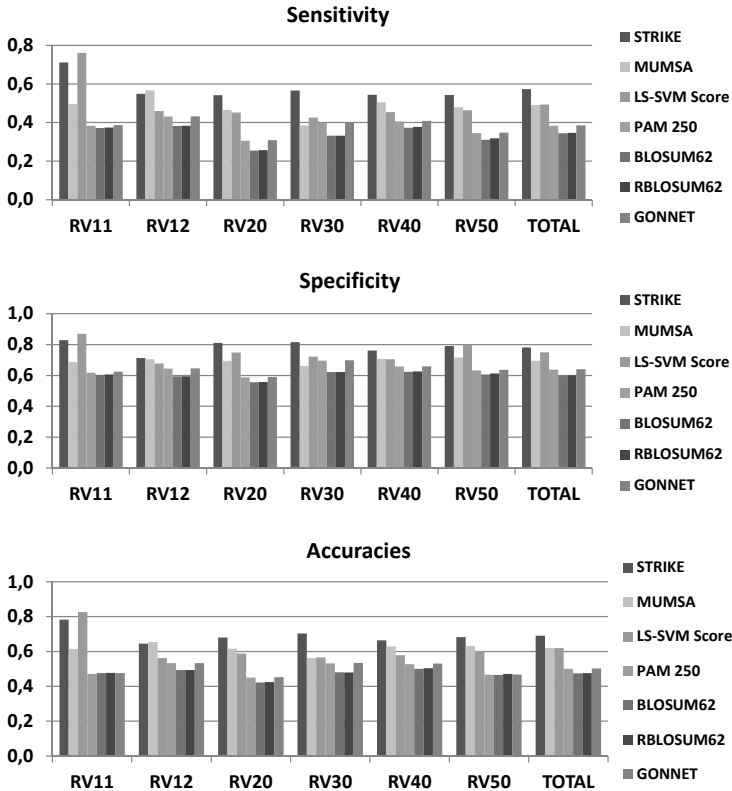
**Table 2.** Pearson correlation between evaluation scores and BALIScore with respect to each of the subset in BALiBASE. The correlation is also shown according to the BALiBASE subsets.

	RV11	RV12	RV20	RV30	RV40	RV50	TOTAL
STRIKE	0.775	0.516	0.374	0.564	0.597	0.734	0.653
PAM 250	0.112	0.107	0.229	0.345	0.121	0.115	0.148
BLOSUM62	0.136	0.131	0.197	0.230	0.062	-0.118	0.104
RBLOSUM62	0.129	0.130	0.191	0.226	0.061	-0.117	0.101
MUMSA	0.629	0.641	0.749	0.611	0.443	0.717	0.698
LS-SVM Score	<b>0.846</b>	<b>0.761</b>	<b>0.839</b>	<b>0.681</b>	<b>0.765</b>	<b>0.780</b>	<b>0.858</b>



**Fig. 2.** Graphical correlation between BALIScore and the remaining evaluation systems

performed in order to know the accuracy of each score deciding which of two alignments is the best one. The alignment considered by BALIScore as the best for each pairwise comparison was chosen as the gold standard. Then, this comparison was calculated according to the accuracy, sensitivity and specificity measures, obtained for a total of 11990 pairwise comparisons (11 alignments taken in pairs for 218 sets of sequences). A pairwise comparison was considered true (positive



**Fig. 3.** Sensitivity, specificity and accuracy obtained for the pairwise comparison of alignments for each score scheme. Values are shown according to the BALiBASE subsets.

or negative) when a specific score scheme agreed with the BALiscore selecting the best alignment in such comparison. Otherwise, if both scores differed, the comparison is considered a false negative or false positive.

Therefore, the obtained specificity, sensitivity and accuracy measures for the provided scores are shown in Figure 3. The alignments were divided into the BALiBASE subsets in order to see whether the improvement could depend on the sequence similarities. As shown in this figure, the LS-SVM evaluation algorithm usually outperforms the remaining scores in the three measures excepting the STRIKE score. In the case of STRIKE, LS-SVM score is significantly better for the RV11 subset. This is an interesting finding due to this subset is composed by alignments with less similar sequences and, therefore, it is harder to obtain accurate alignments in such subset. Thus, as the LS-SVM procedure included further biological information, this allowed selecting the most accurate alignment. Additionally, regarding the remaining subsets of alignments, LS-SVM was found between the three most accurate scores, obtaining similar values to

MUMSA and STRIKE. However, taking the previously shown correlations into account, the provided LS-SVM score in general determined more accurately the quality associated to these alignments. This score could even be applied in the future for the optimization of some less accurate alignments or for novel MSA tools which build alignments according to the provided LS-SVM evaluation.

## 4 Conclusions

In this work, a novel scoring scheme for multiple sequence alignments has been proposed. This algorithm takes advantage of several biological sources to build a dataset of heterogeneous features. Such dataset is used to train a least squares support vector machine (LS-SVM) which provides an evaluation for each alignment according to the extracted biological features. The proposed evaluation was assessed by using the BALiBASE benchmark. This benchmark provides an accurate score, BALiscore, which was used to compare the results of the LS-SVM approach against other known scores. A significant improvement in terms of the correlation with the BALiscore was shown. Additionally, the accuracy obtained when pairwise alignments were compared was calculated. In this case, the LS-SVM score showed similar results as MUMSA or STRIKE. However, our score outperformed them in the RV11 dataset, where alignments are harder to align due to more distant sequences. For this reason, the LS-SVM score can be considered an adequate evaluation scheme in order to be applied in future MSA methodologies.

## References

1. Apweiler, R., Bairoch, A., Wu, C.H., Barker, W.C., Boeckmann, B., Ferro, S., Gasteiger, E., Huang, H.Z., Lopez, R., Magrane, M., Martin, M.J., Natale, D.A., O'Donovan, C., Redaschi, N., Yeh, L.S.L.: Uniprot: the universal protein knowledgebase. *Nucleic Acids Res.* 32, D115–D119 (2004)
2. Berman, H., Westbrook, J., Feng, Z., Gilliland, G., Bhat, T., Weissig, H., Shindyalov, I., Bourne, P.: The protein data bank. *Nucleic Acids Research* 28(1), 235–242 (2000)
3. Bradley, R.K., Roberts, A., Smoot, M., Juvekar, S., Do, J., Dewey, C., Holmes, I., Pachter, L.: Fast Statistical Alignment. *PLoS Computational Biology* 5(5) (2009)
4. Camon, E., Magrane, M., Barrell, D., Lee, V., Dimmer, E., Maslen, J., Binns, D., Harte, N., Lopez, R., Apweiler, R.: The gene ontology annotation (goa) database: sharing knowledge in uniprot with gene ontology. *Nucleic Acids Res.* 32, D262–D266 (2004)
5. Dayhoff, M.O., Schwartz, R.M., Orcutt, B.C.: A model of evolutionary change in proteins. *Atlas of Protein Sequence and Structure* 5(3), 345–352 (1979)
6. De Brabanter, K., Karsmakers, P., Ojeda, F., Alzate, C., De Brabanter, J., Pelckmans, K., De Moor, B., Vandewalle, J., Suykens, J.A.K.: Ls-svmlab: a matlab toolbox for least squares support vector machines, v1.8 (2011)
7. Do, C., Mahabhashyam, M., Brudno, M., Batzoglou, S.: ProbCons: Probabilistic consistency-based multiple sequence alignment. *Genome Research* 15(2), 330–340 (2005)

8. Edgar, R.: MUSCLE: multiple sequence alignment with high accuracy and high throughput. *Nucleic Acids Research* 32(5), 1792–1797 (2004)
9. Estévez, P.A., Tesmer, M., Perez, C.A., Zurada, J.M.: Normalized mutual information feature selection. *IEEE Transactions on Neural Networks* 20(2), 189–201 (2009)
10. Finn, R.D., Mistry, J., Tate, J., Coghill, P., Heger, A., Pollington, J.E., Gavin, O.L., Gunasekaran, P., Ceric, G., Forslund, K., Holm, L., Sonnhammer, E.L.L., Eddy, S.R., Bateman, A.: The pfam protein families database. *Nucleic Acids Res.* 38, D211–D222 (2010)
11. Henikoff, S., Henikoff, J.G.: Amino-acid substitution matrices from protein blocks. In: *Proceedings of the National Academy of Sciences of the United States of America*, vol. 89(22), pp. 10915–10919 (1992)
12. Katoh, K., Misawa, K., Kuma, K., Miyata, T.: MAFFT: a novel method for rapid multiple sequence alignment based on fast Fourier transform. *Nucleic Acids Research* 30(14), 3059–3066 (2002)
13. Kemena, C., Notredame, C.: Upcoming challenges for multiple sequence alignment methods in the high-throughput era. *Bioinformatics* 25(19), 2455–2465 (2009)
14. Kemena, C., Taly, J.F., Kleinjung, J., Notredame, C.: Strike: evaluation of protein msas using a single 3d structure. *Bioinformatics* 27(24), 3385–3391 (2011)
15. Lassmann, T., Sonnhammer, E.: Kalign - an accurate and fast multiple sequence alignment algorithm. *BMC Bioinformatics* 6 (2005)
16. Li, H., Homer, N.: A survey of sequence alignment algorithms for next-generation sequencing. *Briefings in Bioinformatics* 11(5), 473–483 (2010)
17. Lin, K., Kleinjung, J., Taylor, W.R., Heringa, J.: Testing homology with contact accepted mutation (cao): a contact-based markov model of protein evolution. *Computational Biology and Chemistry* 27(2), 93–102 (2003)
18. Notredame, C., Higgins, D., Heringa, J.: T-Coffee: A novel method for fast and accurate multiple sequence alignment. *Journal of Molecular Biology* 302(1), 205–217 (2000)
19. O’Sullivan, O., Suhre, K., Abergel, C., Higgins, D., Notredame, C.: 3DCoffee: Combining protein sequences and structures within multiple sequence alignments. *Journal of Molecular Biology* 340(2), 385–395 (2004)
20. Pei, J.: Multiple protein sequence alignment. *Current Opinion in Structural Biology* 18(3), 382–386 (2008)
21. Pei, J., Grishin, N.V.: PROMALS: towards accurate multiple sequence alignments of distantly related proteins. *Bioinformatics* 23, 802–808 (2007)
22. Styczynski, M.P., Jensen, K.L., Rigoutsos, I., Stephanopoulos, G.: BLOSUM62 miscalculations improve search performance. *Nature Biotechnology* 26(3), 274–275 (2008)
23. Suykens, J.A.K., Van Gestel, T., De Brabanter, J., De Moor, B., Vandewalle, J.: *Least Squares Support Vector Machines*. World Scientific Pub. Co. Inc., Singapore (2003)
24. Szabo, A., Novak, A., Miklos, I., Hein, J.: Reticular alignment: A progressive corner-cutting method for multiple sequence alignment. *BMC Bioinformatics* 11 (2010)
25. Thompson, J., Higgins, D., Gibson, T.: ClustalW: Improving the sensitivity of progressive multiple sequence weighting, position-specific gap penalties and weight matrix choice. *Nucleic Acids Research* 22(22), 4673–4680 (1994)
26. Thompson, J., Koehl, P., Ripp, R., Poch, O.: BALiBASE 3.0: Latest developments of the multiple sequence alignment benchmark. *Proteins-Structure Function and Bioinformatics* 61(1), 127–136 (2005)



# Animal Vibrissae: Modeling and Adaptive Control of Bio-inspired Sensors

Carsten Behn, Tonia Schmitz, Hartmut Witte, and Klaus Zimmermann

Ilmenau University of Technology, Faculty of Mechanical Engineering,  
Max-Planck-Ring 12, 98693 Ilmenau, Germany  
{carsten.behn,hartmut.witte,klaus.zimmermann}@tu-ilmenau.de  
<http://www.tu-ilmenau.de/mb>

**Abstract.** The reception of vibrations is a special sense of touch, important for many insects and vertebrates. The latter realize this reception by means of hair-shaped vibrissae in the mystacial pad, to acquire tactile information about their environments. The system models have to allow for stabilizing and tracking control while nevertheless being able to detect superimposed solitary excitations. Controllers have to be adaptive in view of both the randomness of the external signals to be suppressed and the uncertainty of system data. We presents mechanical models and an improved adaptive control strategy that avoids identification but renders the system sensitive.

**Keywords:** Vibrissa, tactile sensor, mechanical model, adaptive control.

## 1 Motivation

In addition to their visual and auditory sense, mice and rats use a sophisticated sensory system to acquire tactile information about their surroundings. They employ a sophisticated tactile sensory system for this purpose: hair-shaped vibrissae or whiskers. The tactile hairs are located in the mystacial pad, are either used passively to sense environmental forces (wind, contact with an obstacle) or actively, when they are rhythmically moved to scan objects or surfaces. Disregarding different types of such sensors we set up various mechanical models of a single vibrissa/whisker to describe their modes of operation (passive and active vibrissae): vibrissae are either used passively to sense environmental forces, e.g., wind, or actively, when they are rhythmically moved to scan objects or surfaces (“whisking”).

The tenor of our investigations is from biomimetics. The main focus is not on “copying” the solution from biology/animality, rather on detecting the main features, functionality and algorithms of the considered biological systems to implement them in (here: mechanical) models and to develop ideas for prototypes. For this, a well-founded analysis of the biological paradigm (e.g., anatomy, functionality of a vibrissae) is important, mostly guaranteed by means of an intensive

and critical literature study. Then a implementation of these specific characteristics of the vibrissa is needed for the detection of useful information in challenging surroundings in a mechanical model.

The global goal is not to construct prototypes with one-to-one properties of a vibrissa, rather the models shall exhibit its main features, which shall be easier to handle as the ones from literature.

## 2 The Biological Paradigm

### 2.1 Anatomy

The vibrissa itself (made of dead material) is mainly used as a lever for the force transmission. But, in contrast to ordinary hairs, vibrissae are stiffer and have a hollow conical shape, [31]. The mystacial vibrissae are arranged in an array of columns and rows around the snout, see Fig. 1, [31]. Each vibrissa in the mystacial pad is embedded in and supported by its own **follicle-sinus complex** (FSC). The FSC is characterized by its exceptional arrangement of blood vessels, neural connections and muscles, see [9] for a schematic drawing. It is assumed that the rodents can control the viscoelastic properties of the vibrissa's support by regulating the blood supply to the sinus (like a blood sac), [7].

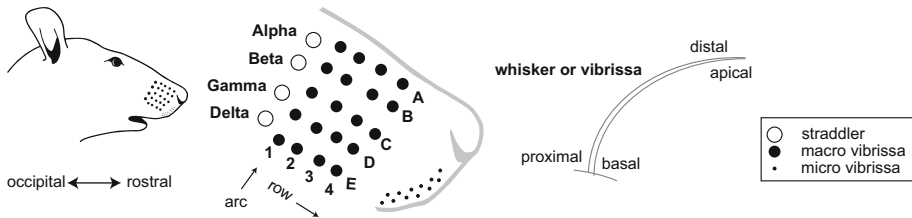


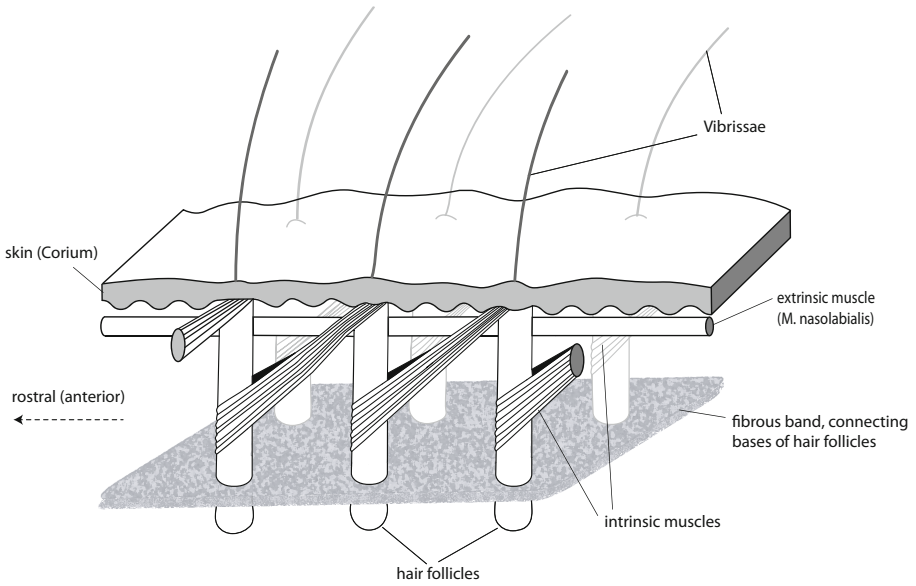
Fig. 1. Schematic drawing of the mystacial pad, [31]

The **musculature** is divided in **extrinsic and intrinsic** ones, see Fig. 2.

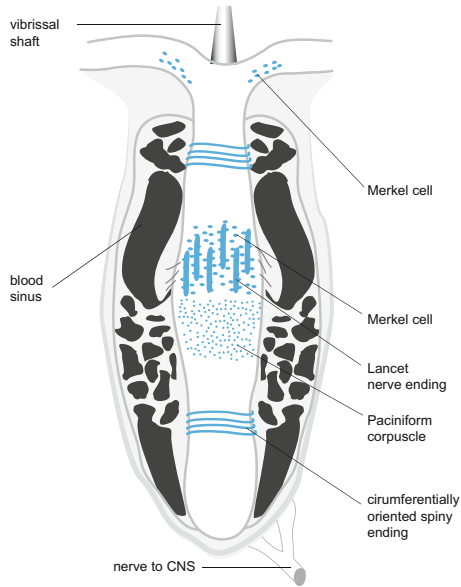
### 2.2 Functionality

The functionality of these vibrissae vary from animal to animal and is best developed in rodents, especially in mice and rats, [19]. In the following we discuss the various elements of the FSC and their important properties for the reception of vibrations.

1. **Mechanoreceptors:** The detection of contact forces is made possible by the pressure-sensitive mechanoreceptors in the support of the vibrissa, see Fig. 3. These mechanoreceptors are stimulated due to the vibrissa displacements in the FSC. The nerves (see Fig. 3) transmit the information through several processing units to the CNS. The receptor cells offer the fundamental principle 'adaptation'.



**Fig. 2.** Schematic drawing of neighboring mystacial follicles, which can be moved by extrinsic and intrinsic muscles, [1]



**Fig. 3.** Follicle-sinus complex (FSC) of a vibrissa with various types of receptors (blue). Adapted from [9] and [26].

2. The vibrissa returns passively to the initial position through the **fibrous band**.
3. Intrinsic and extrinsic musculature: The vibrissae can be moved either passively (e.g., by wind), or actively through alternate contractions of the intrinsic and extrinsic muscles, see Fig. 2. The resulting rhythmic pro- and retractions of the vibrissa, called whisking, are used to scan surfaces and objects. Relevant information can be perceived by adjusting the frequency and amplitude of the oscillation to each task. By observing rats accomplishing several tasks, [4] could distinguish two main whisking patterns: **exploratory whisking**, i.e., rodents explore their environment with large amplitude sweeps in a low frequency (5–15 Hz) range, and **foveal whisking**, i.e., rodents palpate object surfaces with small amplitude, high frequency (15 – 25 Hz) movements.

Summarizing, the complex FSC- and muscle-system enables the rodents to use their vibrissae in two different ways (modes of operation): In the **passive mode**, the vibrissae are being deflected by external forces (e.g., wind). They return to their rest position passively — thus without any muscle activation. In the **active mode**, the vibrissae are swung back- and forward by alternate contractions of the intrinsic and extrinsic muscles. By adjusting the frequency and amplitude of the oscillations, the rodents are able to investigate object surfaces and shapes amazingly fast and with high precision, [16].

How the animals convert these multiple contacts with single objects into coherent information about their surroundings is still unclear.

### 2.3 Control Strategies

Every biological sensory system has the ability to constantly adapt its sensitivity to its current environment in a way that enables it to distinguish the relevant information from the multitude of negligible stimuli ( $\rightarrow$  *adaptive system*). Several **control strategies** enhance the relevance-oriented stimulus processing:

- a feedback loop (closed-loop control system) enables the rodents to immediately react to an object contact: they slow down the concerned vibrissae, diminishing the occurring wear-out effect on the hair, [21], [22],
- depending on the mode (passive or active) and the expectations of the rodent, the neuron’s reaction is being suppressed, enhanced or left unaltered, [6], [5], [10],
- the rodents can probably modify the stiffness of the vibrissa support by varying the pressure in the blood-sinus, [7], and by doing so, specifically alter the properties of the vibrissa in motion.

Therefore, this biological sensor system is highly interesting for applications in the field of autonomous robotics, since tactile sensors can offer reliable information, where conventional sensors fail (in dark, smoky or noisy environments).

### 3 State of the Art in Modeling

Since the author in [27] tried to determine the position of a robot arm with vibrissa-like sensors (made of guitar strings), the demand for technical vibrissae grew steadily. In the meantime, these tactile sensors often complement or even replace optical sensors (as mentioned above) in their two main fields of application: flow measurements in micro technology and autonomous robotics. Especially in the latter field, technical vibrissae are currently just used to avoid collisions (merely used as contact sensors with a binary output, [25]). In the last decade, the number of scientific works in which the capabilities of the tactile sensors were improved, grew significantly. As in 1996 the development of robots equipped with artificial vibrissae and driving along walls, see [18], was seen as a considerable achievement, the recently developed robots with a similar configuration managed to distinguish objects on the basis of their surface texture ([11], [29], [33], [12], [24]), or to determine form and position of nearby objects, [28].

In the majority of papers found in literature, the development of innovative technical whiskers was based on analytical investigations of mechanical models of vibrissa. In order to analyze the mechanical and especially the dynamical behavior of the vibrissa, the physical principles of the paradigm have to be identified and to be modeled. Usually two types of models are used to analyze the mechanical behavior of the vibrissa: rigid body models or continuum models.

There are a lot of sophisticated rigid body models in literature, we mention an excerpt: A model of the FSC is considered in [20] and [22]. A model of a single vibrissa with the neighboring muscle-systems are investigated in [4]. In [17] the authors developed a mechanical model of the vibrissa, focussing on the relationship between the various muscle contractions and the resulting vibrissa motion. Furthermore, three vibrissa / follicle units, linked by spring and damping elements, were incorporated in the model so that the influence of the intrinsic muscle slings on their neighboring follicles could also be considered. The authors in [23] set up a model for the stimulus transmission. The model consists of two parts – the *mechanical part* has components representing the vibrissa shaft from stimulus contact point to base, and internal components of FSC. The *electrical (control) part* is given therein as a Simulink flow chart.

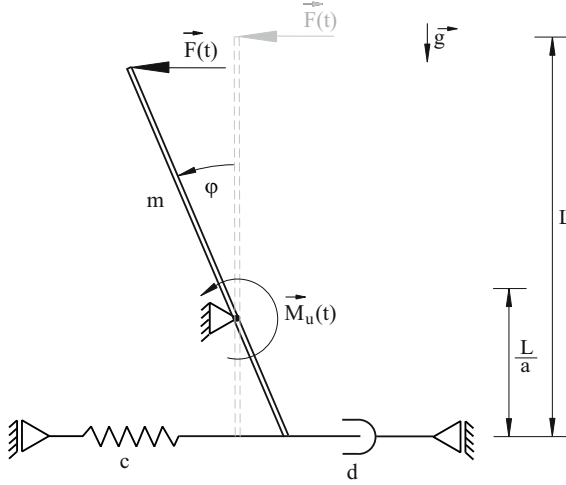
A more detailed overview is given in [1]. The most of these models exhibit a high complexity due to the goal of an exact modeling of the biological paradigm as possible, see [14] and [15] for complex models of a complete vibrissa row and neighboring tissue.

Our **global goal** is to *present models more transparent and to use more stringent mechanics and mathematical analysis to exploit them*. The goal is **not** to recreate an exact copy of the biological system, but *to implement in a mechanical model the specific characteristics of the vibrissa needed for the detection of useful information in challenging surroundings (principle goal of theoretical bionics)*. We point out, that we focus on a single vibrissa and not on a tuft of various vibrissae. Therefore, these models can be transferred to model a *carpal vibrissa* (i.e., vibrissa at extremities in mammals), too.

## 4 Modeling and Control

### 4.1 Model with Single DOF

A first model of a single vibrissa serves as the level of stimulus reception. The center of rotation of the thin rod-like vibrissa lies at skin level, a viscoelastic element located beneath it, represents the compliance of the FSC, see Fig.4.



**Fig. 4.** Mechanical model of a vibrissa:  $d$  - viscous damping coefficient,  $c$  - spring constant,  $m$  - mass of the rod,  $L$  - length of the rod,  $\mathbf{F}(t)$  - disturbing force,  $\mathbf{M}_u(t)$  - control torque

The equations of motion are:

$$\begin{aligned}
 J_{0z} \ddot{\varphi}(t) &= \left(L - \frac{L}{a}\right) \mathbf{F}(t) \cos(\varphi(t)) - c \frac{L^2}{a^2} \cos(\varphi(t)) \sin(\varphi(t)) \\
 &\quad - d \frac{L^2}{a^2} \dot{\varphi}(t) \cos^2(\varphi(t)) + \left(\frac{L}{2} - \frac{L}{a}\right) mg \sin(\varphi(t)) + \mathbf{M}_u(t).
 \end{aligned} \tag{1}$$

The ability of the rodents to either stabilize or swing their vibrissa actively, was implemented with a control torque  $\mathbf{M}_u(t)$  (calculated due to the feedback law of the following adaptive high-gain controller):

$$\left. \begin{aligned}
 e(t) &:= \varphi(t) - \varphi_{\text{ref}}(t) \\
 \mathbf{M}_u(t) &= -[k(t)e(t) + \kappa k(t)\dot{e}(t)] \\
 \dot{k}(t) &= \begin{cases} \gamma (||e(t)|| - \lambda)^2, & \text{if } ||e(t)|| \geq \lambda + 1 \\ \gamma (||e(t)|| - \lambda)^{0.5}, & \text{if } (\lambda + 1) > ||e(t)|| \geq \lambda \\ 0, & \text{if } (||e(t)|| < \lambda) \wedge (t - t_E < t_d) \\ -\sigma k(t), & \text{if } (||e(t)|| < \lambda) \wedge (t - t_E \geq t_d) \end{cases} \forall t.
 \end{aligned} \right\} \tag{2}$$

This adaptive control algorithm (2) (improved one compared to the ones in [2] and [3]) has the ability to compensate *unknown* disturbance forces in the passive

as well as in the active mode: the rod-like vibrissa follows the reference signal  $\varphi_{\text{ref}}$  within the margin of tolerance  $\lambda$  (i.e.,  $\lambda$ -tracking). This is similar to the rodents reaction: they suppress the perception of a *bothering* permanent vibrissa deflection (here: keeping the motion of the rod in the  $\lambda$ -tube), while still staying sensitive for an *interesting* sudden deflection.

## 4.2 Simulation of the Single Vibrissa Model

Now, we choose the following parameters matching the biological paradigm, see [17] and [1]:

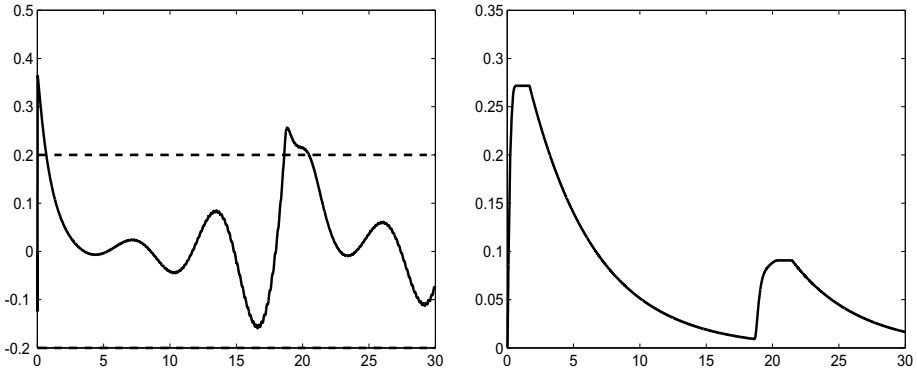
- vibrissa:  $m = 0.000\,003\text{ kg}$ ,  $c = 5.7 \frac{\text{N}}{\text{m}}$ ,  $d = 0.2 \frac{\text{Ns}}{\text{m}}$ ,  $L = 0.04\text{ m}$ ,  $a = \frac{L}{10} = 0.004\text{ m}$ ,  $(\varphi(0), \dot{\varphi}(0)) = (0\text{ rad}, 0 \frac{\text{rad}}{\text{s}})$ ;
- environment:  $t \mapsto F(t) = 0.1 \cos(t) + 2 e^{-(t-20)^2}\text{ N}$ , which represents a (small) permanent oscillation with a gust of wind, and  $g = 9.81 \frac{\text{m}}{\text{s}^2}$ ;
- $\lambda$ -tracker (2):  $\lambda = 0.2 \approx 0.064\pi$ ,  $\gamma = 50$ ,  $\sigma = 0.2$ ,  $t_d = 1\text{ s}$  and  $k_0 = 0$ ;
- reference signal to be tracked:

The active mode has to be implemented with reference signals performing periodical oscillations enabling the rod to either explore its surroundings or to scan specific objects – and since rodents use two different kinds of oscillations depending on the task, the exploratory and foveal whisking are simulated by two different reference signals. Rodents employ large amplitude sweeps in a low frequency range (5 – 15 Hz) to investigate their environment. As the range of movement of the biological vibrissa amounts to ca.  $100^\circ = 1.74\text{ rad}$ , the amplitude of the exploratory reference signal (3) can be chosen to  $A = \frac{1.74}{2} \approx 0.8\text{ rad}$ . The frequency of the signal  $\varphi_{\text{ref}1}(t)$  has been set to  $f = 5\text{ Hz}$  according to the findings in [4]. Foveal whisking has been implemented with the reference signal (4), using an amplitude of  $A = 0.2\text{ rad} \approx 12^\circ$  and a frequency of  $f = 25\text{ Hz}$ , since rodents scan specific objects with small amplitude, high frequency movements (15 – 25 Hz).

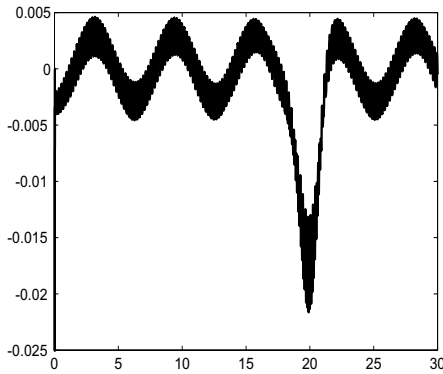
$$t \mapsto \varphi_{\text{ref}1}(t) = 0.8 \sin(2\pi 5 t)\text{ rad} \quad \text{exploratory whisking} \quad (3)$$

$$t \mapsto \varphi_{\text{ref}2}(t) = 0.2 \sin(2\pi 25 t)\text{ rad} \quad \text{foveal whisking} \quad (4)$$

Applying controller (2), we simulate the vibrissa in active mode 1, i.e., we  $\lambda$ -track reference signal (3). We obtain the results presented in Fig. 5 and 6. Here, one cannot clearly see the advantage of two alternating exponents in observing the excitation peak in the gain parameter. We have a good tracking result. The gain parameter  $k(\cdot)$  increases very fast in the beginning of the simulation. This is due to the “switching on” of the controller. It forces  $e$  fast into the tube at cost of a high  $k$ . The gain  $k(\cdot)$  immediately decreases after a  $t_d$ -stay of  $e$  in the tube, see Fig. 5. The error  $e$  is forced back into the  $\lambda$ -tube very fast because of the modified adaptation rule. This is on the expense of a tolerable overshooting of  $k$  at the beginning.



**Fig. 5.** Error and  $\lambda$ -tube (left), gain parameter  $k(\cdot)$  (right), all vs. time  $t$



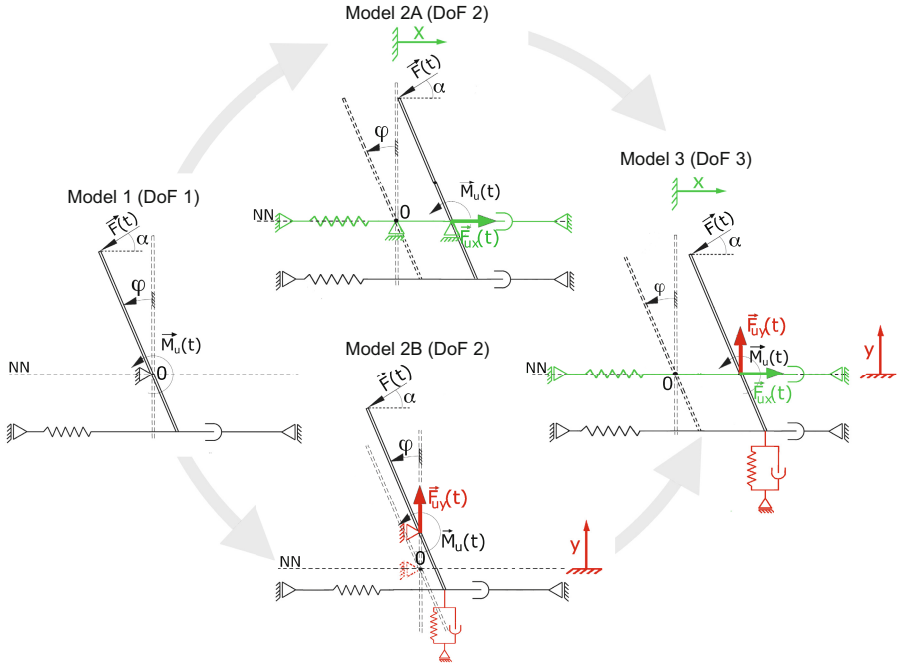
**Fig. 6.** Control torque  $M_u$  vs.  $t$

### 4.3 Models with Higher DOF

The considered single rod-like vibrissa with  $DoF = 1$  is not sufficient to model the complex behavior of the animal vibrissae. We should increase the  $DoF$  in the following. Three innovative mechanical models with a stiff, rod-like vibrissa are being developed, see Fig. 7. The degree of freedom ( $DoF$ ) is being successively increased from 1 to 3, to investigate the impact of different supports on the sensory capabilities of the system.

In **model 1** the rod has one rotational degree of freedom: the angular deflection  $\varphi(t)$ . The control torque  $\mathbf{M}_u(t)$  simulates the rodent's ability to regulate the deflection of the vibrissa by means of their intrinsic musculature. In **model 2A** the rod has, in addition to the rotational, a linear degree of freedom: the lateral translational motion of the pivot point (following the information found in [4] and [17]). A control force  $\mathbf{F}_{ux}(t)$  simulates the rodent's ability to alter the position of the pivot point through contractions of the extrinsic musculature. In **model 2B** the rod has two degrees of freedom as well: the angular deflection





**Fig. 7.** Innovative mechanical models with a rigid, rod-like vibrissa, ( $x$ : lateral direction,  $y$ : longitudinal direction)

as in the models 1 and 2A, and a longitudinal translational motion of the vibrissa. A control force  $F_{uy}(t)$  determines the longitudinal position of the pivot point. This force is not simulating any natural musculature. In **model 3** the models 2A and 2B are being combined, thus the rod possesses three degrees of freedom, which enables it to perform a rotatory deflection, as well as lateral and longitudinal displacements.

The implementation of the linear degree of freedom in the longitudinal direction is based on findings in [13], revealing that vibrissae experience considerable forces in longitudinal direction when touching an object. Furthermore, the authors in [30] found out that the rodent's neurons react strongly to the longitudinal displacements of the vibrissa – which leads to the assumption that they provide relevant information about their environment.

The examined mechanical models all meet the basic requirements for high-quality sensor systems: they react with sensitivity to occurring disturbance forces, the response time is short, and the disturbance force can be identified. Still the performances of the models differ greatly from one another, especially with respect to the force identification. The steady increase of the *DoF* from model 1 ( $DoF = 1$ ), via models 2A, 2B ( $DoF = 2$ ) to model 3 ( $DoF = 3$ ) revealed the significant benefits of the respective direction of motion. Thus, although the enhancement of model 1 with a translational *DoF* in  $x$ -direction

led to an improvement of the sensibility in model 2A, the additional *DoF* in  $y$ -direction was by far more relevant for the identification of the disturbance force: in model 2B the force can be identified in the passive, as well as in the active mode – and this for angles of attack reaching from  $0^\circ$  to  $90^\circ$ . Yet the positive characteristics of the models 2A and 2B could not be fully united in model 3: the interaction between the translational displacement in  $x$  with the angular deflection  $\varphi$  impeded, especially in the active mode, the identification of the disturbance force. While the models 1 and 2A are only suitable for applications with forces acting mostly horizontally, the models 2B and 3 can also provide reliable information in widely unknown surroundings. Furthermore, model 2B can be used in the passive, as well as in the active mode.

## 5 Conclusion and Outlook

The goal of this work was to present the theoretical context needed to examine the mechanical and in particular the dynamical characteristics of the biological vibrissa. Moreover, these theoretical aspects were to be interpreted with respect to the biological vibrissa, as well as for a technical implementation of it. Inspired by this biological sensory system, several types of mechanical models were developed based on findings in the literature.

The focus was on rigid body systems. At the beginning, a single vibrissa system consisting of one rigid rod was investigated. The investigations have shown that adaptive control is promising in application to vibrissa systems: it allowed to describe the two main modes of operation of vibrissae – passive and active one. We switched back to the analysis of a single vibrissa and increased its *DoF*. We presented three models with a stiff rod-like vibrissa, taking into account the viscoelastic support in the mystacial pad (FSC and skin). The muscles (extrinsic and intrinsic) enabling the animals to whisk actively were simulated by adaptive control algorithms. Numerical simulations with chosen perturbation forces showed that specific control variables contain adequate information on the force to be identified.

Nevertheless, all models offer the drawback that they consist of one rigid element. One may think of object localization, in this case the rigid body may break or get locked. Hence, further and present investigations are directed to more compliant vibrissa systems: first to rigid multi-body systems and, second to continuum systems (e.g., beams).

## References

1. Behn, C.: Mathematical Modeling and Control of Biologically Inspired Uncertain Motion Systems with Adaptive Features. Habilitation thesis, submitted to Ilmenau University of Ilmenau, Germany (2013)
2. Behn, C., Steigenberger, J.: Improved Adaptive Controllers For Sensory Systems - First Attempts. In: Awrejcewicz, J. (ed.) Modeling, Simulation and Control of Nonlinear Engineering Dynamical Systems, pp. 161–178. Springer, Amsterdam (2009)

3. Behn, C., Steigenberger, J.: Experiments in adaptive control of uncertain mechanical systems. *International Review of Mechanical Engineering* 4(7), 886–898 (2010)
4. Berg, R.W., Kleinfeld, D.: Rhythmic Whisking by Rat: Retraction as Well as Protraction of the Vibrissae Is Under Active Muscular Control. *Journal of Neurophysiology* 89, 104–117 (2003)
5. Curtis, J.C., Kleinfeld, D.: Seeing What the Mouse Sees with Its Vibrissae: A Matter of Behavioural State. *Neuron* 50(4), 524–526 (2006)
6. Derdikman, D., Yu, C., Haidarliu, S., Bagdasarian, K., Arieli, A., Ahissar, E.: Layer-Specific Touch-Dependent Facilitation and Depression in the Somatosensory Cortex during Active Whisking. *The Journal of Neuroscience* 26(37), 9358–9547 (2006)
7. Dörfl, J.: The musculature of the mystacial vibrissae of the white mouse. *Journal of Anatomy* 135, 147–154 (1982)
8. Dörfl, J.: The innervation of the mystacial region of the white mouse – A topographical study. *Journal of Anatomy* 142, 173–184 (1985)
9. Ebara, S., Kumamoto, K., Matsuura, T., Mazurkiewicz, J.E., Rice, F.L.: Similarities and Differences in the Innervation of Mystacial Vibrissal Follicle-Sinus Complexes in the Rat and Cat: A Confocal Microscopic Study. *The Journal of Comparative Neurology* 449, 103–119 (2002)
10. Fanselow, E.E., Nicolelis, M.A.L.: Behavioral Modulation of Tactile Responses in the Rat Somatosensory System. *The Journal of Neuroscience* 19(17), 7603–7616 (1999)
11. Fend, M., Bovet, S., Yokoi, H.: An Active Artificial Whisker Array for Texture Discrimination. In: *Proceedings of 2003 IEEE/RSJ International Conference on Intelligent Robots and Systems*, pp. 1044–1049 (2003)
12. Fend, M.: Whisker-Based Texture Discrimination on a Mobile Robot. In: Capcarrère, M.S., Freitas, A.A., Bentley, P.J., Johnson, C.G., Timmis, J. (eds.) *ECAL 2005. LNCS (LNAI)*, vol. 3630, pp. 302–311. Springer, Heidelberg (2005)
13. Gopal, V., Hartmann, M.: Using hardware models to quantify sensory data acquisition across the rat vibrissal array. *Bioinspiration & Biomimetics* 2, 135–145 (2007)
14. Haidarliu, S., Simony, E., Golomb, D., Ahissar, E.: Muscle Architecture in the Mystacial Pad of the Rat. *The Anatomical Record* 293, 1192–1206 (2010)
15. Haidarliu, S., Simony, E., Golomb, D., Ahissar, E.: Collagenous Skeleton of the Rat Mystacial Pad. *The Anatomical Record* 294, 764–773 (2011)
16. Hartmann, M.J., Solomon, J.H.: Robotic whiskers used to sense features: Whiskers mimicking those of seals or rats might be useful for underwater tracking or tactile exploration. *NATURE* 443, 525 (2006)
17. Hill, D., Bermejo, R., Zeigler, P., Kleinfeld, D.: Biomechanics of the Vibrissa Motor Plant in Rat: Rhythmic Whisking Consists of Triphasic Neuromuscular Activity. *The Journal of Neuroscience* 28, 3438–3455 (2008)
18. Jung, D., Zelinsky, A.: Whisker based mobile robot navigation. In: *Proceedings of the 1996 IEEE/RSJ International Conference on Intelligent Robots and Systems 1996 (IROS 1996)*, pp. 497–504 (1996)
19. Jin, T.-E., Witzemann, V., Brecht, M.: Fiber Types of the Intrinsic Whisker Muscle and Whisking Behavior. *The Journal of Neuroscience* 24(13), 3386–3393 (2004)

20. Mitchinson, B., Gurney, K.N., Redgrave, P., Melhuish, C., Pipe, A.G., Pearson, M., Gilhespy, I., Prescott, T.J.: Empirically inspired simulated electro-mechanical model of the rat mystacial follicle-sinus complex. *Proceedings of the Royal Society B* 271, 2509–2516 (2004)
21. Mitchinson, B., Pearson, M., Melhuish, C., Prescott, T.J.: A Model of Sensorimotor Coordination in the Rat Whisker System. In: Nolfi, S., Baldassarre, G., Calabretta, R., Hallam, J.C.T., Marocco, D., Meyer, J.-A., Miglino, O., Parisi, D. (eds.) *SAB 2006. LNCS (LNAI)*, vol. 4095, pp. 77–88. Springer, Heidelberg (2006)
22. Mitchinson, B., Martin, C.J., Grant, R.A., Prescott, T.J.: Feedback control in active sensing: rat exploratory whisking is modulated by environmental contact. *Proceedings of the Royal Society B* 274, 1035–1041 (2007)
23. Mitchinson, B., Arabzadeh, E., Diamond, M.E., Prescott, T.J.: Spike-timing in primary sensory neurons: a model of somatosensory transduction in the rat. *Biological Cybernetics* 98(3), 185–194 (2008)
24. N’Guyen, S., Pirim, P., Meyer, J.-A.: Tactile texture discrimination in the robot-rat “Psikharpax”. In: *BIOSIGNALS 2010 – Proceedings of 3rd Int. Conf. on Bio-Inspired Systems and Signal Processing*, pp. 74–81 (2010)
25. Prescott, T., Pearson, M., Mitchinson, B., Sullivan, J., Pipe, A.: Whisking with Robots - From Rat Vibrissae to Biomimetic Technology for Active Touch *IEEE Robotics and Automation Magazine* 16(3), pp. 42–50 (2009)
26. Rice, F.L., Mance, A., Munher, B.L.: A comparative light microscopic analysis of the sensory innervation of the mystacial pad. I. Innervation of vibrissal follicle-sinus complexes. *The Journal of Comparative Neurology* 252, 154–174 (1986)
27. Russell, R.A.: Closing the sensor-computer-robot control loop. *Robotics Age* 6, 15–20 (1984)
28. Schultz, A.E., Solomon, J.H., Peshkin, M.A., Hartmann, M.J.: Multifunctional Whisker Arrays for Distance Detection, Terrain Mapping, and Object Feature Extraction. In: *Proceedings of 2005 IEEE International Conference on Robotics & Automation*, pp. 2588–2593 (2005)
29. Seth, A.K., McKinstry, J.L., Edelman, G.M., Krichmar, J.L.: Texture discrimination by an autonomous mobile brain-based device with whiskers. In: *Proceedings of the IEEE International Conference on Robotics and Automation (ICRA 2004)*, San Diego, USA, pp. 4925–2930 (2004)
30. Stüttgen, M., Kullmann, S., Schwarz, C.: Responses of Rat Trigeminal Ganglion Neurons to Longitudinal Whisker Stimulation. *The Journal of Neurophysiology* 100, 1879–1884 (2008)
31. Voges, D., Carl, K., Klauer, G., Uhlig, R., Behn, C., Schilling, C., Witte, H.: Structural characterisation of the whisker system of the rat. *IEEE Sensors Journal* 12(2), 332–339 (2012)
32. Wineski, L.E.: Facial morphology and vibrissal movement in the golden hamster. *Journal of Morphology* 183, 199–217 (1985)
33. Yokoi, H., Fend, M., Pfeifer, R.: Development of a Whisker Sensor System and Simulation of Active Whisking for Agent Navigation. In: *Proceedings of 2004 IEEE/RSJ International Conference on Intelligent Robots and System*, pp. 607–612 (2004)

# Brain Signal Based Continuous Authentication: Functional NIRS Approach

Michitaro Shozawa, Ryota Yokote, Seira Hidano, Chi-Hua Wu,  
and Yasuo Matsuyama

Waseda University, Department of Computer Science and Engineering,  
Tokyo, 169-8555, Japan  
{michi,rrryokote,hidano,gigiwu,yasuo}@wiz.cs.waseda.ac.jp  
<http://www.wiz.cs.waseda.ac.jp>

**Abstract.** A new approach to continuous authentication is presented. The method is based on a combination of statistical decision machines for brain signals. Functional Near InfraRed Spectroscopy (NIRS) is used to measure brain oxyhemoglobin changes for each subject to be authenticated. Such biosignal authentication is expected to be a viable complementary method to traditional static security systems. The designed system is based on a discriminant function which utilizes the average weight vector of one-versus-one support vector machines for NIRS spectra. By computing a histogram of Mahalanobis distances, high separability among subjects was recognized. This experimental result guarantees the utility of brain NIRS signals to the continuous authentication.

**Keywords:** Continuous authentication, brain activities, NIRS, SVM.

## 1 Introduction

Continuous authentication is a method to identify uninterruptedly whether a subject is an eligible person or not. On the other hand, traditional authentication methods are static or one-time by using a password, a PIN (Personal Identification Number), an electro-magnetic card or a physical key. Such static authentication does not consider the weakness to impersonation at all. Therefore, a combination of both methods is expected to realize a better authentication system to the rapidly sophisticated and convolved ICT world.

For the continuous authentication, it is considered that biosignals can match well to its system configuration [1]. In this paper, we discuss a continuous authentication method which uses brain signals. This motivation is based on our observations on BMI (Brain Machine Interface) up to now [2], [3]:

- (1) NIRS patterns of brain signals were applicable to generate BMI commands.
- (2) The brain patterns were dependent on subjects.
- (3) This individuality appeared as temporal patterns.

In addition to such a technological applicability, we can find situations where the continuous authentication by brain signals are useful:

- (a) To a superuser of a computer system, an operating system periodically requests to type in a “sudo password.” This is quite cumbersome since the interval is usually set short. If the period is set too long, it undermines the system security because of the possibility of the impersonation. In such a situation, a continuous authentication combined with a crisp one-time method is ideal.
- (b) After an allowed usage of a special-purpose vehicle by a static authentication it becomes necessary to prevent impersonated operators. Periodic sudo-like authentication during the operation would lead to an accident in such a situation.
- (c) Driving a utility car also gives a situation where a continuous authentication is helpful. In addition to the impersonation, this case includes a detection of a driver’s abrupt change from a normal state. Daily use of a motor cycle shares this case since an operator’s helmet can be a wearable gear for the signal detector.

Since brain signal’s measurement devices have become more compact with less prices, BMI with continuous authentication will be more ubiquitous in our daily life. By understanding this trend, we selected a NIRS machine (Near InfraRed Spectroscopy). This system gives brain oxyhemoglobin changes which are less susceptible to ambient noises than EEGs (ElectroEncephaloGrams). Also, the total device is compact.

The organization of this paper is as follows. In Section 2, basic properties of the NIRS for BMI are explained. In Section 3, preprocessing and the main recognition method using a set of machine learning strategies are explained. In Section 4, experiments based on an averaged SVM weight vector from NIRS spectra are conducted. Results measured by Mahalanobis distances show promising separability of a subject from others. Section 5 gives concluding remarks to further sophistications of the system.

## 2 Near InfraRed Spectroscopy and Brain Activity Measurement

### 2.1 NIRS Machine

There are several types of NIRS machines for the brain signal measurement. For this paper’s continuous authentication, we used NIRO-200 [4]. Among possible measurements, oxyhemoglobin changes of subject’s local areas of brains will be used in later experiments. This is a set of time series expressed by  $\Delta O_2Hb \mu M$ .

Figure 1 illustrates a monitor of the NIRS machine (left bottom corner) as well as two subjects. An actual shape of a probe can be seen from the left subject. The right subject, who is under an actual task of typing, wears a head belt so that unnecessary optical noise is avoided. As can be observed from this figure, the restraint to the subject is moderate.

The NIRS sampling frequency is 6 Hz due to this machine’s capability. This speed is not very fast but it is appropriate to the continuous authentication.



**Fig. 1.** Brain NIRS measurement under typing

In contrast, EEG machines accept sampling of much higher frequencies. But, EEG is easily contaminated by ambient noise like fluorescent illumination and eye blinking.

## 2.2 Data Collection

By considering that the NIRS measurement is a class of optics, outdoor measurements under strong sunlight were avoided. Instead, subjects were seated in a room under fluorescent light (see Figure 1).

Methods to obtain training data and test data are explained by using numbers specified in Table 1.

**Table 1.** Numbers appearing in data collection

symbol	explanation	number
S	number of subjects	10
2K	number of measurements per subject	40
M	total number of NIRS time series	$M=2KS=400$
N	number of samples in a time series	60 (10 seconds)
L	number of reduced dimensions	$(N/2)/3=10$

Training and test data sets for the continuous authentication system to be designed were collected as follows.

**Subjects:**  $S = 10$  sound male and female students of twenties are subjects.

**Tasks:** Each subject operates typing a keyboard.

**Data set:** One sample data is a one-dimensional NIRS time series of 10 seconds out of a 60 second typing. Each subject gives  $2K = 40$  data sets. Half of them is used for the training in machine learning. The rest is used for performance testing. Thus, there are  $M = 2KS = 400$  time series of brain NIRS prepared.

Each data set has a label of a subject's name which is not used for the authentication per se.

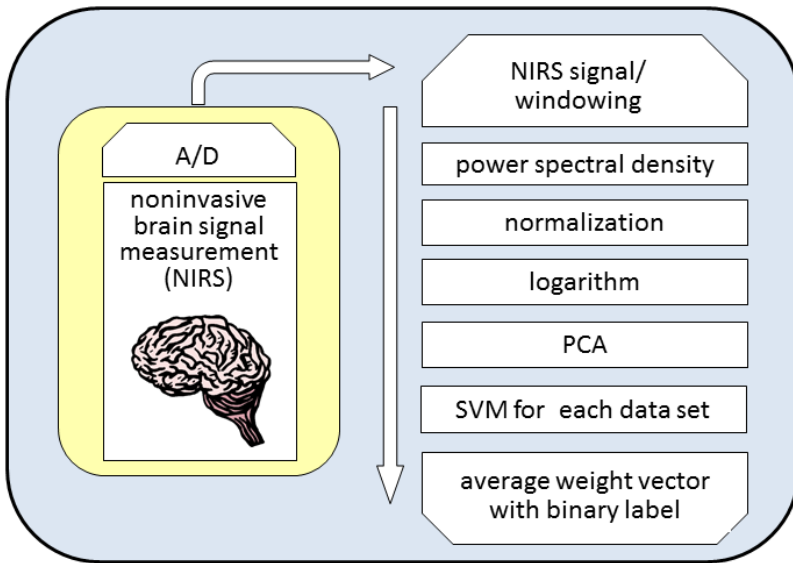
### 3 Recognizer: Learning Phase

The recognition in this paper indicates a decision that each data supplier is correctly identified to be eligible or not.

#### 3.1 Recognizer Design

NIRS data are time series. But, our preliminary observation indicated that a combination of low frequency periodicities, which are not affected by power supply frequencies (50 or 60 Hz), can convey each subject's individuality very well. Therefore, we set the signal essence to be a set of spectra.

Let  $\{x(n)\}_{n=0}^{N-1}$  be an NIRS time series from a subject. The number of samples is  $N = 60$  (1 channel, 6 fps, 10 seconds). Then, the total recognizer consists of the following 6 steps. Figure 2 illustrates a path from a brain NIRS signal to the end of the machine learning steps.



**Fig. 2.** Learning of the average SVM weight vector

Each step is explained as follows.

**Step 1:**  $M/2$  labeled sample time series for training are selected. One of such time series is denoted by  $\{x(n)\}_{n=0}^{N-1}$ . This set is multiplied by a Hamming window [5]. This modified time series is re-denoted by  $\{x(n)\}_{n=0}^{N-1}$ .



**Step 2:** The time series is transformed to  $\{X(m)\}_{m=0}^{N-1}$  by FFT (Fast Fourier Transformation). Actually,  $N/2$  FFT points contain non-overlapping information.

**Step 3:** Compute the logarithm of normalized power spectrum.

$$v_m = \log \frac{X(m)^2}{\sum_{i=0}^{N/2-1} X(i)^2}, \quad (m = 0, \dots, N/2 - 1). \quad (1)$$

Then, we regard this series as an  $N/2$ -dimensional vector  $\mathbf{v}$ . Since there are  $K = 20$  training data with the same subject label, this vector is re-denoted by  $\mathbf{v}_k$ , ( $k = 0, \dots, K - 1$ ).

**Step 4:** Using  $K$  sample vectors  $\{\mathbf{v}_k\}_{k=0}^{K-1}$ , the vector dimension of  $N/2 = 30$  is reduced to  $L = (N/2)/3 = 10$ . That is, the following Principal Component Analysis (PCA) [6] is conducted.

$$\mathbf{m} = \sum_{k=0}^{K-1} \mathbf{v}_k / K, \quad (2)$$

$$\mathbf{C} = \sum_{k=0}^{K-1} (\mathbf{v}_k - \mathbf{m})(\mathbf{v}_k - \mathbf{m})^T / K, \quad (3)$$

$$\mathbf{E}_L = \text{col}(\mathbf{e}_1, \dots, \mathbf{e}_l, \dots, \mathbf{e}_L), \quad (4)$$

$$\mathbf{V} = \mathbf{E}_L^T. \quad (5)$$

Here,  $\mathbf{E}_L$  is the orthonormal matrix of the first  $L$  eigenvectors of  $\mathbf{C}$  in its descending order. There is no need of sphering in Equation (5). By using these matrices, a set of reduced dimensional vectors is computed.

$$\mathbf{z}_k = \mathbf{V} \mathbf{v}_k, \quad (k = 0, \dots, K - 1). \quad (6)$$

The above PCA procedure was introduced to defend against over-fitting. Preliminary experiments supported this necessity.

**Step 5:** Given a training data set of  $\{\mathbf{z}_k\}_{k=0}^{K-1}$ , a weight vector  $\mathbf{w}$  of a support vector machine [7] is computed.

$$y_k = \mathbf{w}^T \mathbf{z}_k + b, \quad (k = 0, \dots, K - 1). \quad (7)$$

Here, each weight vector  $\mathbf{w}$  is computed against impersonated subjects.

**Step 6:** Re-denote each weight vector by  $\mathbf{w}_{sk}$  where  $s$  is an index for each subject. Then, the average weight vector is computed.

$$\bar{\mathbf{w}} = \sum_{s \in S} \sum_{k \in K} \mathbf{w}_{sk} / SK. \quad (8)$$

Note that the average of SVM biases is not needed in the discriminant analysis in experiments. Therefore, the bias is set to zero.

Before closing this subsection, we give a set of reasonings for the choices appearing in the above algorithm steps.

**Hamming window:**

This windowing is a standard method to reduce unnecessary spectral side lobes appearing in the case of the rectangular window. There was very little difference between the Hamming and other windows.

**Selection of  $L$ :**

Any integer of  $5 \leq L \leq 20$  was applicable, which reflects the following observations.

- (1) The maximum of  $L$  is 30 since the number of the spectral points is 60.
- (2) The number  $L$  needs to be reduced because there is a learning phase for the recognizer design.
- (3) The case of  $L = 5$  can contain more than 90% of the total power.
- (4) The choice of  $L$  may affect the shape of the separating hyperplane. But, the case of the SVM is less sensitive than those of the linear discriminant analysis and the ridge regression.

The choice of  $L = 10$  resulted from preliminary experiments guided by the above reasons.

### 3.2 Recognizer: Test Phase

After the learning phase, the learned vector  $\bar{\mathbf{w}}$  is applied to estimate the subject's matching.

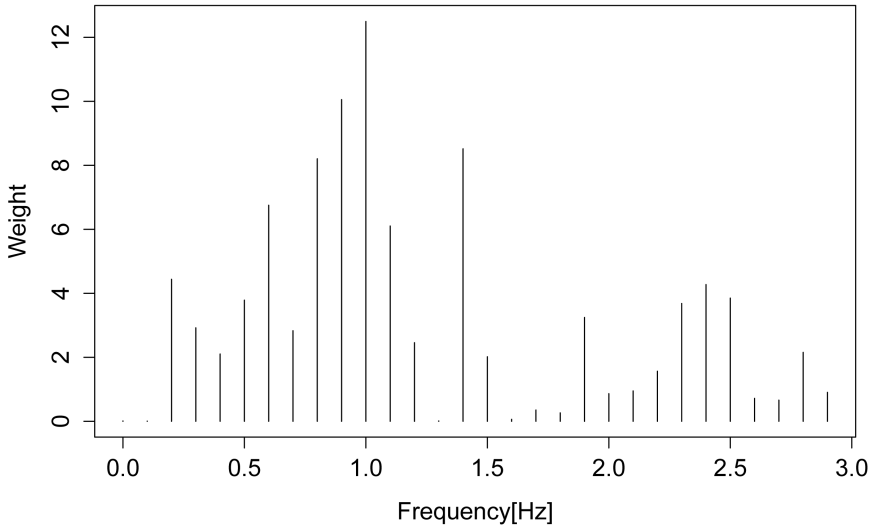
**Step 1:** A test data of unknown subject  $\{x(n)\}_{n=0}^{N-1}$  is given.

**Step 2:**  $\mathbf{V}^T \bar{\mathbf{w}}$  is computed. After discarding unnecessary components, a dichotomy decision based on the Mahalanobis distance to clusters is conducted.

## 4 Experiments for Performance Evaluation

### 4.1 Weight Vector

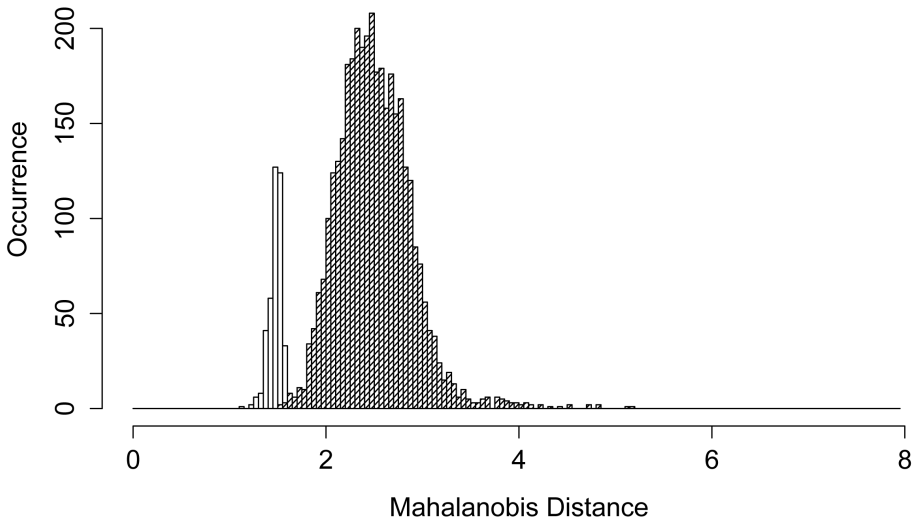
As was explained in Section 2.2,  $K = 20$  training data were given from each of  $S = 10$  subjects. Figure 3 illustrates the resulting weight vector  $\mathbf{V}^T \bar{\mathbf{w}}$ . In this figure, the horizontal axis stands for  $N/2 = 30$  column positions of the average weight vector which correspond to spectral frequencies. The vertical axis specifies each column's magnitude which does not have a unit. One can observe from this figure that the spectral range of  $0.5 \sim 1.5$  Hz is responsible for the separation ability among subjects.



**Fig. 3.** Learned average weight vector

## 4.2 Cross Validation

Since there are  $K = 20$  test data sets for each of  $S = 10$  subjects, we can measure the performance of the average vector  $\bar{\mathbf{w}}$  by using  $S$ -fold cross validation. The collection of margins which decides whether the subject is the right person or not



**Fig. 4.** Mahalanobis distance for identification

can give a histogram. We illustrate this result by computing the Mahalanobis distance. Figure 4 illustrates the result in view of a histogram. The horizontal axis stands for the Mahalanobis distance. The vertical axis is the total number of subjects reflecting the result of the authentication. There are two clusters in this figure. The left distribution with a sharp peak is the collection of results that the input data was identified to be a rightful subject's one. The right distribution which is more flat specifies cases that the measured data came from different subjects.

### 4.3 FNMR-FMR Rate

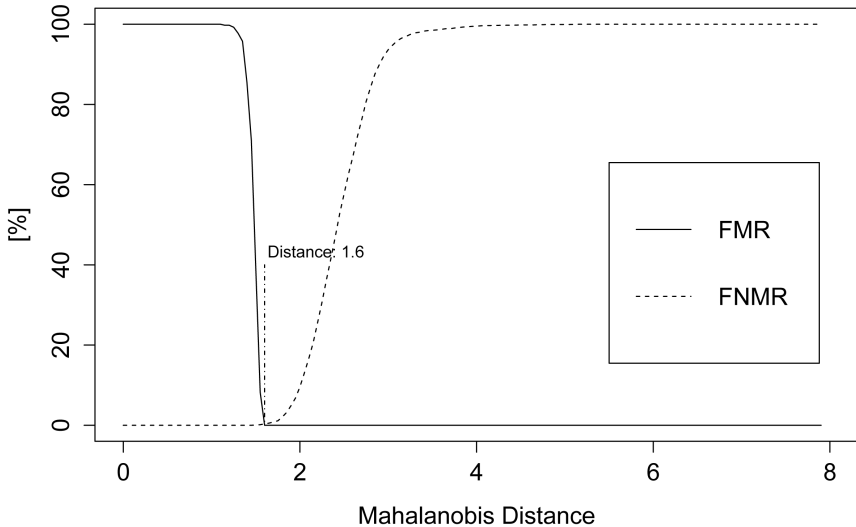
Figure 4 is quite appealing that the continuous authentication system of Figure 2 is effective. But, we need more confidence that this system deserves to be a practical one. This can be verified by a curve of the FNMR-FMR (False Non-Matching Rate versus False Matching Rate):

$$\text{FNMR}(t) = \int_t^{s_{max}} f_G(s)ds \tag{9}$$

$$\text{FMR}(t) = \int_{s_{min}}^t f_I(s)ds \tag{10}$$

Here,  $f_G(s)$  is the genuine distribution form right persons.  $f_I(s)$  the impostor distribution from illegal persons. The region of integration is

$$s_{min} \leq t \leq s_{max}. \tag{11}$$



**Fig. 5.** FNMR-FMR curve for performance identification

Figure 5 is the resulting FNMR-FMR curve by sliding a threshold  $t$  on the horizontal axis of Figure 4. The vertical line around the crossing of two curves specifies the EER (Equal Error Rate) which is the position that

$$\text{FNMR}(1.6) = \text{FMR}(1.6) = 0.0035 = 0.35\%. \quad (12)$$

This means that more than 99% of the continuous authentication was successful. By observing Figure 5 and Equation (12), one finds that this paper's system of Figure 2, which is based on the NIRS, outperforms by far than other brain signal based systems [8].

Before closing this section, it is necessary to explain the effect of tasks forced to subjects. Figures 4 and 5 were with a task of typing a keyboard. In addition to this experiment, we measured the authentication of no-task subjects. Its resulting histogram showed strong similarity to Figure 4. A little difference was that the two sharp peaks become a little bit more flat having longer tails. This means that the designed continuous authentication system by the NIRS signal is robust against "task-and-rest."

## 5 Concluding Remarks

There will be further sophistications on the system of Figure 2 so that the performance appeared in Figure 4 and Figure 5 can be improved more.

**More NIRS probes:** Increasing the number of probes is a promised performance improvement, provided the total system remains within a moderate price.

**Utilization of nonlinear kernels:** In this paper, we aimed at the lightest system. Therefore, methods of the machine learning and the test were all linear except for the logarithm on the power spectrum. Although the results described in Figures 4 and 5 were satisfactory as a baseline trial, an inclusion of nonlinear mechanisms can improve the performance. It is a use of nonlinear kernels in PCA and SVM.

**ICA after PCA:** In the designed system of this paper, a process of PCA was included. But, PCA coordinates are forced to be orthogonal. Because of this restriction, ICA (Independent Component Analysis) gives better non-orthogonal coordinates. For this type of systems, the coordinate comparison method, which overcomes the axis ordering indeterminacy of ICA [9], and the rapid computation method [10] will become essential.

**Dynamic Continuous Authentication:** The learned average weight vector of Figure 3 may be tuned up by including the data while a genuine subject is operating a target system.

**Attaining 100% Authentication:** In any authentication by human biosignals, FNMR and FMR of Equations (9) and(11) always exist. But, by allowing repeated recognition with an appropriate threshold, the final authentication rate can approach to 100% from this paper's EER of 99.65%.

## References

1. Traore, I., Ahmed, A.A.E. (eds.): *Continuous Authentication Using Biometrics: Date Models and Metrics*. IGI Global, Hershey (2012)
2. Matsuyama, Y., Matsushima, F., Nishida, Y., Hatakeyama, T., Ochiai, N., Aida, S.: Multimodal belief integration by HMM/SVM-embedded Bayesian network: Applications to ambulating PC operation by body motions and brain signals. In: Alippi, C., Polycarpou, M., Panayiotou, C., Ellinas, G. (eds.) *ICANN 2009, Part I. LNCS*, vol. 5768, pp. 767–778. Springer, Heidelberg (2009)
3. Matsuyama, Y., Noguchi, K., Hatakeyama, T., Ochiai, N., Hori, T.: Brain signal recognition and conversion towards symbiosis with ambulatory humanoids. In: Yao, Y., Sun, R., Poggio, T., Liu, J., Zhong, N., Huang, J. (eds.) *BI 2010. LNCS*, vol. 6334, pp. 101–111. Springer, Heidelberg (2010)
4. Hamamatsu Photonics: *NIRO 200 document*, Shizuoka, Japan (2003)
5. Oppenheim, A.V., Schafer, R.W.: *Digital Signal Processing*. Prentice-Hall, Upper Saddle River (1975)
6. Jolliffe, I.T.: *Principal Component Analysis*, 2nd edn. Springer, New York (2002)
7. Boser, B.E., Guyon, I.M., Vapnik, V.N.: A training algorithm for optimal margin classifiers. In: Haussler, D. (ed.) *5th Annual ACM Workshop on COLT*, pp. 144–155. ACM Press, Pittsburgh (1992)
8. Nakanishi, I., Baba, S., Li, S.: Evaluation of brain waves as biometrics for driver authentication using simplified driving simulator. In: *Proc. Int. Conf. on Biometrics and Kansei Engineering*, pp. 71–76 (2011)
9. Katsumata, N., Matsuyama, Y.: Database retrieval for similar images using ICA and PCA bases. *Engineering Applications of Artificial Intelligence* 18, 705–717 (2005)
10. Yokote, R., Matsuyama, Y.: Rapid algorithm for independent component analysis, *J. Signal and Information Processing* 3, 275–285 (2012)

# Risk Prediction of Femoral Neck Osteoporosis Using Machine Learning and Conventional Methods

Tae Keun Yoo<sup>1</sup>, Sung Kean Kim<sup>2,3</sup>, Ein Oh<sup>1</sup>, and Deok Won Kim<sup>2,3,\*</sup>

<sup>1</sup>Department of Medicine, Yonsei University College of Medicine  
fawoo2@yuhs.ac, bluerose1186@gmail.com

<sup>2</sup>Department of Medical Engineering, Yonsei University College of Medicine

<sup>3</sup>Graduate Program in Biomedical Engineering, Yonsei University, Seoul, Korea  
{sdm04sdm, kdw}@yuhs.ac

**Abstract.** Screening femoral neck osteoporosis is important to prevent fractures of the femoral neck. We developed machine learning models with the aim of more accurately identifying the risk of femoral neck osteoporosis in postmenopausal women and compared those to a conventional clinical decision tool, osteoporosis self-assessment tool (OST). We collected medical records based on the Korea National Health and Nutrition Surveys. The training set was used to construct models based on popular machine learning algorithms using various predictors associated with osteoporosis. The learning models were compared to OST. Support vector machines (SVM) had better performance than OST. Validation on the test set showed that SVM predicted femoral neck osteoporosis with an area under the curve of the receiver operating characteristic of 0.874, accuracy of 80.4%, sensitivity of 81.3%, and specificity of 80.5%. The machine learning methods may be effective tools for identifying postmenopausal women at high risk for osteoporosis.

**Keywords:** Screening, machine learning, risk assessment, clinical decision tool, support vector machine.

## 1 Introduction

Fracture due to osteoporosis is one of the major factors of disability and death in elderly people [15]. According to the World Health Organization (WHO) report, femoral neck osteoporosis was the best predictive factor for fracture risk and the most common fracture site was proximal femur [8]. Osteoporosis is common in postmenopausal women but is asymptomatic until a fracture occurs. WHO estimates that 30% of all postmenopausal women have osteoporosis, which is defined as bone mineral density (BMD) 2.5 standard deviations below the young healthy adult mean ( $T\text{-score} \leq -2.5$ ) [8]. Dual X-ray absorptionmetry (DEXA) of total hip, femoral neck, and lumbar spine is the most widely used tool for diagnosing osteoporosis. However,

---

\* This work was supported by the National Research Foundation of Korea (NRF) grant funded by the Korea government (MEST) (No. 2012R1A2A2A03045612).

mass screening using DEXA is not widely recommended for evaluating BMD as it is expensive and hazardous due to X-ray radiation [16]. Therefore, selecting patients for DEXA is an important task for cost-effective screening for osteoporosis.

A number of epidemiological studies have developed clinical decision tools for osteoporosis risk assessment to select postmenopausal women for the measurement of BMD. The purpose of these clinical decision tools is to help estimate the risk for osteoporosis, not to diagnose osteoporosis. The osteoporosis self-assessment tool (OST) is one of the clinical decision tools, which is a simple formula based on age and body weight [10]. Although OST uses only two factors to predict osteoporosis risk, it has been shown to have good sensitivity with an appropriate cutoff value [19]. However, the decision tool has the limitation of low accuracy for clinical use [18].

Machine learning is an area of artificial intelligence research which uses statistical methods for data classification. Several machine learning techniques have been applied in clinical settings to predict disease, and have shown higher accuracy for diagnosis than classical methods [7]. Support vector machines (SVM), random forests (RF), and artificial neural networks (ANN) have been widely used approaches in machine learning [7].

The SVM is based on mapping data to a higher dimensional space through a kernel function and choosing the maximum-margin hyper-plane that separates training data [3]. RF grows many classification trees built from a random subset of predictors and bootstrap samples [2]. ANN is comprised of several layers and connections which mimic biological neural networks to construct complex classifiers [6]. Logistic regression (LR) is another machine learning technique. LR is the gold standard method for analyzing binary medical data because it provides not only a predictive result, but also yields additional information such as a diagnostic odds ratio [1].

Several studies have shown that SVM, RF, and ANN could help predict low BMD using diet and lifestyle habit data [5,14,17,22]. Although these studies considered risk factors, they did not select informative variables that could contribute to osteoporosis. Moreover, previous studies had no objective comparisons of the performance of osteoporosis prediction developed by epidemiological data among the machine learning methods and clinical decision tools. Therefore, a structural design is needed for constructing the models along with a comparative study of various analytical methods for predicting osteoporosis risk.

In this study, we developed the prediction models for femoral neck osteoporosis using various machine learning methods including SVM, RF, ANN, and LR. We compared the performance of machine learning methods and OST using accuracy and area under the curve (AUC) of the receiver operating characteristic (ROC).

## 2 Materials and Methods

### 2.1 Data Source

We collected data from Korean postmenopausal women based on the Korea National Health and Nutrition Examination Surveys (KNHANES V-1) conducted in 2010. BMD was measured by DEXA using Hologic Discovery (Hologic Inc., Bedford,

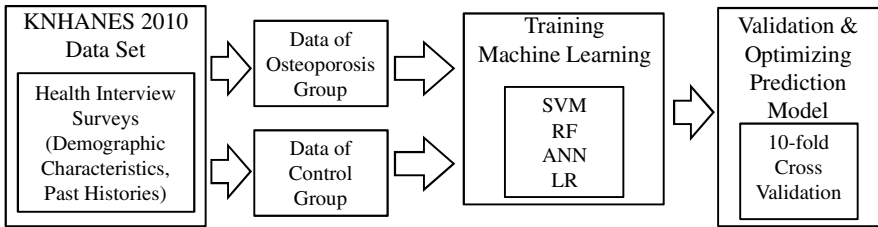


MA). Patients who were determined to have postmenopausal status were included in this study. We categorized the postmenopausal women into a control group and an osteoporotic group with low BMD ( $T\text{-score} \leq -2.5$ ) at femoral neck.

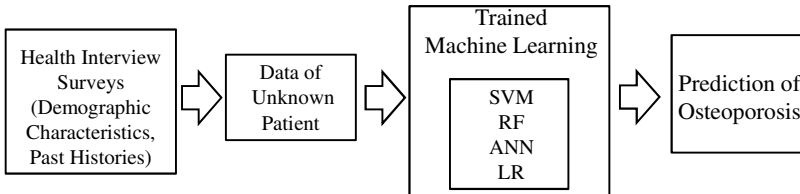
## 2.2 Data Analysis

The data were separated randomly into two independent data sets: training and test sets. The training set, comprised of 60% (1000 patients) of the entire dataset, was used to construct models based on SVM, RF, ANN, and LR. The clinical decision tool for screening osteoporosis, OST, was calculated according to its formula. The prediction models were internally validated using 10-fold cross validation [11]. We designed the 10-fold cross validation not only to assess performance, but also to optimize prediction models using machine learning techniques. We used 10-fold cross validation on the training set, and the performance was measured on the test set. The test set, comprised of 40% (674 patients) of the entire dataset, was used to assess ability to predict osteoporosis in postmenopausal women. Figure 1 shows the overview of trained machine learning models to predict osteoporosis.

### A. Machine Training



### B. State Classification



**Fig. 1.** Overview of models to predict osteoporosis. The flow of training machine learning models (A) and the flow of state classification with unknown data (B).

## 2.3 Model Selection and Validation

We used the 10-fold cross validation scheme to construct machine learning models. The purpose of the machine learning models was to predict osteoporosis risk using the health interview surveys concerning demographic characteristics and past histories listed in Table 1. Due to high dimensionality, variable selection was a necessary technique to make an effective prediction model and to improve prediction performance [20]. We adopted a feature selection method of wrapper subset evaluation for SVM,

RF, and ANN [4,7]. Although construction of the classifier has a high computational loading, wrapper approach can obtain the optimal feature subset by training and testing a specific machine learning model [20]. We determined the order of the variables with the embedded method of each machine learning method and decreased the number of variables to determine the best subset using backward elimination [20]. The remaining features that indicated the highest accuracy in 10-fold cross validation were the selected subset for prediction. For LR, we used the backward stepwise method for variable selection.

Data sets in this study were class-imbalanced because the control group contained significantly more samples than the osteoporotic group. Therefore, it was important to improve prediction models for the imbalanced data. To obtain the optimal result, we adopted a grid search in which a range of parameter values were tested using 10-fold cross validation strategy. We found the best classification model and employed its parameters for prediction. The optimal model of SVM was found using a Gaussian kernel function with a penalty parameter  $C$  of 100 and scaling factor  $\sigma$  of 30. In RF, the optimal number of trees was 100, and the number of predictors for each node was 3. The optimal ANN was set with 3 nodes of a hidden layer and learning rate of 0.1.

Due to the imbalanced data problem, prediction accuracy might not be a good criterion for assessing performance since the minor class has less influence on accuracy

**Table 1.** Characteristics of postmenopausal women

Variable*	Without osteoporosis at femoral neck (n = 1343)	With osteoporosis at femoral neck (n = 331)	P-value†
Age (years)	61.0±8.7	72.79±8.7	<0.001
Height (cm)	154.2±5.4	149.0±6.1	<0.001
Weight (kg)	58.2±8.3	51.4±8.5	<0.001
BMI (kg/m <sup>2</sup> )	24.4±3.2	23.1±3.2	<0.001
Waist circumference (cm)	82.5±9.1	80.6±9.6	<0.001
Pregnancy	4.4±2.2	5.0±2.5	<0.001
Duration of menopause (years)	12.4±9.3	24.8±10.2	<0.001
Duration of breast feeding (months)	53.0±46.5	87.3±58.3	<0.001
Estrogen therapy	256 (19.1)	17 (5.1)	<0.001
Hypertension	498 (37.1)	169 (51.1)	<0.001
Hyperlipidemia	195 (14.5)	32 (9.7)	0.011
Diabetes mellitus	142 (10.6)	40 (12.1)	0.242
Osteoarthritis	344 (24.5)	108 (32.6)	0.007
Rheumatoid arthritis	39 (2.9)	17 (5.1)	0.058
History of fracture	173 (12.9)	66 (19.9)	<0.001

\* Table values are given as mean ± standard deviation or number (%) unless otherwise indicated.

† P-values were obtained by t-test and chi-square test.

BMI: body mass index

than the major class [21]. Therefore, we evaluated diagnostic abilities including not only accuracy, but also AUC, sensitivity, and specificity.

$$\text{Sensitivity} = \text{TP} / (\text{TP} + \text{FN}) \tag{1}$$

$$\text{Specificity} = \text{TN} / (\text{TN} + \text{FP}) \tag{2}$$

$$\text{Accuracy} = (\text{TP} + \text{TN}) / (\text{TP} + \text{TN} + \text{FP} + \text{FN}) \tag{3}$$

- True positive (TP): No. of osteoporotic women correctly identified as osteoporosis.
- True negative (TN): No. of healthy women correctly identified as normal
- False positive (FP): No. of healthy women incorrectly identified as osteoporosis
- False negative (FN): No. of osteoporotic women incorrectly identified as normal

The AUC is known as a strong predictor of performance, especially with regard to imbalanced problems [13]. To compare the performance of models, we generated the ROC curves and selected cut-off points as the points on the ROC curve closest to the upper left corner. We used MATLAB 2010a (Inc., Natick, MA) for the analysis of machine learning and SPSS 18.0 (SPSS Inc., Chicago, IL) for LR and statistical analysis.

### 3 Results

Three hundred thirty-one (19.8%) of 1674 postmenopausal women had osteoporosis at femoral neck. Table 1 shows the characteristics of postmenopausal women categorized by the presence of osteoporosis. Table 2 summarizes the results of variable selection used in the machine learning methods. While OST selected only

**Table 2.** Variable selection in machine learning for osteoporosis risk of femoral neck

Variables	Machine learning methods			
	SVM	RF	ANN	LR
Age	O	O	O	O
Height	O	O	O	
Weight	O	O	O	O
Body mass index	O	O	O	
Waist circumference		O		
Pregnancy		O	O	
Duration of menopause	O	O	O	O
Duration of breast feeding	O	O	O	
Estrogen therapy	O			
Hypertension	O	O		
Hyperlipidemia	O	O		O
Diabetes mellitus	O	O	O	O
Osteoarthritis	O	O	O	O
Rheumatoid arthritis				
History of fracture			O	

SVM: support vector machines, RF: random forests, ANN: artificial neural networks, LR: logistic regression

two variables to obtain simplicity, the machine learning methods except LR selected more than 10 variables for better performance. In 10-fold cross validation, we found that more complex discriminating functions such as SVM and RF showed better performance than simple linear functions such as LR and OST.

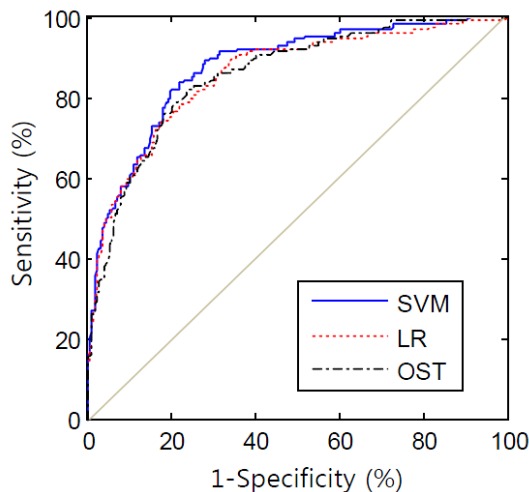
Additionally, to assess the performance of the models for predicting osteoporosis, we applied our methods to a test set composed of the independent data. Table 3 shows the results of classifying the test set for selecting women at risk of osteoporosis at femoral neck. As a result, the SVM model was the best discriminator between controls and women with osteoporosis.

SVM predicted osteoporosis risk with an AUC of 0.874, an accuracy of 80.4%, sensitivity of 81.3%, and specificity of 80.5%. Figure 2 shows the ROC curves of SVM, LR, and OST in predicting osteoporosis at femoral neck. Because SVM had the highest AUC among the machine learning methods, we compared their ROC curves. LR was also included for comparison with SVM and OST. The AUCs of SVM, LR and OST were 0.874, 0.855, and 0.855, respectively (Table 3).

**Table 3.** Diagnostic performance of osteoporosis risk assessment methods

	AUC	Accuracy (%)	Sensitivity (%)	Specificity (%)
SVM	0.874	80.4	81.3	80.5
RF	0.867	77.6	81.3	76.6
ANN	0.845	77.1	82.1	75.9
LR	0.855	76.6	82.9	75.0
OST	0.855	77.6	79.8	77.0

AUC: area under the curve, SVM: support vector machines, RF: random forests, ANN: artificial neural networks, LR: logistic regression, OST: osteoporosis self-assessment tool



**Fig. 2.** Receiver operating characteristic (ROC) curves of support vector machines (SVM), logistic regression (LR), and osteoporosis self-assessment tool (OST) in predicting osteoporosis risk at femoral neck

## 4 Discussion and Conclusion

We investigated a new approach based on machine learning techniques for predicting femoral neck osteoporosis risk in postmenopausal women using data from the KNHANES V-1. To our knowledge, we first performed comparisons of the performance of osteoporosis prediction between the machine learning and conventional methods using population-based epidemiological data. Among the machine learning and conventional methods, the SVM model discriminated more accurately between women with osteoporosis and control women. In other words, SVM was more effective in analyzing the epidemiological underlying patterns of osteoporosis compared with the other methods.

Our proposed SVM model included age, height, weight, body mass index, duration of menopause, duration of breast feeding, estrogen therapy, hypertension, hyperlipidemia, diabetes mellitus, and osteoarthritis as predictors (Table 2). Similar to earlier studies concerning prediction for osteoporosis [9,10], our results suggest that age and weight are most closely associated with the development of osteoporosis. However, our findings also demonstrated different factors involved in osteoporosis such as height, duration of menopause, duration of breast feeding, and presence of chronic diseases such as hypertension, hyperlipidemia, diabetes mellitus, and osteoarthritis. Our prediction model was able to consider these chronic diseases in combination using a SVM model characterized by nonlinearity and high dimension. Because the SVM model delicately handled a separating space composed of these factors in high dimension, it was possible to consider all factors for the improvement of sensitivity and specificity in predicting osteoporosis.

Women experience menopause at 50 years old on average [23]. Accordingly, when we regard the Korean women who are over 50 years old as potential menopausal population, menopausal women account for 31.8% of all women in Korea. The 31.8% corresponds to around 8.5 million [12]. Although SVM showed small improvement of 2.8% in accuracy compared to OST, the 2.8% corresponds to approximately 238,000, which is not small population.

In conclusion, the most important finding of this study is the identification of postmenopausal women at high risk of osteoporosis at femoral neck to increase the possibility of appropriate treatment before fracture occurs. Machine learning methods might contribute to the advancement of clinical decision tools and understanding about the risk factors for osteoporosis. Further studies should be targeted at constructing an extended prediction model for progressive osteoporosis through the collection of prospective data, and the simultaneous prediction of osteopenia and osteoporosis using multi-category classification.

## References

1. Bishop, C.M.: *Pattern Recognition and Machine Learning*. Springer, New York (2006)
2. Breiman, L.: Random forests. *Mach. Learn.* 45(1), 5–32 (2001)
3. Cortes, C., Vapnik, V.: Support-vector networks. *Mach. Learn.* 20(3), 273–297 (1995)

4. Dash, M., Liu, H.: Consistency-based search in feature selection. *Artif. Intell.* 151(1-2), 155–176 (2003)
5. De Cos Juez, F.J., Suárez-Suárez, M.A., Sánchez Lasheras, F., Murcia-Mazón, A.: Application of neural networks to the study of the influence of diet and lifestyle on the value of bone mineral density in post-menopausal women. *Math. Comput. Model.* 54(7-8), 1665–1670 (2011)
6. Dreiseitl, S., Ohno-Machado, L.: Logistic regression and artificial neural network classification models: a methodology review. *J. Biomed. Inform.* 35(5-6), 352–359 (2002)
7. Hsieh, C.H., Lu, R.H., Lee, N.H., Chiu, N.T., Hsu, M.H., Li, Y.C.: Novel solutions for an old disease: diagnosis of acute appendicitis with random forest, support vector machines, and artificial neural networks. *Surgery* 149(1), 87–93 (2011)
8. Kanis, J.A.: Assessment of fracture risk and its application to screening for postmenopausal osteoporosis: synopsis of a WHO report. *Osteoporos. Int.* 4(6), 368–381 (1994)
9. Khosla, S., Melton III, L.J.: Osteopenia. *N. Engl. J. Med.* 356, 2293–2300 (2007)
10. Koh, L.K., Sedrine, W.B., Torralba, T.P., Kung, A., Fujiwara, S., Chan, S.P., Huang, Q.R., Rajatanavin, R., Tsai, K.S., Park, H.M., Reginster, J.Y.: A simple tool to identify Asian women at increased risk of osteoporosis. *Osteoporos. Int.* 12(8), 699–705 (2001)
11. Kohavi, R.: A study of cross-validation and bootstrap for accuracy estimation and model selection. *IJCAI* 14, 1137–1145 (1995)
12. Korean National Statistical Office (2010), <http://www.kosis.kr>
13. Kotsiantis, S., Kanellopoulos, D., Pintelas, P.: Handling imbalanced datasets: A review. *GESTS Int. T. Comput. Sci. Eng.* 30, 25–36 (2006)
14. Lix, L.M., Yogendran, M.S., Leslie, W.D., Shaw, S.Y., Baumgartner, R., Bowman, C., Metge, C., Gumel, A., Hux, J., James, R.C.: Using multiple data features improved the validity of osteoporosis case ascertainment from administrative databases. *J. Clin. Epidemiol.* 61(12), 1250–1260 (2008)
15. Marshall, D., Johnell, O., Wedel, H.: Meta-analysis of how well measures of bone mineral density predict occurrence of osteoporotic fractures. *BMJ* 312(7041), 1254–1259 (1996)
16. Nayak, S., Roberts, M.S., Greenspan, S.L.: Cost-effectiveness of different screening strategies for osteoporosis in postmenopausal women. *Ann. Intern. Med.* 155(11), 751–761 (2011)
17. Ordóñez, C., Matías, J.M., de Cos Juez, J.F., García, P.J.: Machine learning techniques applied to the determination of osteoporosis incidence in post-menopausal women. *Math. Comput. Model.* 50(5-6), 673–679 (2009)
18. Raisz, L.G.: Screening for osteoporosis. *N. Engl. J. Med.* 353, 164–171 (2005)
19. Richey, F., Gourlay, M., Ross, P.D., Sen, S.S., Radican, L., Ceulaer, F.D., Sedrine, W.B., Ethgen, O., Bruyere, O., Reginster, J.Y.: Validation and comparative evaluation of the osteoporosis self-assessment tool (OST) in a Caucasian population from Belgium. *QJM* 97(1), 39–46 (2004)
20. Saeys, Y., Inza, I., Larrañaga, P.: A review of feature selection techniques in bioinformatics. *Bioinformatics* 23(19), 2507–2517 (2007)
21. Sun, Y., Kamel, M.S., Wong, A.K.C., Wang, Y.: Cost-sensitive boosting for classification of imbalanced data. *Pattern Recogn.* 40(12), 3358–3378 (2007)
22. Walid, M., Ahmad, S., Fadi, C., Dima, R.: Intelligent predictive osteoporosis system. *Int. J. Comput. Appl.* 32, 28–30 (2011)
23. Yeun, E.J.: A study on the health promoting lifestyle practices of middle-aged women in Korea. *J. Korean Soc. Health Educ. Promo.* 17(1), 41–59 (2000)

# Out of Core Computation of HSPs for Large Biological Sequences

Andrés Rodríguez Moreno, Óscar Torreño Tirado, and Oswaldo Trelles Salazar

Dept. of Computer Architecture, University of Málaga, Spain,  
Campus de Teatinos, 29071  
ortrelles@uma.es

**Abstract.** Bioinformatics is facing a post-genomic era characterized by the release of large amounts of data boosted by the scientific revolution in high throughput technologies. This document presents an approach to deal with such a massive data processing problem in a paradigmatic application from which interesting lessons can be learned. The design of an out-of-core and modular implementation of traditional High-scoring Segment Pairs (HSPs) applications removes the limits of genome size and performs the work in linear time and with controlled computational requirements. Regardless of the expected huge I/O operations, the full system performs faster than state-of-the-art references providing additional advantages such as monitoring and interactive analysis, the exploitation of important intermediate results, and giving the specific nature of the modules, instead of monolithic software, enabling the plugging of external components to squeeze results.

**Keywords:** HSPs, out-of-core, comparative genomics.

## 1 Introduction

New, massively parallel data acquisition technologies in the life sciences are changing bottlenecks in biology and biomedical research from data acquisition to data interpretation. This is leading to a shift from the theory-driven experiments of the last fifty years back to traditional observation-driven theory building, but with orders of magnitude more data to analyze. The adaptation and creation of software is needed to enable bioinformatics' tools to deal with this massively growing rate of data. Only one example: just on February 2012, a miniaturized device -the size of a USB memory stick- has been announced as designed to make DNA sequencing universally accessible (costs below \$900 using Oxford Nanopore Technologies [1]). Still scientists are racing to develop methods that are fast and cheap enough to allow individual to get his or her genome sequenced, thus truly ushering in the era of personalized medicine based on genetics. But not only is the human genome of interest. At present, hundreds of different organisms, in all kingdoms, have been sequenced and thousands of on-going projects have put Comparative Genomics in the spotlight to provide the methods to study the relationships among this flood of data.

From a different perspective, huge-data handling problems are fundamental as the increasing speed of computers, storage and networks are not keeping up with the increasing speed of data generation. This issue has two dimensions. First, there is the fundamental dilemma of analysis procedures that show quadratic calculation time relative to input size (e.g. 'all versus all' computational strategies; the large usage of statistical tools such as maximum likelihood, Bayesian analysis, etc). Second, most software for computational biology is designed for single-CPU computers (i.e. dotplot [2]). Since conventional analysis software is used for much larger data than originally designed for, the limits of computing, as well as those of memory capacity, are being reached. This fact produces a pressing need to both retrofit trusted software and also create new software.

A dotplot is the traditional and simple way to compare biological sequences. Basically, a dotplot is a visual representation of the similarities shared by two sequences, one arranged horizontally and the other vertically. The dotplot is built up by comparing each residue in the horizontal sequence against each residue in the vertical sequence. A dot is placed in the intersection coordinates when both residues are identical. Thus, regions of the sequences sharing substantial areas of similarity will be revealed by diagonal stretches. Sliding windows combined with stringency thresholds are the standard method to remove noise produced by random matches.

Dotplots were designed to deal with genes and proteins, therefore the solution space of the original implementation of dotplot becomes impractical for processing with single CPUs when working with larger datasets, such as the mega-sized chromosomes of higher eukaryotes (for example, a 30x30MB comparison could take 25 days on a single CPU). Enhanced solutions can reduce the computational search space, normally to a linear complexity  $O(N+M)$  but is still unaffordable for massive exercises.

Many extensions of the basic dotplot methodology have been proposed. These include interactive usage [3, 4], statistical filtering and the use of other symbols than dots to discriminate among matches of different similarity [5], the use of biophysical features of the residues for scoring [6], and the simultaneous study of several dotplots as a way to perform some forms of multiple alignments [7]. Concerning how this information is presented to the user, strong improvements have been made from the early simple monochrome representations with virtually no possibility of performing an interactive analysis. Color coding was introduced to represent the information [8], and a simple window based zooming and panning approach was proposed in [9]. Dotter [10] introduces a 'Greyramp tool' to interactively adjust the score cut-offs for displaying dots, so the separation between noise and signal can be fine-tuned interactively, and in our previous work [11] we proposed the use of image processing filters in the framework of mathematical morphology to enforce the signal/noise ratio and extend the notion of sequences comparison to structural analysis. In the web domain [12] offers a full menu and mouse-driven application, and [13] presents a web-server application to align genomic sequences.

Another way for representing the similarities between biological sequences is to use HSPs (High-scoring Segment Pairs), sub-segments from two sequences that share a high level of similarity. There are some reference programs for computing HSPs



(i.e. similarity between biological sequences) such as Blast [14] and Megablast [15] for large sequences, also MUMmer application [16] uses HSPs for fast sequence alignment, and there are several other programs that somehow perform HSPs calculations such as Gepard [17] for dotplot visualization. To reduce the computational space and accelerate data processing most of the mentioned programs use some kind of pre-processing step. In this pre-processing step, when genomes replaced sequences as input, the limitations of HSPs calculation become evident: the computational complexity and the memory consumption of the algorithms, which rises with the product of the length of the sequences and the window-size becomes a problem due to the algorithm works in an in-core fashion. Of equal importance, the interactive analysis and visual exploration of the solution space would require handling the dotplot matrix in memory, which also rise with the second power of the average sequence length.

In our case, the pre-processing step follows a similar approach but working in an out-of-core fashion, to avoid memory consumption limitations. The approach consists on a Blast-like strategy also implemented in Megablast and more recently in Gepard application with important time reduction, allowing the comparison of human chromosome 1 (more than 300Mbp) in approximately one hour. Concretely, this step produces a dictionary of words or k-mers that contains a list of occurrences of each k-mer in the sequence. To perform the calculation of the dictionary we use a sliding window of length  $k$  that runs along the sequence one nucleotide each time. All the components in the window must be in the 'ACGT' alphabet, if not the word will be discarded. Then k-mers included in the dictionary are used as prefixes for the rapid identification of matching words, the position of the word in each sequence is used as seed point (i.e. coordinate) from where to try to extend the local sequence alignment.

In the way to accelerate computation the organization of the data corresponding to k-mers' position is usually worked out in-core, as we have said before. This advantage turns into a disadvantage since for large sequences an appropriate value of  $k$  is needed (the size of the word or k-mer). Currently, typical values are around 10 which lead to 1,048,576 putative entries. Although array-based memory is manageable in terms of main memory, the number of repeats for  $k=10$  can be high for chromosomal sequences. With this the number of putative hits or seed points becomes high and therefore the computation unaffordable. On the other hand, using a larger value for  $k$  to reduce the number of repetitions would force the limits of main memory. For instance, with  $k=20$ , more than 1TB of possible entries could be expected, it does not require the complete  $4^{32}$  address space of the naive implementation.

The exact number of k-mers in a sequence of length  $L$  is  $L-k+1$  which can be managed in main memory, but requires more complex data management structures and procedures (i.e. prefix trees) that could slowing down the complete process. To overcome this problem it is possible to work out-of-core, i.e. using the hard disk as temporary storage. The slower access time of storage devices is by far compensated in several ways: (a) the size is unbound of  $k$  which will reduce the number of repetitions and the computational space; (b) it is able to recover –without additional processing time- all  $k'$ -mers for  $k' < k$ , thus keeping all the sensitiveness for the identification of true signals; (c) the already computed dictionaries of words remain available for subsequent processing when comparing against other genomes; (d) combining the

reduction of the computational space with a modular implementation allows fine-grained monitoring of execution, and the storage of intermediate results on disk allows the development of simple additional modules for exhaustive analysis, and finally; (e) the elapsed time is short enough even to allow an interactive analysis.

This document reports the design of software modules that enable comparative genomics. Our development is illustrated with the implementation of HSPs calculation at genome scale with linear time and controlled memory requirements, trying to tackle the problem in memory consumption faced by the state of the art reference programs. Several tests will be presented later on to demonstrate the utility of the strategy. Detailed material (including more tests) and open source code are available to reproduce results (<http://www.bitlab-es.com/dotplot>).

## 2 Methods

We have addressed the out-of-core implementation from two complementary perspectives. On the one hand we have designed, developed and implemented an I/O library (SFILE) to reduce the number of access to disk storage at the same time keeping controlled memory demands. This library uses a general buffering strategy plus pre-fetching that perform well in most sequence analysis applications. On the other hand we have reformulated the internals of the application to overcome the memory limitation of the original codes.

In short, the SFILE library is designed to provide buffered management of large sequences. The library implements the classical methods available in files systems, such as open, close, read, write, seek, etc. From the programmer's perspective the library hides the complexity of keeping partial sequences loaded into memory. The program can point or make reference to any position of a given sequence and the software provides efficient access to such piece of data. The library is built on top of the library function layer of the operating system and uses the FILE module of C language to map the functionality. Detailed information about the SFILE API is provided as Supplementary Material.

At the same time, the optimization of the HSPs calculation has been addressed in a twofold strategy: on one side we focus on the reduction of the computational space, which is application specific, and on the other side on the modularization of the process which is a classic engineering concept: one tool for one specific task. Following these criteria we identify the following main sections in the design:

**Computational Space Reduction.** As mentioned above, to reduce the computational space we have followed similar strategies as state-of-the-art solutions, based on the rapid identification of k-mers present in both sequences, to be used as seed points to extend local fragments.

The main contribution to deal with this problem is to work out-of-core, i.e. using the hard disk as temporary storage and the SFILE library. The slower access time of storage devices is by far compensated in several ways:

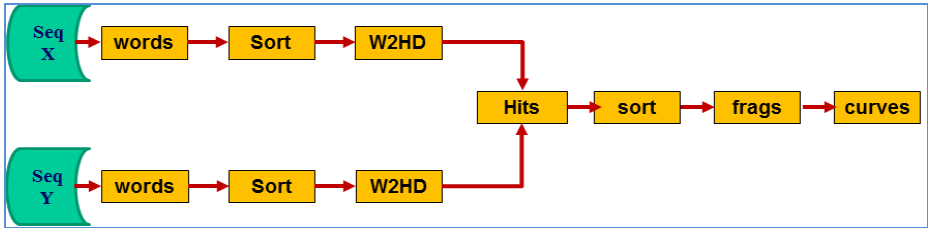
1. It is possible to extend the prefix length to any arbitrary value (e.g. by default  $k=32$ ), which, despite producing the same number of words (in practical terms  $L-k+1$ , with  $L \gg k$ ), does not mean any loss of sensitivity, since a collection of prefixes of length  $K$  contains all the prefixes with  $k < K$ .
2. Greater  $k$  values produce a lower number of words sharing the same prefix, thus the number of potential seed points to extend the alignment is much shorter.
3. By using proximity criterion is it possible to reduce the number of seed-points yet further
4. A pre-visualization of seed-points can help in selecting the most appropriate  $k$  value

**The Modular Organization.** The second aspect to enhance the implementation is based on the modular organization of the full process, removing dependencies and repetitive actions when processing collections of data sets. Thus, the full application is aimed for using on multiple data analysis, allowing parameter sensitivity studies as well as all-against-all comparisons of a collection of genomes. With these ideas in mind we organize the process in a workflow that includes the next steps (see figure 1):

1. Create the dictionaries for each sequence or genome. This section involves the following steps:
  - (a) Production of words, compressed storage on disk (4 bases per byte) including word position.
  - (b) Sorting by word.
  - (c) Creating a hash table on disk. This table has two components: the hash header (the word, the starting position of the word within an array with the list of words-repeats positions) and the array of positions of words in the sequence.
2. Determine the hits that will be used as seed points for fragments. This involves the following steps:
  - (a) Producing all the combinations (positions) of the same word in the two sequences
  - (b) Sorting the hits by diagonal and offset
  - (c) Optional reduction of the number of hits by proximity.
3. Local fragments detection
4. Visualization and further data analysis.

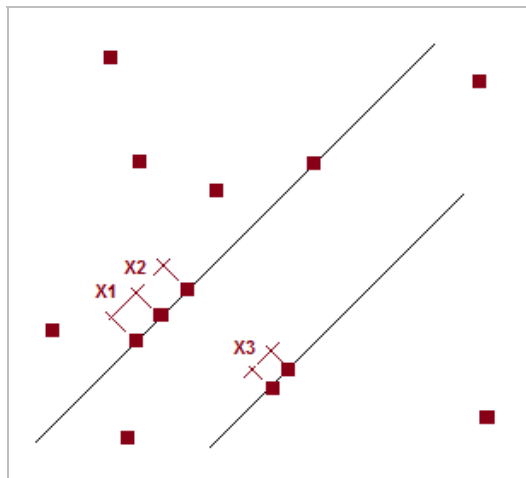
In the first section of the workflow, a collection of  $k$ -mers ( $k=32$  by default) including their position in the sequence, is stored on disk, avoiding low complexity regions. The words are then ordered according to their content. It is worth observing that this intermediate result can be post processed to obtain the frequency of  $k$ -mers for any value of  $k$ . The ‘word to hash in disk’ (w2hd) program produces a hash table that corresponds to an “inverted index” in which the position of each word in the sequence

is recorded. It is most important to observe that this dictionary, when stored in the disk device does not need to be obtained any more, and it is available for later usage when compared against any other sequence. This section must be executed once for each sequence involved in the specific study.



**Fig. 1.** Workflow for HSPs calculation and dotplot representation. The two branches on the left represent the dictionary computation, followed by its detection and finally the fragment extension step.

The second section corresponds to the identification of seed points. If a word  $w_i$  appears  $n$  times in the first sequence at positions  $p_j$  ( $j=1 \dots n$ ); and the same word  $w_i$  appears  $m$  times in the second sequence in positions  $p_k$  ( $k=1 \dots m$ ), a hit will occur in all  $(p_j, p_k)$  coordinates (see figure 2). For each hit, a diagonal number can be defined as  $d=(p_j - p_k)$ . All these “hits” are putative starts of local alignments (with  $k$  identities at the beginning). Using a proximity approach you can reduce the number of hits, by which all those hits on the same diagonal and at a predefined distance are grouped as a big-hit (see figure 2). Later filters can select those seeds for processing that fulfill a given big-hit size). Ordering the hits by diagonal and offset and joining together closest hits does this.



**Fig. 2.** The showed points are the hits produced into the  $(p_j, p_k)$  coordinates. X1, X2, and X3 represent distances between hits of the same diagonal of less than a given threshold  $D$ . The involved hits will be joined into a big hit, reducing considerably the computational space.

Finally, a local fragment (un-gapped similarity) is defined as a sub-string matching sequence whose positive accumulated score cannot be increased by extending the fragment at either of its extremes. A fragment starts in a cell with a positive score (the seed points identified in the previous section, using a scoring-matrix system), and eventually grows an accumulating score, until the overall fragment score becomes negative or the matrix diagonal ends. The fragment boundaries are the start cell and the cell with maximum accumulated score. The algorithm continues searching in the next cell or in the next diagonal matrix for the next fragment. When using k-mers as seed points the algorithm also extend the fragment in the reverse direction.

The main output from the whole process is the set of HSPs identified, among other values, by the starting coordinates in sequences, length, score and similarity levels. This info can easily be used to draw the full dotplot or to be used as input for any visualization process, or to produce the list of aligned fragments, etc. We provide the representation as a PNG image and text-based fragments.

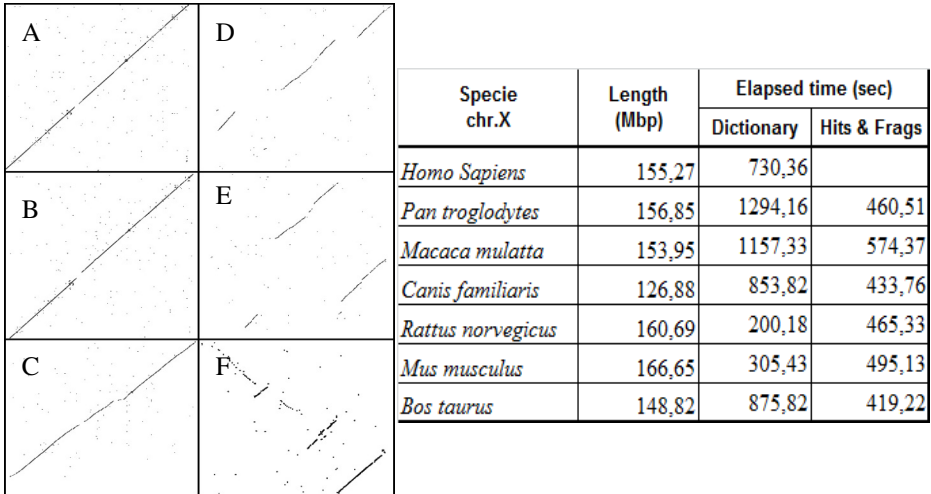
## 3 Results

### 3.1 Benchmarking

The benchmarks reported in this document have been performed in the SGI Altix UltraViolet 1000 system, an extra-large symmetric multiprocessor with up to 2048 computational cores along with 16 TB of RAM, available at the Scientific Computing facilities of the Johannes Kepler University (JKU) in Linz, Austria. All results shown in this section correspond to sequential -single core- execution of each module. Exhaustive data using other diverse collections of data are available as supplementary material (<http://www.bitlab-es.com/dotplot>).

The exercise shown at figure 3 describes the dotplot comparison of human (*Homo sapiens*) chromosome X against the same chromosome in several other species. Figure displays the dotplots for *Pan troglodytes*, *Macaca mulatta*, *Canis familiaris*, *Mus musculus*, *Rattus norvegicus*, and *Bos taurus*. In all cases, we take into account the execution time of each module, since this is the worst situation. Obviously, in the case we have compared human chromosome X against chimpanzee, macaque, rat, mouse, etc. it was only necessary to obtain the human-dictionary once, but to facilitate comparison we include this time in all the tables.

Rather than the relatively short time needed to complete an experiment, is important to realize that this tool allows performing exhaustive studies with affordable resources. This opens a window for exhaustive comparative genome analysis, such as detection of main evolutionary events, new models that can be evaluated experimentally, for inter-species evolutionary distance, the composition of the k-mers dictionaries for each species, etc. Detailed information about these experiments (including several other species) is available in the supplementary material (<http://www.bitlab-es.com/dotplot>).



**Fig. 3.** Above on the left, the HSPs found, represented by dotplots of human chromosome X against (from top-bottom and left to right) chimpanzee (A), macaque (B), dog (C), rat (D), mouse (E) and domestic cow (F). The table on the right describes the sequence size and the elapsed time needed to compute the dotplot in the two main steps: building the dictionaries and computing hits (seed points) and un-gapped local fragments.

### 3.2 Discussion

The proposed implementation compares quite well with the reference software for short sequences. It is much faster than Dotter and it is as fast as Gepard even when it pre-computes the dictionaries. Gepard reports 40 seconds for 5Mbp genomes [17], compared with 20 seconds in our implementation on an equivalent hardware platform. For longer sequences, however, our method notoriously outperforms existing ones. We need -on average- no more than ten minutes to compare chromosome 1 from different species (all with more than 120 Mbp), this time results are widely better than the estimated 382 years needed by Dotter (estimated from results in [10]) or the approximate 1 hour needed by Gepard [17].

But the strength of our approach is that it actually works without the limitation of available main memory. We have downloaded latest versions of both Gepard and Dotter applications and tried to run a test comparison of human chromosome X (155 Mbp) against chimpanzee (156Mbp) without success. Both programs soon abort execution because of running out of memory. The test has been carried on a computer with eight gigabytes of available memory and an Intel Xeon E5405 @ 2GHz as main processor. In the same computer, our implementation deals with the process out-of-core and achieves the task in less than fifteen minutes (using a single core): ten minutes for building the dictionaries (this step result is reusable for next comparisons) and less than five minutes for computing hits (seed points) and un-gapped local fragments.

The implementation shows really good performance with some points to analyze. Traditionally, bioinformatics programs, as well as any computational development, try to perform their work with data in the main memory as efficient as possible. However, the rate of growth of the volume of data is far greater than that of RAM memory, even nowadays when -for some special infrastructures- the amount of available memory could be in the range of some TB. The main reason for this coding style lies in the access-time gap between main and external (i.e. hard disks) memory, which is about 6 orders of magnitude.

However, nowadays there is no way to keep all data in core and therefore there is a pressing need to re-design trusted software and also creates new software strategies. It is valid to exploit the particular flow of data of each specific application, but general software should be the programmer's final target. In this sense, in this document we explain how both approaches have been combined to better exploit the advantages of each one. In this out-of-core implementation the following advantages can be mentioned:

1. It removes any dependence of  $k$ , enabling small prefixes for short sequences and bigger values of  $k$  for chromosomes. We identify as 32 the maximum value of  $k$  that results of interest in this type of applications (identical words). Greater values of  $k$  do not produce enough seed points to identify all the signals even with 100Mbp datasets.
2. Working in disk allows keeping the dictionaries of words computed in previous invocations of the program in the secondary storage, reducing the processing demand in multiple comparative studies.
3. The modular implementation stores the intermediate results on disk, which allows developing small and simple software components for exhaustive analysis of intermediate data such as words frequencies, words structure, comparative studies, extreme frequencies analysis, annotation for functional genomics, visualization tools, etc.
4. Several additional features are incorporated into the algorithm such as different scoring schemes to allow the detection of remote homologous regions, or  $k$ -mer size to fine tuning sensitivity, etc.
5. The elapsed time is short enough even to allow for interactive analysis.

## 4 Conclusions

This document presents (a) a new software library to deal with long sequences in out-of-core fashion; and (b) a HSPs calculation and dotplot implementation based on an enhanced reduction of the computational space combined with a modular implementation that -apart from an encouraging run time- presents several remarkable advantages, as presented in the Discussion section (independence of  $K$  value, reduction of complexity, fast and accurate performance, etc.).

Additionally, new, simple and small software components can be easily added to this framework enabling the extension of capabilities in the spirit of software developer collaboration. The incorporation of new modules does not represent any new

re-coding of the current architecture. Some examples currently available are: frequency of k-mers, over and underrepresented set of words, pre-visualization tools for monitoring, full composition of local un-gapped fragments including their alignment, etc.

A full battery of benchmark exercises demonstrates the effectiveness of the implementation, even in a single-core machine. Ongoing work to use our cloud and multi-processor developments obtains linear speedups. This software aims to facilitate a massive comparison of full genomes, and to carry out more complex evolutionary studies, helping to identify evolution events such as inversions, translocations, gene duplication and ending with providing new insight and experimental data to contrast the evolutionary models of populations and species.

**Acknowledgements.** This work has been partially supported by the Spanish National Institute of Bioinformatics (INB-ISCI), the RIRAAF network (RD12/0013/0013), Mr.SymBioMath (EU grant agreement number 324554) and Proyecto Motriz de Excelencia de la Junta de Andalucía (P10-TIC-6108). We would like to thank the JKU, the Institute for Bioinformatics team for fruitful discussions and hosting Prof. Trelles as a visiting professor; and Johann Messner, sysman of the UV1000-JKU for his invaluable support.

## References

1. Oxford Nanopore Technologies, <http://www.nanoporetech.com/news/press-releases/view/39>
2. Gibbs, A.J., McIntyre, G.A.: The diagram, a method for comparing se-quences, Its use with aminoacid and nucleotide sequences. *Eur. J. Biochem.* 16, 1–11 (1970)
3. Maizel, J.V., Lenk, R.P.: Enhanced Graphic Matrix Analysis of Nucleic Acid and Protein Sequences. In: *Proc. of the National Academy of Science, USA* 78, vol. 12, pp. 7665–7669. *Genetics* (1981)
4. Staden, R.: An interactive graphics program for comparing and aligning nucleic acid and amino acid sequences. *Nucleic Acids Research* 10(9), 2951–2961 (1982)
5. Pustell, J., Kafatos, F.C.: A convenient and adaptable package of computer programs for DNA and protein sequence management, analysis and homology determination. *Nucl. Acids Res.* 12, 643–655 (1984)
6. Argos, P.: A sensitive procedure to compare aminoacids. *J. Mol. Biol.* 193, 385–396 (1987)
7. Vingron, Argos: Motif recognition and alignment for many sequences by com-parison of dot-matrices. *J. Mol. Biology* 218(1) (1991)
8. Reisner, H., Bucholtz: The use of various properties of amino acids in color and monochrome dot-matrix analyses for protein homologies. *Bioinformatics* 4(3), 395–402 (1988)
9. Nedde, D.N., Ward, M.O.: Visualizing relationships between nucleic acid sequences using correlation images. *CABIOS* 9(3), 331–335 (1993)
10. Sonnhammer, E.L.L., Durbin, R.: A dot-matrix program with dynamic thres-hold control suited for genomic DNA and protein sequence analysis. *Gene.* 167, GC1–GC10 (1995)
11. Trelles, O., et al.: An Image processing approach to DotPlots: An X window-based program for interactive analysis of dotplots derived from sequence and structural data. *CABIOS* 11(3), 301–308 (1995)



12. Junier, T., Pagni, M.: DotLet: Diagonal plots in a web-browser. *Bioinformatics* 16(2), 178–179 (2000)
13. Schwartz, S.: PipMaker: a web server for aligning two genomic DNA sequences. *Genome Res.* 10, 577–586 (2000)
14. Altschul, S.F., Gish, W., Miller, W., Myers, E.W., Lipman, D.J.: Basic local alignment search tool. *J. Mol. Biol.* 215, 403–410 (1990)
15. Zhang, Z., et al.: A greedy algorithm for aligning DNA sequences. *J. Comp. Biol.* 7, 203–214 (2000)
16. Kurtz et al.: Versatile and open software for comparing large genomes. *Genome Biol.*, 5, R12 (2004)
17. Krumsiek, J., et al.: Gepard: a rapid and sensitive tool for creating dotplots on genome scale. *Bioinformatics* 23(8), 1026–1028 (2007), doi:10.1093/bioinformatics

# Bio-Cirrus: A Framework for Running Legacy Bioinformatics Applications with Cloud Computing Resources

Tor Johan Mikael Karlsson<sup>1</sup>, Óscar Torreño Tirado<sup>1</sup>, Daniel Ramet<sup>1</sup>,  
Juan Lago<sup>4</sup>, Juan Falgueras Cano<sup>2</sup>, Noura Chelbat<sup>3</sup>, and Oswaldo Trelles<sup>1</sup>

<sup>1</sup> Department of Computer Architecture, University of Málaga,  
Campus de Teatinos, 29071 Málaga, Spain

<sup>2</sup> Department of Languages and Computer Sciences, University of Málaga,  
Campus de Teatinos, 29071 Málaga, Spain

<sup>3</sup> Institute for Bioinformatics, Johannes Kepler University, Linz-Austria

<sup>4</sup> Fundacion Iavante, Consejería de Salud, Junta de Andalucía, Spain

**Abstract.** Technological advances in biological and biomedical data acquisition are creating mountains of data. Existing legacy applications are unable to process this data without using new strategies. However, some workloads in bioinformatics are easily parallelized by splitting the data, running legacy applications in parallel and then join the partial results into one final result. In this paper, we present Bio-Cirrus, a software package which facilitates this process. Our software consists of a user-friendly client (jORCA) for accessing Web Services and enacting workflows, and a module (Mr. Cirrus) for processing the data with a map/reduce style approach. Bio-Cirrus binaries and documentation are freely available at <http://www.bitlab-es.com/cloud> under the Creative Commons Attribution-No Derivative Works 2.5 Spain License and its source code is available under request. (GPL v3 license).

## 1 Introduction

Bioinformatics is currently facing a post-genomic era characterized by the release of large amounts of data due to technical breakthroughs in high-throughput technologies [16]. Such data offer biologists unprecedented opportunities to increase the understanding of the functions and dynamics of individual cells on the one end and entire populations on the other, for example meta-genomic studies of all the micro-organisms' genomes of a sample, genome re-sequencing and polymorphism discovery, mutation mapping and alternative splicing identification. The potential for biomedicine is equally promising with personalized medicine and implications on human health and drug discovery.

To effectively process and analyze such data, it is becoming more and more important to employ advanced high performance computing (HPC) strategies [11]. One of the main restrictions to increase the adoption of HPC in bioinformatics seems to lie in the lack of trained programmers capable of designing, developing, and using the right HPC programming tools. Map/Reduce (MR)

frameworks (for example Hadoop [15]) efficiently take advantage of computing resources. Therefore, a transitory solution could be to facilitate the porting of legacy applications (software written for an earlier operating system or hardware platform). This is straightforward for those applications in bioinformatics which present *embarrassingly parallel* workloads, i.e. where the input data can be split and processed *independently* in parallel. Cloud Computing (CC) provides an attractive alternative to traditional HPC centers for computational and storage resources because users only pay for CC resources actually used.

This paper is organized as follows; we present the Bio-Cirrus software framework in Section 2. In Section 3, we discuss Bio-Cirrus and compare the speedup of our approach with a reference implementation using Hadoop Streaming on different cluster sizes. Finally, we conclude the paper in Section 4.

## 2 The Bio-Cirrus Software Framework

Bio-Cirrus is a software framework which aims to simplify the transition to using CC resources for bioinformatics legacy (command-line) applications. Our approach uses a parallel strategy (Section 2.1) for processing data using CC resources. In addition, Bio-Cirrus allows end-users to access these applications through a consistent and user-friendly interface (Section 2.2).

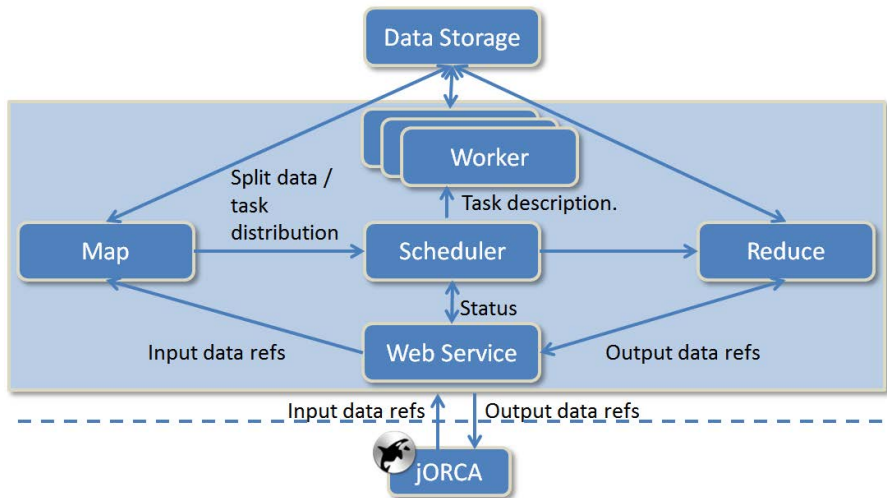
### 2.1 The Mr. Cirrus Framework

The software suite Mr. Cirrus (Map-Reduce for High Level Cloud Computing) consists of three major software modules (see Figure 1):

- Map: This initial module splits the input data and prepares an initial mapping of tasks. The output of this module is essentially the distribution of the computational load, the chunks of data and the reduce task.
- Scheduler: This module is in charge of invoking the tasks prepared in the initial module. The scheduler will assign tasks dynamically to each available worker.
- Reduce: The final module collects the partial results and composes a final, global result.

The initial implementation of Mr. Cirrus was a Message Passing Interface (MPI) application, which provides a parallel execution environment for sequential applications in multiprocessors, cluster of computer machines and IaaS clouds [14]. Mr. Cirrus has also been implemented for the following CC platforms: Amazon Web Services (AWS) [2], IBM SmartCloud [3] and Microsoft Azure [6,9]. Obviously, the legacy applications running on the different applications must be executable on the CC platform, for example, the Azure version of Mr. Cirrus can only be used with legacy applications which run on Windows 2008.

**Data Distribution Strategy in Mr. Cirrus.** In Mr Cirrus, the map stage is configurable and determines the data distribution which typically depends on



**Fig. 1.** Overview of Bio-Cirrus with the computational framework Mr. Cirrus in the middle part and the end-user client software jORCA in the lower part. Note that jORCA only submits data references to previously prepared data during Web-Service invocation.

the legacy application. It is essential to distribute data in such a way that each computing node minimizes the waiting time before starting to process data. This section gives examples of such strategies for two typical bioinformatics applications: dotplot and blast.

Dotplot[8] is a simple way to compare biological sequences where the similarities of the sequences are represented visually with one sequence arranged horizontally and the other vertically. For dotplot data, the dot matrix is built by comparing two sequences  $S_x$  and  $S_y$ . The simplest distribution is to allot the computational space  $L_x$  and  $L_y$  (the lengths of the respective sequences) to equal lengths. The two sequences are split in  $N_x$  and  $N_y$  chunks. Mr Cirrus will process them independently using the available computing nodes for each set  $S_i$  where  $i = 1 \dots N_x$  and  $S_j$  where  $j = 1 \dots N_y$ . This will produce partial results  $RES(i, j)$  which are combined in the reduce step to produce the final dot matrix.

BLAST [4] is a well-known application for comparing biological sequences. When performing a BLAST, we often have a large amount of sequences. The strategy in this case is to split these sequences in several files, where each file has a similar number of sequences. It is important to note that this variant can cause efficiency problems when the number of sequences are too small or the lengths of the sequences are very different. This will limit the efficiency of the system because the longer sequences determine the overall performance.

In both cases, it is important to ensure that the map stage minimizes the start latency and provide a simple final reduce step. We have used Guided Self Scheduling (GSS) [13] and modified Guided Self Scheduling (mGSS) [17] which sends light jobs at the beginning of the process to minimize the scheduling cost.

## 2.2 The jORCA Client

The jORCA client [12] was developed to facilitate the integrated usage of Web-Services (WS) in bioinformatics. jORCA uses the Modular programmatic application interface (MAPI) [10] to obtain a uniform representation of metadata related to WS (such as tools, datatypes, WS registries). MAPI is organized in separate modules which solve specific tasks, for example one module is used to invoke services, another module to obtain metadata about WS, etc.

jORCA facilitates the usage by generating a consistent and clear user interface for heterogeneous WS. Additionally, jORCA requires tool developers to map the input/output parameter datatypes to shared data taxonomy, which is essential to increase interoperability among WS (service composition). The client is extensible for new WS protocols and metadata repositories.

The following improvements of jORCA have been implemented to integrate jORCA with Mr. Cirrus:

### **Component for Transfer of Data to Network Connected Data Storage.**

jORCA now supports data transfer to network connected data storage. A standardized GUI has been developed to upload/download data and it is possible to extend the supported types of data storage. Initial implementations include Microsoft Azure blob storage and support for SFTP and Amazon EC2 storage is under development. For the Azure blob storage, users can specify a storage account and credentials which are then used to generate temporary keys which are used by jORCA to authenticate against the blob storage API. The jORCA component for transferring data to Azure blob storage uses a special type of blobs (page blobs), which allows the component to upload parts of the data and, if necessary, resume interrupted transfers.

### **Component for Invoking WS Using Data References.**

We have also specified and implemented support for invoking a RESTful WS front-end for Mr. Cirrus from jORCA. The WS provides an interface to submit a job specifying the required WS parameters as data references to data already uploaded on cloud data storage, see Figure 1. The submission creates a new resource (addressable via a unique URL). The resource can be polled for status and, when ready, for the final result. Therefore, these call-by-reference invocations greatly facilitate invocation of a series of WS (i.e. a pipeline or more complex workflow) because the jORCA client does not need to download the intermediate result and upload again to the subsequent WS. Not only is this more efficient but it also saves cost because data transfers between applications running in the cloud and the storage services are typically free of charge. The WS front-end has been implemented in C# (for Windows Azure) and Java (for AWS).

The deployment model for the front-end WS in Bio-Cirrus implies that the size of the computational cluster is known in advance for a specific service. When data are prepared in the map step, it is not necessary to know the cluster size. For example, it is possible to split the data in several ways (fixed size, GSS and

mGSS), see Section 2.1. The data distribution strategy will produce  $N$  chunks where  $N$  is typically much larger than the available compute units. Naturally, this model fits better on a private cloud where we have permanent access to the computational cluster. On a commercial cloud, it is not economically efficient to maintain a large cluster used only occasionally.

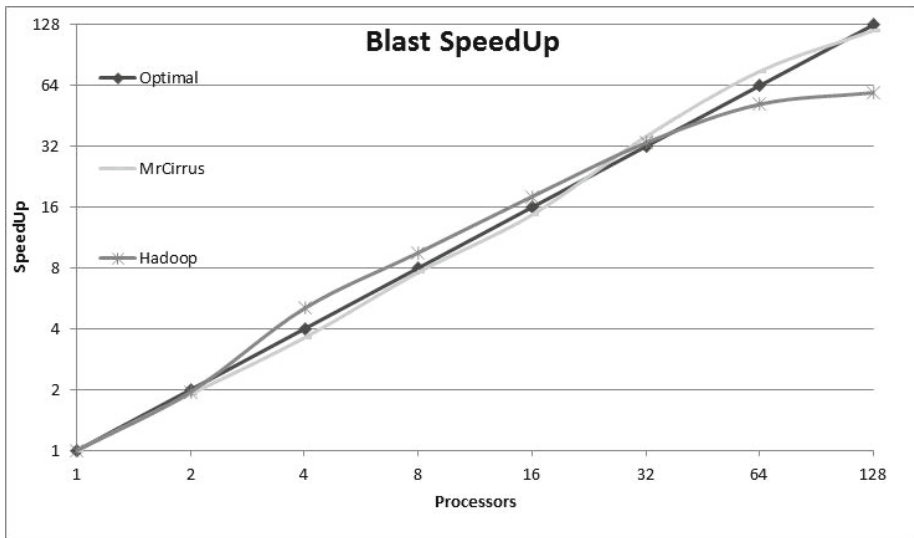
The WS front-end can be registered with the Flipper [5] application in any of the WS metadata repositories supported by jORCA.

### 3 Discussion

Bioinformatics is an extremely active field where new applications and web-services are developed constantly. Bio-Cirrus aims to simplify the transition of these applications to run on cloud computing architectures. Although not all bioinformatics applications are suitable for parallel implementation due to their irregular computational patterns, data dependencies, etc., bioinformatics is a clearly a good domain to evaluate Bio-Cirrus.

The legacy application we have chosen to evaluate Bio-Cirrus with is BLAST. We will search for similarities between a collection of singletons (approximately 160,000 sequences with average size of 530 residues, 85.4 Mb) against the collection of contigs (120,000, 76.9 Mb) obtained as a result of a Next Generation Sequencing (NGS) DNA-assembly process using reads from Olive tree samples [8]. It was not possible to group these singletons into contigs during the assembly process. The rationale of the scenario, from a biological point of view, is to perform an additional verification of singletons that could match with some specific contigs.

To enable us to evaluate the performance of Mr Cirrus, we have developed a reference implementation based on Hadoop [15] with similar characteristics as Mr Cirrus. Hadoop provides a set of libraries for the distributed processing of large data sets across clusters of computers using a simple programming model. Nowadays, there are several Cloud providers offering Hadoop-based services, for example Amazon Elastic Map/Reduce [1]. We used Hadoop Streaming, deployed on Amazon Elastic Map Reduce [1], which lets us create and run Map/Reduce jobs with any executable or script as the mapper and reducer functions. We have developed a bash script that acts as a wrapper between the sequential program and the Hadoop Streaming library. In our reference implementation, Amazon S3 buckets are used to store input data and binaries. When the master node is started, data and binaries are downloaded to the local file system of the master. Once downloaded, these files are uploaded to Hadoop Distributed File System (HDFS) [7] so that all cluster nodes (running Hadoop) can access them. HDFS is a distributed file system designed to run on commodity hardware. HDFS is highly fault-tolerant and provides high throughput access to large data sets (in the range of gigabytes or terabytes). An HDFS instance may consist of hundreds or thousands of server machines (resizable dynamically), each storing part of the file system's data. Because of the fact that the probability of failure in a node is high, a HDFS component is always non-functional.



**Fig. 2.** This graph shows the speedup of the Blast benchmark using 1, 2, 8, 16, 32, 64 and 128 processing entities running on Amazon WS using Mr.Cirrus and Hadoop Streaming respectively. The time to deploy the clusters or the time to upload/download the input/output files were not included in the measurements, only the time for the computing nodes to download their input data, process the data and upload the result to the storage. Please note that, in some cases, the Hadoop Streaming representation and Mr.Cirrus get speedups higher than the theoretical optimal but this is most likely because the most commonly used variables in blast have enough space in the processor cache (much faster than the RAM memory) which distorts the results.

The strategy used to distribute partial input data among the cluster nodes is important. In the case of Bio-Cirrus, the data distribution is defined explicitly in the map stage (see Section 2.1). In our reference implementation using Hadoop, the data distribution is performed implicitly by HDFS. As you can see in Figure 2, the Hadoop version performs better with a little number of processors because the size of the chunk files to distribute is higher, and thus the synchronizing time between nodes is lower than the compute time. However, when the number of processors grows (32 is the inflection point in the graph), Mr.Cirrus performs better due to the effective synchronization mechanism (mGSS).

## 4 Conclusions

Breakthroughs in bioinformatics data acquisition have provided researchers with material to obtain important new knowledge. However, the sheer scale of the data makes it necessary to employ techniques from high performance computing (HPC). Ideally, legacy applications can be rewritten to take advantage of parallel computing but, as an intermediate solution, porting legacy applications using

map/reduce strategies could be an effective solution in many cases. Clearly, the potential of using CC for bioinformatics data processing is promising.

This document presents the software framework Bio-Cirrus which aims to facilitate the transfer of bioinformatics applications to run on CC architectures and provide consistent and user friendly interfaces. In Section 3, we show that the speed-up obtained using the computational component of Bio-Cirrus (Mr.Cirrus) is comparable to Hadoop and, when the number of processing entities grows large, Mr.Cirrus has an advantage due to its effective synchronization strategy. The jORCA application is able to provide a simple and standardized interface for end-users due to the standardized web-service front-end.

In conclusion, Bio-Cirrus provides an integrated solution which supports all necessary steps for transferring legacy applications in bioinformatics to run on cloud computing architectures, starting from the deployment of the legacy application using Mr.Cirrus, deployment and registration of a web-service front-end using Flipper and discovery and invocation of the web-service using jORCA.

**Acknowledgements.** This work has been partially supported by the Spanish National Institute of Bioinformatics (INB-ISCI), the RIRAAF network (RD12/0013/0013), Mr.SymBioMath (EU grant agreement number 324554) and Proyecto Motriz de Excelencia de la Junta de Andalucía (P10-TIC-6108).

## References

1. Amazon Elastic Map Reduce, <http://aws.amazon.com/elasticmapreduce/>
2. Amazon Web Services, <http://aws.amazon.com/>
3. IBM SmartCloud, <http://www.ibm.com/cloud-computing/us/en/>.
4. Program parameters for blastall,  
<http://www.ncbi.nlm.nih.gov/staff/tao/URLAPI/blastall/>
5. The Flipper Web Service Registration Tool,  
<http://chirimoyo.ac.uma.es/flipper/>
6. Windows Azure Storage API,  
<http://msdn.microsoft.com/en-us/library/windowsazure/dd179355.aspx>
7. Borthakur, D.: The Hadoop Distributed File System: Architecture and Design,  
[http://hadoop.apache.org/common/docs/r0.18.0/hdfs\\_design.pdf](http://hadoop.apache.org/common/docs/r0.18.0/hdfs_design.pdf)
8. Gibbs, A.J., McIntyre, G.A.: The diagram, a method for comparing sequences. *European Journal of Biochemistry* 16(1), 1–11 (1970)
9. Karlsson, J., Torreño, O., Ramet, D., Klambauer, G., Cano, M., Trelles, O.: Enabling large-scale bioinformatics data analysis with cloud computing. In: 2012 IEEE 10th International Symposium on Parallel and Distributed Processing with Applications (ISPA), pp. 640–645. IEEE (2012)
10. Karlsson, J., Trelles, O.: MAPI: a software framework for distributed biomedical applications. *Journal of Biomedical Semantics* 4(1), 4 (2013)
11. Parsons, M.: Multiple challenges for multicore processors (2009),  
<http://www.isgtw.org/?pid=1001952>
12. Martín-Requena, V., Ríos, J., García, M., Ramírez, S., Trelles, O.: JORCA: easily integrating bioinformatics Web Services. *Bioinformatics* 26(4), 553–559 (2010)



13. Polychronopoulos, C.D., Kuck, D.J.: Guided Self-Scheduling: A Practical Scheduling Scheme for Parallel Supercomputers. *IEEE Transactions on Computers* C-36(12), 1425–1439 (1987)
14. Ramet, D., Lago, J., Karlsson, J., Falgueras, J., Trelles, O.: Mr-Cirrus: Implementación de Map-Reduce bajo MPI para la ejecución paralela de programas secuenciales. In: *Proceedings of XXII Jornadas de Paralelismo, Las Palmas de Gran Canaria, España* (2011)
15. Taylor, R.: An overview of the Hadoop/MapReduce/HBase framework and its current applications in bioinformatics. *BMC Bioinformatics* 11(suppl. 12), S1+ (2010)
16. Trelles, O., Prins, P., Snir, M., Jansen, R.C.: Big data, but are we ready? *Nature Reviews Genetics* 12(3), 224–224 (2011)
17. Trelles-Salazar, O., Zapata, E.L., Carazo, J.M.: On an efficient parallelization of exhaustive sequence comparison algorithms on message passing architectures. *Computer applications in the biosciences: CABIOS* 10(5), 509–511 (1994)

# Activity Recognition Based on a Multi-sensor Meta-classifier

Oresti Baños\*, Miguel Damas, Héctor Pomares, and Ignacio Rojas

Department of Computer Architecture and Computer Technology,  
Research Center for Information and Communications  
Technologies of the University of Granada (CITIC-UGR)  
C/Periodista Daniel Saucedo Aranda s/n, 18071 Granada, Spain  
{oresti,mdamas,hpomares,irojas}@atc.ugr.es  
<http://citic.ugr.es>

**Abstract.** Ensuring ubiquity, robustness and continuity of monitoring is of key importance in activity recognition. To that end, multiple sensor configurations and fusion techniques are ever more used. In this paper we present a multi-sensor meta-classifier that aggregates the knowledge of several sensor-based decision entities to provide a unique and reliable activity classification. This model introduces a new weighting scheme which improves the rating of the impact that each entity has on the decision fusion process. Sensitivity and specificity are particularly considered as insertion and rejection weighting metrics instead of the overall accuracy classification performance proposed in a previous work. For the sake of comparison, both new and previous weighting models together with feature fusion models are tested on an extensive activity recognition benchmark dataset. The results demonstrate that the new weighting scheme enhances the decision aggregation thus leading to an improved recognition system.

**Keywords:** Meta-classifier, Sensor network, Decision fusion, Weighted decision, Aggregation, Activity recognition, Human Behavior.

## 1 Introduction

The assessment of human behavior has been demonstrated of worth value for its several applications in healthcare [3], rehabilitation [1], industrial maintenance [16] or gaming [11] among others. Even when relevant contributions have been provided in the last years to the activity recognition field, there are still several open issues respectively referring to systems reliability, robustness, pervasiveness and seamless of usage. The use of multiple sensor configurations appears in this context as a means to efficiently overcome some of these issues.

In wearable computing, several studies have already demonstrated the importance of monitoring different body parts to increase activity detection capabilities [7,15]. To do so, more than one sensor is normally required to be attached

---

\* Corresponding author.

at various body locations. However, obtrusiveness has traditionally been one of the main controversial drawbacks against the wearing of multiple sensors, since their size and ergonomic limitations may difficult their use in life-long conditions. Nonetheless, progressive sensors miniaturization and cost reductions are supporting a new generation of devices that may be embedded in garments and textiles [2], with the aim of integrating tens, hundreds or even thousands of these sensors in a very reduced area [8].

Together with this mainstream technologies, sensor fusion has become a hot topic in activity recognition. Sensor fusion applies to different levels of the activity recognition chain, including signal fusion, feature fusion and classification decision fusion. Thus for example, [13] combines features extracted from different signal domains (respiration and acceleration) to recognize a set of 13 types of activities of varying intensities; [18] uses the fusion of 3D acceleration and angular velocity signals for spotting up to eight regular daily activities; the relationship between activity intensity and physiological response is also leveraged in [14] through correlating motion with heart rate or skin temperature data, which improves the accuracy of activity detection. At a higher level [12] fuses the classification scores provided by support vector machines (SVM) and gaussian mixture models (GMM) that operate on acceleration and electrocardiogram data. In [10] the fusion concept is also incorporated in a more sophisticated hierarchical model that combines information from dynamically-selected acceleration sensor nodes.

In this work we present a multi-sensor meta-classifier that incorporates an improved version of the weighting scheme introduced in a previous work [4]. This improvement allow us to independently weight the positive (insertion) and negative (rejection) decisions yielded by each decision making entity, instead of using the same value for both. This way is more problem-sensitive and supports the use of potential decision entities even when their classification or rejection capabilities are unbalanced. The rest of the paper is organized as follows. In Section 2 the meta-classifier structure and the decision weighting scheme are described. Section 3 presents the main results obtained for the meta-classifier when tested on an activity recognition benchmark dataset. The proposed model is also compared with a previous hierarchical version and a standard feature fusion model. Finally, main conclusions and future steps are presented in Section 4.

## 2 Multi-sensor Meta-classifier

Meta-classification is a prominent subfield of machine learning which shares conceptual basis with other state-of-the-art meta-algorithms such as stacking, boosting or mixture of experts among others. In this paper we refer to this as those models based on the aggregation of the decision provided by several sources or nodes of information. In the model presented here the decisions are provided by different level classification entities (hierarchical classification). Moreover, each decision is particularly rated according to each entity classification capabilities (e.g., from the sensor informativeness). This weighting procedure supports

an optimal exploitation of the classification potential of each individual entity, thus allowing for the definition of a precise collective knowledge structure.

The structure of the meta-classifier is very similar to the one presented in [4]. This consists of three classification levels or stages. The first level is composed by a set of  $M$  by  $N$  binary or base classifiers ( $c_{mn}, \forall m = 1, \dots, M, n = 1, \dots, N$ ) which respectively specialize in the discrimination of the activity or class  $n$  by using the information from the sensor or node  $m$ . The second classification level is defined through  $M$  node or source classifiers ( $S_m, \forall m = 1, \dots, M$ ) which defines through the decision fusion of each sensor associated binary classifiers. On top of the model (third level) the fusion of the decisions given by the source classifiers provides the eventually yielded activity classification.

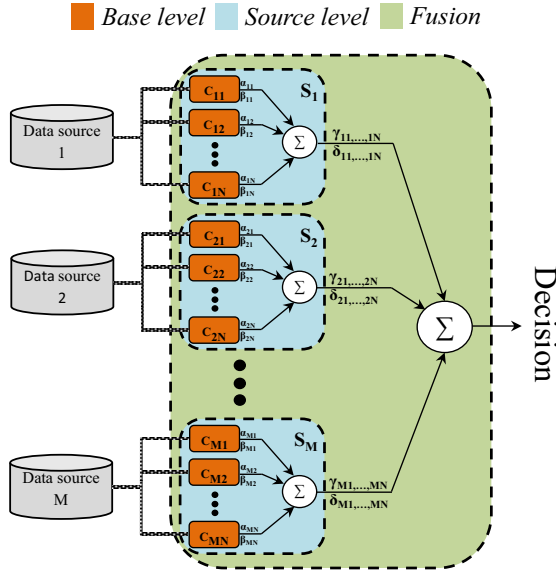
The model training requires from just a few steps. Firstly, the training dataset is partitioned in three equally-distributed parts. One of these partitions is used to train the base classifier entities. Afterwards, another partition is used to test the performance of the binary classifiers. From here, statistical metrics are obtained and later used to define the first level of weighting parameters. Once the models are trained and the metrics obtained the source classifiers are almost defined. Then, the weighting parameters for the second level are assessed. To that end, the third yet unused part of the dataset is considered now for the evaluation of the source classifiers performance. From the test statistics the second level weights may be obtained. At this point the source classifiers are completely defined. The meta-classifier is by extension defined as the sources classifiers and weights are, thus completing the final stage of the model. The final structure may be seen in Figure 1.

In the following the computation of the first level and second level weights as well as the suggested decision fusion scheme are presented. As was already introduced, two parameters are used both to weight classifications/insertions and rejections. At the class level these parameters are defined as  $\alpha_{mn}$  and  $\beta_{mn}$  which respectively represent the insertion and rejection weights for  $c_{mn}$ . The values of  $\alpha_{mn}$  and  $\beta_{mn}$  are obtained from the performance assessment of  $c_{mn}$ . In particular,  $\alpha_{mn}$  corresponds to the sensitivity whilst  $\beta_{mn}$  to the computed specificity. We have selected these performance parameters since they represent well the insertion and rejection capabilities of the classifier. From the statistical theory, given  $TP_{mn}$  (true positives) the number of correctly identified samples,  $FP_{mn}$  (false positives) the incorrectly identified samples,  $TN_{mn}$  (true negatives) the number of correctly rejected samples and  $FN_{mn}$  (false negatives) the incorrectly rejected samples, all specifically for the classifier  $c_{mn}$ ,  $\alpha_{mn}$  and  $\beta_{mn}$  may be defined as:

$$\alpha_{mn} = \frac{TP_{mn}}{TP_{mn} + FN_{mn}} \quad (1)$$

$$\beta_{mn} = \frac{TN_{mn}}{TN_{mn} + FP_{mn}} \quad (2)$$

These weights represent the importance that each base classifier will have on the source classifier decision scheme. A specific voting algorithm is considered



**Fig. 1.** Meta-classifier scheme.  $\alpha_{mn}$  and  $\beta_{mn}$ , and  $\gamma_m$  and  $\delta_m$  correspond to the insertion/rejection weights for the base level and source level respectively.

at this stage to fuse the base classifier individual decisions on a unique decision for each source respectively. For a source  $m$ , given a sample  $x_{m_k}$  to be classified and being  $q$  the class predicted by the classifier  $c_{mn}$ , if such class belongs to the class of specialization ( $q = n$ ), the classifier will set its decision to  $\alpha_{mn}$  for the class  $n$  and 0 for the rest of the classes. Otherwise ( $q \neq n$ ), the decision is set to 0 for the class  $n$  and  $\beta_{mn}$  for the others. In summary, the classifier  $c_{mn}$  weighted decision ( $WD_{mn}$ ) for the class  $q$  may be defined as ( $\forall \{q, n\} = 1, \dots, N$ ):

$$WD_{mn}(x_{m_k}) = \begin{cases} \alpha_{mn}, & x_{m_k} \text{ classified as } q & (\forall q = n) \\ 0, & x_{m_k} \text{ not classified as } q & (\forall q = n) \\ \beta_{mn}, & x_{m_k} \text{ not classified as } q & (\forall q \neq n) \\ 0, & x_{m_k} \text{ classified as } q & (\forall q \neq n) \end{cases} \quad (3)$$

The aggregation of the weighted decisions provided by each base classifier for the  $m$ -th source classifier ( $S_m$ ) may be computed as follows:

$$O_m(x_{m_k}) = \sum_{n=1}^N WD_{mn}(x_{m_k}) \quad (4)$$

The class predicted by  $S_m$  is the class  $q$  for which the source classifier output is maximized:

$$q_m(x_{m_k}) = \operatorname{argmax}_q (O_m(x_{m_k})) \quad (5)$$

For the next level, similar parameters to  $\alpha_{mn}$  and  $\beta_{mn}$  are considered, here defined as  $\gamma_m$  (insertions) and  $\delta_m$  (rejections). Nonetheless, the way they are computed varies slightly with respect to the above described. At the source level the classifiers are not binary but multiclass models. Therefore, the evaluation of each source classifier requires to extend sensitivity and specificity concepts to the multiclass case (see details in [17]). According to this generalization,  $\gamma_m$  and  $\delta_m$  may be described as:

$$\gamma_m = \langle \gamma_{m1}, \gamma_{m2}, \dots, \gamma_{mn} \rangle = \left\langle \frac{TP_{m1}}{TP_{m1} + FN_{m1}}, \frac{TP_{m2}}{TP_{m1} + FN_{m2}}, \dots, \frac{TP_{mn}}{TP_{mn} + FN_{mn}} \right\rangle \quad (6)$$

$$\delta_m = \langle \delta_{m1}, \delta_{m2}, \dots, \delta_{mn} \rangle = \left\langle \frac{TN_{m1}}{TN_{m1} + FP_{m1}}, \frac{TN_{m2}}{TN_{m1} + FP_{m2}}, \dots, \frac{TN_{mn}}{TN_{mn} + FP_{mn}} \right\rangle \quad (7)$$

where  $\{TP/TN/FP/FN\}_{mn}$  refer to the previous described classification and rejection counting values, but now computed for each class  $k$  across the confusion matrix results obtained from the evaluation of  $S_m$  ( $\forall m = 1, \dots, M, n = 1, \dots, N$ ). The source level weights are used in a different manner than in the class level. Besides the decisions are now made in a multiclass way, the weights are used to reward or penalize those classes that are classified or not by each source classifier. Accordingly, given  $q_m$  the decision of  $S_m$  for the sample  $x_{m_k}$ , the set of weighted decisions from this classifier is defined as:

$$WD_m(q_m(x_{m_k})) = \begin{cases} \gamma_{mn}, & n = q_m(x_{m_k}) \\ -\delta_{mn}, & n \neq q_m(x_{m_k}) \end{cases} \quad (\forall n = 1, \dots, N) \quad (8)$$

Now, for a sample  $x_k$  defined through the corresponding samples delivered by each source ( $x_{1_k}, \dots, x_{M_k}$ ), the aggregation of the source level weighted decisions is calculated as follows:

$$O(x_k) = O(\{x_{1_k}, \dots, x_{M_k}\}) = \sum_{p=1}^M WD_p(q_p(x_{p_k})) \quad (9)$$

Finally, and similarly to (5), the eventually yielded class  $q$  is obtained as:

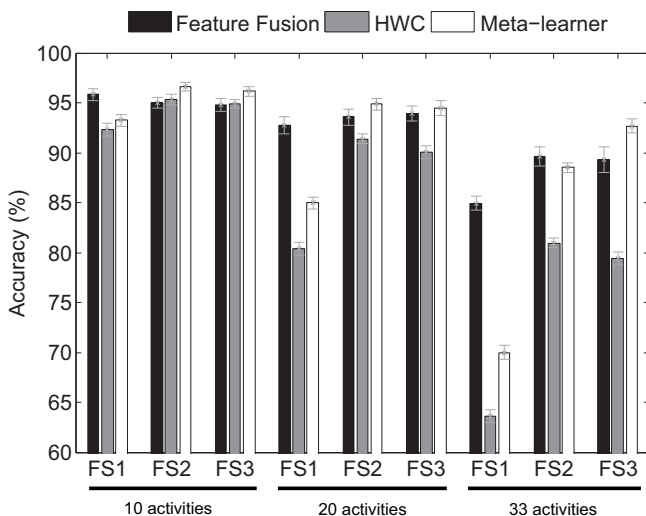
$$q = \underset{q}{\operatorname{argmax}}(O(x_k)) \quad (10)$$

### 3 Results and Discussion

For the evaluation of the proposed model an activity recognition benchmark dataset is used [6]. This dataset comprises motion data (namely acceleration, rate of turn and magnetic field) recorded for 17 volunteers performing 33 fitness

activities while wearing a set of nine inertial sensors attached to different parts of their bodies. For the sake of simplicity, the 3D acceleration data from the so-defined “ideal-placement” recordings are here considered. Three feature sets (FS) are respectively extracted for evaluation: FS1=’mean’, FS2=’mean and standard deviation’ and FS3=’mean, standard deviation, maximum, minimum and mean crossing rate’. All features are computed over a non-overlapping sliding window (6 seconds size). C4.5 decision trees (DT, [9]), which have been extensively and successfully applied in previous activity recognition problems, are used both for the multiclass classifiers and the binary or base classifiers. For all models a ten-fold random-partitioning cross validation process is applied across all subjects and activities. The process is repeated 100 times for each method to ensure statistical robustness.

In Figure 2 the results for the feature fusion (feature vector composed by the feature extracted from all sensors), hierarchical weighted classifier (HWC, [4]) and the here proposed meta-classifier are shown. FS1, FS2 and FS3 are respectively evaluated on these models for three activity recognition problems of increasing complexity (10 activities, 20 activities and 33 -all- activities). The meta-classifier clearly outperforms in all cases the recognition capabilities of the HWC, which appears to be the less reliable of the tested models. For some cases the accuracy improvement is of up to 13% as for the experiment with 33 activities and FS3. This systematic enhancement demonstrates that the rating



**Fig. 2.** Accuracy results from the evaluation of the fusion models when tested on different complexity activity recognition datasets.  $FS_i$  refers to the feature set extracted from the raw acceleration data. The 10 activities dataset refers to the activities  $\{1, 2, 18, 20, 23, 25, 30, 31, 32\}$ , the 20 activities to  $\{1, 2, 3, 7, 12, 13, 17, 18, 19, 20, 21, 23, 25, 27, 28, 29, 30, 31, 32, 33\}$  while the 33 activities dataset comprises all (see [6] for indices equivalence).

of not just the insertions (HWC) but also the rejections translates into a more precise weighting of the decisions yielded by each classifier. Moreover, specificity and sensitivity also contribute to a more balanced description of the classification capabilities than for the use of the overall accuracy.

The differences between the meta-classifier and the feature fusion model are not very significant. Nevertheless, the feature fusion model demonstrates a more regular performance for all problems and feature sets, whereas the meta-classifier shows a significant performance worsening for the 20 and 33 activities problems when FS1 is used. Normally, the more complex (#activities) the problem is the more features are required. Therefore, these reduced recognition capabilities are associated to the limited discrimination potential of the binary classifiers when just a feature (FS1) is considered. Nevertheless, this is shown to be compensated when a richer feature vector is used. In either case, it must be borne in mind that one of the main drawbacks of the feature fusion models is the drop on their activity assessment capabilities during realistic daily-living conditions [5]. A simple anomaly on one of the sensors may potentially affect the whole fusion process and lead to misclassifications. The proposed meta-classifier could deal with this and similar issues since the sources or sensors are independently evaluated and the fusion applies only to the individual yielded decisions.

## 4 Conclusions and Future Work

In this paper we have presented a meta-classifier scheme for multi-sensor activity recognition that may nevertheless be applied to other multi-source classification problems. The model improves the classification performance of a previous hierarchical fusion version through the weighting of both insertions and rejections at base (activity) and source (sensor) levels. The meta-classifier demonstrates to be sensitive to weak base classifiers, which translates into a significant drop on the recognition capabilities as the number of activities (complexity) increases. Nevertheless, the use of richer feature sets significantly increases the recognition potential. Next steps will aim to compare the robustness capabilities of the proposed meta-classifier against feature fusion models when dealing with complex activity recognition issues such as concept drift and diverse sensor anomalies.

**Acknowledgments.** This work was partially supported by the HPC-Europa2 project (no. 228398), the Spanish CICYT Project SAF2010-20558, Junta de Andalucía Project P09-TIC-175476 and the FPU Spanish grant AP2009-2244.

## References

1. Albert, M.V., Toledo, S., Shapiro, M., Kording, K.: Using mobile phones for activity recognition in parkinson's patients. *Frontiers in Neurology* 3(158) (2012)
2. Amft, O., Lukowicz, P.: From backpacks to smartphones: Past, present, and future of wearable computers. *IEEE Pervasive Computing* 8(3), 8–13 (2009)



3. Avci, A., Bosch, S., Marin-Perianu, M., Marin-Perianu, R., Havinga, P.: Activity recognition using inertial sensing for healthcare, wellbeing and sports applications: A survey. In: 2010 23rd International Conference on Architecture of Computing Systems (ARCS), pp. 1–10 (2010)
4. Banos, O., Damas, M., Pomares, H., Rojas, F., Delgado-Marquez, B., Valenzuela, O.: Human activity recognition based on a sensor weighting hierarchical classifier. *Soft. Computing* 17, 333–343 (2013)
5. Banos, O., Damas, M., Pomares, H., Rojas, I.: On the use of sensor fusion to reduce the impact of rotational and additive noise in human activity recognition. *Sensors* 12(6), 8039–8054 (2012)
6. Banos, O., Damas, M., Pomares, H., Rojas, I., Attila Toth, M., Amft, O.: A benchmark dataset to evaluate sensor displacement in activity recognition. In: Proceedings of the 2012 ACM Conference on Ubiquitous Computing, UbiComp 2012, pp. 1026–1035. ACM, New York (2012)
7. Bao, L., Intille, S.S.: Activity recognition from user-annotated acceleration data. *Pervasive Computing* 23, 1–17 (2004)
8. Cherenack, K., van Pieterse, L.: Smart textiles: Challenges and opportunities. *Journal of Applied Physics* 112(9), 091301 (2012)
9. Duda, R.O., Hart, P.E., Stork, D.G.: *Pattern Classification*, 2nd edn. Wiley Interscience (2000)
10. Gao, L., Bourke, A.K., Nelson, J.: Activity recognition using dynamic multiple sensor fusion in body sensor networks. In: 2012 Annual International Conference of the IEEE Engineering in Medicine and Biology Society (EMBC), August 28–September 1, pp. 1077–1080 (2012)
11. Kailas, A.: Capturing basic movements for mobile platforms embedded with motion sensors, pp. 2480–2483 (2012); cited By (since 1996) 0
12. Li, M., Rozgic, V., Thatte, G., Sangwon, L., Emken, A., Annavaram, M., Mitra, U., Spruijt-Metz, D., Narayanan, S.: Multimodal physical activity recognition by fusing temporal and cepstral information. *IEEE Transactions on Neural Systems and Rehabilitation Engineering* 18(4), 369–380 (2010)
13. Liu, S., Gao, R.X., John, D., Staudenmayer, J.W., Freedson, P.S.: Multisensor data fusion for physical activity assessment. *IEEE Transactions on Biomedical Engineering* 59(3), 687–696 (2012)
14. Martin, H., Bernardos, A.M., Tarrío, P., Casar, J.R.: Enhancing activity recognition by fusing inertial and biometric information. In: 2011 Proceedings of the 14th International Conference on Information Fusion (FUSION), pp. 1–8 (July 2011)
15. Maurer, U., Smailagic, A., Siewiorek, D.P., Deisher, M.: Activity recognition and monitoring using multiple sensors on different body positions. In: International Workshop on Wearable and Implantable Body Sensor Networks, BSN 2006, pp. 113–116 (2006)
16. Stiefmeier, T., Roggen, D., Ogris, G., Lukowicz, P., Tröster, G.: Wearable activity tracking in car manufacturing. *IEEE Pervasive Computing Magazine* 7(2), 42–50 (2008)
17. Ward, J.A., Lukowicz, P., Gellersen, H.W.: Performance metrics for activity recognition. *ACM Trans. Intell. Syst. Technol.* 2(1), 6:1–6:6 (2011)
18. Zhu, C., Sheng, W.: Human daily activity recognition in robot-assisted living using multi-sensor fusion. In: IEEE International Conference on Robotics and Automation, ICRA 2009., pp. 2154–2159 (May 2009)

# Indoor Activity Recognition by Combining One-vs.-All Neural Network Classifiers Exploiting Wearable and Depth Sensors

Benoît Delachaux, Julien Rebetz,  
Andres Perez-Uribe, and Héctor Fabio Satizábal Mejia

IICT, HEIG-VD, University of Applied Sciences Western Switzerland (HES-SO)  
benoit.delachaux@gmail.com, {julien.rebetz, andres.perez-uribe,  
hector-fabio.satizabal-mejia}@heig-vd.ch

**Abstract.** Activity recognition has recently gained a lot of interest and appears to be a promising approach to help the elderly population pursue an independent living. There already exist several methods to detect human activities based either on wearable sensors or on cameras but few of them combine the two modalities. This paper presents a strategy to enhance the robustness of indoor human activity recognition by combining wearable and depth sensors. To exploit the data captured by those sensors, we used an ensemble of binary one-vs-all neural network classifiers. Each activity-specific model was configured to maximize its performance. The performance of the complete system is comparable to lazy learning methods ( $k$ -NN) that require the whole dataset.

**Keywords:** Smart home, Activity recognition, Artificial neural networks, One-vs-all binary classifier fusion, Wireless sensors, Depth sensors

## 1 Introduction

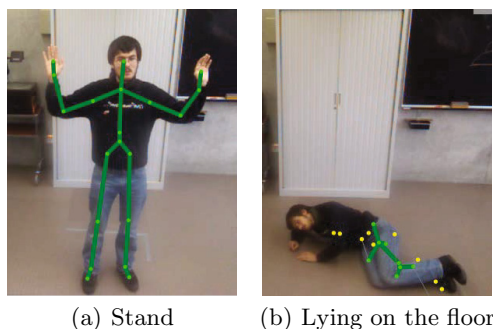
Supporting the quality of life of aging population is one of the greatest challenges facing our societies nowadays. With age comes neurodegenerative diseases, memory loss, increased risks of falls, and broken limbs. However, smart home technologies offer new opportunities to help the elderly population pursue an independent living. In our work, we are interested in using activity recognition to build applications that can help people with cognitive or memory problems. We focus on indoor environments, such as an apartment, which can be equipped with static sensors (e.g., Kinect depth cameras). In addition, the users can also carry wearable sensors which can be hidden in clothes or in accessories (e.g., a watch or a smartphone). In this context, an activity recognition system should be able to (i) recognise a wide range of activities, (ii) be flexible with regards to loss of one or more sensor modalities.

There are numerous previous works in activity recognition [7, 10, 13]. Many works target a medical application: for instance, Amft et al. [1] use a variety of on-body sensors to perform dietary monitoring and therefore help patients

with their nutrition. They use multiple modalities (accelerometers, microphones and electromyogram) to detect various activities like chewing, swallowing, drinking, cutting, eating soup. Hondori et al. [5] present a system that helps monitor various dining activities of post-stroke patients using a Kinect camera and accelerometers. Kepski et al. [6] built a system that uses the Kinect and a single accelerometer to perform fall detection.

In this paper, we explore the possibility of a smart home system that would recognize high-level daily activities (e.g., eating, cleaning, drinking, reading) using artificial neural networks, for instance to help people with memory loss, by recording a visual log of their daily activities. It has been shown that such a system can help those people by acting as a cognitive compensation system [3], and at the same time, given that memory loss can be frustrating, it can provide a positive feedback letting them remember their recent activities.

This contribution is organized as follows: In Section 2, we present the dataset we used to conduct our experiments. In Section 3, we explain the various steps of our activity recognition pipeline. Section 4 discusses the results we obtained and finally Section 5 presents our conclusions.



**Fig. 1.** Kinect extracted skeleton for two sample poses. The skeleton is overlaid in green, with yellow dots indicating the joints with a low confidence score reported by the sensor. The skeleton provided by the Kinect is reliable when the person is standing in front of the sensor, but it is unreliable when parts of the person’s body are occluded.

## 2 Dataset

Several activity recognition datasets are available and allow researchers to benchmark their algorithms. However, even recent datasets [9] do not include depth-sensors. Our dataset consists of recordings of typical daily living activities performed by one subject so far, but we are working on a database where several subjects will take part in the recordings<sup>1</sup>. The recording environment simulates the setup of a small apartment with one Kinect camera per room. We decided

<sup>1</sup> The current database is available upon request. The complete database involving several subjects will be available on our website <http://ape.iict.ch> soon.

to use Kinect and accelerometer sensors because they are both relatively cheap hardware (when compared to motion capture setup, for example) and are not too invasive for the user of our system. In addition to its skeleton tracking capabilities, the Kinect can also be used as a camera and therefore allows us to show pictures of the activities to the user, which are more easily interpretable than text labels as shown by Browne et al. [3]. In order to respect the privacy of the person, the system might not store the video after having been processed (i.e., it will only store the snapshots, the duration of the activities, etc.).

During the sequence, the subject performs various daily activities including: *Read, Sleep, Sit idle, Dress, Undress, Brush teeth, Clean a table, Work at the computer, Tidy up the wardrobe, Pick something up, and Sweep the floor*, repeating each activity multiple times. The duration of the first recording is 2176 seconds, which corresponds to 65'057 samples. Each sample consists of the skeleton<sup>2</sup> of the person, obtained from the Kinect sensor, placed at a height of around 2 m in the rooms, using the Microsoft's SDK [12], and the 3-axis acceleration from 5 wireless inertial measurement units (IMU) from Shimmer Research<sup>3</sup>, placed on the wrists, ankles and on the back. In addition, for each timestamp the Kinect also gives us a RGB image that we used to label the data (by hand) and validate our system. Figure 1 shows two examples of Kinect captures with the extracted skeleton overlaid in green. An in-house software was used to synchronize the accelerometers with the Kinect. Figure 2 shows the activity labels of the whole sequence used in our experiments.

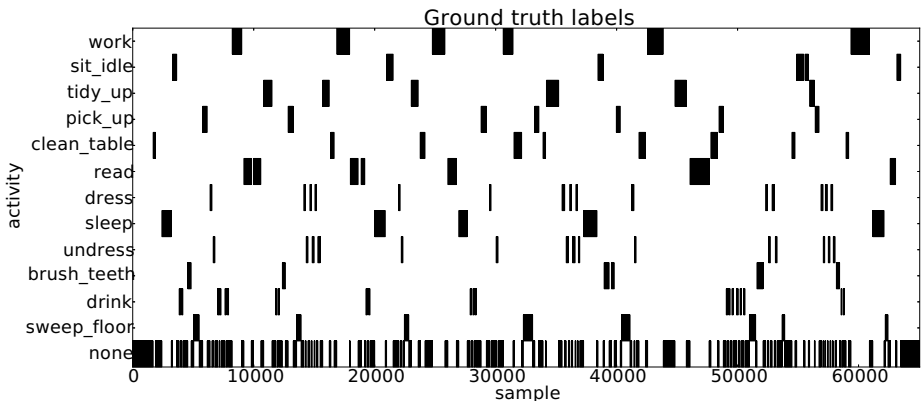


Fig. 2. Activity labels corresponding to the sequence of 65'057 samples

### 3 Learning Pipeline

Activity recognition was achieved by combining a set of binary classifiers based on feedforward artificial neural networks (i.e., Multi-layer Perceptrons).

<sup>2</sup> The Kinect sensor tracks the position (relative to the sensor) of 20 body joints at a rate of about 30hz.

<sup>3</sup> <http://shimmer-research.com>

We decided to use a one-vs-all approach [4] and trained a neural network for each activity. Each individual neural network was trained to distinguish all the samples belonging to one activity from a randomly chosen set of samples belonging to all other activities. The main reason for this choice is that different activities might require different features. For example, one might assume that the position of the feet is not relevant to detect the *drink* activity.

Our learning pipeline consists of the following steps: acceleration and skeleton acquisition, signal filtering, window-size selection, neural network complexity (number of hidden neurons) selection, and input selection, for each individual binary classifier. We performed parameter exploration to help us choose the best value for each parameter of this learning pipeline, when possible. This means that running the whole pipeline can be quite time-consuming, but most parameters (e.g., window size, topology) that are found optimal on our test sequences are likely to be near-optimal on new similar sequences that our system might encounter in the future.

**Acceleration and Skeleton Acquisition.** We used 5 three-axis accelerometers. Two were placed on the legs, one on the back and one on each wrist of the subject. This is a subtotal of  $3 * 5 = 15$  inputs from the accelerometers. In addition, we used the following information from the Kinect skeleton data : the position of the person in the room, the position of left and right hands, elbows and hips, and the position of each hand relative to the corresponding shoulder. This gives a subtotal of  $3 * 9 = 27$  inputs from the Kinect. So we have a total number of  $15 + 27 = 42$  input values for each frame.

**Signal Filtering.** We used a 1Hz low-pass filter to only consider the low frequency components of the subject's movements. Hence, we mostly kept data about the posture of the subject when performing an activity. Indeed, most of the activities we are interested in have quite different postures.

**Window Size Selection.** After the signal has been filtered, we used a sliding window to extract feature vectors. We tried window sizes between 10 and 100 samples, and chose the one that gave us the least validation error. We used the absolute error  $\epsilon = |y_{ground\ truth} - y_{predicted}|$  to evaluate the training performance of each single neural network for this step. Although not all activities have the same optimal window size, we used a single window size for all activities (for simplicity). We chose a window size of 30 samples, which was a good choice for almost all activities. We tested two overlapping settings for our sliding windows: 50% and "99%" (just slide the window by one value). The windows are used to sub-sample the original time-series by computing the mean.

**Topology Selection.** Since we used one-vs-all networks, specific to each activity, such networks have a single output unit indicating whether the input corresponds to the execution of the given activity (1) or not (0). We used sigmoidal output neurons, thus output values between 0 and 1 represent the neural network's certainty regarding the classification of a particular input pattern. Since we found that networks with a single hidden layer were sufficiently complex for

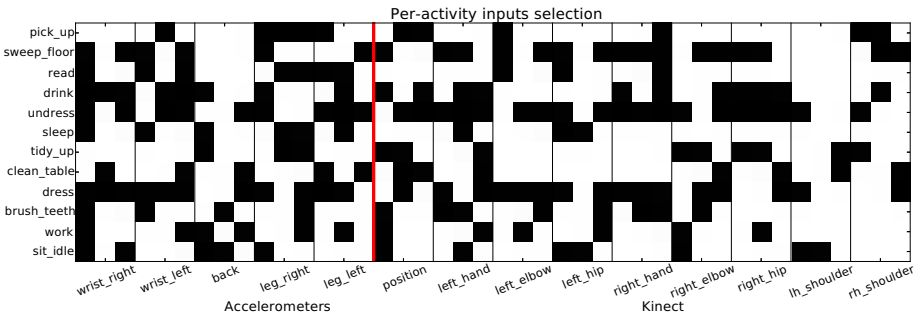
our classification problem, the topology selection consisted on (i) determining the number of hidden units and (ii) selecting the inputs features.

**Neural Network Complexity (hidden units).** To determine the number of hidden units used in our networks, we tried values between 1 and 8 and performed a training/validation procedure using the whole dataset. From these results, we chose for each activity, the best number of hidden units (e.i., the one that minimizes the classification error); those numbers are reported in the table below. Hidden units used the hyperbolic tangent function.

**Table 1.** Number of hidden units chosen for each activity

sweep_floor	drink	brush_teeth	undress	sleep	dress	read	clean_table	pick_up	tidy_up	sit_idle	work
4	8	7	7	8	8	1	5	8	8	5	4

**Binary Classifiers’ Inputs Selection.** As an additional optimisation, for each activity-specific neural network classifier, we used the sensitivity matrix method [11] to select the subset of inputs with the highest relevance in the task of one-vs-all classification, using the whole dataset. Figure 3 shows the set of selected inputs for each activity-specific binary classifier.



**Fig. 3.** Matrix showing the selected inputs for each class. Each modality has 3 axis (x, y, z). For each activity, we select a different set of inputs (rows). A black square indicates that the input has been selected for the corresponding activity. On the left are the features computed from accelerometers, on the right the features computed from the Kinect (the red line shows the separation).

**Binary Classifiers’ Training and Fusion.** Each Multi-Layer Perceptron (MLP) implementing an activity-specific one-vs-all binary classifier was trained using the FENNIX software<sup>4</sup>, developed by one of the authors. In particular, we used the Backpropagation algorithm [2] during 50 and 250 epochs, a decreasing learning rate from 0.025 to 0.001, and a momentum term of 0.7. The output of the ensemble of binary classifiers was the action having the highest classification certainty value (i.e., the highest activity-specific one-vs-all classifier’s output value), provided that such a value was greater than 0.7. Otherwise, we considered the recognized activity as being the *none* activity, which is a special class for unknown activities.

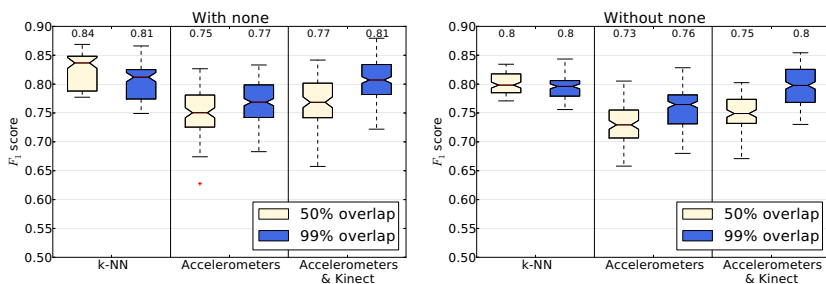
<sup>4</sup> <http://fennix.sourceforge.net>

## 4 Results

To evaluate the performance of our system, we compared it to a  $10$ -NN ( $k$  Nearest Neighbors) classifier, which is often used as a benchmark classifier for activity recognition tasks. We chose  $k = 10$  here because this gave the best results after some limited testing of the values of  $k$ . We performed two-fold cross-validation, by creating 10 different training/validation pairs by sliding the training data window by 10% each time. Then, for each of the training/validation pair, we performed 20 runs, where we trained our model using the corresponding training set, and then proceeded to evaluate its validation performance, using the rest of the dataset. Therefore, a total of 200 runs is performed per experiment. To compute the resulting performance of the classifier, we used the average (over all classes) of the  $f(1)$  score [8] shown in Equation 1, which estimates how accurately it classifies a particular activity as such. In Equation 1,  $precision = \frac{tp}{tp+fp}$ ,  $recall = \frac{tp}{tp+fn}$ ,  $tp$  are the true positives,  $fp$  are the true negatives, and  $fn$  are the false negatives.

$$f(1) = 2 \cdot \frac{\text{precision} \cdot \text{recall}}{\text{precision} + \text{recall}} \quad (1)$$

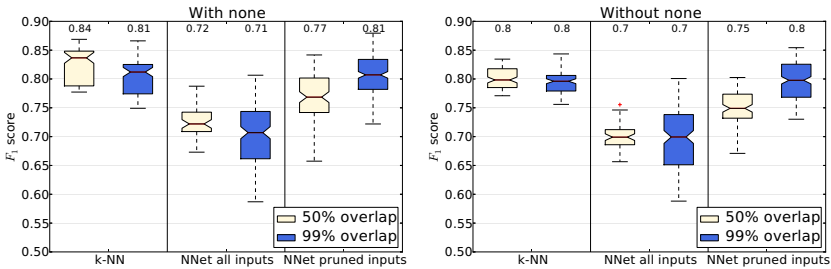
To fully profit from the use of both wearable and static sensors, we implemented a *model switching* capability within the activity recognition system as follows: given that the skeleton data provided by the Kinect has a quality flag for each joint and frame, indicating the confidence in the reported joint position, when this flag was low for most of the joints being tracked, we considered that the Kinect data was not reliable and we relied on a model based only on the accelerometers, to recognize the activity being performed. To achieve this, we trained two models: one using both the wearable and the static depth-based sensors, and a second one using only the wearable accelerometers.



**Fig. 4.** Influence of model switching on classification performances ( $k$ -NN is shown for comparison). There are two plots: one where we take the none class into account and one where we do not. The window overlap parameter is indicated by the color. The number on top of each boxplot show the value of the median, for ease of comparison.

To evaluate the usefulness of *model switching* on our dataset, we compared the performance of a model using only the accelerometers and the one of a model using *model switching*. The results are shown on Figure 4. Notice that using *model switching* improves performances by about 5% when using a single frame window overlap (“99%”). The gain is less important when using a 50% window overlap. One of the reasons that might explain this is that when using “99%” window overlap, we have roughly 14 times more data (windows have a length of 30) to train our network. We can also see that using *model switching* allows us to get performances very close to  $k$ -NN.

Figure 4 shows the overall performances of our system with and without input pruning. We see that input pruning based on the sensitivity matrix method [11] gives us a considerable performance improvement (around 14%), when using a “99%” window overlap, whereas the performance improvement is of around 7%, when using a 50% window overlap. As we mentioned before, this is likely due to the fact that having more window overlap means more training data. We also see that we get performances that are comparable to  $k$ -NN, which is an encouraging result, given that we do not use the whole dataset to classify the input patterns.



**Fig. 5.** Classification performance ( $f(1)$  score) for our pipeline. On the left,  $k$ -NN is used as a benchmark. There are two plots: one where we take the none class into account and one where we do not. Then, in the middle of each plot, the performance of our models without input pruning is shown and on the right are the results for our models with input pruning. The window overlap parameter is indicated by the color. The number on top of each boxplot indicates the value of the median, for ease of comparison.

## 5 Conclusions

This paper presents an activity recognition system built using activity-specific one-vs-all artificial neural networks. The experiments demonstrated that the performance of the system is comparable with a  $k$ -NN classifier but with the advantage that, once trained, the training database can be discarded. This makes it possible to use this kind of system on an embedded device like a smartphone or a tablet. We also showed that input pruning and custom configuration of each activity-specific model can be used to improve the performance of the system.



Last but not least, we showed that the combination of wearable motion sensors and static depth sensors can enhance not only the performance, but the robustness of indoor activity recognition systems by taking advantage of one modality when the other one is not reliable. Our results are quite encouraging, but further tests with several subjects are required in order to verify to a greater extent the generalization performance of such a system. Moreover, given that our aim is to work towards activity recognition democratization, we will try to use as few sensors as possible in the future.

**Acknowledgements.** This work was funded by the Hasler Foundation and the RCSO-TIC of the HES-SO. We thank our colleagues from the Wearable Computing Lab. ETH, for useful discussions as well as L. Heim, O. Hüsser and F. Tièche from the HE-ARC/HES-SO for their contribution regarding the use of the Kinect SDK.

## References

1. Amft, O., Tröster, G.: Recognition of dietary activity events using on-body sensors. *Artificial Intelligence in Medicine* 42(2), 121–136 (2008)
2. Bishop, C.: *Neural networks for pattern recognition*. OUP, USA (1995)
3. Browne, G., et al.: Sensecam improves memory for recent events and quality of life in a patient with memory retrieval difficulties. *Memory* 19(7), 713–722 (2011)
4. Garcia-Pedrajas, N., Ortiz-Boyer, D.: An empirical study of binary classifier fusion methods for multiclass classification. *Information Fusion* 12(2), 111–130 (2011)
5. Hondori, H., et al.: Monitoring intake gestures using sensor fusion (microsoft kinect and inertial sensors) for smart home tele-rehab setting. In: 2012 1st Annual IEEE Healthcare Innovation Conference (2012)
6. Kepski, M., Kwolek, B.: Fall detection on embedded platform using kinect and wireless accelerometer. In: Miesenberger, K., Karshmer, A., Penaz, P., Zagler, W. (eds.) ICCHP 2012, Part II. LNCS, vol. 7383, pp. 407–414. Springer, Heidelberg (2012)
7. Lara, O.D., et al.: Centinela: A human activity recognition system based on acceleration and vital sign data. *Pervasive and Mobile Computing* 8(5), 717–729 (2012)
8. Rijsbergen, C.J.V.: *Information Retrieval*, 2nd edn. Butterworth-Heinemann, Newton (1979)
9. Roggen, D., et al.: Collecting complex activity data sets in highly rich networked sensor environments. In: *Proceedings of the Seventh International Conference on Networked Sensing Systems (INSS)*, pp. 233–240. IEEE CSP (2010)
10. Sagha, H., et al.: Benchmarking classification techniques using the Opportunity human activity dataset. In: *IEEE International Conference on Systems, Man, and Cybernetics* (2011)
11. Satizábal M, H.F., Pérez-Urbe, A.: Relevance metrics to reduce input dimensions in artificial neural networks. In: de Sá, J.M., Alexandre, L.A., Duch, W., Mandic, D.P. (eds.) ICANN 2007. LNCS, vol. 4668, pp. 39–48. Springer, Heidelberg (2007)
12. Shotton, J., et al.: Real-time human pose recognition in parts from single depth images. In: *Computer Vision and Pattern Recognition (CVPR)*, pp. 1297–1304. IEEE (2011)
13. Stiefmeier, T., et al.: Wearable activity tracking in car manufacturing. *IEEE Pervasive Computing* 7(2), 42–50 (2008)

# On Galois Connections and Soft Computing\*

F. García-Pardo, I.P. Cabrera, P. Cordero, and Manuel Ojeda-Aciego

Department of Applied Mathematics, University of Malaga, Spain  
{fgarciap, ipcabrera, pcordero, aciego}@uma.es

**Abstract.** After recalling the different interpretations usually assigned to the term Galois connection, both in the crisp and in the fuzzy case, we survey on several of their applications in Computer Science and, specifically, in Soft Computing.

**Keywords:** Galois connection, Adjunction, Preorder, Fuzzy sets.

## 1 Introduction

Galois connections are ubiquitous; together with adjunctions, their close relatives, occur in a number of research areas, ranging from the most theoretical to the most applied. In a rather poetic tone, the preface of [8] reads, *Galois connections provide the structure-preserving passage between two worlds of our imagination*; and we should add that these two worlds can be so different that the slightest relationship could be seldom ever imagined.

The term *Galois connection* was coined by Øystein Ore [29] (originally, spelled *connexion*) as a general type of correspondence between structures, obviously named after the Galois theory of equations which is an example linking subgroups of automorphisms and subfields. Ore generalized to complete lattices the notion of *polarity*, introduced by Birkhoff [4] several years before, as a fundamental construction which yields from any binary relation two inverse dual isomorphisms. Later, when Kan introduced the *adjoint functors* [19] in a categorical setting, his construction was noticed to greatly resemble that of the Galois connection; actually, in some sense, both notions are interdefinable. The importance of Galois connections/adjunctions quickly increased to an extent that, for instance, the interest of category theorists moved from universal mapping properties and natural transformations to adjointness.

When examining the literature, one can notice a lack of uniformity in the use of the term Galois connection, mainly due to its close relation to adjunctions and that, furthermore, there are two versions of each one. In this paper, after recalling the different interpretations usually assigned to the term Galois connection, both in the crisp and in the fuzzy case, we briefly survey on several of their applications in Computer Science and, specifically, in Soft Computing.

---

\* Partially supported by the Spanish Science Ministry projects TIN12-39353-C04-01, TIN11-28084 and TIN09-14562-C05-01, and Junta de Andalucía project FQM-5233.

## 2 Galois Connections vs. Adjunctions

This section is devoted to establish the different definitions of Galois connection, their characterization and the relation among them. For this purpose, the results will be formulated in the most general framework of preordered sets, that are sets endowed with a reflexive and transitive binary relation.

For a preordered set  $\mathbb{A} = (A, \leq)$ , its *dual* set is  $\mathbb{A}^{op} = (A, \geq)$ . We denote  $a^\downarrow = \{x \in A : x \leq a\}$  and  $a^\uparrow = \{x \in A : x \geq a\}$ . Let  $f : (A, \leq) \rightarrow (B, \leq)$  be a map between preordered sets.

- $f$  is *isotone* if  $a \leq b$  implies  $f(a) \leq f(b)$ , for all  $a, b \in A$ .
- $f$  is *antitone* if  $a \leq b$  implies  $f(b) \leq f(a)$ , for all  $a, b \in A$ .

In the particular case in which  $A = B$ ,

- $f$  is *inflationary* (also called *extensive*) if  $a \leq f(a)$  for all  $a \in A$ .
- $f$  is *deflationary* if  $f(a) \leq a$  for all  $a \in A$ .
- $f$  is *idempotent* if  $f \circ f = f$ .
- $f$  is a *closure operator* if it is inflationary, isotone and idempotent.
- $f$  is a *kernel operator* if it is deflationary, isotone and idempotent.

For a more detailed study of closure and kernel operators we refer to [7].

**Definition 1 (Galois Connections/Adjunctions).** Let  $\mathbb{A} = (A, \leq)$  and  $\mathbb{B} = (B, \leq)$  be preordered sets,  $f : A \rightarrow B$  and  $g : B \rightarrow A$  be two mappings. The pair  $(f, g)$  is called  $a^\dagger$

- Right Galois Connection between  $\mathbb{A}$  and  $\mathbb{B}$ , denoted by  $(f, g) : \mathbb{A} \dashv \mathbb{B}$ , if

$$a \leq g(b) \text{ if only if } b \leq f(a) \quad \text{for all } a \in A \text{ and } b \in B.$$

- Left Galois Connection between  $\mathbb{A}$  and  $\mathbb{B}$ , we write  $(f, g) : \mathbb{A} \dashv \mathbb{B}$ , if

$$g(b) \leq a \text{ if only if } f(a) \leq b \quad \text{for all } a \in A \text{ and } b \in B.$$

- Adjunction between  $\mathbb{A}$  and  $\mathbb{B}$ , denoted by  $(f, g) : \mathbb{A} \rightleftharpoons \mathbb{B}$ , if

$$a \leq g(b) \text{ if only if } f(a) \leq b \quad \text{for all } a \in A \text{ and } b \in B.$$

- Co-Adjunction between  $\mathbb{A}$  and  $\mathbb{B}$ , denoted by  $(f, g) : \mathbb{A} \rightleftharpoons \mathbb{B}$ , if

$$g(b) \leq a \text{ if only if } b \leq f(a) \quad \text{for all } a \in A \text{ and } b \in B.$$

All of the previous notions can be seen in the literature, in fact, one can even find the same term applied to different notions of connection/adjunction. Although it is true that the four definitions are strongly related, they do not have exactly the same properties; hence, it makes sense to specifically describe what is the

---

<sup>1</sup> The arrow notation for the different versions is taken from [31].

relation between the four notions stated above, together with their corresponding characterizations.

The following theorem states the existence of pairwise biunivocal correspondences between all the notions above. The transition between the two types of adjunctions (connections) relies on using the opposite ordering in *both* preordered sets, whereas the transition between adjunctions to connections and vice versa relies on using the opposite ordering in *just one* of the posets.

**Theorem 1.** *Let  $\mathbb{A} = (A, \leq)$  and  $\mathbb{B} = (B, \leq)$  be preordered sets,  $f : A \rightarrow B$  and  $g : B \rightarrow A$  be two mappings. Then, the following conditions are equivalent*

1.  $(f, g) : \mathbb{A} \leftrightarrow \mathbb{B}$
2.  $(f, g) : \mathbb{A}^{op} \dashv \mathbb{B}^{op}$ .
3.  $(f, g) : \mathbb{A} \rightleftharpoons \mathbb{B}^{op}$ .
4.  $(f, g) : \mathbb{A}^{op} \rightleftharpoons \mathbb{B}$

Observe that, as a direct consequence of this theorem, any property about Galois connections can be extended by duality to the other kind of connections.

*Remark 1.* Obviously, the ordering in which the mappings appear in the pair determines the kind of Galois connection or adjunction. Thus,

1.  $(f, g)$  is a right (left, resp.) Galois connection between  $\mathbb{A}$  and  $\mathbb{B}$  if and only if  $(g, f)$  is a right (left, resp.) Galois connection between  $\mathbb{B}$  and  $\mathbb{A}$ .
2.  $(f, g)$  is an adjunction between  $\mathbb{A}$  and  $\mathbb{B}$  if and only if  $(g, f)$  is a co-adjunction between  $\mathbb{B}$  and  $\mathbb{A}$ .

Any preordered set  $(A, \leq)$  induces an equivalence relation in  $A$  defined as:

$$a_1 \approx a_2 \quad \text{if and only if} \quad a_1 \leq a_2 \quad \text{and} \quad a_2 \leq a_1 \quad \text{for } a_1, a_2 \in A. \quad (1)$$

The notions of maximum and minimum in a poset can be extended to preordered sets as follows: an element  $a \in A$  is a *p-maximum* (*p-minimum* resp.) for a set  $X \subseteq A$  if  $a \in X$  and  $x \leq a$  ( $a \leq x$ , resp.) for all  $x \in X$ . The set of p-maximum (p-minimum) of  $X$  will be denoted as  $\text{p-max } X$  ( $\text{p-min } X$ , resp.). Observe that, in a preordered set, different elements can be p-maximum for a set  $X$ , but, in this case,  $a_1, a_2 \in \text{p-max } X$  implies  $a_1 \approx a_2$ .

**Theorem 2.** *Let  $\mathbb{A} = (A, \leq)$ ,  $\mathbb{B} = (B, \leq)$  be two preordered sets,  $f : A \rightarrow B$  and  $g : B \rightarrow A$  be two mappings. The following conditions are equivalent:*

- i)  $(f, g) : \mathbb{A} \leftrightarrow \mathbb{B}$ .
- ii)  $f$  and  $g$  are antitone maps, and  $g \circ f, f \circ g$  are inflationary maps.
- iii)  $f(a)^\downarrow = g^{-1}(a^\uparrow)$  for all  $a \in A$ .
- iv)  $g(b)^\downarrow = f^{-1}(b^\uparrow)$  for all  $b \in B$ .
- v)  $f$  is antitone and  $g(b) \in \text{p-max } f^{-1}(b^\uparrow)$  for all  $b \in B$ .
- vi)  $g$  is antitone and  $f(a) \in \text{p-max } g^{-1}(a^\uparrow)$  for each  $a \in A$ .

Theorem 1 and Theorem 2 provide characterizations for the different Galois connections/adjunctions that are summarized in Table 1.

**Table 1.** Summary of definitions and equivalent characterizations

<i>Galois Connections</i>	
Right Galois Connections between $\mathbb{A}$ and $\mathbb{B}$ $(f, g): \mathbb{A} \dashv \vdash \mathbb{B}$	Left Galois Connections between $\mathbb{A}$ and $\mathbb{B}$ $(f, g): \mathbb{A} \dashv \vdash \mathbb{B}$
$b \leq f(a) \Leftrightarrow a \leq g(b)$ for all $a \in A$ and $b \in B$	$f(a) \leq b \Leftrightarrow g(b) \leq a$ for all $a \in A$ and $b \in B$
$f$ and $g$ are antitone and $g \circ f$ and $f \circ g$ are inflationary	$f$ and $g$ are antitone and $g \circ f$ and $f \circ g$ are deflationary
$f(a)^\downarrow = g^{-1}(a^\uparrow)$ for all $a \in A$	$f(a)^\uparrow = g^{-1}(a^\downarrow)$ for all $a \in A$
$g(b)^\downarrow = f^{-1}(b^\uparrow)$ for all $b \in B$	$g(b)^\uparrow = f^{-1}(b^\downarrow)$ for all $b \in B$
$f$ is antitone and $g(b) \in \text{p-max } f^{-1}(b^\uparrow)$ for all $b \in B$	$f$ is antitone and $g(b) \in \text{p-min } f^{-1}(b^\downarrow)$ for all $b \in B$
$g$ is antitone and $f(a) \in \text{p-max } g^{-1}(a^\uparrow)$ for all $a \in A$	$g$ is antitone and $f(a) \in \text{p-min } g^{-1}(a^\downarrow)$ for all $a \in A$
<i>Adjunctions</i>	
Adjunction between $\mathbb{A}$ and $\mathbb{B}$ $(f, g): \mathbb{A} \rightleftarrows \mathbb{B}$	co-Adjunction between $\mathbb{A}$ and $\mathbb{B}$ $(f, g): \mathbb{A} \rightleftarrows \mathbb{B}$
$f(a) \leq b \Leftrightarrow a \leq g(b)$ for all $a \in A$ and $b \in B$	$b \leq f(a) \Leftrightarrow g(b) \leq a$ for all $a \in A$ and $b \in B$
$f$ and $g$ are isotone, $g \circ f$ is inflationary and $f \circ g$ is deflationary	$f$ and $g$ are isotone, $g \circ f$ is deflationary and $f \circ g$ is inflationary
$f(a)^\uparrow = g^{-1}(a^\downarrow)$ for all $a \in A$	$f(a)^\downarrow = g^{-1}(a^\uparrow)$ for all $a \in A$
$g(b)^\uparrow = f^{-1}(b^\downarrow)$ for all $b \in B$	$g(b)^\downarrow = f^{-1}(b^\uparrow)$ for all $b \in B$
$f$ is isotone and $g(b) \in \text{p-max } f^{-1}(b^\downarrow)$ for all $b \in B$	$f$ is isotone and $g(b) \in \text{p-min } f^{-1}(b^\uparrow)$ for all $b \in B$
$g$ is isotone and $f(a) \in \text{p-min } g^{-1}(a^\downarrow)$ for all $a \in A$	$g$ is isotone and $f(a) \in \text{p-max } g^{-1}(a^\uparrow)$ for all $a \in A$

**Theorem 3.** Let  $\mathbb{A} = (A, \leq), \mathbb{B} = (B, \leq)$  be two preordered sets,  $f : A \rightarrow B$  and  $g : B \rightarrow A$  be two mappings. If  $(f, g): \mathbb{A} \rightleftarrows \mathbb{B}$ , where  $\rightleftarrows \in \{\dashv, \vdash, \rightleftarrows, \rightleftarrows\}$ , then,  $(f \circ g \circ f)(a) \approx f(a)$ , for all  $a \in A$ , and  $(g \circ f \circ g)(b) \approx g(b)$  for all  $b \in B$ . Moreover,

1. If  $(f, g)$  is a left and right Galois connection (adjunction and co-adjunction resp.) then  $(g \circ f)(a) \approx a$  for all  $a \in A$  and  $(f \circ g)(b) \approx b$  for all  $b \in B$ .
2. If  $(f, g)$  is a (left or right) Galois connection and a (co-) adjunction then  $f(a_1) \approx f(a_2)$  for all  $a_1, a_2 \in A$  with  $a_1 \leq a_2$ , and  $g(b_1) \approx g(b_2)$  for all  $b_1, b_2 \in B$  with  $b_1 \leq b_2$ .

Moreover, for any preordered set  $\mathbb{A} = (A, \leq)$ , the quotient set  $A/\approx$  with the relation defined as “ $[a_1] \leq [a_2]$  iff  $a_1 \leq a_2$ ” is a partial ordered set (poset) denoted as  $\mathbb{A}/\approx$ . Theorem 2 allows to translate Galois connections to the quotient posets as follows.

**Theorem 4.** Let  $\mathbb{A} = (A, \leq)$  and  $\mathbb{B} = (B, \leq)$  be two preordered sets and let  $\rightleftarrows \in \{\dashv, \vdash, \rightleftarrows, \rightleftarrows\}$ . If  $(f, g): \mathbb{A} \rightleftarrows \mathbb{B}$  then  $(f_\approx, g_\approx): \mathbb{A}/\approx \rightleftarrows \mathbb{B}/\approx$  where  $f_\approx([a]) = [f(a)]$  and  $g_\approx([b]) = [g(b)]$  for all  $a \in A$  and  $b \in B$ .

Since any equivalence relation is a preorder, Galois connections between two sets endowed with equivalence relations can be considered. But the properties that we obtain on these cases are not significative as the following corollary shows.

**Corollary 1.** Let  $\mathbb{A} = (A, \leq), \mathbb{B} = (B, \leq)$  be two preordered sets,  $f : A \rightarrow B$  and  $g : B \rightarrow A$  be two mappings.

1.  $(f, g)$  is a left and right Galois connection (adjunction and co-adjunction, resp.) if and only if  $f_{\approx}$  and  $g_{\approx}$  are inverse mappings ( $g_{\approx} = f_{\approx}^{-1}$ ).
2.  $(f, g)$  is a right and left Galois connection, and adjunction and a co-adjunction if and only if both relations  $\leq$  are equivalence relations and  $f_{\approx}$  and  $g_{\approx}$  are inverse mappings.

*Example 1.* Consider the set  $\mathbb{P}$  of propositional logic programs on a finite set  $\{p_1, p_2, \dots, p_n\}$  of propositional symbols, and  $\mathbb{B}^n$  the set of chains of  $n$  digits, which will be interpreted as assignments of truth-value to the corresponding propositional symbol. Define  $\mathbb{P}_1 \leq \mathbb{P}_2$  if and only if their least models satisfy  $lm(\mathbb{P}_1) \subseteq lm(\mathbb{P}_2)$ . This relation is reflexive and transitive, but not antisymmetric.

We define a mapping  $f: \mathbb{P} \rightarrow \mathbb{B}^*$  by assigning to each program  $P$  the chain of Boolean values corresponding to the least model of  $P$ . Conversely, a mapping  $g: \mathbb{B}^* \rightarrow \mathbb{P}$  assigns to each chain in  $\mathbb{B}^*$  the (trivial) program consisting just of the fact corresponding to the propositional symbols with truth-value 1. It is not difficult to check that  $(f, g)$  is both an adjunction and a co-adjunction.  $\square$

In the particular case of posets, from Theorem 3 and Theorem 2, we obtain:

**Theorem 5.** *Let  $\mathbb{A} = (A, \leq)$  and  $\mathbb{B} = (B, \leq)$  be posets. If  $(f, g): \mathbb{A} \rightleftharpoons \mathbb{B}$  where  $\rightleftharpoons \in \{\leftarrow, \rightarrow, \rightrightarrows, \rightleftharpoons\}$  then  $g \circ f \circ g = g$  and  $f \circ g \circ f = f$  and therefore*

- If  $(f, g): \mathbb{A} \leftarrow \mathbb{B}$  then  $g \circ f$  and  $f \circ g$  are closure operators.
- If  $(f, g): \mathbb{A} \rightarrow \mathbb{B}$  then  $g \circ f$  and  $f \circ g$  are kernel operators.
- If  $(f, g): \mathbb{A} \rightrightarrows \mathbb{B}$  then  $g \circ f$  is a closure operator and  $f \circ g$  is a kernel operator.
- If  $(f, g): \mathbb{A} \rightleftharpoons \mathbb{B}$  then  $g \circ f$  is a kernel operator and  $f \circ g$  is a closure operator.

### 3 Fuzzy Galois Connections

Since Lotfi Zadeh introduced Fuzzy Set Theory by considering the unit interval as truthfulness/membership degree structure, a wide range of algebraic structures has been used to this aim. The most usual structure in this context is that of residuated lattice,  $\mathbb{L} = (L, \vee, \wedge, 1, 0, \otimes, \rightarrow)$ , introduced in the 1930s by Dilworth [9] and used in the context of fuzzy logic by Goguen [14]. Thus, an  $\mathbb{L}$ -fuzzy set is a mapping from the universe set to the membership values structure  $X: U \rightarrow L$  where  $X(u)$  means the degree in which  $x$  belongs to  $X$ . Given  $X$  and  $Y$  two  $\mathbb{L}$ -fuzzy sets,  $X$  is said to be *included in*  $Y$ , denoted as  $X \subseteq Y$ , if  $X(u) \leq Y(u)$  for all  $u \in U$ . An  $\mathbb{L}$ -fuzzy binary relation on  $U$  is an  $\mathbb{L}$ -fuzzy subset of  $U \times U$ ,  $\rho: U \times U \rightarrow L$ , and it is said to be:

- *reflexive* if  $\rho(a, a) = 1$  for all  $a \in U$ .
- *transitive* if  $\rho(a, b) \otimes \rho(b, c) \leq \rho(a, c)$  for all  $a, b, c \in U$ .
- *symmetric* if  $\rho(a, b) = \rho(b, a)$  for all  $a, b \in U$ .
- *antisymmetric* if  $\rho(a, b) = \rho(b, a) = 1$  implies  $a = b$ , for all  $a, b \in U$ .

An  $\mathbb{L}$ -fuzzy preordered set is a pair  $(U, \rho_U)$  in which  $\rho_U$  is a reflexive and transitive  $\mathbb{L}$ -fuzzy relation. A (crisp) preordering can be given from  $(U, \rho_U)$  by considering

its 1-cut ( $a \leq_U b$  iff  $\rho_U(a, b) = 1$ ). If  $\rho_U$  is antisymmetric then  $(U, \rho_U)$  is said to be an  $\mathbb{L}$ -fuzzy poset and, in this case,  $(U, \leq_U)$  is a (crisp) poset. From now on, when no confusion arises, we will omit the prefix “ $\mathbb{L}$ ”.

For any fuzzy preordered set  $\mathbb{U} = (U, \rho_U)$ , its dual fuzzy preordered set is defined as  $\mathbb{U}^{op} = (U, \rho_U^{-1})$  where  $\rho_U^{-1}(a, b) = \rho_U(b, a)$  for all  $a, b \in U$ .

For every element  $a \in U$ , the fuzzy extension of upper and lower closure  $a^\uparrow$  and  $a^\downarrow : U \rightarrow L$  are given by  $a^\downarrow(u) = \rho_U(u, a)$  and  $a^\uparrow(u) = \rho_U(a, u)$  for all  $u \in U$ .

A *p-maximum* (resp. *p-minimum*) for a fuzzy set  $X$  is an element  $a$  satisfying

- $X(a) = 1$  and
- $X \subseteq a^\downarrow$  (resp.  $X \subseteq a^\uparrow$ ).

Observe that *p-minimum* and *p-maximum* elements are not necessarily unique. If the fuzzy relation is antisymmetric, then *p-maximum* (*minimum*, resp.) is a singleton.

Let  $\mathbb{A} = (A, \rho_A)$  and  $\mathbb{B} = (B, \rho_B)$  be fuzzy preordered sets. A mapping  $f : A \rightarrow B$  is said to be

- *isotone* if  $\rho_A(a_1, a_2) \leq \rho_B(f(a_1), f(a_2))$  for each  $a_1, a_2 \in A$ .
- *antitone* if  $\rho_A(a_1, a_2) \leq \rho_B(f(a_2), f(a_1))$  for each  $a_1, a_2 \in A$ .

Moreover, a mapping  $f : A \rightarrow A$  is said to be

- *inflationary* if  $a \leq_A f(a)$  for all  $a \in A$ .
- *deflationary* if  $f(a) \leq_A a$  for all  $a \in A$ .

The definition of *idempotent* mapping, *closure* operator and *kernel* operator follows in the same way as crisp case.

**Definition 2 (Fuzzy Galois Connections/Adjunctions).** Let  $\mathbb{A} = (A, \rho_A)$ ,  $\mathbb{B} = (B, \rho_B)$  be fuzzy preordered sets,  $f : A \rightarrow B$  and  $g : B \rightarrow A$  be two mappings.

- $(f, g) : \mathbb{A} \dashv \mathbb{B}$ , if  $\rho_A(a, g(b)) = \rho_B(b, f(a))$  for all  $a \in A$  and  $b \in B$ .
- $(f, g) : \mathbb{A} \dashv \overleftarrow{\mathbb{B}}$ , if  $\rho_A(g(b), a) = \rho_B(f(a), b)$  for all  $a \in A$  and  $b \in B$ .
- $(f, g) : \mathbb{A} \overleftarrow{\dashv} \mathbb{B}$ , if  $\rho_A(a, g(b)) = \rho_B(f(a), b)$  for all  $a \in A$  and  $b \in B$ .
- $(f, g) : \mathbb{A} \overleftarrow{\dashv} \overleftarrow{\mathbb{B}}$ , if  $\rho_A(g(b), a) = \rho_B(b, f(a))$  for all  $a \in A$  and  $b \in B$ .

*Remark 2.* Theorem 1 can be straightforwardly extended to the fuzzy case and, therefore, any property given for fuzzy Galois connection can be translated to the other cases.

As far as we know, all the fuzzy extension of the notions of Galois connections (and adjunctions) in the literature are given on the particular case of considering the fuzzy poset (with the properties induced by the truthfulness values structure) in which elements are fuzzy sets and the fuzzy relation is related to the assertion "to be a subset of" in a fuzzy setting (see Equation 2).

*Example 2.* Let  $\mathbb{L} = (L, \vee, \wedge, 1, 0, \otimes, \rightarrow)$  be a complete residuated lattice and  $U$  be the universe set. Then  $(\mathbb{L}^U, \cup, \cap, U, \emptyset, \otimes, \rightarrow)$  is a complete residuated lattice

where  $(X \cup Y)(u) = X(u) \vee Y(u)$ ,  $(X \cap Y)(u) = X(u) \wedge Y(u)$ ,  $\emptyset(u) = 0$ ,  $U(u) = 1$ ,  $(X \otimes Y)(u) = X(u) \otimes Y(u)$  and  $(X \rightarrow Y)(u) = X(u) \rightarrow Y(u)$  for all  $u \in U$ .

The  $\mathbb{L}$ -fuzzy binary relation “to be a subset of” is defined as follows

$$S(X, Y) = \bigwedge_{u \in U} (X(u) \rightarrow Y(u)) \tag{2}$$

Thus, the inclusion of fuzzy sets  $\subseteq$  can be obtained from  $S$  as follows:  $X \subseteq Y$  if and only if  $S(X, Y) = 1$ . Observe that  $(\mathbb{L}^U, \subseteq)$  is a complete lattice.

Let  $f : A \rightarrow B$  be a mapping,  $f : \mathbb{L}^A \rightarrow \mathbb{L}^B$  and  $f^{-1} : \mathbb{L}^B \rightarrow \mathbb{L}^A$  defined as

$$f(X)(b) = \bigvee \{X(x) \mid f(x) = b\} \quad f^{-1}(Y)(a) = Y(f(a)) \tag{3}$$

for all  $b \in B, a \in A$ . Then,  $(f, f^{-1}) : (\mathbb{L}^A, S) \rightleftharpoons (\mathbb{L}^B, S)$ .

**Notation 1** *From now on, we will use the following notation just introduced in (3): for a mapping  $f : A \rightarrow B$  and a fuzzy subset  $Y$  of  $B$ , the fuzzy set  $f^{-1}(Y)$  is defined as  $f^{-1}(Y)(a) = Y(f(a))$ , for all  $a \in A$ .*

*Example 3 (See [2]).* Let  $\mathbb{L} = (L, \vee, \wedge, 1, 0, \otimes, \rightarrow)$  be a complete residuated lattice. Let  $A, B$  be two sets and  $I : A \times B \rightarrow L$  be an  $\mathbb{L}$ -fuzzy relation. For all  $X \in \mathbb{L}^A$  and  $Y \in \mathbb{L}^B$ , define

$$X^\Delta(b) = \bigwedge_{a \in A} (X(a) \rightarrow I(a, b)) \quad Y^\nabla(a) = \bigwedge_{b \in B} (Y(b) \rightarrow I(a, b))$$

The pair  $(\Delta, \nabla)$  is a fuzzy Galois connection between  $(\mathbb{L}^A, S_A)$  and  $(\mathbb{L}^B, S_B)$ .  $\square$

**Theorem 6.** *Let  $\mathbb{L} = (L, \vee, \wedge, 1, 0, \otimes, \rightarrow)$  be a complete residuated lattice,  $\mathbb{A} = (A, \rho_A), \mathbb{B} = (B, \rho_B)$  be  $\mathbb{L}$ -fuzzy preordered sets and  $f : A \rightarrow B$  and  $g : B \rightarrow A$  be two mappings. The following conditions are equivalent:*

- i)  $(f, g) : \mathbb{A} \leftrightarrow \mathbb{B}$ .*
- ii)  $f$  and  $g$  are antitone maps, and  $g \circ f, f \circ g$  are inflationary maps.*
- iii)  $f(a)^\downarrow = g^{-1}(a^\uparrow)$  for all  $a \in A$ .*
- iv)  $g(b)^\downarrow = f^{-1}(b^\uparrow)$  for all  $b \in B$ .*
- v)  $f$  is antitone and  $g(b) \in \text{p-max } f^{-1}(b^\uparrow)$  for all  $b \in B$ .*
- vi)  $g$  is antitone and  $f(a) \in \text{p-max } g^{-1}(a^\uparrow)$  for each  $a \in A$ .*

*Proof.* According to Remark 2, it suffices to prove that *i), ii), iii)* and *v)* are equivalent. Observe that  $f(a)^\downarrow(b) = \rho_B(b, f(a))$  and  $g^{-1}(a^\uparrow)(b) = \rho_A(a, g(b))$  by the definition (see Notation 1) then *i)* and *iii)* are trivially equivalent.

**i)  $\Rightarrow$  ii)** Let  $a \in A$ . As  $\rho_B$  is reflexive,  $1 = \rho_B(f(a), f(a))$  and by hypothesis,  $\rho_A(a, g(f(a))) = \rho_B(f(a), f(a)) = 1$ , thus,  $g \circ f$  is inflationary. Given  $a_1, a_2 \in A$ , it holds that  $\rho_A(a_1, a_2) = \rho_A(a_1, a_2) \otimes 1 = \rho_A(a_1, a_2) \otimes \rho_A(a_2, g(f(a_2)))$ . Being  $\rho_A$  transitive,  $\rho_A(a_1, a_2) \leq \rho_A(a_1, g(f(a_2))) = \rho_B(f(a_2), f(a_1))$ . That is,  $f$  is antitone. Similarly, we prove that  $f \circ g$  is inflationary and  $g$  is antitone.



- ii)  $\Rightarrow$  v)  $f$  is antitone, by the hypothesis. For all  $b \in B$ , since  $f \circ g$  is inflationary,  $1 = \rho_B(b, f(g(b))) = f^{-1}(b^\uparrow)(g(b))$ . On the other hand, since  $\rho_A$  is transitive,  $g(b)^\downarrow(a) = \rho_A(a, g(b)) \leq \rho_A(a, g(f(a))) \otimes \rho_A(g(f(a)), g(b))$ . As  $g \circ f$  is inflationary and  $g$  antitone,  $g(b)^\downarrow(a) \leq 1 \otimes \rho_A(g(f(a)), g(b)) = \rho_A(g(f(a)), g(b)) \geq \rho_B(b, f(a)) = f^{-1}(b^\uparrow)(a)$ .
- v)  $\Rightarrow$  i) It is sufficient to prove that  $\rho_B(b, f(a)) \geq \rho_A(a, g(b))$ . Firstly note that  $f^{-1}(b^\uparrow)(g(b)) = 1$  is equivalent to  $f \circ g$  being inflationary. Then,

$$\begin{aligned} \rho_B(b, f(a)) &\geq \rho_B(b, f(g(b))) \otimes \rho_B(f(g(b)), f(a)) \\ &= 1 \otimes \rho_B(f(g(b)), f(a)) \geq \rho_A(a, g(b)) \end{aligned}$$

□

Remark 2 and Theorem 6 provide similar characterizations for the different fuzzy Galois connections/adjunctions that are summarized in Table 1.

As we have mentioned at the beginning of this section, any fuzzy preordered set  $\mathbb{A} = (A, \rho_A)$ , defines a (crisp) preordered set  $\mathbb{A}_c = (A, \leq_A)$  where  $a \leq_A b$  iff  $\rho_A(a, b) = 1$ . It is also straightforward that the pair  $\mathbb{A}/\approx = (A/\approx, \rho_{A/\approx})$  where  $\approx$  is the equivalence relation given by

$$a \approx b \text{ if and only if } \rho_A(a, b) = \rho_A(b, a) = 1 \tag{4}$$

and  $\rho_{A/\approx}$  is defined as  $\rho_{A/\approx}([a], [b]) = \rho_A(a, b)$  is a fuzzy poset. Moreover, any mapping  $f$  between fuzzy preordered sets defines a mapping  $f_\approx$  between the quotient poset in the same way as in Theorem 4.

**Theorem 7.** Let  $\mathbb{A} = (A, \rho_A)$  and  $\mathbb{B} = (B, \rho_B)$  be two fuzzy preordered sets and two mappings  $f: A \rightarrow B$  and  $g: B \rightarrow A$ . Then, for  $\Leftrightarrow \in \{\leftarrow, \rightarrow, \Leftarrow, \Rightarrow\}$ ,

1.  $(f, g): \mathbb{A} \Leftrightarrow \mathbb{B}$  implies  $(f, g): \mathbb{A}_c \Leftrightarrow \mathbb{B}_c$ .
2.  $(f, g): \mathbb{A} \Leftrightarrow \mathbb{B}$  if and only if  $(f_\approx, g_\approx): \mathbb{A}/\approx \Leftrightarrow \mathbb{B}/\approx$ .

The following example shows that the converse of item 1 above is not true.

*Example 4.* Let  $\mathbb{L}$  be the (product) residuated lattice  $([0, 1], \sup, \inf, 1, 0, \cdot, \rightarrow)$ . Let  $\mathbb{A} = (A, \rho_A)$  such that  $A = \{a, b\}$ ,  $\rho_A(a, a) = \rho_A(b, b) = 1$ ,  $\rho_A(a, b) = 0.5$  and  $\rho_A(b, a) = 0.2$  and let  $I$  be the identity mapping on  $A$ . Then  $(I, I): \mathbb{A}_c \leftarrow \mathbb{A}_c$  but  $(I, I)$  is not a Galois connection between  $\mathbb{A}$  and  $\mathbb{A}$  because  $0.5 = \rho_A(a, I(b)) \neq \rho_A(b, I(a)) = 0.2$ . □

Observe that, contrariwise to the crisp case, nontrivial fuzzy relations exist that are both equivalencies and partial orders. They are known as fuzzy equalities and are strongly reflexive ( $\rho(a, b) = 1$  iff  $a = b$ ), symmetric and transitive fuzzy relations. Obviously, in these cases, antitone and isotone maps coincide. But there exist nontrivial mappings between fuzzy posets (not fuzzy equalities) that are both antitone and isotone as the following example shows.

*Example 5.* Let  $\mathbb{L}$  be the (product) residuated lattice  $([0, 1], \sup, \inf, 1, 0, \cdot, \rightarrow)$ . Consider  $\mathbb{A} = (\{a, b, c\}, \rho)$  such that  $\rho$  is the  $\mathbb{L}$ -fuzzy preorder given by the table

below, then the map  $f: A \rightarrow A$  with  $f(a) = f(c) = b$  and  $f(b) = a$  is antitone and isotone.

$\rho$	$a$	$b$	$c$
$a$	1	0.5	0.3
$b$	0.5	1	0.2
$c$	0.2	0.1	1

□

**Theorem 8.** Let  $\mathbb{A} = (A, \rho_A)$  and  $\mathbb{B} = (B, \rho_B)$  be fuzzy preordered sets and  $\Leftrightarrow \in \{\leftarrow, \rightarrow, \Leftarrow, \Rightarrow\}$ . If  $(f, g): \mathbb{A} \Leftrightarrow \mathbb{B}$  then, for all  $a \in A, b \in B$ , the following relations hold  $(f \circ g \circ f)(a) \approx f(a)$  and  $(g \circ f \circ g)(b) \approx g(b)$ . Moreover,

- If  $(f, g)$  is both left and right Galois connection (resp., adjunction and co-adjunction) then  $(g \circ f)(a) \approx a$  and  $(f \circ g)(b) \approx b$  for all  $a \in A$  and  $b \in B$ .
- If  $(f, g)$  is a (left or right) Galois connection and a (co-) adjunction then, for all  $a_1, a_2 \in A$ ,  $\rho_A(a_1, a_2) = 1$  implies  $f(a_1) \approx f(a_2)$  and, for all  $b_1, b_2 \in B$ ,  $\rho_B(b_1, b_2) = 1$  implies  $g(b_1) \approx g(b_2)$ .

**Corollary 2.** Let  $\mathbb{A} = (A, \rho_A)$  and  $\mathbb{B} = (B, \rho_B)$  be two fuzzy posets.

- If  $(f, g): \mathbb{A} \leftarrow \mathbb{B}$  then  $g \circ f$  and  $f \circ g$  are closure operators.
- If  $(f, g): \mathbb{A} \rightarrow \mathbb{B}$  then  $g \circ f$  and  $f \circ g$  are kernel operators.
- If  $(f, g): \mathbb{A} \Leftarrow \mathbb{B}$  then  $g \circ f$  is closure operator and  $f \circ g$  is kernel operator.
- If  $(f, g): \mathbb{A} \Rightarrow \mathbb{B}$  then  $g \circ f$  is kernel operator and  $f \circ g$  is closure operator.

## 4 Applications to Computer Science and Soft Computing

Out of the plethora of applications of Galois connections that can be found in CS-related research topics, we have selected just a few to comment a little bit about them. Applications range from the mathematics of program construction to data analysis and formal concept analysis.

**Program Construction.** Some authors propose the use of Galois connections (actually, adjunctions), as suitable calculational specifications: in [25] one can see how to simplify and easily handle data structures problems when using Galois connections. On the other hand, [27] considers them as program specifications, helping in the process of deriving and using an algebra of programming. Another common usage is based on that a Galois connection is a correspondence between two complete lattices that consists of an *abstraction* and *concretisation* functions.

**Constraint Satisfaction Problems (CSPs).** In this context, a well-known Galois connection between sets of relations and sets of (generalized) functions was used in [18] to investigate the algorithmic complexity of CSPs. Continuing this idea, [6] established a link between certain *soft* constraint languages and sets of certain sets determined by algebraic constructs called weighted polymorphisms, resulting in an alternative approach to the study of tractability in valued constraint languages. This approach was recently used in [20] generalizing the notions of polymorphisms and invariant relations to arbitrary categories.

**Logic.** There are strong links between Galois connections and logic. The first one arose in Lawvere's paper on the foundational value of category theory. This is made explicit in [30] which formally defines a Galois Connection (adjunction) between sets of sentences and classes of semantic structures.

In [17] the Information Logic of Galois Connections (ILGC) is introduced as a convenient tool for approximate reasoning about knowledge. Actually, they use adjunctions introduced as generalized rough approximation operations based on information relations. ILGC turns out to be the usual propositional logic together with two modal connectives. This natural inclusion of modal connectives in the framework, enables the study of such as intuitionistic logic [33,11].

**Mathematical Morphology.** Galois connections can be seen as well in the mathematical structure of morphological operations, in the research area known as mathematical morphology. In [15] the authors note the duality between the morphological operations of dilation and erosion, and identify them as the components of an adjunction (by the way, making the proper distinction between Galois connections and adjunctions). Originally, mathematical morphology was applied on binary images, but later extended to grayscale by applying techniques from the fuzzy realm, specifically, using fuzzy Galois connections (adjunctions); a survey on classical and fuzzy approaches of mathematical morphology can be found in [28]. Later, in [22] a further generalization based on lattices is given aimed at unifying morphological and fuzzy algebraic systems. The benefits of considering the different links, in terms of Galois connections, that can be established is exploited in [5], clarifying the links between different approaches in the literature and giving conditions for their equivalence. Recently, mathematical morphology is being studied using ideas and results from formal concept analysis [1].

**Information Processing and Data Analysis.** Another use of Galois connections (adjunctions) can be seen in [12], where Galois connections are generalized from complete lattices to flow algebras (an algebraic structure more general than idempotent semirings, in which distributivity is replaced by monotonicity and the annihilation property is ignored).

Another interesting application can be found in the theory of relational systems: in [16] it was shown that every Galois connection between complete lattices determines an Armstrong system (a closed set of dependencies). More recently, [21] proved the converse, for any given Armstrong system it is possible to define a Galois connection which generates the original Armstrong system.

In [32] the author focuses on the different applications of Galois connections (both types, termed polarities and axialities) to different theories of qualitative data analysis. Specifically, the paper studies some links between axialities (adjunctions) and the area of data analysis.

**Formal Concept Analysis (FCA).** The notion of polarity, given by Birkhoff, is precisely that used by Ganter and Wille in order to define the derivation operators in crisp FCA. In this context, it is well-known that the concept lattices induced by Galois connections and by adjunctions are naturally isomorphic. Authors indistinctly use one or the other approach, for instance [26] considers

the problem of attribute reduction by using axialities (adjunctions) inspired by the reduction method in rough set theory.

The introduction of fuzzy Galois connections [2] lead to the systematic development of fuzzy FCA. In this framework, the fuzzy concept lattices generated from Galois connections and from adjunction need not be isomorphic. In [3] it is shown that the expected isomorphism depends largely on the way the notion of a complement is defined, the usual based on a residuum w.r.t. 0, is replaced by one based on residua w.r.t. arbitrary truth degrees.

Different extensions of fuzzy FCA consider even more general frameworks, some of them use a sub-interval rather than a precise value of the lattice to refer to what extent an object satisfies an attribute [10,23]. Usually, these extensions require to provide a sound minimal set of algebraic requirements for interval-valued implications in order to obtain a Galois connection. Anyway, there are approaches in which this vicissitude can be circumvented [24].

## 5 Conclusions

We have surveyed some applications of Galois connections and adjunctions in Computer Science and Soft Computing. The greater generality of the fuzzy case, which allows to see a single crisp notion from very different perspectives, suggests that it is worth to consider these notions either in a more general setting or by weakening its requirements [13].

## References

1. Alcalde, C., Burusco, A., Díaz, J.C., Fuentes-González, R., Medina, J.: Fuzzy property-oriented concept lattices in morphological image and signal processing. In: Rojas, I., Joya, G., Cabestany, J. (eds.) IWANN 2013, Part II. LNCS, vol. 7903, pp. 246–253. Springer, Heidelberg (2013)
2. Bělohlávek, R.: Fuzzy Galois connections. *Mathematical Logic Quarterly* 45(4), 497–504 (1999)
3. Belohlavek, R., Konecny, J.: Concept lattices of isotone vs. antitone Galois connections in graded setting: Mutual reducibility revisited. *Information Sciences* 199, 133–137 (2012)
4. Birkhoff, G.: *Lattice theory*, vol. 25. Amer. Mathematical Society (1967)
5. Bloch, I.: Duality vs. adjunction for fuzzy mathematical morphology and general form of fuzzy erosions and dilations. *Fuzzy Sets and Systems* 160, 1858–1867 (2009)
6. Cohen, D.A., Creed, P., Jeavons, P.G., Živný, S.: An algebraic theory of complexity for valued constraints: Establishing a galois connection. In: Murlak, F., Sankowski, P. (eds.) MFCS 2011. LNCS, vol. 6907, pp. 231–242. Springer, Heidelberg (2011)
7. Davey, B., Priestley, H.: *Introduction to Lattices and Order*, 2nd edn. Cambridge University Press (2002)
8. Denecke, K., Erné, M., Wismath, S.L.: *Galois connections and applications*, vol. 565. Springer (2004)
9. Dilworth, R.P., Ward, M.: Residuated lattices. *Transactions of the American Mathematical Society* 45, 335–354 (1939)

10. Djouadi, Y., Prade, H.: Interval-valued fuzzy Galois connections: Algebraic requirements and concept lattice construction. *Fundamenta Informaticae* 99(2), 169–186 (2010)
11. Dzik, W., Järvinen, J., Kondo, M.: Intuitionistic propositional logic with Galois connections. *Logic Journal of the IGPL* 18(6), 837–858 (2010)
12. Filipiuk, P., Terepeta, M., Nielson, H., Nielson, F.: Galois connections for flow algebras. In: Bruni, R., Dingel, J. (eds.) *FMOODS/FORTE 2011*. LNCS, vol. 6722, pp. 138–152. Springer, Heidelberg (2011)
13. Frascella, A.: Fuzzy Galois connections under weak conditions. *Fuzzy Sets and Systems* 172(1), 33–50 (2011)
14. Goguen, J.A.: L-fuzzy sets. *J. Math. Anal. Appl.* 18, 145–174 (1967)
15. Heijmans, H.J.A.M., Ronse, C.: The algebraic basis of mathematical morphology I. dilations and erosions. *Computer Vision, Graphics, and Image Processing* 50(3), 245–295 (1990)
16. Järvinen, J.: Pawlak’s information systems in terms of Galois connections and functional dependencies. *Fundamenta Informaticae* 75, 315–330 (2007)
17. Järvinen, J., Kondo, M., Kortelainen, J.: Logics from Galois connections. *Int. J. Approx. Reasoning* 49(3), 595–606 (2008)
18. Jeavons, P.: On the algebraic structure of combinatorial problems. *Theoretical Computer Science* 200(1), 185–204 (1998)
19. Kan, D.M.: Adjoint functors. *Transactions of the American Mathematical Society* 87(2), 294–329 (1958)
20. Kerkhoff, S.: A general Galois theory for operations and relations in arbitrary categories. *Algebra Universalis* 68(3), 325–352 (2012)
21. Kondo, M., Soneda, S., Yoshii, B.: Armstrong systems and Galois connections. In: *Proc IEEE Intl Conf on Granular Computing, GrC 2011*, pp. 342–344 (2011)
22. Maragos, P.: Lattice image processing: a unification of morphological and fuzzy algebraic systems. *J. of Mathematical Imaging and Vision* 22(2-3), 333–353 (2005)
23. Medina, J.: Multi-adjoint property-oriented and object-oriented concept lattices. *Information Sciences* 190, 95–106 (2012)
24. Medina, J., Ojeda-Aciego, M.: On multi-adjoint concept lattices based on heterogeneous conjunctors. *Fuzzy Sets and Systems* 208, 95–110 (2012)
25. Melton, A., Schmidt, D.A., Strecker, G.E.: Galois connections and computer science applications. In: Poigné, A., Pitt, D.H., Rydeheard, D.E., Abramsky, S. (eds.) *Category Theory and Computer Programming*. LNCS, vol. 240, pp. 299–312 (1986)
26. Mi, J.-S., Leung, Y., Wu, W.-Z.: Approaches to attribute reduction in concept lattices induced by axialities. *Knowledge-Based Systems* 23(6), 504–511 (2010)
27. Mu, S.-C., Oliveira, J.: Programming from Galois connections. *Journal of Logic and Algebraic Programming* 81(6), 680–704 (2012)
28. Nachtgael, M., Kerre, E.E.: Classical and fuzzy approaches towards mathematical morphology. *Studies in Fuzziness and Soft Computing* 52, 3–57 (2000)
29. Ore, Ø.: Galois connections. *Trans. Amer. Math. Soc.* 55, 493–513 (1944)
30. Smith, P.: The Galois connection between syntax and semantics. Technical report, Univ Cambridge (2010)
31. Valverde-Albacete, F.J., Peláez-Moreno, C.: Extending conceptualisation modes for generalised formal concept analysis. *Information Sciences* 181, 1888–1909 (2011)
32. Wolski, M.: Galois connections and data analysis. *Fundamenta Informaticae* 60, 401–415 (2004)
33. Zhou, L.: Intuitionistic fuzzy residuated logic and Galois connection. In: *Proc. of 2nd Pacific-Asia Conf on Circuits, Communications and System (PACCS)*, pp. 249–252. IEEE (2010)

# A Proximity-Based Method for Discovery of Generalized Knowledge and Its Incorporation to the Bousi~Prolog System

Pascual Julián-Iranzo<sup>1</sup> and Clemente Rubio-Manzano<sup>2</sup>

<sup>1</sup> Department of Information Technologies and Systems,  
University of Castilla-La Mancha, Spain

`Pascual.Julian@uclm.es`

<sup>2</sup> Department of Information Systems, University of the Bío-Bío, Chile  
`clrubio@ubiobio.cl`

**Abstract.** In this work, a proximity-based generic method for discovery of generalized knowledge is presented and implemented in the framework of a fuzzy logic programming language with a weak unification procedure that uses proximity relations to model uncertainty. This method makes use of the concept of  $\lambda$ -block characterizing the notion of equivalence when working with proximity relations. When the universe of discourse is composed of concepts which are related by proximity, the sets of  $\lambda$ -blocks extracted from that proximity relation can be seen as hierarchical sets of concepts grouped by abstraction level. Then, each group (forming a  $\lambda$ -block) can be labeled, with user help, by way of a more general descriptor in order to simulate a generalization process based on proximity. Thanks to this process, the system can learn concepts that were unknown initially and reply queries that it was not able to answer. The novelty of this work is that it is the first time a method, with analogous features to the one aforementioned, has been implemented inside a fuzzy logic programming framework. In order to check the feasibility of the method we have developed a software tool which have been integrated into the Bousi~Prolog system.

**Keywords:** Fuzzy Logic Programming, Proximity/Similarity Relations, Discovery of Generalized Knowledge.

## 1 Introduction

Logic programming is a declarative programming paradigm well suited for knowledge representation and the inference of new knowledge from old one. However, logic programming does not allow to represent and to manage vagueness in a natural way due to the lack of specific tools and, particularly, by its rigid query answering process. This may be a real limitation when modeling some problems. By instance, logic programming has not a direct ability to manage concepts which are related by its meaning. Hence, it would be interesting to have mechanisms allowing to relate approximate knowledge inside a domain and to grade

such a relation in the context of a logic programming framework. This was the aim that motivates the apparition of similarity-based logic programming [4,10] and proximity-based logic programming [7].

A practical realization of both approaches is *Bousi~Prolog*<sup>1</sup> (BPL, for short) [8], a fuzzy logic language where the classical unification algorithm used in logic programming has been replaced by a new algorithm based on proximity/similarity relations. Hence, its operational mechanism is a variant of the SLD resolution rule introduced in [11]. We have studied how to apply *Bousi~Prolog* for: flexible query answering, advanced pattern matching [6], information retrieval, where textual information is selected or analyzed using an ontology, text cataloging [5], flexible data bases, knowledge-base systems or approximate reasoning [8]. The following example helps to understand the main aspects of the syntax and semantics of this language.

*Example 1.* Suppose a fragment of a database that stores a semantic network with information about people's names and eye colors, as well as the approximate relation between black, brown, green and blue eyes.

```
% BPL directive
:- transitivity(no).

% FACTS
is_a(john, person).      is_a(peter, person).      is_a(mary, person).
eye_color(john,black).  eye_color(peter,brown).  eye_color(mary,blue).

% PROXIMITY EQUATIONS
black~brown =0.8.  green~gray =0.8.  gray~blue =0.8.
brown~green =0.5.  brown~gray =0.5.  green~blue =0.5.  brown~blue =0.2.
```

In a standard Prolog system, if we ask about whether *mary's* eye color is *green*, “?- eye\_color(mary, green)”, the system fails. However *Bousi~Prolog* allows us to obtain the answer “Yes with 0.5”. This is because the BPL system is capable of using the proximity equations for the inference process.

The fact of relating concepts by their meaning, throw open the door to manage linguistic phenomena based on those relationships. For instance: synonymy, antonymy or generality. In this work the spotlight becomes focussed on the last concept.

In a proximity/similarity-based logic programming framework, because of the use of proximity equations in order to relate concepts, we can extract new generalized knowledge from those proximity equations. To be specific, we are interested in the automatization of this generalization process. Therefore the aim of this paper is to present a proximity-based generic method for the discovery of generalized knowledge in the framework of a fuzzy logic programming language with a weak unification procedure that uses proximity equations to model uncertainty. More precisely, we want to implement this method and to integrate it within the BPL system.

<sup>1</sup> *Bousi~Prolog* is publicly available at the URL: <http://dectau.uclm.es/bousi>

Providing the BPL system with this ability improves its operational mechanism, supporting inductive learning of new concepts and, hence, the power to infer new knowledge that the system was unable to infer initially. Then, this is an additional step towards the goal of consolidating **Bousi~Prolog** as a true programming language for soft computing, in general, and computing with words, in particular, since the generalization process is part of ordinary reasoning and a system aiming at to fit the computing with words agenda should manage these cognitive process.

## 2 Knowledge Generalization and Related Work

Generalization is a fundamental property for human reasoning. Given two concepts,  $C_1$  and  $C_2$ ,  $C_1$  is a generalization of  $C_2$  if (i) each instance of  $C_2$  is also a instance of  $C_1$ ; (ii) there exists instances of  $C_1$  which are not instances of  $C_2$ . Equivalently, it is said that  $C_2$  is a specialization of  $C_1$ . For example, “animal” is a generalization of “bird” because every “bird” is an “animal”, and there are animals which are not birds. Linguistic generalization/specialization is well defined by means of the pair superordinate/hyponym.

In software systems, generalization processing has been handled with many different techniques. Particularly, it has been performed using thesauri that provide the pair superordinate/hyponym or ontologies where a hierarchy relation between concepts is represented and supported. Another solution has been the abstraction of knowledge from specific knowledge [9].

In order to carry out this task, data mining techniques have been employed, which simulate the generalization process from the mined data selected according to a criterion. The output of this process is a hierarchy, structured by levels, where the top level contains the most general data and the next levels contains more specific data. Ideally, the bottom level contains the initial mined data. For example, given the data set {“Sweden”, “Denmark”, “United Kingdom”, “Germany”, “France”, “Italy”, “Spain”, “Portugal”}, it can be performed a generalization process such that the original set is divided in the subgroups {“Sweden”, “Denmark”, “United Kingdom”}, {“Germany”, “France”} and {“Italy”, “Spain”, “Portugal”}, attending to a location criterion, and then, respectively assigned to them the more general descriptors: “Northern Europe”, “Western Europe”, and “Southern Europe”. Finally these concepts, in the new abstraction level, are also grouped and the more general descriptor “Europe” is assigned to the new aggregation. This technique is named “attributed-oriented induction” [3] and it allows to obtain a concept hierarchy starting from the elemental data available in the considered system. A fuzzy extension of this technique was applied in [1] for the discovery of abstract knowledge in fuzzy databases. In that work similarity classes were used as grouping units. We aim to extend the reach of this mechanism and transfer it to a fuzzy programming framework that works with proximity relations, allowing the discovery of concepts starting from the proximity  $\lambda$ -blocks which characterize this kind of fuzzy relations.



### 3 Proximity Relations

A *binary fuzzy relation* on a (crisp) set  $U$  is a fuzzy subset on  $U \times U$  (that is, a mapping  $U \times U \rightarrow [0, 1]$ ). If  $R$  is a fuzzy relation on  $U$ , the  $\lambda$ -cut  $\mathcal{R}_\lambda = \{\langle x, y \rangle \mid \mathcal{R}(x, y) \geq \lambda\}$  (which is an ordinary relation on  $U$ ). There are some important properties that fuzzy relations may have: **Reflexive**, if  $\mathcal{R}(x, x) = 1$  for any  $x \in U$ ; **Symmetric**, if  $\mathcal{R}(x, y) = \mathcal{R}(y, x)$  for any  $x, y \in U$ ; and **Transitive**, if  $\mathcal{R}(x, z) \geq \mathcal{R}(x, y) \wedge \mathcal{R}(y, z)$  for any  $x, y, z \in U$  (where the operator ‘ $\wedge$ ’ is the minimum of two elements).

A *proximity relation* is a binary fuzzy relation which is reflexive and symmetric. A proximity relation is characterized by a set  $\Lambda = \{\lambda_1, \dots, \lambda_n\}$  of approximation levels. We say that a value  $\lambda \in \Lambda$  is a *cut value*. A special, and well-known, type of proximity relations are *similarity relations*, which are nothing but transitive proximity relations. There exists a close relation between similarity relations and equivalence relations: the  $\lambda$ -cut of a similarity relation  $\mathcal{R}$  on  $U$ ,  $\mathcal{R}_\lambda$ , is an equivalence relation on  $U$ . Proximity relations are more complicated in this respect. For a proximity on a set  $U$ , the notion of equivalence class splits into two different concepts: the blocks and the classes of proximity. Given a proximity relation  $\mathcal{R}$  on a set  $U$ , a *proximity block of level  $\lambda$*  (or  $\lambda$ -block) is a subset of  $U$  such that the restriction of  $\mathcal{R}_\lambda$  to this subset is a total relation, and maximal with this property. The effective computations of  $\lambda$ -blocks in a proximity relation is a difficult matter which is linked with the problem of finding all maximal cliques on an undirected graph [2]. On the other hand, the *proximity class of level  $\lambda$*  (or  $\lambda$ -Class) of an element  $x \in U$  is the subset  $\mathcal{K}_\lambda(x) = \{y \in U \mid \mathcal{R}(x, y) \geq \lambda\}$  of those elements of  $U$  that are approximate to  $x$  (at a certain level  $\lambda$ ). Observe that, for the special case of a similarity relation,  $\lambda$ -blocks and  $\lambda$ -classes coalesce. Hence, in this case  $\lambda$ -blocks can be computed efficiently computing the corresponding  $\lambda$ -classes. The following example illustrate the concept of  $\lambda$ -block in a proximity relation.

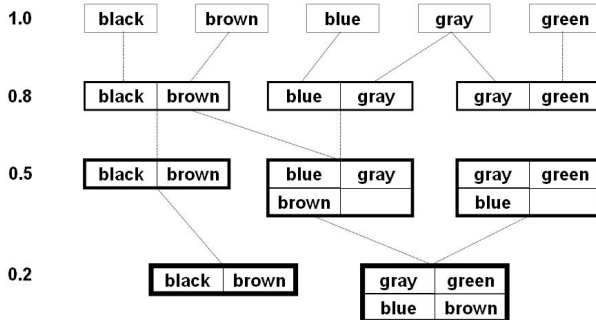


Fig. 1. Blocks diagram for the proximity relation of Example 2

*Example 2.* Let  $\mathcal{R}$  be the proximity relation generated by the proximity equations in Example 1. Figure 1 describe “level by level” the blocks structure of this proximity relation, which is characterized by a set  $\Lambda = \{0.2, 0.5, 0.8, 1\}$  of approximation levels. In particular, for the cut value  $\lambda=0.5$ , there exist three blocks of level 0.5:

$$\mathcal{B}_1^{0.5} = \{brown, green, gray\}, \mathcal{B}_2^{0.5} = \{green, gray, blue\}, \mathcal{B}_3^{0.5} = \{black, brown\}.$$

On the other hand, the classes of level 0.5 for each one of the elements are:

$$\begin{aligned} \mathcal{K}_{0.5}(black) &= \{black, brown\}. \\ \mathcal{K}_{0.5}(brown) &= \{brown, black, gray, green\}. \\ \mathcal{K}_{0.5}(blue) &= \{blue, gray, green\}. \\ \mathcal{K}_{0.5}(gray) &= \{gray, blue, green, brown\}. \\ \mathcal{K}_{0.5}(green) &= \{green, gray, blue, brown\}. \end{aligned}$$

Note also that the block diagram of Figure 1 determines completely  $\mathcal{R}$ .

In this paper we are interested in proximity relations on syntactic domains representing concepts. When the universe of discourse is composed of concepts which are related under a particular abstraction criterion, a proximity relation can model the closeness of this concepts. Then, the sets of  $\lambda$ -blocks extracted from that proximity relation can be seen as sets of concepts grouped by abstraction criterion that form a hierarchy of abstraction levels. Then, each  $\lambda$ -block can be labeled by way of a more general descriptor in order to simulate a generalization process based on proximity relations.

*Example 3.* Attending to an abstraction criterion of location, the relationships between the concepts of the set  $\{canada, usa, mexico\}$ , can be model by a proximity relation whose entries may be:  $\mathcal{R}(canada, usa) = 0.8$ ,  $\mathcal{R}(canada, mexico) = 0.5$ ,  $\mathcal{R}(usa, mexico) = 0.8$ , which is characterized by the set  $\Lambda = \{0.5, 0.8, 1\}$  of approximation levels. At level  $\lambda = 0.5$ , there exist only one block  $\mathcal{B}_1^{0.5} = \{canada, usa, mexico\}$  that can be labeled by the more general descriptor “north\_america”.

## 4 A Generic Approximation

The management of a generalization process in the context of a fuzzy logic language based on weak unification pass through representing generalization in an explicit way by means of the addition of specific proximity equations. On the contrary, some difficulties can arise when launching queries where a generalization process is involved. For instance, considering Example 1, if we ask about people with “light” eyes, the system is unable to answer that query because the generalized information that green, blue or gray eyes are light eyes was not modeled. A solution to this problem, as we are proposing, would be to produce the additional proximity equations thru a semi-automatic generalization process able to classify concepts into groups on the basis of user choices identifying each concept with a more general descriptor.

In the sequel, we propose a method to handle the generalization process in the context of a proximity-based logic programming language. In order to do that, it is necessary an algorithm capable to obtain proximity  $\lambda$ -blocks. Informally, a step by step definition of the method is as follows: 1) start from a set of proximity equations (defined by a user or taken from a thesaurus); 2) generate a proximity or a similarity relation to suit; 3) execute the algorithm to generate proximity  $\lambda$ -blocks<sup>2</sup>; 4) the concepts grouped by  $\lambda$ -blocks which are susceptible to generalization are labeled by means of a unique abstract descriptor identifying each one among the others (this step needs human intervention); 5) new proximity equations are generated, putting in relation this new abstract descriptor with each element belonging to the generalized set described by that descriptor, thus completing a hierarchy level; 6) the new set of proximity equations, characterizing a hierarchy of concepts, are loaded into a fuzzy logic programming system based on weak unification. Then, these new concepts can participate in the inference process, allowing the programmer to launch queries on concepts that were initially unknown for the system and that have been generated semi-automatically.

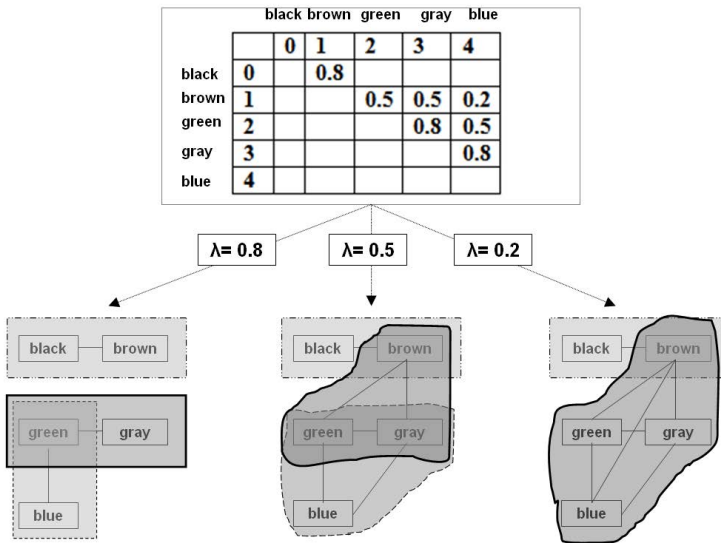


Fig. 2. Generating Proximity Blocks

The formalization of some aspects of this method are discussed next. First, we define an algorithm that automatically computes a hierarchy of concepts from the set of proximity equations.

<sup>2</sup> Note that, for the special case of similarity relations,  $\lambda$ -classes will be used instead of  $\lambda$ -blocks.

**Algorithm 1**

**Input:** A set of proximity equations,  $E$ , and a set of approximation levels  $\Lambda = \{\lambda_1, \dots, \lambda_n\}$ .

**Output:** A hierarchy of proximity blocks,  $\mathcal{J}$ .

**Inicialisation:**  $\mathcal{J} := \emptyset$ ;  $\mathcal{R} := \text{generateProximityRel}(E)$ .

**for each level**  $\lambda \in \Lambda$ :

1.  $PB^\lambda := \text{generateProximityBlocks}(\mathcal{R}_\lambda)$

2. **insert**  $PB^\lambda$  **in**  $\mathcal{J}$

**Return**  $\mathcal{J}$

where `generateProximityBlocks` is a procedure that generates all blocks of a certain approximation level. This procedure is based on a fuzzy version of the well-known algorithm for finding all maximal cliques of an undirected graph [2]. This works like a fuzzy clustering algorithm based on *lambda*-cuts of  $\mathcal{R}$ , i.e., in each step cliques of elements connected by proximity are computed.

The following items show the behavior of the initial steps of our method and Algorithm 1 for the particular case of Example 1:

1. A set  $\Lambda$  of proximity levels is created from a set of proximity equations. In this case:  $\Lambda = \{1.0, 0.8, 0.5, 0.2\}$ .
2. Each element (constant, function or predicate symbol) occurring in a proximity equation is added to an array  $A$ . In the present case:  $A = \{\textit{black}, \textit{brown}, \textit{green}, \textit{gray}, \textit{blue}\}$ . Then, a graph  $G$  of dimension  $N \times N$  (being  $N$  the length of the array) is created (see Figure 2). The graph  $G$  is representing the proximity relation  $\mathcal{R}$  induced by the set of proximity equations.
3. Afterwards, a crisp subgraph  $G_\lambda$  representing the  $\lambda$ -cut of  $\mathcal{R}$  is created, the idea is that two elements of  $A$  are connected at level  $\lambda$  if:  $G[i][j] \geq \lambda$  or  $G[j][i] \geq \lambda$  ( $i, j=1, \dots, N$ ). This is the input for the `generateProximityBlocks` procedure, that, as it was mentioned, computes all maximal cliques ( $\lambda$ -blocks) of the crisp subgraph. For instance, given the subgraph:  $G_{0.8} = \{G[\textit{black}][\textit{brown}], G[\textit{green}][\textit{gray}], G[\textit{gray}][\textit{blue}]\}$ , the maximal cliques  $\mathcal{C}_1 = \{\textit{black}, \textit{brown}\}$ ,  $\mathcal{C}_2 = \{\textit{green}, \textit{blue}\}$ ,  $\mathcal{C}_3 = \{\textit{green}, \textit{gray}\}$  are obtained. Figure 2 gives a partial intuition of how this is done: note that cliques (0.8-blocks) are maximal connected subgraphs where each element of a clique is connected with the other elements.
4. Finally, a hierarchy of the corresponding  $\lambda$ -blocks is built at each iteration step, as previously was formalized in Algorithm 1.

Once we have got the hierarchy of proximity blocks  $\mathcal{J}$ , the second step consists in the selection of some  $\lambda$ -block  $\mathcal{B}_k^\lambda \in PB^\lambda \subseteq \mathcal{J}$  and the later labeling of it with an abstract descriptor  $d_k$ . Then, for each element  $e_j \in \mathcal{B}_k^\lambda$ , we generate the proximity equation “ $e_j \sim d_k = \alpha_{jk}$ ”, where the approximation degree  $\alpha_{jk} \equiv \mathcal{R}(e_j, d_k)$  is computed as follows: i) the user selects a set  $R = \{r_1, \dots, r_n\}$  of typical representative elements in  $\mathcal{B}_k^\lambda$  that best fit the notion described by  $d_k$ ; ii)  $\alpha_{jk} = (1/n) \sum_{i=1}^n \mathcal{R}(e_j, r_i)$ , that is, an average of the closeness of  $e_j$  w.r.t. the considered representative concepts of the block. Note that, if an element  $e_j$  is related to the elements of a set  $D = \{d_1, \dots, d_m\}$  of abstract descriptors, the approximation degree  $\alpha_{jk}$  should be normalized to the value  $\alpha'_{jk} = \alpha_{jk} / \sum_{i=1}^m \alpha_{ji}$ ,

in order to fulfill the consistency criterion:  $\sum_{i=1}^m \mathcal{R}(e_j, d_i) = 1$ . Later, the set of proximity equations automatically generated can participate in the inference process of a fuzzy programming language based on weak unification.

*Example 4.* For the proximity relation in Example 1 the 0.5-blocks generated by the above mentioned algorithm are:  $\mathcal{B}_1^{0.5} = \{brown, green, gray\}$ ,  $\mathcal{B}_2^{0.5} = \{green, gray, blue\}$  and  $\mathcal{B}_3^{0.5} = \{black, brown\}$ . Then the user might assign the more general descriptors “mixed” to  $\mathcal{B}_1^{0.5}$ , “light” to  $\mathcal{B}_2^{0.5}$  and “dark” to  $\mathcal{B}_3^{0.5}$ . Also, he might choose the following sets of representative elements:  $\{brown\}$  for  $\mathcal{B}_1^{0.5}$ ,  $\{gray, blue\}$  for  $\mathcal{B}_2^{0.5}$  and  $\{black\}$  for  $\mathcal{B}_3^{0.5}$ . Then, after this choice phase, our method generates the additional proximity equations:

`mixed~brown=0.48.    mixed~green=0.6.    mixed~gray=0.45.    dark~brown=0.52.`  
`light~green=0.4.    light~gray=0.55.    light~blue=1.0.    dark~black=1.0.`

These proximity equations can be load into a proximity-based logic programming system, as is the case of `Bousi~Prolog`, so when asking the system about people who have “light” eyes, the system will answer “`X=mary`” with approximation degree 1.0.

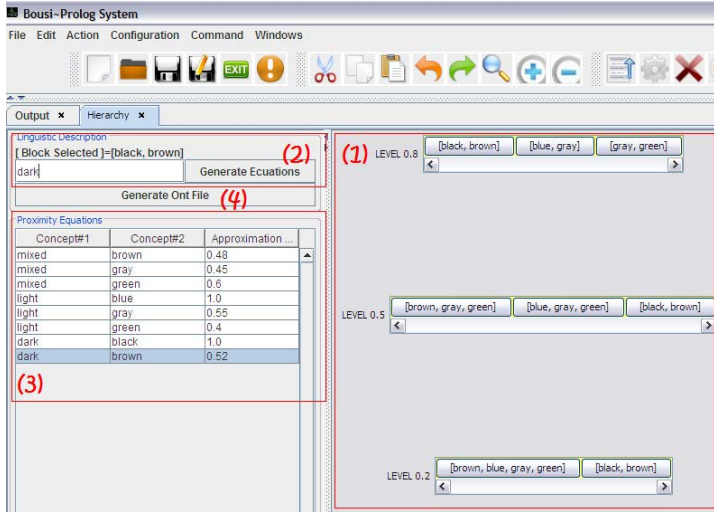
Note that this technique can be seen as a generalization process where the user controls the selection of the more appropriate descriptor for a proximity  $\lambda$ -block. More widely, this method can be understood as an abstraction process which: 1) improves, by means of data summaries, the comprehension of the ontology defined by the proximity equations; and 2) gives the user more freedom in order to define his own generalization. Finally observe that, when the proximity relation  $\mathcal{R}$  is a similarity, the notion of “proximity block”, used in the description of Algorithm 1, becomes a “similarity class” which can be computed more efficiently.

## 5 A Tool for Discovery of Abstract Knowledge

For the practical materialization of the generalization method described in the last section, a tool (see Figure 3) has been built and integrated into the BPL system. This tool allows the automatization of the proximity  $\lambda$ -block generation process, facilitates the assignment of an abstract descriptor to each one of the groupings of concepts (selected by the user from the set of generated  $\lambda$ -blocks) and generates the corresponding proximity equations <sup>3</sup>.

The user of this tool has at his disposal graphical windows that facilitate the interaction with the system: The Hierarchy Displayer Window (1) that shows the structure of the generated hierarchy and allows the selection of a  $\lambda$ -block clicking on it. Once a  $\lambda$ -block is selected, its information will become available in the Descriptor Selection Window (2) which, in addition, has a text field box where the user can introduce the descriptor that is going to be linked with a group of concepts. After the choice of a descriptor, the user can, at the push of the button “Generate Equations”, generate the proximity equations which are displayed in the Equations Displayer Window (3). Finally, they can be loaded into the BPL system pushing the button “Load Proximity Equations”.

<sup>3</sup> Note that, in Figure 3, the 1-blocks are singletons and they are not represented.



**Fig. 3.** A display of the tool for discovery of generalized knowledge

The tool has been implemented in Java 7. For this task, two software layers have been built. A domain layer which is responsible for the whole functionality of the described method and it is composed by four classes: the Block class which is mainly a list of sets of blocks; the Level class composed of a list of objects belonging to the Block class, along with a field “degree” indicating the level; the Hierarchy class consists of a list of objects in the Level class, and the Generator class which implements a fuzzy extension of the clique algorithm [2]. The second layer is the representation layer. It has the function of implementing the graphical interface of the tool.

## 6 Conclusions and Future Work

In this paper we have proposed and implemented a proximity-based generic method for discovery of generalized knowledge in the context of a fuzzy logic programming language with a weak unification procedure based on proximity relations (or similarity relations more restrictively). The generalization method can be understood as modeling a knowledge abstraction process. In order to prove its feasibility, this method has been integrated as a tool into the Bousi~Prolog system. Thanks to the new tool we accomplish the goal of managing a generalization process, in a semi automatic way, starting from the semantic knowledge represented by a set of proximity relations.

Some of the advantages of this proposal are: i) the learned descriptors are fixed once and used many times, adding new knowledge (this can be considered a learning process where the user teaches the system new concepts on the basis

of the existing knowledge); ii) block analysis can contribute to ontology tuning and lead to a form of information comprehension; iii) gives users the freedom to define the most convenient generalization. However we can signal out possible limitations: i) the user has to intervene in the choice of descriptors; ii) block generation can be non-affordable in time, if you are working with a great amount of proximity equations.

Regarding future work lines, we want to make more flexible the automatic generation of proximity equations allowing, for example, to establish relations between general descriptors of the same abstraction level, that currently are disposed in a hierarchy (and only relate with descriptors of the superior/inferior level). On the other hand we like to improve the efficiency of the block generation algorithm. All in all, we desire continue enhancing the **Bousi~Prolog** system in order to transform it in a effective tool to the development of soft computing applications.

## References

1. Angryk, R.A., Petry, F.E.: Discovery of Abstract Knowledge from Non-Atomic Attribute Values in Fuzzy Relational Databases. In: *Modern Information Processing: From Theory to Applications* (2005)
2. Bron, C., Kerbosh, J.: Algorithm 457: Finding All Cliques of an Undirected Graph. *Communications of ACM* 16(9) (1973)
3. Cai, Y., Cercone, N., Han, J.: Attribute-Oriented Induction in Relational Databases. In: *Proc. IJCAI 1989*, pp. 26–36 (1989)
4. Formato, F., Gerla, G., Sessa, M.I.: Similarity-based Unification. *Fundam. Inform.* 41(4), 393–414 (2000)
5. Romero, F.P., Julián-Iranzo, P., Ferreira-Satler, M., Gallardo-Casero, J.: Classifying unlabeled short texts using a fuzzy declarative approach. *Language Resources and Evaluation* (2012), <http://dx.doi.org/10.1007/s10579-012-9203-2>
6. Julián, P., Rubio, C., Gallardo, J.: **Bousi~Prolog**: A Prolog Extension Language for Flexible Query Answering. *ENTCS*, vol. 248, pp. 131–147. Elsevier (2009)
7. Julián, P., Rubio, C.: A Declarative Semantics for **Bousi~Prolog**. In: *Proc. of 11th ACM SIGPLAN Symposium on PPDP 2009*, pp. 149–160 (2009)
8. Julián, P., Rubio, C.: **Bousi~Prolog** - A Fuzzy Logic Programming Language for Modeling Vague Knowledge and Approximate Reasoning. In: *Proc. of IJCCI (ICFC-ICNC)*, pp. 93–98 (2010)
9. Lee, D.H., Kim, M.H.: Database Summarization Using Fuzzy ISA Hierarchies. *IEEE Transactions on Systems, Man and Cybernetics—part B* 27(1), 68–78 (1997)
10. Sessa, M.I.: Approximate Reasoning by Similarity-based SLD Resolution. *Theoretical Computer Science* 275, 389–426 (2002)
11. Robinson, J.A.: A Machine-oriented Logic Based on the Resolution Principle. *Journal of the ACM* 12(1), 23–41 (1965)

# Fuzzy Property-Oriented Concept Lattices in Morphological Image and Signal Processing\*

Cristina Alcalde<sup>1</sup>, Ana Burusco<sup>2</sup>, Juan Carlos Díaz<sup>3</sup>,  
Ramón Fuentes-González<sup>2</sup>, and Jesús Medina-Moreno<sup>3,\*\*</sup>

<sup>1</sup> Dpt. Matemática Aplicada, Universidad del País Vasco UPV/EHU, Spain  
c.alcalde@ehu.es

<sup>2</sup> Dpt. Automática y Computación, Univ. Pública de Navarra, Spain  
{burusco,rfuentes}@unavarra.es

<sup>3</sup> Dpt. of Mathematics, University of Cádiz, Spain  
{juancarlos.diaz,jesus.medina}@uca.es

**Abstract.** Fuzzy property-oriented concept lattices are a formal tool for modeling and processing incomplete information in information systems. This paper relates this theory to fuzzy mathematical morphology, which scope, for instance, is to process and analyze images and signals. Consequently, the theory developed in the concept lattice framework can be used in these particular settings.

**Keywords:** Rough sets, fuzzy sets, fuzzy mathematical morphology.

## 1 Introduction

Mathematical Morphology is a theory concerned with the processing and analysis of images or signals using filters and other operators that modify them, these morphological filters are obtained by means of two basic operators, the *dilation* and the *erosion*.

The fundamentals of this theory (initiated by G. Matheron [15] and J. Serra [16]), are in the set theory, the integral geometry and the lattice algebra. Actually this methodology is used in general contexts related to activities as the information extraction in digital images, the noise elimination or the pattern recognition.

This theory has been developed in a fuzzy environment. For instance, a new type of *fuzzy morphological image processing* has been given in [2, 5–8, 13, 14] using *L*-fuzzy sets as images and structuring elements.

On the other hand, fuzzy concept lattices and fuzzy rough sets are two formal tools for modeling and processing incomplete information in information systems and, therefore, they are also used to extract information from these systems.

Another important concept lattice setting is the fuzzy property-oriented concept lattice framework [12], which arises as a fuzzy generalization of Rough

---

\* Partially supported by Spanish Ministry of Science and FEDER funds through project TIN09-14562-C05-03 and Junta de Andalucía project P09-FQM-5233.

\*\* Corresponding author.



Set Theory and in which a set of objects and a set of attributes are assumed, following the view point of Formal Concept Analysis.

Recently, an interesting relation between  $L$ -fuzzy concept lattices and fuzzy mathematical morphology has been introduced in [1]. In this paper we have extended this relation to the case of fuzzy property-oriented concept lattices. The main difference in this case is the non-consideration of negation operators. Moreover, this relation is taken into account in two practical examples, about binary images and digital signals.

Furthermore, the main result of this paper provides that the theory developed in both frameworks can be merged in order to prove new results and the algorithms given for the calculus of fuzzy concepts, or fixed points of closure operators, can be applied to fuzzy mathematical morphology and vice versa.

## 2 Preliminaries

First of all, this section recalls the fuzzy property-oriented concept lattices introduced in [12], which use the isotone Galois connections presented in [9]. Later, several basic notions of mathematical morphology are presented.

### 2.1 L-Fuzzy Property-Oriented Concept Lattice

A complete residuated lattice  $(L, *, 1)$  is the considered carrier in this framework. On this structure, a fuzzy (formal) context is assumed,  $(X, Y, R)$ , where  $R: X \times Y \rightarrow L$  is a fuzzy relation between the sets  $X$  and  $Y$ , where  $X$  can be interpreted as a set of objects and  $Y$  as a set of properties (attributes).

For a fuzzy context  $(X, Y, R)$ , two mappings  $R_{\exists}: L^X \rightarrow L^Y$  and  $R^{\forall}: L^Y \rightarrow L^X$  can be defined:

$$R_{\exists}(A)(y) = \sup\{A(x) * R(x, y) \mid x \in X\} \tag{1}$$

$$R^{\forall}(B)(x) = \inf\{I(R(x, y), B(y)) \mid y \in Y\} \tag{2}$$

for all  $A: Y \rightarrow L$ ,  $B: X \rightarrow L$ ,  $x \in X$  and  $y \in Y$ , where  $I$  is the residuated implication associated with the conjunctive  $*$ .

The pair  $(R_{\exists}, R^{\forall})$  forms an isotone Galois connection [9].

Hence, a *property-oriented concept* (or, a *concept based on rough set theory*) of  $(X, Y, R)$  is a pair  $(A, B) \in L^X \times L^Y$  such that  $B = R_{\exists}(A)$  and  $A = R^{\forall}(B)$ ,  $B$  is called the properties,  $A$  is called the objects of the concept  $(A, B)$ .

The set of all property-oriented concepts of  $(X, Y, R)$  is denoted by  $\mathcal{P}(X, Y, R)$ , it is a complete lattice [12], which is called the *property-oriented concept lattice of  $(X, Y, R)$*  (or, the *concept lattice of  $(X, Y, R)$  based on rough set theory*) [12]. For that isotone Galois connection  $(R_{\exists}, R^{\forall})$  and lattice  $\mathcal{P}(X, Y, R)$  interesting properties have been proven, e.g., in [3, 4, 9, 12].

### 2.2 Mathematical Morphology in Binary Images and Grey Scale Images

In this theory images  $A$  from  $X = \mathbb{R}^n$  or  $X = \mathbb{Z}^n$  (digital images, or signals when  $n=1$ ) are analyzed.

The *morphological filters* are defined as operators  $F: \wp(X) \rightarrow \wp(X)$  that transform, simplify, clean or extract relevant information from these images  $A \subseteq X$ , information that is encapsulated by the filtered image  $F(A) \subseteq X$ .

These morphological filters are obtained by means of two basic operators, the *dilation*  $\delta_S$  and the *erosion*  $\varepsilon_S$ , that are defined in the case of binary images with the *sum* and *difference of Minkowski* [16], respectively.

$$\delta_S(A) = A \oplus S = \bigcup_{s \in S} A_s \quad \varepsilon_S(A) = A \ominus \check{S} = \bigcap_{s \in \check{S}} A_s$$

where  $A$  is an image that is treated with another  $S \subseteq X$ , that is called *structuring element*, or with its opposite  $\check{S} = \{-x \mid x \in S\}$  and where  $A_s$  represents a translation of  $A$ :  $A_s = \{a + s \mid a \in A\}$ .

The structuring image  $S$  represents the effect that we want to produce over the initial image  $A$ .

We can compose these operators dilation and erosion associated with the structuring element  $S$  and obtain the basic filters *morphological opening*  $\gamma_S: \wp(X) \rightarrow \wp(X)$  and *morphological closing*  $\phi_S: \wp(X) \rightarrow \wp(X)$  defined by:

$$\gamma_S = \delta_S \circ \varepsilon_S \quad \phi_S = \varepsilon_S \circ \delta_S$$

The opening  $\gamma_S$  and the closing  $\phi_S$  over these binary images verify the two conditions that characterize the morphological filters: They are isotone and idempotent operators.

These operators will characterize some special images (the  $S$ -open and the  $S$ -closed ones) that will play an important role in this work.

### 2.3 Fuzzy Mathematical Morphology

A new type of *fuzzy morphological image processing* has been developed [2, 5–8, 13, 14] using  $L$ -fuzzy sets  $A$  and  $S$  (with  $X = \mathbb{R}^2$  or  $X = \mathbb{Z}^2$ ) as images and structuring elements.

In this framework, *fuzzy morphological dilations*  $\delta_S: L^X \rightarrow L^X$  and *fuzzy morphological erosions*  $\varepsilon_S: L^X \rightarrow L^X$  are defined using some operators of the fuzzy logic.

In the literature, (see [2, 5, 10, 14]), erosion and dilation operators are introduced associated with the residuated pair  $(*, I)$  as follows:

If  $S: X \rightarrow L$  is an image that we take as *structuring element*, then we consider the following definitions associated with  $(L, X, S)$

**Definition 1.** [5] *The fuzzy erosion of the image  $A \in L^X$  by the structuring element  $S$  is the  $L$ -fuzzy set  $\varepsilon_S(A) \in L^X$  defined as:*

$$\varepsilon_S(A)(x) = \inf\{I(S(y - x), A(y)) \mid y \in X\} \quad \forall x \in X$$

*The fuzzy dilation of the image  $A$  by the structuring element  $S$  is the  $L$ -fuzzy set  $\delta_S(A)$  defined as:*

$$\delta_S(A)(x) = \sup\{S(x - y) * A(y) \mid y \in X\} \quad \forall x \in X$$

Then we obtain fuzzy erosion and dilation operators  $\varepsilon_S, \delta_S: L^X \rightarrow L^X$ .

### 3 Relation between Both Theories

First of all, we will associate any fuzzy image  $S \in L^X$  with the fuzzy relation  $R_S \in L^{X \times X}$ , defined, for all  $x, y \in X$ , as:

$$R_S(x, y) = S(y - x)$$

Hence, the fuzzy erosion and dilation are as follows:

$$\varepsilon_S(A)(x) = \inf\{I(R_S(x, y), A(y)) \mid y \in X\}$$

$$\delta_S(A)(x) = \sup\{R_S(y, x) * A(y) \mid y \in X\}$$

and the following results can be proven.

**Proposition 1.** *Let  $(L, X, S)$  be the triple associated with the structuring element  $S \in L^X$ . Let  $(L, X, X, R_S)$  be the  $L$ -fuzzy property-oriented context whose incidence relation is the relation  $R_S$  associated with  $S$ . Then the operators erosion  $\varepsilon_S$  and dilation  $\delta_S$  in  $(L, X, S)$  are related to the derivation operators  $(R_S)^\forall$  and  $(R_S)^\exists$  in the  $L$ -fuzzy property-oriented context  $(L, X, X, R_S)$  by:*

$$\varepsilon_S(A) = (R_S)^\forall(A)$$

$$\delta_S(A) = (R_S)^\exists(A)$$

for all  $A \in L^X$ .

*Proof.* Taking into account the definitions of  $(R_S)^\forall$  and  $(R_S)^\exists$ , given in Equations (2) and (1), for each  $x \in X$  the following equations hold:

$$\varepsilon_S(A)(x) = \inf\{I(R_S(x, y), A(y)) \mid y \in X\} = (R_S)^\forall(A)(x), \quad \text{for all } A \in L^X$$

Analogously,

$$\delta_S(A)(x) = \sup\{R_S(y, x) * A(y) \mid y \in X\} = (R_S)^\exists(A)(x), \quad \text{for all } A \in L^X$$

□

As a consequence, the dilation and erosion hold the properties of the isotone Galois connection  $(R_\exists, R^\forall)$ .

**Proposition 2.** *Given a structuring element  $S \in L^X$ , where  $(L, \preceq)$  is a complete lattice and  $X$  a set of objects, we have*

1.  $\varepsilon_S: L^X \rightarrow L^X$  and  $\delta_S: L^X \rightarrow L^X$  are isotone operators.
2.  $\varepsilon_S \circ \delta_S: L^X \rightarrow L^X$  is a closure operator.
3.  $\delta_S \circ \varepsilon_S: L^X \rightarrow L^X$  is an interior operator.
4.  $\varepsilon_S \circ \delta_S \circ \varepsilon_S = \varepsilon_S$
5.  $\delta_S \circ \varepsilon_S \circ \delta_S = \delta_S$
6.  $\delta_S(A_1) \preceq A_2$  if and only if  $A_1 \preceq \varepsilon_S(A_2)$ , for all  $A_1, A_2 \subseteq X$

The next result proves the connection between the outstanding morphological elements and the  $L$ -fuzzy property-oriented concepts.

**Theorem 1.** *Let  $S \in L^X$  and its associated relation  $R_S \in L^{X \times X}$ , the following statements are equivalent:*

1. *The pair  $(A, B) \in L^X \times L^X$  is an  $L$ -fuzzy property-oriented concept of the context  $(L, X, X, R_S)$ .*
2.  *$A$  is  $S$ -closed and  $B$  is the  $S$ -dilation of  $A$ .*
3.  *$B$  is  $S$ -open and  $A$  is the  $S$ -erosion of  $B$ .*

*Proof.* 1.  $\implies$  2. *Given an  $L$ -fuzzy property-oriented concept  $(A, B)$  of the  $L$ -fuzzy property-oriented context  $(L, X, X, R_S)$ , we have that  $B = (R_S)_{\exists}(A)$  and, Proposition 1,  $B = \delta_S(A)$ , that is,  $B$  is the  $S$ -dilation of  $A$ .*

*Moreover, it is fulfilled that  $\phi_S(A) = \varepsilon_S(\delta_S(A)) = \varepsilon_S(B) = (R_S)^{\forall}(B) = A$ , which proves that  $A$  is  $S$ -closed.*

2.  $\implies$  3. *By hypothesis and Proposition 2(5), the following chain of equalities is obtained:*

$$\gamma_S(B) = \delta_S(\varepsilon_S(B)) = \delta_S(\varepsilon_S(\delta_S(A))) = \delta_S(\phi_S(A)) = \delta_S(A) = B$$

*which shows that  $B$  is  $S$ -open. On the other hand, taking into account that  $A$  is  $S$ -closed,  $A = \phi_S(A) = \varepsilon_S(\delta_S(A)) = \varepsilon_S(B)$  holds, that is,  $A$  is the  $S$ -erosion of  $B$ .*

3.  $\implies$  1. *Given the  $L$ -fuzzy property-oriented context  $(L, X, X, R_S)$ , since  $A$  is the  $S$ -erosion of  $B$ , by hypothesis, and, using Proposition 1, we obtain that  $(R_S)^{\forall}(B) = \varepsilon_S(B) = A$ .*

*In order to prove the other equality, we consider the other hypothesis,  $B$  is  $S$ -open, and Proposition 1, and the equalities  $(R_S)_{\exists}(A) = \delta_S(A) = \delta_S(\varepsilon_S(B)) = \gamma(B) = B$  hold.*

*Thus,  $(A, B)$  is a property-oriented concept of the context  $(L, X, X, R_S)$ .  $\square$*

Now, we present two interesting examples in which the results above are applied. The first one is about the interpretation of one binary image (crisp case) as a property-oriented concept.

*Example 1.* *Since two dimensional images are assumed, the considered referential set is  $X = \mathbb{R}^2$ . If  $L = \{0, 1\}$  the maps  $A: \mathbb{R}^2 \rightarrow L$  are interpret as two dimensional images. The elements of  $X$  are denoted as  $\bar{x} = (x_1, x_2) \in \mathbb{R}^2$ .*

The structuring binary image  $S$  is

$$S = \{(x_1, x_2) \in \mathbb{R}^2 \mid x_1^2 + x_2^2 \leq w^2\}$$

where  $w$  is a positive number. Hence, the associated incidence relation  $R_S \subseteq \mathbb{R}^2 \times \mathbb{R}^2$  is defined, for each  $\bar{x} = (x_1, x_2)$ ,  $\bar{y} = (y_1, y_2)$ , as

$$R_S(\bar{x}, \bar{y}) = S(\bar{y} - \bar{x}) = \begin{cases} 1 & \text{if } (y_1 - x_1)^2 + (y_2 - x_2)^2 \leq w^2 \\ 0 & \text{otherwise} \end{cases}$$

From these data the assumed context is  $(\{0, 1\}, \mathbb{R}^2, \mathbb{R}^2, R_S)$ . Hence, for  $A \in L^{\mathbb{R}^2}$  and for each  $\bar{x} = (x_1, x_2) \in \mathbb{R}^2$  the dilation operator is

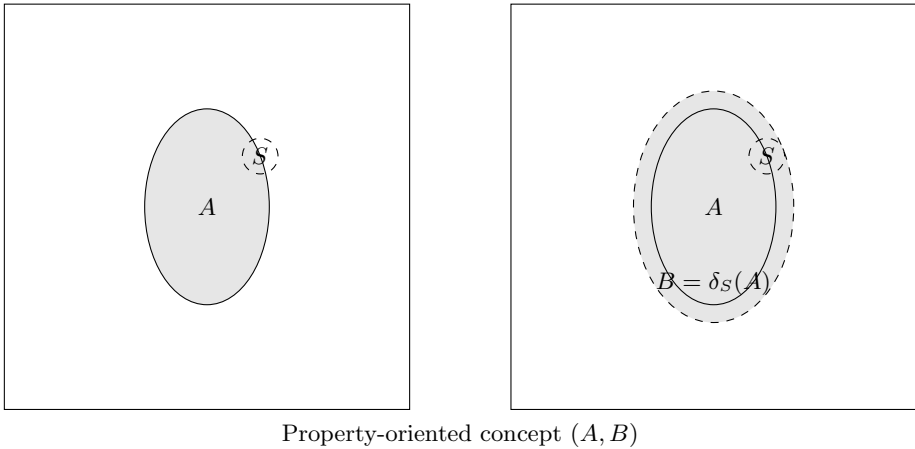
$$\begin{aligned} \delta_S(A)(\bar{x}) &= (R_S)_{\exists}(A)(\bar{x}) \\ &= \sup\{R_S(\bar{y}, \bar{x}) * A(\bar{y}) \mid \bar{y} \in \mathbb{R}^2\} \\ &= \sup\{A((y_1, y_2)) \mid (x_1 - y_1)^2 + (x_2 - y_2)^2 \leq w^2\} \\ &= \begin{cases} 1 & \text{if there exists } (y_1, y_2) \in \mathbb{R}^2 \text{ such that } A((y_1, y_2)) = 1 \\ & \text{and } (y_1 - x_1)^2 + (y_2 - x_2)^2 \leq w^2 \\ 0 & \text{otherwise} \end{cases} \end{aligned}$$

Hence, given a set  $A$ , the dilation of  $A$  is the set  $A$  union with the set formed by all points  $(x_1, x_2)$  of  $\mathbb{R}^2$ , such that the distance between  $(x_1, x_2)$  and a point of  $A$  is less or equal to  $w$ .

On the other hand, the erosion operator is:

$$\begin{aligned} \varepsilon_S(A)(\bar{x}) &= (R_S)^{\forall}(A)(\bar{x}) \\ &= \inf\{I(R_S(\bar{x}, \bar{y}), A(\bar{y})) \mid \bar{y} \in X\} \\ &= \inf\{A((y_1, y_2)) \mid (x_1 - y_1)^2 + (x_2 - y_2)^2 \leq w^2\} \\ &= \begin{cases} 0 & \text{if there exists } (y_1, y_2) \in \mathbb{R}^2 \text{ such that } A((y_1, y_2)) = 0 \\ & \text{and } (y_1 - x_1)^2 + (y_2 - x_2)^2 \leq w^2 \\ 1 & \text{otherwise} \end{cases} \end{aligned}$$

Fig. 1 shows an example of property-oriented concept. The pair  $(A, B)$  is a property-oriented concept of the context  $(\{0, 1\}, \mathbb{R}^2, \mathbb{R}^2, R_S)$  because  $\phi(A) = A$  and  $B = \delta_S(A)$ .



**Fig. 1.** A property-oriented concept of the context  $(\{0, 1\}, \mathbb{R}^2, \mathbb{R}^2, R_S)$

The second example interprets one open digital signal as a fuzzy property-oriented concept.

*Example 2.* If  $X \subseteq Z$  and  $L = \{0, 0.1, 0.2, \dots, 0.9, 1\}$  then the maps  $A: X \rightarrow L$  can be interpreted as 1-D discrete signals.

In this example the considered referential set is  $X = \{0, 1, 2, \dots, 21, 22\}$ . The structuring binary image  $S$  is the crisp set  $S = \{-1, 0, 1\}$ .

Hence, the associated incidence relation  $R_S \subseteq X \times X$  is defined, for each  $(x, y) \in X \times X$ , as

$$R_S(x, y) = S(y - x) = \begin{cases} 1 & \text{if } |y - x| \leq 1 \\ 0 & \text{otherwise} \end{cases}$$

From these data the considered context is  $(L, X, X, R_S)$ . Here, for  $A \in L^X$  and for each  $x \in X$  the dilation and erosion operators are

$$\delta_S(A)(x) = \sup\{R_S(y, x) * A(y) \mid y \in X\} = \sup\{A(y) \mid |x - y| \leq 1\}$$

$$\varepsilon_S(A)(x) = \inf\{I(R_S(x, y), A(y)) \mid y \in X\} = \inf\{A(y) \mid |y - x| \leq 1\}$$

In Fig. 2 a particular discrete signal  $A$  and its dilation  $B = \delta_S(A)$  are assumed. It can be directly checked that the pair  $(A, B)$  satisfies  $\phi(A) = A$  and  $B = \delta_S(A)$  and, therefore, it is a property-oriented concept of the context  $(L, X, X, R_S)$ .

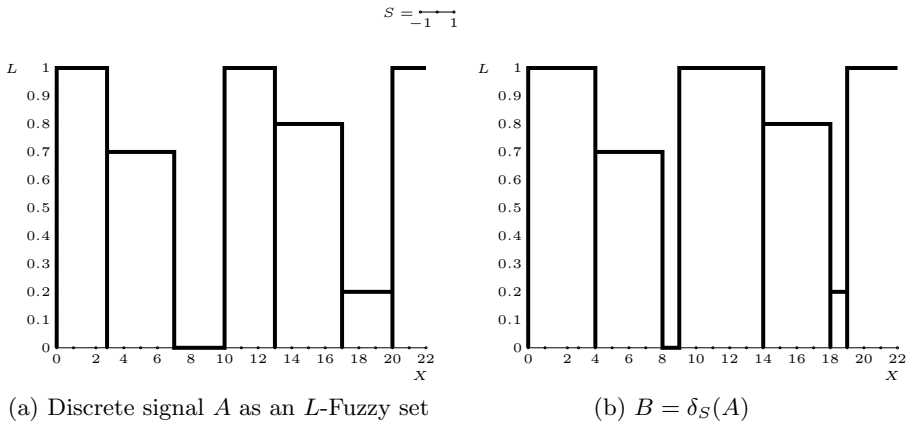


Fig. 2. Discrete signals

## 4 Conclusions and Future Work

This paper relates fuzzy property-oriented concept lattices and fuzzy mathematical morphology, in which no negation operators are considered, and two practical examples have been analyzed. As a consequence, the theory developed

in both frameworks can be merged in order to prove new results and the algorithms given for fuzzy concept lattices can be applied to fuzzy mathematical morphology and vice versa.

In the future, we will study the theory of concept lattices to process and analyze images and signals using the filters and the operators considered in fuzzy mathematical morphology. Moreover, the result obtained will be applied to practical examples.

## References

1. Alcalde, C., Burusco, A., Fuentes-González, R.: An interpretation of the L-Fuzzy Concept Analysis as a tool for the Morphological Image and Signal Processing. In: Proc. of CLA 2012, Fuengirola, Málaga, pp. 81–92 (2012)
2. De Baets, B.: Fuzzy morphology: a logical approach. In: Ayyub, B., Gupta, M. (eds.) *Uncertainty Analysis, Engineering and Science: Fuzzy Logic, Statistics and neural network Approach*, pp. 53–67. Kluwer Academic Publishers (1997)
3. Bartl, E., Bělohávek, R., Konecny, J., Vychodil, V.: Isotone galois connections and concept lattices with hedges. 4th International IEEE Conference “Intelligent Systems”, 15.24–15.28 (2008)
4. Bělohávek, R.: Concept lattices and order in fuzzy logic. *Annals of Pure and Applied Logic* 128, 277–298 (2004)
5. Bloch, I., Maître, H.: *Fuzzy Mathematical Morphologies: a comparative study*. Télécom Paris 94D001 (1994)
6. Bloch, I.: Duality vs. adjunction for fuzzy mathematical morphology and general form of fuzzy erosions and dilations. *Fuzzy Sets and Systems* 160, 1858–1867 (2009)
7. Burillo, P., Fuentes-González, R., Frago, N.: Inclusion grade and fuzzy implication operators. *Fuzzy Sets and Systems* 114, 417–429 (2000)
8. Burillo, P., Frago, N., Fuentes-González, R.: Generation of Fuzzy Mathematical Morphologies. *Mathware & Soft Computing* VIII (1), 31–46 (2001)
9. Georgescu, G., Popescu, A.: Non-dual fuzzy connections. *Arch. Math. Log.* 43(8), 1009–1039 (2004)
10. Goutsias, J., Heijmans, H.J.A.M.: *Fundamenta Morphologicae Mathematicae. Fundamenta Informaticae* 41, 1–31 (2000)
11. Heijmans, H.J.A.M.: *Morphological Image Operators*. Academic Press Inc. (1994)
12. Lai, H., Zhang, D.: Concept lattices of fuzzy contexts: Formal concept analysis vs. rough set theory. *International Journal of Approximate Reasoning* 50(5), 695–707 (2009)
13. Maragos, P.: Lattice Image Preprocessing: A Unification of Morphological and Fuzzy Algebraic Systems. *Journal of Mathematical Imaging and Vision* 22, 333–353 (2005)
14. Mas, M., Monserrat, M., Torrens, J.: S-implications and R-implications on a finite chain. *Kybernetika* 40(1), 3–20 (2004)
15. Matheron, G.: *Random Sets and Integral Geometry*. Wiley, New York (1975)
16. Serra, J.: *Image Analysis and Mathematical Morphology*. Academic Press I (fourth printing 1990) and II (second printing 1992)
17. Soille, P.: *Morphological Image Analysis*, 2nd edn. Springer (2004)

# Automated Inference with Fuzzy Functional Dependencies over Graded Data

José Manuel Rodríguez-Jiménez, Pablo Cordero, Manuel Enciso,  
and Angel Mora

Universidad de Málaga, Spain

{jmrodriguez,amora}@ctima.uma.es, pcordero@uma.es, enciso@lcc.uma.es

**Abstract.** Fuzzy set theory has proved to be a successful paradigm to extend the database relational model, augmenting its skill to capture uncertainty. This capability may be considered in two levels: the data itself and the constraints defined to adjust the database schema to the real system. When constraints are considered, it is necessary to design methods to reason about it and not only a way to express them. This situation leads to an ambitious goal: the design of automated reasoning methods. Highly-expressive data models are not useful without an automated reasoning method. In this work we introduce an automated method to infer with fuzzy functional dependencies over a high level generalization of the relational model and provide its completeness result.

## 1 Introduction

From the 70's, the relational model [1] has become a standard in the database area. In these years some extensions of the original model have been proposed in order to achieve a more expressive model for some environments and real applications. In [2] we showed a discussion about the interest of an adequate extension of Codd's model. This request is not only a logicians matter but also interesting for the database community: "When one leaves business data processing, essentially all data is uncertain or imprecise" [3].

Fuzzy Set Theory has provided a generalization of the relational model in order to incorporate to the data some degree of uncertainty, vagueness, truthlikeness, incompleteness and imprecision. We emphasize three research lines in fuzzy databases corresponding to the use of fuzzy membership values [4, 5], possibility distributions [6, 7] or similarity relations [8–10]. Apart of this, another outstanding topic in fuzzy databases is the fuzzification of the constraints. In [2], an study of the main works related with this topic is presented. The main conclusion is the necessity of a proper definition of Fuzzy Functional Dependency (FFD).

In [11–14], the authors have presented some extensions of the relational model, several definitions of FFDs and complete axiomatic systems to reason with them. Nevertheless, these axiomatic systems are not designed to build automated method to make inference with fuzzy functional dependencies. Beside that, there are two dimensions to categorize [2] the wide range of FFD definitions: the way



in which vagueness is incorporated to the data and level of fuzzification of the functional dependency.

In [15, 16] we have introduced two definitions of FFD together with the corresponding sound and complete axiomatic systems and their automated reasoning method. Both definitions incorporate different levels of fuzzification of the dependency while data remain crisp. In [2], we establish this classification and introduce a general FFD definition. In the relational model, the atomic element is the attribute value. Our approach associates a degree to each value of the attribute, providing the maximum level of uncertainty in tables. A sound and complete axiomatic system for these dependencies has been also introduced in [2]. As a future work, the need for an automated reasoning method for this approach was suggested and it constitutes the goal of this paper.

The paper is organized as follows: Section 2 shows the notions of *Fuzzy Attributes Tables* and Fuzzy Functional Dependencies for this model. The Simplification Logic for Fuzzy Functional Dependencies appears in Section 3. Section 4 introduces the automated reasoning method for this fuzzy functional dependencies. It directly uses the rules of logic to decide whether a formula may be inferred from a theory. Soundness and completeness of the automated reasoning method is provided in Section 5. The paper ends with a conclusion section.

## 2 Preliminaries

We assume that basic notions related to Fuzzy Logic are known. In this framework, it is usual to replace the truthfulness value set  $\{0, 1\}$  (false and true) for the interval  $[0, 1]$  (*truth degrees*) enriched with some operations. The basic approach is to consider the following lattice:  $([0, 1], \min, \max, 0, 1)$ . This approach may be enhanced by adding a t-norm (triangular norm) and a *residuated implication* defined over the t-norm. This is only a particular case of a residuated lattice.<sup>1</sup>

Our approach uses the unit interval  $[0, 1]$ , the infimum (denoted by  $\wedge$ ) as the universal quantifier, the supremum (denoted by  $\vee$ ) as the existential quantifier, an arbitrary left-continuous t-norm (denoted by  $\otimes$ ) as the conjunction and the residuum defined by  $a \rightarrow b = \sup\{x \in [0, 1] \mid x \otimes a \leq b\}$ . That is, the system of truth values is the residuated complete lattice  $([0, 1], \vee, \wedge, 0, 1, \otimes, \rightarrow)$  where  $([0, 1], \otimes, 1)$  is a commutative monoid and  $(\otimes, \rightarrow)$  is an adjoint pair ( $a \otimes b \leq c$  iff  $a \leq b \rightarrow c$ ).

### 2.1 Fuzzy Functional Dependencies

In this subsection, we show the basic concepts of the Relational Model, with emphasis on functional dependencies, and its fuzzy extension that we will use in this paper. Considering a family of sets  $\{D_a \mid a \in \Omega\}$ , named *domains*, indexed in a finite non-empty set  $\Omega$  of elements, named *attributes*, a relation is a subset

---

<sup>1</sup> There is a wide range of extensions of the notion of residuated lattice. Some of them obtained by including new operations as, for example, multiadjoint lattices [17]. Other ones by relaxing the properties of the operations as in the case of multi-lattices [18].

of the cartesian product of the domains  $R \subseteq \mathbb{D} = \prod_{a \in \Omega} D_a$ . The elements in this product  $t = (t_a)_{a \in \Omega} \in \mathbb{D}$  will be named *tuples*.

Now, some issues concerning the database notation are summarized: Given  $A, B \subseteq \Omega$ ,  $AB$  denotes  $A \cup B$  and  $D_A$  denotes  $\prod_{a \in A} D_a$ . Let  $t \in R$  be a tuple, then  $t_{/A}$  denotes the *projection* of  $t$  to  $D_A$ ; that is, if  $t = (t_a)_{a \in \Omega}$  then  $t_{/A} = (t_a)_{a \in A}$ .

**Definition 1.** A formula  $A \mapsto B$ , where  $A, B \subseteq \Omega$ , is named a functional dependency (FD). A relation  $R \subseteq \mathbb{D}$  is said to satisfy  $A \mapsto B$  if, for all tuples  $t_1, t_2 \in R$ ,  $t_{1/A} = t_{2/A}$  implies that  $t_{1/B} = t_{2/B}$ .

In the literature, some very similar definitions of functional dependency have been proposed [11, 12, 14, 19, 20]. The first step in order to fuzzify the model is considering similarity relations instead of the equality. Thus, each domain  $D_a$  is provided with a similarity relation  $\rho_a : D_a \times D_a \rightarrow [0, 1]$ , that is, a reflexive ( $\rho_a(x, x) = 1$  for all  $x \in D_a$ ) and symmetric ( $\rho_a(x, y) = \rho_a(y, x)$  for all  $x, y \in D_a$ ) fuzzy relation. Given  $A \subseteq \Omega$ , the extension to the set  $\mathbb{D}$  is the following: for all  $t, t' \in \mathbb{D}$ ,

$$\rho_A(t, t') = \bigwedge_{a \in A} \rho_a(t_a, t'_a) \quad (1)$$

The definition of fuzzy functional dependency used in this paper, presented in [21], is the following.

**Definition 2.** A fuzzy functional dependency (FFD) is an expression  $A \xrightarrow{\vartheta} B$  where  $A, B \subseteq \Omega$  and  $\vartheta \in [0, 1]$ . A relation  $R \subseteq \mathbb{D}$  is said to satisfy  $A \xrightarrow{\vartheta} B$  if,

$$\vartheta \leq \bigwedge_{t, t' \in R} \rho_A(t, t') \rightarrow \rho_B(t, t') \quad (2)$$

## 2.2 Fuzzy Attributes Tables

As we have motivated in the previous subsection, database fuzzy extensions are fundamented on the establishment of similarity relations between values of the domains. Nevertheless, in most of these extensions the table definition remains classical [11, 12, 19].

Since the value of each attribute is the atomic element in the classical relational model, if we would like to introduce uncertainty at the ground level, the values assigned to each attribute in each tuple has to be capable to be fuzzified. Thus, we propose to introduce a rank associated to each value which indicates the truthfulness degree of the value of this attribute in this tuple. This approach provides the maximum level of uncertainty in fuzzy tables.

*Example 1.* A company decided to make an questionnaire where the age is a relevant data. The obtained results are:  $(Ann, 26)$ ,  $(Albert, 33)$  and  $(Dave, 43)$ . Nevertheless, we would like to enrich the model by adding a grade that informs us about the truthlikeness of the age. This situation may be modeled introducing a degree for each value in the Age attribute, providing the following three tuples:  $(Ann, 26/1)$ ,  $(Albert, 33/0.9)$  and  $(Dave, 43/0.6)$ .

This extension of the classical relational table is named *Fuzzy Attributes Tables* and constitutes a generalization of other fuzzy data tables appeared in the literature [11, 12, 19]. That is, for each tuple  $t = (t_a)_{a \in \Omega} \in \mathbb{D}$ , we consider a map  $R: \mathbb{D} \rightarrow [0, 1]^{\Omega}$  or, equivalently  $R: \mathbb{D} \times \Omega \rightarrow [0, 1]$ , which renders a tuple of truth values  $R(t) = (r_a)_{a \in \mathcal{A}}$ .

For each tuple  $t$ ,  $t_a$  denotes the value of the attribute  $a$  in the tuple  $t$  and  $R(t)(a)$  is the truthfulness of the value  $t_a$ . We would like to remark that, it is possible that  $R(t)(a) = 0$  for all attribute  $a \in \Omega$ .

When we work with Fuzzy Attributes Tables, we also consider similarity relations in domains in the same way as previous works [15, 21, 22]. Fuzzy Attributes Table is an extension of the original table in the classical relational model by adding the degree of certainty to the values of each attribute.

*Example 2.* We consider a table to store some patients with a mark from infection in their skin. The table is built with the set of attributes  $\mathcal{A} = \{n, a, p, c, l\}$  where  $n$  represent the name,  $a$  the age,  $p$  the percent of extension in the skin,  $c$  the mark color,  $l$  the localization in the skin.

The domain of the attributes are  $D_n = \{\text{John, Peter, Ann, Dave, Peter}\}$ ,  $D_a = \{n \in \mathbb{N} \mid 0 \leq n \leq 120\}$ ,  $D_p = \{n \in \mathbb{N} \mid 0 \leq n \leq 100\}$ ,  $D_c = \{\underline{\text{B}}\text{lack, } \underline{\text{B}}\text{rown, } \underline{\text{P}}\text{urple, } \underline{\text{R}}\text{ed, } \underline{\text{Y}}\text{ellow}\}$  and  $D_l = \{\underline{\text{A}}\text{rm, } \underline{\text{F}}\text{ace, } \underline{\text{F}}\text{oot, } \underline{\text{H}}\text{and, } \underline{\text{L}}\text{eg}\}$ . We build the similarity relations in each domain  $D_a$  as follows:

$\rho_c$	<u>b</u>	<u>w</u>	<u>p</u>	<u>r</u>	<u>y</u>		$\rho_l$	<u>a</u>	<u>f</u>	<u>o</u>	<u>h</u>	<u>l</u>
	1	0.7	0.4	0.3	0.1			1	0.2	0.4	0.9	0.4
	0.7	1	0.5	0.4	0.2			0.2	1	0.2	0.2	0.2
	0.4	0.5	1	0.8	0.2			0.4	0.2	1	0.6	0.8
	0.3	0.4	0.8	1	0.1			0.9	0.2	0.6	1	0.3
	0.1	0.2	0.2	0.1	1			0.4	0.2	0.8	0.3	1

$$\rho_n(t_n, t'_n) = \begin{cases} 1 & \text{if } t_n = t'_n \\ 0 & \text{if } t_n \neq t'_n \end{cases} \quad \rho_a(t_a, t'_a) = 1 - \frac{|t_a - t'_a|}{\max_a - \min_a} \quad \rho_p(t_p, t'_p) = 1 - \frac{|t_p - t'_p|}{100}$$

And finally, we consider the following Fuzzy Attributes Table.

<u>name</u>	<u>age</u>	<u>percent</u>	<u>colour</u>	<u>localization</u>
Ann/1	26/0.9	2/0.8	Brown/0.8	Hand/0.8
Albert/1	33/0.7	4/0.7	Black/0.6	Leg/0.9
Mary/1	21/0.6	7/0.6	Purple/0.9	Arm/0.9
Dave/1	43/0.4	4/0.9	Yellow/0.8	Foot/0.8
Peter/1	24/0.1	3/0.7	Brown/0.7	Arm/0.6

The information represented in the table corresponds to the patient’s names and the description about their infection. Note that the name attribute is crisp, as a particular case.

The next step to provide a notion of Fuzzy attribute table over domains with similarity relations is to relate the similarity degree between two values of an attribute (in two tuples) with their truthfulness degree.

**Definition 3.** Thus, let  $R$  be a fuzzy attributes table and let  $t, t' \in R$  two tuples, for all  $a \in \Omega$ , the relative similarity degree is defined as

$$\rho_a^R(t, t') = (R(t)(a) \otimes R(t')(a)) \rightarrow \rho_a(t_a, t'_a)$$

The above definition may be generalized to subsets of attributes  $A \subseteq \Omega$  as usual, that is,  $\rho_A^R(t, t') = \bigwedge_{a \in A} \rho_a^R(t, t')$

The definition of the relative similarity relation presented in Definition 3 may be used in Equation (2) so that the definition of fuzzy functional dependency remains with no change.

**Definition 4.** A fuzzy functional dependency is an expression  $A \xrightarrow{\vartheta} B$  where  $A, B \subseteq \Omega$ ,  $A \neq \emptyset$  and  $\vartheta \in [0, 1]$ . A Fuzzy Attributes Table  $R$  is said to satisfy  $A \xrightarrow{\vartheta} B$  if the following condition holds:

$$\vartheta \leq \bigwedge_{t, t' \in \mathbb{D}} \rho_A^R(t, t') \rightarrow \rho_B^R(t, t')$$

*Example 3.* The Fuzzy Attributes Table given in Example 2 is a model of the fuzzy functional dependency

$$colour, percent \xrightarrow{0.6} localization$$

for the Łukasiewicz t-norm ( $a \otimes b = \max\{0, a + b - 1\}$ ) and its residuum ( $a \rightarrow b = \min\{1 - a + b, 1\}$ ).

### 3 A Logic for the Management of Fuzzy Functional Dependencies for Fuzzy Attribute Tables

Some complete axiomatic system over several kind of FFDs have been defined [11–13]. However, like in the case of classical FDs and the Armstrong’s Axioms, these fuzzy inference systems are not oriented to develop automated method to manipulate FFDs. A logic for the management of FFDs over fuzzy attribute tables, named FSL, was introduced in [2]. In the axiomatic system of this logic, the transitivity role is played by a novel rule, named *simplification rule*, which opens the door to define automated reasoning methods.

In this section, FSL is introduced. Its language is the following:

**Definition 5.** Given a finite set of attribute symbols  $\Omega$ , we define the language

$$\mathbb{L} = \{A \xrightarrow{\vartheta} B \mid \vartheta \in [0, 1] \text{ and } A, B \in 2^\Omega\}$$

Concerning the semantic, the models are given by a fuzzy attribute table  $R: \mathbb{D} \rightarrow [0, 1]^\Omega$  over a family of domains  $\{(D_a, \rho_a) \mid a \in \Omega\}$ . We say that  $R \models A \xrightarrow{\vartheta} B$  if  $R$  satisfies  $A \xrightarrow{\vartheta} B$ ,  $R \models \Gamma$  means that  $R$  satisfies every FFD in the set  $\Gamma$  and  $\Gamma \models A \xrightarrow{\vartheta} B$  denotes that  $R \models \Gamma$  implies  $R \models A \xrightarrow{\vartheta} B$ .

**Definition 6.** *The axiomatic system for FSL has one axiom scheme and three inference rules:*

$$\begin{array}{ll}
 \text{[Ax]} \text{ Reflexive Axioms:} & \vdash A \xrightarrow{1} A \\
 \text{[InR]} \text{ Inclusion Rule:} & A \xrightarrow{\vartheta_1} B \vdash A \xrightarrow{\vartheta_2} B' \\
 & \text{when } \vartheta_2 \leq \vartheta_1 \text{ and } B' \subseteq B. \\
 \text{[CoR]} \text{ Composition Rule:} & A \xrightarrow{\vartheta_1} B, C \xrightarrow{\vartheta_2} D \vdash AC \xrightarrow{\vartheta_1 \wedge \vartheta_2} BD \\
 \text{[SiR]} \text{ Simplification Rule:} & A \xrightarrow{\vartheta_1} B, C \xrightarrow{\vartheta_2} D \vdash C \cdot B \xrightarrow{\vartheta_1 \otimes \vartheta_2} D \cdot B \\
 & \text{when } A \subseteq C \text{ and } A \cap B = \emptyset.
 \end{array}$$

The next definition presents the well known notions of *syntactic inference* ( $\vdash$ ) and *equivalence* ( $\equiv$ ).

**Definition 7.** *Let  $\Gamma, \Gamma' \subseteq \mathbb{L}$  and  $\varphi \in \mathbb{L}$ . We say that  $\varphi$  is (syntactically) inferred from  $\Gamma$ , denoted  $\Gamma \vdash \varphi$ , if there exist  $\varphi_1 \dots \varphi_n \in \mathbb{L}$  such that  $\varphi_n = \varphi$  and, for all  $1 \leq i \leq n$ , we have that  $\varphi_i$  belongs to  $\Gamma$ , is an axiom or is obtained by applying the inference rules to formulas in  $\{\varphi_j \mid 1 \leq j < i\}$ .*

*$\Gamma$  and  $\Gamma'$  are said to be equivalent, denoted  $\Gamma \equiv \Gamma'$ , if  $\Gamma \vdash \varphi'$ , for all  $\varphi' \in \Gamma'$ , and  $\Gamma' \vdash \varphi$ , for all  $\varphi \in \Gamma$ .*

**Theorem 1** ([2]). *The axiomatic system of FSL is sound and complete.*

## 4 Automated Reasoning for Fuzzy Functional Dependencies

The aim of this section is to propose an automated reasoning method to decide if a formula  $A \xrightarrow{\vartheta} B$  can be derived from a theory  $\Gamma$  (a set of fuzzy functional dependencies). That is, an automated algorithm to compute the membership function for the closure of  $\Gamma$  defined as follows:

$$\Gamma^+ = \{A \xrightarrow{\vartheta} B \mid \Gamma \vdash A \xrightarrow{\vartheta} B\} \quad (3)$$

Notice that, as a consequence of [InR],  $\Gamma^+$  assigns an infinite set of pairs  $(B, \vartheta)$  to every set  $A$ . If the set  $B$  is also fixed then  $\Gamma^+$  gives an interval (consequence of [InR]) whose supremum will be denoted as  $\vartheta_{A,B}^+$

$$\vartheta_{A,B}^+ = \sup\{\vartheta \in [0, 1] \mid A \xrightarrow{\vartheta} B \in \Gamma^+\} \quad (4)$$

On the other hand, if we fix the value of  $\vartheta$  then a subset of  $2^\Omega$  is obtained. This set is finite and, by [InR] and [CoR], is an ideal of  $(2^\Omega, \subseteq)$ . The maximum element of this ideal will be denoted by  $A_\vartheta^+$ .

$$A_\vartheta^+ = \max\{B \subseteq \Omega \mid A \xrightarrow{\vartheta} B \in \Gamma^+\} \quad (5)$$

And finally, for each set of attributes  $A$ , the closure of  $A$  is defined as

$$A^+ = \{(a, \vartheta_{A,\{a\}}^+) \mid a \in \Omega, 0 < \vartheta_{A,\{a\}}^+\} \quad (6)$$

The following proposition is straightforward from definition.

**Proposition 1.** *Let  $\Gamma$  be a set of fuzzy functional dependencies,  $A, B \subseteq \Omega$  and  $\vartheta \in (0, 1]$ . The following properties are equivalent.*

1.  $\Gamma \vdash A \xrightarrow{\vartheta} B$
2.  $\vartheta \leq \vartheta_{A,B}^+$
3.  $B \subseteq A_{A,B}^+ = \text{Cut}_{\vartheta}(A^+)$  where  $\text{Cut}_{\vartheta}(A^+) = \{a \in \Omega \mid (a, \eta) \in A^+ \text{ with } \eta \geq \vartheta\}$

Thus, the method to solve the implication problem (i.e. to test if  $\Gamma \vdash A \xrightarrow{\vartheta} B$ ) is strongly based on the computation of  $A^+$ . Algorithm 1 computes  $A^+$  di-

---

**Algorithm 1.** Closure Algorithm

---

```

Data:  $\Gamma, A$ 
Result:  $A^+$ 
begin
   $X := \{(x, 1) \mid x \in A\};$ 
  repeat
     $X_{old} := X;$ 
     $\Sigma := \emptyset;$ 
    foreach  $B \xrightarrow{\vartheta} C \in \Gamma$  do
      1   if there exists  $b \in B$  such that  $b \neq a$  for all  $(a, \kappa) \in X$  then  $\eta := 0$ 
      2   else  $\eta := \min\{\kappa \mid (b, \kappa) \in X \text{ with } b \in B\};$ 
      3   if  $\eta \otimes \vartheta \neq 0$  then  $X := X \sqcup \{(c, \eta \otimes \vartheta) \mid c \in C\};$ 
      4   if  $\eta \neq 1$  and  $C \not\subseteq \text{Cut}_{\vartheta}(X)$  then
         $\Sigma := \Sigma \cup \{B \setminus \text{Cut}_1(X) \xrightarrow{\vartheta} C \setminus \text{Cut}_{\vartheta}(X)\}$ 
       $\Gamma := \Sigma;$ 
    until  $X = X_{old};$ 
  return " $A^+$  is "  $X$ 
end

```

---

rectly based on FSL as the next section proves. Now, some comments about this algorithm are given:

- Observe that, in the lines labeled with the numbers 1 and 2 in Algorithm 1, the computed degree is

$$\eta = \sup\{\kappa \mid B \subseteq \text{Cut}_{\kappa}(X)\} \tag{7}$$

So, when  $\eta = 1$  (see condition in Line 4) the inclusion  $B \subseteq \text{Cut}_1(X)$  holds.

- On the other hand, in Line 3, a kind of union is used that is defined as:

$$A \sqcup B = \{(x, \sigma(x)) \mid \text{there exists } \eta \text{ with } (x, \eta) \in A \cup B\} \tag{8}$$

where

$$\sigma(x) = \begin{cases} \eta & \text{if } (x, \eta) \in A \text{ and } x \neq y \text{ for all } (y, \kappa) \in B \\ \kappa & \text{if } (x, \kappa) \in B \text{ and } x \neq y \text{ for all } (y, \eta) \in A \\ \eta \vee \kappa & \text{if } (x, \eta) \in A \text{ and } (x, \kappa) \in B \end{cases} \tag{9}$$

*Example 4.* In this example  $abc^+$  are going to be computed from the set

$$\Gamma = \{cd \xrightarrow{0.6} e, ac \xrightarrow{0.7} def, f \xrightarrow{0.5} dg, de \xrightarrow{0.9} ch, dh \xrightarrow{0.4} a\}$$

by considering the Lukasiweicz product. The initial set  $X$  is  $\{(a, 1), (b, 1), (c, 1)\}$  and the sketch of the trace of Algorithm 1 is the following:

1. For  $cd \xrightarrow{0.6} e$ , since there does not exist  $\kappa$  such that  $(d, \kappa) \in X$ , then  $\eta = 0$ . Moreover,  $\eta \otimes 0.6 = 0$  and  $\{e\} \not\subseteq \text{Cut}_{0.6}(X) = \{a, b, c\}$ . So,  $X = \{(a, 1), (b, 1), (c, 1)\}$  and  $\Sigma = \{d \xrightarrow{0.6} e\}$ .
2. For the formula  $ac \xrightarrow{0.7} def$  we have that  $\eta = 1$  and  $\eta \otimes 0.7 = 0.7$ . Then

$$X = \{(a, 1), (b, 1), (c, 1), (d, 0.7), (e, 0.7), (f, 0.7)\}$$

$$\text{and } \Sigma = \{d \xrightarrow{0.6} e\}.$$

3. For  $f \xrightarrow{0.5} dg$ , since  $(f, 0.7) \in X$ ,  $\eta = 0.7$  and  $\eta \otimes 0.5 = 0.2$ . Thus,

$$X = \{(a, 1), (b, 1), (c, 1), (d, 0.7), (e, 0.7), (f, 0.7), (g, 0.2)\}$$

$$\text{and } \Sigma = \{d \xrightarrow{0.6} e, f \xrightarrow{0.5} g\}.$$

4. Considering  $de \xrightarrow{0.9} ch$ ,  $\eta = \min\{0.7, 0.7\} = 0.7$  and  $\eta \otimes 0.9 = 0.6$ . Then

$$\begin{aligned} X &= X \sqcup \{(c, 0.6), (h, 0.6)\} \\ &= \{(a, 1), (b, 1), (c, 1), (d, 0.7), (e, 0.7), (f, 0.7), (g, 0.2), (h, 0.6)\} \end{aligned}$$

and  $\Sigma$  remains without changes.

5. For  $dh \xrightarrow{0.4} a$ , since  $\eta = 0.6$ ,  $\eta \otimes 0.4 = 0$  and  $\{a\} \subseteq \text{Cut}_{0.4}(X)$ , then there is no change in either  $A$  or  $\Sigma$ .
6. Now,  $\Gamma = \{d \xrightarrow{0.6} e, f \xrightarrow{0.5} g\}$  and, since  $X_{old} \neq X$ , the sets are initialized as  $X_{old} := X$  and  $\Sigma = \emptyset$ .
7. For  $d \xrightarrow{0.6} e$ ,  $\eta = 0.7$  and  $\eta \otimes 0.6 = 0.3$ . Therefore,  $X$  and  $\Sigma$  remain invariant.
8. For  $f \xrightarrow{0.5} g$ ,  $\eta = 0.7$  and  $\eta \otimes 0.5 = 0.2$ . Therefore,  $X$  does not change and  $\Sigma = \{f \xrightarrow{0.5} g\}$ .

Thus, since  $X_{old} = X$ , the algorithm returns:

$$abc^+ = \{(a, 1), (b, 1), (c, 1), (d, 0.7), (e, 0.7), (f, 0.7), (g, 0.2), (h, 0.6)\}$$

*Example 5.* Let  $\Gamma = \{cd \xrightarrow{0.6} e, ac \xrightarrow{0.7} def, f \xrightarrow{0.5} dg, de \xrightarrow{0.9} ch, dh \xrightarrow{0.4} a\}$  and  $\otimes$  be the Lukasiweicz product. To decide if  $\Gamma \vdash abc \xrightarrow{0.5} dh$  holds, we first compute  $abc^+$  (see Example 4)

$$abc^+ = \{(a, 1), (b, 1), (c, 1), (d, 0.7), (e, 0.7), (f, 0.7), (g, 0.2), (h, 0.6)\}$$

Since  $\{d, h\} \subseteq \text{Cut}_{0.5}(abc^+) = \{a, b, c, d, e, f, h\}$ , then the answer is affirmative.

**Table 1.** Algorithm’s schema

$B \xrightarrow{\vartheta} C \in \Gamma$	$\Sigma$	$X$
$\Gamma = \{cd \xrightarrow{0.6} e, ac \xrightarrow{0.7} def, f \xrightarrow{0.5} dg, de \xrightarrow{0.9} ch, dh \xrightarrow{0.4} a\}$		
$cd \xrightarrow{0.6} e$	$\emptyset$	$\{(a, 1), (b, 1), (c, 1)\}$
$ac \xrightarrow{0.7} def$	$\{d \xrightarrow{0.6} e\}$	$\{(a, 1), (b, 1), (c, 1)\}$
$f \xrightarrow{0.5} dg$	$\{d \xrightarrow{0.6} e, f \xrightarrow{0.5} g\}$	$\{(a, 1), (b, 1), (c, 1), (d, 0.7), (e, 0.7), (f, 0.7)\}$
$de \xrightarrow{0.9} ch$	$\{d \xrightarrow{0.6} e, f \xrightarrow{0.5} g\}$	$\{(a, 1), (b, 1), (c, 1), (d, 0.7), (e, 0.7), (f, 0.7), (g, 0.2)\}$
$dh \xrightarrow{0.4} a$	$\{d \xrightarrow{0.6} e, f \xrightarrow{0.5} g\}$	$\{(a, 1), (b, 1), (c, 1), (d, 0.7), (e, 0.7), (f, 0.7), (g, 0.2), (h, 0.6)\}$
$\Gamma = \{d \xrightarrow{0.6} e, f \xrightarrow{0.5} g\}$		
$d \xrightarrow{0.6} e$	$\emptyset$	$\{(a, 1), (b, 1), (c, 1), (d, 0.7), (e, 0.7), (f, 0.7), (g, 0.2), (h, 0.6)\}$
$f \xrightarrow{0.5} g$	$\{f \xrightarrow{0.5} g\}$	$\{(a, 1), (b, 1), (c, 1), (d, 0.7), (e, 0.7), (f, 0.7), (g, 0.2), (h, 0.6)\}$

### 5 Soundness and Completeness

The following theorem is one of the cornerstones of Algorithm 1.

**Theorem 2.** *Let  $\Gamma$  be a set of fuzzy functional dependencies,  $A \subseteq \Omega$ ,  $a \in \Omega$  and  $\vartheta \in (0, 1]$ . The following equivalencies hold.*

$$(a, \vartheta) \in A^+ \text{ if and only if } \Gamma \cup \{\emptyset \xrightarrow{1} A\} \vdash \emptyset \xrightarrow{\vartheta} a \tag{10}$$

$$\text{if and only if } \Gamma \cup \{\emptyset \xrightarrow{1} x \mid x \in A\} \vdash \emptyset \xrightarrow{\vartheta} a \tag{11}$$

Basically, the algorithm considers the set  $\Gamma \cup \{\emptyset \xrightarrow{1} x \mid x \in A\}$  and applies to it transformations that preserve the equivalence. Specifically, the equivalences applied are the following.

**Lemma 1.** *Let  $A = \{a_i \mid i \in I\} \subseteq \Omega$  and  $B, C \subseteq \Omega$  be finite sets of attributes and  $\{\vartheta_i \mid i \in I\} \cup \{\vartheta\} \subseteq (0, 1]$ . The following equivalency holds:*

$$\{\emptyset \xrightarrow{\vartheta_i} a_i \mid i \in I\} \cup \{B \xrightarrow{\vartheta} C\} \equiv \{\emptyset \xrightarrow{\vartheta_i} a_i \mid i \in I\} \cup \{B \setminus A_1 \xrightarrow{\vartheta} C \setminus A_\vartheta\} \tag{12}$$

where  $A_\vartheta = \{a_i \mid \vartheta \leq \vartheta_i\}$  and particularly  $A_1 = \{a_i \mid \vartheta_i = 1\}$ .

*Proof.* The following sequence proves the derivation

$$\{\emptyset \xrightarrow{\vartheta_i} a_i \mid i \in I\} \cup \{B \xrightarrow{\vartheta} C\} \vdash B \setminus A_1 \xrightarrow{\vartheta} C \setminus A_\vartheta$$

- $\emptyset \xrightarrow{1} A_1$  ..... By [CoR] from hypothesis  $\{\emptyset \xrightarrow{1} a_i \mid a_i \in A_1\}$ .
- $B \setminus A_1 \xrightarrow{1 \otimes \vartheta} C \setminus A_1$  ..... By [SiR] from 1. and  $B \xrightarrow{\vartheta} C$ .
- $B \setminus A_1 \xrightarrow{\vartheta} C \setminus A_\vartheta$  ..... By [InR] from 2. and  $C \setminus A_\vartheta \subseteq C \setminus A_1$  because  $A_1 \subseteq A_\vartheta$ .



On the other hand, the following sequence proves the converse derivation

$$\{\emptyset \xrightarrow{\vartheta_i} a_i \mid i \in I\} \cup \{B \setminus A_1 \xrightarrow{\vartheta} C \setminus A_\vartheta\} \vdash B \xrightarrow{\vartheta} C$$

1.  $B \cap A_1 \xrightarrow{1} B \cap A_1$  ..... By [Ax].
2.  $B \xrightarrow{1 \wedge \vartheta} (C \setminus A_\vartheta) \cup (B \cap A_1)$  ..... By [CoR] from 1. and hypothesis.
3.  $\emptyset \xrightarrow{\vartheta} A_\vartheta$  ..... By [InR] and [CoR] from hypothesis  $\{\emptyset \xrightarrow{\vartheta_i} a_i \mid a_i \in A_\vartheta\}$ .
4.  $B \xrightarrow{\vartheta} (C \setminus A_\vartheta) \cup (B \cap A_1) \cup A_\vartheta$  ..... By [CoR] from 2. and 3.
5.  $B \xrightarrow{\vartheta} C$  ..... By [InR] from 4.

□

As particular cases of the equivalence given in the previous lemma, if  $C \subseteq A_\vartheta$  then

$$\{\emptyset \xrightarrow{\vartheta_i} a_i \mid i \in I\} \cup \{B \xrightarrow{\vartheta} C\} \equiv \{\emptyset \xrightarrow{\vartheta_i} a_i \mid i \in I\} \quad (13)$$

and, if  $B \subseteq A_1$ , then

$$\{\emptyset \xrightarrow{\vartheta_i} a_i \mid i \in I\} \cup \{B \xrightarrow{\vartheta} C\} \equiv \{\emptyset \xrightarrow{\vartheta_i} a_i \mid i \in I\} \cup \{\emptyset \xrightarrow{\vartheta} c \mid c \in C \setminus A_\vartheta\} \quad (14)$$

Equivalence (15) is used in Algorithm 1 in two steps (Line 3 and Line 6), Equivalence (14) is used in the combination of Line 3 and Line 4 and Equivalence (13) is used in Line 3.

**Lemma 2.** *Let  $A = \{a_i \mid i \in I\} \subseteq \Omega$  and  $B, C \subseteq \Omega$  be finite sets of attributes and  $\{\vartheta_i \mid i \in I\} \cup \{\vartheta\} \subseteq (0, 1]$ . If  $B \subseteq A$  and  $\eta = \min\{\vartheta_i \mid i \in I\}$  then*

$$\{\emptyset \xrightarrow{\vartheta_i} a_i \mid i \in I\} \cup \{B \xrightarrow{\vartheta} C\} \vdash \{\emptyset \xrightarrow{\eta \otimes \vartheta} c \mid c \in C\} \quad (15)$$

*Proof.* It is straightforward from [InR] and [SiR]. □

Lemma 2 is used in Line 5 of Algorithm 1. Now we introduce the completeness result and outline its proof.

**Theorem 3 (Soundness and Completeness).** *Given a set of fuzzy functional dependencies  $\Gamma$  and a set of attributes  $A$ , Algorithm 1 returns  $A^+$ .*

*Proof.* The soundness is consequence of Lemmas 1 and 2. Tarski's fixed-point theorem ensures that the algorithm finishes because the sequence of the sets  $A$  is growing simultaneously with the decrease of the set  $\Gamma$ . Regarding completeness, when the algorithm finishes, any formula  $\emptyset \xrightarrow{\eta} B$  that can be derived from  $\{\emptyset \xrightarrow{\vartheta} a \mid (a, \vartheta) \in A\} \cup \Gamma$  can be also derived from  $\{\emptyset \xrightarrow{\vartheta} a \mid (a, \vartheta) \in A\}$  by [InR] and [CoR]. □

## 6 Conclusions

In [2] we have introduced the Simplification Logic for the management of fuzzy functional dependencies over fuzzy attribute tables,  $\mathbb{FSL}$ , and we have outlined its advantages. In this paper we show that the design of the  $\mathbb{FSL}$  axiomatic system provides a way to define automated reasoning methods for fuzzy functional dependencies. Specifically, we present a sound and complete automated reasoning method to solve the implication problem. This provides a framework with a high expressive power useful for the applications.

**Acknowledgment.** Supported by Grants TIN2011-28084 of the Science and Innovation Ministry of Spain, and No. P09-FQM-5233 of the Junta de Andalucía.

## References

1. Codd, E.F.: The relational model for database management: version 2. Addison-Wesley Longman Publishing Co., Inc., Boston (1990)
2. Cordero, P., Enciso, M., Mora, A., de Guzmán, I.P., Rodríguez-Jiménez, J.M.: Specification and inference of fuzzy attributes. In: FOCCI, pp. 107–114 (2011)
3. Abiteboul, S., et al.: The lowell database research self-assessment. Communications of the ACM 48, 111–118 (2005); ACM ID: 1060718
4. Giardina, C., Sack, I., Sinha, D.: Fuzzy field relational database. Report 8332, Elect. Engng. and Computer Science Dept., Stevens Institute of Technology, Hoboken, NJ (1983)
5. Baldwin, J.: Knowledge engineering using a fuzzy relational inference language. In: Proc. IFAC Conf. on Fuzzy Information, Knowledge Representation, and Decision Processes, Marseille, France, pp. 15–23 (1983)
6. Prade, H., Testemale, C.: The connection between lipskios approach to incomplete information data bases and zadeh's possibility theory. In: Proc. Int. Conf. Systems Meth., pp. 402–408 (1982)
7. Prade, H., Testemale, C.: Generalizing database relational algebra for the treatment of incomplete or uncertain information and vague queries. Information Sciences 34, 115–143 (1984)
8. Buckles, B.P., Perty, F.: A fuzzy representation of data for relational databases. Fuzzy Sets and Systems 7, 213–216 (1982)
9. Buckles, B.P., Perty, F.: Fuzzy databases and their applications. In: Fuzzy Inform. Decision Process, pp. 361–371 (1982)
10. Buckles, B.P., Perty, F.: Uncertainty models in information and database systems. J. Inform. Sci. 11, 77–87 (1985)
11. Yahia, S.B., Ounalli, H., Jaoua, A.: An extension of classical functional dependency: dynamic fuzzy functional dependency. Information Sciences 119, 219–234 (1999)
12. Tyagi, B., Sharfuddin, A., Dutta, R., Tayal, D.K.: A complete axiomatization of fuzzy functional dependencies using fuzzy function. Fuzzy Sets and Systems 151, 363–379 (2005)
13. Bělohávek, R., Vychodil, V.: Data tables with similarity relations: Functional dependencies, complete rules and non-redundant bases. In: Li Lee, M., Tan, K.-L., Wuwongse, V. (eds.) DASFAA 2006. LNCS, vol. 3882, pp. 644–658. Springer, Heidelberg (2006)

14. Sözat, M.I., Yazici, A.: A complete axiomatization for fuzzy functional and multivalued dependencies in fuzzy database relations. *Fuzzy Sets and Systems* 117, 161–181 (2001)
15. Cordero, P., Enciso, M., Mora, A., de Guzmán, I.P.: A complete logic for fuzzy functional dependencies over domains with similarity relations. In: Cabestany, J., Sandoval, F., Prieto, A., Corchado, J.M. (eds.) *IWANN 2009, Part I*. LNCS, vol. 5517, pp. 261–269. Springer, Heidelberg (2009)
16. Cordero, P., Enciso, M., Mora, A., de Guzmán, I.P., Rodríguez-Jiménez, J.M.: An efficient algorithm for reasoning about fuzzy functional dependencies. In: Cabestany, J., Rojas, I., Joya, G. (eds.) *IWANN 2011, Part II*. LNCS, vol. 6692, pp. 412–420. Springer, Heidelberg (2011)
17. Medina, J., Ojeda-Aciego, M.: Dual multi-adjoint concept lattices. *Information Sciences* 225, 47–54 (2013)
18. Medina, J., Ojeda-Aciego, M., Ruiz-Calviño, J.: Fuzzy logic programming via multilattices. *Fuzzy Sets and Systems* 158, 674–688 (2007)
19. Raju, K.V.S.V.N., Majumdar, A.K.: Fuzzy functional dependencies and lossless join decomposition of fuzzy relational database systems. *ACM Trans. Database Syst.* 13, 129–166 (1988)
20. Belohlavek, R., Vychodil, V.: Relational model of data over domains with similarities: An extension for similarity queries and knowledge extraction. In: *IEEE International Conference on Information Reuse and Integration*, pp. 207–213 (2006)
21. Cordero, P., Enciso, M., Mora, A., de Guzmán, I.P.: A complete logic for fuzzy functional dependencies over t-norms. In: *XV Spanish Conference on Fuzzy Logic and Technology*, pp. 205–210 (2010)
22. Cordero, P., Enciso, M., Mora, A., de Guzmán, I.P.: Reasoning about fuzzy functional dependencies. In: *XIV Spanish Conference on Fuzzy Logic and Technology*, pp. 121–126 (2008)

# On the Classification of Fuzzy-Attributes in Multi-adjoint Concept Lattices\*

Maria Eugenia Cornejo<sup>1</sup>, Jesús Medina-Moreno<sup>2,\*\*</sup>, and Eloisa Ramírez<sup>1</sup>

<sup>1</sup> Dpt. de Estadística e I.O. University of Cádiz, Spain

{[mariaeugenia.cornejo](mailto:mariaeugenia.cornejo@uca.es),[eloisa.ramirez](mailto:eloisa.ramirez@uca.es)}@uca.es

<sup>2</sup> Dpt. de Matemáticas. University of Cádiz, Spain

[jesus.medina@uca.es](mailto:jesus.medina@uca.es)

**Abstract.** In formal concept analysis, attribute reduction is an important preprocessing in order to obtain concept lattices, which provides fundamental information of the attributes, as well. This importance is increased in the fuzzy case.

This paper presents, in the general fuzzy framework of multi-adjoint concept lattices, a classification of the fuzzy-attributes of a context, which provides interesting properties of the attributes and its application to reduce the computational complexity for building this kind of concept lattices.

**Keywords:** Formal concept analysis, fuzzy sets, attribute classification.

## 1 Introduction

Formal concept analysis was introduced by R. Wille in the eighties, and it is one of the effective mathematical tools for conceptual data analysis and knowledge processing. This formal tool has a lot of applications, there are papers ranging from ontology merging [18] to diverse fields of application such as the Semantic Web [2, 4, 5].

Attribute reduction is a fundamental part in Formal Concept Analysis since the complexity for building the concept lattice is exponential in the number of attributes and objects. In knowledge systems usually appear unnecessary attributes which considerably increase the computational time for obtaining the concept lattice, hence it is very important knowing the unnecessary attributes at the beginning.

Therefore, this line is widely studied in the classical case [11, 13, 21, 22]. In the fuzzy extensions of concept lattices, we can remark [12]. Other interesting viewpoints in order to reduce the complexity for building the fuzzy concept lattices are the use of *truth stressers* (which is also called *hedges*) in the concept-forming operators [1, 9, 10], and the granularity [8]. However, these methodologies decrease the complexity reducing the size of the fuzzy concept lattices.

---

\* Partially supported by the Spanish Science Ministry projects TIN2009-14562-C05-03 and TIN2012-39353-C04-04, and by Junta de Andalucía project P09-FQM-5233.

\*\* Corresponding author.

This paper presents a first prospect about attribute reduction in multi-adjoint concept lattices [14, 16]. These concept lattices are a fuzzy generalization of classical formal concept analysis, which embeds other fuzzy extensions, and in which the basic operators, taken into account in the concept-forming operators, are the adjoint triples [3]. Specifically, the corresponding definitions of attribute reduction theory will be given in this fuzzy framework, several properties and a classification of fuzzy attributes will be made. As a consequence of this last result, the unnecessary fuzzy attributes can be located and erased, therefore, a reduct is easily obtained, from which the whole multi-adjoint concept lattice is built.

## 2 Preliminaries

This section presents a sketch of attribute reduction theory in formal concept analysis and the general fuzzy framework of multi-adjoint concept lattices [16].

### 2.1 Attribute Reduction in Formal Concept Analysis

Attribute reduction was already studied by B. Ganter and R. Wille in [6]. For that, they considered the irreducible elements of the concept lattice. This consideration was taken into account in [15] in order to present an attribute classification assuming the definitions given in Rough Set Theory [17].

First of all, the definitions of finer, consistent set, reduct and core on concept lattices will be recalled.

**Definition 1.** *Given two concept lattices  $\mathfrak{B}(A_1, B, R_1)$  and  $\mathfrak{B}(A_2, B, R_2)$ . If for any  $(X, Y) \in \mathfrak{B}(A_2, B, R_2)$  there exists  $(X', Y') \in \mathfrak{B}(A_1, B, R_1)$  such that  $X = X'$ , then we say that  $\mathfrak{B}(A_1, B, R_1)$  is finer than  $\mathfrak{B}(A_2, B, R_2)$  and we will write:*

$$\mathfrak{B}(A_1, B, R_1) \leq \mathfrak{B}(A_2, B, R_2)$$

If  $\mathfrak{B}(A_1, B, R_1) \leq \mathfrak{B}(A_2, B, R_2)$  and  $\mathfrak{B}(A_2, B, R_2) \leq \mathfrak{B}(A_1, B, R_1)$ , then these two concept lattices are said to be *isomorphic* to each other, and we will write:

$$\mathfrak{B}(A_1, B, R_1) \cong \mathfrak{B}(A_2, B, R_2)$$

Considering a context  $(A, B, R)$ , a subset of attributes,  $Y \subseteq A$  and the restriction relation  $R_Y = R \cap (Y \times B)$ , the triple  $(Y, B, R_Y)$  is also a formal context, which can be interpreted as a *subcontext* of the original one. Hence, we can apply the mappings  $\downarrow$  and  $\uparrow$ , which will be rewritten in this subcontext as  $\downarrow^Y$  and  $\uparrow_Y$ . It is clear that, given  $X \subseteq B$ , we obtain that  $X^{\uparrow_Y} = X^{\uparrow} \cap Y$ .

If  $(A, B, R)$  is a formal context, we can easily verify that for any  $Y \subseteq A$ , such that  $Y \neq \emptyset$ ,  $\mathfrak{B}(A, B, R) \leq \mathfrak{B}(Y, B, R_Y)$  holds.

**Definition 2.** *Given a context  $(A, B, R)$ , if there exists a set of attributes  $Y \subseteq A$  such that  $\mathfrak{B}(A, B, R) \cong \mathfrak{B}(Y, B, R_Y)$ , then  $Y$  is called a *consistent set* of  $(A, B, R)$ . Moreover, if  $\mathfrak{B}(Y \setminus \{y\}, B, R_{Y \setminus \{y\}}) \not\cong \mathfrak{B}(A, B, R)$ , for all  $y \in Y$ , then  $Y$  is called a *reduct* of  $(A, B, R)$ .*

*The core of  $(A, B, R)$  is the intersection of all the reducts of  $(A, B, R)$ .*

**Theorem 1 ([22]).** *Let  $(A, B, R)$  be a formal context,  $Y \subseteq A$  and  $Y \neq \emptyset$ . Then,  $Y$  is a consistent set if and only if  $\mathfrak{B}(Y, B, R_Y) \leq \mathfrak{B}(A, B, R)$ .*

Pawlak [17] proposed three types of attributes for rough set theory, which were introduced in a formal context in [22]. Now, this definition will be recalled considering the notation in [20] to denote the subsets of attributes.

**Definition 3.** *Given an index set  $\Lambda$ , a formal context  $(A, B, R)$  and the set  $\{Y_i \mid Y_i \text{ is a reduct, } i \in \Lambda\}$  of all reducts of  $(A, B, R)$ . The set of attributes  $A$  can be divided into the following three parts:*

1. *Absolutely necessary attributes (core attribute)  $C_f = \bigcap_{i \in \Lambda} Y_i$ .*
2. *Relatively necessary attributes  $K_f = (\bigcup_{i \in \Lambda} Y_i) \setminus (\bigcap_{i \in \Lambda} Y_i)$ .*
3. *Absolutely unnecessary attributes  $I_f = A \setminus (\bigcup_{i \in \Lambda} Y_i)$ .*

The pre-processing of attribute reduction in formal concept analysis aims at classifying the attributes from the irreducible elements in  $\mathfrak{B}(A, B, R)$ . Therefore, the definition of irreducible elements of a lattice must be introduced.

**Definition 4.** *Given a lattice  $(L, \leq)$ , such that  $\wedge, \vee$  are the meet and the join operators, and an element  $x \in L$  verifying*

1. *If  $L$  has a top element  $\top$ , then  $x \neq \top$ .*
2. *If  $x = y \wedge z$ , then  $x = y$  or  $x = z$ , for all  $y, z \in L$ .*

*we call  $x$  meet-irreducible ( $\wedge$ -irreducible) element of  $L$ . Condition (2) is equivalent to*

- 2'. *If  $x < y$  and  $x < z$ , then  $x < y \wedge z$ , for all  $y, z \in L$ .*

*Hence, if  $x$  is  $\wedge$ -irreducible, then it cannot be represented as the infimum of strictly greatest elements.*

*A join-irreducible ( $\vee$ -irreducible) element of  $L$  is defined dually.*

## 2.2 Multi-Adjoint Concept Lattices

The considered operators in the forming-concept operators are the adjoint triples, which are generalizations of a triangular norm (t-norm) and its residuated implication [7].

**Definition 5.** *Let  $(P_1, \leq_1)$ ,  $(P_2, \leq_2)$ ,  $(P_3, \leq_3)$  be posets and  $\&: P_1 \times P_2 \rightarrow P_3$ ,  $\swarrow: P_3 \times P_2 \rightarrow P_1$ ,  $\nwarrow: P_3 \times P_1 \rightarrow P_2$  be mappings, then  $(\&, \swarrow, \nwarrow)$  is an adjoint triple with respect to  $P_1, P_2, P_3$  if:*

$$x \leq_1 z \swarrow y \quad \text{iff} \quad x \& y \leq_3 z \quad \text{iff} \quad y \leq_2 z \nwarrow x \tag{1}$$

*where  $x \in P_1$ ,  $y \in P_2$  and  $z \in P_3$ .*

Condition (1) is also called *adjoint property*. Note that the commutativity and associativity properties are not assumed for the conjunctor  $\&$ . Moreover, assuming different adjoint triples adds more flexibility to the language [16].

**Definition 6.** A multi-adjoint frame  $\mathcal{L}$  is a tuple

$$(L_1, L_2, P, \preceq_1, \preceq_2, \leq, \&_1, \swarrow^1, \nwarrow_1, \dots, \&_n, \swarrow^n, \nwarrow_n)$$

where  $(L_1, \preceq_1)$  and  $(L_2, \preceq_2)$  are complete lattices,  $(P, \leq)$  is a poset and, for all  $i = 1, \dots, n$ ,  $(\&_i, \swarrow^i, \nwarrow_i)$  is an adjoint triple with respect to  $L_1, L_2, P$ .

Multi-adjoint frames are denoted as  $(L_1, L_2, P, \&_1, \dots, \&_n)$ .

A *multi-adjoint context* is a tuple consisting of sets of objects, attributes and a fuzzy relation among them; in addition, the multi-adjoint approach also includes a function which assigns an adjoint triple to each pair of objects and attributes.

**Definition 7.** Let  $(L_1, L_2, P, \&_1, \dots, \&_n)$  be a multi-adjoint frame, a context is a tuple  $(A, B, R, \sigma)$  such that  $A$  and  $B$  are non-empty sets (usually interpreted as attributes and objects, respectively),  $R$  is a  $P$ -fuzzy relation  $R: A \times B \rightarrow P$  and  $\sigma: A \times B \rightarrow \{1, \dots, n\}$  is a mapping which associates any element in  $A \times B$  with some particular adjoint triple in the frame.

Given a multi-adjoint frame and a context for that frame, the forming-concept operators are denoted as  $\uparrow: L_2^B \rightarrow L_1^A$  and  $\downarrow: L_1^A \rightarrow L_2^B$  and are defined, for all  $g \in L_2^B$ ,  $f \in L_1^A$  and  $a \in A$ ,  $b \in B$ , as

$$g^\uparrow(a) = \inf\{R(a, b) \swarrow^{\sigma(b)} g(b) \mid b \in B\} \tag{2}$$

$$f^\downarrow(b) = \inf\{R(a, b) \nwarrow_{\sigma(b)} f(a) \mid a \in A\} \tag{3}$$

These two arrows form a Galois connection [16], and so the notion of concept is defined as usual: a *multi-adjoint concept* is a pair  $\langle g, f \rangle$  satisfying that  $g \in L_2^B$ ,  $f \in L_1^A$  and that  $g^\uparrow = f$  and  $f^\downarrow = g$ .

Given  $g \in L_2^B$  (resp.  $f \in L_1^A$ ), the *closure concept of  $g$*  (resp.  *$f$* ) is the concept  $\langle g^\uparrow, g^\uparrow \rangle$  (resp.  $\langle f^\downarrow, f^\downarrow \rangle$ ). Finally, the definition of concept lattice in this framework is introduced.

**Definition 8.** The multi-adjoint concept lattice associated with a multi-adjoint frame  $(L_1, L_2, P, \&_1, \dots, \&_n)$  and a context  $(A, B, R, \sigma)$  is the set

$$\mathcal{M} = \{\langle g, f \rangle \mid g \in L_2^B, f \in L_1^A \text{ and } g^\uparrow = f, f^\downarrow = g\}$$

in which the ordering is defined by  $\langle g_1, f_1 \rangle \preceq \langle g_2, f_2 \rangle$  if and only if  $g_1 \preceq_2 g_2$  (equivalently  $f_2 \preceq_1 f_1$ ).

It was proven in [16] that  $(\mathcal{M}, \preceq)$  is really a complete lattice, together with a representation theorem, which generalizes the classical one and different other fuzzy generalizations.

---

<sup>1</sup> Note that the notation of  $L_2^B$  and  $L_1^A$  is considered to the set of mappings  $g: B \rightarrow L_2$ ,  $f: A \rightarrow L_1$ , respectively.

### 3 Fuzzy-Attribute Reduction

Following the similar steps to classical setting, first of all, a characterization of the  $\wedge$ -irreducible elements of a multi-adjoint concept lattice will be presented. From now on, we will consider a multi-adjoint concept lattice  $\mathcal{M}$  associated with a multi-adjoint frame  $(L_1, L_2, P, \&_1, \dots, \&_n)$ , a context  $(A, B, R, \sigma)$ , an index set  $I$ , such that  $A = \{a_i \mid i \in I\}$ , and the following specific family of fuzzy subsets of  $L_1^A$ .

**Definition 9.** For each  $a_i \in A$ , the fuzzy subsets of attributes  $\phi_{i,x_i} \in L_1^A$  defined, for all  $x \in L_1$ , as

$$\phi_{i,x}(a) = \begin{cases} x & \text{if } a = a_i \\ 0 & \text{if } a \neq a_i \end{cases}$$

will be called fuzzy-attributes. The set of all fuzzy-attributes will be denoted as  $\Phi = \{\phi_{i,x} \mid a_i \in A, x \in L_1\}$ .

Considering these fuzzy subsets of attributes, the following result characterizes the  $\wedge$ -irreducible elements of a multi-adjoint concept lattice.

**Theorem 2.** The set of  $\wedge$ -irreducible elements of  $\mathcal{M}$ ,  $M_F(A, B, R, \sigma)$ , is:

$$\left\{ \langle \phi_{i,x}^\downarrow, \phi_{i,x}^\uparrow \rangle \mid \phi_{i,x}^\downarrow \neq \bigwedge \{ \phi_{j,x_j}^\downarrow \mid \phi_{j,x_j} \in \Phi, \phi_{i,x}^\downarrow \prec_2 \phi_{j,x_j}^\downarrow \} \text{ and } \phi_{i,x}^\downarrow \neq \perp_A^\downarrow \right\}$$

In the previous set, the expression  $\phi_{i,x}^\downarrow \neq \bigwedge \{ \phi_{j,x_j}^\downarrow \mid \phi_{i,x}^\downarrow \prec_2 \phi_{j,x_j}^\downarrow \}$  may be replaced by  $\phi_{i,x}^\downarrow \prec_2 \bigwedge \{ \phi_{j,x_j}^\downarrow \mid \phi_{i,x}^\downarrow \prec_2 \phi_{j,x_j}^\downarrow \}$ , since both are equivalent. However, we prefer using the inequality in order to emphasize the difference.

As a consequence of this theorem, the  $\wedge$ -irreducible elements are directly obtained from the fuzzy-attributes and these are only considered to compute them.

*Example 1.* Let us consider a shorter example than the one given in [19], in which, the goal is to find out the best day to walk. Hence, a suitable definition of *walking time* is assumed and the theory of concept lattices is used to obtain the best day satisfying this definition. In this introductory example, we have only considered the weak-end and we will analyze the built concept lattice.

Let  $([0, 1], [0, 1], [0, 1], \leq, \leq, \leq, \&_G)$  be the multi-adjoint frame where  $\&_G$  is the commutative Gödel conjunctor. The considered context is formed by the set of objects and attributes:

$$\begin{aligned} A &= \{\text{warm, cold, poor in rain, calm wind}\} \\ B &= \{\text{Fri, Sat, Sun}\} \end{aligned}$$

and the relationship  $R: A \times B \rightarrow P$ , which is defined in Fig. 1.



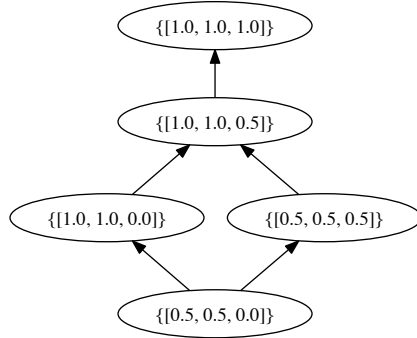
**Fig. 1.** Table Example 1

$R$	Fri	Sat	Sun
warm	1.0	1.0	0.0
cold	0.5	0.5	0.5
poor in rain	1.0	1.0	0.5
calm wind	0.5	0.5	0.0

From the context  $(A, B, R, \sigma)$ , a concept lattice  $(\mathcal{M}, \preceq)$  with the following 5 concepts is built.

- $C_0 = \langle \{0.5/\text{Fri}, 0.5/\text{Sat}\}, \{1.0/\text{warm}, 1.0/\text{cold}, 1.0/\text{poor in rain}, 1.0/\text{calm wind}\} \rangle$
- $C_1 = \langle \{1.0/\text{Fri}, 1.0/\text{Sat}\}, \{1.0/\text{warm}, 0.5/\text{cold}, 1.0/\text{poor in rain}, 0.5/\text{calm wind}\} \rangle$
- $C_2 = \langle \{0.5/\text{Fri}, 0.5/\text{Sat}, 0.5/\text{Sun}\}, \{1.0/\text{cold}, 1.0/\text{poor in rain}\} \rangle$
- $C_3 = \langle \{1.0/\text{Fri}, 1.0/\text{Sat}, 0.5/\text{Sun}\}, \{0.5/\text{cold}, 1.0/\text{poor in rain}\} \rangle$
- $C_4 = \langle \{1.0/\text{Fri}, 1.0/\text{Sat}, 1.0/\text{Sun}\}, \{0.5/\text{cold}, 0.5/\text{poor in rain}\} \rangle$

The Hasse diagram of this lattice is shown in Figure 2, in which each node represents the fuzzy extension of each concept.



**Fig. 2.** The Hasse diagram of  $(\mathcal{M}, \preceq)$

The concept  $C_4$  is the closure concept of the fuzzy-attributes  $\phi_{a,0.0}$ , for all  $a \in A$ , and  $\phi_{\text{cold},0.5}$  and  $\phi_{\text{poor in rain},0.5}$ , as well. The rest of closure concepts are:

$$\begin{aligned}
 \langle \phi_{\text{warm},0.5}^\downarrow, \phi_{\text{warm},0.5}^\uparrow \rangle &= \langle \phi_{\text{warm},1.0}^\downarrow, \phi_{\text{warm},1.0}^\uparrow \rangle = \langle \phi_{\text{calm wind},0.5}^\downarrow, \phi_{\text{calm wind},0.5}^\uparrow \rangle = C_1 \\
 &\qquad \qquad \qquad \langle \phi_{\text{cold},1.0}^\downarrow, \phi_{\text{cold},1.0}^\uparrow \rangle = C_2 \\
 \langle \phi_{\text{poor in rain},1.0}^\downarrow, \phi_{\text{poor in rain},1.0}^\uparrow \rangle &= C_3 \\
 \langle \phi_{\text{calm wind},1.0}^\downarrow, \phi_{\text{calm wind},1.0}^\uparrow \rangle &= C_0
 \end{aligned}$$

Consequently, the concepts in  $(\mathcal{M}, \preceq)$  are associated with, at least, one fuzzy-attribute in  $\Phi$ . Considering the Hasse diagram (Fig. 2), the set of  $\wedge$ -irreducible elements is

$$M_F(A, B, R, \sigma) = \{C_1, C_2, C_3\}$$

Furthermore, these concepts satisfy the conditions of the previous theorem, namely, they are concepts  $\langle \phi_{i,x}^\downarrow, \phi_{i,x}^{\downarrow\uparrow} \rangle$  associated with fuzzy-attributes satisfying  $\phi_{i,x}^\downarrow \neq \bigwedge \{ \phi_{j,x_j}^\downarrow \mid \phi_{i,x}^\downarrow \prec_2 \phi_{j,x_j}^\downarrow \}$  and  $\phi_{i,x}^\downarrow \neq \perp_A^\downarrow$ . For instance, given  $C_2 = \langle \phi_{\text{cold},1.0}^\downarrow, \phi_{\text{cold},1.0}^{\downarrow\uparrow} \rangle$ , it is not possible to express this element as intersection of elements  $\phi_{j,x_j}^\downarrow$ , such that  $\phi_{\text{cold},1.0}^\downarrow \prec_2 \phi_{j,x_j}^\downarrow$ ; and  $\phi_{\text{cold},1.0}^\downarrow$  is not the top-element.

However,  $\phi_{\text{calm wind},1.0}^\downarrow$  is the intersection of  $\phi_{\text{warm},1.0}^\downarrow$  and  $\phi_{\text{cold},1.0}^\downarrow$  and so,  $C_0 = \langle \phi_{\text{calm wind},1.0}^\downarrow, \phi_{\text{calm wind},1.0}^{\downarrow\uparrow} \rangle$  is not a  $\wedge$ -irreducible concept.  $\square$

In order to give a classification of fuzzy-attributes in the multi-adjoint framework, several definitions introduced in [17] must be extended. The first one introduces the extension of a consistent set.

**Definition 10.** A subset of fuzzy-attributes,  $\Psi \subseteq \Phi$ , is called fuzzy-consistent set of  $(A, B, R, \sigma)$ , if for each  $\langle g, f \rangle \in \mathcal{M}(A, B, R, \sigma)$ , there exists a family  $\{ \phi_{j,x_j} \}_{j \in J} \subseteq \Psi$ , such that  $g = \bigwedge_{j \in J} \phi_{j,x_j}^\downarrow$ .

Moreover, if each element  $\phi_{k,x_k} \in \{ \phi_{j,x_j} \}_{j \in J}$ , satisfies that  $\Psi \setminus \{ \phi_{k,x_k} \}$  is not fuzzy-consistent, then  $\Psi$  is called fuzzy-reduct set of  $(A, B, R, \sigma)$ .

The core of  $(A, B, R, \sigma)$  is the intersection of all the fuzzy-reducts of  $(A, B, R, \sigma)$ .

This definition arises from the classical definition and considering that each element  $\langle g, f \rangle \in \mathcal{M}(A, B, R, \sigma)$  is the infimum of concepts in  $\mathcal{M}(A, B, R, \sigma)$ . Therefore, proving that there exists  $\langle g', f' \rangle$  in the concept lattice  $\mathcal{M}(Y, B, R_Y, \sigma_{Y \times B})$ , such that  $g = g'$ , is equivalent to proving that there exists a family of  $\wedge$ -irreducible elements  $\langle g_j, f_j \rangle \in M_F(Y, B, R_Y, \sigma_{Y \times B})$ , such that  $g = \bigwedge_{j \in J} g_j$ .

Following the classical case, three different types of fuzzy-attributes will be considered. The set of fuzzy-reducts of  $(A, B, R, \sigma)$  will be denoted as  $\{ \Psi_\lambda \subseteq \Phi \mid \Psi_\lambda \text{ is a fuzzy-reduct, } \lambda \in \Lambda \}$ , where  $\Lambda$  is an index set.

**Definition 11.** The set of fuzzy-attributes can be divided into the following three types:

1. Absolutely necessary fuzzy-attributes (core fuzzy-attributes):

$$C_\Phi = \{ \phi_{i,x_i} \in \Phi \mid \phi_{i,x_i} \in \bigcap_{\lambda \in \Lambda} \Psi_\lambda \}$$

2. Relatively necessary fuzzy-attributes:

$$K_\Phi = \{ \phi_{i,x_i} \in \Phi \mid \phi_{i,x_i} \in \bigcup_{\lambda \in \Lambda} \Psi_\lambda \setminus \bigcap_{\lambda \in \Lambda} \Psi_\lambda \}$$

3. Absolutely unnecessary fuzzy-attributes:

$$I_\Phi = \{\phi_{i,x_i} \in \Phi \mid \phi_{i,x_i} \notin \bigcup_{\lambda \in \Lambda} \Psi_\lambda\}$$

Several technical results must be given before introducing the classification of fuzzy-attributes. The first proposition presents a characterization of fuzzy-reducts by  $\wedge$ -irreducible elements.

**Proposition 1.** *A subset of fuzzy-attributes,  $\Psi \subseteq \Phi$ , is a fuzzy-consistent set of  $(A, B, R, \sigma)$ , if and only if, for each  $\langle g, f \rangle \in M_F(A, B, R, \sigma)$ , there exists  $\phi_{j,x_j} \in \Psi$ , such that  $g = \phi_{j,x_j}^\downarrow$ .*

This result can be rewritten as follows.

**Corollary 1.**  *$\Psi \subseteq \Phi$  is a fuzzy-consistent set of  $(A, B, R, \sigma)$  if and only if*

$$M_F(A, B, R, \sigma) \subseteq \{\langle \phi_{i,x}^\downarrow, \phi_{i,x}^\downarrow{}^\uparrow \rangle \mid \phi_{i,x} \in \Psi\}$$

The following proposition provides a mechanism to interchange elements in a fuzzy-reduct, which is very useful.

**Proposition 2.** *A fuzzy-reduct  $\Psi$  and an element  $\phi_{j,x_j} \in \Psi$ , such that there exists  $\phi_{i,x_i} \in \Phi$  satisfying that  $\phi_{i,x_i} \notin \Psi$  and  $\phi_{i,x_i}^\downarrow = \phi_{j,x_j}^\downarrow$ . Then, the set  $\Psi' = \Psi \setminus \{\phi_{j,x_j}\} \cup \{\phi_{i,x_i}\}$  is a fuzzy-reduct of  $(A, B, R, \sigma)$ .*

Next, we show that each fuzzy-attribute associated with a  $\wedge$ -irreducible element is in, at least, one fuzzy-reduct.

**Proposition 3.** *Given  $\phi_{j,x_j} \in \Phi$ , we have that there exists a fuzzy-reduct  $\Psi$ , with  $\phi_{j,x_j} \in \Psi$ , if and only if  $\langle \phi_{j,x_j}^\downarrow, \phi_{j,x_j}^\downarrow{}^\uparrow \rangle \in M_F(A, B, R, \sigma)$ .*

Finally, the following theorem classifies the fuzzy-attributes.

**Theorem 3.** *Given a formal context  $(A, B, R, \sigma)$ , the following equivalences are obtained:*

1.  $\phi_{i,x_i} \in I_\Phi$  if and only if  $\langle \phi_{i,x_i}^\downarrow, \phi_{i,x_i}^\downarrow{}^\uparrow \rangle \notin M_F(A, B, R, \sigma)$ .
2.  $\phi_{i,x_i} \in K_\Phi$  if and only if  $\langle \phi_{i,x_i}^\downarrow, \phi_{i,x_i}^\downarrow{}^\uparrow \rangle \in M_F(A, B, R, \sigma)$  and there exists  $\phi_{j,x_j} \in \Phi$ ,  $\phi_{i,x_i} \neq \phi_{j,x_j}$ , such that  $\langle \phi_{i,x_i}^\downarrow, \phi_{i,x_i}^\downarrow{}^\uparrow \rangle = \langle \phi_{j,x_j}^\downarrow, \phi_{j,x_j}^\downarrow{}^\uparrow \rangle$ .
3.  $\phi_{i,x_i} \in C_\Phi$  if and only if  $\langle \phi_{i,x_i}^\downarrow, \phi_{i,x_i}^\downarrow{}^\uparrow \rangle \in M_F(A, B, R, \sigma)$  and  $\langle \phi_{i,x_i}^\downarrow, \phi_{i,x_i}^\downarrow{}^\uparrow \rangle \neq \langle \phi_{j,x_j}^\downarrow, \phi_{j,x_j}^\downarrow{}^\uparrow \rangle$ , for all  $\phi_{j,x_j} \in \Phi$ ,  $\phi_{i,x_i} \neq \phi_{j,x_j}$ .

Note that these results generalize the classical ones, and they are important, since, for instance, we can know the classification of each fuzzy-attribute of each attribute in  $A$ , which helps us to recognize several properties of each (crisp) attribute.

*Example 2.* Considering Example 1, by Theorem 3(1), the absolutely unnecessary fuzzy-attributes are:  $\phi_{\text{warm},0.0}$ ,  $\phi_{\text{cold},0.0}$ ,  $\phi_{\text{cold},0.5}$ ,  $\phi_{\text{poor in rain},0.0}$ ,  $\phi_{\text{poor in rain},0.5}$ ,  $\phi_{\text{calm wind},0.0}$ ,  $\phi_{\text{calm wind},1.0}$ .

By Theorem 3(2), since  $C_1$  is  $\wedge$ -irreducible and it is the closure of  $\phi_{\text{warm},0.5}$ ,  $\phi_{\text{warm},1.0}$  and  $\phi_{\text{calm wind},1.0}$ , we have that these fuzzy-attributes are relatively necessary attributes:

$$K_f = \{\phi_{\text{warm},0.5}, \phi_{\text{warm},1.0}, \phi_{\text{calm wind},0.5}\}$$

Finally,  $C_2$  and  $C_3$  are  $\wedge$ -irreducible concepts and they only are the closure of the fuzzy-attributes  $\phi_{\text{cold},1.0}$  and  $\phi_{\text{poor in rain},1.0}$ , respectively. Therefore, by Theorem 3(3), the set of absolutely necessary fuzzy-attributes is:

$$C_f = \{\phi_{\text{cold},1.0}, \phi_{\text{poor in rain},1.0}\}$$

As a consequence, several reducts are obtained. For example, we can consider the fuzzy-reduct:

$$\Psi = \{\phi_{\text{warm},1.0}, \phi_{\text{cold},1.0}, \phi_{\text{poor in rain},1.0}\}$$

in which only three attributes, with the maximum truth-value, are assumed to build the fuzzy concept lattice. This fact also shows the importance of these attributes and that they must be considered with the maximum value of the lattice. Note that the number of fuzzy-attributes (the cardinality of  $\Phi$ ), in this simple example, is 12.

Next, by Theorems 2 and 3, a detailed classification of the fuzzy-attributes of another fuzzy concept lattice will be provided.

## 4 A Worked Out Example

The considered multi-adjoint formal frame is  $(L, \preceq, \&_G)$ , where  $L = \{0, 0.5, 1\}$  and  $\&_G$  is the Gödel conjunctor defined on  $L$ . The context is  $(A, B, R, \sigma)$ , where  $A = \{a_1, a_2, a_3, a_4, a_5\}$ ,  $B = \{b_1, b_2, b_3\}$ ,  $R: A \times B \rightarrow L$  is given by Table 1, and  $\sigma$  is constant.

**Table 1.** Relation  $R$

$R$	$b_1$	$b_2$	$b_3$
$a_1$	0.5	1	0
$a_2$	0.5	1	0.5
$a_3$	0.5	0.5	0.5
$a_4$	1	1	0.5
$a_5$	1	0.5	1
$a_6$	1	1	0.5

The concept lattice  $(\mathcal{M}, \preceq)$ , associated with the framework and context considered, has 10 concepts listed below.

- $C_0 = \langle \{0.5/b_1, 0.5/b_2\}, \{1.0/a_1, 1.0/a_2, 1.0/a_3, 1.0/a_4, 1.0/a_5\} \rangle$
- $C_1 = \langle \{0.5/b_1, 1.0/b_2\}, \{1.0/a_1, 1.0/a_2, 0.5/a_3, 1.0/a_4, 0.5/a_5\} \rangle$
- $C_2 = \langle \{1.0/b_1, 0.5/b_2\}, \{1.0/a_1, 0.5/a_2, 0.5/a_3, 1.0/a_4, 1.0/a_5\} \rangle$
- $C_3 = \langle \{0.5/b_1, 0.5/b_2, 0.5/b_3\}, \{1.0/a_2, 1.0/a_3, 1.0/a_4, 1.0/a_5\} \rangle$
- $C_4 = \langle \{1.0/b_1, 1.0/b_2\}, \{1.0/a_1, 0.5/a_2, 0.5/a_3, 1.0/a_4, 0.5/a_5\} \rangle$
- $C_5 = \langle \{0.5/b_1, 1.0/b_2, 0.5/b_3\}, \{1.0/a_2, 0.5/a_3, 1.0/a_4, 0.5/a_5\} \rangle$
- $C_6 = \langle \{1.0/b_1, 0.5/b_2, 0.5/b_3\}, \{0.5/a_2, 0.5/a_3, 1.0/a_4, 1.0/a_5\} \rangle$
- $C_7 = \langle \{1.0/b_1, 1.0/b_2, 0.5/b_3\}, \{0.5/a_2, 0.5/a_3, 1.0/a_4, 0.5/a_5\} \rangle$
- $C_8 = \langle \{1.0/b_1, 0.5/b_2, 1.0/b_3\}, \{0.5/a_2, 0.5/a_3, 0.5/a_4, 1.0/a_5\} \rangle$
- $C_9 = \langle \{1.0/b_1, 1.0/b_2, 1.0/b_3\}, \{0.5/a_2, 0.5/a_3, 0.5/a_4, 0.5/a_5\} \rangle$

The Hasse diagram of this lattice is shown in Figure 3.

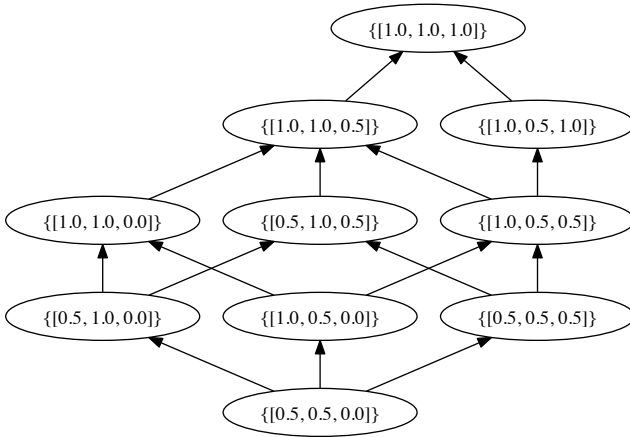


Fig. 3. The Hasse diagram of  $(\mathcal{M}, \preceq)$

The fuzzy-attributes are:  $\langle \phi_{a,0.0}^\downarrow, \phi_{a,0.0}^\uparrow \rangle = C_9$ , for all  $a \in A$ ,  $\langle \phi_{2,0.5}^\downarrow, \phi_{2,0.5}^\uparrow \rangle$ ,  $\langle \phi_{3,0.5}^\downarrow, \phi_{3,0.5}^\uparrow \rangle$ ,  $\langle \phi_{4,0.5}^\downarrow, \phi_{4,0.5}^\uparrow \rangle$ ,  $\langle \phi_{5,0.5}^\downarrow, \phi_{5,0.5}^\uparrow \rangle$  and  $\langle \phi_{6,0.5}^\downarrow, \phi_{6,0.5}^\uparrow \rangle$  are  $C_9$ , and the rest of concepts are

$$\begin{array}{ll}
 \langle \phi_{1,0.5}^\downarrow, \phi_{1,0.5}^\uparrow \rangle = C_4 & \langle \phi_{1,1.0}^\downarrow, \phi_{1,1.0}^\uparrow \rangle = C_1 \\
 \langle \phi_{2,1.0}^\downarrow, \phi_{2,1.0}^\uparrow \rangle = C_5 & \langle \phi_{3,1.0}^\downarrow, \phi_{3,1.0}^\uparrow \rangle = C_3 \\
 \langle \phi_{4,1.0}^\downarrow, \phi_{4,1.0}^\uparrow \rangle = \langle \phi_{6,1.0}^\downarrow, \phi_{6,1.0}^\uparrow \rangle = C_7 & \langle \phi_{5,1.0}^\downarrow, \phi_{5,1.0}^\uparrow \rangle = C_8
 \end{array}$$

Hence, the concepts associated with the fuzzy-attributes of  $\Phi$  are  $C_1, C_3, C_4, C_5, C_7, C_8$  and  $C_9$ . Referring to the Hasse diagram, it is not difficult to see that the concepts  $C_4 = \langle \phi_{1,0.5}^\downarrow, \phi_{1,0.5}^\uparrow \rangle = \langle \phi_{1,1.0}^\downarrow, \phi_{1,1.0}^\uparrow \rangle, C_5 = \langle \phi_{2,1.0}^\downarrow, \phi_{2,1.0}^\uparrow \rangle,$

$C_7 = \langle \phi_{4,1.0}^\downarrow, \phi_{4,1.0}^{\downarrow\uparrow} \rangle = \langle \phi_{6,1.0}^\downarrow, \phi_{6,1.0}^{\downarrow\uparrow} \rangle$  and  $C_8 = \langle \phi_{5,1.0}^\downarrow, \phi_{5,1.0}^{\downarrow\uparrow} \rangle$  are the set of  $\wedge$ -irreducible elements of  $\mathcal{M}$ , that is

$$M_F(A, B, R, \sigma) = \{C_4, C_5, C_7, C_8\}$$

Once computed the  $\wedge$ -irreducible elements of the concept lattice, Theorem 3 can be applied and the classification of the fuzzy attributes is obtained. For instance,  $\phi_{1,1.0}$  and  $\phi_{3,1.0}$  belong to  $I_\Phi$ , because  $C_1 = \langle \phi_{1,1.0}^\downarrow, \phi_{1,1.0}^{\downarrow\uparrow} \rangle$  and  $C_3 = \langle \phi_{3,1.0}^\downarrow, \phi_{3,1.0}^{\downarrow\uparrow} \rangle$  are not in  $M_F(A, B, R, \sigma)$ .

Furthermore,  $\phi_{4,1.0}$  belongs to  $K_\Phi$ , since  $C_7 = \langle \phi_{4,1.0}^\downarrow, \phi_{4,1.0}^{\downarrow\uparrow} \rangle$  is  $\wedge$ -irreducible,  $M_F(A, B, R, \sigma)$ , and, if we consider  $\phi_{6,1.0} \in L_1^A$ , we have that  $\phi_{4,1.0} \neq \phi_{6,1.0}$  and  $\langle \phi_{4,1.0}^\downarrow, \phi_{4,1.0}^{\downarrow\uparrow} \rangle = \langle \phi_{6,1.0}^\downarrow, \phi_{6,1.0}^{\downarrow\uparrow} \rangle$ . Analogously, the fuzzy-attribute  $\phi_{6,1.0}$  also belongs to  $K_\Phi$ .

The other fuzzy-attributes are in the core, for example,  $\phi_{1,0.5}$  is in  $C_\Phi$ , because  $C_4 = \langle \phi_{1,0.5}^\downarrow, \phi_{1,0.5}^{\downarrow\uparrow} \rangle \in M_F(A, B, R, \sigma)$  and there does not exist  $\phi_{i,x_i} \in L_1^A$  with  $\phi_{i,x_i} \neq \phi_{1,0.5}$ , such that  $\langle \phi_{i,x_i}^\downarrow, \phi_{i,x_i}^{\downarrow\uparrow} \rangle = \langle \phi_{1,0.5}^\downarrow, \phi_{1,0.5}^{\downarrow\uparrow} \rangle$ .

Finally, the classification of the fuzzy-attributes is the following:

$$\begin{aligned} I_\Phi &= \{\phi_{1,0.0}, \phi_{1,1.0}, \phi_{2,0.0}, \phi_{2,0.5}, \phi_{3,0.0}, \phi_{3,0.5}, \\ &\quad \phi_{3,1.0}, \phi_{4,0.0}, \phi_{4,0.5}, \phi_{5,0.0}, \phi_{5,0.5}, \phi_{5,1.0}, \phi_{6,1.0}\} \\ K_\Phi &= \{\phi_{4,1.0}, \phi_{6,1.0}\} \\ C_\Phi &= \{\phi_{1,0.5}, \phi_{2,1.0}, \phi_{5,1.0}\} \end{aligned}$$

As a consequence, two possible fuzzy-reducts arise:  $\Psi_1 = \{\phi_{1,0.5}, \phi_{2,1.0}, \phi_{5,1.0}, \phi_{4,1.0}\}$  and  $\Psi_2 = \{\phi_{1,0.5}, \phi_{2,1.0}, \phi_{5,1.0}, \phi_{6,1.0}\}$ .

## 5 Conclusions and Future Work

Several interesting results in fuzzy attribute reduction theory have been introduced and a classification of the fuzzy-attributes has been given, which provides important properties of the attributes. This has been considered in a worked out example and the corresponding reducts are easily obtained.

For further work, a classification of the crisp attributes will be given considering the introduced results, and an attribute reduction mechanism will be presented keeping the original concept lattice and without losing information.

## References

1. Bělohávek, R., Vychodil, V.: Reducing the size of fuzzy concept lattices by hedges. In: The 2005 IEEE International Conference on Fuzzy Systems, pp. 663–668 (2005)
2. Beydoun, G.: Formal concept analysis for an e-learning semantic web. Expert Systems with Applications 36(8), 10952–10961 (2009)
3. Cornejo, M., Medina, J., Ramírez, E.: A comparative study of adjoint triples. Fuzzy Sets and Systems 211, 1–14 (2012)

4. Formica, A.: Concept similarity in fuzzy formal concept analysis for semantic web. *International Journal of Uncertainty, Fuzziness and Knowledge-Based Systems* 18(2), 153–167 (2010)
5. Formica, A.: Semantic web search based on rough sets and fuzzy formal concept analysis. *Knowledge-Based Systems* 26, 40–47 (2012)
6. Ganter, B., Wille, R.: *Formal Concept Analysis: Mathematical Foundation*. Springer (1999)
7. Hájek, P.: *Metamathematics of Fuzzy Logic*. In: *Trends in Logic*. Kluwer Academic Publishers (1998)
8. Kang, X., Li, D., Wang, S., Qu, K.: Formal concept analysis based on fuzzy granularity base for different granulations. *Fuzzy Sets and Systems* 203, 33–48 (2012)
9. Konecny, J.: Isotone fuzzy galois connections with hedges. *Information Sciences* 181(10), 1804–1817 (2011)
10. Konecny, J., Medina, J., Ojeda-Aciego, M.: Intensifying hedges and the size of multi-adjoint concept lattices with heterogeneous conjunctors. In: *The 9th International Conference on Concept Lattices and Their Applications*, pp. 245–256 (2012)
11. Kumar, C.A., Srinivas, S.: Concept lattice reduction using fuzzy k-means clustering. *Expert Systems with Applications* 37(3), 2696–2704 (2010)
12. Li, L., Zhang, J.: Attribute reduction in fuzzy concept lattices based on the t-implication. *Knowledge-Based Systems* 23(6), 497–503 (2010)
13. Medina, J.: Relating attribute reduction in formal, object-oriented and property-oriented concept lattices. *Computers & Mathematics with Applications* 64(6), 1992–2002 (2012)
14. Medina, J., Ojeda-Aciego, M.: Multi-adjoint t-concept lattices. *Information Sciences* 180(5), 712–725 (2010)
15. Medina, J., Ojeda-Aciego, M.: Towards attribute reduction in multi-adjoint concept lattices. In: *The 7th International Conference on Concept Lattices and Their Applications*, pp. 92–103 (2010)
16. Medina, J., Ojeda-Aciego, M., Ruiz-Calviño, J.: Formal concept analysis via multi-adjoint concept lattices. *Fuzzy Sets and Systems* 160(2), 130–144 (2009)
17. Pawlak, Z.: Rough sets. *International Journal of Computer and Information Science* 11, 341–356 (1982)
18. Phan-Luong, V.: A framework for integrating information sources under lattice structure. *Information Fusion* 9, 278–292 (2008)
19. Umbreit, S.: *Formale Begriffsanalyse mit unscharfen Begriffen*. PhD thesis, Halle, Saale (1995)
20. Wang, X., Zhang, W.: Relations of attribute reduction between object and property oriented concept lattices. *Knowledge-Based Systems* 21, 398–403 (2008)
21. Wei, L., Qi, J.-J.: Relation between concept lattice reduction and rough set reduction. *Knowledge-Based Systems* 23(8), 934–938 (2010)
22. Zhang, W., Wei, L., Qi, J.: Attribute reduction in concept lattice based on discernibility matrix. In: Ślęzak, D., Yao, J., Peters, J.F., Ziarko, W.P., Hu, X. (eds.) *RSFDGrC 2005*. LNCS (LNAI), vol. 3642, pp. 157–165. Springer, Heidelberg (2005)

# Can Machine Learning Techniques Help to Improve the Common Fisheries Policy?\*

María Pérez-Ortiz<sup>1</sup>, Rosa Colmenarejo<sup>2</sup>,  
Juan Carlos Fernández Caballero<sup>1</sup>, and César Hervás-Martínez<sup>1</sup>

<sup>1</sup> Department of Computer Sciences and Numerical Analysis, University of Cordoba,  
Albert Einstein Building, Campus of Rabanales, Córdoba, Spain

{i82perom,jfcaballero,chervas}@uco.es

<sup>2</sup> Department of General Economics, Law Sciences and Sociology,  
Faculty of Economics, ETEA-University of Córdoba, Córdoba, Spain

rosa.colmenarejo@telefonica.net

**Abstract.** The overcapacity of the European fishing fleets is one of the recognized factors for the lack of success of the Common Fisheries Policy. Unwanted non-targeted species and other incidental fish likely represent one of the causes for the overexploitation of fish stocks; thus there is a clear connection between this problem and the type of fishing gear used by vessels. This paper performs an environmental impact study of the Spanish Fishing Fleet by means of ordinal classification techniques to emphasize the need to design an effective and differentiated common fish policy for “artisan fleets”, that guarantees the maintenance of environmental stocks and the artisan fishing culture.

**Keywords:** Machine learning, Ordinal Classification, Commitment to sustainability, Common Fisheries Policy, Fleet Overcapacity.

## 1 Introduction

“Commitment to Sustainability” is a common statement of intentions used in large companies. Since 2009, the Common Fisheries Policy (CFP) has been revised in order to address the real threat of depletion of fishing grounds in the near future [1]. The CFP reform begins to admit the political failure of previous plans as reflected in the conclusions of the external audit made on European fisheries [2] where it was shown that fleet capacity has not been reduced; indeed, it has caused an alteration in European Union (EU) markets since it has failed to establish an effective monitoring system on catches and discards.

Meanwhile, the EU has attempted to control the evolution of community fishing fleets through the so-called Multi-Annual Guidance Programmes (MAGPs), simultaneously applied to the successive CFPs, where the member state fleet capacity has been measured using aggregate Tonnage and the Engine Power of

---

\* This work has been partially subsidized by the TIN2011-22794 project of the Spanish Ministerial Commission of Science and Technology (MICYT), FEDER funds and the P2011-TIC-7508 project of the “Junta de Andalucía” (Spain).



fishing vessels in order to obtain a standardized measure for all member states. As Pascoe and Gréboval noted [3], although Tonnage and Engine Power affect the vessel's catching ability, the fishing capacity as the ability of a vessel to catch fish is a highly complex concept which depends on multiple-inputs that must be addressed. While the MAGPs program was operating, the EU reduced the number of vessels, along with the crew members, the gross tonnage (GT) and the power (kW) of its fleet, applying "Fishing capacity-Effort reduction" and "Vessel Renewal and Modernisation" policies. However, the average size of the fishing boat was significantly greater. In this sense, this paper seeks to characterize the Spanish Fishing Fleet according to the environmental impact of each vessel using for this purpose the gears declared (note that the gear information about a vessel may be unknown or wrong in some cases) in order to compute an understandable and predictable model which can be used to identify the complex patterns which influence the commitment to sustainability.

However, the classification problem in this paper is considered as a different setup to the standard one, as the variable to predict is not numerical or nominal, but ordinal, so categories have a natural order. The major problem with this kind of classification is that there is not a precise notion of the distance between categories and there are some misclassification errors which should be more penalized. To cope with this issue, a cost-sensitive decision tree hybridized with an ordinal cost matrix is used to penalize misclassification errors according to the distance in ranking to the true class.

The remainder of the paper is organized as follows. Section 2 shows a brief analysis about Machine Learning (ML) methods for solving the abovementioned problem. Section 3 explains the methodology constructed. Section 4 shows the experimental data design. In Section 5 the results are shown and discussed. And finally, some conclusions are drawn in Section 6.

## 2 Background

The ML paradigm is a scientific discipline related to Artificial Intelligence. It is based on the design and development of methods and algorithms that could yield patterns or prediction rules from a set of input data in order to make intelligent decisions. Very different paradigms such as regression, classification and time-series are usually included in this multidisciplinary research area.

There are several works in the literature that have addressed the characterization of the fishing fleet using statistical techniques: In the case of Piniella et al. [4], the Artisanal Fishing Fleet in Andalusia (2007) was analysed by using regression techniques in order to evaluate the relation between the various variables characterizing a fleet. Another example is in the work of Castro et al. [5], where a multivariate analysis, a clustering and time-series methodologies were conducted in order to identify métiers by target species inferred from the species composition of landings, applied to Spanish longliners operating in non-Spanish European waters. Similarly, Pauly et al. [6] assessed the problem of determining the global trends in fishing efforts. Also, in a recent work, Crilly and Esteban [7]

conducted a cost-benefit analysis of social, economic and environmental factors of the United Kingdom North Sea cod fishery, comparing the two main fishing gears declared in this area: trawlers (mobile) and gillnets (static). The results show that the environmental impacts caused by the trawlers are more costly than the value of their landings, whereas gillnets generate positive value for society. Similar conclusions were obtained by Gascuel et al. [8] using the Celtic Sea and the North Sea as case studies to show a clearly highlighted contrast between fleet segments, based on the ecological impact and economic performances of the major fleets operating within each ecosystem. Villasante [9] showed in 2010 an update of the EU fishing fleet assuming that the tonnage probably represents the most appropriate indicator to measure fishing capacity and extending the four fish sectors of the Galician fishing fleet to the EU, demonstrating how the Tonnage and Power had decreased since 1987, whereas the productivity rate, in terms of catch value, had increased significantly. The author concludes that the largest fishing vessels have increased their capacity under the application of the CFP, despite many attempts to address the problem of overcapacity.

In order to help link the concepts of “fleet capacity” and of “fishing effort”, this paper presents a characterization of the gears employed by the Spanish Fishing Fleet, according to its commitment to the sustainability of its registered gear, by following a previous classification of fishing gears provided by the Food and Agriculture Organization in 1990. Specifically, we make use of a specific learning paradigm known as ordinal classification [10]. The use of this methodology is mainly justified by the existing ordinal rank among the classes, as these classes correspond to the use of different kinds of gears, which determine the environmental impact of the vessels. Thus, the classes in the problem are ordered according to this environmental impact (from lowest to highest).

### 3 Ordinal Classification

The goal in classification is to assign an input vector  $\mathbf{x} \in \mathbb{R}^d$ ,  $d$  being the data dimensionality, to one of the  $K$  classes  $\mathcal{C}_k$ . To do so, a given algorithm is trained according to some labeled data  $\{\mathbf{x}, \mathbf{y}\}$ , where  $\mathbf{y}_i$  is the category assigned to pattern  $\mathbf{x}_i$ . In the case of ordinal classification there is a ranking among the classes, so this kind of classification needs to be treated differently. One of the main approaches developed for ordinal classification focuses on the use of cost matrices, where several errors were considered when misclassifying a pattern. The usual cost matrix used for weighting the errors for the case of  $K = 10$  can be seen in Table 1 and it is known as the standard absolute cost matrix. From this matrix, one could notice that when classifying a pattern from class  $\mathcal{C}_1$  in  $\mathcal{C}_1$  the associated error is obviously zero, as the pattern has been correctly classified. However, when misclassifying it with a different class, the associated error varies according to its order, since the implicit order among categories becomes an important issue when classifying, e.g. misclassifying a pattern from  $\mathcal{C}_1$  (the one which presents the minimal environmental impact) with  $\mathcal{C}_{10}$  should be clearly more penalized than when misclassifying it with class  $\mathcal{C}_2$ . More formally, in

**Table 1.** Matrix elements represent the cost applied to each kind of error

Predicted Category	Real category									
	$\mathcal{C}_1$	$\mathcal{C}_2$	$\mathcal{C}_3$	$\mathcal{C}_4$	$\mathcal{C}_5$	$\mathcal{C}_6$	$\mathcal{C}_7$	$\mathcal{C}_8$	$\mathcal{C}_9$	$\mathcal{C}_{10}$
$\mathcal{C}_1$	0	1	2	3	4	5	6	7	8	9
$\mathcal{C}_2$	1	0	1	2	3	4	5	6	7	8
$\mathcal{C}_3$	2	1	0	1	2	3	4	5	6	7
$\mathcal{C}_4$	3	2	1	0	1	2	3	4	5	6
$\mathcal{C}_5$	4	3	2	1	0	1	2	3	4	5
$\mathcal{C}_6$	5	4	3	2	1	0	1	2	3	4
$\mathcal{C}_7$	6	5	4	3	2	1	0	1	2	3
$\mathcal{C}_8$	7	6	5	4	3	2	1	0	1	2
$\mathcal{C}_9$	8	7	6	5	4	3	2	1	0	1
$\mathcal{C}_{10}$	9	8	7	6	5	4	3	2	1	0

the ordinal classification paradigm, the outcome space is ordered, so the classes present a ranking structure:  $\mathcal{C}_1 \prec \mathcal{C}_2 \prec \dots \prec \mathcal{C}_K$ , where  $\prec$  denotes this order.

In this work, different classical Decision Tree algorithms (C4.5 and Logistic Model Tree) have been hybridized with an ordinal cost matrix to induce an ordinal ranking among the classes of the problem. Therefore, all the tree growing and pruning procedure change, in such a way that instead of minimizing the number of errors, regardless of cost, they take into account ordinal cost errors. Thus, these techniques are considered as post-processor decision trees, which both implement cost-sensitive specialization by seeking to specialize leaves for high misclassification cost classes in favor of leaves for low misclassification cost classes. For further information about cost-sensitive tree induction algorithms, see [11,12].

Nonetheless, the choice of this technique for the classification problem is not arbitrary. Cost-sensitive decision trees have been chosen due to their easy interpretability (which is a necessary requirement in many real-world applications) and their close relation to the problem of ordinal regression through the use of cost matrices. Although really complex and successful algorithms have been developed in the ordinal regression paradigm (many of them derived from existing nominal techniques such as the Support Vector Machine or Kernel Discriminant Analysis), very little effort has been made to design interpretable methodologies in order to extract direct knowledge from them.

## 4 Design of the Sample

This study focuses on the Spanish fleet, as a preview of subsequent research, that should be extended to other EU state members. The sample design is:

1. The complete status of the current Spanish fleet (2012) is obtained from the “Fleet Register On the Net”, part of the Fisheries and Maritime Affairs of the European Commission.
2. Variables such as Port Code, IRCS, Loa, Tonnage, Power, first gear and second gear were selected in order to study the factors that influence the environmental impact of a vessel. First, port codes were classified according

to their region resulting in the characterization in Table 2. In that vein, Table 2 also summarises the main characteristics of the database (the different variables involved and the number of patterns, classes and attributes).

3. Following a 1990 FAO report [13] where different gears were categorized, the gears presented in the Spanish Fleet have been classified in this paper according to their environmental impact (from lowest to highest), as can be seen in Fig. 1, primarily dependent on whether the gear is static or towed, and secondly, whether it is located in the demersal or pelagic zones.
4. Finally, the entire Spanish Fleet was then classified taking its declared main and secondary gear into account (see Table 3 and Fig. 1).

**Table 2.** Characteristics of the dataset constructed

Patterns: 10460, Classes: 10, Attributes: 6					
Variable	Description	Type	Values	Mode	Source
Zone	Zone assigned to a Port (see the legend of this Table)	Nom	{1,2,3,4,5}	2	OWN
IRCS Code	Has the vessel the International Radio Call Sign?	Bin	{0,1}	0	EUFR
Loa	Vessel length, expressed in metres (m)	Num	[2.8, 116]	10.91	EUFR
Ton Gt	Total capacity of the vessel, expressed in volumetric tons of 100 cubic feet	Num	[0.12, 4406]	37.98	EUFR
Main Power	Main vessel engine power, in Kilowatts (Kw)	Num	[0, 5854.3]	85.74	EUFR
Auxiliary Power	Auxiliar vessel engine power, in Kilowatts (Kw)	Num	[0, 3980.87]	21.75	EUFR
Zone 1 - Basque Country, Cantabria and Asturias; Zone 2 - Galiza; Zone 3 - West Andalusia					
Zone 4 - East Andalusia, Valencia, Alicante, Balearic Islands and Catalonia; Zone 5 - Canary Islands; Nom = Nominal; Bin = Binary; Num = Numeric; EUFR = EU Fleet Register					

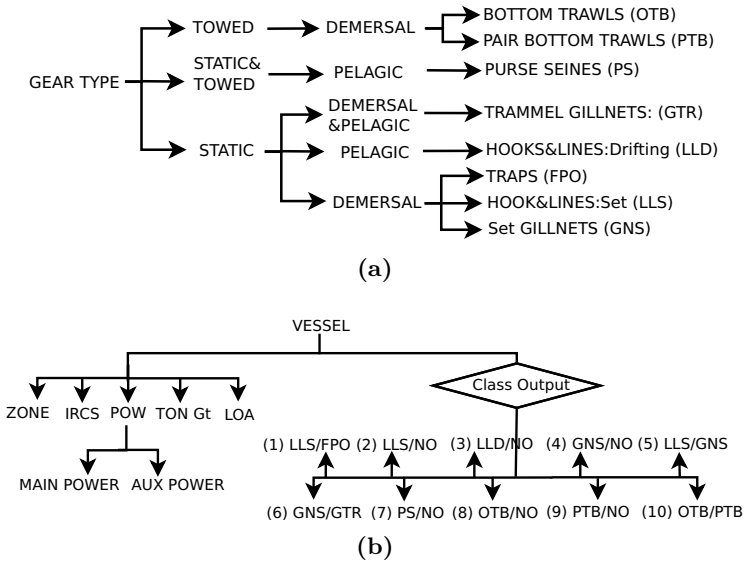
**Table 3.** Description of Spanish Fleet registered Gear (Nédélec 1990)

Spanish Fleet Gear Declared	Code	ISSCFG	Static/Towed	Pelagic/Demersal
Otter	OTB	03.1.2	T	D
Pair	PTB	03.1.3	T	D
Purse Seines	PS	01.0.0	M	P
Trammel nets	GTR	07.5.0	S	DP
Drifting Longlines	LLD	09.4.0	S	P
Pots	FPO	08.2.0	S	D
Set Longlines	LLS	09.3.0	S	D
Set Gillnets	GNS	07.1.0	S	D
ISSCFG = International Standard Statistical Classification of Fishing Gear				
GR = Gross Registered; PF= Power/Fishery				

The study of this sample has also shown that most of the vessels are concentrated in only a part of the total number of classes of the problem studied. In fact, the dataset presents an unbalanced nature (the pattern distribution being {245, 187, 873, 57, 86, 7187, 671, 970, 9, 175}).

## 5 Results

Several state-of-the-art approaches that have been proposed in the domain of ML have been tested for the problem. The methodologies tested are based on Logistic Regression (Logistic and Logistic Model Tree), Decision Tree learning (C4.5), Bayesian Approaches (NaiveBayes) and Artificial Neural Networks (Multilayer Perceptron), although the study is focused on the use of Decision Trees



**Fig. 1.** a) Spanish Fleet Declared Gear classification according to its environmental impact (Nédélec 1990). b) Dataset to classify the Spanish Fishery Fleet according to previous gear categorization (Eurostat).

because of their interpretability (specifically Cost-sensitive Decision Trees), that can provide us with some useful information about the model. Furthermore, some ordinal classification state-of-the-art methods have been tested for comparison purposes (Support Vector for Ordinal Regression [14] and Discriminant Learning for Ordinal Regression [15]).

A 5-fold partitioning technique has been used in order to divide the dataset and analyse how selected algorithms generalise on unseen data, dividing the data into 80% for training and 20% for testing.

Evaluating the performance of a classification algorithm is a fundamental aspect of ML since it is very important to understand the quality of certain algorithms but it is also a difficult issue. The experimental results obtained can be seen in Table 4, where two evaluation metrics were considered: the well-known accuracy measure (*Acc*), which is the rate of correctly classified patterns although it does not consider the order relation among the categories. The Mean Absolute Error (*MAE*), which is average deviation in absolute value of the predicted class from the true class [16]. This metric is specially designed for ordinal regression and its values range from 0 to  $K - 1$  (maximum deviation in number of ranks between two labels),  $K$  being the number of classes in the problem.

Concerning the results in Table 4, one can notice that decision tree methodologies (C4.5 and Logistic Model Tree) are those with higher performance, even better than the results of some of the methods specially proposed for ordinal classification. In this sense, the Logistic Model Tree achieved the best results when

**Table 4.** Mean and Standard deviation for Accuracy (Acc) and Mean Absolute Error (MAE) values from the 5 models obtained for the test sets

Algorithm	Acc (%)	MAE
Standard nominal classifiers		
C4.5	89.22 ± 0.36	0.341 ± 0.019
LMT	<b>89.62 ± 0.45</b>	0.344 ± 0.022
SLogistic	88.03 ± 0.38	0.383 ± 0.017
MLogistic	88.14 ± 0.39	0.379 ± 0.018
MLP	88.47 ± 0.39	0.363 ± 0.017
NaiveBayes	84.81 ± 0.54	0.468 ± 0.029
Ordinal classifiers		
Support Vector for Ordinal Regression	85, 14 ± 0, 78	0, 347 ± 0, 009
Discriminant Learning for Ordinal Regression	77, 95 ± 0, 79	0, 483 ± 0, 017
Hybridized techniques		
Cost-sens. C4.5	89.31 ± 0.34	<b>0.321 ± 0.011</b>
Cost-sens. LMT	<i>89.54 ± 0.33</i>	<i>0.326 ± 0.020</i>
Cost-sens. C4.5 (Best model)	89.87	0.307

Best method is in bold face and the second best is in italics

taking into account the *Acc*, but failed when considering the *MAE* measure, since C4.5 presented lower results. However, this technique presented slightly lower performance in *Acc*. With regard to the hybridization of the decision trees with the ordinal cost matrix, the obtained *Acc* values remain almost invariant, however, a considerable improvement can be seen in *MAE* values. Moreover, the results obtained provide evidence that the variables selected for the problem were appropriate and robust enough to perform the classification of vessels, due to the high ratio of well-classified patterns achieved by most of the algorithms.

Taking the Mean Average Error into account, which actually reports ordinal errors, it is seen that the mean value obtained is very low, thus showing that the ordering performed on the gears is correct; in addition, the techniques used in this paper are able to capture this order information, thus avoiding serious ordinal errors when classifying, which is an important issue for the prediction model. The cost-sensitive C4.5 method is chosen for the interpretation of the best model since it achieves the minimum mean *MAE* value. This model has been included in a webpage<sup>1</sup>.

Concerning the interpretation of the best model, several conclusions can be drawn. Firstly, it can be noted that the IRCS Code variable does not contribute much information about the end-point variable since it does not appear in many nodes of the tree. However, there is a clear relation between the top-rated classes and the vessels presenting the IRCS. On the other hand, the zone variable is clearly determining for classification. For example, class 3 only appears for zone 5, which demonstrates the need to perform different studies according to the zone, and develop different policies accordingly. This is also the case with the

<sup>1</sup> <http://www.uco.es/grupos/ayrna/en/partitions-and-datasets/#MLforCFP>

Loa variable, which influences the classification notably (e.g. classes  $\mathcal{C}_3$  and  $\mathcal{C}_6$  are characterized by a lower loa value). It can also be noticed that when presenting patterns under the similar variable conditions (i.e. patterns at the same tree leaf), classification is performed by considering the Main Power and Auxiliary Power variables (determining these the membership to adjacent classes in the ordinal scale). In particular, for low classes ( $\mathcal{C}_1$  to  $\mathcal{C}_3$ ), very low values for the Auxiliary Power variable are given (mostly 0). Finally, for those classes which are at the top of the ordinal scale, the Tonnage, the Auxiliary Power and the Loa present very high values. The analysis has also shown the need to take individual note of the two types of powers of a vessel since they have different impacts on the model.

## 6 Conclusions

In this paper, the notion of cost-sensitive decision tree for ordinal regression is explored in order to construct a comprehensible and predictive model to understand where the real “lack of commitment” to sustainability is located in the Spanish Fishing Fleet. The results show evidence that some of the variables selected for the vessels (port zone, size of the loa, tonnage, main power and auxiliary power) are highly significant and appropriate for determining the classification, and their use enables the model to classify the fleet accordingly. Furthermore, the ordinal methodology constructed is able to properly capture the implicit class ordering of the data showing competitiveness with other ordinal regression state-of-the-art algorithms.

## References

1. Stokstad, E.: Ecology. global loss of biodiversity harming ocean bounty. *Science* 314(5800), 745 (2006)
2. Union, E.: of Auditors, E.C.: Have EU Measures Contributed to Adapting the Capacity of the Fishing Fleets to Available Fishing Opportunities? (pursuant to Article 287 (4), Second Subparagraph, TFEU) Special report (European Court of Auditors). Publications Office of the European Union (2011)
3. Pascoe, S., Gréboval, D.: Measuring capacity in fisheries. In: *FAO Fisheries Technical 445*, Food and Agriculture Organiz. of the United Nations (FAO), Rome (2003)
4. Piniella, F., Soriguer, M., Fernández-Engo, M.: Artisanal fishing in andalusia: A statistical analysis of the fleet. *Marine Policy* 31, 573–581 (2007)
5. Castro, J., Punzón, A., Pierce, G.J., Marín, M., Abad, E.: Identification of métiers of the northern spanish coastal bottom pair trawl fleet by using the partitioning method clara. *Fisheries Research* 102(12), 184–190 (2010)
6. Anticamaraa, J., Watsona, R., Gelchua, A., Paulya, D.: Global fishing effort (1950–2010): Trends, gaps and implications. *Fisheries Research* 107, 131–136 (2010)
7. Crilly, R., Esteban, A.: Small versus large-scale, multifleet fisheries: The case for economic and environmental access criteria in european fisheries. *Marine Policy* 37, 20–27 (2012)

8. Gascuel, D., Merino, G., Döring, R., Druon, J., Goti, L., Macher, C., Soma, K., Travers-Trolet, M., Mackinson, S.: Towards the implementation of an integrated ecosystem fleet-based management of european fisheries. *Marine Policy* 36, 1022–1032 (2012)
9. Villasante, S.: Global assessment of the european union fishing fleet: An update. *Marine Policy* 34(3), 663–670 (2010)
10. Gutiérrez, P.A., Pérez-Ortiz, M., Fernández-Navarro, F., Sánchez-Monedero, J., Hervás-Martínez, C.: An Experimental Study of Different Ordinal Regression Methods and Measures. In: Corchado, E., Snášel, V., Abraham, A., Woźniak, M., Graña, M., Cho, S.-B. (eds.) HAIS 2012, Part II. LNCS, vol. 7209, pp. 296–307. Springer, Heidelberg (2012)
11. Webb, G.I.: Cost sensitive specialisation. In: Foo, N.Y., Göbel, R. (eds.) PRICAI 1996. LNCS, vol. 1114, pp. 23–34. Springer, Heidelberg (1996)
12. Lomax, S., Vadera, S.: A survey of cost-sensitive decision tree induction algorithms. *ACM Comput. Surv.* 16, 1–16 (2013)
13. Food and Agriculture Organization of the United Nations: Cwp handbook of fishery statistical standards. Technical report
14. Chu, W., Keerthi, S.S.: Support vector ordinal regression. *Neural Computation* 19, 792–815 (2007)
15. Sun, B.Y., Li, J., Wu, D.D., Zhang, X.M., Li, W.B.: Kernel discriminant learning for ordinal regression. *IEEE Transactions on Knowledge and Data Engineering* 22, 906–910 (2010)
16. Baccianella, S., Esuli, A., Sebastiani, F.: Evaluation measures for ordinal regression. In: Proceedings of the Ninth Intern. Conf. on Intelligent Systems Design and Applications (ISDA 2009), Pisa, Italy (2009)



# Integration of Fuzzy Systems and Genetic Algorithm in Permeability Prediction

Ahmad Ja'fari and Rasoul Hamidzadeh Moghadam

Mining Engineering Department, Sahand University of Technology, Tabriz, Iran  
{a\_jafari, hamidzadeh}@sut.ac.ir

**Abstract.** Determine an appropriate distribution of reservoir parameters is a challenge in reservoir engineering. Permeability is one of special reservoir parameters which its modeling is more complicated because there is no direct tool to determine permeability distribution. This problem is more critical in carbonate reservoir because of the fracture effects on measurements. The most reliable way of permeability calculation is laboratory analysis of cores, but this method could not provide a thorough permeability profile in the desired field. In recent years, different methods and algorithms used to predict permeability. One of the most common methods is artificial intelligent methods such as ANN, FL and GA. This paper provides a way to compare the ability of different fuzzy methods to predict permeability from well logs in one of southern Iranian carbonate reservoirs. Sugeno type fuzzy inference system (SFIS), adaptive neuro-fuzzy inference system (ANFIS) and locally linear neuro-fuzzy (LLNF) used to predict permeability. One third of all data used for test the fuzzy systems. Mean square error (MSE) and correlation coefficient (CC) of the test dataset used to select the best method in permeability determination. In final step genetic algorithm is applied to combine different method results to obtain a final model. This algorithm minimizes an error function. This function consists of SFIS, ANFIS and LLNF model predictions. The ability of different methods are compared to find an appropriate method for permeability prediction.

**Keywords:** permeability prediction, SFIS, ANFIS, LLNF, GA.

## 1 Introduction

Permeability, which measures the ability of a rock to transmit fluids, is one of the most important properties of reservoir rocks. Estimation of permeability is important in determining the well completion strategy and the resulting productivity (Cuddy, 1998). Reservoir management and development requires accurate knowledge of permeability. Depending on the available data, permeability can be determined by analyzing well test data, core data, or well log data (Balan et al., 1995). Well test interpretation provides a reliable in situ measure of average permeability. When there are no well test data, taking core measurements in a laboratory is another way to estimate permeability. However, both well test data and core data are expensive to obtain (Chen and Lin, 2006). Well log data can be used to estimate permeability if

limited core data are also available. Well logging is performed for almost all wells. Many correlations have been widely studied to estimate permeability using well log data with the aid of available core-measured permeability (Balan et al., 1995).

Artificial intelligent tools were a common way of un-sampled property prediction from well logs recently. Many authors applied different methods separately to predict an un-sample property. Abdurraheem et al. 2007 used fuzzy logic to predict permeability from well logs, they shown that subtractive clustering provide better predictions compare to grid partitioning technique. Cuddy (1998) implemented fuzzy logic for litho-facies and permeability prediction. The fuzzy prediction technique was calibrated in a cored well and "blind tested" in another well to see how well it fitted the actual core permeabilities. Amabeoku et al. (2005) used fuzzy logic to model and predict permeability in cored wells by calibrating core permeability against conventional open-hole logs. Beiraghdar et al. (2010) use a locally linear neuro-fuzzy model to predict permeability from well logs. Many other authors applied a combination of different AI methods to predict un-sampled properties. Kakhodaie et al. (2009) provide a committee machine to predict petrophysical data from seismic attributes. They used Larsen, Mamdani and Sugeno type fuzzy inference system and a pattern search genetic algorithm to combine the prediction of these methods. Chen and Lin (2006) introduce a committee machine to predict permeability from well logs. They used empirical formula, neural network and genetic algorithm to improve their predictions. Wong et al. (2000) proposed multiple networks resulting in a smaller error for permeability prediction when compared with multiple linear regression and other neural networks. Labani et al (2010) applied a committee machine with intelligent system to predict NMR log parameters from conventional well log data. Ja'fari and H. Moghadam (2012) integrate ANFIS, NN and GA to determine porosity and permeability from log data. Their method shows that the combined prediction provides better results than any methods individually. In this study different fuzzy models (SFIS, ANFIS and LLNF) combined using GA tool to predict permeability from conventional well logs. The method applied to a dataset from one of southern Iranian carbonate reservoir.

## **2 Theory and Methodology**

The application of AI tools such as fuzzy logic and NN is evolving as an oil field technology. Over the last few years several studies have been conducted in the field of petroleum engineering by applying AI. The major applications are seismic data processing and interpretation, well logging, reservoir mapping and engineering (El Ouahed et al 2005). The aim of this study is to focus on different fuzzy methods to predict permeability in un-cored wells. A brief description of different methods is described here.

### 2.1 Sugeno Type Fuzzy Inference System

Fuzzy logic is a convenient way to map an input space to an output space. Fuzzy logic was first introduced by Zadeh (1965). As the name suggested, it deals with the concept of partiality. Fuzziness or vagueness refers to not only crisp definition of conventional Boolean logic (e.g. true or false) but also continuous form of anything in between (i.e. partially true and partially false). The partial membership behavior can be characterized deterministically and mathematically by fuzzy sets (or fuzzy membership functions) and a set of fuzzy "if-then" rules (or fuzzy rules). In other words, descriptive uncertainties can be quantified (Tran, 2004). Complete theoretical descriptions of fuzzy logic (fuzzy sets, memberships and rules) can be found in Kosko (1992).

Fuzzy inference is the process of formulating the mapping from a given input to an output using fuzzy logic. Fuzzy inference process comprises of five parts: fuzzification of the input variables, application of the fuzzy operator (AND or OR) in the antecedent, implication from the antecedent to the consequent, aggregation of the consequents across the rules, and defuzzification (Matlab help). Figure 2 represent a schematic diagram of this, which is shown by Lee (2004) and Kadkhodaie Ilkhchi (2009).

The most important differences among fuzzy inference systems are the types of the output membership functions and the implication methods. The output membership functions for SFIS are either linear or constant (Sugeno 1985). A typical rule in a Sugeno fuzzy model has the form:

$$\text{If Input1}=x_0 \text{ and Input2}=y_0, \text{ then } z=p_1x_0+q_1y_0+r$$

For a zero-order Sugeno model, the output level is a constant (p=q=0). The output level,  $z_i$ , of each rule, is weighted by the firing strength  $\alpha_i$  of the rule. The final output of the system is the weighted average of all rule outputs, computed as follows:

$$\text{final output} = \frac{\sum_{i=1}^n \alpha_i z_i}{\sum_{i=1}^n \alpha_i} \tag{1}$$

A graphical illustration of SFIS is shown in Figure 1.

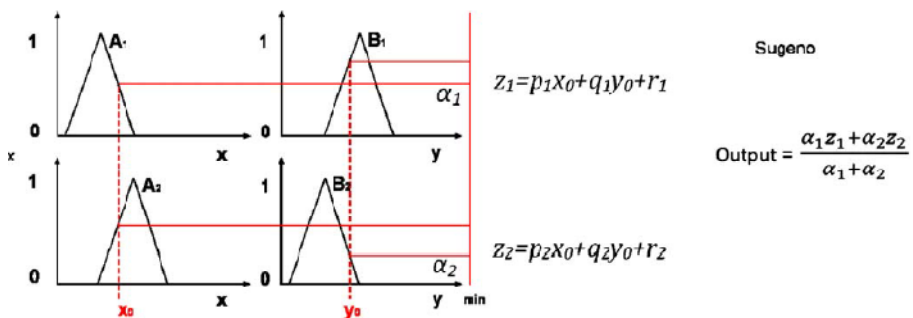


Fig. 1. Schematic of SFIS (Kadkhodaie et al., 2009)

## 2.2 Adaptive Neuro-fuzzy Inference System

In recent years, considerable attention has been devoted to the use of hybrid NN–fuzzy logic approaches as an alternative for pattern recognition, clustering, statistical and mathematical modelling. It has been shown that NN models can be used to construct internal models that capture the presence of fuzzy rules. Neuro-fuzzy modeling is a technique for describing the behavior of a system using fuzzy inference rules using a NN structure. The model has a unique feature in which it can express linguistically the characteristics of complex nonlinear systems (Nikravesh *et al* 2003). The formulation between input and output data is performed through a set of fuzzy if–then rules. Normally, fuzzy rules are extracted through a fuzzy clustering process. Subtractive clustering (Chiu 1994) is one of the effective methods for constructing a fuzzy model. The effectiveness of a fuzzy model is related to the search for the optimal clustering radius, which is a controlling parameter for determining the number of fuzzy if–then rules. Fewer clusters might not cover the entire domain, and more clusters (resulting in more rules) can complicate the system behavior and may lead to lower performance (Kadkhodaie-Ilkhchi *et al* 2009). Depending on the case study, it is necessary to optimize this parameter for construction of the fuzzy model. The basic idea behind the neuro-adaptive learning techniques is very simple. These techniques provide a method for the fuzzy modelling procedure to learn information about a dataset, in order to compute the membership function parameters that best allow the associated fuzzy inference system to track the given input/output data. The Sugeno fuzzy model was proposed by Tagaki, Sugeno and Kang in an effort to formulate a systematic approach to generalized fuzzy rules from an input–output dataset. A typical fuzzy rule in a Sugeno fuzzy model has the following format:

$$\text{if } x \text{ is } A \text{ and } y \text{ is } B \text{ then } z = f(x, y)$$

where  $A$  and  $B$  are the fuzzy sets in the antecedent;  $z = f(x, y)$  is a crisp function in the consequent. When  $f(x, y)$  is a constant, then we have the zero-order Sugeno fuzzy model, which can be viewed as a special case of the Mamdani fuzzy inference system. If  $f(x, y)$  is a first-order function, then we have a first-order Sugeno fuzzy model. Consider a first-order Sugeno fuzzy inference system which contains two rules.

$$\text{Rule 1: if } X \text{ is } A1 \text{ and } Y \text{ is } B1, \text{ then } f_1 = p_1x + q_1y + r_1.$$

$$\text{Rule 2: if } X \text{ is } A2 \text{ and } Y \text{ is } B2, \text{ then } f_2 = p_2x + q_2y + r_2.$$

Figure 2(a) illustrates graphically the fuzzy reasoning mechanism to derive an output  $f$  from a given input vector  $[x, y]$ . The firing strength  $w_1$  and  $w_2$  are usually obtained as the product of the membership grades in the premise part, and the output  $f$  is the weighted average of each rule's output. To facilitate the learning or adaptation of the Sugeno fuzzy model, it is convenient to put the fuzzy model into the framework of adaptive networks that can compute gradient vectors systematically. The resultant network architecture is called ANFIS, and is shown in figure 2(b), where nodes within the same layer perform functions of the same type. Layer 1: each node in this layer generates membership grades of a linguistic label. Parameters in this layer are referred to as the premise parameters. Layer 2: each node in this layer calculates the firing strength of a rule via multiplication. Layer 3: node  $i$  in this layer calculates the ratio of the  $i$ th rule's firing strength to the total of all firing strength. Layer 4: node  $i$  in this

layer computes the contribution of the  $i$ th rule towards the overall output. Layer 5: the single node in this layer computes the overall output as the summation of contribution from each rule (Jang2000).

The constructive adaptive network shown in figure 2(b) is functionally equivalent to the fuzzy inference system shown in figure 2(a). There are two methods that ANFIS learning employs for updating membership function parameters: back propagation (which calculates error signals (the derivative of the squared error with respect to each node’s output) recursively from the output layer backward to input nodes. This learning rule is exactly the same as the back propagation learning rule used in the common feed forward NN) for all parameters (a steepest descent method) and a hybrid method consisting of back propagation for the parameters associated with the input membership functions, and leastsquares estimation for the parameters associated with the output membership functions (Matlab user’s guide 2007).

### 2.3 Locally Linear Neuro-fuzzy with Model Tree

The fundamental approach with the LLNF model is dividing the input space into small linear subspaces with fuzzy validity functions. Any produced linear part with its validity function can be described as a fuzzy neuron. Thus, the total model is a neuro-fuzzy network with one hidden layer, and a linear neuron in the output layer which simply calculates the weighted sum of the outputs of locally linear neurons (Gholipoor et al. 2007). Figure 3 demonstrate a schematic of LLNF model.

$$\hat{y}_i = w_{i0} + w_{i1}u_1 + w_{i2}u_2 + \dots + w_{ip}u_p$$

$$\hat{y} = \sum_{i=1}^M \hat{y}_i \phi_i(\underline{u}) \tag{2}$$

where  $\underline{u} = [u_1, u_2, \dots, u_p]^T$  is the model input, M is the number of LLM neurons,  $w_{ij}$  denotes the LLM parameters of the  $i$ th neuron, and p is the size of input vector. For proper modeling, it is necessary that the Gaussian validity functions be normalized.

$$\phi_i(\underline{u}) = \frac{\mu_i(\underline{u})}{\sum_{j=1}^M \mu_j(\underline{u})} \tag{3}$$

$$\mu_i(\underline{u}) = \exp\left(-\frac{1}{2}\left(\frac{(u_1 - c_{i1})^2}{\sigma_{i1}^2} + \dots + \frac{(u_p - c_{ip})^2}{\sigma_{ip}^2}\right)\right) \tag{4}$$

There are two sets of learning parameters: the rule consequent parameters of the LLMs ( $w_{ij}$ s) and the rule premise parameters of validity functions ( $\sigma_{ij}$ s and  $c_{ij}$ s). Since the learning algorithm searches for locally linear models, supposing that the  $c_{ij}$ s and  $\sigma_{ij}$ s are known, the least square technique is a reasonable choice for tuning the LLMs parameters (Nejadfar et al., 2013). Several methods can be used for the approximation of rule premises (parameter of hidden layer). Tree based methods are appropriate for their simplicity and intuitive constructive algorithm (Mirmomeni et al. 2009).

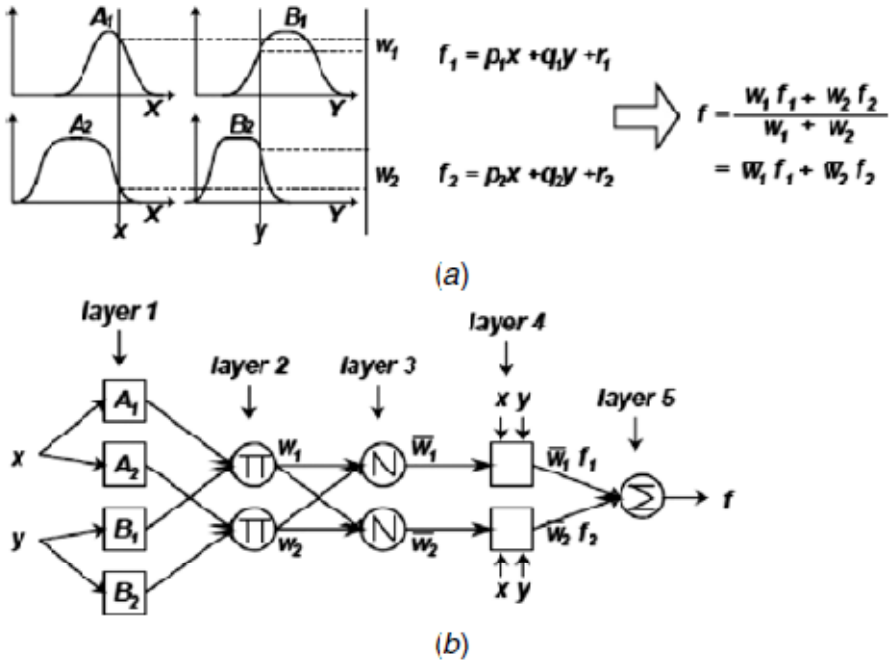


Fig. 2. (a) First-order Sugeno fuzzy model; (b) corresponding ANFIS architecture (Jang 2000)

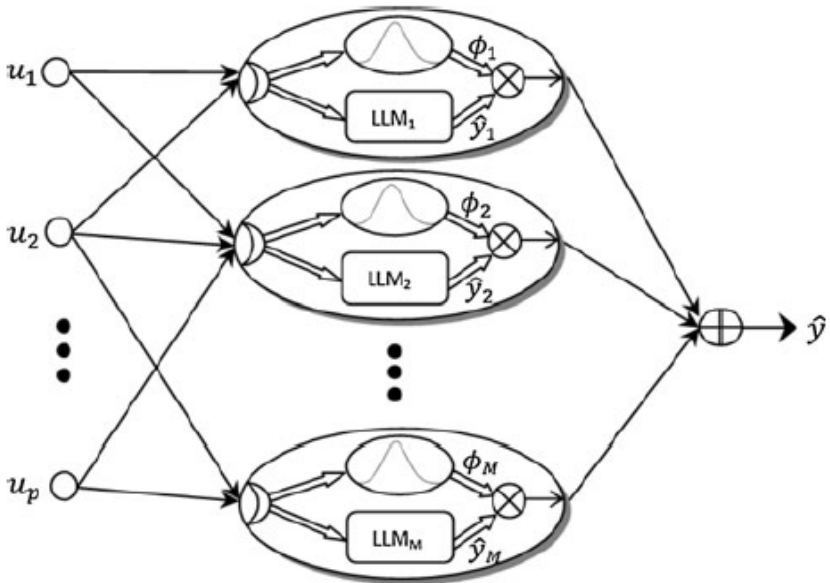


Fig. 3. Structure of LLNF (Nejadfard et al. 2013)

In each iteration, the one locally linear neuron with the worst performance is subdivided. In  $p$  dimensional input space, for all possible orthoaxial sets of subdivisions, the performance index is calculated and the one with best performance is selected. Hence, the LLM neuron becomes divided into two equal halves on the selected input dimension. Based on such a division, the centers  $c_{ij}$  and standard deviations  $r_{ij}$  of the two new neurons are computed and the fuzzy validity functions are updated. The centers of new validity functions are the centers of the new hypercubes. The standard deviation determines the support area for Gaussian validity functions. Each division of input space is assigned as support area for the corresponding validity function as well. A schematic of the algorithm used here is shown in figure 4.

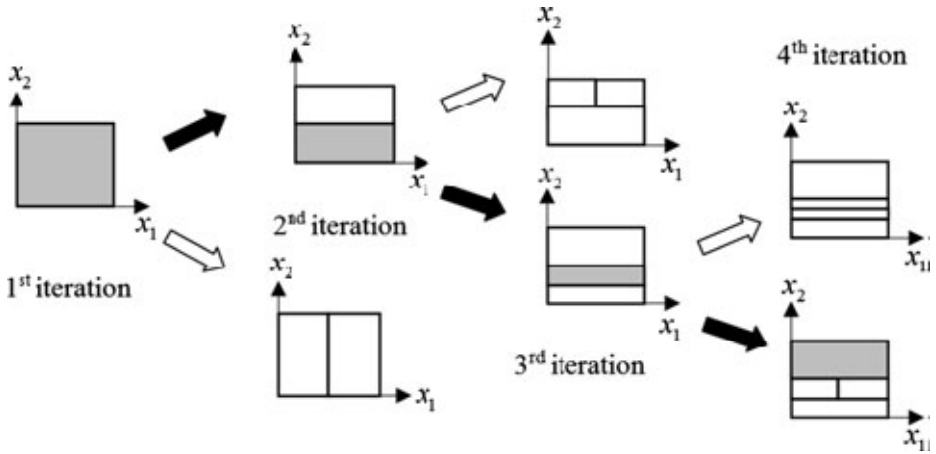


Fig. 4. First four iteration of LOLIMOT training algorithm (Mirmomeni et al. 2009)

**2.4 Genetic Algorithm**

GAs was first introduced in the field of AI by Holland(1975). These algorithms mimic processes from the Darwinian theories of natural evolution in which winners survive to reproduce and pass along ‘good’ genes to the next generation, and ultimately, a ‘perfect’ species is evolved. Hence the term ‘genetic’ was adopted as the name of the mathematical algorithms (Huang *et al* 1998).The GA works by firstly encoding the parameters of a given estimator as chromosomes (binary or floating-point).This is followed by populating a range of potential solutions. Each chromosome is evaluated by a fitness function. The better parent solutions are reproduced and the next generation of solutions (children) is generated by applying the genetic operators (crossover and mutation). The children solutions are evaluated and the whole cycle repeats until the best solution is obtained (Tamhane *et al* 2000, Labani *et al* 2010).

### 3 Data Preparation and Modeling

The above described methods are integrated to predict permeability in an Iranian carbonate reservoir from conventional well logs. Dataset composed of well logs and conventional core analysis data. Regression analysis applied to determine more appropriate log data from a suit of well logs. Sonic, neutron porosity, photo-electric factor, resistivity, gamma ray and bulk density logs are selected because of their higher correlation coefficients by permeability. Table 1 summarizes the CC of the dataset.

**Table 1.** Correlation coefficient of well logs and permeability

	DT	NPHI	RHOZ	log(Rxo)	PEF	GR	log(K)
DT	1						
NPHI	0.700784	1					
RHOZ	-0.92765	-0.66458	1				
log(Rxo)	-0.40164	-0.57199	0.538567	1			
PEF	-0.20588	-0.15033	0.093485	-0.03	1		
GR	0.436083	0.010164	-0.52331	-0.40278	-0.2116	1	
log(K)	0.758737	0.695619	-0.70051	-0.45621	-0.23766	0.205702	1

Dataset is divided into two parts as training and testing datasets. Different fuzzy systems are trained using train dataset and validated using test dataset which are not participated in training of the model.

Clustering methods can be used to clustering input dataset to train the fuzzy systems better. Subtractive clustering method applied here for SFIS and ANFIS. Different clustering radiuses were applied and the system is trained by these radiuses. The best radius is selected based on correlation coefficient and mean square error while applying the testing set to the trained system. Table 2 provides information about SFIS using different clustering radiuses. Radiuses start with 0.05 and increase by 0.05. Some of the best performances of the algorithm are summarized.

Regarding to data in table 2 clustering radius of 0.4 is bolded. This radius provides the highest CC and lowest MSE for our test dataset.

The same procedure is done for ANFIS training and validation. Different clustering radiuses applied and the results is summarizes in table 3. Results show a clustering radius of 0.9 with highest CC and lowest MSE. This radius selected as the optimum clustering radius for ANFIS model. Note that the training and testing datasets are same for all algorithms and tried to determine an optimum method to predict permeability using these algorithms by a reasonable judgment.



**Table 2.** Performance of SFIS with different clustering radiuses

Clustering Radius	Test CC	Test MSE
0.05	0.784828	0.020593
0.10	0.774934	0.022174
0.15	0.066292	0.023806
0.20	0.856565	0.013288
0.25	0.876732	0.010987
0.30	0.876241	0.011138
0.35	0.886203	0.010108
<b>0.40</b>	<b>0.887279</b>	<b>0.010024</b>
0.45	0.882533	0.010410
0.50	0.880221	0.010571
0.55	0.878480	0.010669
0.60	0.872855	0.011218
0.65	0.871860	0.011298
0.70	0.876562	0.010900
0.75	0.876518	0.010892
0.80	0.877741	0.010780
0.85	0.875678	0.010897
0.90	0.883008	0.010280
0.95	0.883345	0.010250
1.00	0.882983	0.010289

**Table 3.** Performance of ANFIS with different clustering radiuses

Clustering Radius	Test CC	Test MSE
0.1	0.734966	0.030189
0.2	0.841352	0.014313
0.3	0.804725	0.017472
0.4	0.865821	0.011825
0.5	0.868407	0.01164
0.6	0.837793	0.014704
0.7	0.829975	0.015793
0.8	0.837213	0.015249
<b>0.9</b>	<b>0.888307</b>	<b>0.009903</b>
1	0.887909	0.009931

The third algorithm which used to predict permeability was LLNF. By means of LOLIMOT algorithm, both the number of neurons and the parameters of LLMs are trained. Table 4 summarizes the training and testing procedure of this algorithm. Data demonstrate that after 5 neurons by increase number of neurons the training error decreases but the test error doesn't decrease any more. So this can be used to determine optimum number of neurons for permeability prediction. The CC of this algorithm for test data set is better than both previous ones. This can verify the strength of LLNF to predict permeability from well log data in present dataset.

**Table 4.** Performance of LLNF with different No. of parts

No of Parts	training CC	training MSE	test CC	test MSE
1	0.810702	0.018842	0.822663	0.015258
2	0.85783	0.014561	0.877942	0.010716
3	0.876325	0.012772	0.880322	0.010504
4	0.885677	0.011868	0.877718	0.010874
5	0.897748	0.010696	0.879046	0.010925
6	0.901733	0.010281	0.877508	0.011123
<b>7</b>	<b>0.908348</b>	<b>0.009621</b>	<b>0.887413</b>	<b>0.01024</b>
8	0.910311	0.009425	0.882055	0.010773
9	0.915118	0.008938	0.876151	0.011212
10	0.920496	0.008396	0.884541	0.010596
11	0.924747	0.007968	0.872399	0.0119
12	0.928325	0.007601	0.877342	0.011502
13	0.930344	0.007393	0.875677	0.011684
14	0.934114	0.007006	0.877777	0.011978
15	0.936025	0.006811	0.877483	0.011976
16	0.936743	0.006737	0.877531	0.011987
17	0.937592	0.006652	0.878007	0.012067
18	0.941038	0.006298	0.871913	0.012903
19	0.944545	0.005944	0.870022	0.013036
20	0.945297	0.005866	0.876472	0.012563

In order to apply GA method we need a cost function. This cost function can be minimized by GA to obtain the optimum condition for our problem. The cost function here is defined as an error function:

$$MSE = \sum_{i=1}^n (w_1 SFIS_i + w_2 ANFIS_i + w_3 LLNF_i - T_i)^2 \tag{5}$$

$w_1, w_2$  and  $w_3$  are the weight factors and  $T_i$  is target values. The initial population size is set to 20 which specifies the number of individuals in each generation, and the initial range is [0, 1] which specifies the range of the individuals in the initial population. The initial population is generated with a random process covering the entire problem space. The maximum number of generations that specifies the maximum number of GA iterations is set to 100. The next generation is produced using crossover and mutation operators with default functions in the GA toolbox.

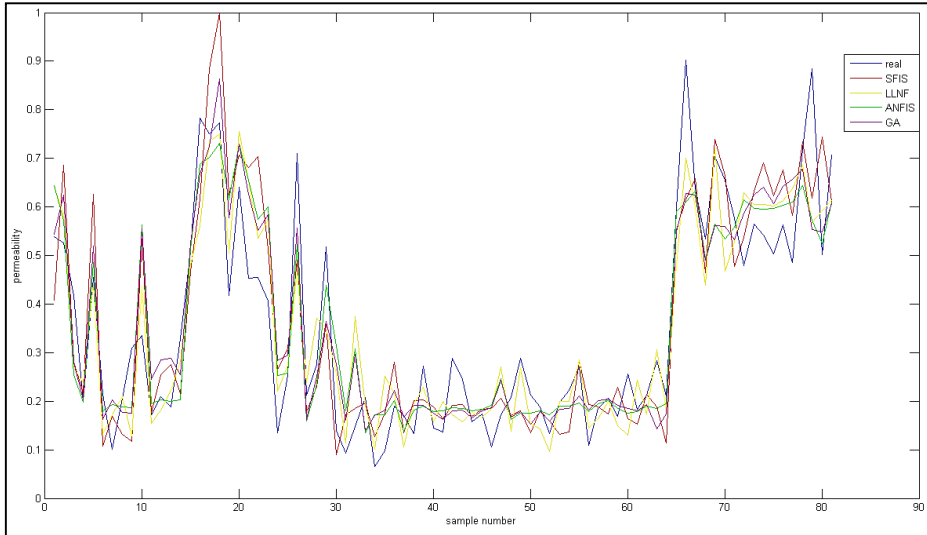
The defined algorithm applied on training data and the results of that is validated using test dataset. The following formula describe the weight factors of each data for final prediction.

$$MSE = \sum_{i=1}^n (0.115 * SFIS_i + 0.229 * ANFIS_i + 0.66 * LLNF_i - T_i)^2 \quad (6)$$

Results show that this algorithm can improve CC of the test dataset, but not so much. Table 5 summarizes the results of these algorithms. Figure 6 compare test dataset and each algorithm predictions.

**Table 5.** Summary of different applied methods

Algorithm	MSE	CC
SFIS	0.887279	0.010024
ANFIS	0.888307	0.009903
LLNF	0.887413	0.01024
Combined (GA)	0.8881	0.0106



## 4 Conclusion

Different fuzzy based methods were applied to predict permeability. The performance of each method is evaluated using a test dataset which is not participated in training. The results show that the ability of all methods are approximately same for all algorithms with a little differences. ANFIS provide the best correlation coefficient and also least mean square error for this dataset. The LLNF model also can predict with a lower MSE than combined method. Using different decision making scenarios like MSE and CC can chose different algorithms for prediction but ANFIS here provide the most powerful one regard to MSE and CC. Results show that all the fuzzy algorithms can mimic the real data trends to some extent.

## References

- Abdulraheem, A., Sabakhi, E., Ahmed, M., Vantala, A., Raharja, I., Korvin, G.: Estimation of Permeability From Wireline Logs in a Middle Eastern Carbonate Reservoir Using Fuzzy Logic. In: 15th SPE Middle East Oil & Gas Show and Conference, Bahrain, March 11-14 (2007)
- Amabeoku, M.O., Lin, C., Khalifa, A.A., Cole, J., Dahan, M., Jarlow, J., Ajufo, A.: Use of Fuzzy-Logic Permeability Models To Facilitate 3D Geocellular Modeling and Reservoir Simulation: Impact on Business. In: International Petroleum Technology Conference, pp. 21–23 (November 2005)
- Balan, B., Mohaghegh, S., Ameri, S.: State-of-the-art in permeability determination from well log data: part 1-A comparative study, model development. Paper SPE 30978 Presented at the SPE Eastern Regional Conference and Exhibition, West Virginia, pp. 17–21 (September 1995)
- Beiraghdar, Y., Nabi-Bidhendi, M., Lucas, C.: The Prediction of Permeability in a Carbonate Reservoir Using Adaptive Neurofuzzy Inference System. In: 1st International Petroleum Conference & Exhibition (2010)
- Chen, C.H., Lin, Z.S.: A committee machine with empirical formulas for permeability prediction. *Computers & Geosciences* 32, 485–496 (2006)
- Chiu, S.: Fuzzy model identification based on cluster estimation. *J. Intell. Fuzzy Syst.* 2, 267–278 (1994)
- Cuddy, S., J.: Litho-Facies and Permeability Prediction from Electrical Logs using Fuzzy Logic. In: Paper SPE 49470 Presented at 8th Abu Dhabi International Petroleum Exhibition and Conference (1998)
- El Ouahed, A.K., Tiab, D., Mazouzi, A.: Application of artificial intelligence to characterize naturally fractured zones in Hassi Messaoud Oil Field, Algeria. *J. Pet.Sci. Eng.* 49, 122–141 (2005)
- Gholipour, A., Lucas, C., Araabi, B.N., Mirmomeni, M., Shafiee, M.: Extracting the main patterns of natural time series for long-term neurofuzzy prediction. *Neural Comput. & Applic.* 16, 383–393 (2005)
- Holland, J.: *Adaptation in natural and artificial systems*. University of Michigan Press, Ann Harbor (1975)
- Ja'fari, A., Moghadam, R.H.: Integration of ANFIS, NN and GA to determine core porosity and permeability from conventional well log data. *J. Geophys. Eng.* 9, 473–481 (2012)

- Jang, R.: Input Selection for ANFIS Learning. Department of Computer and Science. National Hua University, Hsinchu (2000)
- Kadkhodaie-Ilkhchi, A., Rezaee, M.R., Rahimpour-Bonab, H., Chehrazi, A.: Petrophysical data prediction from seismic attributes using committee fuzzy inference system. *Computers & Geosciences*, 2314–2330 (2009)
- Kosko, B.: *Neural Networks and Fuzzy Systems: A Dynamical Systems Approach to Machine Intelligence*, ch. 1, 5. Prentice Hall, New Jersey (1992)
- Labani, M.M., Kadkhodaie-Ilkhchi, A., Salahshoor, K.: Estimation of NMR log parameters from conventional well log data using a committee machine with intelligent systems: A case study from the Iranian part of the South Pars gas field, Persian Gulf Basin. *Journal of Petroleum Science and Engineering*, 175–185 (2010)
- Lee, K.H.: *First Course on Fuzzy Theory and Applications*, p. 335. Springer, Berlin (2004)
- MATLAB user's Guide 2007 Fuzzy logic and Neural Network toolboxes. MATLAB CD-ROM Mathworks, Inc. (2007)
- Mirmomeni, M., Lucas, C., Shafiee, M., Araabi, B.N., Kamaliha, E.: Fuzzy descriptor systems and spectral analysis or chaotic time series prediction. *Neural Comput. & Applic.* 18, 991–1004
- Nejadfard, A., Yazdanpanah, M.J., Hassanzadeh, I.: Friction compensation of double inverted pendulum on a cart using locally linear neuro-fuzzy model. *Neural Comput. & Applic.* 22, 337–347 (2013)
- Nikravesh, M., Aminzadeh, F., Zadeh, L.A.: *Soft Computing and Intelligent Data Analysis in Oil Exploration*. Elsevier (2003)
- Tamhane, D., Wong, P.M., Aminzadeh, F., Nikravesh, M.: Soft computing for intelligent reservoir characterization. In: *SPE Asia Pacific Conference on Integrated Modeling for Asset Management*, Yokohama, Japan, pp. 25–26. SPE 59397 (April 2000)
- Tran, N.H.: *Characterization and Modeling of Naturally Fractured Reservoirs*. Ph.D. Thesis, University of New South Wales, Australia (2004)
- Wong, P.M., Jang, M., Cho, S., Gedeon, T.D.: Multiple permeability predictions using an observational learning algorithm. *Computers & Geosciences* 26(8), 907–913 (2000)
- Zadeh, L.A.: Fuzzy sets *Information and Control*, vol. 8, pp. 338–353 (1965)

# Annotating “Fuzzy Chance Degrees” When Debugging XPath Queries

Jesús M. Almendros-Jiménez<sup>1,\*</sup>,  
Alejandro Luna Tedesqui<sup>2</sup>, and Ginés Moreno<sup>2</sup>

<sup>1</sup> Dep. of Informatics, University of Almería, Spain  
jalmen@ual.es

<sup>2</sup> Dep. of Computing Systems, University of Castilla-La Mancha, Spain  
Alejandro.Luna@alu.uclm.es, Gines.Moreno@uclm.es

**Abstract.** In this paper we present a method for debugging XPath queries which has been implemented with the fuzzy logic language MALP by using the FLOPER tool developed in our group. We describe how XPath expressions can be manipulated for obtaining a set of alternative queries matching a given XML document. For each new proposed query, we give a “chance degree” that represents an estimation on its deviation w.r.t. the initial expression. Our work is focused on providing to the programmers a repertoire of paths which can be used to retrieve answers.

**Keywords:** XPath, Fuzzy (Multi-adjoint) Logic Programming, Debugging.

## 1 Introduction

The eXtensible Markup Language (XML) is widely used in many areas of computer software to represent machine readable data. XML provides a very simple language to represent the structure of data, using tags to label pieces of textual content, and a tree structure to describe the hierarchical content. XML emerged as a solution to data exchange between applications where tags permit to locate the content. XML documents are mainly used in databases. The XPath language [1] was designed as a query language for XML in which the path of the tree is used to describe the query. XPath expressions can be adorned with boolean conditions on nodes and leaves to restrict the number of answers of the query. XPath is the basis of a more powerful query language (called XQuery) designed to join multiple XML documents and to give format to the answer.

In spite of the simplicity of the XPath language, the programmer usually makes mistakes describing the path in which the data are allocated. Typically, the programmer omits some of the tags of the path, adds more than necessary, and also uses similar but wrong tag names. When the query does not match to

---

\* The author’s work has been supported by the Spanish Ministry MICINN and Ingenieros Alborada IDI under grant TRA2009-0309, and the Junta de Andalucía (proyecto de excelencia) under grant TIC-6114.

the tree structure of the XML tree, the answer is empty. However, we can also find the case in which the query matches to the XML tree but the answer does not satisfy the programmer. Due to the inherent flexibility of XML documents, the same tag can occur at several positions, and the programmer could find answers that do not correspond to her (his) expectations. In other words, (s)he finds a correct path, but a wrong answer. We can also consider the case in which a boolean condition is wrong, expressing a wrong range, and several boolean conditions that do not hold at the same time. When the programmer does not find the answer is looking for, there is a mechanism that can try to debug the query. In XPath there exists an operator, denoted by ‘//’, that permits to look for the tag from that position. However, it is useless when the tag is present at several positions, since even though the programmer finds answers, does not know whether they are close to her (his) expectations.

XPath debugging has to take into account the previous considerations. Particularly, there is an underlying notion of *chance degree*. When the programmer makes mistakes, the number of bugs can be higher or lower, and the chance degree is proportional to them. Moreover, there are several ways on which each bug can be solved, and therefore the chance degree is also dependent from the number of solutions for each bug, and the quality of each solution. The quality of a solution describes the number of changes to be made. Finally, there is a case in which we have also focused our work. The case in which the mistake comes from a similar but wrong used tag. Here, the chance degree comes from the semantic closeness of the used tag.

Our proposed XPath debugging technique is guided by the programmer that initially establishes a value (i.e., a real value between 0 and 1), used by the debugger to penalize bugs in a proportional way. Additionally, we assume that the debugger is equipped with a table of similarities, that is, pairs of similar words with an assigned value in the range [0..1]. It makes possible that chance degrees be computed from similarity degrees.

The debugger reports a set of annotated paths by using an extended XPath syntax incorporating three annotations: `JUMP`, `SWAP` and `DELETE`. `JUMP` is used to represent that some tags have been added to the original expression, `SWAP` is used to represent that a tag has been changed by another one and, `DELETE` is used to represent that a tag has been removed. Moreover, the reported XPath expressions updates the original XPath expression, that is: case `JUMP` incorporates ‘//’ at the position in which the bug is found; case `SWAP` includes the new tag; and finally case `DELETE` removes the wrong tag.

Additionally, our proposal permits the programmer to test the reported XPath expressions. The annotated XPath expressions can be executed in our tool (<http://dectau.uclm.es/fuzzyXPath/>) in order to obtain a ranked set of answers w.r.t. the chance degree. It facilitates the process of debugging because programmers can visualize answers to each query in a very easy way. Our implementation has been developed on top of the recently proposed fuzzy XPath extension [2,3], which uses *fuzzy logic programming* to provide a fuzzy taste to XPath expressions. The implementation has been coded with the fuzzy logic programming

language MALP and developed with the FLOPER tool designed in our research group and freely accessible from <http://dectau.uclm.es/floper/>.

Although our approach can be applied to standard (crisp) XPath expressions, chance degrees in XPath debugging fits well with our proposal. Particularly, XPath debugging annotations can be seen as annotations of XPath expressions similar to the proposed DEEP and DOWN of fuzzy XPath [2,3]. DEEP and DOWN serve to annotate XPath expressions and to obtain a ranked set of answers depending on they occur, more deeply and from top to down. Each answer is annotated with a *RSV (Retrieval Status Value)* which describes the degree of satisfaction of the answer. Here JUMP, SWAP and DELETE penalize the answers of annotated XPath expressions. DEEP and JUMP have, in fact, the same behavior: JUMP proportionally penalizes answers as deep as they occur. Moreover, in order to cover with SWAP, we have incorporated to our framework similarity degrees. Finally, let us remark that the current work is an extension of our previous published work [4].

The structure of the paper is as follows. After summarizing in Section 2 our fuzzy extension of XPath [2,3], in Section 3 we describe our debugging technique. Implementation details are drawn in Section 4.

## 2 Fuzzy XPath

In this section we summarize the main elements of our proposed fuzzy XPath language described in [2,3]. We firstly incorporate two structural constraints called DOWN and DEEP to which a certain degree of relevance is associated. So, whereas DOWN provides a ranked set of answers depending on the path they are found from “top to down” in the XML document, DEEP provides a ranked set of answers depending on the path they are found from “left to right” in the XML text. Both structural constraints can be used together, assigning importance’s degrees with respect to the distance to the root XML element.

Secondly, our fuzzy XPath incorporates fuzzy variants of *and* and *or* for XPath conditions. Crisp *and* and *or* operators are used in standard XPath over boolean conditions, and enable to impose boolean requirements on the answers. XPath boolean conditions can be referred to attribute values and node content, in the form of equality and range of literal values, among others. However, the *and* and *or* operators applied to two boolean conditions are not precise enough when the programmer does not give the same value to both conditions. For instance, some answers can be discarded when they could be of interest by the programmer, and accepted when they are not of interest. Besides this, programmers would need to know in which sense a solution is better than another. When several boolean conditions are imposed on a query, each one contributes to satisfy the programmer’s preferences in a different way and perhaps, the programmer’s satisfaction is distinct for each solution.

We have enriched the arsenal of operators of XPath with fuzzy variants of *and* and *or*. Particularly, we have considered three versions of *and*: *and+*, *and*, and *and-* (and the same for *or*: *or+*, *or*, *or-*) which make more flexible the composition of fuzzy conditions. Three versions for each operator that come for free from our adaptation of fuzzy logic to the XPath paradigm.



One of the most known elements of fuzzy logic is the introduction of fuzzy versions of classical boolean operators. *Product*, *Lukasiewicz* and *Gödel* fuzzy logics are considered as the most prominent logics and give a suitable semantics to fuzzy operators. Our contribution is now to give sense to fuzzy operators into the XPath paradigm, and particularly in programmer’s preferences. We claim that in our work the fuzzy versions provide a mechanism to force (and debilitate) conditions in the sense that stronger (and weaker) programmer preferences can be modeled with the use of stronger (and weaker) fuzzy conditions. The combination of fuzzy operators in queries permits to specify a ranked set of fuzzy conditions according to programmer’s requirements.

Furthermore, we have equipped XPath with an additional operator that is also traditional in fuzzy logic: the average operator *avg*. This operator offers the possibility to explicitly give weight to fuzzy conditions. Rating such conditions by *avg*, solutions increase its weight in a proportional way. However, from the point view of the programmer’s preferences, it forces the programmer to quantify his(er) wishes which, in some occasions, can be difficult to measure. For this reason, fuzzy versions of *and* and *or* are better choices in some circumstances.

Finally, we have equipped our XPath based query language with a mechanism for thresholding programmer’s preferences, in such a way that programmer can request that requirements are satisfied over a certain percentage.

The proposed fuzzy XPath is described by the following syntax:

```

xpath := ['deep-down'] path
path := literal | text() | node | @att | node/path | node//path
node := QName | QName[cond]
cond := xpath op xpath | xpath num-op num
deep := DEEP=num
down := DOWN=num
deep-down := deep | down | deep ';' down
num-op := > | = | < | <>
fuzzy-op := and | and+ | and- | or | or+ | or- | avg | avg{num,num}
op := num-op | fuzzy-op

```

Basically, our proposal extends XPath as follows:

- **Structural constraints.** A given XPath expression can be adorned with  $\llbracket \text{DEEP} = r_1; \text{DOWN} = r_2 \rrbracket$  which means that the *deepness* of elements is penalized by  $r_1$  and that the *order* of elements is penalized by  $r_2$ , and such penalization is proportional to the distance (i.e., the length of the branch and the weight of the tree, respectively). In particular,  $\llbracket \text{DEEP} = 1; \text{DOWN} = r_2 \rrbracket$  can be used for penalizing only w.r.t. document order. *DEEP* works for *//*, that is, the deepness in the XML tree is only computed when descendant nodes are explored, while *DOWN* works for both */* and *//*. Let us remark that *DEEP* and *DOWN* can be used several times on the main *path* expression and/or any other *sub-path* included in conditions.
- **Flexible operators in conditions.** We consider three fuzzy versions for each one of the classical conjunction and disjunction operators (also called

$\&_P(x, y) = x * y$	$ _P(x, y) = x + y - x * y$	<i>Product: and/or</i>
$\&_G(x, y) = \min(x, y)$	$ _G(x, y) = \max(x, y)$	<i>Gödel: and+/or-</i>
$\&_L(x, y) = \max(x + y - 1, 0)$	$ _L(x, y) = \min(x + y, 1)$	<i>Luka.: and-/or+</i>

**Fig. 1.** Fuzzy Logical Operators

```

<bib>
  <name>Classic Literature</name>
  <book year="2001" price="45.95">
    <title>Don Quijote de la Mancha</title>
    <author>Miguel de Cervantes Saavedra</author>
    <references>
      <novel year="1997" price="35.99">
        <name>La Galatea</name>
        <author>Miguel de Cervantes Saavedra</author>
        <references>
          <book year="1994" price="25.99">
            <title>Los trabajos de Persiles y Sigismunda</title>
            <author>Miguel de Cervantes Saavedra</author>
          </book>
        </references>
      </novel>
    </references>
  </book>
  <novel year="1999" price="25.65">
    <title>La Celestina</title>
    <author>Fernando de Rojas</author>
  </novel>
</bib>

```

**Fig. 2.** Input XML document in our examples

connectives or aggregators) describing *pessimistic*, *realistic* and *optimistic* scenarios, see Figure 1. In XPath expressions the fuzzy versions of the connectives make harder to hold boolean conditions, and therefore can be used to debilitate/force boolean conditions. Furthermore, assuming two given *RSV*s  $r_1$  and  $r_2$ , the *avg* operator is obviously defined with a fuzzy taste as  $(r_1 + r_2)/2$ , whereas its *priority-based* variant, i.e.  $avg\{p_1, p_2\}$ , is defined as  $(p_1 * r_1 + p_2 * r_2)/p_1 + p_2$ .

In general, a fuzzy XPath expression defines, w.r.t. an XML document, a sequence of subtrees of the XML document where each subtree has an associated *RSV*. XPath conditions, which are defined as fuzzy operators applied to XPath expressions, compute a new *RSV* from the *RSVs* of the involved XPath expressions, which at the same time, provides a *RSV* to the node. In order to illustrate these explanations, let us see some examples of our proposed fuzzy version of XPath according to the XML document shown of Figure 2.

*Example 1.* Let us consider the fuzzy XPath query of Figure 3 requesting *title*'s penalizing the occurrences from the document root by a proportion of 0.8 and 0.9 by nesting and ordering, respectively, and for which we obtain the file listed in Figure 3. In such document we have included as attribute of each subtree, its corresponding *RSV*. The highest *RSVs* correspond to the main *books* of the

Document	RSV computation
<code>&lt;result&gt;</code>	
<code>&lt;title rsv="0.8000"&gt;Don Quijote de la Mancha&lt;/title&gt;</code>	$0.8000 = 0.8$
<code>&lt;title rsv="0.7200"&gt;La Celestina&lt;/title&gt;</code>	$0.7200 = 0.8 * 0.9$
<code>&lt;title rsv="0.2949"&gt;Los trabajos de Persiles y ...&lt;/title&gt;</code>	$0.2949 = 0.8^5 * 0.9$
<code>&lt;/result&gt;</code>	

**Fig. 3.** Execution of the query `«/bib[DEEP=0.8;DOWN=0.9]/title»`

Document	RSV computation
<code>&lt;result&gt;</code>	
<code>&lt;title rsv="1.00"&gt;Los trabajos de Persiles y ...&lt;/title&gt;</code>	$1.00 = (3 * 1 + 1 * 1)/(3 + 1)$
<code>&lt;title rsv="0.25"&gt;Don Quijote de la Mancha&lt;/title&gt;</code>	$0.25 = (3 * 0 + 1 * 1)/(3 + 1)$
<code>&lt;/result&gt;</code>	

**Fig. 4.** Execution of the query `«//book[@year<2000 avg{3,1} @price<50]/title»`

Document	RSV computation
<code>&lt;result&gt;</code>	
<code>&lt;title rsv="0.25"&gt;Don Quijote de la Mancha&lt;/title&gt;</code>	$0.25 = (3 * 0 + 1 * 1)/(3 + 1)$
<code>&lt;title rsv="0.0625"&gt;Los trabajos de ...&lt;/title&gt;</code>	$0.0625 = 0.5^4 * (3 * 1 + 1 * 1)/(3 + 1)$
<code>&lt;/result&gt;</code>	

**Fig. 5.** Execution of the query `«/bib[DEEP=0.5]/book[@year<2000 avg{3,1} @price<50]/title»`

document, and the lowest RSVs represent the *books* occurring in nested positions (those annotated as related *references*).

*Example 2.* Figure 4 shows the answer associated to a search of books, possibly referenced *directly or indirectly* from other books, whose publishing year and price are relevant but the year is three times more important than the price. Finally, in Figure 5 we combine both kinds of (structural/conditional) operators, and the ranked list of solutions is reversed, where “*Don Quijote*” is not penalized with DEEP.

### 3 Debugging XPath

In this section we propose a debugging technique for XPath expressions. Our debugging process accepts as inputs a query  $Q$  preceded by the `[DEBUG=r]` command, where  $r$  is a real number in the unit interval. For instance, `«[DEBUG=0.5]/bib/book/title»`.

Assuming an input XML document like the one depicted in Figure 2, the debugging produces a set of alternative queries  $Q_1, \dots, Q_n$  packed into an output XML document with the following structure (see also Figure 6):

```

<result>
<query cd="r1" attributes1> Q1 </query>
...
<query cd="rn" attributesn> Qn </query>
</result>

```

```

<result>
  <query cd="1.0">/bib/book/title</query>
  <query cd="0.8" book="novel">/bib/[SWAP=0.8]novel/title</query>
  <query cd="0.5" book="//">/bib/[JUMP=0.5]/title</query>
  <query cd="0.5" bib="//">/[JUMP=0.5]/book/title</query>
  <query cd="0.45" book="" title="name">/bib/[DELETE=0.5][SWAP=0.9]name</query>
  <query cd="0.4" bib="//" book="novel">/[JUMP=0.5]/[SWAP=0.8]novel/title</query>
  <query cd="0.25" book="" title="//">/bib/[DELETE=0.5][JUMP=0.5]/title</query>
  <query cd="0.25" book="//" book="">/bib/[JUMP=0.5]/[DELETE=0.5]title</query>
  <query cd="0.25" bib="" book="//">/[DELETE=0.5][JUMP=0.5]/book/title</query>
  <query cd="0.25" bib="//" book="//">/[JUMP=0.5]/[JUMP=0.5]/title</query>
  <query cd="0.25" bib="">/[JUMP=0.5]/[DELETE=0.5]book/title</query>
  <query cd="0.225" title="//" title="//" title="name">
    /bib/book/[JUMP=0.5]/[JUMP=0.5][SWAP=0.9]name</query>
  <query cd="0.225" bib="" book="//" title="name">
    /[DELETE=0.5][JUMP=0.5][SWAP=0.9]name</query>
  <query cd="0.225" bib="//" book="" title="name">
    /[JUMP=0.5]/[DELETE=0.5][SWAP=0.9]name</query>
  <query cd="0.2" bib="" book="//" book="novel">
    /[DELETE=0.5][JUMP=0.5][SWAP=0.8]novel/title</query>
  .....
</result>

```

Fig. 6. Debugging query «[DEBUG=0.5]/bib/book/title»

where the set of alternative queries is ordered with respect to the CD key. This value measures the chance degree of the original query with respect to the new one, in the sense that as much changes are performed on  $Q_i$  and as more *traumatic* they are with respect to  $Q$ , then the CD value becomes lower.

In Figure 6, the first alternative, with the highest CD, is just the original query, thus, the CD is 1, whose further execution should return «Don Quijote de La Mancha». Our debugger runs even when the set of answers is not empty, like in this case. The remaining options give different CD's depending on the chance degree, and provide XPath expressions annotated with JUMP, DELETE and SWAP commands.

In order to explain the way in which our technique generates the attributes and content of each *query* tag in the output XML debugging document, let us consider a generic path  $Q$  of the form: «[DEBUG=r]/tag<sub>1</sub>/.../tag<sub>i</sub>/tag<sub>i+1</sub>/...», where we say that tag<sub>i</sub> is at level  $i$  in the original query. So, assume that when exploring the input query  $Q$  and the input XML document  $D$ , we find that tag<sub>i</sub> in  $Q$  does not occurs at level  $i$  in (a branch of)  $D$ . Then, we consider the following three situations.

### 3.1 Swapping Case

Instead of tag<sub>i</sub>, we find tag'<sub>i</sub> at level  $i$  in the input XML document  $D$ , where tag<sub>i</sub> and tag'<sub>i</sub> are two similar terms with similarity degree  $s$ . Then, we generate an alternative query by adding the attribute tag<sub>i</sub>="tag'<sub>i</sub>" and replacing in the original path the occurrence "tag<sub>i</sub>/" by "[SWAP= s]tag'<sub>i</sub>/". The second query proposed in Figure 6 illustrates this case:

« <query cd="0.8" book="novel">/bib/[SWAP=0.8]novel/title</query> »

Let us observe that : 1) we have included the attribute `<book="novel">` in order to suggest that instead of looking now for a *book*, finding a *novel* should be also a good alternative, 2) in the path we have replaced the tag *book* by *novel* and we have appropriately annotated the exact place where the change has been performed with the annotation `[SWAP=0.8]` and 3) the CD of the new query has been adjusted with the *similarity degree* 0.8 of the exchanged tags.

Now, it is possible to launch with our *FuzzyXPath* interpreter, the execution of the (fuzzy) XPath queries `</bib/novel/title>` and `</bib/[SWAP=0.8]novel/title>`. In both cases we obtain the same result, i.e., `<La Celestina>` but with different RSV (or *Retrieval Status Value*): 1 and 0.8, respectively.

### 3.2 Jumping Case

Even when  $tag_i$  is not found at level  $i$  in the input XML document  $D$ ,  $tag_{i+1}$  appears at a deeper level (i.e., greater than  $i$ ) in a branch of  $D$ . Then, we generate an alternative query by adding the attribute  $tag_i="//"$ , which means that  $tag_i$  has been jumped, and replacing in the path the occurrence `"tag_i/"` by `"[JUMP=r]//"`, where  $r$  is the value associated to `DEBUG`.

This situation is illustrated by the third and fourth queries in Figure 6, where we propose to jump tags *book* and *bib*. The execution of the queries returns different results, and as more tags are jumped, the resulting CD's become lower. Let us see the results of `</bib/[JUMP=0.5]//title>` and `</[JUMP=0.5]//book/title>`, respectively:

```
<result>
  <title rsv="0.5">Don Quijote de la Mancha</title>
  <title rsv="0.5">La Celestina</title>
  <title rsv="0.03125">Los trabajos de Persiles y Sigismunda</title>
</result>
```

```
<result>
  <title rsv="0.5">Don Quijote de la Mancha</title>
  <title rsv="0.03125">Los trabajos de Persiles y Sigismunda</title>
</result>
```

### 3.3 Deletion Case

This scenario emerges when at level  $i$  in the input XML document  $D$ , we found  $tag_{i+1}$  instead of  $tag_i$ . So, the intuition tell us that  $tag_i$  should be removed from the original query  $Q$  and hence, we generate an alternative query by adding the attribute  $tag_i=""$  and replacing in the path the occurrence `"tag_i/"` by `"[DELETE=r]"`, being  $r$  the value associated to `DEBUG`.

This situation is illustrated by the fifth query in Figure 6, where the deletion of the tag *book* is followed by a swapping of similar tags *title* and *name*. The CD *0.45* associated to this query is defined as the *product* of the values

associated to both `DELETE` (*0.5*) and `SWAP` (*0.9*), and hence the chance degree of the original one is lower than the previous examples. So, the execution of query `«/bib/[DELETE=0.5][SWAP=0.9]name»`, should produce the XML-based output:

```
<result>
  <name rsv="0.45">Classic Literature</name>
</result>
```

As we have seen in the previous example, the combined use of one or more debugging commands (`SWAP`, `JUMP` and `DELETE`) is not only allowed but also frequent. In other words, it is possible to find several debugging points.

When executing a query like `«/[DELETE=0.5][JUMP=0.5]//[SWAP=0.9]name»`, with several changes on its body (w.r.t. the original goal) and a CD *0.225* quite low, the RSV of the result is low too, since it has been obtained by multiplying the three values associated to the deletion of the tag *bib* (*0.5*), jumping the tag *book* (*0.5*) and the swapping of *title* by *name* (*0.9*):

```
<result>
  <name rsv="0.225">Classic Literature</name>
  <name rsv="0.028125">La Galatea</name>
</result>
```

It is important to note that the wide range of alternatives proposed by our technique (Figure 6 is still incomplete), reveals its high level of flexibility: programmers are free to use the alternative queries to execute them, and to inspect results up to their intended expectations.

Finally, we would like to remark that even when we have worked with a very simple query with three tags in our examples, our technique works with more complex queries with large paths and connectives in boolean conditions, as well as `DEBUG` used in several places on the query. For instance, in Figure 7, we show the result of debugging the following query: `«[DEBUG=0.7]/bib/[DEBUG=0.6]book/[DEBUG=0.5]title»`.

## 4 Some Implementation Hints with MALP and FLOPER

In this section we assume familiarity with logic programming and its most popular language Prolog [5], for which MALP [6] (*Multi-Adjoint Logic Programming*<sup>1</sup>) allows a wide repertoire of *fuzzy connectives* connecting atoms in the bodies of clauses. Although the core of our application is written with (fuzzy) MALP rules, our implementation is based on the following items:

1. We have reused/adapted several modules of our previous Prolog-based implementation of (crisp) XPath described in [9,10].
2. We have used the SWI-Prolog library for loading and writing XML files, in order to represent a XML document with Prolog term<sup>2</sup>.

<sup>1</sup> See also [7,8] and visit <http://dectau.uclm.es/floper> for downloading our FLOPER system.

<sup>2</sup> The notion of *term* (i.e., data structure) is just the same in MALP as in Prolog.

```

<result>
  <query cd="1.0">/bib/book/title</query>
  <query cd="0.8" book="novel">/bib/[SWAP=0.8]novel/title</query>
  <query cd="0.7" bib="//">/[JUMP=0.7]//book/title</query>
  <query cd="0.6" book="//">/bib/[JUMP=0.6]//title</query>
  <query cd="0.56" bib="//" book="novel">/[JUMP=0.7]//[SWAP=0.8]novel/title</query>
  <query cd="0.54" book="" title="name">/bib/[DELETE=0.6][SWAP=0.9]name</query>
  <query cd="0.42" bib="" book="//">/[DELETE=0.7][JUMP=0.6]//book/title</query>
  <query cd="0.42" bib="//" book="//">/[JUMP=0.7]//[JUMP=0.6]//title</query>
  <query cd="0.378" bib="" book="//" title="name">
    /[DELETE=0.7][JUMP=0.6]//[SWAP=0.9]name</query>
  <query cd="0.378" bib="//" book="" title="name">
    /[JUMP=0.7]//[DELETE=0.6][SWAP=0.9]name</query>
  <query cd="0.336" bib="" book="//" book="novel">
    /[DELETE=0.7][JUMP=0.6]//[SWAP=0.8]novel/title</query>
  <query cd="0.3" book="" title="//">/bib/[DELETE=0.6][JUMP=0.5]//title</query>
  <query cd="0.2646" bib="//" bib="" book="" title="name">
    /[JUMP=0.7]//[DELETE=0.7][DELETE=0.6][SWAP=0.9]name</query>
  .....
</result>

```

Fig. 7. Debugging of the query «[DEBUG=0.7]/bib/[DEBUG=0.6]book/[DEBUG=0.5]title»

```

[element(bib, [],
  [element(book, [year=2001, price=45.95],
    [element(title, [], [Don Quijote de la Mancha]),
     element(author, [], [Miguel de Cervantes Saavedra]),
     element(publications, [],
       [element(book, [year=1997, price=35.99],
         [element(title, [], [La Galatea]),
          element(author, [], [Miguel de Cervantes Saavedra]),
          element(publications, [], ...)]...)],)]))

```

Fig. 8. A Prolog term representing a XML document

3. The parser of XPath has been extended to recognize new keywords such as `DEBUG` and others like `DEEP`, `DOWN`, `avg`, etc. with their proper arguments.
4. Each tag is represented as a data-term of the form: `element(Tag, Attributes, Subelements)`, where `Tag` is the name of the XML tag, `Attributes` is a Prolog list containing the attributes, and `Subelements` is a Prolog list containing the sub-elements (i.e. subtrees) of the tag. For instance, the document of Figure 2 is represented in SWI-Prolog like in Figure 8.
5. A predicate called `fuzzyXPath` where `fuzzyXPath(+ListXPath, +Tree, +Deep, +Down)` receives four arguments: (1) `ListXPath` is the Prolog representation of an XPath expression; (2) `Tree` is the term representing an input XML document and (3) `DEEP/DOWN`.
6. The evaluation of the query generates a *truth value* which has the form of a tree, called *tv tree*. Basically, the `fuzzyXPath` predicate traverses the Prolog tree representing a XML document annotating into the *tv tree* the corresponding `DEEP/DOWN` values. These actions directly revert on the new predicate `debugQuery` implementing the ideas described in this work.
7. Finally, the *tv tree* is used for computing the output of the query, by multiplying the recorded values. A predicate called `tv_to_elem` has been implemented to output the answer in a pretty way.

```

tv(0.9, [[]],
  tv(0.9, [element(title, [], [Don Quijote de la Mancha]), []],
    tv(1, [[]], [],
      tv(1, [[]],
        tv(0.9, [[]],
          tv(0.9, [element(title, [], [La Galatea]), []],
            tv(1, [[]], [],
              tv(1, [[]],
                tv(0.9, [[]],
                  tv(0.9, [element(title, [], [Los trabajos de Persiles..]), ...]),
                )
              )
            )
          )
        )
      )
    )
  )
tv(0.8, [[]],
  tv(0.9, [element(title, [], [La Celestina]), [], []]), ...

```

**Fig. 9.** Example of a XML output in *MALP*

More details about our implementation of the flexible version of the XPath interpreter and debugger reported in this paper are available on: <http://dectau.uclm.es/fuzzyXPath/> (please, try with the on-line tools).

## 5 Conclusions and Future Work

In this paper we have presented an approach for XPath debugging. The result of the debugging process of a XPath expression is a set of alternative queries, each one associated to a chance degree. We have proposed `JUMP`, `DELETE` and `SWAP` operators that cover the main cases of programming errors when describing a path about a XML document. Our implemented and tested approach has a fuzzy taste in the sense that XPath expressions are debugged by relaxing the shape of path queries with chance degrees.

Although XML files are extensively used in many applications, the debugging of XPath queries has not been studied enough in the literature. Some authors have explored this topic [11], where the functional logic language TOY has been used for debugging XPath expressions. There the debugger is able to assist the programmer when a tag is wrong, providing alternative tags, and to trace executions. The current work can be considered as an extension of the quoted work. Here, our debugging technique gives to programmers a chance degree for each proposed alternative by annotating wrong-points on XPath expressions. We have based our approach in the works [12,13], where XPath relaxation is studied by giving some rules for query rewriting: axis relaxation, step deletion and step cloning, among others. However, they do not give chance degrees associated to wrong XPath expressions.

We are nowadays introducing *thresholding* techniques on our fuzzy XPath in order to increase its performance when dealing with massive XML files. Our idea is to create filters for prematurely disregarding those superfluous computations dealing with non-significant solutions. In [14] we have reported some successful thresholding-based techniques specially tailored for MALP.



## References

1. Berglund, A., Boag, S., Chamberlin, D., Fernandez, M., Kay, M., Robie, J., Siméon, J.: XML path language (XPath) 2.0. W3C (2007)
2. Almendros-Jiménez, J.M., Luna Tedesqui, A., Moreno, G.: A Flexible XPath-based Query Language Implemented with Fuzzy Logic Programming. In: Bassiliades, N., Governatori, G., Paschke, A. (eds.) RuleML 2011 - Europe. LNCS, vol. 6826, pp. 186–193. Springer, Heidelberg (2011)
3. Almendros-Jiménez, J., Luna, A., Moreno, G.: Fuzzy logic programming for implementing a flexible xpath-based query language. *Electronic Notes in Theoretical Computer Science*, vol. 282, pp. 3–18. Elsevier Science (2012)
4. Almendros-Jiménez, J.M., Luna, A., Moreno, G.: A XPath Debugger based on Fuzzy Chance Degrees. In: Herrero, P., Panetto, H., Meersman, R., Dillon, T. (eds.) OTM-WS 2012. LNCS, vol. 7567, pp. 669–672. Springer, Heidelberg (2012)
5. Lloyd, J.: *Foundations of Logic Programming*. Springer, Berlin (1987)
6. Medina, J., Ojeda-Aciego, M., Vojtáš, P.: Similarity-based Unification: a multi-adjoint approach. *Fuzzy Sets and Systems* 146, 43–62 (2004)
7. Morcillo, P.J., Moreno, G.: Programming with Fuzzy Logic Rules by Using the FLOPER Tool. In: Bassiliades, N., Governatori, G., Paschke, A. (eds.) RuleML 2008. LNCS, vol. 5321, pp. 119–126. Springer, Heidelberg (2008)
8. Morcillo, P.J., Moreno, G., Penabad, J., Vázquez, C.: Fuzzy Computed Answers Collecting Proof Information. In: Cabestany, J., Rojas, I., Joya, G. (eds.) IWANN 2011, Part II. LNCS, vol. 6692, pp. 445–452. Springer, Heidelberg (2011)
9. Almendros-Jiménez, J.M.: An Encoding of XQuery in Prolog. In: Bellahsene, Z., Hunt, E., Rys, M., Unland, R. (eds.) XSym 2009. LNCS, vol. 5679, pp. 145–155. Springer, Heidelberg (2009)
10. Almendros-Jiménez, J., Becerra-Terón, A., Enciso-Baños, F.J.: Querying XML documents in logic programming. *TPLP* 8(3), 323–361 (2008)
11. Almendros-Jiménez, J., Caballero, R., García-Ruiz, Y., Sáenz-Pérez, F.: XPath query processing in a functional-logic language. *Electron. Notes Theor. Comput. Sci.*, vol. 282, pp. 19–34 (May 2012)
12. Fazzinga, B., Flesca, S., Furfaro, F.: On the expressiveness of generalization rules for XPath query relaxation. In: *Proceedings of the Fourteenth International Database Engineering & Applications Symposium*, pp. 157–168. ACM (2010)
13. Fazzinga, B., Flesca, S., Furfaro, F.: XPath query relaxation through rewriting rules. *IEEE Transactions on Knowledge and Data Engineering* 23(10), 1583–1600 (2011)
14. Julián, P., Medina, J., Morcillo, P.J., Moreno, G., Ojeda-Aciego, M.: A static pre-process for improving fuzzy thresholded tabulation. In: Cabestany, J., Rojas, I., Joya, G. (eds.) IWANN 2011, Part II. LNCS, vol. 6692, pp. 429–436. Springer, Heidelberg (2011)

# Designing and Evolving an Unreal Tournament™ 2004 Expert Bot

Antonio M. Mora<sup>1</sup>, Francisco Aisa<sup>1</sup>, Ricardo Caballero<sup>1</sup>,  
Pablo García-Sánchez<sup>1</sup>, Juan Julián Merelo<sup>1</sup>,  
Pedro A. Castillo<sup>1</sup>, and Raúl Lara-Cabrera<sup>2</sup>

<sup>1</sup> Departamento de Arquitectura y Tecnología de Computadores,  
Universidad de Granada, Spain

{amorag,jmerelo,pgarcia,pedro}@geneura.ugr.es,  
francisco\_aisa@hotmail.com, rcabamo@gmail.com

<sup>2</sup> Depto. Lenguajes y Ciencias de la Computación  
University of Málaga, Spain

raul@lcc.uma.es

**Abstract.** This work describes the design of a bot for the first person shooter Unreal Tournament™ 2004 (UT2K4), which behaves as a human expert player in 1 vs. 1 death matches. This has been implemented modelling the actions (and tricks) of this player, using a state-based IA, and supplemented by a database for ‘learning’ the arena. The expert bot yields excellent results, beating the game default bots in the hardest difficulty, and even being a very hard opponent for the human players (including our expert). The AI of this bot is then improved by means of three different approaches of evolutionary algorithms, optimizing a wide set of parameters (weights and probabilities) which the expert bot considers when playing. The result of this process yields an even better rival; however the noisy nature of the fitness function (due to the pseudo-stochasticity of the battles) makes the evolution slower than usual.

## 1 Introduction

A *bot* is an autonomous agent which tries to behave as a human player, normally fighting against some other humans/bots in a computer game. There are different types of bots in addition to the opponents, such as the cooperative players (try to aid the main player). They essentially refer to an Artificial Intelligence (AI) engine which is able to perform the same actions in a game as a human player.

First Person Shooter games (FPS) are one of the most profitable area in the study/implementation of bots due to their usual open-code philosophy. They are games where the player can only see the hands and the current weapon of his character, and has to fight against enemies by shooting to them. They usually have a multiplayer fighting mode placed in a limited arena.

Unreal game series follows this philosophy to make it easy the game-modding (modification), including with every copy of the game an editor (UnrealEd), an own programming language (UnrealScript), and a compiler, to add/change

almost whatever the user desires: scenarios, items, characters; just with a few constraints. The state-based AI engine is also open.

Moreover, some additional tools have arisen some years ago, such as GameBots<sup>1</sup>, a *mod* that allows the control of characters (bots) in the game through network connections to other programs. The game sends character's sensory information to the client program, which can decide the actions the bot will take. These actions are sent back to the game which interprets them for the bot movement, shooting, jumping, etc. It was initially released for the Unreal sequel *Unreal Tournament™* (*UT*) and later implemented for *UT 2003*. Over the basis of that tool, it was later launched *Pogamut*<sup>2</sup>, which defines an interface (using GameBots architecture) to program the bots externally using Java. It was implemented for Unreal Tournament™ 2004 (*UT2K4*).

These open-code possibilities and external tools are the main reasons why this game environment has been widely considered in the computational intelligence researching field [1,2,3].

This work is also embedded in the *UT2K4* environment, and uses *Pogamut* for implementing a bot which we have named *UT Expert Bot (E-Bot)*. Its behaviour (AI) follows a shape of Finite State Machine (based in two levels of states), that describes a complex set of rules. These rules are based in the knowledge of an *UT2K4* Spanish expert player and are focused on *1 vs 1 Death Match battle*. It has been modelled according to his experience, including several tricks, as the humans players do, for getting a better behaviour in the game. We have considered the rules defined in the official competitions of *UT2K4* for human players, such as: there are some items forbidden (U-Damage), weapons are not respawned and the match runs for 15 minutes, not for a number of frags (number of enemies killed).

Once *E-Bot* has been completely defined and tested (it beats the default game bots in the hardest difficulty levels), we have designed some evolutionary approaches based on the application of a Genetic Algorithm (GA)[4] for optimizing the set of parameters (weights, probabilities, thresholds) which the rules of behaviour apply, following previous approaches [3,5], but considering an own created behavioural model as the main difference with regard to these works, where the standard AI in the game was improved.

A GA is an algorithm where a population of possible solutions (called individuals) are evolved by means of selection and recombination/mutation to create a new set of candidates that compete using their fitness (quality of adaptation) with the rest of solutions, until a stop criterion (i.e. number of generations) is met. Fitness function is a quality function that gives the grade of adaptation of an individual respect the others. This function usually models the problem to solve.

## 2 State of the Art

Bots have been widely used in games since 1992, when *Quake™* became the first known game in including autonomous characters. It presented not only the

---

<sup>1</sup> <http://gamebots.sourceforge.net/>

<sup>2</sup> <http://pogamut.cuni.cz/main/tiki-index.php>

option of playing against machine-controlled bots, but also the possibility to modify them or create new ones. Some AI approaches arose such as the SOAR Quakebot [6], which modelled a human-like behaviour.

Unreal™ appeared some years later, being as stated in the previous section, the first game in including an easily programming environment and a more powerful language, thus plenty of bots were developed. However just a few of them applied metaheuristics or complex AI techniques, and most of these bots were based in predefined hard-coded scripts.

The studies involving computer games and the improvement of some components of the characters' AI appeared some years ago [7], but the use of metaheuristics to study (and improve) specifically the behaviour of the bots inside FPSs, have arisen in the last few years. We started our research in this field in 2001, publishing our results in national conferences (in Spanish). We applied a Genetic Algorithm to improve the parameters in the bots AI core (as later several authors did [8]), and to change the way of controlling the bots by automatically redefining, by means of Genetic Programming, the standard set of rules of the main states.

Some other evolutionary approaches have been published, such as [9], where evolution and co-evolution techniques have been applied, or [2] in which an evolutionary rule-based system has been applied. The two latter developed inside the Unreal Tournament™ 2004 environment (UT2K4).

There are several studies involving other techniques, such as Self-Organizing Maps, Machine Learning, or Neural Networks, to cite a few. Another line of research involves the human-like bots (which try to imitate the human's behaviour) [1]. There is even a competition which searches for the 'most human' bot [10] in UT2K4.

Our work is devoted to present and study two ideas: first a human-like bot, based in a human expert knowledge modelling is described; second the bot is improved by means of evolutionary computation, as in previous works [3,5], but starting from an own created AI engine, not the standard one.

### 3 UT2K4 Expert Bot

The design of the expert bot (*E-Bot*) AI is based in the knowledge of an expert (human) player, *Me\$\$!@h*, who belongs to the best Spanish UT2K4 clan, *Trauma Reactor (dRâ)*, and who has participated in some European championships. He is one of the authors of the paper and has designed and implemented the main work flow of the bot's behaviour. As a summary, *E-Bot* is implemented considering hierarchical states (primary and secondary), a set of rules to decide the correspondent states, and a (simple) database.

Some tips have to be taken into account as part of the **expert knowledge** to model. Thus, the items and weapons are critically valuable in a *1 vs 1 Death Match*. It is even more important to consider the respawn *timing* of each of them, i.e. the time it takes to appear again once an item has been picked up. The importance grows in this mode since if one player picks one item/weapon,

he/she prevents the opponent for profiting it (while he/she does, of course). Expert players must control this time in order to move to a known respawn area in the moment an item appears. These conditions (timing and locations) depend on the map, which the player should know (or learn).

The main items include: *Shields* (provide protection points), *Health packs* (health points), and *Adrenaline* (which can provide the player special states such as invisibility or faster movement).

*Weapons* in UT2K4 have been ‘carefully’ designed to be all of them equally useful and important (as a difference to other games), so there is no absolutely better weapon than the rest. Everyone has a perfect moment to use and take advantage over other weapons. The choice of this moment is an expert decision that depends on several factors such as the player’s and enemy’s health, the distance to enemy or the height/level where it is placed. The considered weapons are: *Shield Gun*, *Assault Rifle*, *Link Gun*, *Bio Rifle*, *Minigun*, *Rocket Launcher*, *Flak-Cannon*, *Shock Rifle*, and *Lightning Gun*.

The *movement* is another key factor in UT2K4, since it could mean the difference between win or lose. Players usually move jumping, in order to avoid being shot easily. This is a problem of our approach because Pogamut movement module does not implement the jump.

The proposed E-Bot uses a ‘simple’ **database**, which stores the location of every (new) item it finds while moving around the maps (searching for enemies or just exploring to learn), as the human players do the first times in a new arena. Additional information could be stored, but we think this is enough for this initial version.

The use of Pogamut implies we cannot consider the FSM defined in the UT2K4 bot’s AI, thus, a complete AI engine has been designed and implemented. However, we have profited Pogamut’s high-level functions, such as basic navigation from point to point in a map, or the so-called *listeners* (triggers for detecting events).

The *E-Bot*’s AI module considers two levels of states: primary and secondary. The first ones correspond to general actions to perform: Attack, Hunt, Retreat, Greedy and Camp in this initial version. The secondary states are devoted to perform additional tasks within the main action flow (offensive and defensive profiles, pickup items or weapons, among others). For instance, the bot can decide attacking to the enemy, but if it has low health search for any health pack at the same time.

The comparisons and decisions required to choose the state are quite complex, because they consider several factors and situations that the human expert knows. For instance, the comparison of weapons depends on several parameters and weights, because of the existing balance between the power and usefulness of all of them, which could mean that a weapon is the best in a specific situation (different levels, hidden opponent, close/far enemy), but that weapon would be the worst on a different position.

The AI engine (composed by a huge system of rules) at a time chooses the primary state, but while the bot is performing the actions associated to it, the

engine continues checking conditions (for instance the timing of every item), receiving sensory information, checking the bot status, etc. This way, a secondary state can be also set. However the engine can stop and change, at any time, both the primary and/or the secondary state, depending of the conditions, received information and status, giving an extra ‘flexibility’ level to the FSM.

As a general summary, the bot tends to be defensive if its health is lower than the enemy’s, unless the latter has a critical health level, so the bot will attack him to win a frag. In similar health conditions the attitude depends on the weaponry (in comparison with the enemy’s weapons). If the bot’s health is good, it is quite aggressive.

The value of the expert bot has been tested in an experiment, consisting in four different *1 vs 1 - Death Match* combats against a standard UT2K4 game bot, held in two different maps. The bots have been fighting, respecting championship rules, during 15 minutes. The results of every match as well as the average are shown in Table 1.

**Table 1.** Scores (number of frags) of the test fights between *E-Bot* and a Standard UT2K4 bot in the hardest difficulty (*StdBot*). Match 1 (m1) and 2 (m2) in every map.

<i>Map</i>	<i>E-Bot</i>	<i>StdBot</i>
<i>DM-Ironic</i>	13 (m1), 26 (m2)	6 (m1), 8 (m2)
<i>DM-Idoma</i>	23 (m1), 25 (m2)	15 (m1), 8 (m2)
Average	21.75	9.25

As it can be seen *E-Bot* outperforms the standard game bot, even in the hardest difficulty level, which is a challenge for a medium level player.

## 4 Evolution of the UT2K4 Expert Bot

Following previous approaches [8,3,5], the expert bot will be improved. To this end, the set of parameters which act as thresholds, weights, priorities and conditions, and which finally determine the final behaviour of the bot, will be optimized by means of a Genetic Algorithm (GA)[4], which can evolve their values searching for the best combination, i.e. the set of values which performs better in a battle. Following this idea, we have designed and tested a GA-based bot, named *GE-Bot*<sup>3</sup>, following different approaches.

### 4.1 First Approach: chromosome-143

In this approach the *chromosome scheme* has 143 genes, grouped in six different blocks: having 2 genes for health levels, 3 genes for distance, 5 genes to value the risk, 1 gene for time to see an enemy, 6 genes for items priority, and 126 genes related to weapons selection.

<sup>3</sup> The source code of both *E-Bot* and *GE-Bot* can be downloaded from <https://github.com/franaisa/EvolutionaryBot> under a GPL license.

The *fitness function* has been defined as:

$$f = \begin{cases} 3 + (damP/damR) & \text{if } (frags + 1) = deads \\ (2 \cdot frags - deads) + (damP/damR) & \text{if } frags > deads \\ (3/2) + (damP/damR) & \text{if } frags = deads \\ frags/deads & \text{if } frags < deads \end{cases} \quad (1)$$

Where *frags* is the number of enemy kills the bot has obtained, *deads* is the number of own deads, *damP* is the total damage produced by the bot, and *damR* is the total damage it has received. This function rewards the individuals with a positive balance (more frags than deads) and a high number of frags. In addition individuals which perform a high amount of damage to the enemies are also rewarded, even if they have not got a good balance.

The *evaluation of an individual* consists in setting the values of the chromosome in the *E-Bot* AI engine, then a 1 vs 1 combat is launched between this and a standard *E-Bot*. After the time limit defined, the fitness value is computed for the individual. There is a high pseudo-stochastic component in these battles, since the results do not depend completely on our bot, but also on the enemy's actions which we cannot control. Thus, the fitness function is considered as noisy [11], since an individual could be valued as good in one combat, but yield very bad results in another match.

An *elitist selection mechanism* has been applied, remaining the best four individuals in the next population. The rest of population is considered as parents.

The *uniform crossover* operator (every gene of a descendent has the same probability of belonging to each one of the parents) has been applied in two steps: on the one hand it is used with the elite, yielding two descendents by combining the best individual with a random one in the best four chosen. On the other hand, the rest of the offspring is formed as a random combination of the rest of parents (in pairs). Finally, four random individuals are included in the population (they substitute the four worse) to add diversity.

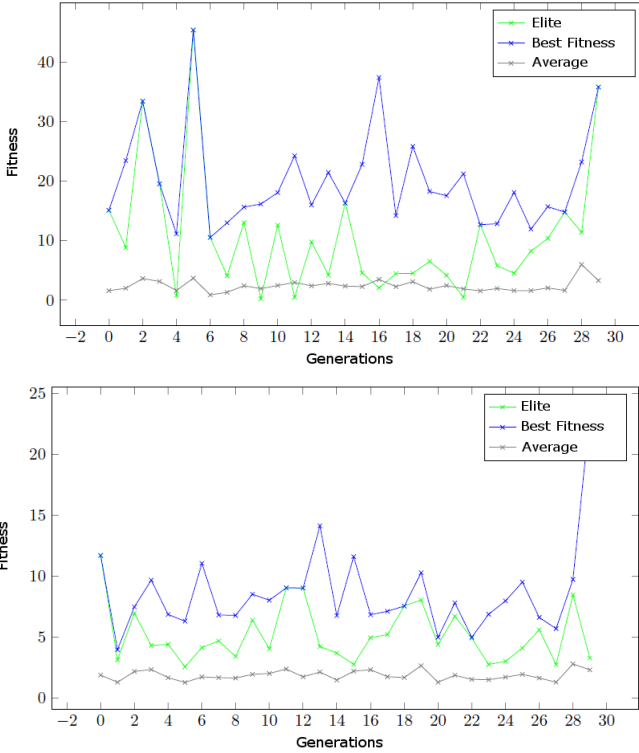
The *mutation mechanism* is performed on every descendent. It changes with a probability  $1/chromosome\_size$  the value of every gen in a  $\pm 10\%$  rate.

Some experiments were conducted to test this approach for the *GE-Bot*. All of them (and next) have been conducted in the map DM-Ironic, since it is one of the most used maps in competitions, and has a design that offers almost any possible fighting situation: different levels, hidden zones, viewpoints and camping areas.

Firstly, the algorithm is tested considering as parameter setting: *30 generations, 30 individuals, and 15 minutes every evaluation*, taking 10 running days.

Figure 1 shows the best and average fitness evolution in the run, considering one (left side) and three (right side) evaluations per individual.

As it can be seen on the left subfigure, the evolution is highly noisy, as commented when the fitness function was defined, due to the pseudo-stochasticity of combats. In order to deal with this effect, some evaluations (different matches) per individual have been performed, as it is recommended [12]. This second experiment has taken one month of computational time and is plotted on the right side subfigure. An improvement in the fitness evolution tendency is shown.



**Fig. 1.** Fitness evolution of the best, elite and average in 30 generations for the first approach of GE-Bot (143 genes chromosome, 1 evaluation (left) and 3 evaluations (right) per individual).

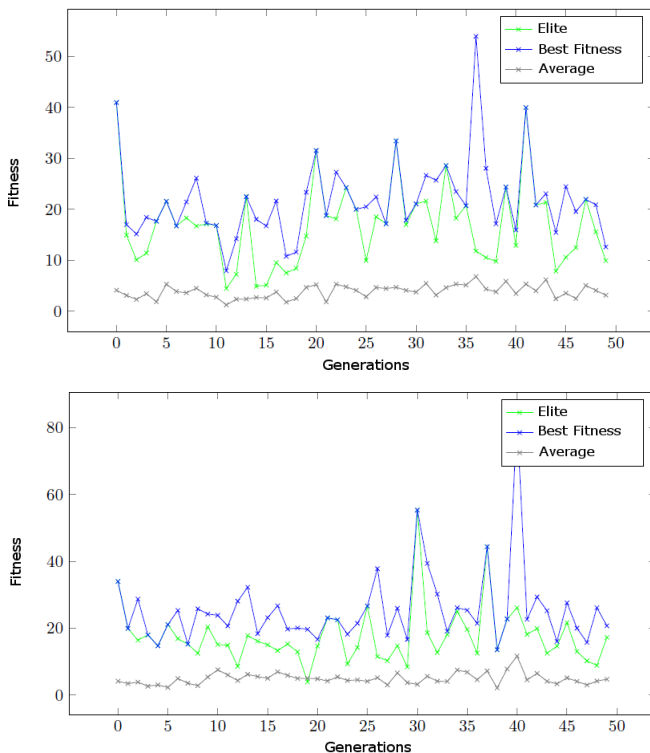
The best fitness graphs proved the noise nature of the function, so even considering three matches for every evaluation, and having followed an elitist scheme, the best values oscillate without a clear tendency. The average results show a lightly improvement tendency, which let us think in a good (but slow) evolution and improvement of individuals (parameters) or results. The reasons of these light tendencies and high oscillations might be two: first reason could be the chromosome length, since the evolution of 143 genes might take much more generations; the second reason could be the inclusion of diversity enhancement mechanisms, such as the uniform crossover or the random generation of some individuals (which substitute the four worst).

**4.2 Second Approach: chromosome-26**

Since the chromosome length implies a high number of generations (and so, huge computational time) are required for a good optimization process, the *chromosome scheme* was redefined considering 26 genes, by reducing the weapons block to just 9 genes (one associated to the priority of each weapon). This representation is less precise from the expert’s AI performance point of view, but with a



more approachable size. The rest of the algorithm terms and operators remained the same. Results are presented in Figure 2 (two runs of ten), with a different parameter setup, due to the expected computational time reduction, so, in order to perform a more complete evolution, *the number of generations has been increased to 50, being the population again 30 individuals and considering this time 5 minutes for evaluating every individual.* The running time of this experiment has been 5 days per run.



**Fig. 2.** Fitness evolution of the best, elite and average in 50 generations for the second approach of GE-Bot (26 genes chromosome). Two different runs.

As it is shown, there are again fluctuations and light improving tendencies. The oscillations seem to be lighter, but what is happening is that the resulting values have been reduced (due to the shorter battle time). The average fitness tendency on the other hand is less clear this time. Thus, the reduction in the evaluation time just has meant an improvement in the computational cost.

### 4.3 Third Approach: Fitness and Operators Redefinition

According to the second conclusion reached by the end of Subsection 4.1, the evolution in this problem is quite difficult, so it would be recommended the

implementation of mechanisms to increase the exploitation of solutions rather than increasing diversity (as it has been done).

Firstly, the fitness function has been redefined in order to take into account more elements of the individual/bot performance during a match, i.e. the most important items for survive and the best weapons for our bot (the most useful according to the defined FSM). They have been included in some terms of the evaluation function as follows:

$$f = \begin{cases} (frags - deads) + s2 + \frac{s1}{2} + \frac{tS/10}{d+1} \\ + \frac{tL/10}{d+1} + \log((damP - damR) + 1) & \text{if } frags \geq deads \\ \frac{frags}{deads} + s2 + \frac{s1}{2} + \frac{tS/10}{d+1} \\ + \frac{tL/10}{d+1} + \log((damP - damR) + 1) & \text{if } frags < deads \end{cases} \quad (2)$$

Where *frags*, *deads*, *damP* and *damR* are the same as in Equation 1. *s1* and *s2* refers respectively to the number of Shields and Super Shields the bot has picked up. *tS* is the time the bot has used the Shock Rifle, and *tL* refers to the time it has used the Lightning Gun. The term frags is the most important and the rest are weighted to have lower relevance.

The GA scheme has been changed to a stationary approach in order to increase the selective pressure and get a higher convergence factor. Thus the best 15 individuals are considered for the new population. They also are one of the parents for generating the offspring and the other parents are selected using a probability roulette wheel from the rest of population. The crossover and mutation operators remains the same as in the other approaches.

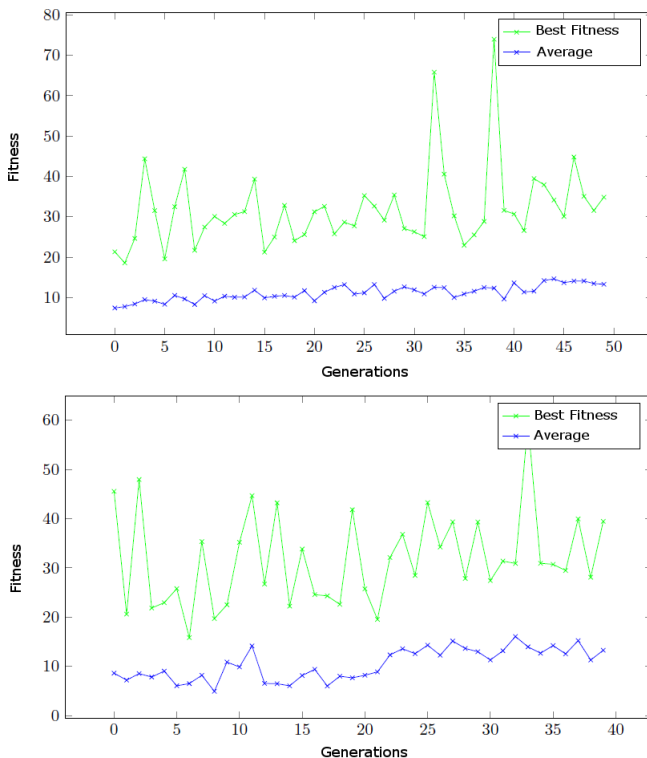
Figure 3 shows the results of two runs (of ten), considering the same parameter configuration as in the last approach.

As it can be seen, the results are better than in previous approaches, showing a ‘softer’ fitness tendency (with less fluctuations), and a clear improving, with the generations, in the average results.

## 5 Expert Bot versus Evolved Bots

A last test has been performed confronting the best individuals of the *GE-Bot* approaches against *E-Bot*, since they have been optimized for beating it (they have fought against it during the evolution). The average results of four matches are shown in Table 2. They have been held in the same two maps and for 15 minutes each.

The results show that the *GE-Bots* with a higher number of generations and smaller chromosome perform better than the one with the higher length. This result should be expected, since the chromosome length is a key factor in the evolution, because it defines the search space size, so long individuals need a higher number of generations. In this case, we just have performed (due to the huge computational time required) 30 generations for 143 genes which are clearly insufficient, according to the experiments results. The evolved for longer *GE-Bots* (50 generations) yield a very good performance beating *E-Bot* in average.



**Fig. 3.** Fitness evolution of the best, and average in 50 generations for the third approach of GE-Bot (26 genes chromosome, complex fitness function and stationary scheme).

**Table 2.** Average scores (number of frags) of the test fights between the three approaches of *GE-Bot* versus *E-Bot*. 4 battles in two maps: DM-Ironic and DM-Idoma.

	Score		
GE-Bot: 143chr-30gen-3evals	4.2	13.2	E-Bot
GE-Bot: 26chr-50gen-1evals	15.3	7.8	E-Bot
GE-Bot: 26chr-50gen-1evals-complexfitness	17.5	6.2	E-Bot

Finally, the last approach considering the complex fitness function performs better than the rest, because it is less influenced by the noisy nature of the evaluation function due to the consideration of additional (and important) factors to compute it.

## 6 Conclusions and Future Work

In this work, a human-like bot for the First Person Shooter game Unreal Tournament™ 2004 (UT2K4) has been described. It models the expert knowledge

of a Spanish high-level player so, it has been named Expert-Bot (*E-Bot*). Its behaviour is based in a shape of finite state machine with two levels of states (primary and secondary), each of them with an associated priority for performing actions. This work flow is flexible, so the AI engine can alter/change it depending on the conditions or status (bot's or enemy's). Moreover, the bot uses a database for 'learning' the maps, as a human player would do the first time it navigates around a new arena. *E-bot* has been designed for fighting in 1 vs 1 death match mode, considering the official competition rules.

Then a Genetic Algorithm (GA) has been implemented to improve the parameters (thresholds, weights, priorities) that the bot's AI considers in its behavioural rule system. The evolved expert bot, named *GE-Bot* has been tested considering different approaches (chromosome length, number of generations, scheme, fitness function, crossover), along with an evaluation consisting in repeated battles which are rated once they have finished, for assigning an average fitness value to every individual in the population. The aim is to deal with the noisy nature of the fitness function, since it depends on the results of the battles, which can vary for the same individual from time to time, regarding to the situation in the map or the enemy's actions which we cannot predict.

Some experiments have been conducted, firstly proving that *E-Bot* outperforms the standard UT2K4 bots, even in the hardest difficulty level. The result-to-effort ratio for *GE-Bot* is not very good, since the extremely high computation time that every experiment takes (from 5 to 30 days), has limited the number of generations and runs performed, so the improvement is not substantial. However, the results yielded show that the best approaches are those which consider a smaller chromosome size, and a higher number of generations, rather than wasting time in repeated evaluations. Moreover, the approach following a stationary scheme and a fitness function that considers items and weapons use gets the best performance and results. Both approaches have improved the results of *E-Bot* and have beaten it in a set of test battles. However, the evolution is not as good as desired and some repetitions of the evaluations could definitely help to improve this tendencies. We will consider this as the first future work line.

According to the expert's opinion, the bots do not perform as well as expected (from the behavioural point of view). This way, another line of research will be the improvement of *E-Bot* in its main flaw, the movement. Thus, the possibility of jumping must be included in its actions, in order to get a harder opponent (more difficult to kill). Once the behaviour has been improved, several research could be conducted with regard to the evolutionary approaches, since the results in this paper can be considered as preliminary. A better noisy fitness dealing could be an interesting issue to address.

Finally, another option to study could be the optimization of *E-Bot* for multiplayer and team modes, which are so far the most famous among the players.

**Acknowledgements.** This paper has been funded in part by project TIN2011-28627-C04-02 (ANYSELF), projects P08-TIC-03903 (EVORQ) and P10-TIC-6083 (DNEMESIS) awarded by the Andalusian Regional Government,

and project 83 (CANUBE) awarded by the CEI-BioTIC UGR. The authors are very grateful to the Pogamut developers, specially to Michal Bida and Jakub Gemrot, by their dedication and support which has definitely aided to finish this work.

## References

1. Soni, B., Hingston, P.: Bots trained to play like a human are more fun. In: IEEE International Joint Conference on Neural Networks, IJCNN 2008, pp. 363–369 (2008)
2. Small, R., Bates-Congdon, C.: Agent Smith: Towards an evolutionary rule-based agent for interactive dynamic games. In: IEEE Congress on Evolutionary Computation, CEC 2009, pp. 660–666 (2009)
3. Mora, A.M., Montoya, R., Merelo, J.J., Sánchez, P.G., Castillo, P.Á., Laredo, J.L.J., Martínez, A.I., Espacia, A.: Evolving bot AI in Unreal™. In: Di Chio, C., et al. (eds.) EvoApplications 2010, Part I. LNCS, vol. 6024, pp. 171–180. Springer, Heidelberg (2010)
4. Goldberg, D.E.: Genetic Algorithms in search, optimization and machine learning. Addison Wesley (1989)
5. Mora, A.M., Moreno, M.A., Merelo, J.J., Castillo, P.A., Arenas, M.G., Laredo, J.L.J.: Evolving the cooperative behaviour in unreal; bots. In: Yannakakis, G.N., Togelius, J. (eds.) CIG, pp. 241–248. IEEE (2010)
6. Laird, J.E.: It knows what you're going to do: Adding anticipation to a quake-bot. In: Artificial Intelligence and Interactive Entertainment SS-00-02. AAAI 2000 Spring Symposium Series (2000)
7. Laird, J.E.: Using a computer game to develop advanced AI. *Computer*, 70–75 (2001)
8. Cole, N., Louis, S.J., Miles, C.: Using a genetic algorithm to tune first-person shooter bots. In: Proceedings of the IEEE Congress on Evolutionary Computation 2004, pp. 139–145 (2004)
9. Priesterjahn, S., Kramer, O., Weimer, A., Goebels, A.: Evolution of human-competitive agents in modern computer games. In: IEEE World Congress on Computational Intelligence, WCCI 2006, pp. 777–784 (2006)
10. 2K-Games: The 2k botprize competition (2012), <http://www.botprize.org>
11. Mora, A.M., Fernández-Ares, A., Merelo, J.J., García-Sánchez, P., Fernandes, C.M.: Effect of noisy fitness in real-time strategy games player behaviour optimisation using evolutionary algorithms. *J. Comput. Sci. Technol.* 27(5), 1007–1023 (2012)
12. Mora, A.M., Fernández-Ares, A., Merelo-Guervós, J.-J., García-Sánchez, P.: Dealing with noisy fitness in the design of a RTS game bot. In: Di Chio, C., et al. (eds.) EvoApplications 2012. LNCS, vol. 7248, pp. 234–244. Springer, Heidelberg (2012)

# Evolving the Strategies of Agents for the ANTS Game

José Carpio<sup>1</sup>, Pablo García-Sánchez<sup>2</sup>, Antonio M. Mora<sup>2</sup>, Juan Julián Merelo<sup>2</sup>,  
Jesús Caraballo<sup>1</sup>, Fermín Vaz<sup>1</sup>, and Carlos Cotta<sup>3</sup>

<sup>1</sup> Dept. of Computer Science, University of Huelva, Spain

<sup>2</sup> Dept. of Computer Architecture and Technology, University of Granada, Spain

<sup>3</sup> Dept. of Computer Languages and Computer Sciences, Málaga, Spain

jose.carpio@dti.uhu.es

**Abstract.** This work studies the performance and the results of the application of Evolutionary Algorithms (EAs) for evolving the decision engine of a program, called in this context *agent*, which controls the player's behaviour in an real-time strategy game (RTS). This game was chosen for the Google Artificial Intelligence Challenge in 2011, and simulates battles between teams of ants in different types of maps or mazes. According to the championship rules the agents cannot save information from one game to the next, which makes impossible to implement an EA 'inside' the agent, i.e. on game time (or on-line), that is why in this paper we have evolved this engine off-line by means of an EA, used for tuning a set of constants, weights and probabilities which direct the rules. This evolved agent has fought against other successful bots which finished in higher positions in the competition final rank. The results show that, although the best agents are difficult to beat, our simple agent tuned with an EA can outperform agents which have finished 1000 positions above the untrained version.

## 1 Introduction

Real-Time Strategy (RTS) games are a sub-genre of strategy-based videogames in which the contenders control a set of units and structures that are distributed in a playing arena. The game objective is normally eliminating all the enemy units. It is usually possible to create additional units and structures during the course of the game, at a cost in resources. Another usual feature is their real time nature, so the player is not required to wait for the results of other players' moves as in turn-based games. Starcraft<sup>TM</sup>, Warcraft<sup>TM</sup> and Age of Empires<sup>TM</sup> are some examples of RTS games.

The 2011 edition of the Google AI Challenge [5] was conducted with an RTS game named ANTS, in which the players control a set of ants that must 'fight' against the colonies of the rest of players in a grid with labyrinthine paths. The ants must gather food for generating new individuals and get an advance over the rivals. The fighting between ants is solved following some rules, but as a thumb rule, the higher number of ants are grouped, the easier will be to win a fight.

Thus, this is a RTS where the AI must be implemented at both commented levels: on the one hand, the ants must be grouped and specialized (explorers, fighters, gatherers), on the other hand each individual should have a particular behaviour to get a global emergent behaviour.

As a first approximation, a behavioural engine (for both levels) was designed by defining a set of states and rules guided by several parameters. This agent participated in the contest and finished in position 2076.

Then the initial engine has been improved by means of a Evolutionary Algorithms (EAs)[2]. They are a class of probabilistic search and optimisation algorithms inspired in darwinistic evolution theory. There are some types, including the extended Genetic Algorithms (GAs)[4], but the main features are common to all of them: a population of possible solutions (individuals) of the target problem, a selection method that favours better solutions and a set of evolutionary operators that act upon the selected solutions. After an initial population is created (usually randomly), the selection mechanism and the operators (crossover, mutation, etc) are successively applied to the individuals in order to create new populations that replace the older one. The candidates compete using their fitness (quality of adaptation). This process guarantees that the average quality of the individuals tends to increase with the number of generations. Eventually, depending on the type of problem and on the efficiency of the EA, the optimal solution may be found.

To conduct the evolution (in the evaluation step), every candidate agent in the population has fought against three different enemies (in two different approaches): a deterministic agent who finished in rank 993, and two very competitive agents which got position 1 and 165.

According to the results the agent has performed quite good, and has been able to beat bots which finished almost 1000 positions better than it in the competition.

## 2 State of the Art

AI in games has become the most interesting element in actual games from the player's point of view, once the technical components (graphics and sound) have reached almost an upper bound. They mostly request opponents exhibiting intelligent behaviour, or just better human-like behaviours [9].

Researchers have also found it an interesting area from the early nineties, so this scope has presented an exponential grown in several videogames and fields, mainly starting with the improvement of FPS Bot's AI, the most prolific type of game [8,12], and following with several games such as Super Mario [19], Pac-Man [10] or Car Racing Games [14], to cite a few.

The RTS games research area presents an emergent component [18] as a consequence of the commented two level AIs (units and global controllers). RTS games usually correspond to vast search spaces that traditional artificial intelligence techniques fail to play at a human level. As a mean to address it, authors in [15] proposed to extract behavioural knowledge from expert demonstrations which could be used to achieve specific goals. There are many research

problems involving the AI for RTSs, including: planning with uncertainty or incomplete information, learning, opponent modelling, or spatial and temporal reasoning [1].

However, most of the RTS games in industry are basically controlled by a fixed script (i.e. a pre-established behaviour independent of inputs) that has been previously programmed, so they are predictable for the player some combats later. Falke et al. [3] tried to improve the user's gaming experience by means of a learning classifier system that can provide dynamically-changing strategies that respond to the user's strategies.

Evolutionary Algorithms (EAs), have been widely used in this field [16,7], but they are not frequently used on-line (in real-time) due to the high computational cost they require. In fact, the most successful proposals for using EAs in games corresponds to off-line applications [17], that is, the EA works previously the game is executed (played), and the results or improvements can be used later during the real-time game. Through off-line evolutionary learning, the quality of bots' intelligence in commercial games can be improved, and this has been proven to be more effective than opponent-based scripts. For instance, in [11] an agent trained with an EA to play in the previous Google AI Challenge is presented.

In the present work, EAs are also used, and an off-line Genetic Algorithm (GA) is applied to improve a parametrised behaviour model (set of rules), inside a RTS named ANTS.

### 3 The Google AI Challenge

This section describes the game scenario where the bots will play. The ANTS game was used as base for the Google AI Challenge 2011 (GAIC)<sup>1</sup> [6]. An ANTS match takes place on a map (see Figure 1) that contains several anthills. The game involves managing the ant community in order to attack (and destroy) the maximum number of enemy hills. Initially, game players have one or more hills and each hill releases the first ant. Then, the bot has to control it in order to reach food and generate another ant. Game is based on a turn system (1000 turns in official games). For each turn, participants have a limited time to develop a strategy with the ant community, i.e. decide the set of simple steps (just one cell in one direction) that every ants must perform. Before turn time-over, the bot should return a witness indicating that tasks have been finished. If the witness is not sent before time-over, the player receives the 'timeout' signal. This signal carries penalty points and the inability to make more movements until game finish. However, this does not entail game disqualification.

If the player has accumulated enough points before 'timeout', she could win. For each captured hill, the player receives two points and if one of our hills is captured, she misses a point.

There are two strong constraints (set by the competition rules) which determine the possible methods to apply to design a bot: a simulated turn takes *just*

<sup>1</sup> <http://ants.aichallenge.org/>



one second, and the bot is *not allowed to store any kind of information between games* about its former actions, about the opponent's actions or about the state of the game (i.e., the game's map).

Thus, if desired, it is mandatory to perform an off-line (not during the match) fine-tuning or adaptation in order to improve an agent's behaviour. In this work, an evolutionary algorithm has been applied. Therefore, the goal in this paper is to design a bot/agent and improve it using an extra GA layer that consider a set of representative maps and enemies to train and adapt the bot for being more competitive, in order to fight the enemy, conquer its anthills, and finally win the game.

## 4 Algorithm and Experimental Setup

In this section the strategy to evolve is presented. A Genetic Algorithm (GA) is used to improve parameters of a basic agent. In order to improve the agent two different type of fitness functions and six different maps have been used.

### 4.1 Behavioural Rules and Parameters

The basic behaviour of our bot is mainly based in a Greedy strategy to prioritize multiple tasks entrusted to the ants:

```

IF enemy hill in sight
    attack the hill
ELSE IF food in sight
    pick up the food
    ELSE IF enemy ants in sight
        attack the ants
    ELSE IF non-explored zone in sight
        explore the area randomly
  
```

The second part of the strategy, is a *lefty movement*, i.e. follow a straight line until water/obstacle is found, and then, walks to the left bordering it.

In order to perform a parameter optimization using genetic algorithms, we have defined a set in the above specified bot's rules. They are:

- *food\_distance*: Maximum distance to go get food, i.e. ants ignores food that is at a distance greater than this value.
- *time\_remaining*: Margin time we have for one turn to finish without a 'time-out penalty'. Higher values indicate that more actions are performed, but as previously explained, the player receives a penalty.
- *distance\_my\_ant\_attack* and *distance\_hill\_attack*: These parameters are used to determine the attack priority. *Distance\_my\_ant\_attack* means that we have one ant partner close enough to take advantage when attacking enemy ants. In this situation, the *distance\_hill\_attack* is taking into account in order to change ant objective. If another enemy ant is close to our hill, our ant give priority to this more dangerous situation for our interest. In this case an ant is sacrificed to keep alive our anthill.

- *turns\_lefty*: Maximum number of consecutive turns in which an ant lefty strategy can be used. After that number of turns, ants community change to Greedy strategy.

## 4.2 Genetic Algorithm

A GA has been used to evolve the previously presented parameters. Thus each individual in the population is represented by an array of integers, where each number indicates the value of one of the parameters previously explained.

The *fitness function*, which determines the individual's adaptation to the environment, is based on launching a game against several opponents, in a certain number of turns and a specific map. The score for the agent after that game will determine the degree of kindness and individual adaptation to the problem we want to solve, knowing the individual that maximizes the score. Two different fitness functions have been studied:

- Basic fitness: it only considers the score obtained by our agent in the battle.
- Hierarchical fitness: the fitness is a tuple of the following elements in order: My score, enemy's score (negative), number of my own ants and number of enemy's ants (negative). A lexicographical order is applied to compare two individuals.

The considered operators have been:

- *selection*: choose half of population with individuals who obtained the highest scores in the games for improving the convergence component.
- *crossover*: multi-point crossover has been performed, mixing some parts of the parents to create the offspring.
- *mutation*: changes parameter values in an individual randomly (inside a range) with certain probability.

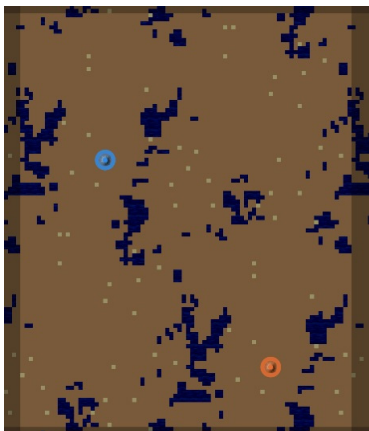
In order to achieve evolution it has been added an extra layer to the game implementation that allows us to store best individuals (set of parameters), and let to evolve the population in future generations.

## 4.3 Experimental Setup

Six maps have been considered in order to perform the bot evolution. All of them are provided by the competition organizers in a tools package. Three maps are mazes with different level of difficulty and the rest are open walking areas. Figure 1 shows two examples of different type of maps. The circles mark hills positions with one colour for each team/player. The blue areas represent water that ants cannot cross, nor walk on it, small points represent food and the rest are land where ants can move. Some other relevant information about maps is detailed in Table 1.

**Table 1.** Maps

	Name	Type	#competitors	Rows	Cols	#Hills
<b>map1</b>	random_walk_p02_01	Open	2	100	80	1
<b>map2</b>	random_walk_p02_05	Open	2	52	70	1
<b>map3</b>	maze_p02_05	Maze	2	66	66	2
<b>map4</b>	maze_p02_34	Maze	2	108	138	1
<b>map5</b>	maze_p02_42	Maze	2	72	126	2
<b>map6</b>	cell_maze_p02_10	Open maze	2	42	142	2



(a) Map 1: open map



(b) Map 3: maze/labyrinth type

**Fig. 1.** Two different example maps considered in the experiments

The experiments conducted try to analyze the performance of the implemented approaches (GA + fitness function) in each of the six maps. Both have considered 64 individuals in the population, a crossover rate equal to 0.3, a mutation rate of 0.1 and a stop criterion set to 20 generations. Every agent is evolved in the six maps 10 times in order to get a reliable fitness value; i.e trying to avoid the ‘noisy nature’ [13] of game playing as a valuation function for an individual when the opponent is non-deterministic. The reason is the same agent (individual) could be valued as very good or very bad depending on the combat result, which in turn depends on the enemy’s actions and the game events.

## 5 Results and Analysis

Firstly it is important to notice that all the selected competitors which have been considered as opponents in the evolution got higher final rankings than our bot, who finished in rank 2076. They are a deterministic agent who finished in rank 993, and two very competitive and non-deterministic agents which got position

**Table 2.** Results of ten battles between the evolved bot (using two fitness functions) and three different opponents with higher final ranks in the Google AI 2011 Competition. The scores, number of own and enemy's ants and the average number of turns to finish the match are presented, along with the standard deviation in each case.

	<b>maxScore</b>	<b>maxMyAnts</b>	<b>maxEnemyAnts</b>	<b>meanTurns</b>
Basic fitness vs. Bot993.				
<b>map1</b>	3,00 ± 0,00	84,08 ± 43,82	66,50 ± 49,20	416,87 ± 125,94
<b>map2</b>	3,00 ± 0,00	68,08 ± 39,10	60,67 ± 34,92	425,64 ± 90,26
<b>map3</b>	6,00 ± 0,00	39,91 ± 15,65	186,91 ± 63,74	318,28 ± 124,63
<b>map4</b>	1,00 ± 0,00	8,64 ± 0,67	12,00 ± 0,00	150,00 ± 0,00
<b>map5</b>	5,42 ± 0,51	36,00 ± 27,24	228,75 ± 89,91	428,93 ± 189,53
<b>map6</b>	6,00 ± 0,00	46,25 ± 59,21	111,25 ± 20,82	221,18 ± 104,35
Hierarchical fitness vs. Bot993.				
<b>map1</b>	3,00 ± 0,00	154,56 ± 28,84	2,67 ± 1,50	481,33 ± 48,26
<b>map2</b>	3,00 ± 0,00	97,67 ± 37,83	3,00 ± 2,18	486,78 ± 79,99
<b>map3</b>	6,00 ± 0,00	45,00 ± 8,85	118,33 ± 19,49	266,00 ± 55,57
<b>map4</b>	1,00 ± 0,00	9,22 ± 0,44	12,00 ± 0,00	150,00 ± 0,00
<b>map5</b>	4,67 ± 0,50	73,78 ± 71,10	226,89 ± 57,61	706,78 ± 262,88
<b>map6</b>	5,00 ± 1,15	104,11 ± 107,52	77,89 ± 58,10	519,44 ± 262,51
Hierarchical fitness vs. Bot165.				
<b>map1</b>	0,00 ± 0,00	33,58 ± 2,97	101,17 ± 7,83	183,42 ± 7,29
<b>map2</b>	0,17 ± 0,39	31,08 ± 8,54	122,00 ± 49,41	221,17 ± 86,06
<b>map3</b>	0,00 ± 0,00	35,33 ± 9,72	98,83 ± 10,99	186,50 ± 9,26
<b>map4</b>	0,00 ± 0,00	34,75 ± 9,75	99,17 ± 10,96	184,92 ± 9,11
<b>map5</b>	0,00 ± 0,00	32,50 ± 10,51	101,75 ± 12,19	186,25 ± 9,18
<b>map6</b>	0,00 ± 0,00	31,50 ± 10,91	103,10 ± 12,80	188,00 ± 9,08
Hierarchical fitness vs. Bot1.				
<b>map1</b>	0,00 ± 0,00	31,00 ± 34,00	109,00 ± 95,00	185,00 ± 198,00
<b>map2</b>	0,00 ± 0,00	17,00 ± 23,00	119,00 ± 132,00	156,00 ± 175,00
<b>map3</b>	0,00 ± 0,00	16,00 ± 17,00	118,00 ± 147,00	160,00 ± 186,00
<b>map4</b>	0,00 ± 0,00	14,00 ± 17,00	130,00 ± 120,00	166,00 ± 160,00
<b>map5</b>	0,00 ± 0,00	20,00 ± 31,00	112,00 ± 108,00	149,00 ± 147,00
<b>map6</b>	0,00 ± 0,00	21,00 ± 19,00	127,00 ± 131,00	172,00 ± 171,00

165 and the winner of the competition. Table 2 shows the obtained results in ten combats performed once the evolution has been completed.

It could be noticed the small standard deviation present in most of the results, due to the small variations in the combat scores. It is zero in many cases because there are very few possible values (i.e. in maps with only two hills, max\_score will be 0, 1 or 3 points). In addition, when a bot is good, it wins most of times and the other way round. Thus in the evolutionary process after 20 generations the system evolves always to reach max score.

For the same reason it can be seen in the table that our bot can not beat those in positions 165 and 1, since they are much more sophisticated in its defined behavioural engine. However, the evolution of the agent gets higher number of own ants and decreases the number of enemy ants.

Moreover, our evolved agent wins on all maps to the robot that ended in ranking 993, more than 1000 positions above the initial version (without optimization). The number of ants is the main difference between basic fitness and hierarchical fitness, and this feature allows to use more effective attack techniques. In maps 5 and 6, the score is lower than the obtained with basic fitness in some cases. However, the number of own ants doubles those obtained with a basic fitness. This invites us to improve strategies in such type of maps to achieve a better use of the large community of generated ants.

## 6 Conclusions and Future Work

This paper presents the design of an agent (bot) that plays in the RTS ANTS game proposed for the Google AI Challenge 2011. Starting with a combination of two basic behaviours (Lefty and Greedy) and a set of parameters, an Evolutionary Algorithm (EA) is used to fine-tune them and thus modify the agent's behaviour.

This bot is evolved in six maps provided by Google, and fighting three different bots that participated in the contest: those who finished in positions 993, 165 and the winner. Two different fitness functions have been tested: a basic function that only takes into account the final score (the number of conquered anthills in a run), and a hierarchical fitness, where the number of player's ants, turns, and enemy ants are also used to compare individuals.

Results show that, even evolving the parameters of two simple strategies, the agent is capable to win harder opponents. On the other hand, the same strategy is not affective against a medium-ranked bot, so it is clear that the enemy behaviour affects to the off-line training algorithms with an specific strategy. However genetic optimization is enough to beat a competitor who is above more than 1000 positions in the ranking.

We conclude that parameters optimization using EA significantly improves agent performance in RTS games and this technique would obtain better results combined with good planning strategies.

For future work, new combination of strategies will be studied and more different fitness functions will be analysed: for example, combining all maps in each fitness calculation. Because the stochastic behaviour of some robots also affects the fitness, an study of how this fitness is affected during the algorithm run will be performed. As demonstrated, the behaviour of the enemies is also a very important key to analyse for designing a all-terrain bot: an agent should adapt to these different behaviours. Also, using a quick map analysis in each turn to set the parameters obtained in this work could be studied to adapt the agent accordingly. A map analysis could be performed, for example, counting the number of direction changes in a period of time. If many direction changes occurs by collisions with walls, means that bots are fighting in a map with maze pattern. Once map type has been detected, bot can choose suitable parameter group for the map. The combination of the Greedy and Lefty actions also will be studied in other RTS games, as the previous Google AI Contest games.

**Acknowledgements.** This work has been funded in part by projects P08-TIC-03903 (Andalusian Regional Government), and TIN2011-28627-C04-02 (Spanish Ministry of Science and Innovation), and by the FPU Grant 2009-2942.

## References

1. Buro, M.: Call for AI research in RTS games. In: Proc. AAAI workshop on Challenges in Game AI, pp. 139–141 (2004)
2. Eiben, A., Smith, J.E.: What is an evolutionary algorithm? In: Rozenberg, G. (ed.) Introduction to Evolutionary Computing, pp. 15–35. Addison Wesley (2005)
3. Falke-II, W., Ross, P.: Dynamic strategies in a real-time strategy game. In: Cantú-Paz, E., et al. (eds.) GECCO 2003. LNCS, vol. 2724, pp. 1920–1921. Springer, Heidelberg (2003)
4. Goldberg, D.E.: Genetic Algorithms in search, optimization and machine learning. Addison Wesley (1989)
5. Google. Google AI Challenge 2011: ANTS (2011), <http://aichallenge.org/>
6. Holdum, K.H., Kaysø-Rørdam, C., Østergaard, C.: Google ai challenge 2011: Ants. Jørgen Villadsen, 11 (2011)
7. Jang, S.H., Yoon, J.W., Cho, S.B.: Optimal strategy selection of non-player character on real time strategy game using a speciated evolutionary algorithm. In: IEEE Symposium on Computational Intelligence and Games, CIG 2009, pp. 75–79. IEEE (2009)
8. Laird, J.E.: Using a computer game to develop advanced ai. Computer 7(34), 70–75 (2001)
9. Lidén, L.: Artificial stupidity: The art of intentional mistakes. AI Game Programming Wisdom 2, 41–48 (2004)
10. Martín, E., Martínez, M., Recio, G., Saez, Y.: Pac-mAnt: Optimization based on ant colonies applied to developing an agent for ms. pac-man. In: 2010 IEEE Conference on Computational Intelligence and Games, CIG 2010, pp. 458–464 (2010)
11. Mora, A.M., Fernández-Ares, A., Merelo-Guervós, J.-J., García-Sánchez, P.: Dealing with noisy fitness in the design of a RTS game bot. In: Di Chio, C., et al. (eds.) EvoApplications 2012. LNCS, vol. 7248, pp. 234–244. Springer, Heidelberg (2012)
12. Mora, A.M., Moreno, M.A., Merelo, J.J., Castillo, P.A., García-Arenas, M.I., Laredo, J.L.J.: Evolving the cooperative behaviour in Unreal™ bots. In: Proc. 2010 IEEE Conference on Computational Intelligence and Games, CIG 2010, pp. 241–248 (2010)
13. Mora, A.M., Fernández-Ares, A., Merelo Guervós, J.J., García-Sánchez, P., Fernandes, C.M.: Effect of noisy fitness in real-time strategy games player behaviour optimisation using evolutionary algorithms. J. Comput. Sci. Technol. 27(5), 1007–1023 (2012)
14. Onieva, E., Pelta, D.A., Alonso, J., Milans, V., Prez, J.: A modular parametric architecture for the torcs racing engine. In: Proc. 2009 IEEE Symposium on Computational Intelligence and Games, CIG 2009, pp. 256–262 (2009)
15. Ontañón, S., Mishra, K., Sugandh, N., Ram, A.: Case-based planning and execution for real-time strategy games. In: Weber, R.O., Richter, M.M. (eds.) ICCBR 2007. LNCS (LNAI), vol. 4626, pp. 164–178. Springer, Heidelberg (2007)

16. Ponsen, M., Munoz-Avila, H., Spronck, P., Aha, D.W.: Automatically generating game tactics through evolutionary learning. *AI Magazine* 27(3), 75–84 (2006)
17. Spronck, P., Sprinkhuizen-Kuyper, I., Postma, E.: Improving opponent intelligence through offline evolutionary learning. *International Journal of Intelligent Games & Simulation* 2(1), 20–27 (2003)
18. Sweetser, P.: Emergence in games. *Game Development* (2008)
19. Togelius, J., Karakovskiy, S., Koutnik, J., Schmidhuber, J.: Super mario evolution. In: *IEEE Symposium on Computational Intelligence and Games, CIG 2009*, pp. 156–161 (2009)

# Interactive Techniques for Entertainment Applications Using Mobile Devices

José Luis Gutiérrez Rivas<sup>1,\*</sup>, Pedro Cano Olivares<sup>2</sup>, and Javier Díaz Alonso<sup>1</sup>

<sup>1</sup> Department of Computer Architecture  
{jlgutierrez, jdiaz}@ugr.es  
<http://atc.ugr.es>

<sup>2</sup> Software Engineering Department  
pcano@ugr.es  
<http://lsi.ugr.es>

**Abstract.** User interaction experience has been lately the main focus of the industry of entertainment. High rendered graphics and huge computing process have been lagging behind for paving the way to the user experience interaction in which the way the user gets involved with the system is a key point. For this reason, we present along with this paper an enhancement for video games and museum applications that is able to increase user experience by separating the display from the controller side, using mobile phones as tracking devices. For this purpose, we have implemented a system architecture based on a Bluetooth peer-to-peer model that establishes a strong connection between mobile phones and desktop applications. The utilization of mobile phones has been revealed as a fundamental element in user experience due to its ease of use and its widespread adoption among society, which makes possible to enter the competitive market of entertainment.

**Keywords:** Virtual Reality, Bluetooth, Accelerometers, Tracking, 3D models.

## 1 Introduction

It is clear that mobile technologies have experienced a considerable boom over the last few years. Part of this growth comes from the appearance of new advanced computing telephones that offers a bigger processing performance: smartphones [1]. The concept of these devices comes from a melting together of different apparatus, such as computers, telephones, music players, cameras, applications (software, web services) and networks (telephone and data), people use in their daily basis.

Smartphones offer the possibility to install software, which leads to a new business idea, the development of applications and the utilization of the best fit operating system on hardware devices. There are multiple different types of applications, which are aimed to utilities, entertainment, productivity, search

---

\* Corresponding author.



tools, social networking, etc., but it is obvious that gaming applications and those which are related to the entertainment of users are creating a very competitive place for software companies products, such as Sony, Samsung, HTC, LG, Apple, Nokia, etc.

In the meantime, the video games and consoles industry has been suffering from a stagnation derived from the lack of innovation in their products [2]. While companies were putting their efforts in improving CPU speed and GPU enhancements, they realized that users were not interested in those features as much as before. For this reason video games companies started to invest in I+D and focus both software (SW) and hardware (HW) in new directions, where user experience and interaction were key points of the product. On that basis new consoles, such as Nintendo Wii [3], and peripherals, such as Microsoft Kinect [4] and Sony Move [5], have appeared on the scene giving rise to a new era in video games field, in which the most important feature of the product resides on the user interaction with the virtual reality (VR) environment [6].

Video games companies are not the only ones that can take profit of this situation. One of this market shares belongs to applications aiming the technical support for museums. It is true that museums are culture providers and exhibitors but it is mandatory to assume that the way they reach citizens has fallen behind in terms of technology and the coverage of the population [7]. Nowadays, young people are more closely related to technology than ever since they have grown up in a world in which every task in their daily basis is accomplished or accompanied by an electronic device. For this reason a way to grant the increase of the interest of young people in museums might be based on providing them with new entertainment and interaction methods that are closer to the new technology trends.

Moreover, not only young people can take profit of these enhancements. New technologies can play a significant role in supporting elderly people and allowing them to lead high-quality lives. One of the most difficult problems in adopting technology has been that of user interfaces which are often not well-suited for elderly users, as growing old inevitably changes the physical and cognitive capabilities of humans. Touchable interfaces and the utilization of larger icons have helped to the paradigm in the context of supporting elderly users in their everyday lives [8].

This paper shows the development of applications that are focused on these new trends, new interaction techniques for video games and new business ideas for museums by the utilization of mobile devices and their capabilities in terms of connectivity and tracking. Section 3 presents the design and Section 3.1 the implementation of the architecture used for this work. Section 3.2 describes the material used for the implementation of an Android video game, and Section 3.3 shows the development and components involved in the museum application. Finally we state in Section 4 the results and conclusions extracted from the described work as well as the future and ongoing work in Section 5.

## 2 Interactive Techniques for Entertainment Applications

One of the key points of our development was the integration of tracking capabilities as the main source of user experience that is the order of the day for video games. Tracking technologies include different HW elements such as accelerometers, gyroscopes, gravity and proximity sensors, which make mobile devices a complete development platform with a powerful tool-chain for user experience enhancements. Furthermore, tracking features in Android applications provide a huge versatility thanks to the possibility to develop a complete and customizable user interaction interface. For example, there are already devices that provide these features (i.e. Wiimote [9]) but, in addition to the expensive costs they are exposed to, their interface and logic are restricted and closed to the original idea they were developed for; in other words, they are not customizable.

On the other hand, museums also need to maintain citizens interest that leads to an increase of new and returning visits [7]. The idea of the second application is also related to the mobile business but applied to the interaction of real elements that people can find in museums such as sculptures, figures, paintings, furniture, etc. Most parts of these museum elements are not available for real public interaction because of wear, which means that many times, users are not able to walk around a sculpture or figure in order to see its details. Add in this fact the update mechanism for the information/legend that corresponds to these elements is a tedious process in which involves printing a new plaque with the new content. This leads inevitably to an expensive update process and it is where our business idea approach has a place for museums.

Our development consists of two applications. The first application consists of a mobile-mobile video game in which the display side and the controller side are separated into two different devices. One of them used as a rendering display device, and the other one as a tracking one, exchanging data through a wireless connection.

The other application maintains the same concept, but it is targeted to mobile-desktop applications for museums. It offers the same services as a tourist guide but including the possibility to interact with the elements that exist inside rooms. The idea is to download the application whenever you are to your mobile device. Your device could display 3D models that you are able to interact with or even to obtain information from them. When the user selects a 3D model, this is displayed on a screen of the room can interact with the model and also navigate in a virtual world.

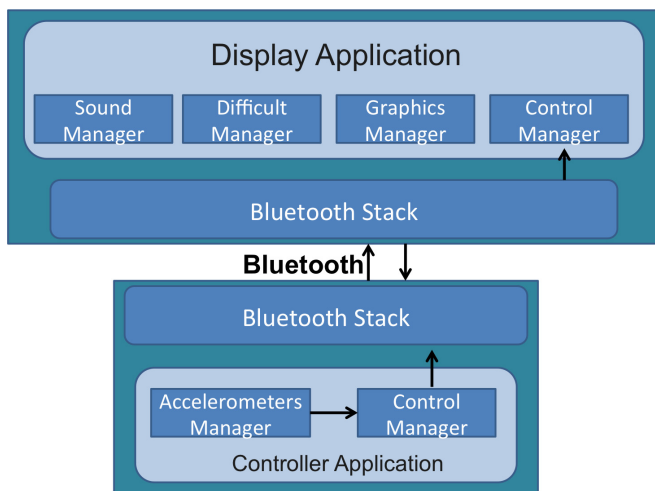
In addition to this, another key point of our study regards to the utilization of own user devices that means a reduction in the maintenance costs of hardware elements for museums since they do not need to maintain any technical support service caused by the wear of these items.

The following Section 3 presents the implementation of both applications.

### 3 Framework Design

Our system presents an architecture to support the design and implementation of mobile games and museum applications using two intercommunicated devices, one for tracking user moves and control and another one as a display device for rendering 3D models.

First, we proposed a Nintendo Wiimote as the controller device, nevertheless, we experimented a considerable communication delay between this controller and Android devices. Since communication delays are not permissible in video games for a correct user interaction, we consider the utilization of other devices. After some tests, we obtained an unappreciable communication delay between two Android devices so that we decided to use them as the display and the controller device respectively.



**Fig. 1.** System architecture model for mobile-mobile and mobile-desktop applications as controller and display devices with Bluetooth message passing functionalities

The point of departure of this work is based on the client-server model architecture previously for desktop games using mobile devices [1]. Analogous to this architecture, our system architecture includes a communication protocol that follows the peer-to-peer (P2P) model using Bluetooth (BT) as Fig. 1 shows.

The display side application includes sound, graphical and control managers as well as a manager to handle BT events. These BT events are implemented in the BT stack which exchanges data between the display and controller applications. The same way the display application handles BT events, the controller application also includes a BT handler, with the exception of using it to send the accelerometers values and commands to the display side.

### 3.1 Implementation

For the architecture implementation, the platform and OS selected has been Android which offers a complete BT development framework based on Java, which allows compatibility with desktop applications. Moreover, Android offers OpenGL ES. as a 3D render engine. On the other hand, for the desktop architecture implementation we have developed the system using Java3D as the rendering system on the top of BlueCove layer, which allows communication between Android and desktop applications.

At first sight, it may initially seem that the need to use two mobile/tablet devices could represent a cost problem but actually, tablets and mobiles have become so prevalent that they are usually both present in any household. Moreover, we offer an all-in-one affordable solution that allows the customization of the device interface whilst big companies normally force users to invest in new peripherals to enhance playing experience. A clear example of this are the previously mentioned Microsoft Kinect and PlayStation Move. Tracking devices that are mandatory for playing several exclusive Microsoft and Sony games. In fact, users are not able to play them by using any other devices which represents an important barrier to the entertainment market.

Next Sections 3.2 and 3.3 present the utilization and implementation of the described development framework for a mobile-mobile game application and for a mobile-desktop museum application.

### 3.2 Mobile-Mobile Application

The first application scenario of this system architecture (Fig. 1) focuses the development of an Android video game application using two devices. One of the devices is used as a screen display and commander receiver while the other is used as a tracking device.

The game consists in a retro-style space ship adventure (Fig. 2) in which the user drives a space ship that must plough through the space crossing geometric figures to score points while avoiding meteors that are also flying all around the space and destroy the ship. The user has a limited number of lives that run out when a meteor impacts the space ship. This part of the video game is executed on the display application.

Regarding movements, the space ship is controlled by another application that runs on the controller application, a smartphone. It captures user motion from accelerometers and gyroscopes. The accelerometers compute the acceleration and direction in which the user has realized a movement and the gyroscope the user position respecting the coordinate axes. Every time the controller detects motion, it is captured by an event and sent to the display application using the BT communication.

In terms of user experience, the fact of separating the display and the controller functions into different devices improve visualization and usability. The problem is that by using the same device for both tasks causes a loss of vision when the display is over a certain vision angle [10]. This is translated into a



**Fig. 2.** Game concept of the mobile-mobile application. At the top, the display device rendering the graphic part of the game and receiving commands from the controller application through Bluetooth (at the bottom).

lack of usability and user experience. This problem has been lately identified by video game companies such as Sony, which has developed their last portable PS Vita [11] with touchable capabilities on the back side. This guarantees touchable functions even with just one screen without interfering visualization.

For this reason, we developed our video game on two devices: the controller and the display application. The following sections describes the implementation of both sides.

**Controller Application Implementation.** This application is responsible for sending commands and the accelerometer values to the display application. It does not require of a high performance HW since it is only focused on capturing motion and sending commands. For this reason almost any low-cost mobile device would be suitable for this purpose.

We have implemented a Java class as a global object to control the game status and store the values from the accelerometers. This class is called *RemoteDevice* and is composed of three types of attributes: accelerometer values, state of the game on controller side (playing, paused...) and the selected space ship model. Accelerometer values are capture as a coordinates vector  $[x,y,z]$  corresponding to x, y and z axes as Fig. 3 shows.

In order to ensure the capture of accelerometer values, we have created a function that captures the event that is launched when accelerometer's values change. This function is called *onSensorChanged*. After updating the accelerometer values, *bluetoothSendAccelerometers* function prepares a command buffer object composed of four bytes. The first byte is used to indicate the display



**Fig. 3.** Mobile-mobile game application. Left: The center image shows the 3D rendering of the display device running. The lower-right-hand corner presents the customized interface of the controller device. Right: Mobile accelerometers for  $[x,y,z]$  axes.

application the command that the user is executing on the controller application and must be executed. These command types regard to pausing, resuming and restarting the game and are interpreted later on on the display application.

The main layer is composed of several icon-like buttons as Fig. 3 shows. The game interface includes a BT button, which is used to establish the BT communication between both devices. When it is pushed, the device lists all the BT devices that are in its BT coverage. By clicking on a device, the application attempts to connects. There is also a cross-like button. It is actually composed by four buttons: top, down, left and right. These button are used in the selection screen so that the user choses different space ships. In addition to this, a confirmation button is used to confirm options such as space ship selection, and also to stop and resume the game. A try again button is used when the user runs all his lives out the game stops and shows a *Game Over* screen. Finally, an auxiliary button (Help Button) shows a help message when pressed. The help message depends on the status of the game. When there is no BT connection establish, it shows instructions to establish the connection, otherwise the message is related to the game instructions.

It is important to remark that this screen interface is totally customizable, making it possible to add or remove buttons and features when required.

**Display Application Implementation.** The display application runs the graphical engine of the video game and executes the commands sent by the controller. The graphic engine has been implemented with the Android version of OpenGL ES that Android NDK provides.

The same way the controller application instantiates a *remoteDevice* object, the display application has its own *remoteDevice*. Both objects have as attributes the  $x$ ,  $y$  and  $z$  coordinates, game status (selecting space ship, playing and dead), the BT connection status and the chosen space ship model but in addition to this, the display application has more attributes related to the global variables

of the game. This refers to lives number, score, game features, difficulty level, timers that controls the progress of the game to change the difficulty level, the OpenGL renderer and several *MediaPlayer* objects that plays different sounds of the game.

When the application is initialized, a BT connection is launched waiting for incoming connections. This BT connection has been performed as paired by using the Bluetooth object from the Android SDK. The BT connection is implemented as a listener that performs six functions: *bluetoothWrite()*, *bluetoothRead()*, *onConnecting()*, *onConnected()*, *onConnectionFailed()* and *onConnectionLost()*. These functions runs as the following state diagram (Fig. 4) shows:

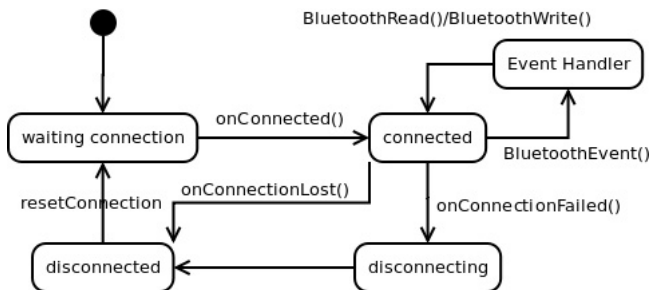


Fig. 4. State diagram of the Bluetooth connection between devices

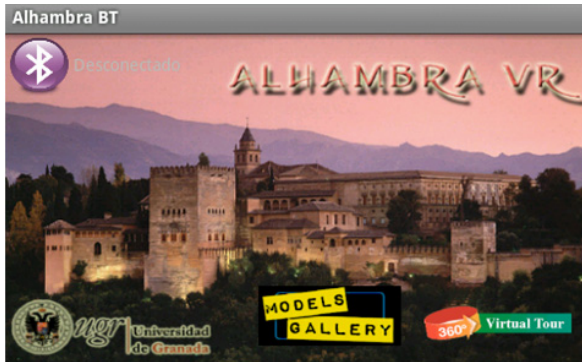
The initial state of the display application remains waiting for incoming BT requests. When the controller application establishes a connection with the display, in both sides *onConnected()* is executed and a BT paired is performed. After pairing, the display application runs the OpenGL render and the game starts by driving the user into the selection screen. Among *Connected* state, both applications are able to exchange BT packages by using *bluetoothWrite()* and *bluetoothRead()* when the BT event handler is triggered.

When the user exits the controller application, the Android *OnDestroy()* function evokes the unpairing between both devices. The display side receives this request and performs *onConnectionLost()* that resets the BT connection. After the BT reboot, the display application is ready again to receive incoming BT requests. *onConnectionFailed()* works in the same way as *onConnectionLost()* except that it is executed after expiring a BT idle timer.

### 3.3 Museum Application

The museum application consists also in two applications. The first application is a desktop application running Java3D and displaying 3D models. The other one is an interactive application to control the displayed 3D models and virtual scenario. On this occasion, however, both of them are implemented using different architecture devices. The display application has been implemented in Java

and runs on a desktop computer and the controller application has been implemented for Android devices. Android mobiles allow users to interact with the virtual environment by using their own devices. This makes possible an immediate availability of the interaction resources that are available at the museum, otherwise user would have to wait for their availability.



**Fig. 5.** Museum controller application. User side application that allows the interaction with a list of 3D models on the desktop application. Buttons available: Bluetooth connection, 3D models gallery and Virtual Tour.

The main concept of the application is based on a controller application running on an Android device to interact with the elements of a museum in a 3D virtual scenario. The museum provides a screen that is connected to a desktop computer, which is running the display application. This application is playing a custom video while it is waiting for incoming BT connections. The BT connection has been implemented using the Java BlueCove library. When the connection is established, the video stops and the application starts to show the 3D models that users can interact with.

For the controller application, the museum offers a QR code [12] that is available for visitors to download the application. Then the user runs the application (Fig. 5), its interface is displayed to the user showing all the interacting possibilities with the 3D models. The controller interface is exposed in Fig. 5.

The interface offers to the user two main options apart from the BT connector: a model gallery for model interaction and a virtual tour. The model gallery shows up a list of the available 3D models than can be displayed and then interacted by the user on the screen of the display application (Fig. 6). This interaction includes zooming, color change, rotation, translation and the possibility of showing information of the models on the controller device.

Moreover, the virtual tour offers the possibility of a third-person navigation through a virtual room like the room in which the user lies. Along with this room the objects that can be rendered are distributed all along the scene. The user is able to approximate to these objects using the device accelerometers





**Fig. 6.** Left: The center picture shows the navigation through the Virtual Tour, and the top-right-hand square shows the closer object to the user position. Right: User interface of the controller application. Shows 3D model selection menu, zooming bar and the information button.

that are sent to the desktop application the same way the previous described video game in section 3.2 describes. By this the user can rotate and translate along the room looking for different 3D models. When the user collides with a model, the Java3D render of the desktop application runs the viewer of the model and the controller application interface changes in order to provide the user the interaction possibilities previously described. When the user stops viewing a model, he/she is returned to the virtual tour.

Whenever the user exits the application, the initial demo video runs again waiting for a new incoming BT connection.

## 4 Conclusions

We have implemented a system architecture to use mobiles as powerful and customizable devices to control entertainment applications using a BT P2P communication model. This approach has been applied to two different examples, a mobile-mobile video game with tracking capabilities and a mobile-desktop application to interact with 3D models in a virtual environment for museums.

Regarding the mobile-mobile application, we have developed an Android Virtual Reality video game with a 3D render, OpenGL ES. The game consists in two applications that run in two different devices. One of the application is considered as a display device using OpenGL ES, and the other one has been designed to be running on an Android smartphone. We have included the possibility of exchanging tracking data and user commands between applications through a BT connection. This has created a solid communication system between both devices. By this, we made possible to transfer tracking values and commands from the controller application to the display device.

A key point of the development of the controller application is the utilization the device accelerometers and the Android Sensors API to add user tracking capabilities [9]. This application is registering the user tracking every time there

is a change in its status by capturing a sensor event. Thanks to this, we have improved the user experience hence the user interacts with the game with his arm's move instead of the typical button-interface. This makes the user get immersed into a VR environment. In addition to this, using different devices for controlling and displaying the game ensures a good user interaction experience since, the touchable screen and the torsion angle derived from the tracking movement, does not interfere with the display of the game as occurs in single screen devices and consoles that joins control and display. This also lead us the opportunity to focus only on the specific tasks of each application, avoiding any device overhead and preventing the display application of any graphic lack or slow-down produced by motion/control capture.

On the other hand, the utilization of an Android device as a tracking controller has made possible the creation of a suitable interacting interface that is completely customizable. Unlikely to other HW tracking devices, such as Wiimote, Kinect, PS Move, our controller is an all-in-one device designed for our system requirements in terms of interface, software and communication protocols. This provides the system with a high level of versatility as opposed to its competitors. Moreover, we made possible the utilization of a mobile device, which is nowadays a daily basis of human beings.

In addition to this, we have developed a new business idea application for museums using a desktop computer and an Android device. This concept includes Java3D for graphic rendering and BlueCove to provide communication between devices. This application increases considerably the user experience of the traditional museum technical support. Moreover, it is a new business idea that guarantees a considerable savings in terms of hardware since the device itself is provided by the user and not by the museum that can be subject to physical wear.

## 5 Future Work

We have planned to enhance the graphic aspects of the video game as well as to add multiuser features to our mobile-mobile and mobile-desktop applications. Currently, both applications allow only one connection at the same time. The video game would aim to a multi-player system in which one of the devices acts as a display screen, and more than one user connect to the display device at the same time with their mobiles. Users' mobiles would be the controllers again and the game type could be a collaborative game as well as a multi-player adventure. Moreover, adding the possibility for the user to modify the controller interface in real-time would provide a new interface interaction concept to the controller application. Equally, the addition of multiuser features for the mobile-desktop application would make possible several users to interact with the desktop application and the 3D models.

In terms of technology, we are planning to integrate the Qualcomm Augmented Reality library. The idea is to provide and improve the game interaction with a higher user experience derived from the overlapping of additional virtual

information to the display of the game. This would make possible to use the game in wide-open spaces, becoming the real world the new virtual environment.

To end with, we are planning to invest in increasing our scope aiming to video surveillance and applications for the automotive domain. Our efforts are focusing in designing applications for these domains that could take the advantage of using mobile devices and their sensors and the lower price of its components since these are very competitive markets and business savings are very significant.

**Acknowledgement.** This work has been supported by the FP7 project TOMSY: Topology Based Motion Synthesis for Dexterous Manipulation (Grant Agreement number FP7-270436).

## References

1. Malfatti, S., dos Santos, F.F., dos Santos, S.R.: Using mobile phones to control desktop multiplayer games. In: 2010 Brazilian Symposium on Games and Digital Entertainment, SBGAMES, pp. 230–238 (November 2010)
2. Dominic, A.: Video game genre, evolution and innovation. *Journal for Computer Game Culture* 2 (2009)
3. Wingrave, C.A., Williamson, B., Varcholik, P.D., Rose, J., Miller, A., Charbonneau, E., Bott, J., LaViola Jr., J.J.: The wiimote and beyond: Spatially convenient devices for 3d user interfaces. *IEEE Computer Graphics and Applications* 30, 71–85 (2010)
4. Corporation, M.: Microsoft kinect (February 2013)
5. Entertainment, S.C.: Playstation move motion capture (February 2013)
6. Burdea, G.C., Coiffet, P.: Virtual reality technology. In: *Virtual Reality Technology* (2003)
7. Squire, K.: Rethinking the role of educational and social science research in digital gaming. *Journal of Computer Game* 2 (2002)
8. Häikiö, J., Wallin, A., Isomursu, M., Ailisto, H., Matinmikko, T., Huomo, T.: Touch-based user interface for elderly users. In: *Proceedings of the 9th International Conference on Human Computer Interaction with Mobile Devices and Services, MobileHCI 2007*, pp. 289–296. ACM, New York (2007)
9. Vajk, T., Bamford, W., Coulton, P., Edwards, R.: Using a mobile phone as a wii-like controller for playing games on a large public display. *Int. J. Comput. Games Technol.* 2008, 4:1–4:6 (2008)
10. Rukzio, E., Leichtenstern, K., Callaghan, V., Holleis, P., Schmidt, A., Chin, J.: An experimental comparison of physical mobile interaction techniques: Touching, pointing and scanning. In: Dourish, P., Friday, A. (eds.) *UbiComp 2006*. LNCS, vol. 4206, pp. 87–104. Springer, Heidelberg (2006)
11. S. C. Entertainment, Playstation vita (February 2013)
12. D. W. Incorporated, Qr code essentials (April 2013)

# Car Setup Optimization via Evolutionary Algorithms

Carlos Cotta<sup>1</sup>, Antonio J. Fernández-Leiva<sup>1</sup>, Alberto Fuentes Sánchez<sup>2</sup>,  
and Raúl Lara-Cabrera<sup>1</sup>

<sup>1</sup> Dept. Lenguajes y Ciencias de la Computación, ETSI Informática,  
University of Málaga, Campus de Teatinos, 29071 - Málaga, Spain

{ccottap,afdez,raul}@lcc.uma.es

<sup>2</sup> elvetto@hotmail.com

**Abstract.** Car racing is a successful genre of videogames, as proved, for example, by the racing simulator saga, Gran Turismo. In this genre of games, players not only race but they are also involved in the process of setting up the car, assuming the role of a technician/mechanic/engineer. Generally, this configuration deals with a large set of parameters that range from the amount of fuel loaded into the car to the tire pressure and type. This article compares different proposals for optimizing this process using evolutionary computation techniques to make several suggestions for a simulated international competition for car racing setup optimization.

## 1 Introduction

Artificial intelligence (AI) in games has become very important so much so that there are even international conferences that only focus on this topic, or provide tracks and special sessions devoted to this area. These conferences frequently include competitions in order to compare and discuss different proposals of AI applied to videogames.

The GECCO conference proposed simulating the days before a race, when mechanics and drivers work together on the car setup to discover which car setup is the best for the circuit. The goal of this competition was to design an evolutionary algorithm to search for the best car setup in a racing car simulator thereby replacing the team of mechanics and drivers, in the search for the best car setup in a racing car simulator. This article describes different algorithms and analyzes their performance within the framework of the aforementioned competition.

There is a related competition, the *Simulated Car Racing Championship*, where each participant has to submit a controller to drive a car. This is a very active competition with a lot of controllers submitted and a wide range of AI techniques are used to develop them. [1] presents an autonomous racing car controller with several context-dependent behavioral modules the parameters of which have been optimized by evolutionary strategies. For example, [6] exhibits a tuned-by-hand modular architecture combined with a simple fuzzy system, while in [3,7] the authors use fuzzy systems in order to implement the controller. Another example that uses an on-line neuroevolution system is presented in [2].

## 2 The Competition

The competition is linked to *TORCS*<sup>1</sup> (The Open Racing Car Simulator), which is a multi-platform racing simulator, that can also be used as both a game in itself and as a research platform because it includes artificial players and comparisons between them. The competition, called “Optimizing Car Setup”, is based on 3 tracks or grand prizes. The participants have to provide evolutionary algorithms to optimize the best car setup for each track. The contest is divided into two consecutive phases: optimization and evaluation. During the optimization phase, the evolutionary algorithm should optimize the car parameters for a fixed amount of playing time (i.e. game tics): 10 million tics. Then, the best car setup is used to compete for a certain number of tics (time units), the maximum distance covered by a car using this configuration. Then, all the distances of the participants are compared with each other and these participants are ranked according to the distance reached; the player with the longest distance earns 10 points, while the second and third earn eight and six points, respectively. The rest of the players from the fourth to the eighth position receive five to one point, respectively.

A real-valued vector of 50 elements represents the parameters of a car setup. The competition software provides an API to evaluate these parameters in a race and returns useful information such as the best lap time, the maximum speed, the distance raced and the damage the car has suffered during the race. Through the API, it is possible to specify the amount of game tics to use in the assessment of a car setup. The game tics spent for an evaluation will be subtracted from the total amount of playing time available. The evaluation process ends when it reaches 10 million games tics or it spends more than 2 hours of computing time.

### 2.1 The Architecture

*TORCS* is available as a standalone application, in which the bots (non-human players, in other words, the cars) are compiled as separate modules of the game and then loaded into the main memory prior to the start of a race. The cars available in *TORCS* have several parameters that should be optimized for each circuit, such as the angle of the wings or the suspension’s parameters. These parameters make *TORCS* an ideal testing framework for optimization algorithms based on evolutionary computation. However, this architecture has two problems: (a) there is no separation between the bots and the simulation engine so that bots have full access to all the data structures that represent the track and the car; this information might be used to create game cheating Artificial Intelligence (AI), and (b) *TORCS* architecture restricts the choice of the programming language used to develop the bots.

---

<sup>1</sup> <http://sourceforge.net/projects/torcs/>

The competition software modified TORCS to cope with these problems and it extended the original architecture as follows:

1. TORCS is structured as a client-server application: the bots run as an external process and connect to the race server through an UDP connection.
2. It is possible to change the car parameters during the race; in the original TORCS the parameters were loaded at the start of each race.
3. The competition software creates a physical separation between the optimizer and the server of the race, building an abstraction layer, which removes the restriction of which programming language is used for the bots. Moreover, it only allows access to a set of parameters defined by the contest designer, and it prevents the possibility of exploiting some specific domain knowledge.

An optimization process involves a server and a client. At the beginning of the process, the client identifies the server and establishes a connection between them; then the latter sends some information to the former, namely the number of parameters to be optimized and the number of available ticks. After this, the simulation begins and the individuals sent by the client are evaluated.

For each evaluation, the client sends the server a request to evaluate a list of values of the parameters to be optimized as well as the duration of the evaluation expressed as a number of game tics. The evaluation (i.e. the race) is in itself a black box and the designer does not have access to it; this aspect of the game raises an interesting and hard challenge in the design of the game's AI. As soon as the evaluation is complete, the server returns the result to the client encoded as four values: *distraced* (i.e., distance raced), *topspeed* (i.e., maximum speed reached during the race), *damage* (i.e., damage to the car), and *bestlap* (i.e., best lap time)

Once the simulation is over, the client must send the server the best solution found. The final solution is the only result considered for the competition. During the competition, the final solution produced by each competitor will be compared with the others to assess the best optimization strategy and this will be scored according to the rules shown in the previous section.

### 3 A Steady-State Algorithm

The first proposal is an evolutionary steady-state algorithm. Individuals are selected in pairs from a population, using a binary tournament method of two parents (i.e. the parent with the best fitness is selected), subsequently they are combined into one individual and mutated (with a probability of 1.0). This new individual is added to the new population and the whole process is repeated a certain number of generations.

Each parameter was a real value and each of them was encoded as a 10-bit binary value. There were 50 parameters to optimize so each individual of the population was an array of 500 bits (50 \* 10-bit real genes). With this

representation, the implementation of the converter had a way to translate the binary representation to a real-value vector.

On the other hand, we had to establish a fitness function to evaluate the quality of each individual. As mentioned above, the server returns four values: *bestlap*, *distraced*, *topspeed* and *damage*. At this point, we considered a single fitness to optimize:

$$C_1 * \text{distraced} + C_2 * \text{topspeed} + C_3 * (1000 - \text{bestlap}) + C_4 * \text{damage} \quad (1)$$

$C_i$  are real constants that provide weights to the four values to optimize in Eq. (1). The value of this fitness corresponds to the mono-objective version of our evolutionary algorithm.

## 4 Experimental Analysis

This section includes a description of the experiments conducted in order to evaluate the performance of the mono-objective algorithm that was described in the last section. An analysis of the performance of this proposal during the contest held at the conference EVO-GAMES 2010 is also presented here.

For the experiments, we decided to set the following parameters: 10 runs of the algorithm with a population of 50 individuals and 20 generations. The number of tics for the simulation was set to 10000 and 5000 for the evaluation of each individual in the population and the evaluation for each solution of the optimization respectively.

For a competitive solution, first we had to find the appropriate values for the constants  $C_i$  (for  $i \in [1, 4]$ ) in the expression (1), and for that we considered various combinations of values. The results of the fitness functions were tested on four different circuits (i.e., Speedway, wheel1, Olethros, and E-track 4). Table 1 shows the fitness function that were proposed for the study. As there are a lot of combinations to consider, we only present the data from some of these. The left hand column shows the fitness function used to train our proposal and the right hand column shows the total score after training in the four aforementioned circuits.

Prior to running the experiments, we had to find the appropriate values for the constants  $C_i$  in the fitness definition (1). Table 1 shows the score obtained from different combinations of these values.

The best performance of the mono-objective algorithm was achieved with the combination of values ( $C_1 = 0.6$ ,  $C_2 = 2.5$ ,  $C_3 = 0.15$  and  $C_4 = 0.05$ ), so the mono-objective algorithm's fitness function was the following:

$$0.6 * \text{distraced} + 2.5 * \text{topspeed} + 0.15 * (1000 - \text{bestlap}) + 0.05 * \text{damage} \quad (2)$$

We submitted the mono-objective evolutionary algorithm to the EVO-\* competition, which specified the following rules:

- The contest involved 3 tracks.
- Only 22 parameters out of 50 to optimize.

**Table 1.** Score obtained by using different  $C_i$  values in the fitness function

Fitness Function (1)	Total Points
$0.6 * \text{distraced} + 2.5 * \text{topspeed} + 0.15 * (1000 - \text{bestlap}) + 0.05 * \text{damage}$	29
$0.6 * \text{distraced} + 3 * \text{topspeed} - \text{bestlap} - 0.1 * \text{damage}$	19
$0.7 * \text{distraced} + 1.5 * \text{topspeed} - 0.1 * \text{bestlap} - 0.05 * \text{damage}$	19
$0.6 * \text{distraced} + 1.5 * \text{topspeed} - 0.25 * \text{bestlap} - 0.05 * \text{damage}$	17
$0.25 * \text{distraced} + 0.25 * \text{topspeed} - 0.25 * \text{bestlap} - 0.25 * \text{damage}$	12
$0.25 * \text{distraced} + \text{topspeed} - 0.25 * \text{bestlap} - 0.25 * \text{damage}$	12
$\text{distraced} + 0.25 * \text{topspeed} - 0.25 * \text{bestlap} - 0.25 * \text{damage}$	8
$\text{distraced} + \text{topspeed} - 0.25 * \text{bestlap} - 0.25 * \text{damage}$	8
$0.6 * \text{distraced} + 0.25 * \text{topspeed} - 0.15 * \text{bestlap} - 0.05 * \text{damage}$	6
$0.25 * \text{distraced} + 10 * \text{topspeed} - 0.25 * \text{bestlap} - \text{damage}$	5
$0.6 * \text{distraced} + 2.5 * \text{topspeed} + 0.15 * (1000 - \text{bestlap}) - 0.05 * \text{damage}$	5
$0.25 * \text{distraced} + 0.25 * \text{topspeed} + 0.25 * \text{bestlap} + 0.25 * \text{damage}$	0
$0.25 * \text{distraced} + 0.25 * \text{topspeed} - 0.25 * \text{bestlap} + 0.25 * \text{damage}$	0
$0.25 * \text{distraced} + 0.25 * \text{topspeed} + 0.25 * \text{bestlap} - 0.25 * \text{damage}$	0

- The simulation time was 1 million games tics.
- The optimization algorithm ran 10 times in each circuit.
- The best solution was scored according to the distance covered in 10000 game tics.

The results for each of the three tracks considered in the competition are presented in Table 2 (note that Fuentes/Cotta/Fdez/Cab is our mono-objective algorithm).

**Table 2.** Distance Average and final classification in the 2010-competition: Distance(Points)

Competitor	CG Track	Poli-Track	Dirt-3	Distance Points
Muñoz (MOEA)	9831.83 (10)	7654.01 (6)	6128.29 (8)	23614.13 24
García-Sáez (PSO)	8386.77 (6)	7979.86 (10)	5021.41 (5)	21388.04 21
Walz (PSO)	8408.25 (8)	7304.54 (5)	5336.88 (6)	21049.77 19
Fuent-Cotta-Fdez-Cab (GA)	7553.21 (4)	5931.47 (4)	6263.40 (10)	19748.08 18
Muñoz-Martín-Sáez (EA)	8167.60 (5)	7718.36 (8)	4629.33 (4)	20515.29 17

Each track was won by a different competitor. Our driver won in *Dirt-3* and the difference between the second and the fourth classified, was really small (only 3 points). The winner of the competition used a multi-objective algorithm (MOEA) to optimize the four parameters considered in the competition (i.e., *distraced*, *topspeed*, *bestlap* and *damage*).

## 5 Multi-Objective Evolutionary Proposals

We also considered two multi-objective algorithms that are described next. Initially we considered several possibilities and finally decided to create two



multi-objective algorithms using SPEA2 [8], specifically the implementation of this algorithm provided by the ECJ<sup>2</sup> library.

In order to use a multi-objective algorithm, it is necessary to add a new field to the population that corresponds to Pareto file size. This file corresponds to a part of the subpopulation and the size of the file cannot be larger than the size of the population.

Another peculiarity of the SPEA2 implementation from the ECJ library is that the fitness includes two elements: an array of floating point values representing the fitness values (0.0 is the worst and infinity is the best) and another value representing the SPEA2 fitness that identifies the individual status. The individuals are sorted by fitness value, so the best individual is the one with the lowest value.

In addition to this algorithm, we also propose a modification of SPEA2 multi-objective algorithm that is capable of finding a set of characteristics for the best individual in the Pareto archive, using a feature selection algorithm.

The feature selection algorithm used for this study consists of a Principal Component Analysis (PCA) [4,5]. To implement PCA, we used the method included in Matlab<sup>3</sup>. This method, which has been applied to each candidate, returns several variables among which a set of characteristics can be found.

The method to obtain the pattern vector is as follows. Candidate solutions are executed ten times in four tracks/races and we consider a Pareto file with size 10. Each individual for each circuit should have a file of 100 individuals resulting from the simulation. Then, the Pareto front of non-dominated individuals is computed.

Each of these individuals are then evaluated in all four tracks, obtaining their distances raced. These distances are grouped into a matrix that is passed to the Matlab function in order to calculate the principal components. These values are involved in the process of selecting the best individual.

## 6 Experimental Analysis Including MOEAs

In this section, we have compared our results obtained in the aforementioned experiments and those obtained by the participants of the competition held in GECCO 2009.

For the multi-objective evolutionary algorithm, we consider a population of 50 individuals, 20 generations and 10000 game tics for the simulation and evaluation. Different candidates were run 3 times on the same tracks that were previously used for single objective. Table 3 shows some of the fitness combinations that were considered (first column) and the score obtained by SPEA2 to optimize in this context.

The best combination for our multi-objective algorithm was minimizing Best-lap and maximizing the fitness used by the mono-objective algorithm explained above.

<sup>2</sup> <http://cs.gmu.edu/~eclab/projects/ecj/>

<sup>3</sup> <http://www.mathworks.es/help/toolbox/stats/princomp.html>

**Table 3.** Results obtained using different fitness combinations

Fitness combinations	Total
$f[0] = \text{min bestlap}, f[1] = \text{Single-objective fitness}$	36
$f[0] = \text{min bestlap}$	32
$f[0] = \text{min bestlap}, f[1] = \text{max distraced}$	27
$f[0] = \text{min bestlap}, f[1] = \text{min } f[0] - \text{damage}$	16
$f[0] = \text{min bestlap}, f[1] = \text{max topspeed}$	15
$f[0] = \text{distraced}$	13
$f[0] = \text{distraced}, f[1] = \text{topspeed}, f[2] = \text{min bestlap}, f[3] = \text{min damage}$	13

The experiments with a variation of the multi-objective algorithm (based on PCA) had the following characteristics: two versions of the proposals were considered: one with a Pareto file size of 5 and another with a size of 10. Each version, in turn, had two versions: one version with the fitness previously considered in SPEA2, and the second one considered by directly optimizing the four main parameters of the competition (i.e., distraced, topspeed, bestlap, and damage). The evaluation was performed with the same scenario as in the previous experiments. Table 4 contains all the results.

**Table 4.** Score obtained using different parameters

Drivers	Total
4 fitness and 5 not dominated	25
4 fitness and 10 not dominated	27
2 fitness and 5 not dominated	36
2 fitness and 10 not dominated	28

The best variation of the multi-objective algorithm is the result of combining a Pareto file size 5 with the fitness: minimizing bestlap and maximizing the fitness used by the mono-objective algorithm. Table 5 shows the overall score obtained by the three proposals described above and the three drivers submitted to the contest GECCO-2009. In this table, the best performance corresponds to our SPEA2 multi-objective algorithm (without PCA).

Note that the winner in the evo-\*2010 competition, as displayed in Section 4, is a multi-objective algorithm (MOEA) similar to our best proposal, as shown here. In fact, our two multi-objective proposals were much more competitive than the single-objective proposal that was sent to the competition. So we are led to think that either of these two proposals could have obtained better results.

## 6.1 Additional Comments

Three parameters were disabled in the experiments: fuel consumption, car damage and the time limit per turn. The reader may wonder why and the answer is

**Table 5.** Overall score of the proposals submitted to GECCO 2009

	Driver	Speedway	ETRACK	Olethros	Wheel	Total
Multi-objective		10	5	8	8	31
	V&M&C	4	8	5	10	27
	Jorge	8	4	10	4	26
Multi-objective	PCA	3	10	6	6	25
Single-objective		5	6	4	5	20
	Luigi	6	3	3	3	15

simple: the objective of this contest was to find the best solution for a car, but, during the training, the car may suffer variations. One of these changes is the damage done to the car. If a car collides with an object it is likely to deform the chassis and all the data obtained from then may not be reliable because it is conditioned by the crash. Fuel consumption leads to the same data reliability problem. In each lap the car consumes fuel and in turn it weights less, becoming easier and faster to drive.

## 7 Conclusions

In this article, we have considered different proposals based on evolutionary computation to set up a car in a racing simulator. In order to achieve this, we have used an international contest in which there were several parameters to be optimized.

The nature of the competition and experimental analysis has shown that multi-objective evolutionary algorithms are a good solution to the problem. Focusing on our proposals, the best proposal is based on the SPEA2, although it is true that we can not underestimate the work done by the single-objective algorithm. That defined the fitness function and this was used in our best multi-objective algorithm as one of the objectives to be optimized.

The results obtained by a variant of our multi-objective algorithm with search patterns was good (better than the results obtained by the single-objective algorithm) and this makes us think that the calculation of the principal components is a good technique to take into account for the future, although it requires further in depth studies.

There are several lines open such as trying new fitness functions for our single-objective algorithm or searching a classification algorithm to find better patterns for the multi-objective.

**Acknowledgements.** This work is partially supported by Spanish MICINN under project ANYSELF<sup>4</sup> (TIN2011-28627-C04-01), and by Junta de Andalucía under project P10-TIC-6083 (DNEMESIS<sup>5</sup>).

<sup>4</sup> <http://anyself.wordpress.com/>

<sup>5</sup> <http://dnemesis.lcc.uma.es/wordpress/>

## References

1. Butz, M., Lonkeker, T.: Optimized sensory-motor couplings plus strategy extensions for the torcs car racing challenge. In: IEEE Symposium on Computational Intelligence and Games, CIG 2009, pp. 317–324 (2009)
2. Cardamone, L., Loiacono, D., Lanzi, P.L.: On-line neuroevolution applied to the open racing car simulator. In: IEEE Congress on Evolutionary Computation, CEC 2009, pp. 2622–2629 (2009)
3. Ho, D., Garibaldi, J.: A fuzzy approach for the 2007 cig simulated car racing competition. In: IEEE Symposium On Computational Intelligence and Games, CIG 2008, pp. 127–134 (2008)
4. Jolliffe, I.: *Principal Component Analysis*, 2nd edn. Series in Statistics. Springer, New York (2002)
5. Krzanowski, W.: *Principles of Multivariate Analysis: A User's Perspective*. Oxford University Press, New York (1988)
6. Onieva, E., Pelta, D., Alonso, J., Milanés, V., Perez, J.: A modular parametric architecture for the torcs racing engine. In: IEEE Symposium on Computational Intelligence and Games, CIG 2009, pp. 256–262 (2009)
7. Perez, D., Recio, G., Saez, Y., Isasi, P.: Evolving a fuzzy controller for a car racing competition. In: IEEE Symposium on Computational Intelligence and Games, CIG 2009, pp. 263–270 (2009)
8. Zitzler, E., Laumanns, M., Thiele, L.: *Spea2: Improving the strength pareto evolutionary algorithm*. Tech. rep., Swiss Federal Institute of Technology (ETH) Zurich (2001)

# Numerical Implementation of Gradient Algorithms\*

Miguel Atencia<sup>1</sup>, Yadira Hernández<sup>2</sup>, Gonzalo Joya<sup>2,3</sup>, and Francisco Sandoval<sup>3</sup>

<sup>1</sup> Departamento de Matemática Aplicada, Universidad de Málaga, Spain

<sup>2</sup> Facultad de Matemática y Computación, Universidad de La Habana, Cuba

<sup>3</sup> Departamento de Tecnología Electrónica, Universidad de Málaga, Spain

Campus de Teatinos, 29071 Málaga, Spain

matencia@ctima.uma.es

**Abstract.** A numerical method for computational implementation of gradient dynamical systems is presented. The method is based upon the development of geometric integration numerical methods, which aim at preserving the dynamical properties of the original ordinary differential equation under discretization. In particular, the proposed method belongs to the class of discrete gradients methods, which substitute the gradient of the continuous equation with a discrete gradient, leading to a map that possesses the same Lyapunov function of the dynamical system, thus preserving the qualitative properties regardless of the step size. In this work, we apply a discrete gradient method to the implementation of Hopfield neural networks. Contrary to most geometric integration methods, the proposed algorithm can be rewritten in explicit form, which considerably improves its performance and stability. Simulation results show that the preservation of the Lyapunov function leads to an improved performance, compared to the conventional discretization.

**Keywords:** Gradient Systems, Hopfield Neural Networks, Geometric Integration.

## 1 Introduction

Algorithms that include some sort of gradient computation are pervasive in machine learning literature and, in fact, in all branches of mathematics and computer science. A non-exhaustive list could include backpropagation [7], recurrent neural networks [8,9] or parameter estimation [3,4]. The performance of such algorithms is a direct consequence of their dynamical behaviour, i.e. the fact that states follow a trajectory such that the gradient of some function, usually a target function of some optimization problem, is forced to decrease. Many algorithms have a natural description in continuous time, i.e. they are formally defined as

---

\* This work has been partially supported by FEDER funds (through project no. TIN2010-16556 from the Spanish Government and project no. P08-TIC-04026 from the Junta de Andalucía), and the Agencia Española de Cooperación Internacional para el Desarrollo (project no. A2/038418/11).

Ordinary Differential Equations (ODEs), so that they should be discretized in order to be implemented as a practical algorithm on a digital computer, which is intrinsically a discrete system. In general, numerical methods used to discretize a continuous system will destroy the dynamical properties.

The recent approach of *geometric numerical integration* aims at designing numerical methods for ODEs that preserve the qualitative properties of the original ODE [13,6]. This approach has been rather fruitful in providing numerical methods for Hamiltonian systems, whereas few methods have been proposed that preserve the Lyapunov function of gradient systems. To the best of our knowledge, the main proposals in this regard comprise the *discrete gradient* methods [12] and the projection methods [5]. On one hand, projection methods are too involved and, although they are formally explicit, they require solving a nonlinear equation at every step. Projection methods have the advantage that arbitrary order can be achieved but, when preservation of the gradient structure is the main aim and accuracy is not crucial, discrete gradient methods are more appealing. However, on the other hand, no practical implementations of discrete gradient methods have been pursued. Therefore, in this contribution we construct a discrete gradient method for the implementation of Hopfield neural networks.

In Section 2 we briefly recall the definition of discrete gradient methods. Hopfield neural networks are presented as an interesting case in point in Section 3. The main contribution of this paper is the construction of a discrete gradient method for continuous Hopfield networks, which is the subject of Section 4. Some experimental results shown in Section 5 support the performance of the proposed implementation. Finally, Section 6 gathers the conclusions and suggest some directions for further research.

## 2 Numerical Methods Based on Discrete Gradients

In this section we recall, for the sake of completeness, the process of construction of a numerical method that preserves the Lyapunov function of an ODE, by means of a discrete gradient. Further details can be found in references [12].

First of all, consider an ODE  $\frac{dy}{dt} = f(y)$  with the usual assumptions about existence and uniqueness of solutions, so that a trajectory  $y(t)$  is defined for each initial value  $y_0 = y(0)$ . The trajectories  $y(t)$  are defined on the real  $n$ -dimensional vectorial space  $\mathbb{R}^n$ . The interesting case for our exposition is the existence of—at least—one equilibrium  $y_f$ , i.e. a point where  $f(y_f) = 0$  holds. We assume further that such equilibrium is asymptotically stable, which amounts to both stability in the sense of Lyapunov *and* attractiveness; in other words, all trajectories  $y(t)$  that start in a neighbourhood of  $y_f$  remain in a—possibly different—neighbourhood and tend to the equilibrium, i.e.:  $\lim_{t \rightarrow \infty} y(t) = y_f$ . It is well known from the converse Lyapunov function theorems [11] that if an equilibrium is asymptotically stable, then a Lyapunov function exists. Then we assume the explicit knowledge of a function  $V(y)$  that satisfies the conditions

for being a Lyapunov function in a neighbourhood of the equilibrium  $y_f$ . Recall that a Lyapunov function, apart from usual smoothness assumptions, fulfils the condition  $\frac{dV}{dt} \leq 0$  and  $y_f$  must be a—possibly local—minimum of  $V$ . Then, the ODE  $\frac{dy}{dt} = f(y)$  can be written in the *linear-gradient* form:

$$\frac{dy}{dt} = L(y) \nabla V(y) \quad (1)$$

where  $L(y)$  is a symmetric and negative-semidefinite matrix function and  $\nabla V(y)$  is the gradient of the function  $V$ . Arguably the fact that the ODE is explicitly written in the linear-gradient form could have been taken as the starting assumption for the studied systems, however it is worth emphasizing that the linear-gradient form given by Equation (1) is not unique [10].

An ODE that has been rewritten in the form of linear gradient, as in Equation (1), can be discretized by considering the following integration method:

$$\frac{y_{k+1} - y_k}{h} = \tilde{L}(y_k, y_{k+1}, h) \bar{\nabla} V(y_k, y_{k+1}) \quad (2)$$

where  $\tilde{L}$  is an approximation of  $L$  such that  $\tilde{L}(y_k, y_k, 0) = L(y)$  and  $\bar{\nabla} V$  is a *discrete gradient*, i.e. the following conditions are met:

$$\begin{aligned} \bar{\nabla} V(y_k, y_{k+1}) \cdot (y_{k+1} - y_k) &= V(y_{k+1}) - V(y_k) \\ \bar{\nabla} V(y, y) &= \nabla V(y) \end{aligned} \quad (3)$$

It can be proved that the numerical method given by Equation (2) has the same Lyapunov function as the original ODE, regardless the step size  $h$ , thus the approximate discretized trajectories will converge to the same equilibria, provided that initial values are close enough.

Note that there is considerable freedom in the choice of both  $\tilde{L}$  and  $\bar{\nabla} V$  and, in general, the method given by Equation (2) is implicit. In this paper we propose a suitable choice of these functions so that an explicit method for discretization of Hopfield networks is obtained.

### 3 Continuous Hopfield Networks

Hopfield networks comprise a well known neural paradigm that was originally defined as a discrete time recurrent system [8]. Then, a continuous version [9] was proved to be useful for solving, among others, optimization problems. In the Abe formulation [1], the continuous Hopfield network is defined by the following system of ODEs:

$$\frac{du}{dt} = W y - b ; \quad y = \tanh u \quad (4)$$

where  $u$  and  $y$  are  $n$ -dimensional vectors,  $W$  is a zero-diagonal matrix of weights, and  $b$  is a bias vector. Note that the computation of the vector  $y$  is componentwise, i.e.  $y_i = \tanh u_i$  for  $i = 1 \dots n$  is meant. From a biological point of view, the vector  $u$  represents the post-synaptic potentials of the neurons whereas the vector  $y$  represents the action potential, thus  $y$  can be considered an output and  $u$  comprises the internal neuron states. However, mathematically the variables  $y$  are fed back into the ODE so it is convenient to rewrite the model depending only on this vector, which results from the chain rule:

$$\frac{dy}{dt} = \frac{dy}{du} \frac{du}{dt} = (1 - \tanh^2 u) (W y - b) = (1 - y^2) (W y - b) \quad (5)$$

Then, from the dynamical point of view, Hopfield networks are stable systems because a Lyapunov function can be defined as a function of the states  $y$ :

$$V(y) = -\frac{1}{2} y' W y + b' y \quad (6)$$

where the apostrophe  $'$  denotes matrix transpose. We emphasize that the construction of a practical optimization algorithm from Hopfield networks stems from the dynamical properties [2]: since a Lyapunov function is decreasing over time, thus the evolution of the states of the network heads towards a stable equilibrium, where the Lyapunov function presents a—possibly local—minimum. Therefore, an optimization problem where the target function has the same structure of the Lyapunov function given by Equation (6) is solved by matching the target and the Lyapunov function, so that the weights and biases are obtained. Finally, the network is “constructed”, which usually means that some numerical method is used to integrate Equation (4) until the states reach an equilibrium, which provides the minimum. Therefore, using a numerical method that preserves the dynamical properties of the continuous ODE under discretization is a crucial step, since a solution is only obtained by an algorithm that mimics the *correct* dynamical behaviour.

## 4 Discretization of Hopfield Networks

In this section, for the sake of comparison, we describe the conventional discretization that is usually adopted to implement Hopfield networks. Then, we apply the results of Section 2 to define a discrete gradient method that numerically integrates a Hopfield network while preserving the Lyapunov function, regardless of the step size  $h$ .

The usual discretization of Hopfield networks results from replacing the derivative  $\frac{du}{dt}$  by the linear approximation  $\frac{u_{k+1} - u_k}{h}$  in Equation (4) for a chosen  $h$  that should be small enough. Therefore, a two-step iteration that involves both the internal potential  $u$  and the state  $y$  is obtained:

$$u_{k+1} = u_k + h (W y_k - b) ; \quad y_{k+1} = \tanh u_{k+1} \quad (7)$$



The linear approximation is well founded—indeed it is the basis for the well known Euler rule—but it does not guarantee that the resulting numerical method will preserve the dynamical properties of the ODE and, in particular, that it will possess the same Lyapunov function as the continuous dynamical system.

We now present the main contribution of the paper: designing a discrete gradient method for the Hopfield network. First of all, recall that the Hopfield network given by Equation (4) can be cast into the linear gradient form, by eliminating the internal variable  $u$ , as shown in Equation (5). Then, the functions  $\tilde{L}$  and  $\bar{\nabla}$  are chosen with a suitable definition:

$$\begin{aligned} \left(\tilde{L}(y, z, h)\right)_{ii} &= 1 - y_i z_i \\ \left(\bar{\nabla}V(y, z)\right)_i &= \frac{V(z_1 \dots z_i, y_{i+1} \dots y_n) - V(z_1 \dots z_{i-1}, y_i \dots y_n)}{z_i - y_i} \end{aligned} \quad (8)$$

and  $\tilde{L}$  is a diagonal matrix, i.e.  $\left(\tilde{L}(y, z, h)\right)_{ij} = 0$  if  $i \neq j$ . It is straightforward to prove that this choice is consistent with the definition of discrete gradient presented in Section 2. A crucial point of this definition is the fact that the implicit numerical method given by Equation (2) can be rewritten as an explicit method in the particular case of Hopfield networks. After straightforward algebra, the proposed iteration results:

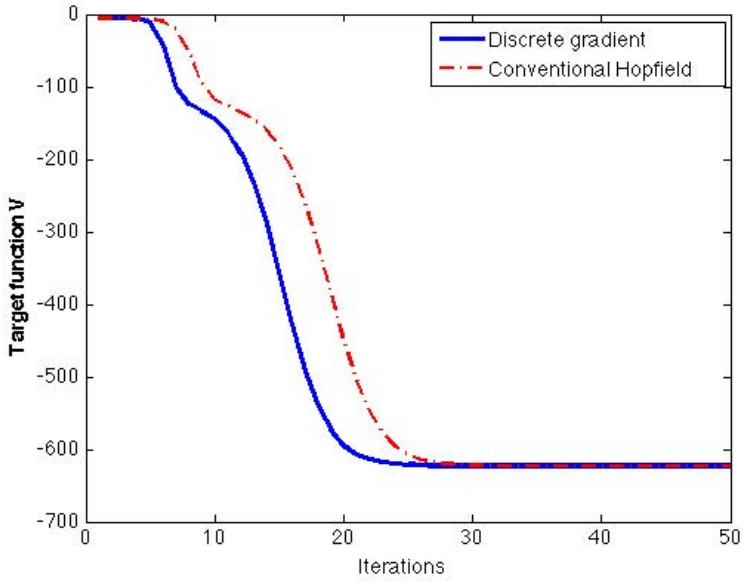
$$(y_{k+1})_i = \frac{(y_k)_i + h (W v^{(i)} - b)_i}{1 + h (y_k)_i (W v^{(i)} - b)_i} \quad (9)$$

where  $v^{(i)}$  is a vector with mixed components:  $(v^{(i)})_j = (y_{k+1})_j$  if  $j < i$  and  $(v^{(i)})_j = (y_k)_j$  if  $j \geq i$ . Note that Equation 9 is an explicit map because the matrix  $W$  has zeros on the diagonal.

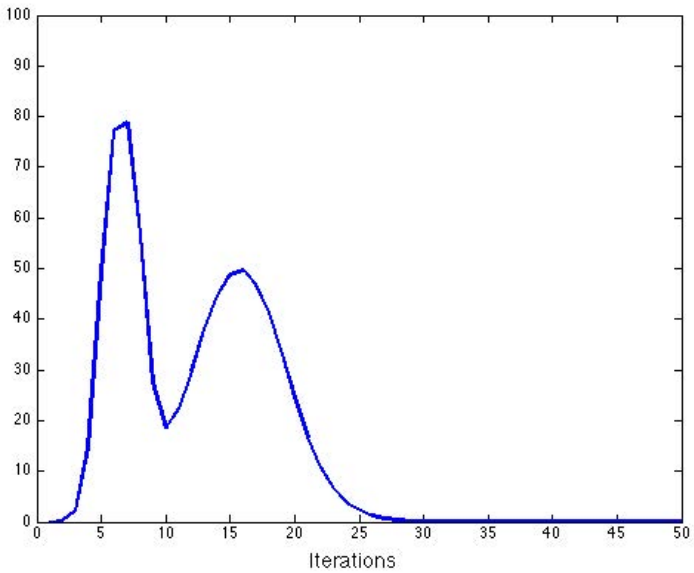
## 5 Experimental Results

In this section we present a summary of our simulation results, which show the superior performance of the discrete gradient numerical method, designed to preserve the Lyapunov function of an ODE. The continuous Hopfield network, as described in Section 3, is used as a case in point since, as mentioned above, its optimization ability is a result of its dynamical properties. In particular, the definition of a Lyapunov function, which is matched to the target function of the optimization problem, proves that the trajectories of the states of Hopfield networks converge to stable equilibria. We measure the performance of a discretization algorithm considering two features of the convergence to the minimum: convergence speed and avoidance of local minima.

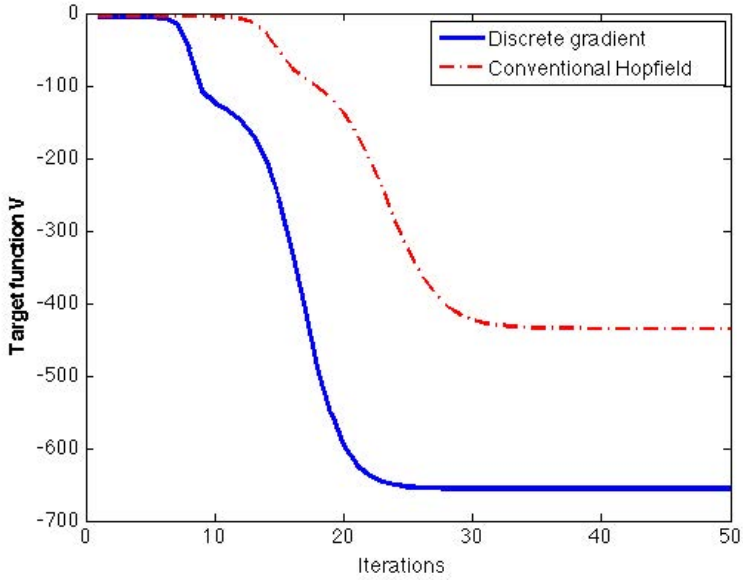
A Hopfield network has been implemented both with the numerical method based upon discrete gradients and the conventional discretization, as presented in Section 4. The same value of the step size  $h$  was assigned for both methods.



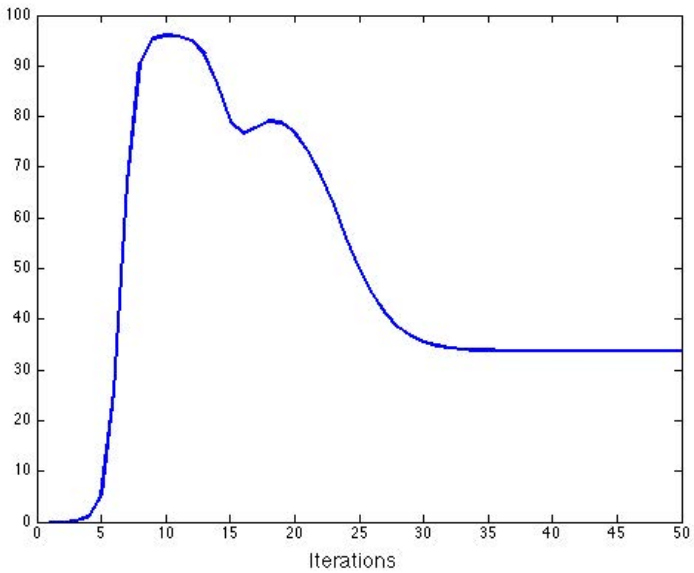
**Fig. 1.** Decrease in target function along trajectories for the conventional Hopfield implementation and the numerical method based upon discrete gradient



**Fig. 2.** Relative outperformance (percentage) of the method of discrete gradient regarding target function decreasing



**Fig. 3.** Decrease in target function along trajectories, considering another initial point: each method converges to a different stable point



**Fig. 4.** Relative outperformance (percentage) of the method of discrete gradient regarding target function decreasing for the same initial point as in Figure 3

A battery of experiments has been performed, by assigning different values to all design parameters of the neural network: dimension—number of neurons—of the network, weight matrix and initial point of the trajectory. The results show a consistent outperformance of the discrete gradient method, both from the point of view of convergence speed and avoidance of local minima. There is certainly a random component, due to the choice of initial point, but in most of the experiments the discrete gradient method converges considerably faster. In a significant number of instances, the discrete gradient method attains a stable equilibrium that corresponds to a lower value of the target function, whereas the conventional Hopfield implementation is stuck at a local minimum. The discrete gradient method, as all algorithms based upon local approximations, is not immune to local minima, but the occasions in which the solution provided by the conventional network is better are exceptional and statistically not significant. Only a portion of these experiments, which is considered to illustrate the conclusions, is here shown for brevity.

In Figure 1, the implementation of an instance of a Hopfield network of dimension  $n = 30$  is depicted, showing the discretization with the discrete gradient method and the conventional Hopfield network. Since the trajectories of the 30 components of the state are not particularly informative, only the values of the target function at each state are presented. The graphs show that both algorithms converge to the same equilibrium, thus the attained value of the target function is the same. However, the discrete gradient method converges significantly faster since, for instance, reaching the value  $V = -600$  requires a 20 percent less in the number of computed iterations, approximately. In Figure 2, the values of the target functions along the simulated trajectories with both methods are shown as the percentage that the discrete gradient method is lower than the value achieved by the conventional method. At some stages of the network evolution, the discrete gradient algorithm provides a value of the target function that is almost 80 percent lower than that of the conventional Hopfield method, using the absolute value of the minimum of both values as a base. Note that faster convergence of a method is a significant finding, since it could mean that a quasi-optimal solution is obtained with reasonable computational cost, where is the computing time of a slower algorithm may be unaffordable.

Similar results are shown in Figures 3 and 4, but now the difference between both methods is qualitative, since a different stable equilibrium is attained, i.e. the solutions obtained by the two methods are different. In Figure 3, again faster decrease of the target function achieved by discrete gradient method is observable and, besides, a significantly lower value is finally attained. This fact confirms that the conventional method has stuck at a local minimum. In Figure 4, the relative improvement in the obtained value of the target function is obtained. Not only the discrete gradient outperforms the conventional method during the network evolution, but also the solution finally obtained is a 40 percent better, approximately.

An exhaustive set of experiments supports that the discrete gradient method outperforms the conventional Hopfield implementation as a rule.

## 6 Conclusions and Future Directions

We have presented the construction of a numerical method for implementation of continuous Hopfield networks. The method is based upon discrete gradients, thus it guarantees the preservation of the Lyapunov function, which is the key to the optimization ability of Hopfield networks. The suitable choice of the functions that define the method leads to an explicit method, which is a considerable advantage concerning both stability and computational cost. Simulation results show that the proposed method provides superior performance compared to the conventional implementation of Hopfield networks.

We suggest that this novel method paves the way for far-reaching advances in the construction of algorithms, beyond the particular case presented. More attention should be paid to the preservation of dynamical properties under discretization and the application of techniques from the geometric integration approach should be widespread. Therefore we are currently engaged in two main directions for expanding the presented results. On the one hand, we are generalizing the discrete gradient method to a wide range of systems, more complex than Hopfield networks. On the other hand, we aim at a deeper theoretical foundation for discrete gradients, in particular developing more accurate, higher-order methods, while preserving the qualitative properties of the dynamical system.

## References

1. Abe, S.: Theories on the Hopfield Neural Networks. In: IEE International Joint Conference on Neural Networks, vol. I, pp. 557–564 (1989)
2. Atencia, M.A., Joya, G., Sandoval, F.: Dynamical Analysis of Continuous Higher Order Hopfield Networks for Combinatorial Optimization. *Neural Computation* 17(8), 1802–1819 (2005)
3. Atencia, M.A., Joya, G., Sandoval, F.: Hopfield Neural Networks for Parametric Identification of Dynamical Systems. *Neural Processing Letters* 21(2), 143–152 (2005)
4. van den Bos, A.: *Parameter estimation for scientists and engineers*. Wiley-Interscience (2007)
5. Calvo, M., Laburta, M.P., Montijano, J.I., Rández, L.: Projection methods preserving lyapunov functions. *BIT Numerical Mathematics* 50(2), 223–241 (2010)
6. Hairer, E.: *Geometric Numerical Integration: Structure-Preserving Algorithms for Ordinary Differential Equations*. Springer, Berlin (2006)
7. Haykin, S.: *Neural Networks*. A Comprehensive Foundation. Macmillan College Publishing Company (1994)
8. Hopfield, J.: Neural networks and physical systems with emergent collective computational abilities. *Proc. Natl. Acad. Sci. USA* 79, 2554–2558 (1982)
9. Hopfield, J.: Neurons with graded response have collective computational properties like those of two-state neurons. *Proc. Natl. Acad. Sci. USA* 81, 3088–3092 (1984)

10. Iserles, A., Peplow, A., Stuart, A.: A unified approach to spurious solutions introduced by time discretisation. Part I: Basic theory. *SIAM J. Numer. Anal.* 28(6), 1723–1751 (1991)
11. Khalil, H.K.: *Nonlinear Systems*. Prentice Hall (2002)
12. McLachlan, R., Quispel, R., Robidoux, N.: Geometric integration using discrete gradients. *Philos. Trans. of the Royal Society of London Series A* 357(1754), 1021–1045 (1999)
13. Stuart, A., Humphries, A.: *Dynamical systems and numerical analysis*. Cambridge University Press (1996)

# A CNN Based Approach for Solving a Hyperbolic PDE Arising from a System of Conservation Laws - the Case of the Overhead Crane

Daniela Danciu

Department of Automatic Control, University of Craiova  
13, A.I. Cuza str., 200585 - Craiova, Romania  
daniela.danciu@automation.ucv.ro

**Abstract.** The paper proposes a neurocomputing approach for numerical solving of a hyperbolic partial differential equation (PDE) arising from a system of conservation laws. The main idea is to combine the method of lines (transforming the mixed initial boundary value problem for PDE into a high dimensional system of ordinary differential equations (ODEs)) with a cellular neural network (CNN) optimal structure which exploits the inherent parallelism of the new problem in order to reduce the computational effort and storage. The method ensure from the beginning the convergence of the approximation and preserve the stability of the initial problem.

**Keywords:** CNN, method of lines, hyperbolic PDE, ODE, conservation laws, neurocomputing, neuromathematics, Courant-Isaacson-Rees rule.

## 1 Introduction

Citing [1], neuromathematics – as a branch of computational mathematics – aims to develop new methods and algorithms for solving both non-formalized (or weakly formalized) and formalized problems by using neural networks’ paradigm. In the case of formalized problems (but not only) there is no need for a learning process based on experimental data in order to obtain the weights of the interconnections. In this case, the neural networks’ structure is based mainly on the “natural parallelism” of the problem itself.

In our opinion, the neuromathematics field is still at its beginning, i.e. there are many aspects which require formalization. A short list of the mathematical problems or tasks arising from natural sciences and engineering applications, which are suitable for solving within the neuromathematics context, comprises [1]:

- high dimensional systems of linear or nonlinear algebraic equations and inequalities – see the list of the problems in [2] or the work [3] to give only a few examples;
- optimization and systems identification problems – there are many approaches and a large area of applications; see e.g. [4–6];
- function approximation and extrapolation;
- (systems of) ordinary differential equations – see e.g. [7, 8];
- partial differential equations – see e.g. [9–12].

Since our present work is related to the problem of numerical solving of ODEs and PDEs by using neural networks, we restrict our attention only on this formalized-type problem. From this point of view, there are proposed several different approaches and methods. [9] discussed the computing problem of the transient response of some mechanical vibrating systems. The authors used the finite element method for reducing the PDEs to a system of ODEs which are then mapped onto a CNN structure. The procedure proposed in [10], and its extension [11], solves ODEs and elliptic PDEs problems by using the collocation method for spatial discretization and two different static neural networks: a multilayer perceptron for solving a minimization problem and a radial basis function network for the construction of some trial solution that satisfies the boundary conditions (BCs). Almost the same idea regarding the inclusion of the BCs in the form of the trial solution is used in [12] for solving the Stokes problem. Other approaches for solving ODEs problems are that of [8] and the references therein.

The present paper is concerned with a neurocomputing approach for numerical solving of an engineering application – a system of conservation laws, the case of the overhead crane. In our case, the problem under consideration is different from those evaluated within the above mentioned approaches: 1) the mathematical model is described by a hyperbolic partial differential equation in one space variable, with space-varying parameters and derivative boundary conditions, 2) the analytical solution is unknown.

The approach we proposed combines the method of lines, used for converting the specific hyperbolic PDE problem to a high-dimensional system of ODEs, with a CNN structure which exploits the local interconnections among the variables of ODEs' system. CNNs are special cases of M-lattice systems. Both CNNs [13] and M-lattice systems [14] had as initial applications those of image processing and pattern recognition. M-lattice systems are inspired by the reaction-diffusion paradigm used by Turing in order to describe the chemical mechanism for morphogenesis (biological pattern formation). As dynamical neural networks having a special structure based on local interconnections, CNNs become desirable for solving ODEs' and PDEs' problems.

The rest of the paper is organized as follows. Section 2 introduces the problem statement and the mathematical model of the system – a non-standard model for the overhead (gantry) crane where two basic simplifying assumptions are overruled: negligible distributed mass of the rope and negligible acceleration of the load mass with respect to the gravity acceleration [15]. Then, there are presented the main steps of the procedure for deducing the approximate system of ODEs via the method of lines. In Section 3 we propose a solution for mapping the systems of ODEs onto a CNN structure and compute the approximate numerical solution. The paper ends with some conclusions.

## 2 The Mathematical Model and the Method of Lines

### 2.1 The Problem Statement

One considers the control model of the overhead crane incorporating the elasticity effects due to the mass distribution along the length of the crane's rod. The control  $u$  in the BCs was calculated in [15] via the control Lyapunov functions and replaced such that the closed loop dynamics is described by the following hyperbolic PDE, written in the standard notations of the PDE field ( $y_{tt} = \frac{\partial^2 y}{\partial t^2}$ ,  $y_\sigma = \frac{\partial y}{\partial \sigma}$ ,  $(a(\sigma))_\sigma = \frac{\partial}{\partial \sigma} a(\sigma)$ )



$$\frac{\rho L}{m} \cdot \frac{L}{g} y_{tt} - \left( \left( 1 + \frac{\rho L}{m} \sigma \right) y_{\sigma} \right)_{\sigma} = 0, \quad t > 0, \quad 0 \leq \sigma \leq 1, \quad (1)$$

with the limit conditions

$$\begin{aligned} \frac{L}{g} \cdot y_{tt}(0,t) = y_{\sigma}(0,t), \quad y(1,t) = X_p \\ \frac{L}{g} \cdot \ddot{X}_p = -(X_p - \bar{X}_p) - f(\dot{X}_p) - \left( 1 + \frac{\rho L}{m} \right) y_{\sigma}(1,t). \end{aligned} \quad (2)$$

The nonlinearity  $f(\cdot)$  verifies the sector condition

$$0 \leq \frac{f(\lambda)}{\lambda} \leq \bar{f}, \quad f(0) = 0, \quad (3)$$

and the notations of variables and parameters are as follows [15]

- $\sigma$  - the rated (to the cable length  $L$ ) arc length along the flexible non-stretching cable,  $\sigma = s/L$  with  $s$  defined in Fig. 1;
- $y$  - the horizontal displacement at time  $t$  of the cable point whose curvilinear abscissa is  $\sigma$ ;
- $y_{\sigma}$  - the angular inclination of the cable at  $\sigma$  with respect to the vertical;
- $X_p$  - the platform abscissa;
- $\bar{X}_p$  - the platform constant reference;
- $\rho$  - the mass per unit length of the cable;
- $m$  - the load mass.

The equations (1) – (2) represent a mixed initial boundary value problem for a hyperbolic PDE. The purpose of this work is to obtain a numerical solution for this problem such that to be ensured the convergence of the approximation and the stability preservation of the initial problem.

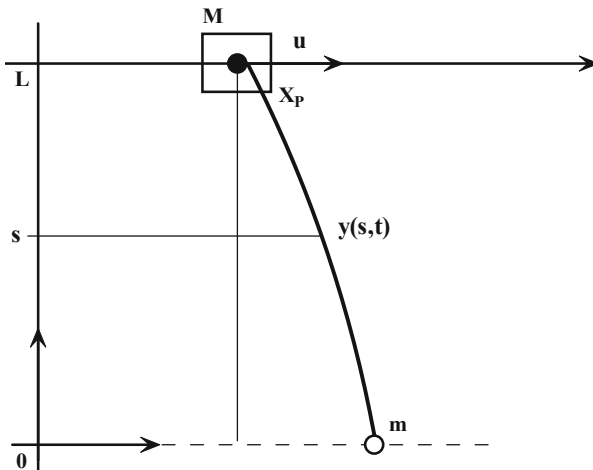


Fig. 1. The overhead crane with flexible cable [15]

The complexity of the problem under consideration is well described in [17]: “The numerical solution of conservation laws is a highly complicated and problem-dependent process.” “In the method of lines, the space and time discretizations of a partial differential equation are decoupled and analyzed independently. First a method is selected to discretize the differential equation in space and incorporate the boundary conditions. The spectrum of this discrete operator is then used as a guide to choose an appropriate method to integrate the equations through time.”

The procedure we propose in order to cope with our problem has two main parts:

1. converting the PDE problem to a high-dimensional system of ODEs via the method of lines,
2. numerical solving of the system of ODEs by using the neural network logical basis.

**2.2 Obtaining the Approximate System of ODEs via the Method of Lines**

In the sequel we shall present the first part of the procedure. We shall use the approach of [18] – Part II in order to deduce the approximate system of ODEs.

S1. Consider the system (1) – (2). One introduces the new distributed variables

$$v(\sigma, t) = y_t(\sigma, t), \quad w(\sigma, t) = y_\sigma(\sigma, t), \tag{4}$$

and write the system in the Friedrichs form

$$\begin{aligned} \frac{\rho L}{m} \cdot \frac{L}{g} v_t - \left( \left( 1 + \frac{\rho L}{m} \sigma \right) w \right)_\sigma &= 0 \\ w_t - v_\sigma &= 0, \quad t > 0, \quad 0 \leq \sigma \leq 1 \\ \frac{L}{g} v_t(0, t) &= w(0, t), \quad \dot{X}_p = v(1, t), \\ \frac{L}{g} \cdot \ddot{X}_p &= -(X_p - \bar{X}_p) - f(\dot{X}_p) - \left( 1 + \frac{\rho L}{m} \right) w(1, t). \end{aligned} \tag{5}$$

Let us remark that the control, obtained via the control Lyapunov functions, is such that the closed loop dynamics of the system has a global asymptotic stable equilibrium at  $v(\sigma) = \bar{v} = 0, w(\sigma) = \bar{w} = 0, \bar{X}_p$  [15].

S2. Denoting

$$\lambda^2(\sigma) = \frac{g}{L} \cdot \frac{m}{\rho L} \left( 1 + \frac{\rho L}{m} \sigma \right) > 0, \quad 0 \leq \sigma \leq 1, \tag{6}$$

one introduces the Riemann invariants  $u_1(\sigma, t)$  and  $u_2(\sigma, t)$  by

$$\begin{aligned} v(\sigma, t) &= \frac{1}{\sqrt{\lambda(\sigma)}} (-u_1(\sigma, t) + u_2(\sigma, t)) \\ w(\sigma, t) &= \frac{1}{\lambda(\sigma)\sqrt{\lambda(\sigma)}} (u_1(\sigma, t) + u_2(\sigma, t)), \end{aligned} \tag{7}$$

S3. One writes the transformed system

$$\begin{aligned} \frac{\partial u_1}{\partial t} + \lambda(\sigma) \cdot \frac{\partial u_1}{\partial \sigma} + \frac{1}{4\lambda(\sigma)} \cdot \frac{g}{L} u_2(\sigma, t) &= 0 \\ \frac{\partial u_2}{\partial t} - \lambda(\sigma) \cdot \frac{\partial u_2}{\partial \sigma} - \frac{1}{4\lambda(\sigma)} \cdot \frac{g}{L} u_1(\sigma, t) &= 0, \end{aligned} \tag{8}$$

with the boundary conditions

$$\begin{aligned} \frac{L}{g} \left( -\frac{d}{dt} u_1(0, t) + \frac{d}{dt} u_2(0, t) \right) &= \frac{1}{\lambda(0)} (u_1(0, t) + u_2(0, t)) \\ \dot{X}_P &= \frac{1}{\lambda(1)} (-u_1(1, t) + u_2(1, t)) \\ \frac{L}{g} \cdot \ddot{X}_P &= -(X_P - \bar{X}_P) - f(\dot{X}_P) - \left( 1 + \frac{\rho L}{m} \right) \frac{1}{\lambda(1)\sqrt{\lambda(1)}} (u_1(1, t) + u_2(1, t)) \end{aligned} \tag{9}$$

and identifies the forward wave  $u_1(\sigma, t)$  and the backward wave  $u_2(\sigma, t)$ .

S4. The discretization of the system, with respect to the spatial variable –  $\sigma$ , is made by taken into consideration the forward and the backward waves. By applying the Euler approximation using the Courant-Isaacson-Rees rule for (8) – (9) we shall obtain a good coupling with the boundary conditions and also, the convergence of the approximation – according to [18]. In the sequel, we consider the discretization step  $h = 1/N$  of the interval  $[0, 1]$  and the following notations:  $\xi_i(t) \approx u_1(ih)$  for  $i = \overline{0, N}$  and  $\eta_j(t) \approx u_2(jh)$  for  $j = \overline{0, N-1}$ . After some tedious but straightforward manipulations, we obtain the following systems of ordinary differential equations:

– for the forward wave  $u_1(\sigma, t)$

$$\begin{aligned} \dot{\xi}_0(t) &= \frac{-3}{4} \cdot \frac{1}{\lambda(0)} \cdot \frac{g}{L} \cdot \xi_0 - \left( N\lambda(0) + \frac{g}{L} \cdot \frac{1}{\lambda(0)} \right) \eta_0 + N\lambda(0)\eta_1 \\ \dot{\xi}_i(t) &= N\lambda(ih)\xi_{i-1} - N\lambda(ih)\xi_i - \frac{g}{L} \cdot \frac{1}{4\lambda(ih)} \eta_i, \quad i = \overline{1, N-1} \\ \dot{\xi}_N(t) &= N\lambda(1)\xi_{N-1} - \left( N\lambda(1) + \frac{g}{L} \cdot \frac{1}{4\lambda(1)} \right) \xi_N - \frac{g}{L} \cdot \frac{1}{4\lambda(1)} V_P \end{aligned} \tag{10}$$

– for the backward wave  $u_2(\sigma, t)$

$$\begin{aligned} \dot{\eta}_j(t) &= -N\lambda(jh)\eta_j + N\lambda(jh)\eta_{j+1} + \frac{g}{L} \cdot \frac{1}{4\lambda(jh)} \xi_j, \quad j = \overline{0, N-2} \\ \dot{\eta}_{N-1}(t) &= -N\lambda((N-1)h)\eta_{N-1} + \frac{1}{4\lambda((N-1)h)} \xi_{N-1} \\ &\quad + N\lambda((N-1)h)\xi_N + N\sqrt{\lambda(1)}\lambda((N-1)h)V_P \end{aligned} \tag{11}$$

– the remaining equations

$$\begin{aligned} \dot{X}_P(t) &= V_P \\ \dot{V}_P(t) &= -2\frac{g}{L} \left(1 + \frac{\rho L}{m}\right) \frac{1}{\lambda(1)\sqrt{\lambda(1)}} \xi_N - \frac{g}{L} X_P \\ &\quad - \frac{g}{L} \left(1 + \frac{\rho L}{m}\right) \frac{1}{\lambda(1)} V_P + \frac{g}{L} \bar{X}_P - \frac{g}{L} f(V_P). \end{aligned} \tag{12}$$

The second part of our procedure is concerned with the numerical solving of the ODEs' systems (10) – (12) by using the neural network logical basis.

### 3 Numerical Approximation by Using CNNs

As already mentioned in Introduction, CNNs or “cell-like neural networks” [1] have some peculiarities of the structure which make them adequate for solving problems having some inherent parallelism and regularities as in the case of the tasks emerging at the solution of PDEs. Based on only local interconnections, one of the key idea of CNNs is that of representing the interactions among the cells by cloning templates – being them translation-invariant or regularly varying templates. To cite [13], “the cloning template is the elementary program of the CNN (an instruction or subroutine) and it can be specified by giving prescribed values, and/or characteristics to the template elements”. Here the authors referred to the case of programmability in VLSI implementation, but the structure of a CNN can be software implemented as well. The dynamics of a cell can be described by

$$\begin{aligned} \dot{x}_{ij}(t) &= -x_{ij} + \sum_{kl \in N_r(ij)} A_{ij,kl} y_{kl} + \sum_{kl \in N_r(ij)} B_{ij,kl} u_{kl} + I_{ij} \\ y_{ij} &= f(x_{ij}) \end{aligned} \tag{13}$$

where the notations are as follows:  $x_{ij}$  – the state variable of the cell  $ij$ ,  $y$  – the output variable,  $u$  – the input (control) variable,  $N_r(ij)$  – the  $r$ -neighbourhood of the cell  $ij$ ,  $A_{ij,kl}$  – the feedback cloning template,  $B_{ij,kl}$  – the control cloning template,  $I_{ij}$  – the bias or an external input. The nonlinearity  $f(\cdot)$  is the unit bipolar ramp function, but in some cases one can consider only the linear part, i.e.  $f(x_{ij}) = x_{ij}$ .

In order to map the systems of ODEs (10) – (11) onto a regularly varying CNN structure, we have first to rearrange them for revealing the so-called “cloning template”. The solution is to assemble the systems' equations by interpolating them in the following manner

$$x^T = [\eta_0 \ \xi_0 \ \eta_1 \ \xi_1 \ \dots \ \eta_{N-1} \ \xi_{N-1} \ \xi_N] \tag{14}$$

and obtaining a  $(2N + 1)$  – dimensional system of ODEs. If we consider, as it is previously suggested,  $f(x_{ij}) = x_{ij}$ , we obtain two inner feedback cloning templates having  $r = 1$  and the general form

$$\begin{aligned} A_1 &= [-g(i) \ h(i) \ g(i)], \ i = \overline{0, N-2} \\ A_2 &= [g(i) \ -h(i) \ -g(i)], \ i = \overline{1, N-1} \end{aligned} \tag{15}$$

where  $g(\cdot)$  and  $h(\cdot)$  depend on the spatial one-dimensional grid points  $i$  and read as

$$g(i) = N\lambda(ih), h(i) = \frac{g}{4L\lambda(ih)} \tag{16}$$

The inner grid points of the  $(2N + 1)$  – dimensional system of ODEs have zero control templates. For them, the dynamics is described by the following equations

$$\begin{aligned} \dot{x}_{2k+1} &= \begin{pmatrix} -g(i) & h(i) & g(i) \end{pmatrix} \begin{pmatrix} x_{2k+1} \\ x_{2k+2} \\ x_{2k+3} \end{pmatrix}, i = \overline{0, N-2}, k = \overline{0, N-2} \\ \dot{x}_{2k} &= \begin{pmatrix} g(i) & -h(i) & -g(i) \end{pmatrix} \begin{pmatrix} x_{2k-2} \\ x_{2k-1} \\ x_{2k} \end{pmatrix}, i = \overline{1, N-1}, k = \overline{2, N} \end{aligned} \tag{17}$$

The cells  $x_{2N-1}$  and  $x_{2N+1}$  of the CNN have as external input controls the speed of the platform  $V_p$ , which represents the output of the second dynamical neural network modelling the equations (12). All the cells  $x_i, i = \overline{1, 2N+1}$  of the CNN have as biases their initial conditions  $x_{i0}$ , which means that within the equations (17) one considers additionally this term.

Let us emphasize the advantages of this rearrangement on the CNNs’ structure and the computational effort:

- It is obtained a CNN having a 5-diagonal matrix of interconnections.
- The two inner templates  $A_1$  and  $A_2$  are such that  $A_1 = -A_2$ , reducing once more the computational effort.
- The elements on the main diagonal of the interconnection matrix are those having as values the terms  $-g(i)$  in both templates.
- There are only four elements within the boundary templates which do not obey the rule of the inner templates and thus have to be separately calculated.
- The other elements of the boundary templates are zero and can be eliminated together with the non-diagonals zeros of the matrix by generating a so-called “sparse matrix”. The sparse matrices specify the positions of the zero elements within a matrix allowing storage optimization and significantly reducing the number of function evaluations [19] – integration, in our case.

Regarding the system (12) it will be mapped onto a normal dynamical neural network (NN2) which will interact with the first one, the CNN. The input signals (or biases) for the entire structure are the initial conditions and the position reference of the platform,  $\overline{X}_p$ .

For the numerical evaluation we borrow from the literature [16] the following data for the parameters of the overhead crane:  $L = 8m, \rho = 3Kg/m, M = 1000Kg, m = 1500kg$ . For the platform we have taken the following values: the reference position  $\overline{X}_p = 3m$ , initial speed  $\overline{V}_{p0} = 0.2m/s$ , initial position  $X_{p0} = 0.3m$ . The initial conditions for  $x_i$  ( $\xi_i$  and  $\eta_i$ ),  $i = \overline{1, 2N+1}$  are random numbers within the interval  $[0, 1]$  with BCs satisfied. The simulations are made by using the Matlab software package.

The numerical solutions for the forward and backward waves are presented in Fig. 2 – Fig. 4. In Fig. 2 it is plotted the time evolution of the two waves while,

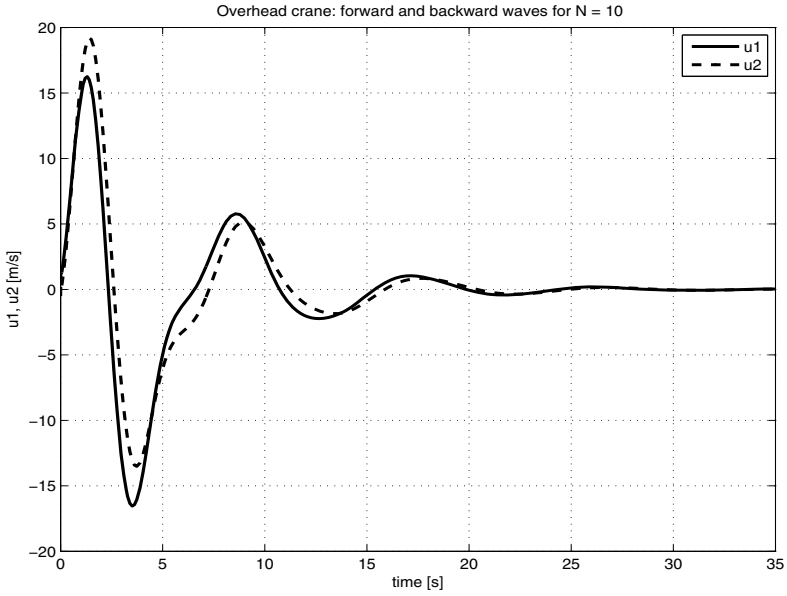


Fig. 2. Time evolution of the forward and backward waves

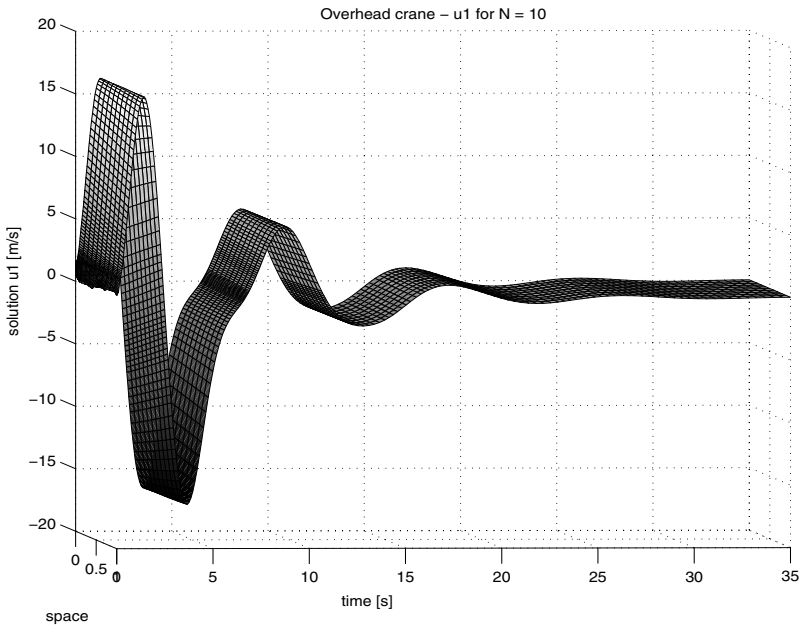
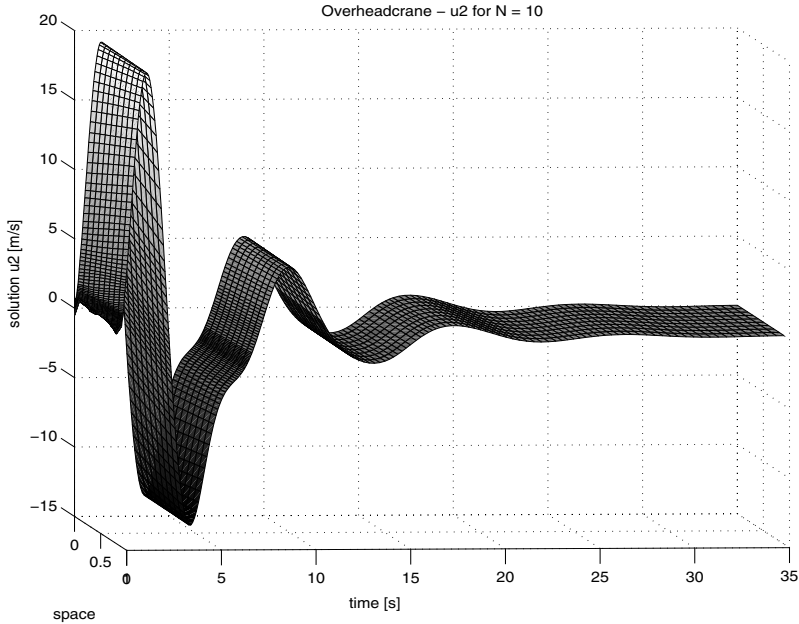


Fig. 3. 3-D plot for the forward wave,  $u_1$ . The space axis corresponds to the normalized length of the cable,  $\sigma \in [0, 1]$



**Fig. 4.** 3-D plot for the backward wave,  $u_2$

Fig. 3 – Fig. 4 are 3-D representation of the solutions. The spatial axis represents the interval  $[0, 1]$ , on which  $\sigma$  varies. It can be seen that the solutions asymptotically converge to the stationary states and this is in accordance with the fact that the partial differential equation (1) corresponds to the already stabilized system, as mentioned in Section 2. In our case,  $N = 10$  is sufficiently large for the convergence of the algorithm.

## 4 Conclusions

The paper proposes a neurocomputing approach for numerical solving of a hyperbolic PDE arising from a system of conservation laws. We took into consideration the model of the overhead crane dynamics which became some kind of benchmark problem for control theory and practice. From this point of view, the numerical solution we have obtained is in accordance with the results of the qualitative analysis made in [15], and this fact recommends the method.

Our approach combines analytical manipulations with numerical computation. It is based mainly on the method of lines for transforming the mixed initial boundary value problem for a hyperbolic PDE into a problem of high dimensional system of ODEs which, due to the inherent parallelism and local regularity, could be mapped onto a CNN structure – after some rearrangements which provide the optimal structure in order to reduce the computational effort and storage.

As already said, our method ensure from the beginning the convergence of the approximation (according to [18]) and, preserve the stability of the initial problem.

## References

1. Galushkin, A.I.: *Neural Network Theory*. Springer, Heidelberg (2010)
2. Guo, D., Zhang, Y.: Novel Recurrent Network for Time-Varying Problems Solving. *IEEE Comp. Intellig. Magazine* 7(4) (2012)
3. Kramer, M.A.: Nonlinear Principal Component Analysis Using Autoassociative Neural Networks. *AIChE Journal* 37(2), 233–243 (1991)
4. Hopfield, J., Tank, D.: 'Neural' Computation of Decisions in Optimization Problems. *Biol. Cyb.* 52, 141–152 (1985)
5. Joya, G., Atencia, M.A., Sandoval, F.: Hopfield Neural Networks for Optimization: Study of the Different Dynamics. *Neurocomputing* 43(1-4), 219–237 (2002)
6. Atencia, M., Joya, G., Sandoval, F.: Robustness of the "Hopfield Estimator" for Identification of Dynamical Systems. In: Cabestany, J., Rojas, I., Joya, G. (eds.) *IWANN 2011, Part II*. LNCS, vol. 6692, pp. 516–523. Springer, Heidelberg (2011)
7. Ramuhalli, R., Udpa, L., Udpa, S.S.: Finite-Element Neural Networks for Solving Differential Equations. *IEEE Trans. Neural Networks* 16(6), 1381–1392 (2005)
8. Filici, C.: On a Neural Approximator to ODEs. *IEEE Trans. Neural Networks* 19(3), 539–543 (2008)
9. Szolgay, P., Voros, G., Eross, G.: On the Applications of the Cellular Neural Network Paradigm in Mechanical Vibrating Systems. *IEEE Trans. Circuits Syst. I* 40(3), 222–227 (1993)
10. Lagaris, I.E., Likas, A.C., Papageorgiou, D.G.: Artificial Neural Networks for Solving Ordinary and Partial Differential Equations. *IEEE Trans. Neural Networks* 9(5), 987–1000 (1998)
11. Lagaris, I.E., Likas, A.C., Papageorgiou, D.G.: Neural-Network Methods for Boundary Value Problems with Irregular Boundaries. *IEEE Trans. Neural Networks* 11(5), 1041–1049 (2000)
12. Baymani, M., Kerayechian, A., Effati, S.: Artificial Neural Networks Approach for Solving Stokes Problem. *Applied Mathematics* 1, 288–292 (2010)
13. Chua, L.O., Roska, T.: The CNN Paradigm. *IEEE Trans. Circuits Syst. I* 40(3), 147–156 (1993)
14. Sherstinsky, A., Picard, R.W.: M-lattice: A novel nonlinear dynamical system and its application to halftoning. In: *Proc. IEEE Int. Conf. on Acoustics, Speech and Signal Processing*, vol. 2, pp. 565–568 (1994)
15. Bobasu, E., Danciu, D., Popescu, D., Răsvan, V.: On dynamics and control for a system of conservation laws - the case of the overhead crane. In: *Proc. 13th IEEE International Carpathian Control Conference*, pp. 52–57 (2012)
16. Piazzì, A., Visioli, A.: Optimal dynamic-inversion-based control of an overhead crane. *Proc. IEE-Control Theory and Applications* 149(5), 405–411 (2002)
17. Hyman, J.M.: A method of lines approach to the numerical solution of conservation laws. In: Vichnevetsky, R., Stepleman, R.S. (eds.) *Adv. Comp. Meth. Part. Diff. Eq. III*, IMACS Publ. House (1979)
18. Halanay, A., Răsvan, V.: Approximations of delays by ordinary differential equations. In: *Recent Advances in Differential Equations*. Academic Press (1981)
19. Matlab, The MathWorks Inc. (2007)



# Reflections on Neural Networks as Repetitive Structures with Several Equilibria and Stable Behavior

Vladimir Răsvan

Department of Automatic Control, University of Craiova  
13, A.I. Cuza str., 200585 - Craiova, Romania  
vladimir.rasvan@automation.ucv.ro

**Abstract.** The structures of the Artificial Intelligence (AI) are sometimes “created” in order to solve specific problems of science and engineering. They may be viewed as dedicated signal processors, with dedicated, in particular repetitive, structure. In this paper such structures of Neural Networks (NN)-like devices are considered, having as starting point the problems in Mathematical Physics. Both the ways followed by such inferences and their outcomes may be quite diverse - one of the paper’s aims is to illustrate this assertion. Next, ensuring global stability and convergence properties in the presence of several equilibria is a common feature of the field. The general discussion on the “emergence” of AI devices with NN structure is followed by the presentation of the elements of the global behavior for systems with several equilibria. The approach is illustrated on the case of the M-lattice; in tackling this application there is pointed out the role of the high gain to ensure both gradient like behavior combined with binary outputs which are required e.g. in image processing.

## 1 Introduction: Some Interacting Sources for Neural Networks Emergence

**A.** We want to start from an interesting *state of the art* due to Grossberg [12], more or less “synchronized” with the start of IWANN conference series. It is said there that in order to “better understanding how we (humans) manage to cope so well in a changing world... new intuitive concepts and mathematical models were needed whereby to analyze these data and link behavior to brain. New mathematical methods were sought to analyze how very large numbers of neural components interact over multiple spatial and temporal scales *via* nonlinear feedback interactions in real time. These methods needed to show how neural interactions may give rise to behaviors in the form of emergent properties”. And to continue with the state of the art: “Many experimentalists were superb at doing one type of psychological or neurobiological data, but rarely read broadly about other types of data. Few read across experimental disciplines, even fewer knew any mathematics or models. The people who were starting to develop Artificial Intelligence (AI) favored symbolic mathematical methods. They typically disparaged *the nonlinear differential equations that are needed to describe adaptive behavior in real time* (our emphasizing)”.

To end this quite large quotation, the problem was and it still is “understanding how neural models function autonomously in a stable fashion despite unexpected changes in

their environments. The contents of these models consists of a small set of equations that describe processes such as activation of Short Term Memory (STM) traces, associative learning by adaptive weights or Long Time Memory (LTM) traces... etc” [12].

On the other hand, one of the sources of the AI emergence had been problem solving - a more algorithmic and easier subject to a formal approach. If we consider a quite known textbook of Artificial Neural Networks (ANN) [9], it is started from the beginning that ANN are “computational networks which attempt to simulate, in a gross manner, the networks of nerve cells (neurons). This simulation is a gross cell-by-cell simulation... It thus differs from conventional (digital or analog) computing machines that serve to replace, enhance or speed-up human brain computation without regard to organization of the computing elements and of their networking... The neural network is in fact a novel computer architecture... relative to conventional computers. *It allows very simple computational operations* (additions, multiplication and fundamental logic elements) to solve mathematically ill-defined problems... The ANN will be (a) *computationally* and algorithmically *very simple* and (b) it will be a self organizing feature to allow it to hold for a wide range of problems” [9]. The following remarks of [9] are also worth mentioning: “Biological systems, in order to be as efficient and as versatile as they certainly are despite their inherent slowness (their basic computational step takes about a millisecond versus less than a nanosecond in today’s electronic computers), can only do so *by converging to the simplest algorithmic architecture that is possible* (our emphasizing)... at the present state of NN their range of adaptability is limited. However, their design is guided to achieve this simplicity and self organization by its gross simulation of the biological network that is (must be) guided by the same principles”.

We deduce from all these considerations two theses that will structure the present survey: i) to infer networked repetitive structures (similar, possibly to ANN) that may be problem oriented or of general purpose (wishful thinking!) and ii) to demonstrate specific global convergence to some steady states accounting for the above mentioned algorithmic architectures.

**B.** If the aforementioned similarity of the biological and artificial NN is generating similar structures with other networked structures, the convergence properties - as qualitative ones - deserve some special attention. The best known property is asymptotic stability of equilibria: it is global for linear systems and for nonlinear ones exhibiting almost linear behavior. In the case of the NN (in fact in the case of AI devices) however, the case of a single globally exponentially stable equilibrium does not apply except, possibly, the solvers of the optimization problems. Most of the cases (e.g. classifiers, associative memories, Cellular NN - CNN) require existence of several equilibria with attractor behavior.

Dynamical systems with several equilibria are known to applied scientists. Their qualitative behavior is described by such concepts as dichotomy, global asymptotics and gradient behavior; especially the last concept is mostly required. Their use turned to be useful and fruitful in synchronization problems: electrical machines [13], phase synchronization [8, 19, 20] and other [13, 25]; for NN good surveys of these notions are [3, 4].

An interesting fact is that the second method of Liapunov is applicable to the multi-equilibria case. The importance of this cannot be underestimated for a system of  $n$

ordinary differential equations - where  $n \in \mathbb{N}$  may be large. The underlying idea goes back to Poincaré. Since the properties of the solutions of a system of differential equations are obtained by system solving, and this may be quite difficult, we are sent to the “qualitative theory” whose initial meaning was “to obtain properties of the solutions without calculating them”. A solution is defined by  $n$  functions and, instead of this the information is grasped from the properties of a single function - suitably chosen.

In the case of time delay systems such a Liapunov like theory is only *in statu nascendi* [6]; the structure of the NN contain sometimes time delays hence such a theory is necessary; it is replaced however by the earlier, by now classical approach of [10, 11].

Taking into account the aforementioned considerations, the aim of this paper is somehow twofold: to display an improved overview of the Liapunov approach to systems with several equilibria and to examine some general structures of NN in the light of this theory. Consequently the paper is organized as follows. The next section is concerned with systems with several equilibria and the Liapunov-like theory with its various extensions, including those of V. M. Popov [22–24] which still await application. A third section considers the general structure attached to the  $M$ -lattice [27, 28], its connection with other structures and its qualitative properties. A fourth section considers the high gain  $M$ -lattice; the paper ends with a section of conclusions.

## 2 Systems with Several Equilibria and Liapunov Theory

**A.** We start with some definitions reproduced from [19, 25], the mathematical framework being the system of Ordinary Differential Equations (ODE)

$$\dot{x} = f(x, t) , \dim x = \dim f = n \tag{1}$$

with  $f : \mathbb{R}^n \times \mathbb{R} \mapsto \mathbb{R}^n$  continuous in both arguments and locally Lipschitz in the first of them. We may state

**Definition 1.** a) Any constant solution of (1) is called equilibrium. The set of equilibria  $\mathcal{E}$  is called stationary set.

b) A solution of (1) is called convergent if it approaches asymptotically some equilibrium:

$$\lim_{t \rightarrow \infty} x(t) = c \in \mathcal{E}$$

c) A solution is called quasi-convergent if it approaches asymptotically the stationary set:

$$\lim_{t \rightarrow \infty} d(x(t), \mathcal{E}) = 0$$

**Definition 2.** System (1) is called monostable if every bounded solution is convergent; it is called quasi-monostable if every bounded solution is quasi-convergent.

**Definition 3.** System (1) is called gradient-like if every solution is convergent; it is called quasi-gradient-like if every solution is quasi-convergent.

It is useful to comment these definitions because there exist also other terms for the same notions. The first definition still concerns a single solution property; the convergence notion is due to M. Hirsch [14–16]. Monostability has been introduced by R. E. Kalman [17]. in [22] the same notion is called mutability. Another term for quasi-monostability is dichotomy [8] since for monostable (quasi-monostable) systems there exists some kind of dichotomic behavior: their solutions are either unbounded or tend to an equilibrium (or to the stationary set) but in any case self sustained oscillations are excluded. Worth mentioning that absence of self sustained oscillations is vital for AI structures, in particular for NN. The quasi-gradient like property is also called global asymptotics [8]. As mentioned, convergence is associated with solutions and monostability and gradient like property with systems. There exist also properties associated with the stationary set.

**Definition 4.** *The stationary set  $\mathcal{E}$  is uniformly stable if for any  $\varepsilon > 0$  there exists  $\delta(\varepsilon)$  such that for any  $t_0$  if  $d(x(t_0), \mathcal{E}) < \delta$  then  $d(x(t), \mathcal{E}) < \varepsilon$  for all  $t \geq t_0$ .*

*The stationary set  $\mathcal{E}$  is uniformly globally stable if it is uniformly Liapunov stable and the system is quasi-gradient-like (has global asymptotics).*

*The stationary set is pointwise globally stable if it is uniformly Liapunov stable and the system is gradient-like.*

In order to establish fulfilment of these properties, the following Liapunov like results are available [8, 19]

**Lemma 1.** *Consider the nonlinear system*

$$\dot{x} = f(x), \dim x = \dim f = n \quad (2)$$

*and assume existence of a continuous function  $V : \mathbb{R}^n \mapsto \mathbb{R}$  that is nonincreasing along any solution of (2). If, additionally, a bounded on  $\mathbb{R}^+$  solution  $x(t)$  for which there exists some  $\tau > 0$  such that  $V(x(\tau)) = V(x(0))$  is an equilibrium then the system is quasi-monostable.*

**Lemma 2.** *If the assumptions of Lemma 1 hold and, additionally,  $V(x) \rightarrow \infty$  for  $|x| \rightarrow \infty$  then system (2) is quasi-gradient-like.*

**Lemma 3.** *If the assumptions of Lemma 2 hold and the set  $\mathcal{E}$  is discrete (i.e. it consists of isolated equilibria only) then system (2) is gradient-like.*

The following remarks from [19] turn to be very useful. Namely, the set  $\mathcal{E}$  being discrete means that every equilibrium of (2) is isolated. If  $f \in \mathcal{C}^1$  and its Jacobian matrix  $J_f(p)$  is nonsingular, then the equilibrium  $p$  is isolated.

**B.** As mentioned, systems with time delays are also present in the field of AI, in particular of the NN - see the aforementioned [10, 11]. The Liapunov like results for such systems are included in the following lemma [6], relying on the Barbashin Krasovskii La Salle invariance principle for infinite dimensional systems [26]

**Lemma 4.** *Assume that for system*

$$\dot{x}(t) = f(x_t) \quad (3)$$

(with the usual notation  $x_t(\cdot) = x(t + \cdot)$ ) there exists a Liapunov functional  $V$  (in the above sense) which, additionally, has the following property: any bounded solution of (3) such that  $V(x_t) \equiv \text{const}$  is an equilibrium. Then the system is dichotomic. If additionally  $V$  is globally defined and radially unbounded then the system is gradient like.

The main difficulty in applying this lemma is, as usually, to find a Liapunov (Krasovskii) functional with the required properties. The standard papers concerning NN-like structures with time lags always tackle systems with a single globally stable equilibrium state whose usefulness sends to e.g. optimization problems.

When the nonlinear functions are e.g. sigmoids if not more general functions restricted to a sector, the counterpart method - the frequency domain inequalities that are due to V. M. Popov - may be applied to systems written in the form of integral equations with several equilibria [18, 19, 21]. We reproduce here the result of [18]

**Lemma 5.** Consider the Volterra integro-differential equation

$$\dot{\sigma}(t) = \alpha(t) - \rho\phi(\sigma(t - \tau)) - \int_0^t \gamma(t - \theta)\phi(\sigma(\theta))d\theta \tag{4}$$

with  $\rho, \tau > 0$  being constants,  $\alpha \in \mathcal{L}^1(0, \infty)$ ,  $\alpha(t) \rightarrow 0$  for  $t \rightarrow \infty$ ,  $|\gamma(t)| \leq \gamma_0 e^{-\lambda t}$ ,  $\lambda > 0$ . Let  $\phi \in \mathcal{C}^1$  be such that

$$-\mu_1 \leq \phi'(\sigma) \leq \mu_2, \mu_i > 0 \tag{5}$$

Let  $\chi(s) = \rho e^{-\sigma\tau} + \tilde{\gamma}(s)$ ,  $s \in \mathbb{C}$ , where  $\tilde{\gamma}(s)$  is the Laplace transform of the kernel  $\gamma(t)$ . Assume that the following frequency domain inequality holds

$$\Re[\chi(i\omega) - \overline{\vartheta_0(\chi(i\omega) + \mu_1^{-1}i\omega)(\chi(i\omega) + \mu_2^{-1}i\omega)}] - \varepsilon|\chi(i\omega)|^2 \geq \delta > 0, \forall \omega \in \mathbb{R} \tag{6}$$

for some  $\delta > 0, \varepsilon > 0, \vartheta_0 \geq 0$  subject to either  $4\vartheta_0\delta > v^2$  or  $4\varepsilon\delta > v_0^2$  where  $v$  and  $v_0$  depend on the properties of the nonlinear functions.

Then any solution of (4) approaches a zero of the nonlinear function  $\phi$  and its derivative approaches 0 for  $t \rightarrow \infty$

Worth mentioning that this lemma awaits extension to the multivariable case (several nonlinear functions). Also the adequate structure of the NN to whom this lemma applies is still to be found.

### 3 Structures of Neural Networks That Are Induced by the Equations of Mathematical Physics

We shall discuss here three different cases, from the point of view of their connection to mathematical physics.

**A.** The first case is that of [29] which is dedicated to the implementation of the self organizing map. Starting from the state of the art at the given moment, it is described an algorithm of achieving the self organizing process of the map by the numerical solution of a wave equation that is similar to the two-dimensional, time dependent

Schrödinger equation: effectively, after reminding the principle of the learning algorithm of the self organizing map, there is presented the modified algorithm based on the Schrödinger equation that creates similar learning results. Summarizing we have the following approach.

The Schrödinger equation in the two dimensional case has the form

$$\alpha \Delta \psi - \beta d(x, y) \psi = -i \frac{\partial \psi}{\partial t}, \quad \alpha = \frac{h}{2\pi m}, \quad \beta = \frac{2\pi}{h} \tag{7}$$

$h$  being at the beginning the Planck constant. Aiming to find an absolute minimum for  $d(x, y)$ , the parameters  $\alpha, \beta$  are considered from the point of view of their impact on the search process. The properties of (7) are such that  $|\psi(x, y, t)|^2$ , which acts as a probability density, approaches asymptotically the local minima.

The searching algorithm (called “the third” in [29]) starts from the remark that  $\alpha\beta = 1/m$  and both  $\alpha$  and  $\beta$  can be “searched” by varying  $h$ , according to the simplest rule

$$\frac{dh}{dt} = -\gamma(h - h_2(t)) \tag{8}$$

where  $h_2(t)$  is the “final value” at the end of the searching process and must decrease slowly to 0; since  $\gamma > 0$ , the solution of the forced equation (8) approaches asymptotically the steady state  $h_2(t)$ ; worth mentioning that steady state may be not necessary an equilibrium but also some special regime (e.g. periodic, almost periodic); in the Liapunov theory this is what is called “basic solution”; when about  $h$ , it is “periodically” re-initialized each time when a new input vector comes to the map. The second step of the searching algorithm is to adapt the weights towards the input vector - proportionally to the probability density  $|\psi(x, y, t)|^2$  that is obtained from the “searched Schrödinger equation”. We have thus a feedback coupled structure which, experimentally works well (according to [29]); its rigorous (i.e. proof based) fundamentals are still waiting to be established (up to our knowledge).

**B.** The  $M$ -lattice structure of [27, 28] has a different source and “evolution”: (bio-)inspired by the paper of A.M. Turing on morphogenesis [30], the following system of reaction diffusion in  $d$  dimensions is considered

$$\frac{\partial \psi}{\partial t} = \underbrace{(D_m \Delta \psi_m - (\nabla \psi_m)v - r_m \psi_m)}_{\text{diffusion and dissipation}} + \underbrace{R_m(\psi_1, \dots, \psi_m)}_{\text{reaction}}, \quad m = 1, \dots, M \tag{9}$$

where  $M$  is the numbers of the “morphogens”, represented by their concentrations,  $\nabla \psi_m$  is the row gradient vector and  $\Delta \psi_m = \text{div grad} \psi_m$  is the Laplacian. It is clear that the linear terms account for dissipation and diffusion while the coupling reaction terms are nonlinear. In particular, the Turing system [30] has two morphogens, no convection, no dissipation.

The inference process is as follows. First the system (with the Turing system as a “toy system”) is partially discretized using the *method of lines* as arising from the numerics of Partial Differential Equations (PDE) to obtain a system of ODE for the morphogens; the periodic Boundary Value Problem (BVP) is considered and a *lattice structure* is thus obtained, with  $N$  equidistant cells. The system is linearized and solved by separation of

the variables using the Discrete Fourier Transform (DFT)- recall the periodicity with respect to the *discretized* space variable. This allows viewing a structure that displays cyclic convolution with Finite Impulse Response (FIR) digital filters. Consequently, a new network structure is inferred, called “*M*-lattice” where *M* does not appear any longer, being thus only the “trace” of the number of morphogens. In fact there will be a single “morphogen” located in *N* cells that are connected through some FIR digital filtering structures; the lattice will be 1-dimensional with some *a priori* boundedness of the state variables, obtained by using sigmoid nonlinear functions. The system structure of the “*M*-lattice” is as follows

$$\dot{x} = Ax - (\nabla_y \Phi(y))^* , y = g(x) , \dim x = N \tag{10}$$

where the  $N \times N$  matrix *A* is real, symmetric and negative definite,  $\nabla_y(\cdot)$  denotes the gradient along the direction of the *N*-vector *y* - assumed to be a row vector, as prescribed by tensor analysis. The “potential function”  $\Phi : \mathbb{R}^N \mapsto \mathbb{R}$  is assumed to be at least  $\mathcal{C}^1$  as smoothness. The entries  $\eta_i$  of the vector *y* are the outputs of the state variables  $\xi_i$  (the entries of the state vector *x*) obtained from the readout sigmoids  $\eta_i = g_i(\xi_i)$ ,  $i = 1, \dots, N$ ,  $g_i$  being the entries of the readout vector map *g*. This is the *smooth* “*M*-lattice” which defines a rather general structure allowing re-discovering Hopfield and Cellular NN (but not only) as special cases [28].

For instance, the continuous time Hopfield NN is obtained from (10) provided *A* is diagonal with negative elements and  $\Phi : \mathbb{R}^N \mapsto \mathbb{R}$  is a multilinear polynomial i.e. its independent variables have the powers 0 and 1 only:

$$A = \text{diag}\{a_1, \dots, a_N\} , \frac{\partial^2 \Phi}{\partial \eta_i \partial \eta_j} = 0 , i, j = 1, \dots, N \tag{11}$$

i.e. the Hessian matrix of  $\Phi$  is zero.

Further, the CNNs are obtained from (10) under the following assumptions: *A* is again diagonal but with equal diagonal elements ( $a_1 = \dots = a_N = a < 0$ ) while  $\Phi$  is such that  $\nabla_y \Phi(y)$  is the product of a symmetric (block-) circulant matrix standing for the discrete cyclic convolution kernel, with a translation invariant FIR digital filter. Therefore

$$\Phi(y) = \frac{1}{2} |Hy|^2 + s^*y + \sigma \tag{12}$$

with *H* the aforementioned (block-)circulant matrix.

As long as the readout nonlinear (“warping”) functions  $g_i(\cdot)$  are smooth, the “*M*-lattice” thus defined may be considered as a special case of the gradient like systems already studied in [2].

We associate to (10) the following “potential energy” function  $\Pi : \mathbb{R}^N \mapsto \mathbb{R}$

$$\Pi(x) = -\frac{1}{2} x^* Ax + \Phi^*(x) \tag{13}$$

where we denoted  $\Phi^*(x) := \Phi(g(x))$  and  $g(x)$  is the readout column vector with the entries  $g_i(\xi_i)$ . Therefore system (10) can be written as a gradient system

$$\dot{x} = -(\nabla_x \Pi(x))^* \tag{14}$$

Like in Classical Mechanics, the equilibria of system (10) are the critical points of the potential energy function  $\Pi(x)$ , its minima being locally asymptotically stable. On the other hand, when discussing global behavior differentiation of  $\Pi(x)$  along the solutions of (13) will give

$$\frac{d}{dt}\Pi(x(t)) = -|\nabla_x \Pi(x(t))|^2 \leq 0 \tag{15}$$

and the function  $\Pi(x(t))$  is non-increasing and constant on the equilibria set only. But  $A$  is a Hurwitz matrix and since the “warping” functions are sigmoids hence their range is bounded, all solutions of (10) are bounded. Since the conditions of Lemma 1 are gathered, the system is quasi-gradient like. In order to obtain the gradient like behavior we need to check that the equilibria of (10) - or at least the interesting ones - are isolated. Compute the Jacobian matrix of (10)

$$J(x) = A - \mathcal{H}_y(\Phi(g(x)))g_x(x) \tag{16}$$

where  $\mathcal{H}_y(\cdot)$  is the Hessian matrix of  $\Phi$  and  $g_x(x)$  is the diagonal matrix with  $g'_i(\xi_i)$  as diagonal entries. Obviously  $J(x)$  is the Hessian matrix of  $\Pi(x)$ ; therefore at least the minima and maxima of  $\Pi(x)$  are isolated. *The gradient like behavior is ensured for the smooth “M-lattice”.*

C. We would like to end this section by mentioning another structure generated by equations of Mathematical Physics - the structure tackled in [5]. It belongs to the more comprehensive class generated when the aforementioned *method of lines* is implemented, in this case for linear and nonlinear hyperbolic PDE, including the systems of conservation laws. Within the framework of this method the space derivatives only are “discretized” i.e. replaced by the corresponding finite differences. Since the details are in [5] we just mention that the derivative of the forward wave must be discretized backwards while the backward wave must be discretized forwards; this rule, due to R. Courant, E. Isaacson and M. Rees, is the only one ensuring matching to the boundary conditions as well as convergence of the approximations to the exact solutions.

### 4 High Gain M-Lattices

The development of the structures called “M-lattices” in order to replace CNNs [27, 28] led to the requirement of having as outputs binary sequences of e.g.  $\pm 1$ s. The proposed approach was a strict saturation of the “warping” readout map: the smooth strictly increasing sigmoid was replaced by

$$g_T(u) = \frac{1}{2} \left( \left| 1 + \frac{u}{T} \right| - \left| \frac{u}{T} - 1 \right| \right) \tag{17}$$

where  $T$  was called “temperature”. The function (17) is only piecewise differentiable since it has angular point at  $u = \pm 1$ . This lack of monotonicity results in existence of non-isolated equilibria. The situation was considered acceptable since there will exist a (possibly dense) set of binary equilibria that could be eventually discriminated. From the point of view of the global behavior, only the quasi-gradient property was obtained in [27, 28] for the newly introduced “M-lattices” called “clipped”: the trajectories are



bounded since  $g_T(u)$  as defined by (17) is bounded, and they tend to the set of equilibria as a whole (in fact the union of all  $\omega$ -limit sets coincides with set of equilibria). But if  $A$  is diagonal then this behavior can be shown to be even gradient like.

Another possibility of obtaining gradient like behavior is to use the *high gain*. This used to be the approach for the so called KWTA neural networks, derived from the Hopfield networks [1]. Following [7] we re-write (10) as

$$\dot{x} = Ax - (\nabla_y \Phi(y))^* , y = g(\lambda x) \tag{18}$$

where  $\lambda > 0$  is a (possibly high) gain. As previously,  $g_i(\sigma)$  are strictly monotonous, continuous, Lipschitz and such that  $\lim_{\sigma \rightarrow \pm\infty} g_i(\sigma) = \pm 1$ .

The energy like Liapunov function will be now

$$\Pi_\lambda(x) = -\frac{1}{2}x^*Ax + \frac{1}{\lambda}\Phi(g(\lambda x)) \tag{19}$$

and system (18) will be written again as

$$\dot{x} = -(\nabla_x \Pi_\lambda(x))^* \tag{20}$$

Therefore

$$\frac{d}{dt}\Pi_\lambda(x(t)) = -|\nabla_x \Pi_\lambda(x(t))|^2 \leq 0 \tag{21}$$

From the smoothness properties of the system the gradient like behavior will follow. On the other hand, considerations as in [1, 7] show that if  $\lambda > 0$  is large enough, the equilibrium output should be in some neighborhood of a “corner” (vertex) of the hypercube  $[-1, 1]^N$ : the outputs will thus have approximately the form of binary sequences and larger is the gain  $\lambda > 0$ , better is the approximation.

The “clipped  $M$ -lattice” also can display some high gain in the un-saturated domain of the readout “warping” map, for low “temperatures” (small  $T > 0$ ) but the high gain approach should normally avoid clipping.

## 5 Some Conclusions

Throughout this paper there was pointed out an important source for generating AI structures - the Mathematical Physics. Two basic classes of outcomes have been discussed: learning algorithms as implemented by iterative processes of solving equations of mathematical physics (the first two applications described in Section 3) and AI structures arising from direct problem solutions in mathematical physics (the application mentioned at the end of Section 3 and which can be seen in detail in these Proceedings).

Our reflections followed the two theses mentioned within the Introduction (Section 1). While the inferences are closer to the engineering philosophy (of rational design), the second thesis implying a rigorous *a posteriori* foundation of the inference concerns the theoretically oriented engineer and the applied mathematician. For this reason there were recalled throughout the paper the more recent topics in Liapunov theory - dealing with the global behavior of the systems with several equilibria; while the Liapunov

standard theory is a very consolidated achievement, this newer part of it is not very popular among the people involved in applications. Moreover, its component dealing with time delay equations is still *in statu nascendi*. In order to illustrate this thesis we tackled the “M-lattice” structure with particular reference to the case containing smooth, namely sigmoid nonlinear functions. There is thus defined a system showed to have gradient like behavior and able to “accept” high gains without de-stabilizing.

In fact the second thesis of the paper states that the global convergence properties are not ensured *a priori* and their separate analysis, based on suitable (“natural”) Liapunov functions remains an urgent task. Coping with this task has been and still is an active field of research, at least for this author [6, 7, 25] (see also [3–5]).

## References

1. Calvert, B.D., Marinov, C.A.: Another k-winners-take-all analog neural network. *IEEE Trans. on Neural Networks* 11(4), 829–838 (2000)
2. Cohen, M., Grossberg, S.: Absolute stability of global pattern formation and parallel memory storage by competitive neural networks. *IEEE Trans. on Syst. Man Cybernetics SMC* 13(5), 815–826 (1983)
3. Danciu, D.: Dynamics of neural networks as nonlinear systems with several equilibria. In: Porto, A.B., Pazos, A., Buno, W. (eds.) *Advancing Artificial Intelligence through Biological Process Applications*, pp. 331–357. Medical Information Science Reference (2008)
4. Danciu, D.: Bio-inspired systems. Several equilibria. Qualitative behavior. In: Cabestany, J., Rojas, I., Joya, G. (eds.) *IWANN 2011, Part II. LNCS*, vol. 6692, pp. 573–580. Springer, Heidelberg (2011)
5. Danciu, D.: A CNN based approach for solving a hyperbolic PDE arising from a system of conservation laws - the case of the overhead crane. In: Rojas, I., Joya, G., Cabestany, J. (eds.) *IWANN 2013, Part II. LNCS*, vol. 7903, pp. 364–374. Springer, Heidelberg (2013)
6. Danciu, D., Răsvan, V.: Dynamics of neural networks - some qualitative properties. In: Sandoval, F., Prieto, A.G., Cabestany, J., Graña, M. (eds.) *IWANN 2007. LNCS*, vol. 4507, pp. 8–15. Springer, Heidelberg (2007)
7. Danciu, D., Răsvan, V.: Gradient like behavior and high gain design of kwta neural networks. In: Cabestany, J., Sandoval, F., Prieto, A., Corchado, J.M. (eds.) *IWANN 2009, Part I. LNCS*, vol. 5517, pp. 24–32. Springer, Heidelberg (2009)
8. Ghelig, A.K., Leonov, G.A., Yakubovich, V.A.: *Stability of Stationary Sets in Control Systems with Discontinuous Nonlinearities*. World Scientific, Singapore (2004)
9. Graupe, D.: *Principles of Artificial Neural Networks*, 2nd edn. *Advanced Series on Circuits and Systems*, vol. 6. World Scientific, Singapore (2007)
10. Grossberg, S.: A prediction theory for some nonlinear functional-differential equations i. learning of lists. *Journ. Math. Anal. Appl.* 21, 643–694 (1968)
11. Grossberg, S.: A prediction theory for some nonlinear functional-differential equations ii. learning of patterns. *Journ. Math. Anal. Appl.* 22, 490–522 (1968)
12. Grossberg, S.: Self-organizing neural networks for stable control of autonomous behavior in a changing world. In: Taylor, J.G. (ed.) *Mathematical Approaches to Neural Networks*, pp. 139–197. Elsevier (1993)
13. Halanay, A., Răsvan, V.: *Applications of Liapunov Methods to Stability. Mathematics and Its Applications*, vol. 245. Kluwer Academic Publishers, Dordrecht (1993)
14. Hirsch, M.: Systems of differential equations which are competitive or cooperative i: Limit sets. *SIAM J. Math. Anal.* 13(2), 167–179 (1982)

15. Hirsch, M.: Systems of differential equations which are competitive or cooperative ii: Convergence almost everywhere. *SIAM J. Math. Anal.* 16(3), 423–439 (1985)
16. Hirsch, M.: Stability and convergence in strongly monotone dynamical systems. *J. Reine Angew. Mathem.* 383, 1–53 (1988)
17. Kalman, R.E.: Physical and mathematical mechanisms of instability in nonlinear automatic control systems. *Trans. ASME* 79(3), 553–566 (1957)
18. Leonov, G.A., Reitmann, V., Smirnova, V.B.: On the global asymptotic stability of ordinary and functional differential equations with multiple equilibria. *Tech. Rep. 07.01.89, TU Dresden* (1989)
19. Leonov, G.A., Reitmann, V., Smirnova, V.B.: Non-local methods for pendulum-like feedback systems. *Teubner Texte zur Mathematik*, vol. 132. Teubner Verlag, Stuttgart-Leipzig (1992)
20. Leonov, G.A., Seledji, S.M.: Systems of phase synchronization for analogue and digital systems techniques. *Nevskii Dialekt, St. Petersburg* (2002) (Russian)
21. Leonov, G.A., Smirnova, V.B.: Asymptotic behavior of the solutions of integro-differential equations with periodic nonlinearities. *Sibirsk. Mat. Zh.* 19(6), 1406–1412 (1978) (Russian)
22. Popov, V.M.: Monotonicity and mutability. *Journ. Diff. Eqs.* 31(3), 337–358 (1979)
23. Popov, V.M.: Monotone gradient systems. *Journ. Diff. Eqs.* 41(2), 245–261 (1981)
24. Popov, V.M.: An index theorem with applications to the control of antagonistic systems. *Rev. Roumaine Math. Pures Appl.* 39(4), 355–363 (1994)
25. Räsvan, V.: Dynamical systems with several equilibria and natural liapunov functions. *Archivum Mathematicum* 34(1), 207–215 (1998)
26. Saperstone, S.: *Semidynamical Systems in Infinite Dimensional Spaces*. Applied Mathematical Sciences, vol. 37. Springer, Heidelberg (1981)
27. Sherstinsky, A.S.: *M*-lattice: a system for signal synthesis and processing based on reaction diffusion. Ph.D. thesis, Massachusetts Institute of Technology (1994)
28. Sherstinsky, A.S., Picard, R.W.: On stability and equilibria of the *m*-lattice. *IEEE Trans. on Circuits and Systems I: Fundamental Theory and Applications* 45(4), 408–415 (1998)
29. Tryba, V., Goser, K.: A modified algorithm for self-organizing maps based on the schrödinger equation. In: Prieto, A.G. (ed.) *IWANN 1991*. LNCS, vol. 540, pp. 33–47. Springer, Heidelberg (1991)
30. Turing, A.M.: The chemical basis of morphogenesis. *Phil. Trans. R. Soc. Lond. B* 237, 37–72 (1952)

# A Retina-Inspired Neurocomputing Circuit for Image Representation

Hui Wei, Qing-song Zuo, and Bo Lang

Lab of Cognitive Algorithm Model, Department of Computer Science,  
Fudan University, Shanghai 200433, China  
{weihui, qingsong\_zuo, 09110240025}@fudan.edu.cn

**Abstract.** Biological vision systems have become highly optimized over millions of years of evolution, developing complex neural structures to represent and process stimuli. Moreover, biological systems of vision are typically far more efficient than current human-made machine vision systems. The present report describes a non-task-dependent image representation schema that simulates the early phase of a biological neural vision mechanism. We designed a neural model involving multiple types of computational units to simulate ganglion cells and their non-classical receptive fields, local feedback control circuits and receptive field dynamic self-adjustment mechanisms in the retina. We found that, beyond the pixel level, our model was able to represent images self-adaptively and rapidly. In addition, the improved representation was found to substantially facilitate contour detection. We propose that this improvement arose because ganglion cells can resize their receptive fields, enabling multi-scale analysis functionality, a neighborhood referring function and a localized synthesis function. The ganglion cell layer is the starting point of subsequent diverse visual processing. The universality of this cell type and its functional mechanisms suggests that it will be useful for designing image processing algorithms in future.

**Keywords:** neural model, non-classical receptive field, feedback control circuits, dynamic self-adjustment mechanism.

## 1 Introduction

We describe a new type of schema for image representation, developed to further our understanding of image processing. Our new schema is based on the simulation of biological processes, because biological visual systems are highly optimized as a result of evolutionary pressures. This system involves modeling retinal ganglion cells and their dynamic properties.

Neuroscience provides a promising approach for understanding image processing. Biological visual systems, especially the vision of higher mammals, can adapt to changing environments. This suggests a biological mechanism to solve the tradeoff problem between performance and cost, optimized by biological evolution. In the

current study, we used the early neuronal vision system as a template for simulation, because in this phase the neural subsystem pre-processes the signals from photoreceptors as well as delivering periodical results to high-level structures for advanced processing. Ganglion cells (GCs) and their receptive fields (RF) are the major micro neural structures in this phase of processing. A number of computational simulations have focused on GCs in the past 20 years, typically focusing on edge or contour detection[1], image enhancement[2], and multi-scale analysis[3], using the GC model. Some recent studies have applied the GC and RF models to represent images[4], and have begun to model much more complex functions of GCs and RFs. Summarizing these studies from the perspective of neural computation reveals two aspects that can be improved upon: (a) referring to more neurobiological findings to construct a more complete neural-processing cell-circuit, and (b) adopting a dynamic receptive field strategy that requires cell-circuits to adjust their receptive fields self-adaptively. As such, the main purpose of this paper is to design a model that takes more consideration of neuronal mechanisms, and uses it as a general schema to represent images.

This paper is arranged into the following sections: In section 2, we formalize the design of the image representation model based on the biological mechanisms of the GC and its RF, and statistically test whether the important features of an image are preserved in our new model. In section 3, 4 and 5 we apply proposed model on segmentation and figure-ground separation. Finally, in section 6, we provide a conclusion.

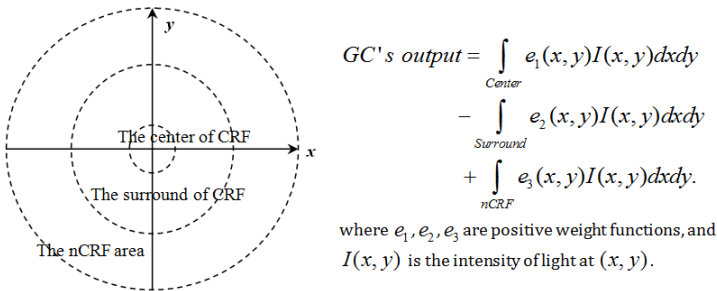


Fig. 1. The spatial structure of the CRF and nCRF and their computational relationships

## 2 The Design of GC-Based Image Representation Array

### 2.1 The Parameter Configuration of Ganglion Cell Computational Model

RFs of GCs have the following biological characteristics (see also in Fig. 1):

- (a) The classical RF (CRF) of a GC comprises two concentric areas, the center and the surround. These two areas have antagonistic effects on the response of the GC;
- (b) Outside the CRF there is a much larger ring area, the non-classical RF (nCRF), which compensates the inhibition that the surround area imposes on the center area.

That is, the response of a GC caused by the nCRF is antagonistic to the response caused by the surround area;

(c) The RF and nCRF are formed by bipolar cells, horizontal cells and amacrine cells[5, 6], which operate through very complex local circuits[7, 8]. Both CRF and nCRF are composed of many sub-regions, and their sizes can vary (see <http://webvision.med.utah.edu/HC.html>, <http://webvision.med.utah.edu/AII.html>).

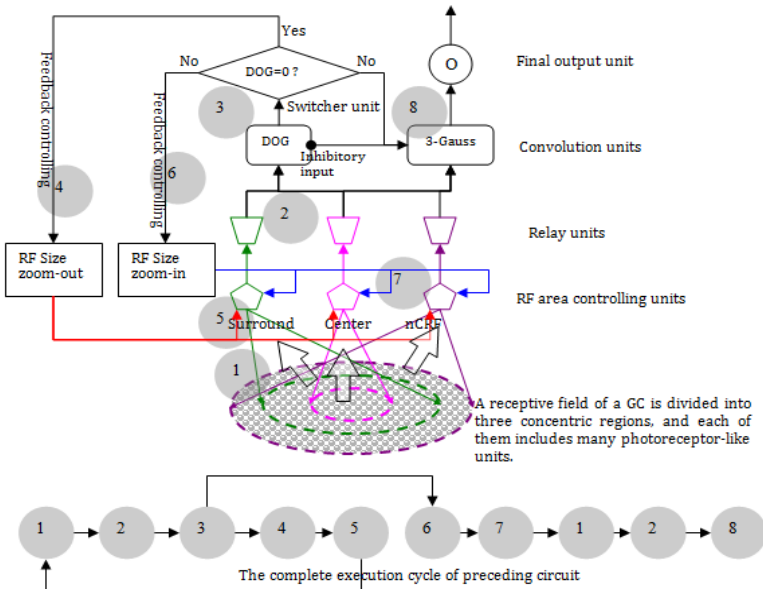


Fig. 2. Inner flowchart of single GC-like module computation

## 2.2 The Design of a Single GC-Like Computational Unit

Although characteristics of the GC discussed above are widely known, finding a way in which to apply them in image understanding (rather than just processing), remains problematic, especially in information integration. A common approach is to apply antagonistic effects in edge detection, but this wastes much of the computational power enabled by the nCRF. According to the neural circuit between a GC and its CRF and nCRF, and also in terms of the GC's electrophysiological characteristics, we propose that the function of GCs is not merely edge-detection. Rather, they may play a crucial role in sampling the whole visual field accurately and economically. An important anatomical finding is that the compression ratio of the number of photoreceptor cells to the number of GCs is approximately 100:1, so the information the brain receives is undergoing substantial selection. From a sampling perspective, we propose that the GC functions as some kind of high-order feature descriptor, particularly involved in detecting homogeneous distributions of stimuli.

After the signal processing function of the GC and the multiple-layer neural structure of the RF were clarified, a brief computational model was designed (see Figure 2), involving a simplification of complex biophysical details regarding the neural construction and control of RFs. Figure 2 shows a conceptual model of the way in which an image is processed by a GC and its RF structure. The functional elements of this model are described in more detail in Table 1.

**Table 1.** Single GC-like module processing algorithm

---

1.	(See gray label 1) Photoreceptor-like units transform RGB values of pixels to wave length like value; and at the beginning the center, surround and nCRF regions have their initial sizes, and all photoreceptor-like units belonging to every region will be summed.
2.	(See gray label 2) All summed RGB-equivalent information is transmitted upwards, through different channels of RF size controlling units, to corresponding relay units, i.e. intensity recording units.
3.	(See gray label 3) A convolution unit DOG executes integration basing on two input streams: from the center and from the surround; once it finished integration, unit DOG submits its output to switcher unit; and switcher unit will decide whether the output is zero or not; at the beginning another convolution unit 3-Gauss is closed, because it is enabled by switcher unit. Unit 3-Gauss will not be triggered until CRF region has been sufficiently expanded.
4.	(See gray label 4) If the output of unit DOG is approaching zero, switcher unit will send positive sign to trigger one of RF area controlling units; this unit will update RF size upwards according to a ratio rule: the center vs. the surround vs. the nCRF = 1:3:3.
5.	(See gray label 5) An instruction of expanding RF is sent to three RF region controlling units; and the center, the surround and the nCRF are expanded simultaneously. Due RF size being changed must cause some photoreceptor units changing their ownerships, so a new round iteration will start.
6.	(See gray label 6) If the output of unit DOG is not zero, switcher unit will send two negative signs out; one is to trigger another RF area controlling unit, which will update RF size downwards according to the same ratio rule.
7.	(See gray label 7) An instruction of shrinking RF is sent to three RF region controlling units, and they will decrease the range of RF; a new, and also the last, round iteration will start.
8.	(See gray label 8) Another negative sign is sent to unit 3-Gauss, and enable it; and at the same time this sign is also sent to unit DOG to shut it down; unit 3-Gauss will receive three instantaneous input streams: from the center, from the surround and from the nCRF, and execute convolution; the final output unit will send the result out.

---

### 2.3 The Design of a Hierarchical Arrays Model

Above, we described the way in which a single GC-like module processes pixels. However real images typically consist of millions of pixels, so a single module is insufficient for processing them. Combining multiple individual modules, we designed a hierarchical multi-layer model to perform this task, in which each layer is an array with a large number of units. In Fig.3, the bottom layer is a pixel-array that

stores an image. The upper layer is a GC-array that plays a similar role to real GCs, and each of them corresponds to the ‘final output unit’ of Fig.3. The middle layer is the receptive field formation layer, which is an array of several types of units corresponding to all other units, except the ‘final output unit’ and the ‘photoreceptor unit’ in Fig.2. These units play similar roles to the bipolar cell, horizontal cell and amacrine cell in the biological retina.

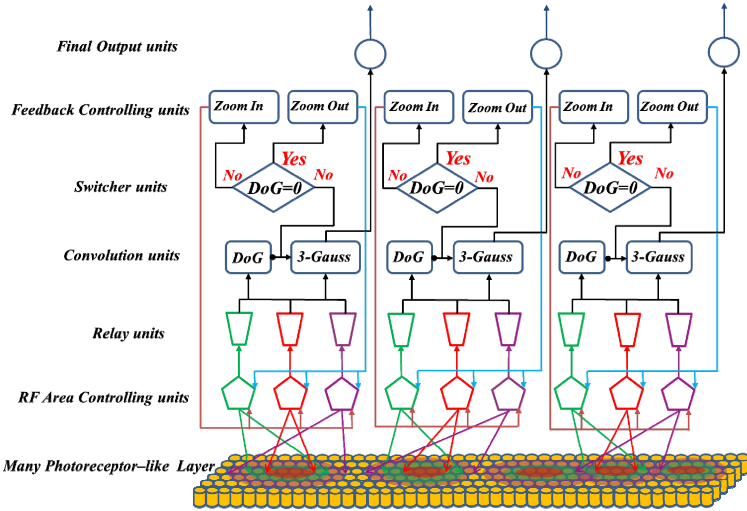


Fig. 3. Hierarchical multi-layer model for image representation

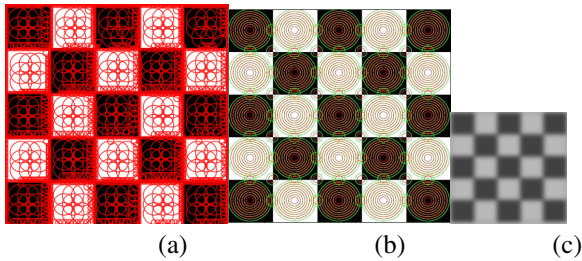


Fig. 4. Dynamic change of RF

To test whether the RFs in our model exhibited self-adaptation, we conducted an experiment with a checkerboard pattern (Fig.4). At the beginning, RFs of random size were located evenly on the board (Fig.4(a)), and became stabilized after the iterations described in Fig.2. The green circles denote the final size of RFs, while red circles denote the size-changing processes (Fig.4(b)). Fig.4(c) shows the visualized results of GC behavior. From this figure, it can be seen that if stimuli in a local area are uniform, RFs tend to expand in size to cover as large an area as possible. In contrast, if



stimuli are sufficiently diverse, the RF tends to shrink in size, obtaining a finer resolution that can identify detail more accurately. This type of dynamic adjustment ability provides an ideal sampling mechanism for representing images.

### 3 GC-Array's Output Promoting Segmentation

As described above, it is clear that the GC array can represent original images faithfully, and that the dimensions of the array are much smaller than the dimensions of the original image. If a computer conducts image processing on the level of the GC array, efficiency should be markedly better than processing conducted on the pixel-level. Segmentation is a particularly important phase for advanced analysis. The following experiment demonstrated that a representation formed by the GC array can markedly promote segmentation. Figure 5 (a) shows a wall texture comprised of stone, while (b) and (c) show two clustering results according to GC outputs. Fine precision was able to highlight details, while coarse precision highlighted the main structure of the image.

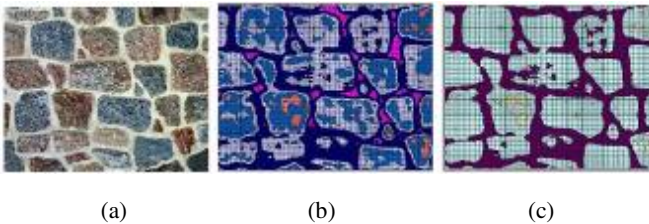


Fig. 5. Segmentation on the GC array is more efficient

### 4 Promoting N-Cut Algorithm

The N-cut algorithm[9] is a widely used method for image segmentation. We tested the effects of running this algorithm on a GC array instead of pixels. Figure 6 shows the results. We applied this algorithm [10] to BMP images and a GC-array, respectively, then compared the two resulting segmentations. The third column shows that the results were improved relative to the use of the algorithm alone. The green circles mark the specific places in which the segmentation was improved. Importantly, there was a dramatic reduction in the required run-time. Thus, a good GC-based representation can improve the efficiency of segmentation without sacrificing performance.

This advantage of the current method was likely related to the much smaller dimensions of the GC-array compared to the original BMP image, which would be expected to greatly reduce the complexity of the graph-based segmentation algorithms. The computational complexity of the min-cut in time is represented by  $O(n^2 \log n)$ , where  $n$  is the number of vertices of graph, and a near-optimal min-cut algorithm's computational complexity is  $O(2nm * \log(n^2/m))$ , where  $m$  is the number of edges [11]. Thus, smaller dimensions must reduce the values of  $n$  and  $m$ .









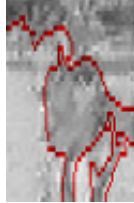





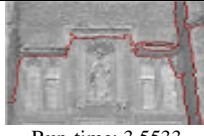



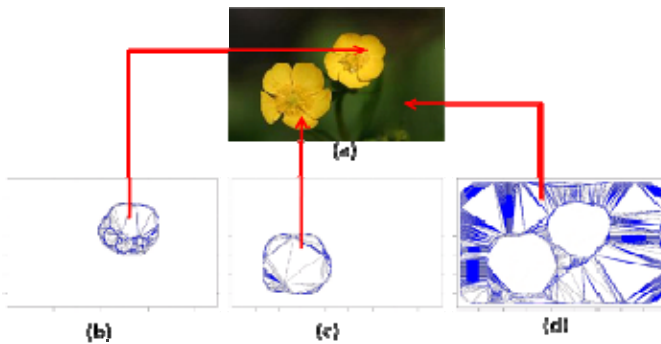
Original picture	N-cut on pixels	N-cut on GC-array
	 <p data-bbox="503 384 666 407">Run-time: 34.2777</p>	 <p data-bbox="742 384 898 407">Run-time: 4.5071</p>
	 <p data-bbox="503 536 666 559">Run-time: 36.1163</p>	 <p data-bbox="747 536 894 559">Run-time: 5.101</p>
	 <p data-bbox="503 772 666 795">Run-time: 19.3885</p>	 <p data-bbox="742 772 898 795">Run-time: 1.5967</p>
	 <p data-bbox="503 913 666 936">Run-time: 23.8193</p>	 <p data-bbox="747 913 894 936">Run-time: 2.8363</p>
	 <p data-bbox="510 1072 671 1095">Run-time: 21.3145</p>	 <p data-bbox="745 1072 894 1095">Run-time: 3.5533</p>
	 <p data-bbox="503 1231 666 1254">Run-time: 69.6711</p>	 <p data-bbox="745 1231 894 1254">Run-time: 4.4497</p>

Fig. 6. Facilitation of the N-cut algorithm by the GC-array

## 5 Promoting Figure-Ground Separation

In traditional segmentation algorithms, a pixel-array is imposed on the original image to denote the position of contours. The main reason for drawing these boundaries is to reveal their locations. However, this does not change the properties of pixels as completely free but not polymer-like entities, meaning that a computer cannot represent or

manipulate pixels in a compound fashion. If no mathematical morphological calculations can follow-up this initial processing, then the significance of drawing these boundaries is limited to presentation only. The GC-array provides an ideal solution for representation purposes, because (a) each GC RF has a regular shape, (b) the position of each GC is fixed, and (c) several neighboring GCs can aid in localization, similarly to GPS. A vectorizable representation schema would be helpful to increase the ease of describing the results of segmentation. Here we first clustered GCs with similar responses and adjacent positions, then combined their receptive fields. We then used some controlling points to construct strict polygons. Finally, a brief representation was obtained through a union of polygons, because any polygon was easy to vectorize with a small number of parameters. These controlling points can be obtained based on the circumferences of receptive fields. Because triangular shapes can be easily formalized by its three vertices, Figure 7 displays the result of applying Delaunay triangulation (similar to the method used in [13] to compensate and represent contours.



**Fig. 7.** Vectorized and formalized representations of segments can be produced by GCs and their RFs. (a) shows the original image; (b) shows a part of the top-right flower; (c) shows a part of the bottom-left flower; (d) shows a part of the background.

## 6 Conclusion

Developing an appropriate method for representing visual stimuli was essential for the evolution of sighted animals. An effective representation system must meet the requirements of expressiveness, efficiency and perceptual soundness. In addition, a representational schema must be able to express all of the necessary information, support the efficient execution of successive processing, and provide a natural schema for expressing the required grouping-knowledge. Our currently proposed GC array and RF model possess all of these attributes.

The current paper tested the possibility of an image representation system based on the physiological mechanisms of GCs and their RFs. Although some biological details of RFs and retinal cells remain unclear, this does not prevent us from designing realistic simulations using appropriate algorithms. The RF is flexible, adapting to changes

in contrast and brightness, and adjusting its filter characteristics according to the localized spatial frequency components of an image. Because the RF sometimes employs a high-pass filter, and sometimes a low-pass filter, it can play multiple roles, representing either fine detail or continuous areas.

**Acknowledgments.** This work was supported by the 973 Program (Project No. 2010CB327900), the NSFC major project (Project No. 30990260) and the National Twelfth 5-Year Plan for Science & Technology (Project No. 2012BAI37B06).

## References

1. Papari, G., Petkov, N.: An improved model for surround suppression by steerable filters and multilevel inhibition with application to contour detection. *Pattern Recogn.* 44, 1999–2007 (2011)
2. Ghosh, K., Sarkar, S., Bhaumik, K.: Image enhancement by high-order Gaussian derivative filters simulating non-classical receptive fields in the human visual system. *Pattern Recognition and Machine Intelligence*, 453–458 (2005)
3. Ghosh, K., Sarkar, S., Bhaumik, K.: A bio-inspired model for multiscale representation of even order gaussian derivatives. In: *Proceedings of the 2004 Intelligent Sensors, Sensor Net-works and Information Processing Conference*, pp. 497–502 (2004)
4. Linde, O., Lindeberg, T.: Object recognition using composed receptive field histograms of higher dimensionality. In: *Proceedings of the 17th International Conference on Pattern Recognition, ICPR 2004*, vol. 2, pp. 1–6 (2004)
5. Dacey, D.M.: The mosaic of midget ganglion cells in the human retina. *The Journal of Neuroscience* 13, 5334–5355 (1993)
6. Trexler, E.B., Li, W., Massey, S.C.: Simultaneous contribution of two rod pathways to AII amacrine and cone bipolar cell light responses. *J. Neurophysiol.* 93, 1476–1485 (2005)
7. Kolb, H., Nelson, R.: Off - alpha and OFF - beta ganglion cells in cat retina: II. Neural circuitry as revealed by electron microscopy of HRP stains. *The Journal of Comparative Neurology* 329, 85–110 (1993)
8. Sjöstrand, J., Olsson, V., Popovic, Z., Conradi, N.: Quantitative estimations of foveal and extra-foveal retinal circuitry in humans. *Vision Res.* 39, 2987–2998 (1999)
9. Shi, J., Malik, J.: Normalized cuts and image segmentation. *IEEE T. Pattern Anal.* 22, 888–905 (2000)
10. <http://www.cis.upenn.edu/~jshi/software/>
11. Dahlhaus, E., Johnson, D.S., Papadimitriou, C.H., Seymour, P.D., Yannakakis, M.: The complexity of multiway cuts..., pp. 241–251. *ACM* (1992)
12. Ren, X.F., Fowlkes, C.C., Malik, J.: Learning probabilistic models for contour completion in natural images. *Int. J. Comput. Vision* 77, 47–63 (2008)

# Evolutionary Approach in Inventory Routing Problem

Dragan Simić<sup>1</sup> and Svetlana Simić<sup>2</sup>

<sup>1</sup> University of Novi Sad, Faculty of Technical Sciences  
Trg Dositeja Obradovića 6, 21000 Novi Sad, Serbia  
dsimic@eunet.rs

<sup>2</sup> University of Novi Sad, Faculty of Medicine  
Hajduk Veljkova 1-9, 21000 Novi Sad, Serbia  
drdragansimic@gmail.com

**Abstract.** Most companies recognize the need for the integration and coordination of various components in logistics and supply chain management as an important factor. This paper presents an evolutionary approach to modeling and optimization on inventory routing problem of inventory management, logistics distribution and supply chain management. The aim of this research is to present different individual evolutionary approach, and to obtain power extension of these hybrid approaches. In general, these evolutionary hybrid approaches are more competitive than classic problem-solving methodology including improved heuristics methods or individual bio-inspired methods and their solutions in inventory management, logistics distribution and supply chain.

**Keywords:** Evolutionary approach, inventory routing problem, genetic algorithms, bio-inspired models, logistics.

## 1 Introduction

Most companies recognize the need for the integration and coordination of various components in a supply Chain Management (SCM) as an important factor in order to remain competitive. Most of the activities in the SCM are inter-related and changes in one part of the SCM are likely to affect the performance of other processes. Inventory management and transportation are two key logistical drivers of the SCM. Other components include production, location, marketing and purchasing [1]. The coordination of these two drivers, often known as the inventory routing problems (IRP), is critical in improving the logistics activities in SCM.

The rest of the paper is organized in the following way. The following section overviews the inventory routing problem, Section 3 elaborates basic approach to evolutionary approach in general. Section 4 shows two implementations of hybrid evolutionary IRP models which are critical in contemporary business and management, and also presented in this section are: (1) hedge-based stochastic inventory routing system; (2) simultaneous delivery and pickup problems with time window. Section 5 concludes the paper.

## 2 Inventory Routing Problem and Related Work

The inventory routing problem dates 30 years back [2]. It can be described as the combination of vehicle routing and inventory management problems, in which a supplier has to deliver products to a number of geographically dispersed customers, subject to side constraints. IRP are among the most important and most challenging extensions of optimizing vehicle routing problem, in which inventory control, routing decisions and delivery scheduling have to be made simultaneously. The IRP represents a non-deterministic polynomial-time hard (NP-hard) problem. The objective is to determine policies that minimize total cost, sum inventory holding and transportation costs, while avoiding stock-out and respecting storage capacity limitations.

The routing component, vehicle routing problem by itself makes the problems difficult. In fact, the problems reduce to the traveling salesman problem when the planning horizon is one, the inventory costs zero, the vehicle capacity infinite, and all customers need to be served. Furthermore, even when only one customer is considered, some variants remain computationally hard [3]. Different solutions on vehicle routing problem based on hybrid artificial intelligent approach are discussed in [4].

This paper is interested in biologically inspired computing, a branch of natural computing which develops algorithms inspired by nature to solve highly complex problems, in particular the problems that cannot be addressed in a satisfactory way by a traditional approach. Under this paradigm, algorithmic models of processes observed in nature are developed and implemented to explore solution spaces. There is a growing interest in bio-inspired algorithms, and the representatives of this trend have been applied to a large variety of problems, including optimization problems.

## 3 Evolutionary Intelligence

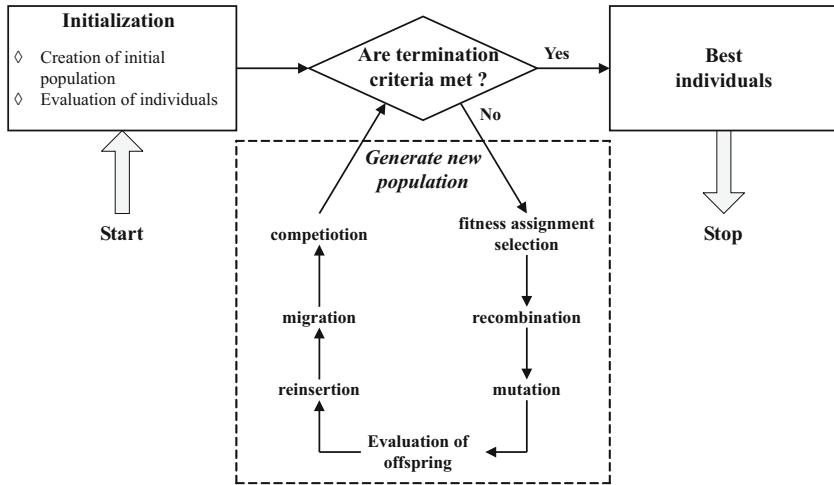
Evolutionary algorithms are modern techniques for searching complex space for an optimum. These meta-heuristics can be differentiated into a quite large set of algorithmic families representing bio-inspired system, which mimic natural evolution. The term “evolutionary” can be used in this case because their basic behavior is drawn from nature and evolution is the basic natural force driving a population of tentative solutions towards the problem regions where the optimal solutions are located.

Evolutionary algorithms have become the method of choice for optimization problems that are too complex to be solved using deterministic techniques such as linear programming. However, most real-world problems involve simultaneous optimization of several mutually concurrent objectives. Multi-objective evolutionary algorithms are able to find optimal trade-offs in order to get a set of solutions that are optimal in an overall sense.

Evolutionary algorithms model natural processes, such as selection, recombination, mutation, migration, locality and neighborhood. Basic structure of a

simple evolutionary algorithm is presented in [5]. Evolutionary algorithms work on populations of individuals instead of single solutions. In this way the search is performed in a parallel manner.

Nevertheless, better results can be obtained by introducing multiple subpopulations. Every subpopulation evolves over a few generations isolated before one or more individuals are exchanged between the subpopulation.



**Fig. 1.** Structure of an extended multi-population evolutionary algorithm (Source [5], p.33)

Multi-population evolutionary algorithm models the evolution of a species in a way more similar to nature than single population evolutionary algorithm. The structure of such an extended multi-population evolutionary algorithm is presented in Fig. 1.

### 4 Hybrid Evolutionary Models

The hybridization of intelligent techniques, draws from different areas of computational intelligence, and has become prevalent because of the growing awareness that they outperform individual computational intelligence techniques. In a hybrid intelligence system, a synergy combination of multiple techniques is used to build an efficient solution to deal with a particular problem [6].

An increasing number of bio-inspired algorithms do not rely on a single search strategy but rather combine various algorithmic ideas. These approaches are referred to as hybrids. The motivation behind hybrids is usually to exploit the strengths of number of individual search strategies in order to obtain a more powerful problem-solving approach.

#### 4.1 Hedge-Based Stochastic Inventory Routing System

This is one of the few studies that use coordinated replenishment policies when both inventory and transportation costs are considered in a supply chain under stochastic demand. A hedge-based stochastic inventory routing system (HSIRS), which is able to deal with multi-product, multi-period replenishment policies with limited vehicle capacity and time window constraints is proposed [7]. There are three goals that should be achieved simultaneously to maximize the net present value or minimize the total cost in this two-echelon food supply chain.

The main concepts of proposed hedge risks in stochastic inventory routing problem (HSIRS) are depicted in (Fig. 2). They could be presented as:

1. First, it is necessary to establish a forecasting model which can effectively deal with the demand heteroskedasticity in a given planning horizon.
2. Second, from the hedge point of view, the inventory portfolio policy can be generated through hedging with Forward Option Pricing Model to maximize the total Net Present Value.
3. Finally, through optimizing delivery schedule, the transportation policy can be generated and solved by Predicting Particle Swarm Optimization (Predicting PSO) algorithm to minimize the total transportation costs.

In order to successfully generate an optimum short-term multi-product replenishment policy based on the long-term effect to maximize NPV for each customer service/store, the objective function, should further be improved to consider the impact of transportation costs and the impact of emergency delivery costs on inventory replenishment policy in the following way: Considered coordinated replenishment and shipment in distribution systems based on both inventory hedge and optimization routing assignment.

The first goal of this research is to minimize demand volatility through Generalized Autoregressive Conditional Heteroskedasticity (GARCH) model forecasting, and the second goal is to generate an optimum short-term multi-product replenishment policy based on the long-term effect to maximize NPV for each customer. Followed by the third goal which is to minimize the total transportation costs incurred in a given planning time horizon. In cases when the planned transport and delivery time is short for the customers, the target customer group is dynamically selected depending on the time of the delivery the customers themselves chose, which differs from other target customer group selection methods which are usually based on division by location of the customer. As the target group has determined with their portfolio ordering policies, the routing and assignment policy can be optimized through Predicting PSO algorithm. As a result, the HSIRS can be generated to deal with a multi-product multi-period stochastic inventory routing problem with capacitated and time window constraints. In the end, the following contributions are considered to be an outcome:



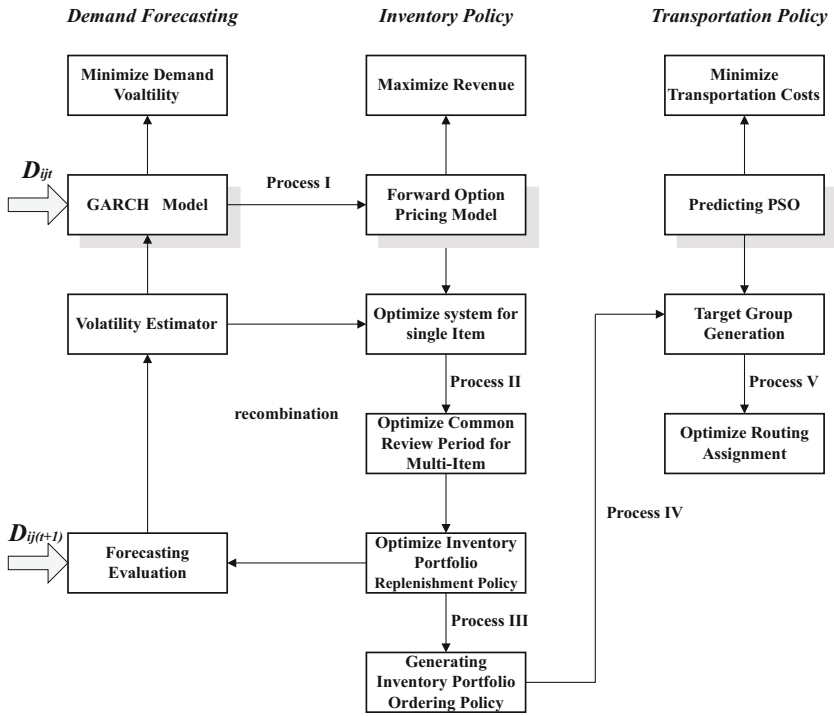


Fig. 2. Hedge-based stochastic inventory-routing system (Source [7], p.1100)

- From the hedge point of view the inventory policy is an asset investment, the GARCH model and Forward Option Pricing Model to hedge demand volatility with maximal net present value successfully integrated.
- An optimal portfolio system can be generated to maximize the net present value under an acceptable service level in a given planning horizon.
- Multiplier system can be generated to further reduce the shortage risks through raising the hedge.
- A target customer group is partitioned to generate the transportation policy at the transportation date.
- Successfully apply the Predicting Particle Swarm Optimization algorithm to solve the VRPTW which is a typically combinatorial problem.

#### 4.2 Simultaneous Delivery and Pickup Problems with Time Window

The customers who require both forward supply service and reverse recycling service within a certain period of time is faced with the problem how to send out a fleet of capacitated vehicles, stationed at a distribution center (DC) to meet the requests with the minimum number of vehicles and minimal transport costs. The greater the number of vehicles, the less the travel costs, therefore,

trade-offs between these two kinds of costs needed to be considered. Based on the simultaneous delivery and pick-up activities of a vehicle, all vehicles should return to the collection center (CC) in order to unload the recycled material. In order to simplify the problem, the distribution center is the same as the collection center.

The traditional design of a genetic algorithm (GA) faced the dilemma of converging too quickly with non-acceptable local optima or converging too slowly

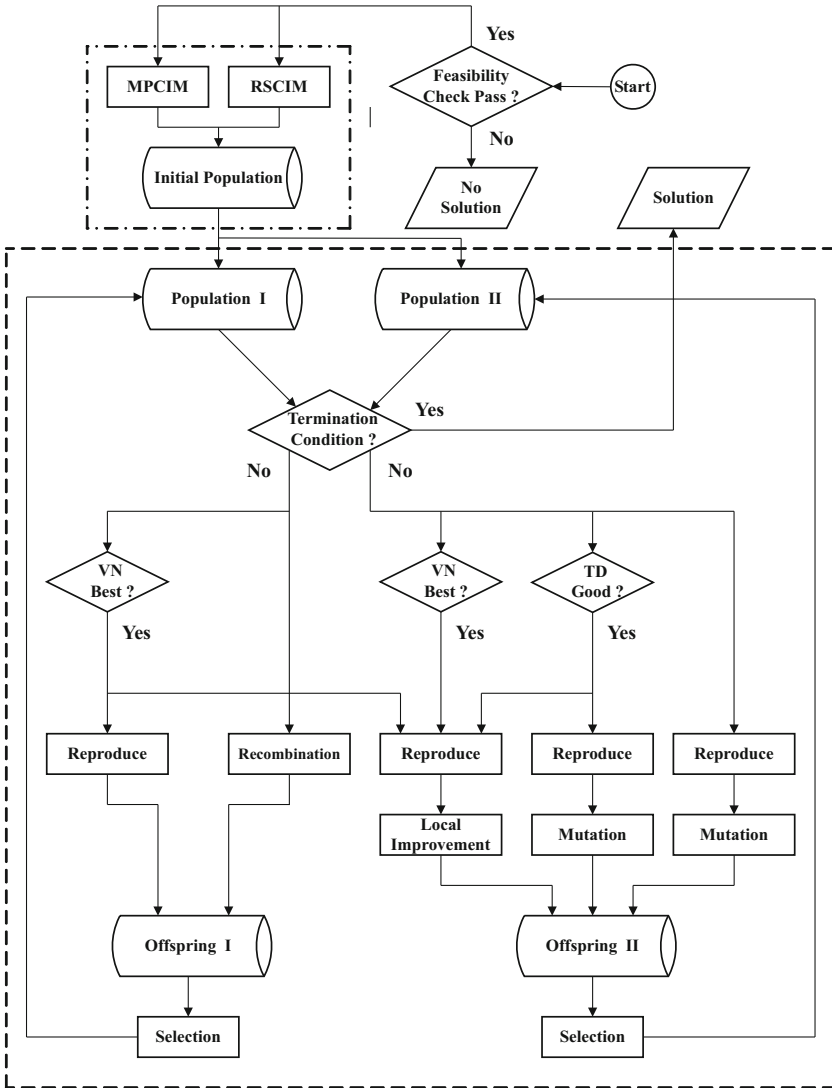


Fig. 3. The framework of the proposed co-evolution genetic algorithm (Source [8], p.87)

and result-ing in exhausting time consumption for deriving an acceptable solution. A co-evolution genetic algorithm [8] was proposed to avoid any of the above mentioned situations. Two simple heuristics (multi-parameter cheapest insertion method - MPCIM, resource service composite modes - RSCIM) used for generating initial population. Based on the framework shown in (Fig. 3), the GA employs two populations for two respective purposes: diversification and intensification.

*Population I* aims to retain the wide searching ability of the proposed GA through three operators: reproducing, recombination and selection, while *population II* aims to reach high quality solutions quickly and improve them continuously through four operators: reproducing, local improvement, crossover, mutation, and selection. In both populations,  $N$  parents generate  $2N$  offspring and then  $2N$  offspring compete with each other for only  $N$  to survive as the parents of the next generation. High class parents include the best individuals of both *population I* and *population II*, plus some good individuals of *population II*.

Instead of using the objective function as a fitness function, the fitness is related to total travel distance and total travel cost. This is motivated by the fact that better individuals are more easily evolved from the ones with the lower total travel distance (TD) than the ones with the lower number of vehicles (NV). The fitness values of the individuals with the minimal TD and the maximal TD are set to be  $4N$  and  $2N + 1$ , respectively. This implies that the individual with the minimal TD has about double probability to be reproduced in comparison to the one with the maximal TD. The fitness is defined as shown below:  $\text{Pr}(\text{individual } k \text{ to be reproduced}) = \text{fitness}/\text{total fitness}$ .

This system is tested and compared with the commercial linear programming software, like ILOG Cplex. Data sets are used from Solomon's vehicle routing problem with time window benchmarks, three 10-customer problems, three 25-customer problems, and three 50-customer problems were revised from Solomon's [9]. These nine small-scale problems were solved by Cplex and the proposed co-evolutionary GA.

### 4.3 Discussion

The first optimization inventory routing module uses a sophisticated Lagrangian relaxation algorithm to solve mixed integer programs with up to 800,000 variables and 200,000 constraints to near optimality. The system, first implemented in October, 1981, has been saving 6% to 10% of total operating costs [2].

The commercial linear programming software could find optimum solutions for the small-scale data set and hence can be used to evaluate the accuracy of the proposed model. It is shown that Cplex is only able to solve five problems optimum, but not more. For those five problems, the proposed co-evolutionary GA is [8] could get their optimum solutions within much shorter time frame (1 ~ 23s). For the other four problems the values with Cplex are poor. Co-evolutionary GA's solutions are much better than Cplex's best solutions, which are presented in more detail in [8].

It can be concluded that complex optimization problems such as inventory routing problem cannot be solved in a satisfactory way with a single artificial intelligence technique nor with a single artificial neural network (ANN). These complex NP-hard problems can successfully be solved to obtain power extension of these hybrid approaches as well as ANN, GA, Tabu Search, Simulated Annealing or hybrid bio-inspired methods and evolutionary algorithms which is discussed in [10].

## 5 Conclusion and Future Work

Due to the NP-hard nature of the inventory routing problem, the paper shows very short review which presents advantage of evolutionary approach in real-world problems. Typical illustration is addressed for evolutionary algorithms, genetic algorithms, predicting particle swarm optimization algorithm, co-evolutionary GA and GARCH model based to solve the multi-product multi-period inventory routing problem with stochastic demand.

It is clear that evolutionary algorithms and their hybrids solutions have shown the best performance up to now. Over the last decade, evolutionary approaches have experienced a rapid growth and have successfully been applied to the design and optimization of highly complex systems such as inventory routing and logistics distribution systems. Finally, hybrid systems for inventory routing problems are not yet mature fields of research and these approaches certainly show great promise for the future work.

**Acknowledgments.** The authors acknowledge the support for research project TR 36030, funded by the Ministry of Science and Technological Development of Serbia.

## References

1. Moin, N.H., Salhi, S.: Inventory Routing Problems: A Logistical Overview. *Journal of the Operational Research Society* 58(9), 1185–1194 (2007)
2. Bell, W.J.L., Dalberto, M., Fisher, M.L., Greenfield, A.J., Jaikumar, R., Kedia, P., Mack, R.G.: Improving the Distribution of Industrial Gases with an On-line Computerized Routing and Scheduling Optimizer. *Interfaces* 13(6), 4–23 (1983)
3. Archetti, C., Bertazzi, L., Laporte, G., Speranza, M.G.: A Branch-and-cut Algorithm for a Vendor Managed Inventory Routing Problem. *Transportation Science* 41(3), 382–391 (2007)
4. Simić, D., Simić, S.: Hybrid Artificial Intelligence Approaches on Vehicle Routing Problem in Logistics Distribution. In: Corchado, E., Snášel, V., Abraham, A., Woźniak, M., Graña, M., Cho, S.-B. (eds.) HAIS 2012, Part III. LNCS, vol. 7208, pp. 208–220. Springer, Heidelberg (2012)
5. Sumathi, S., Hamsapriya, T., Surekha, P.: *Evolutionary Intelligence*. Springer, Heidelberg (2008)
6. Corchado, E., Abraham, A., de Carvalho, A.: *Hybrid Intelligent Algorithms and Applications*. *Information Science* 180(14), 2633–2634 (2010)

7. Chen, Y.M., Lin, C.T.: A Coordinated Approach to Hedge the Risks in Stochastic Inventory-routing Problem. *Computers & Industrial Engineering* 56, 1095–1112 (2009)
8. Wang, H.F., Chen, Y.Y.: A genetic algorithm for the simultaneous delivery and pickup problems with time window. *Computers & Industrial Engineering* 62, 84–95 (2012)
9. Solomon, M.M.: Algorithms for the vehicle routing and scheduling problems with time window constraints. *Operations Research* 35(2), 254–265 (1987)
10. Pham, D.T., Karaboga, D.: *Intelligent Optimisation Techniques: Genetic Algorithms, Tabu Search, Simulated Annealing and Neural Networks*. Springer, Heidelberg (2011)

# BCI-Based Navigation in Virtual and Real Environments

Francisco Velasco-Alvarez<sup>1</sup>, Ricardo Ron-Angevin<sup>1</sup>,  
and Miguel Angel Lopez-Gordo<sup>2</sup>

<sup>1</sup>Dept. of Electronics Technology, E.T.S.I. Telecomunicación, University of Málaga,  
Campus Universitario de Teatinos, 29071, Málaga, Spain  
{fvelasco, rra}@dte.uma.es

<sup>2</sup>Dept. of Systems and Automatic Engineering,  
Electronic and Architecture of Computers and Networks, E. Superior de Ingeniería,  
University of Cádiz, c/ Chile 1, 11002 Cádiz, Spain  
miguel.lopez@uca.es

**Abstract.** A Brain-Computer Interface (BCI) is a system that enables people to control an external device with their brain activity, without the need of any muscular activity. Researchers in the BCI field aim to develop applications to improve the quality of life of severely disabled patients, for whom a BCI can be a useful channel for interaction with their environment. Some of these systems are intended to control a mobile device (e. g. a wheelchair). Virtual Reality is a powerful tool that can provide the subjects with an opportunity to train and to test different applications in a safe environment. This technical review will focus on systems aimed at navigation, both in virtual and real environments.

**Keywords:** Brain-computer interface (BCI), virtual environment (VE), navigation, asynchronous, motor imagery (MI), mental tasks.

## 1 Introduction

A Brain-Computer Interface (BCI) is a system that enables a communication not based on muscular movements but on brain activity. Several methods are used to detect brain activity, some of them by using electrodes implanted in the brain or cortex. However, the most frequently used methods are those in which the recording of the signals is obtained through ‘non-invasive’ means, i.e., the electrodes are not implanted in the brain but placed superficially on the scalp. The brain signals obtained through these methods are called Electroencephalographic (EEG) signals. Several kinds of EEG signals can be detected, resulting in different types of BCIs. Some of them analyze the brain’s response to given stimuli; those are the BCIs based on ‘Event Related Potentials’ (ERPs) [1] and their steady-state versions, in both the visual [2] and the auditory [3] modalities. Other systems process the EEG resulting from voluntary thoughts; among those, the most used are the BCIs based on ‘Sensorimotor Rhythms’ (SMR). These rhythms are specific EEG signals characterised by its frequencies. The main objective of research in the BCI field is to provide disabled people with an alternative communication channel, not based on muscular activity. Due

to different causes, such as Amyotrophic Lateral Sclerosis (ALS), brain paralysis or several brain damages, people can arrive in a state in which they lose their motor capability (usually the control of the eyes remains) but they retain their sensory and cognitive skills. This is the so-called 'locked-in state' (LIS). If all muscular control is lost, then this state is referred to as 'complete locked-in state' (CLIS). Current research is unable to conclude whether or not, in such a state, cognitive skills remain present [4].

Researchers in this field endeavour to develop different applications that can improve the quality of life of these patients establishing alternative communication channels. Research studies have been developed in several areas, such as those dedicated to provide amputee patients with neuroprosthesis movement [5], speller devices [6], 'smart home' control applications [7], EEG-controlled Web browsers [8], training [9] or systems focused on the control of a mobile device (such as a wheelchair). Among the latter, some systems allow subjects to control a real wheelchair in an experimental scenario [10], or a small robot in a real environment that simulates a house [11]. However, in most studies, the subjects participate in experiments with a simulated wheelchair in a Virtual Environment (VE). The objective of this paper is to review the BCI systems aimed at navigation, both in virtual and real environments.

## 2 BCI and Virtual Reality

Before people can use a wheelchair in a real environment, it is necessary to guarantee that they have enough control to avoid dangerous situations. Virtual Reality (VR) is a powerful tool for providing subjects with the opportunity to train with and to test an application in a safe environment. Another advantage of navigating through a VE is that every detail on the environment is under control, so the experiments can be carried out in many different situations and can provide much information on multiple aspects of subjects' performance. On the other hand, VR is used too in order to get a highly immersive scenario that can affect to the results. Regarding the training process, Pineda [12] cites several factors that can enhance learning in a BCI: i) the subject's active engagement, ii) frequent interaction with the environment, iii) feedback presence and iv) existence of links to real world context. VR encourages subjects to be motivated, it allows a suitable interaction, it can provide many kinds of feedback and it can reproduce real world environments. Some examples of BCIs using VR for reasons other than navigation are given in the following.

In [13], a virtual arm appears in a screen placed next to where the subject's real arm is. The representation of movement of the virtual limb is called 'bio-feedback'. In [14], a different kind of feedback is given; a brain is shown on a screen so that the subjects can see their own brain activity. In the same work, two VR BCI-games are presented, one using MI to make a spaceship levitate and the other using Steady-State Visual Evoked Potentials (SSVEP) to keep an avatar balanced. The training performance of a system using classic feedback and another using VR are compared in [15]; the conclusion is that VR enhances performance. The work in [12] uses SMR to make an avatar turn right or left in a video game, whilst other movements are controlled via a keyboard. The popular game World of Warcraft has been adapted to be controlled via a BCI system [16].

### 3 Navigation in Virtual Environments

Early BCI systems aimed at navigation were usually system-paced or asynchronous. In those systems, the subject moved through the VE to fixed locations (determined by the system) and then he was asked to select a new movement. The system showed some kind of signal to cue subjects when the action could take place. Most recent applications let subjects to control the timing of the interaction. These systems are called self-paced or asynchronous. One main advantage of the asynchronous systems is that the freedom to move is usually higher, as subjects do not need only to move among specific locations, but they move freely through the VE.

#### 3.1 Synchronous Systems

Among the synchronous systems, Friedman [17] focuses on the experience of the navigation in highly immersive environments (using a Cave Automatic Virtual Environment, CAVE). Subjects carried out two experiments using two mental tasks: they changed their point of view in a virtual bar; or they moved forward in a virtual street.

A similar experiment is presented in [18]; a navigation paradigm with two mental tasks to move through fixed paths in a virtual apartment is proposed. The right or left hand motor imagery (MI) enabled subjects to select two different commands at each junction, out of three possible commands: turn right or left and move forward.

In [19], subjects moved right or left in a virtual street with both hands MI tasks.

Another work that used SMR to navigate is [20], where subjects performed one MI task to extend a rotating bar that pointed to four possible commands in order to select them; two mental tasks are mapped this way into four navigation commands.

Bayliss in [21] randomly flashed several elements in a virtual apartment, thus evoking the P300 potential in the well-known oddball paradigm (necessarily synchronous). After the selection, an avatar moved towards the object and interacted with it.

The work in [22] used the P300 to compare three different navigation paradigms: i) by means of flashes over the objects, ii) selecting positions of a matrix superimposed to the VE, and iii) selecting ‘tiles’ of a virtual image (square sections of a screen).

In [23], a comparison was established between a BCI-based and a gaze-controlled navigation system, using a screen to project the VE and another one to provide subjects with a command matrix.

Chung [24] describes a SSVEP-based system that allowed subjects to generate low-level commands, but it registered the sequences of these basic commands in order to provide subject-dependant high-level commands.

Finally, Faller [25] presents another SSVEP-based system with three stimuli that subjects used to move with low-level commands in a virtual apartment or in a slalom test avoiding obstacles.

#### 3.2 Asynchronous Systems

Self-paced systems are usually more versatile because the subjects control the timing of the interaction. However, they may be more difficult to control because they need



to support two states: i) one in which subjects do not generate control commands over the system, Non-Control (NC) state; and ii) an Intentional Control (IC) state where they execute control over the system.

As these systems are asynchronous, they mostly use endogenous signals, because these signals let the subjects switch between the two states without the need to wait for an indication from the system. Usually, these systems rely on SMR mental tasks.

The simplest systems to control are those that use only two mental classes. This can be because they only have one active mental task classified versus 'rest', so they only move in one possible direction. Some examples are the works of Leeb [26, 27], where subjects performed feet MI in order to advance in different VE.

By using more tasks, a more versatile system can be achieved; it is the case of [28], in which the classification of left and right hand MI is used to turn an avatar in a VE, and the real movement of the feet is used to move forward.

The same simple classification (both hands MI) has been used in [29] to move through a grid of hexagons. After each turn command, the system forced an advance in the pointed direction. The change between the NC and IC states is achieved by using the parameters 'dwell time' and 'refractory time', when the brain activity must be kept above (or under) certain threshold in order to switch the state.

The work presented in [30] does not use VR techniques, but it shows the blueprint of an apartment. This experiment used three MI tasks: right or left hand MI made an avatar turn both sides, while feet MI made it advance. The switch from the NC to the IC state was achieved with the feet MI task. After that, subjects could choose a turn command. After the turn, the system changed back to the NC state and the avatar started moving in the pointed direction; this movement was kept until subjects stopped it with the feet MI task (which made the system change again to the IC state).

Three mental tasks were used by the Graz group in [31]. In the latter study, both hands and feet MI made an avatar turn and move forward in a virtual park. Subjects switched from the NC to the IC state when one of the three MI tasks was detected.

Three classes were also used in [10], which included some intelligence in the system, providing high-level commands. The executed action after the selection of a command was determined by the knowledge that the system had of the environment, so it 'modulated' the subject intention making the more appropriate movement.

One more work that classifies three MI classes is [32]; MI tasks are not directly interpreted as navigation commands but they are used to move through a decision tree in order to choose among several high level options.

The UMA-BCI group (University of Malaga) continued with the work started in [20], changing the system so it supported the NC and IC states [33]. The use of one hand MI in a NC interface made the system change from the NC to the IC state, and then, with the same MI task subjects could select among three navigation commands that were sequentially pointed by a rotating bar. The selection of a command involved a discrete movement.

On a later experiment [34], the same navigation paradigm was used to provide continuous movements: after the selection of a command the movement was kept while the MI task was above certain threshold.

Finally, a new version of the same paradigm was proposed in [35], in which the visual interface was replaced by auditory cues.

## 4 Navigation in Real Environments

Some the works involving BCIs and robots are preliminary studies preceding the use of the system in a real wheelchair, whereas others are robot-oriented applications in which the robot can complete different actions, not just move in the environment.

### 4.1 Robots

ERP potentials are often used in this kind of system, like [36], where the user watched a screen with the subjective vision of the robot in the environment. Some items were superimposed in the image, which could be selected through an oddball paradigm. These items represented the discrete possibilities of movement.

A similar paradigm, but based on SSVEP potentials is used in [37] to control a car equipped with a video camera.

Some applications let subjects control a robot to perform specific actions, not to move freely in the environment. That is the case of [38], where ERP potentials were used to control a robot that manipulated different objects.

The system in [39] maps two MI tasks into three navigation commands: subjects generated different patterns of MI tasks that corresponded to the three commands.

Three MI tasks are used in [40] to move a humanoid robot in a labyrinth.

Another study that uses MI task is [41]; four MI tasks made the robot move forward, stop, turn right and turn left with discrete movements.

In [42], the same paradigm used in [35] (first visual and then auditory) provided four commands to move a robot in a small maze of corridors with both discrete and continuous movements.

Some experiments are based on high-level commands, letting the system move with intelligence to better perform the action, depending on the specific scenario. In [43], subjects used three mental tasks to select six potential commands. The mapping from three tasks into six commands was achieved through a 'finite state machine'.

Halfway between the low and the high-level commands are the hybrid systems that can adapt their commands. An example is [44], where subjects started performing low-level actions through SSVEP. Once a series of commands had been validated, it was included as a high-level action.

### 4.2 Wheelchairs

Most part of the systems controlling a wheelchair keep the use of-high level commands with some intelligence applied to the wheelchair.

The IDIAP group continued using the paradigm mentioned before [43] to control a real wheelchair. In [45] the probabilities that a command had to be selected depended not only on subjects intention (through SMR-related tasks) but also on the position of the wheelchair regarding obstacles, enabling a 'shared' control.

Another work that uses MI, but with low-level commands is [46]. Three MI tasks moved the wheelchair forward or made it turn. However, this is a hybrid systems because it relied on the actual movement of the cheek for the stop command.

The system presented in [47] is hybrid too: both hands MI tasks were used to make the wheelchair turn, feet MI to make the advance movement slower, and the potential P300 to accelerate.

The group from the University of Zaragoza used the same paradigm described in [36] to control an intelligent wheelchair [48]: with the potential P300 subjects selected fixed positions from a tri-dimensional reconstruction of the real environment.

The P300 is used in [49] to select different objectives pre-known by the system.

The study in [50] describes a SSVEP-controlled wheelchair with four possible low-level commands.

Four commands are used too in [51], but the control is achieved with P300.

Finally, the work of [52] will be mentioned here. This system is hybrid, providing subjects with high-level commands that could be replaced by low-level commands in case the subjects wanted to assume the control in a specific situation.

## 5 Summary

Several navigation systems have been mentioned, whose characteristics will be briefly described next.

Regarding two classifications, there are endogenous and exogenous systems, as well as synchronous and asynchronous. The endogenous and asynchronous systems are those that better fit the control model of a navigation device, as subjects execute the control in a direct way (because of being endogenous) and they can do it at any moment they want (because of being asynchronous).

The mentioned systems use high-level commands ('Go straight and turn right on the next corner' or 'go to the kitchen', for example) and low-level commands ('turn left'). The first are easier to control because subjects do not need to indicate every single movement. On the other hand, the systems based on low-level commands allow users to move with more autonomy, because they can go to any point in the environment, without the limitation of moving among pre-defined locations. Adaptive systems use low-level and high-level commands in different situations.

The more versatile systems are those that provide subjects with more navigation commands. Those cases in which subjects can only move in one direction ('forward') or are controlled with only two commands ('turn left and turn right') provide subjects with little range of action. Systems with three or more commands use to bind the number of commands with the number of mental tasks used to control them. However, as deduced from [53, 54], an increase on the number of mental tasks can reduce the classification accuracy. On the other hand, some systems use less mental tasks to control a device with a higher number of commands (through a mapping of some mental tasks into more commands at the cost of a slower control).

The research in this field is relatively recent; however, the current works show the interest of the different groups, who keep achieving promising results.

**Acknowledgements.** This work was partially supported by the Innovation, Science and Enterprise Council of the Junta de Andalucía (Spain), project P07-TIC-03310, the Spanish Ministry of Science and Innovation, project TEC 2011-26395 and by the European fund ERDF.

## References

1. Kübler, A., Müller, K.R.: An introduction to brain-computer interfacing. In: Dornhege, G., Millán, J.D.R., Hinterberger, T., McFarland, D.J., Müller, K.R. (eds.) *Toward Brain-Computer Interfacing*, G, pp. 1–25. MIT Press, Cambridge (2007)
2. Lopez-Gordo, M.A., Prieto, A., Pelayo, F., Morillas, C.: Use of Phase in Brain-Computer Interfaces based on Steady-State Visual Evoked Potentials. *Neural Process Lett.* 32(1), 1–9 (2010)
3. Lopez-Gordo, M.A., Fernandez, E., Romero, S., Pelayo, F., Prieto, A.: An auditory brain-computer interface evoked by natural speech. *J. Neural Eng.* 9(3), 1–9 (2012)
4. Kübler, A., Nijboer, F., Birbaumer, N.: Brain-computer interfaces for communication and motor control- perspectives on clinical applications. In: Dornhege, G., Millán, J.D.R., Hinterberger, T., McFarland, D.J., Müller, K.R. (eds.) *Toward Brain-Computer Interfacing*, pp. 373–391. MIT Press, Cambridge (2007)
5. Pfurtscheller, G., Müller, G.R., Pfurtscheller, J., Gerner, H.J., Rupp, R.: ‘Thought’-control of functional electrical stimulation to restore hand grasp in a patient with tetraplegia. *Neurosci. Lett.* 351(1), 33–36 (2003)
6. Blankertz, B., Dornhege, G., Krauledat, M., et al.: The Berlin brain-computer interface presents the novel mental typewriter hex-o-spell. In: *Proceedings of the 3rd International Brain-Computer Interface Workshop and Training Course*, Graz, pp. 108–109 (2006)
7. Guger, C., Holzner, C., Grönegree, C., Edlinger, G., Slater, M.: Control of a smart home with a brain-computer interface. In: *Proceedings of the 4th International Brain-Computer Interface Workshop and Training Course*, Graz, pp. 339–342 (2008)
8. Bensch, M., Karim, A.A., Mellinger, J., Hinterberger, T., Tangermann, M., Bogdan, M., Rosenstiel, W., Birbaumer, N.: Nessi: An EEG-controlled web browser for severely paralyzed patients. *Computational Intelligence and Neuroscience* (2007)
9. Ron-Angevin, R., Lopez, M.A., Pelayo, F.: The Training Issue in Brain-Computer Interface: A Multi-disciplinary Field. In: Cabestany, J., Sandoval, F., Prieto, A., Corchado, J.M. (eds.) *IWANN 2009, Part I. LNCS*, vol. 5517, pp. 666–673. Springer, Heidelberg (2009)
10. Galán, F., Nuttin, M., Lew, E., Ferrez, P.W., Vanacker, G., Philips, J., Millán, J.D.R.: A brain-actuated wheelchair: Asynchronous and non-invasive brain-computer interfaces for continuous control of robots. *Clinical Neurophysiology* 119(9), 2159–2169 (2008)
11. Millán, J.D.R., Renkens, F., Mouriño, J., Gerstner, W.: Noninvasive brain-actuated control of a mobile robot by human EEG. *IEEE Trans. Biomed. Eng.* 51(6), 1026–1033 (2004)
12. Pineda, J.A., Silverman, D.S., Vankov, A., Hestenes, J.: Learning to control brain rhythms: Making a brain-computer interface possible. *IEEE Transactions on Neural Systems and Rehabilitation Engineering* 11(2), 181–184 (2003)
13. Krepki, R., Curio, G., Blankertz, B., Müller, K.-R.: Berlin brain-computer interface-the HCI communication channel for discovery. *International Journal of Human Computer Studies* 65(5), 460–477 (2007)
14. Lécuyer, A., Lotte, F., Reilly, R.B., Leeb, R., Hirose, M., Slater, M.: Brain-computer interfaces, virtual reality, and videogames. *Computer* 41(10), 66–72 (2008)
15. Ron-Angevin, R., Díaz-Estrella, A.: Brain-computer interface: Changes in performance using virtual reality techniques. *Neurosci. Lett.* 449(2), 123–127 (2009)
16. Scherer, R., Friedrich, E.C.V., Allison, B., Pröll, M., Chung, M., Cheung, W., Rao, R.P.N., Neuper, C.: Non-invasive brain-computer interfaces: Enhanced gaming and robotic control. In: Cabestany, J., Rojas, I., Joya, G. (eds.) *IWANN 2011, Part I. LNCS*, vol. 6691, pp. 362–369. Springer, Heidelberg (2011)

17. Friedman, D., Leeb, R., Guger, C., Steed, A., Pfurtscheller, G., Slater, M.: Navigating virtual reality by thought: What is it like? *Presence-Teleop. Virt.* 16(1), 100–110 (2007)
18. Leeb, R., Lee, F., Keinrath, C., Scherer, R., Bischof, H., Pfurtscheller, G.: Brain-computer communication: Motivation, aim, and impact of exploring a virtual apartment. *IEEE Trans. Neural Syst. Rehabil. Eng.* 15(4), 473–482 (2007)
19. Fujisawa, J., Touyama, H., Hirose, M.: EEG-based navigation of immersing virtual environment using common spatial patterns. In: *Proceedings - IEEE Virtual Reality (2008)*
20. Ron-Angevin, R., Díaz-Estrella, A., Velasco-Álvarez, F.: A two-class brain computer interface to freely navigate through virtual worlds. *Biomed. Tech.* 54(3), 126–133 (2009)
21. Bayliss, J.D.: Use of the evoked potential P3 component for control in a virtual apartment. *IEEE Trans. Neural Syst. Rehabil. Eng.* 11(2), 113–116 (2003)
22. Donnerer, M., Steed, A.: Using a P300 brain-computer interface in an immersive virtual environment. *Presence-Teleop. Virt.* 19(1), 12–24 (2010)
23. Groenegrass, C., Holzner, C., Guger, C., Slater, M.: Effects of P300-based BCI use on reported presence in a virtual environment. *Presence-Teleop. Virt.* 19(1), 1–11 (2010)
24. Chung, M., Cheung, W., Scherer, R., Rao, R.P.N.: Towards hierarchical BCIs for robotic control. In: *5th International IEEE/EMBS Conference (2011)*
25. Faller, J., Müller-Putz, G., Schmalstieg, D., Pfurtscheller, G.: An application framework for controlling an avatar in a desktop-based virtual environment via a software SSVEP brain-computer interface. *Presence-Teleop. Virt.* 19(1), 25–34 (2010)
26. Leeb, R., Settgast, V., Fellner, D., Pfurtscheller, G.: Self-paced exploration of the Austrian National Library through thought, *Int. J. Bioelectromagnetism* 9, 237–244 (2007)
27. Leeb, R., Friedman, D., Müller-Putz, G.R., Scherer, R., Slater, M., Pfurtscheller, G.: Self-paced (asynchronous) BCI control of a wheelchair in virtual environments: A case study with a tetraplegic. *Computational Intelligence and Neuroscience (2007)*
28. Suh, D., Cho, H.S., Goo, J., Park, K.S., Hahn, M.: Virtual navigation system for the disabled by motor imagery. In: Elleithy, K. (ed.) *Advances in Computer, Information, and Systems Sciences, and Engineering (2006)*
29. Tsui, C.S.L., Gan, J.Q.: Asynchronous BCI control of a robot simulator with supervised online training. In: Yin, H., Tino, P., Corchado, E., Byrne, W., Yao, X. (eds.) *IDEAL 2007. LNCS, vol. 4881, pp. 125–134. Springer, Heidelberg (2007)*
30. Geng, T., Dyson, M., Tsui, C.S., Gan, J.Q.: A 3-class asynchronous BCI controlling a simulated mobile robot. In: *Int. Conf. IEEE Eng. in Med. and Biol. Society, pp. 2524–2527 (2007)*
31. Scherer, R., Lee, F., Schlögl, A., Leeb, R., Bischof, H., Pfurtscheller, G.: Toward self-paced brain-computer communication: Navigation through virtual worlds. *IEEE Trans. Biomed. Eng.* 55(2), 675–682 (2008)
32. Lotte, F., van Langenhove, A., Lamarche, F., Ernest, T., Renard, Y., Arnaldi, B., Lécuyer, A.: Exploring large virtual environments by thoughts using a brain-computer interface based on motor imagery and high-level commands. *Presence-Teleop. Virt.* 19(1), 54–70 (2010)
33. Velasco-Álvarez, F., Ron-Angevin, R.: Asynchronous brain-computer interface to navigate in virtual environments using one motor imagery. In: Cabestany, J., Sandoval, F., Prieto, A., Corchado, J.M. (eds.) *IWANN 2009, Part I. LNCS, vol. 5517, pp. 698–705. Springer, Heidelberg (2009)*
34. Velasco-Álvarez, F., Ron-Angevin, R., Da Silva-Sauer, L., Sancha-Ros, S.: Brain-computer interface: Comparison of two paradigms to freely navigate in a virtual environment through one mental task. In: *Int. Conf. on Broadband and Biomed. Comm., IB2Com (2010)*
35. Velasco-Álvarez, F., Ron-Angevin, R., Da Silva-Sauer, L., Sancha-Ros, S., Blanca-Mena, M.J.: Audio-cued SMR brain-computer interface to drive a virtual wheelchair. In: Cabestany, J., Rojas, I., Joya, G. (eds.) *IWANN 2011, Part I. LNCS, vol. 6691, pp. 337–344. Springer, Heidelberg (2011)*

36. Escolano, C., Antelis, J.M., Minguez, J.: A telepresence mobile robot controlled with a noninvasive brain-computer interface. *IEEE Trans. on Systems, Man, and Cybernetics, Part B: Cybernetics* 42(3), 793–804 (2012)
37. Chang, H., Deng, H., Lee, P., Wu, C., Shyu, K.: Real-time control of an SSVEP-actuated remote-controlled car. In: *SICE Annual Conference* (2010)
38. Bell, C.J., Shenoy, P., Chalodhorn, R., Rao, R.P.N.: Control of a humanoid robot by a non-invasive brain-computer interface in humans. *J. Neural Eng.* 5(2), 214–220 (2008)
39. Wu, L., Liao, H., Hu, J., Lo, P.: Brain-controlled robot agent: An EEG-based eRobot agent. *Ind. Robot.* 35(6), 507–519 (2008)
40. Chae, Y., Jeong, J., Jo, S.: Toward Brain-Actuated Humanoid Robots: Asynchronous Direct Control Using an EEG-Based BCI. *IEEE Trans. on Robotics* 99, 1–14 (2012)
41. Barbosa, A.O.G., Achancaray, D.R., Meggiolar, M.A.: Activation of a mobile robot through a brain computer interface. In: *IEEE Int. Conf. on Robotics and Automation* (2010)
42. Velasco-Álvarez, F., Ron-Angevin, R., Da Silva-Sauer, L., Sancha-Ros, S.: Audio-Cued Motor Imagery-Based Brain-Computer Interface: Navigation Through Virtual and Real Environments. *Neurocomputing* (in press 2013)
43. Millán, J.D.R., Renkens, F., Mouriño, J., Gerstner, W.: Brain-actuated interaction. *Artif. Intell.* 159(1-2), 241–259 (2004)
44. Bryan, M., Green, J., Chung, M., Chang, L., Scherert, R., Smith, J., Rao, R.P.N.: An adaptive brain-computer interface for humanoid robot control. In: *11th IEEE-RAS Int. Conf. on Humanoid Robots* (2011)
45. Vanacker, G., Del, J., Millán, R., Lew, E., Ferrez, P.W., Moles, F.G., Philips, J., Van Brussel, H., Nuttin, M.: Context-based filtering for assisted brain-actuated wheelchair driving. *Computational Intelligence and Neuroscience* (2007)
46. Choi, K., Cichocki, A.: Control of a wheelchair by motor imagery in real time. In: Fyfe, C., Kim, D., Lee, S.-Y., Yin, H. (eds.) *IDEAL 2008. LNCS*, vol. 5326, pp. 330–337. Springer, Heidelberg (2008)
47. Long, J., Li, Y., Wang, H., Yu, T., Pan, J., Li, F.: A hybrid brain computer interface to control the direction and speed of a simulated or real wheelchair. *IEEE Trans. on Neural Systems and Rehab. Eng.* 20(5), 720–729 (2012)
48. Iturrate, I., Antelis, J.M., Kübler, A., Minguez, J.: A noninvasive brain-actuated wheelchair based on a P300 neurophysiological protocol and automated navigation. *IEEE Trans. on Robotics* 25(3), 614–627 (2009)
49. Rebsamen, B., Guan, C., Zhang, H., Wang, C., Teo, C., Ang Jr., M.H., Burdet, E.: A brain controlled wheelchair to navigate in familiar environments. *IEEE Trans. Neural Syst. Rehabil. Eng.* 18(6), 590–598 (2010)
50. Muller, S.M.T., Bastos-Filho, T.F., Sarcinelli-Filho, M.: Using a SSVEP-BCI to command a robotic wheelchair. In: *IEEE Int. Symp. on Ind. Electronics* (2011)
51. Shin, B.-G., Kim, T., Jo, S.: Non-invasive brain signal interface for a wheelchair navigation. In: *Int. Conf. on Control Automation and Systems* (2010)
52. Lopes, A.C., Pires, G., Vaz, L., Nunes, U.: Wheelchair navigation assisted by human-machine shared-control and a P300-based brain computer interface. In: *Int. Conf. on Intelligent Robots and Systems* (2011)
53. Kronegg, J., Chanel, G., Voloshynovskiy, S., Pun, T.: EEG-based synchronized brain-computer interfaces: A model for optimizing the number of mental tasks. *IEEE Trans. Neural Syst. Rehabil. Eng.* 15(1), 50–58 (2007)
54. Obermaier, B., Neuper, C., Guger, C., Pfurtscheller, G.: Information transfer rate in a five-classes brain-computer interface. *IEEE Trans. Neural Syst. Rehabil. Eng.* 9(3), 283–288 (2001)

# A Motor Imagery Based Brain-Computer Interface Speller

Bin Xia, Jing Yang, Conghui Cheng, and Hong Xie

Electrical Engineering Department, Shanghai Maritime University, Shanghai, China  
binxia@shmtu.edu.cn

**Abstract.** Speller is an important application in brain-computer interface researching. In this study, we developed a novel motor imagery based brain-computer interface speller which integrates a 2-D cursor control strategy into a hex-o-spell paradigm to spell a character in two-step. The experimental results (five subjects participated) showed that the average spelling speed is 14.64 characters per minute and that its average information transfer rate is 73.96 bits per minute.

**Keywords:** Motor Imagery, Brain-Computer Interface, Speller.

## 1 Introduction

Brain-computer interface (BCI) system provides a communication channel between the brain and the external world by transforming neural activities into control commands without the participation of peripheral nerves and muscles [1, 2]. For people with severe motor disabilities, BCI help them to control external devices or communicate with other peoples.

The electroencephalogram (EEG) is widely used in BCI research because of its high temporal resolution and recorded easily from the surface of the scalp. BCIs are developed based on different neural activities, such as event related potentials, steady-state evoked potentials (SSVEP), event-related desynchronization/synchronization and slow cortical potentials [3, 4, 5, 6]. The BCI speller is a typical application that allows the paralyzed patients to communicate with the nurse or family. In 1988, Farwell *et al.* introduced the first P300 speller [7]. The classical P300 spelling system was composed of a 6\*6 letter matrix which includes 26 characters, 9 numbers and a SPACE symbol. The basic principle of P300 based BCI is to spell character by detecting the event related potentials with Oddball paradigm. In recent years, P300 spellers have been studied deeply in signal processing algorithm and paradigm design [8, 9].

Researchers also implemented BCI spellers based on SSVEP, but the SSVEP speller cannot provide specific command for each character like P300 based speller. The SSVEP based BCI can only produce several commands without external stimulus device due to the stimulus frequencies are limited by the refresh rates of the screen.

Cecotti developed a SSVEP speller with five stimuli, which include characters group or control command [10]. To spell a character, the user should focus on related stimuli three times. Volosyak *et al.* proposed screen based SSVEP speller with a virtual keyboard and five command stimuli [11]. The user uses five commands to move the cursor to select the character in virtual keyboard. The speeds of screen based SSVEP spellers are not satisfactory because they need several steps to spell a character with spending 4-6 s for each step. The SSVEP BCI also can provide more commands using external stimuli device. Hwang *et al.* developed a SSVEP speller by adopting a QWERTY-style LED keyboard with 30 flicking stimulus [12]. Its average speed is 9.39 letter per minute (LPM) and its average information transfer rate is 40.72 bits per minute. However, one disadvantage of the visual stimuli based speller (P300, SSVEP) is that the subjects will suffer visual fatigue with a long time staring on stimuli.

Motor imagery (MI) based BCI spellers, which normally can provide 3 or 4 commands, also need special designed interface like SSVEP speller. Sbattella developed a motor imagery based speller with language model [13]. The user can use four class motor imagery based BCI to choose a character from four groups. The language model will provide word suggestions and disabled importable character. The best performance of the subject is 3 LPM. The Berlin BCI research group has proposed a speller paradigm, called 'Hex-o-Spell', in which the subject can spell a letter using two-step in a hexagon interface [14]. This system is based on two-class motor imagery BCI, and its speed is between 4.6 and 7.6 LPM for most subjects. One advantage of the MI based speller is no visual stimuli, but the performances of published MI spellers are not comparable with visual stimuli based speller.

In this paper, we focused on motor imagery based speller. To improve the performance of BCI speller, we develop a 2-D cursor control strategy within modified Hex-o-Spell paradigm. Five subjects achieved good performance in online experiments.

## 2 Materials and Methods

### 2.1 2-D Control Paradigm

In our previous study [15], we presented a three-class (left hand, right hand and feet) motor imagery based BCI for 2-D cursor control strategy. The probability  $P_1$ ,  $P_2$ ,  $P_3$ , outputs of three classes Support Vector Machine classifier, are mapped to three vectors, as shown in Fig. 1.(a).  $P_1$  is the probability of the left hand imagery;  $P_2$  and  $P_3$  are the probabilities of the right hand and foot imagery respectively. The angle between two vectors is 120 degree and the norm of a vector is equal to the value of related probability. In the BCI application of 2-D control, vertical and horizontal movements are considered separately [16]. In our 2-D control strategy, the subject can combine two motor imagery tasks simultaneously to directly move the cursor to the target instead of considering horizontal and vertical movement as shown in Fig.1.(b).



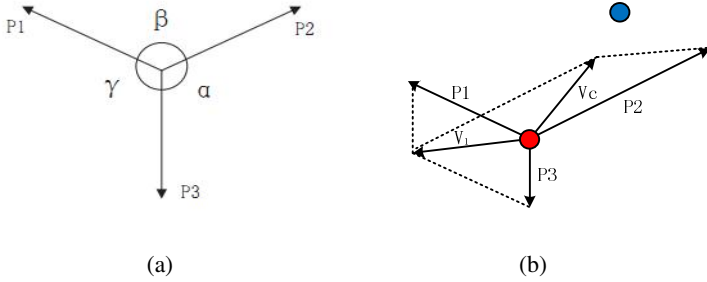


Fig. 1. The mapping of three predict probabilities

## 2.2 Hex-o-Spell Paradigm

**GUI Design.** We adopted a similar ‘Hex-o-Spell’ paradigm in [14], which consists of two-layer structure. In the first layer, 26 letters and 4 symbols (comma, period, space and delete) are divided into six blocks, which are ranged in clockwise (Fig 2.a). There are five letters and a target circle in each block in first five blocks. Block 6 is composed of Z, a target circle and four symbols. In the second layer, a letter/symbol and a target circle are included in each block (from block 1 to block 5) (Fig.2 b). One special command ‘Back’ is assigned in block 6. Each block of the first layer has a related second layer.

The monitor has a dimension of 1440\*838 pixels. The ratio of the size of cursor, target circle and the screen is 0.0003:0.0065:1.

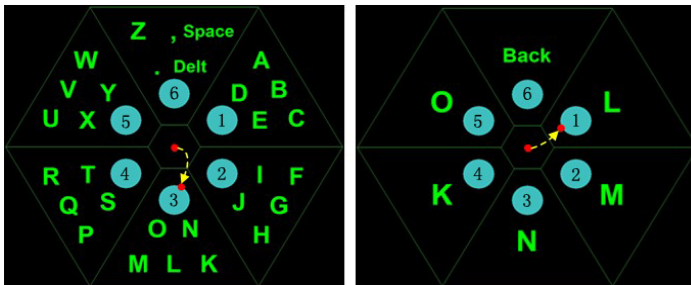


Fig. 2. 2-D cursor control based Hex-o-spell paradigm a. First layer b. Second layer

**Spell Paradigm.** In this paper, we designed a two-step spell paradigm. At the first step, the user can move cursor to reach the target circle of the block (containing the target character) in the first layer. Then the interface will extend to the second layer according to the previous selection. At the second step, the target character will be spelled out in the second layer. The target 1, 3, 5 are located in the same directions of predict probabilities (P2, P3 and P1) respectively. To move the cursor in these directions, the user only need to do one motor imagery task, which means the cursor will

be moved quickly in these directions. To achieve the good performance, we designed the second layer of interface according to the English letter frequency, in which the letters with higher frequency are set in block 1, 3, 5 [17]. For other targets, the user should use a combination of two motor imagery tasks to move the cursor. In this paradigm, two commands are designed to correct the mistake. When a wrong block is chosen in the first layer, the user can choose 'Back' to return to the first layer. If spelled a wrong letter, the user can use 'Delete' to remove it. In this study, moving step is 21 pixels and the output updated every 0.1 second according to the predict probability of classifier.

### 3 Experiments

#### 3.1 Subject

Five healthy subjects aged from 19 to 26 (average  $22 \pm 2.4$ ) participated in this study. Three subjects were naïve (sub1, sub2, sub3) and other two subjects involved in previous MI researches (sub4, sub5). All of the subjects were in good health, and they submitted their consent to be involved in the study. They received a payment for their participation.

#### 3.2 EEG Recording and Signal Processing

EEG signals were acquired by a 16-channel g.USBamp amplifier, and the recording electrodes were placed according to the international 10-20 system. 13 channels (FC3, FCZ, FC4, C5, C3, C1, CZ, C2, C4, C6, CP3, CPZ, CP4) were used to record the EEG data, the ground and reference electrodes were placed on the FZ position and right earlobe. Common Spatial Pattern (CSP) was used to extract the EEG spatial features by maximizing the difference between tasks. To obtain control commands, a linear Support Vector Machine (SVM) classifier was applied to discriminate the three-class MI patterns. EEG signals were sampled at 256 Hz and band-pass filtered between 5-30 Hz.

#### 3.3 Online Experiments

**2-D control training:** All subjects attended a 2-D control training program which includes two steps. At the first step, subjects are asked to attend a three-class motor imagery training program. The training session will stop until classification accuracy for every class is greater than the threshold (85%). This step lasted three days and 2 hours per day for each subject. At the second step, all subjects participated a center out 2-D control experiment. The 2-D control training process ends when the subject can hit the targets over 90% [15]. It lasted one day for 2 hours in this step.

**Online copy spelling experiment:** In order to help the subjects be familiar with the speller interface, each subject will do 2 free spell runs in which the subject is asked to type characters from A to Z (26 letters). Then subjects participate in online copy

experiment. We choose the same 15 words from reference [12], “WOMEN, DESK, WATER, HAND, MEMORY, ZONE, BABY, FACE, TAXI, JUNE, QUICK, VIDEO, GOLF, HOUR, PENCIL”. At the beginning, the system counts down 3 s and the subject can prepare to spell first word. There is 3 seconds interval between two words task (As shown in Fig. 3). All subjects are asked to spell 15 words. If subjects cannot spell the word correctly in one trial in 40 seconds, this trial will end and goes to next. In this experiment, we adopt the no mistake protocol which means the wrong typed letter has to be corrected.



Fig. 3. Online procedure of copy spelling

### 4 Result

To evaluate the performance, we calculated the accuracy, LPM and information transfer rate (ITR) which are widely used to quantify the performance of BCI speller [18]. In this study, the ITR is calculated as following:

$$ITR [bit/min] = [\log_2 N + P \log_2 P + (1 - P) \log_2 \frac{1-N}{N-1}] \frac{60}{\text{trial length}} \tag{1}$$

Where N is the number of classes (N=6) for there are 6 effective blue circles for select and P is the accuracy. Trial length is the average time (second) of each selection for two selection outputs a character in this experiment. The total time is per trial time, so the performance is calculated per trial which 15 trials in all for a run.

All subjects finished the copy spelling experiment. Four subjects achieved 100% accuracy. Only one subject’s accuracy was 94.74%. Sub2 reached the best performance with 18.71 LPM and 96.74 ITR. On average of all subjects, the performance reaches 98.95% of accuracy, 14.64 LPM and 73.96 ITR, which is better than the results in [12].

Table 1. Average Accuracy, LPM and ITR

	Accuracy (%)	LPM	ITR
Sub1	94.74	10.45	45.26
Sub2	100	<b>18.71</b>	<b>96.74</b>
Sub3	100	11.18	57.82
Sub4	100	14.85	76.80
Sub5	100	18.03	93.20
Mean	98.95	14.64	73.96

In this spell paradigm, there are two possible spelling mistakes. The first type of mistake is to choose a wrong block in the first layer, which can be corrected by selecting “Back” in the second layer and no wrong character is outputted. Another type of mistake is to spell a wrong character, which will be corrected by using ‘Delt’. Table 2 shows the details of spelling process of Sub 1. For instance, Sub 1 made two types of mistake in spelling MEMORY.

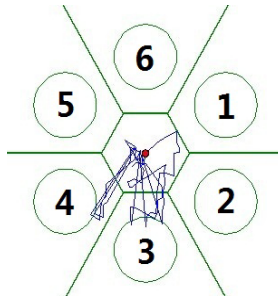
As we discussed above, the user can only use one motor imagery task to select target 1, 3, 5, which means these targets will be selected quickly. We calculated the average time for each target. As shown in Table 3, target 1, 5 are selected quickly for all subjects. But most of the subjects need long time to select target 3. Fig. 4 shows the cursor traces of trials of Sub1. In some trials, the cursor is moved to the other direction at the beginning. And the subject takes a long time to draw it back to the right direction. For each step, the speed vector is composed by three probabilities. If the subject cannot get higher probability for feet imagery, the cursor cannot move to target 3 directly.

**Table 2.** Results of spelling(sub1). “DELTA” denoted as “←” and “BACK” denoted as (back) in the table.

Word	Input results	Effective/total
WOMEN	WOMEN	10/10
DESK	DESK	8/8
WATER	WATER	10/10
HAND	HAND	8/8
MEMORY	ME(back)MK←-ORY	15/18
ZONE	ZK←-ONE	10/12
BABY	BABY	8/8
FACE	FACE	8/8
TAXI	TAXI	8/8
JUNE	JUNE	8/8
QUICK	Q(back)Y←-UICK	13/16
VIDEO	VIDEO	10/10
GOLF	GOLF	8/8
HOUR	HOUR	8/8
PENCIL	PENCIL	12/12
Total		144/152
Accuracy(%)		94.74%
ITR(bits/min)		45.26
LPM(letters/min)		10.45

**Table 3.** Average Time on each direction. *r-h* *l-h* stand for right hand and left imagination, respectively. *f* stands for feet imagination

	1 (r-h)	2 (r-h+f)	3 (f)	4 (l-h+f)	5 (l-h)	6 (l-h+r-h)	Mean
Sub1	1.62	5.50	3.68	1.87	1.67	3.22	2.93
Sub2	1.24	1.62	1.74	2.40	1.31	2.93	1.87
Sub3	2.09	2.31	4.05	3.79	1.39	3.57	2.87
Sub4	1.36	2.91	2.64	2.47	1.34	3.32	2.34
Sub5	1.14	1.97	2.07	2.69	1.14	1.48	1.75
Mean	<b>1.49</b>	2.86	2.83	<b>2.64</b>	<b>1.37</b>	2.90	2.34



**Fig. 4.** Subject1's cursor traces of several trials

## 5 Discussion and Conclusion

The Speller is one of the most popular applications in BCI research area, which provides a communication channel for the paralyzed. Motor imagery BCIs are rarely applied to speller which cannot achieve good performance with limited commands. In Hex-o-Spell paradigm, the subject should turn the arrow clockwise to find the target [14]. In the worst case, the arrow should go across four blocks to target block. After chosen the target block in the first layer, the subject should extend the arrow to choose target letter. In proposed paradigm, the user can directly move the cursor to choose target letter in a short time. In online copy experiment, all subjects can achieve high accuracy because there is 3 s for the subject to prepare next word.

In general, motor imagery based BCI spellers need specific paradigm due to limited commands. Even using well designed paradigm as Hex-o-Spell, it cannot achieve good speed performance. In this study, we combined Hex-o-Spell paradigm with the 2-D cursor control system to build a high speed speller. In online experiment, subjects can spell quickly and precisely. Comparing with other types speller system, such as P300 and SSVEP based speller [10, 11, 12], our results are satisfactory and comparable.

**Acknowledgment.** The work was supported by Innovation Program of Shanghai Municipal Education Commission (Grant No.12ZZ150) and the National Natural Science Foundation of China (Grant No. 61105122) and the Ministry of Transport of the People's Republic of China (Grant No. 2012319810190).

## References

1. Wolpaw, J.R., et al.: Brain-computer interfaces for communication and control. *Clinical Neurophysiology* 113(6), 767–791 (2002)
2. Kübler, A., et al.: Brain–computer communication: Unlocking the locked in. *Psychological Bulletin* 127(3), 358 (2001)
3. Kübler, A., et al.: A Brain–Computer Interface Controlled Auditory Event-Related Potential (P300) Spelling System for Locked-In Patients. *Annals of the New York Academy of Sciences* 1157(1), 90–100 (2009)
4. Pfurtscheller, G., et al.: Self-paced operation of an SSVEP-Based orthosis with and without an imagery-based “brain switch:” a feasibility study towards a hybrid BCI. *IEEE Transactions on Neural Systems and Rehabilitation Engineering* 18(4), 409–414 (2010)
5. Pfurtscheller, G., Neuper, C.: Motor imagery and direct brain-computer communication. *Proceedings of the IEEE* 89(7), 1123–1134 (2001)
6. Mensh, B.D., Werfel, J., Seung, H.S.: BCI competition 2003-data set Ia: combining gamma-band power with slow cortical potentials to improve single-trial classification of electroencephalographic signals. *IEEE Transactions on Biomedical Engineering* 51(6), 1052–1056 (2004)
7. Donchin, E., Spencer, K.M., Wijesinghe, R.: The mental prosthesis: assessing the speed of a P300-based brain-computer interface. *IEEE Transactions on Rehabilitation Engineering* 8(2), 174–179 (2000)
8. Van der Waal, M., et al.: Introducing the tactile speller: an ERP-based brain–computer interface for communication. *Journal of Neural Engineering* 9(4), 045002 (2012)
9. Jin, J., Sellers, E.W., Wang, X.: Targeting an efficient target-to-target interval for P300 speller brain–computer interfaces. *Medical and Biological Engineering and Computing*, 1–8 (2012)
10. Cecotti, H.: A self-paced and calibration-less SSVEP-based brain–computer interface speller. *IEEE Transactions on Neural Systems and Rehabilitation Engineering* 18(2), 127–133 (2010)
11. Volosyak, I., et al.: Evaluation of the Bremen SSVEP based BCI in real world conditions. In: *IEEE International Conference on Rehabilitation Robotics, ICORR 2009. IEEE* (2009)
12. Hwang, H.-J., et al.: Development of an SSVEP-based BCI spelling system adopting a QWERTY-style LED keyboard. *Journal of Neuroscience Methods* (2012)
13. Sbattella, L., Tedesco, R.: A Predictive Speller for A Brain-Computer Interface Based on Motor Imagery
14. Blankertz, B., et al.: The Berlin Brain-Computer Interface presents the novel mental typewriter Hex-o-Spell, pp. 108–109 (2006)
15. Xia, B., et al.: Control 2-dimensional movement using a three-class motor imagery based Brain-Computer Interface. In: *2012 Annual International Conference of the IEEE Engineering in Medicine and Biology Society, EMBC. IEEE* (2012)

16. Li, Y., Long, J., Yu, T., et al.: An EEG-based BCI system for 2-D cursor control by combining Mu/Beta rhythm and P300 potential. *IEEE Transactions on Biomedical Engineering* 57(10), 2495–2505 (2010)
17. What is the frequency of the letters of the alphabet in English? Oxford Dictionary. Oxford University Press (December 29, 2012) (retrieved)
18. Krausz, G., et al.: Critical decision-speed and information transfer in the “Graz Brain–Computer Interface. *Applied Psychophysiology and Biofeedback* 28(3), 233–240 (2003)

# A New Method for BCI Spelling Using a 7 Segments Display

N. Galea-Sevilla<sup>1</sup>, Miriam España<sup>2</sup>, Alberto Guillén<sup>1</sup>, and Ignacio Rojas<sup>1</sup>

<sup>1</sup> Department of Computer Technology and Architecture,  
University of Granada, Spain  
[aguillen@ugr.es](mailto:aguillen@ugr.es)

<sup>2</sup> Department of Experimental Psychology, University of Granada, Spain

**Abstract.** Research on Brain Computer Interfaces (BCI) covers a wide spectrum of applications. In this paper we tackle the problem of spelling words which could be used by people with harmful motor skills. The P300 has been widely used to communicate with the machine using a set of stimuli. For the word spelling problem, several approaches have been proposed although the most popular consists on an array of characters.

The novelty of the work proposed in this paper is that the panel that stimulates the user generating the P300 usually performs better in terms of efficiency and allows a better visual focalisation.

At this preliminary stage of the research, several experiments were carried out using simulated signals showing that, indeed, the new way of stimulating the user could make word spelling faster.

**Keywords:** Brain-Computer Interface, P300, speller.

## 1 Introduction

We propose a new BCI paradigm for writing letters, against the classical matrix 6x6 paradigm by Farwell and Donchin [6] and Hex-o-Spell paradigm by [11]. From a neuroscience point of view, the principal differences between those paradigms and the ours is the managing of overt and covert attention and its relation with P3 potential in a visual search task. We can distinguish between overt and covert attention if we move the eyes to a spatial location to focus on a target or if we do not, establishing in this way our visual field and our peripheral visual field respectively. Covert attention monitors the environment, detecting movements or light changes. Attention can affect perception by altering performance and enhances spatial resolution in visual search (Carrasco, 2011). The performance (measured on time) of a visual search task depends on load [13] and practice [8], being the load the cardinal of the cartesian square of the stimuli-target set and the all-stimuli set: the higher the load is, the smaller the performance becomes and, the higher the practice is, the better the performance is obtained.

Then, in a search context like the BCI paradigms discussed here is, the P3 potential responds to a match between the subject's internal expectancies and



the stimulus presented to him or her: if the subject find what he or she is looking for (a target), a classical P3 (P3b) potential arises. A match is produced when the desired target is illuminated, distinguishing it among the others stimuli, enhancing its saliency and producing a pop-out effect [13]. The amplitude of this P3 is enhanced if the focus of attention is deployed to the target location and decreases if the difficult to discriminate the target increases [7]. Reaching these goals we improve the speed of our system. This is obtained through the minimization of the set of stimuli without reduction of the functionality of the system, independently of the frequency of illumination of the stimuli [5]. The idea has also been used by the Hex-o-Spell paradigm. First, all the stimuli lies within the visual field. This cannot be accomplished by the matrix 6x6 paradigm without the called crowding effect: the impaired recognition or identification of a stimulus that is caused by the presence of nearby distractor stimuli [4]. This crowding effect reduces the P3 amplitude. In the Hex-o-Spell paradigm the matrix 6x6 paradigm's 36 stimuli (letters) are rearranged and grouped into discs (5 stimuli per disc), resulting in 6 discs for selection of the target letter, removing also the crowding effect. With this approach, this paradigm becomes an improvement of the 6x6 matrix paradigm, but introduces a 2-step search process to select the target letter and the overall load is still big (30). In this paper, we propose to reduce the load down to 8 encoding every letter with 7 segments, as usually a digital clock's segments display does (plus an intro symbol). The results obtained are consistent with the facilitation provided by reducing the window size of attention [10]. In our case, the user has to keep in mind every letter composition of segments and the training process is longer. However, with practice, the approach could improve the visual search task.

## 2 Previous Paradigms

The most common paradigm that has been used is based on a matrix of dimension  $6 \times 6$  that contains 36 letters and symbols. A stimulus is defined in this case as to illuminate or change the color of an element in the matrix, a whole row, a whole column or a combination of all of them. As the matrix has many elements, it is difficult to keep all of them visually focalised [12].

From some bibliographics sources it can be taken that BCI-P300 based systems using visual paradigms matrix-based depends considerably on the direction of the visual focalization, that is, the systems' efficiency depends on the user's ability to control saccadic eye movements. This is due to the fact that the stimulus focused has been shown at the same time that an eye movement has been produced by the user, missing the stimulus then in the peripheral visual area where cover attention comes into its own. BCI systems using visual covert attention have been developed but its performance is visibly lower than systems that use overt attention [1].

To solve the effects explained above the symbols size can be enlarged but, in this way, the crowding effect appears because the screen size does not increase and the items are clinging together. The only way to increase the size of the

elements showed without crowding effect is decreasing the amount of it. Unfortunately, this it's not possible in the classic paradigm because a lot of symbols should be lost and so usefulness.

The Hex-o-Spell paradigm carries out the prior strategy cited: it gathers the letters of the alphabet in several sets, resulting in 7 circles. In comparison with the classic paradigm, this one provides less selection errors, greater amplitude on ERP and better classifications. In the classic paradigm, when covert attention is deployed, components P1, N1, P2, N2 and P3 are detected, but in the case that covert attention occurs only components N2 and P3 are detected. Using covert attention in Hex-o-Spell, also components N1 and P2 are detected in addition to components N2 and P3 [12].

### 3 New Paradigm: 7-D Speller

The paradigm developed here is a visual paradigm for writing letters by the selection of the letters using a 7 segments display that flashes one random segment each time. The purpose of this design attempts to find paradigm with fewer items than the classic one because the speed on ERP detection increases as the number of the eligible items goes down [12] [1] [2]. The reduction of the elements could avoid also problems on visual focus and improve the performance of the system.

#### 3.1 Initial Version

On the initial version, letters are represented by segments that are a very close match to real writing strokes.

As auxiliary element, the system have an *enter* symbol which lets make the selection on the letter most similar to the selected segments set up to now. In addition, it has a panel showing the alphabet as a guide.

In the panel guide, the segments that represents every letter are shown. At the begginig of every sequence, the paradigm generator checks the letters which contains the segments that have been selected so far. Afterwards, when a segment is selected, the systems removes from the panel guide the letters that do not contain that segment. The selected segment is accentuated with other colour in the panel guide for every letter and the letter that most closely match to the selection is indicated. If in the next sequence the *enter* symbol is focused, the letter will be selected.

It may happen that the number of unselected segments is bigger than the remaining candidate letters. When this occurs, only the candidate letters are used as the stimuli. Thus, we ever have the less eligible items obtaining the maximun system performance.

#### 3.2 Optimized Version

The original aim to develop this pardigm was to build a letter writting system faster than the existent ones. In a classical 6x6 panel, if the rows and colums are

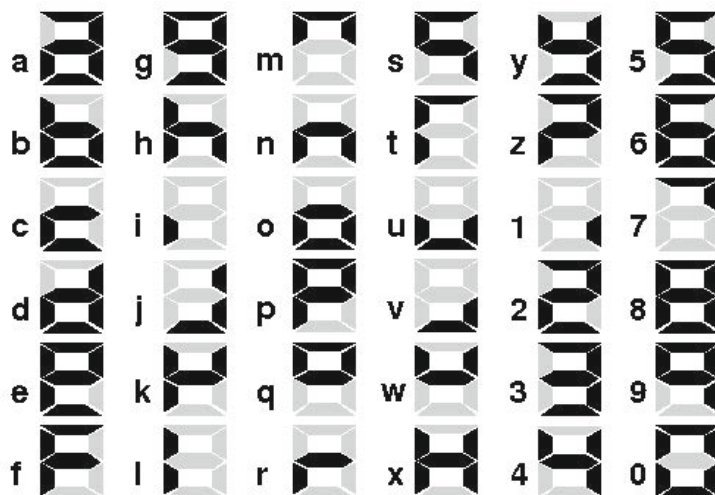


Fig. 1. Initial version

used as stimuli, the user has to choose among 12 different items. In our proposal paradigm, 8 items has to be taken into account for defining a single letter at the most (see Figure 1). There are items like the letter *i* or the number *1* that can be reached with 2 selections. However, there are 8 symbols that require many segments to be selected.

To improve the usefulness of this paradigm, we observe the statistical information about the relative percentage of times that every letter occurs in the spanish language

Since a 7 segments display is being used, there are 7 letters that can be represented by an only segment (the most used ones). The rest of the 19 letters less used plus 2 numbers can be represented using 2 segments and, finally, the remaining 8 numbers can be represented with 3 segments, supposing that numbers are less used than the letters.

The segments that represents every letter are assigned as follows (see Fig. 2):

**The 7 letters more used:** They are represented with only one segment among the ones used for the same letter in the initial version of the system.

**The 19 letters less used plus 2 numbers:** Every segment has been represented with one of the possibles combinations derived from 2 segments. We have tried that the 2 segments that define a letter match with any of the segments used to represent it on the initial version, although in some cases other segments have had to be used for cover all the combinations.

**The remaining numbers:** They are represented with 3 segments which have been chosen in such a way that they have to be common among the segments that represent the less used letters. For example, the letters *j*, *q* and *h* are among the less used ones (0.37%, 0.36% and 0.35% of usage respectively).

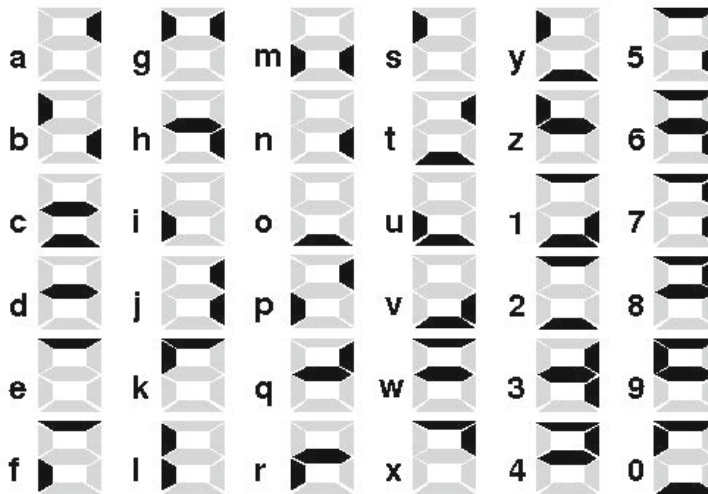


Fig. 2. Optimized version

The letter  $j$  utilises the segments 3 and 6, the letter  $q$  utilises the segments 3 and 5, and the letter  $h$  uses the segments 5 and 6. The common combination for the three of them is formed by the segments 3, 5 and 6 which has been assigned to number 3. In this way, the most frequent letters that are composed by 2 segments can be selected in only 2 steps because its combination is unique considering that there isn't an element composed by 3 segments with that combination.

## 4 Experiments

The system has been tested using a simulator of brain signals which is included in BCI2000 [3]. The signals can be controlled by keyboard, mouse, joystick or other devices. The signal generator does not need any additional further configuration and it is operated as if it was a physical device. There are several parameters that can be adjusted, for the experiments, the configuration below was used:

**Width of the background brain activity:** 30  $\mu V$  (is the typical width in the position Pz in a BCI session).

**P300 generation method:** Vertical mouse movement. When the user sees the stimulus, it moves quickly the mouse up and down just once.

**Width of the Evoqued potential:** 5  $\mu V$  (is the usual width of a P300 evoked potential).

**Input channels:** 16, although the mouse only affects Pz y Cz.

**Type of Reference:** CAR (Common Average Reference); the reference potential is considered as the average of the potentials for all channels.

This configuration was used for both the training and the spelling sessions.

The experiments were carried out with four volunteers with not known brain disease whose age where in the interval [20,65]. Each user made several trial sequences. The results obtained were used to set the parameters for each individual allowing the systems to obtain nearly a 100% of success in the spelling process.

The proposed approach of seven segments was compared against the classical  $6 \times 6$  panel using the same configuration for the stimuli:

**Sequence Type:** random.

**Stimulus length:** 0.20 seconds.

**Interstimulus length:** 0.016 seconds.

**Number of passes on each sequence:** 50 passes although it continues with the next one when the selection condition is satisfied.

**Selection condition:** The score of the selected element has to be a 20% higher than the second stimulus with higher score. There is a minimum of 4 passes before satisfying the condition.

The efficiency of the  $6 \times 6$  panel does not depend on the selected letter, however, for the proposed paradigm this is not true. For the experiments, the paradigm was optimised to select faster the most common used letters in spanish in comparison with less used letters and numbers. Four words were chosen and, for the sake of a fair comparison, two of them have letters that are not common in the spanish language (actually, these words were adopted from other languages): "kayak" and "whisky". The other two words were selected randomly: "prueba" and "electroencefalograma". So it is possible to observe the performance of the paradigm in normal conditions and in the worst of the cases.

Table 1 shows the results obtained in the experiments. As it is shown, for the word "prueba" the new paradigm is a 27% faster than the classical paradigm. For the word "electroencefalograma", the new paradigm is again much faster showing an improvement of a 24.5%. For the foreign words "kayak" and "whisky" the new paradigm was slower (17.78% and 15.11% respectively). This is not surprising since they include very uncommon letters such as "k" and "w" for example. Nonetheless, the improvement for common words is still higher than the performance decrease for the rare words.

## 5 Conclusions and Further Work

This paper has proposed a new paradigm for spelling words using the P300. The novelty of the approach is that instead of a large set of stimuli, it only requires a 7 segments display to represent all the symbols (letters and numbers). This is translated in a better focalization of the stimulus that generates the P300 and, thus, the number of passes through the complete stimuli is smaller.

Another consequence of using less symbols is that it is possible to increase the size of these in the screen minimising the effect of agglomeration (it is possible to increase the distance between them) and increasing the visual focalisation.

**Table 1.** Result comparison for the two different paradigms spelling four words

Paradigm	6 × 6 Panel	7 segment display.	Difference	% of improvement
Word 1:	<i>prueba</i>			
Hits (%)	100	100	0	equal
Time (s)	42.50	31.03	11.47	26.98% faster
Word 2:	<i>electroencefalograma</i>			
Hits (%)	100	98.75	1.25 ≈ 0	nearly equal
Time (s)	41.18	31.09	10.09	24.50% faster
Word 3:	<i>kayak</i>			
Hits (%)	100	100	0	equal
Time (s)	37.51	44.18	-6.67	17.78% slower
Word 4:	<i>whisky</i>			
Hits (%)	100	100	0	equal
Time (s)	37.92	43.65	-5.73	15.11% slower

The new paradigm was compared against the classic 6 × 6 approach. The experiments were carried out using a signal generator included in the BCI2000 software so each individual could simulate the P300 using the mouse. Analysing the results obtained it could be concluded that the new 7-D-speller:

- was a 25% approximately faster than the other paradigm for words that include common letters in spanish language.
- And it was approximately a 16% slower for "foreign" words that include uncommon letters in spanish language.

Although these results seem promising and confirming the psychological motivation, further work can be done:

**Test the system with real EEG** : although the signal generator is quite robust and has been tested by other researchers, the new system will be tested using a real EEG device.

**Optimisation of the word selection** : a word predictor based on a dictionary could be implemented in the system so word writing would be much faster.

## References

1. Aloise, F., Arico, P., Schettini, F., Riccio, A., Salinari, S., Mattia, D., Babiloni, F., Cincotti, F.: A covert attention P300-based brain-computer interface: Geospell Brain-computer interface (BCI) and ergonomics, pp. 538–551 (2012)
2. Brunner, P., Joshi, S., Briskin, S., Wolpaw, J.R., Bischof, H., Schalk, G.: Does the P300 speller depend on eye gaze? *Journal of Neural Engineering* 7(5), 056013 (2010)

3. Schalk, G., Mellinger, J.: Introduction to Brain-Computer Interfacing Using BCI2000. Human-Computer Interaction Series. Springer (2010)
4. Carrasco, M.: Visual attention: The past 25 years. *Vision Research* 51, 1484–1525 (2011)
5. Donchin, E., Arbel, Y.: P300 Based Brain Computer Interfaces: A Progress Report. In: Schmorow, D.D., Estabrooke, I.V., Grootjen, M. (eds.) FAC 2009. LNCS, vol. 5638, pp. 724–731. Springer, Heidelberg (2009)
6. Farwell, L.A., Donchin, E.: Talking off the top of your head: toward a mental prosthesis utilizing eve brain potentials. *EEG Clinical Neurophysiology* 70(6), 510–523 (1988)
7. Kok, A.: On the utility of P3 amplitude as a measure of processing capacity. *Psychophysiology* 38, 557–577 (2001)
8. Schneider, W., Shiffrin, R.M.: Controlled and automatic human information processing: I. Detection, search and attention. *Psychological Review* 84(1), 1–66 (1977a)
9. Shiffrin, R.M., Schneider, W.: Controlled and automatic human information processing: II. Perceptual learning, automatic attending and a general theory. *Psychological Review* 88(2), 127–189 (1977b)
10. Theeuwes, J.: Top-down and bottom-up control of visual selection. *Acta Psychologica* 135, 77–99 (2010)
11. Treder, M.S., Blankertz, B. (C)over attention and visual speller design in an ERP-based brain-computer interface. *Behavioral and Brain Functions*?: *BBF* 6, 28 (2010)
12. Treder, M.S., Blankertz, B. (C)over attention and visual speller design in an ERP-based brain-computer interface. *Behavioral and Brain Functions* 6, 28 (2010)
13. Treisman, A., Gelade, G.: A feature-integration theory of attention. *Cognitive Psychology* 136, 97–136 (1980)

# Motor Imagery EEG-Based Person Verification

Phuoc Nguyen, Dat Tran, Xu Huang, and Wanli Ma

Faculty of Education Science Technology and Mathematics  
University of Canberra, ACT 2601, Australia  
`dat.tran@canberra.edu.au`

**Abstract.** We investigate in this paper the activity-dependent person verification method using electroencephalography (EEG) signal from a person performing motor imagery tasks. Two tasks were performed in our experiments were performed. In the first task, the same motor imagery task of left hand or right hand was applied to all persons. In the second task, only the best motor imagery task for each person was performed. The Gaussian mixture model (GMM) and support vector data description (SVDD) methods were used for modelling persons. Experimental results showed that lowest person verification error rate could be achieved when each person performed his/her best motor imagery task.

**Keywords:** EEG, Person Verification, Brain Computer Interface, SVDD, GMM.

## 1 Introduction

Beside the popular person characteristics such as face, voice, fingerprint, signature and iris, researchers have been investigated other types of biometrics such as ear, gait, hand and dental [1]. Those biometric traits are not universal, and can be subject to physical damage such as dry skin, scars, loss of voice, etc. [2]. In addition, static physical characteristics can be digitally duplicated, such as a photo of a face or a voice recording [3]. On the other hand, brain electrical signals can avoid those limitations, it is hardly to steal because the brain activity is sensitive to the stress and the mood of the person, an aggressor cannot force the person to reproduce his/her mental pass-phrase [4] and it requires living person recording, spontaneous signal, individual uniqueness due to different brain configurations [2].

Brain electrical signal is usually used in diagnosing brain related diseases, but there are very few reported studies on brain electrical activity-based biometrics [5]. Measuring the EEG is a simple non-invasive way to monitor electrical brain activity, but it does not provide detailed information on the activity of single neurons (or small brain areas). Moreover, it is characterized by small signal amplitudes (a few Volts) and noisy measurements [4].

The main applications of authentication systems are access control systems, building gate control, digital multimedia access, transaction authentication, voice mail, or secure teleworking. A research at the Canada's Carleton University uses



the brains response to stimuli, such as sounds or images, as the authentication method called pass-thought. Users will access a protected computer system or building by thinking of their pass-thought. Their brain signals are recorded and features are extracted for matching with authorized users models [6].

Several techniques have been used for brain-wave-based person verification. In [7], Manhattan distances on autoregressive (AR) coefficients with PCA were used to compute thresholds for determining test patterns were clients or impostors, the person verification task from 5 subjects were done in 2 stages. In [8], Independent Component Analysis (ICA) was used to determine dominating brain regions to extract AR features, then a Naive Bayes probabilistic model is employed for person authentication of 7 subjects with Half Total Error Rate (HTER) of 2.2%. In [4], Gaussian mixture models has been applied for person verification task on EEG signal from 9 subjects. Half total error rate of 6.6 % was achieved for imagination left task.

In this paper, we investigate the person verification system using EEG signals of motor imagery tasks. The subjects were required doing the same motor imagery tasks in enrolment and test phases. Experiments were done first using the same task for all subjects, namely motor imagery of left hand or right hand, then they were done using the best motor imagery task for each subjects that can distinguish them. The GMM and SVDD methods were used for modelling the individuals. The rest of the paper is organized as follows: Section 2 describes the brainwave features, Section 3 describes SVDD and GMM modelling techniques, Section 4 depicts the dataset used and parameter setup, finally Section 5 represents person verification results and Section 6 concludes the paper.

## 2 Brainwave Features

### 2.1 Autoregressive (AR) Features

Autoregressive model can be used for a single-channel EEG signal. It is a simple linear prediction formulas that best describe the signal generation system. Each sample in an AR model is considered to be linearly related with respect to a number of its previous samples [9]:

$$y(n) = - \sum_{k=1}^p a_k y(n-k) + x(n) \quad (1)$$

where  $a_k$ ,  $k = 1, 2, \dots, p$ , are the linear parameters,  $n$  denotes the discrete sample time, and  $x(n)$  is the noise input. The linear parameters of different EEG channel were taken as the features.

### 2.2 Power Spectral Density (PSD) Features

Power spectral density (PSD) of a signal is a positive real function of a frequency variable associated with a stationary stochastic process. The PSD is

defined as the discrete time Fourier transform (DTFT) of the covariance sequence (ACS) [10]

$$\phi(\omega) = \sum_{k=-\infty}^{\infty} r(k)e^{-i\omega k} \quad (2)$$

where the auto covariance sequence  $r(k)$  is defined as

$$r(k) = E\{y(t)y^*(t-k)\} \quad (3)$$

and  $y(t)$  is the discrete time signal  $\{y(t); t = 0, \pm 1, \pm 2, \dots\}$  assumed to be a sequence of random variables with zero mean.

In this paper, the Welch's method using periodogram is used for estimating the power of a signal at different frequencies. 12 frequency components in the band 8-30 Hz of different channels was estimated as features. Welch's method can reduce noise but also reduce the frequency resolution as compare to the standard Bartlett's method, which is desirable for this experiments.

### 3 Modelling Techniques

#### 3.1 Support Vector Data Description (SVDD)

Let  $\mathbf{X} = \{\mathbf{x}_1, \mathbf{x}_2, \dots, \mathbf{x}_n\}$  be the normal data set. SVDD [11] aims at determining an optimal hypersphere that encloses all normal data samples in this data set  $\mathbf{X}$  while abnormal data samples are not included. The optimisation problem is formulated as follows

$$\min_{R, c, \xi} \left( R^2 + C \sum_{i=1}^n \xi_i \right) \quad (4)$$

subject to

$$\begin{aligned} \|\phi(\mathbf{x}_i) - \mathbf{c}\|^2 &\leq R^2 + \xi_i & i = 1, \dots, n \\ \xi_i &\geq 0, & i = 1, \dots, n \end{aligned} \quad (5)$$

where  $R$  is radius of the hypersphere,  $C$  is a constant,  $\xi = [\xi_i]_{i=1, \dots, n}$  is vector of slack variables,  $\phi(\cdot)$  is the nonlinear function related to the symmetric, positive definite kernel function  $K(\mathbf{x}_1, \mathbf{x}_2) = \phi(\mathbf{x}_1) \cdot \phi(\mathbf{x}_2)$ , and  $\mathbf{c}$  is centre of the hypersphere.

For classifying an unknown data sample  $\mathbf{x}$ , the following decision function is used:  $f(\mathbf{x}) = \text{sign}(R^2 - \|\phi(\mathbf{x}) - \mathbf{c}\|^2)$ . The unknown data sample  $\mathbf{x}$  is normal if  $f(\mathbf{x}) = +1$  or abnormal if  $f(\mathbf{x}) = -1$ .

In person verification enrolment phase, a smallest hyper sphere is trained to enclose the individual feature vectors. In test phase a feature vector will be accepted belonging to a claimed identity if its distances to the sphere center less than the sphere radius  $R$  and rejected otherwise. The radius  $R$  can be changed larger or smaller as a threshold.

### 3.2 Gaussian Mixture Model (GMM)

Since the distribution of feature vectors in  $X$  is unknown, it is approximately modelled by a mixture of Gaussian densities, which is a weighted sum of  $K$  component densities, given by the equation

$$p(x_t|\lambda) = \sum_{i=1}^K w_i N(x_t, \mu_i, \Sigma_i) \tag{6}$$

where  $\lambda$  denotes a prototype consisting of a set of model parameters  $\lambda = \{w_i, \mu_i, \Sigma_i\}$ ,  $w_i$ ,  $i = 1, \dots, K$ , are the mixture weights and  $N(x_t, \mu_i, \Sigma_i)$ ,  $i = 1, \dots, K$ , are the  $d$ -variate Gaussian component densities with mean vectors  $\mu_i$  and covariance matrices  $\Sigma_i$

$$N(x_t, \mu_i, \Sigma_i) = \frac{\exp\{-\frac{1}{2}(x_t - \mu_i)' \Sigma_i^{-1} (x_t - \mu_i)\}}{(2\pi)^{d/2} |\Sigma_i|^{1/2}} \tag{7}$$

In training the GMM, these parameters are estimated such that in some sense, they best match the distribution of the training vectors. The most widely used training method is the maximum likelihood (ML) estimation. For a sequence of training vectors  $X$ , the likelihood of the GMM is

$$p(X|\lambda) = \prod_{t=1}^T p(x_t|\lambda) \tag{8}$$

The aim of ML estimation is to find a new  $\bar{\lambda}$  parameter model such that  $p(X|\bar{\lambda}) \geq p(X|\lambda)$ . Since the expression in 8 is a nonlinear function of parameters in  $\lambda$  its direct maximisation is not possible. However, parameters can be obtained iteratively using the expectation-maximisation (EM) algorithm [12]. An auxiliary function  $Q$  is used

$$Q(\lambda, \bar{\lambda}) = \sum_{i=1}^T p(i|x_t, \lambda) \log[\bar{w}_i N(x_t, \bar{\mu}_i, \bar{\Sigma}_i)] \tag{9}$$

where  $p(i|x_t, \lambda)$  is the a posteriori probability for acoustic class  $i$ ,  $i = 1, \dots, c$  and satisfies

$$p(i|x_t, \lambda) = \frac{w_i N(x_t, \mu_i, \Sigma_i)}{\sum_{k=1}^c w_k N(x_t, \mu_k, \Sigma_k)} \tag{10}$$

The basis of the EM algorithm is that if  $Q(\lambda, \bar{\lambda}) \geq Q(\lambda, \lambda)$  then  $p(X|\bar{\lambda}) \geq p(X|\lambda)$  [23][24][25]. The following re-estimation equations are found

$$\bar{w}_i = \frac{1}{T} \sum_{t=1}^T p(i|x_t, \lambda) \tag{11}$$

$$\bar{\mu}_i = \frac{\sum_{t=1}^T p(i|x_t, \lambda)x_t}{\sum_{t=1}^T p(i|x_t, \lambda)} \quad (12)$$

$$\bar{\Sigma}_i = \frac{\sum_{t=1}^T p(i|x_t, \lambda)(x_t - \bar{\mu}_i)(x_t - \bar{\mu}_i)'}{\sum_{t=1}^T p(i|x_t, \lambda)} \quad (13)$$

### 3.3 Hypothesis Testing

The verification task can be stated as a hypothesis testing between the two hypotheses: the input is from the hypothesis person, ( $H_0$ ) or not from the hypothesis person ( $H_1$ ).

Let  $\lambda_0$  be the claimed person model and  $\lambda$  be a model representing all other possible people, i.e. impostors. For a given input  $x$  and a claimed identity, the choice is between the hypothesis  $H_0$ :  $x$  is from the claimed person  $\lambda_0$ , and the alternative hypothesis  $H_1$ :  $x$  is from the impostors  $\lambda$ . A claimed person's score  $L(x)$  is computed to reject or accept the person claim satisfying the following rules

$$L(x) \begin{cases} > \theta_L & \text{accept} \\ \leq \theta_L & \text{reject} \end{cases} \quad (14)$$

where  $\theta_L$  are the decision thresholds.

The score used in person verification using GMM models is

$$L_0(x) = \log P(x|\lambda_0) - \log P(x|\lambda) \quad (15)$$

And the score used in person verification using SVDD models is

$$L_0(x) = R - \|x - c_S\| \quad (16)$$

The score (16) with a radius threshold  $R$  checks whether  $x$  is inside or outside the sphere

## 4 Experimental Setup

### 4.1 Datasets

The Graz dataset B in the BCI Competition 2008 comes from the Department of Medical Informatics, Institute of Biomedical Engineering, Graz University of Technology for motor imagery classification problem in BCI Competition 2008 [13]. The Graz B 2008 dataset consists of EEG data from 9 subjects. The subjects were right-handed, had normal or corrected-to-normal vision and were paid for

participating in the experiments. The subjects participated in two sessions contain training data without feedback (screening), and three sessions were recorded with feedback. It consisted of two classes: the motor imagery (MI) of left hand and right hand. Three bipolar recordings (C3, Cz, and C4) were recorded at sampling frequency of 250 Hz.

## 4.2 Feature Extraction

The signals from electrodes C3, C4 and Cz were selected to extract features. The autoregressive (AR) linear parameters and power spectral density (PSD) components from these signals are extracted as features. In details, the power spectral density (PSD) in the band 8-30 Hz was estimated. The Welch's averaged modified periodogram method was used for spectral estimation. Hamming window was 1 second 50% overlap. 12 power components in the frequency band 8-30 Hz were extracted. Besides PSD features, autoregressive (AR) model parameters were extracted. In AR model, each sample is considered linearly related with a number of its previous samples. The AR model has the advantage of low complexity and has been used for person identification and authentication [14] [15] [7]. Burg's lattice-based method was used with the AR model order 21, as a previous study [15] suggested when there were many subjects and epochs.

The resulting feature set consists of  $3 \times (12+21) = 99$  features.

## 5 Experimental Results

For SVDD method, experiments were conducted using 5-fold cross validation training and the best parameters found were used to train models on the whole training set and test on a separate test set. the RBF kernel function  $K(x, x') = e^{-\gamma \|x-x'\|^2}$  was used. The parameters for SVDD training are  $\gamma$  and  $\nu$ . The parameter  $\gamma$  was searched in  $\{2^k : k = 2l + 1, l = -8, -7, \dots, 2\}$ . The parameter  $\nu$  was

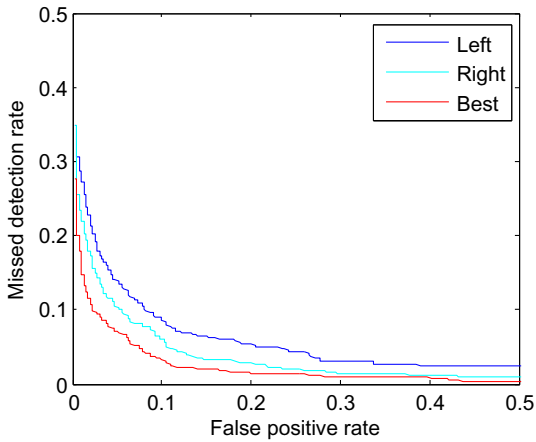
**Table 1.** Equal error rate in training phase of 9 subjects using the left, right or the best motor imagery task of SVDD and GMM methods

Subject	SVDD			GMM		
	Left	Right	Best	Left	Right	Best
B01	0.0471	0.0466	0.0466	0.0998	0.1402	0.0371
B02	0.0502	0.0367	0.0342	0.0571	0.0404	0.0341
B03	0.0310	0.0113	0.0054	0.0013	0.0038	0.0013
B04	0.0912	0.0736	0.0855	0.1054	0.1179	0.0524
B05	0.1699	0.0620	0.0682	0.1964	0.1541	0.0805
B06	0.0857	0.0413	0.0413	0.0497	0.0438	0.0400
B07	0.0528	0.0692	0.0301	0.0313	0.0277	0.0630
B08	0.0746	0.0679	0.0546	0.0608	0.0529	0.0129
B09	0.0742	0.0978	0.0025	0.0625	0.0968	0.0758
Average:	0.0752	0.0563	0.0409	0.0738	0.0753	0.0441

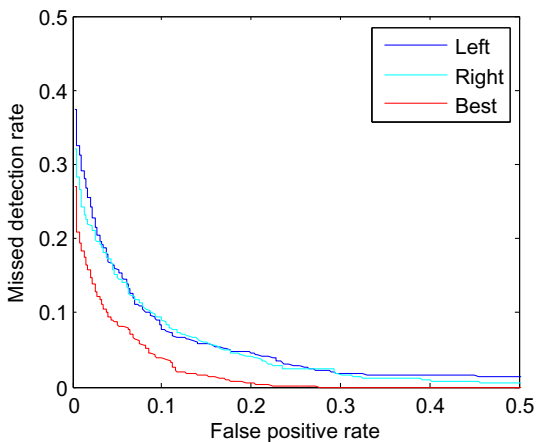
searched in  $\{0.001, 0.01, 0.1\}$ . The best parameters found are  $(\nu = 0.1, \gamma = 2^{-3})$  for left and right hand motor imagery and  $(\nu = 0.1, \gamma = 2^{-5})$  for the best motor imagery of each subjects. For the GMM method, the number of mixtures are set to 64 in model trainings.

Table 1 shows the equal error rate (EER) in training phase of 9 subjects using the left, right or the best motor imagery task of SVDD and GMM methods. Overall the EER is the lowest using the best motor imagery task. The subject B09 can be recognized best with left hand motor imagery task.

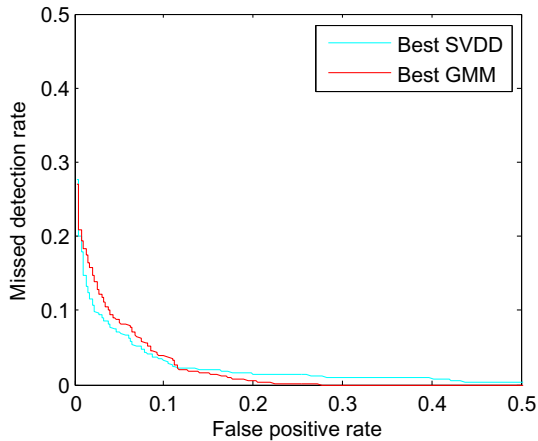
Figures 1 and 2 show the DET curves in test phase of person verification task using EEG signal of left, right and best motor imagery task of SVDD method



**Fig. 1.** DET curves of person verification task using EEG signal of left, right and best motor imagery task of SVDD method



**Fig. 2.** DET curves of person verification task using EEG signal of left, right and best motor imagery task of GMM method



**Fig. 3.** DET curves of person verification task using EEG signal using the best motor imagery task of SVDD and GMM methods

for SVDD and GMM person verification methods respectively. The curves are averaged across targets from DET curves of each target person [16]. Overall, the equal error rate is the lowest using the best motor imagery task.

Figure 3 shows the comparison of DET curves in test phase between SVDD and GMM methods using the best motor imagery task. The SVDD method show slightly lower EER than the GMM method.

## 6 Conclusion

We have investigated the activity-dependent person verification method using brain wave features extracted from EEG signals of motor imagery tasks. The left, right and best motor imagery tasks were used for each subject. The GMM and SVDD methods were used for modelling the individuals. Experimental results have showed that we can use EEG signals of persons performing motor imagery tasks to verify persons and that different motor imagery tasks can be performed by different persons to reduce person verification error rate. For future investigation, more data sets and brain activities will be investigated.

## References

1. Prabhakar, S., Kittler, J., Maltoni, D., O’Gorman, L., Tan, T.: Introduction to the special issue on biometrics: Progress and directions. *IEEE Transactions on Pattern Analysis and Machine Intelligence* 29(4), 513–516 (2007)
2. Riera, A., Soria-Frisch, A., Caparrini, M., Grau, C., Ruffini, G.: Unobtrusive biometric system based on electroencephalogram analysis. *EURASIP Journal on Advances in Signal Processing* 2008, 18 (2008)

3. Damousis, I.G., Tzovaras, D., Bekiaris, E.: Unobtrusive multimodal biometric authentication: the humabio project concept. *EURASIP Journal on Advances in Signal Processing* 2008, 110 (2008)
4. Marcel, S., Millán, J.R.: Person authentication using brainwaves (eeg) and maximum a posteriori model adaptation. *IEEE Transactions on Pattern Analysis and Machine Intelligence* 29(4), 743–752 (2007)
5. Palaniappan, R., Mandic, D.P.: Biometrics from brain electrical activity: A machine learning approach. *IEEE Transactions on Pattern Analysis and Machine Intelligence* 29(4), 738–742 (2007)
6. Thorpe, J., Van Oorschot, P.C., Somayaji, A.: Pass-thoughts: authenticating with our minds. In: *New Security Paradigms Workshop: Proceedings of the 2005 Workshop on New Security Paradigms*, vol. 20, pp. 45–56 (2005)
7. Palaniappan, R.: Two-stage biometric authentication method using thought activity brain waves. *International Journal of Neural Systems* 18(01), 59–66 (2008)
8. He, C., Wang, J.: An independent component analysis (ica) based approach for eeg person authentication. In: *3rd International Conference on Bioinformatics and Biomedical Engineering, ICBBE 2009*, pp. 1–4. IEEE (2009)
9. Sanei, S., Chambers, J.A.: *EEG signal processing*. Wiley-Interscience (2007)
10. Stoica, P., Moses, R.L.: *Spectral analysis of signals*. Pearson/Prentice Hall (2005)
11. Tax, D.M.J., Duin, R.P.W.: Support vector data description. *Machine Learning* 54(1), 45–66 (2004)
12. Tran, D.T.: *Fuzzy Approaches to Speech and Speaker Recognition*. PhD thesis, university of Canberra (2000)
13. Leeb, R., Brunner, C., Müller-Putz, G.R., Schlögl, A., Pfurtscheller, G.: Bci competition 2008–graz data set b. In: *Graz University of Technology, Austria* (2008)
14. Poulos, M., Rangoussi, M., Chrissikopoulos, V., Evangelou, A.: Person identification based on parametric processing of the eeg. In: *Proceedings of the 6th IEEE International Conference on Electronics, Circuits and Systems, ICECS 1999*, vol. 1, pp. 283–286. IEEE (1999)
15. Paranjape, R.B., Mahovsky, J., Benedicenti, L., Koles, Z.: The electroencephalogram as a biometric. In: *Canadian Conference on Electrical and Computer Engineering*, vol. 2, pp. 1363–1366. IEEE (2001)
16. Martin, A., Doddington, G., Kamm, T., Ordowski, M., Przybocki, M.: The det curve in assessment of detection task performance. Technical report, DTIC Document (1997)



# Computer-Aided Diagnosis in Wound Images with Neural Networks

María Navas<sup>1</sup>, Rafael M. Luque-Baena<sup>1</sup>, Laura Morente<sup>2</sup>,  
David Coronado<sup>3</sup>, Rafael Rodríguez<sup>3</sup>, and Francisco J. Veredas<sup>1</sup>

<sup>1</sup> Dpto. Lenguajes y Ciencias de la Computación, Universidad de Málaga, Málaga, Spain  
mnavassanc@gmail.com, rmluque@lcc.uma.es, fvn@uma.es

<sup>2</sup> Escuela Universitaria de Enfermería, Diputación Provincial de Málaga, Málaga, Spain  
lmorente@malaga.es

<sup>3</sup> Wimasis SL, Córdoba, Spain  
{david.coronado,rafael.rodriguez}@wimasis.com

**Abstract.** Pressure ulcer is a clinical pathology of localized damage to the skin and underlying tissue caused by pressure, shear or friction. Diagnosis, care and treatment of pressure ulcers can result in extremely expensive costs for health systems. A reliable diagnosis supported by precise wound evaluation is crucial in order to success on the treatment decision and, in some cases, to save the patient's life. However, current evaluation procedures, focused mainly on visual inspection, do not seem to be accurate enough to accomplish this important task. This paper presents a computer-vision approach based on image processing algorithms and supervised learning techniques to help detecting and classifying wound tissue types which play an important role in wound diagnosis. The system proposed involves the use of the k-means clustering algorithm for image segmentation and a standard multilayer perceptron neural network to classify effectively each segmented region as the appropriate tissue type. Results obtained show a high performance rate which enables to support ulcer diagnosis by a reliable computational system.

## 1 Introduction

The European Pressure Ulcer Advisory Panel (EPUAP) defines a pressure ulcer (PU) as an area of localized damage to the skin and underlying tissue caused by pressure, shear, friction, or a combination of these factors [1–3]. Prevention, care and treatment of PU pathology represent high costs for health services [4] and have important consequences for the health of the affected population, specially for those populations at risk such as elderly people. Recent studies [5] have also shown how mortality rates associated with this pathology have increased in the last few years.

Accurate diagnosis of the wounds is critical in order to proceed with the right diagnosis and appropriate treatment, which in some cases can require surgery. This crucial evaluation is carried out by clinicians using standardized scales or indexes consisting mainly of a visual inspection of the ulcer. However, this technique has been proved to be an inaccurate way to deal with diagnosis of this sort of wounds [6, 7].

Image processing and computational intelligence techniques have been applied in several current studies to address different aspects of this particular problem of wound

diagnosis. One of these aspects involves the partial problem of wound area identification, which has been tackled with different techniques such as contour detection with histogram segmentation, active contours modelling, region growing, clustering approaches or skin texture models [8–10]. Unlike these proposals, other approaches focus on detecting the different tissues existing in the wound, by using diverse segmentation methods—such as histogram thresholding, watersheds, mean-shift smoothing, region growing, classification or graphs— sometimes combined with machine learning strategies [11, 12].

One of the most challenging factors to cope with when working with PU images lies in the very heterogeneous colourations they present, which are related with patient's skin colour and other several anomalies that may be observed in the images, such as erythemas, skin striation, etc. Moreover, boundaries between different tissue regions are usually extremely irregular and vague, which increases the complexity of the tissue segmentation process. The most recent work in this field [13] presents a mean-shift procedure along with a region-growing strategy for effective region segmentation, combined with a complex hybrid approach based on a cascade of single-class classifiers for wound tissue recognition. Although high efficacy rates were obtained, this work presents some significant limitations, since the classifiers are based on an elaborate architecture consisting of neural networks and Bayesian classifiers which were combined to recognize patterns of colour and texture features. Additionally, a complex set of heuristic techniques are needed to be applied to the classifiers' outputs to get the final classification results. In this study, a standard multilayer perceptron approach for PU tissue recognition together with a highly effective image processing procedure is proposed. This latter technique has been devised to extract a richer descriptor set than that obtained in [13], since not only texture and color features are taken into account, but also morphological and topological characteristics are considered.

This paper is structured in four sections, including the introduction given in this Section 1. In Section 2, the methodology followed in this approach is described. Experimental results achieved by this study are shown in Section 3. Finally, conclusions and further works are discussed in Section 4.

## 2 Methodology

Clinicians took color photographs of PUs of patients with home-care assistance. Sacrum and hip PUs were photographed under non-controlled illumination conditions by using a Sony Cybershot<sup>®</sup> W30 digital camera. The images were acquired with flash-light to get well-illuminated scenes, and at a distance of approximately 30–40 cm from the wound plane. Macro-photography focusing was used to ensure well-focused pictures within these short distances. A group of clinical experts selected a total of 113 photographs which were considered to be an appropriate data set for analysis because of the presence of all significant tissue types in PU evaluation.

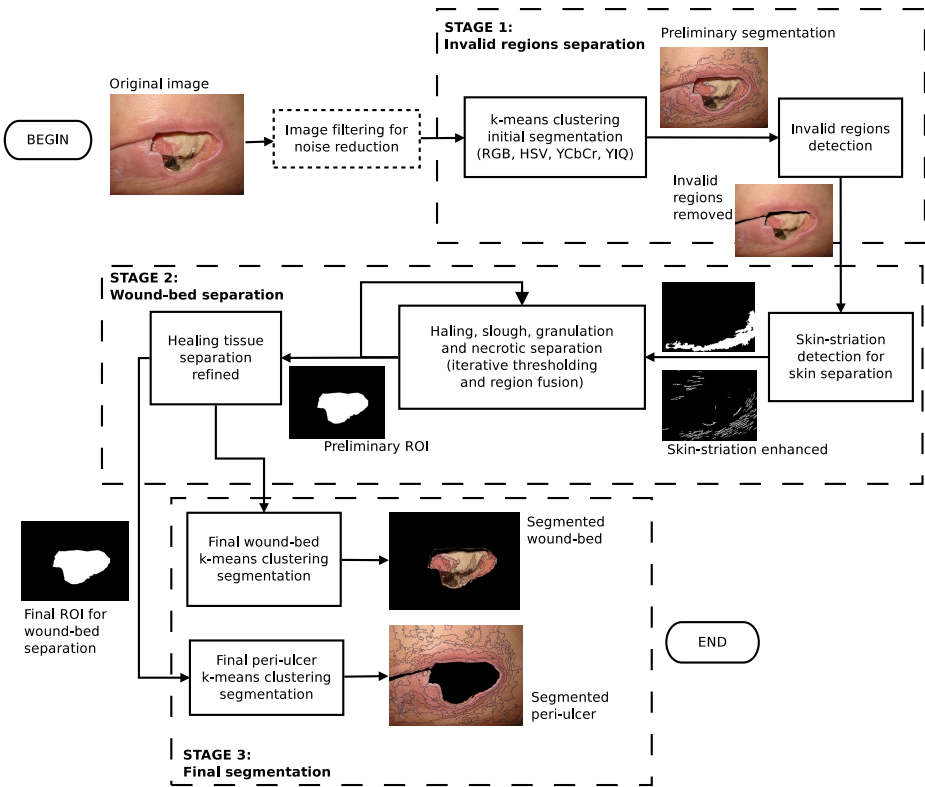
### 2.1 Segmentation Process

After an initial median filtering for noise reduction, a preprocessing procedure is applied to each photograph in order to previously detect and extract those spurious regions

consisting of flash-light reflections, blood stains, shadows, clinical stuff, clinician's fingers, normalization markers, etc. (see Figure 1). If these invalid areas are not removed, the number of regions generated by the segmentation module could negatively increase, affecting seriously the automatic recognition of significant PU tissues. Therefore, these regions are automatically extracted from the image before the segmentation process is initiated. To that end, an appropriate set of colour space transformations and standard deviation filters—which depend on the sort of invalid region needed to be detected—are applied to the images as a previous step to image segmentation. Although specific details of this preprocessing phase could be out of the scope of this paper, some explanations can be provided for the sake of clarity. Thus, flash-light reflections are detected in the HSV colour space as those regions with high saturation and luminance values. On the other hand, white square normalization markers included in the image are extracted by applying morphological transformations [14]. For its part, blood stains, that could hide significant tissues behind them, are identified by detecting those regions with high saturation values in the HSV colour space and low green components in the RGB space. Shadows are extracted from the images by working with the luminance component, which is computed as linear combination of the RGB components; those regions of low luminance and high saturation, that lack flash reflections and present an uniform colour distribution, with a low standard deviation in the center as well as a high standard deviation in the periphery, are considered as shadows. Other spurious regions, such as clinical stuff, clinicians' fingers, background, etc., are detected and removed by having into consideration their typical low luminance values as well as the abrupt transitions with other significant regions in the image.

The objective of the segmentation module is to divide the image into groups of pixels with similar characteristics and make it possible the subsequent classification of the regions obtained. This segmentation process is arranged in three main sequential stages (scheduled in Figure 1), which are based on the specific “center-surround topology” of the ulcer images, with a centred wound-bed that consists of a variable proportion of granulation, slough and necrotic tissues, which is immediately surrounded by epithelial healing tissue (that could present different conditions, such as intact and healthy, macerated, lacerated, eczematous, etc.) and a final periphery mostly consisted of healthy skin.

In a first stage, a simple k-means algorithm has been used (number of groups  $k = 12$ ) to get a preliminary segmentation, by clustering the pixels in the image into separate groups consisted of adjacent pixels with similar colour features. This step makes it possible to work at region-level instead of doing it at pixel-level. Components from four different colour spaces—RGB, HSV, YCbCr and YIQ—have been used for this clustering-based pre-segmentation, in particular S (Saturation), Y (luminance), Q (chrominance) and H (hue) components from those spaces. Of all the components in those four colour spaces, these last four are the ones that best allow the k-means algorithm to separate precisely those intricately tessellated regions of the three different wound-bed tissue types, providing large homogeneously composed skin regions as a expected result. The number of  $k = 12$  groups for the k-means algorithm has been chosen as the minimum number that maximizes the number of resulting segmented regions in the images that include an only tissue type (i.e. homogeneous regions).



**Fig. 1.** The image segmentation process, arranged in three main stages: 1) preprocessing for invalid regions detection, 2) separating the wound-bed area from the peri-ulcer area, and 3) an specific segmentation process is independently applied to each of the two main areas obtained

In a following segmentation stage, some image processing steps have been designed to separate the wound-bed area from the peri-ulcer area (healing and skin regions). In a final stage, an specific segmentation process is independently applied to each of the two main areas obtained, wound-bed and peri-ulcer.

**Wound-Bed Area Detection Stage.** At this point, a subsequent iterative processing stage has been carried out on the regions resulting from the k-means clustering, with the main objective of locating those regions consisting of healing tissue, slough, granulation and necrotic areas. This tissue detection supplies us with information about the wound-bed shape, since healing tissue is mainly arranged along wound-bed edges and delimits the wound-bed area consisted of granulation, slough and necrotic regions. A iterative process applied on the regions obtained from the k-means clustering has been designed, which start with the definition of a new set of colour channels obtained by linear and non-linear transformation of the 12 components from the four colour spaces above. Thresholding strategies based on the distribution of these colour channels in each

different tissue type, allow us to obtain a ROI (Region Of Interest) mask corresponding to an *estimated wound-bed* area.

**Final Segmentation Stage.** Once the wound-bed area is fully separated from the peri-ulcer area, pixels inside and outside that wound-bed are processed in two separated pools, respectively, to get the final segmented image. For pixels in each one of these pools, the k-means ( $k = 12$ ) clustering algorithm is applied again, but using different combinations of color spaces, channels and transformed channels to enhance the separation between clusters in the multi-dimensional feature spaces of the pixels in both areas. The k-means algorithm separates the pixels in each area (*estimated wound-bed* and *peri-ulcer*) into 12 different groups. Even though there could be only four different tissue types inside the *estimated wound-bed* (granulation, slough, necrotic and healing regions) as well as two different tissue classes in the *estimated peri-ulcer* (skin and healing regions), that higher number of clusters than tissue types is used in order to ensure that one and only one tissue type can be found in every region generated by the k-means clustering. At the same time, although the number of resulting regions can be high, region sizes are large enough to extract significant descriptors to be identified as the right tissue type by the subsequent classification process.

A total 15,768 regions are finally obtained from the 113 images after segmentation, with an average 139.54 regions per image (standard deviation 43.88 regions), of which we got an average 66.31 regions per image in the wound-bed area (standard deviation 43.88 regions) and an average 73.23 regions per image in the peri-ulcer area (standard deviation 32.56 regions).

Once the images have been segmented, a set of patterns consisted of topological, morphological, colour and texture descriptors from each one of the segmented regions is extracted. A brief enumeration of these features can be summarized as follows:

– Colour components:

- Components from different colour spaces:
  - \* RGB
  - \* YIQ
  - \* YCbCr
  - \* HSV
- Linear and non-linear combinations of the different components from the colour spaces above, to get transformed colour features.
- Image-level descriptors:
  - \* Percentiles of the transformed colour components intensity levels.
  - \* Estimated threshold for the Cr channel (from the YCbCr colour space).
- Region-level descriptors:
  - \* Mean intensity levels of the transformed colour components.
  - \* Standard deviations of the transformed colour components.
  - \* Mean of the standard deviation filter applied to the region, for all the transformed colour components.

– Topological and morphological components:

- Image-level descriptors:
  - \* Estimation of the radius of the wound-bed in pixels units.

- Region-level descriptors:
  - \* Percentiles of the distribution of the distance of the pixels in the region to the wound-bed border.
  - \* Percentiles of the distribution of the distance of the pixels in the region to the wound-bed center.
  - \* Ratio of the region perimeter belonging to the wound-bed border.
  - \* Ratio of the region perimeter belonging to the image border.
  - \* Ratio of the region area belonging to the preliminary ROI (see Figure 1).
  - \* Ratio of the region area belonging to the first wound-bed area estimation (see Figure 1).
  - \* Ratio of the region area belonging to the final wound-bed area estimation (see Figure 1).

In total, 104 features are used as inputs to the classifiers, which are also supplied with the output value representing the *tissue-class* during the supervised learning phase. A group of 5 expert clinicians from the *Málaga Province Health Services* labelled each region from the set of 113 segmented images, by assigning one of the five possible tissue types (*granulation, slough, necrotic, healing* or *skin*) to each region in the segmented images: these labelled images become the *gold-standards* and give the expected outputs from the classifiers during its supervised training phase.

The tissue class shows an unbalanced distribution in our data, since the prevalence of the different tissue types is quite heterogeneous. Using re-sampling with no replacement contributes to cope with this problem, that could negatively affect the classification process. Figure 2 shows the number of patterns per tissue type used in our experiments with multi-class classifiers (see tables 2 and 3), before and after applying re-sampling<sup>1</sup>.

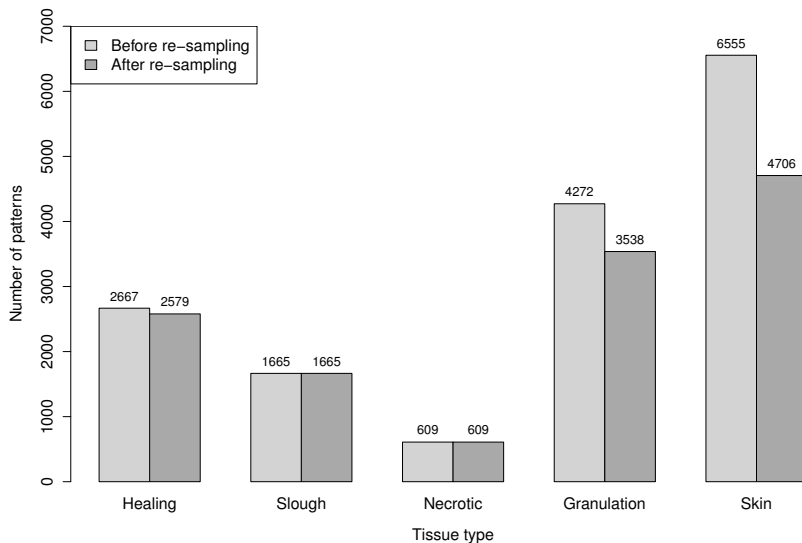
### 3 Experimental Results

In this study, PU diagnosis has been approached as a classification problem. Thus, the design of a pattern recognition system for PU tissue classification has been accomplished by following a supervised approach consisted of two standard three-layer multilayer perceptrons (MLP) (parameters: learning rate = 0.3; momentum = 0.2; one hidden layer of  $(\#classes + \#attributes)/2$  nodes; neurons follow a sigmoid activation function; input patterns are normalized; back-propagation learning rule for 500 *epochs*) specifically trained to classify independently the regions in the *estimated wound-bed* (four tissue classes) and the *estimated peri-ulcer* (two tissue classes), respectively.

The values shown in Table 1 have been generated by a k-fold cross-validation strategy ( $k = 10$ ) using the MLP configuration above. High overall efficacy rates have been obtained in general, although the classifier achieves better results for specific tissue types such as skin and granulation, with high specificity scores for all tissue types.

In order to compare the performance results given by the MLP, a multi-class experiment has been designed to classify all the regions from the segmented images, this time with no distinction between wound-bed or peri-ulcer tissues, i.e. classifying each region

<sup>1</sup> Weka 3.6.8 supervised instance resampling filter, with bias-to-uniform parameter = 0.5.



**Fig. 2.** Numbers of patterns per tissue class, before and after applying re-sampling

as one of the five possible PU tissue classes. Besides the MLP, the following alternative supervised approaches have been also used: a support vector machine (SVM) with polynomial kernel; a decision tree trained with the C4.5 algorithm (with confidence factor = 0.25 and minimum number of instances per leaf = 2); and a Naïves Bayes classifier. The efficacy rates (correctly classified, sensitivity or recall, precision and f-measure) shown in Table 2 have been obtained by running 10 independent executions for each different classifier, with  $k$ -fold stratified cross validation ( $k = 10$ )<sup>2</sup>.

In Table 2, it is possible to observe the high performance rates achieved by the MLP, followed in order by the SVM and the C4.5 algorithm (Naïve Bayes classifier can be considered as a basal-line classifier for comparisons). A *paired Student's T-Test* ( $p = 0.05$ ) used to compare the results of Table 2 provides significant differences in favour of the MLP approach for all of the efficacy measures shown in Table 2.

Figure 3 shows the *ROC curves* corresponding to the classifiers' efficacy rates for a single tissue type, the healing tissue, as an illustrative example (healing tissue is considered as a critical tissue to estimate the wound area). Here, it can be easily observe how the MLP gives the best trade-off between true positive rate (benefits) and false positive rate (cost).

Finally, a similar experiment has been performed to obtain the results in Table 3, where a correlation-based feature subset selection algorithm has been applied to remove those descriptors that may be redundant for classification purposes. This feature selection evaluator favours those feature subsets that are highly correlated with the feature

<sup>2</sup> Weka 3.6.8 has been used to run the classification experiments with standard parameters for all the analysed approaches.

**Table 1.** Performance rates for each tissue class from the MLP approach on patterns in the testing set (data from k-fold cross-validation,  $k = 10$ )

	<i>Balanced Accuracy</i>	<i>Sensitivity</i>	<i>Specificity</i>	<i>Precision</i>	<i>F-Measure</i>
<i>Necrotic</i>	0.907	0.823	0.992	0.828	0.825
<i>Slough</i>	0.875	0.776	0.975	0.808	0.792
<i>Granulation</i>	0.924	0.889	0.959	0.864	0.876
<i>Healing</i>	0.873	0.796	0.949	0.794	0.795
<i>Skin</i>	0.956	0.944	0.968	0.949	0.946
<i>Weighted average</i>	0.919	0.874	0.964	0.874	0.874

**Table 2.** Performance rates (mean  $\pm$  standard deviation) from MLP, SVM, C4.5 (decision tree) and Naïves Bayes classifiers on patterns in testing sets (data from 10 executions for each classifier, with k-fold cross-validation,  $k = 10$ )

	<i>Correctly classified</i>	<i>Sensitivity</i>	<i>Precision</i>	<i>F-Measure</i>
<i>MLP</i>	0.86 $\pm$ 0.01	0.76 $\pm$ 0.04	0.79 $\pm$ 0.04	0.77 $\pm$ 0.02
<i>SVM</i>	0.84 $\pm$ 0.01	0.70 $\pm$ 0.03	0.74 $\pm$ 0.02	0.72 $\pm$ 0.02
<i>C4.5 Decision tree</i>	0.84 $\pm$ 0.01	0.72 $\pm$ 0.03	0.73 $\pm$ 0.02	0.73 $\pm$ 0.02
<i>Naïves Bayes</i>	0.71 $\pm$ 0.01	0.47 $\pm$ 0.03	0.49 $\pm$ 0.02	0.48 $\pm$ 0.02

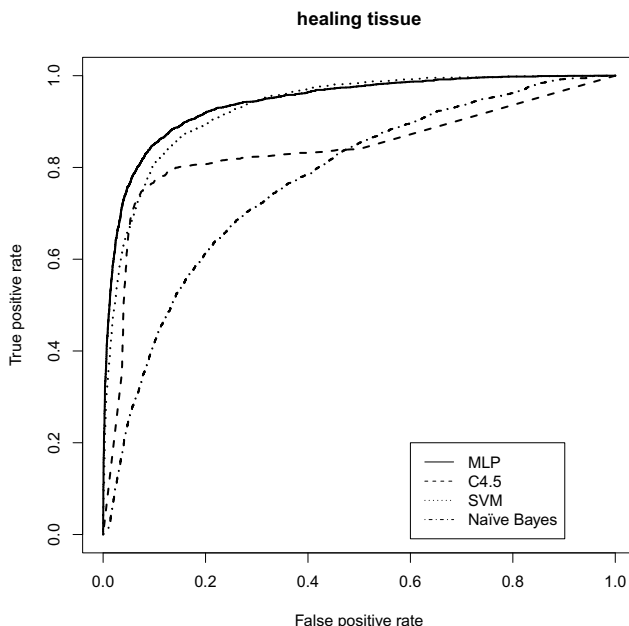
**Table 3.** Performance rates from MLP, SVM, C4.5 (decision tree) and Naïves Bayes classifiers on patterns in testing sets, with feature selection (data from 10 executions for each classifier, with k-fold cross-validation,  $k = 10$ )

	<i>Correctly classified</i>	<i>Sensitivity</i>	<i>Precision</i>	<i>F-Measure</i>
<i>MLP</i>	0.80 $\pm$ 0.01	0.57 $\pm$ 0.07	0.68 $\pm$ 0.05	0.61 $\pm$ 0.03
<i>SVM</i>	0.78* $\pm$ 0.01	0.54 $\pm$ 0.03	0.61* $\pm$ 0.02	0.58* $\pm$ 0.02
<i>C4.5 Decision tree</i>	0.79 $\pm$ 0.01	0.62 <sup>+</sup> $\pm$ 0.03	0.66 $\pm$ 0.02	0.64 <sup>+</sup> $\pm$ 0.02
<i>Naïves Bayes</i>	0.70* $\pm$ 0.01	0.44* $\pm$ 0.03	0.44* $\pm$ 0.02	0.44* $\pm$ 0.02

class (tissue type), meanwhile giving low inter-correlation rates. As a search method for feature selection, greedy best-first with forward direction has been used, giving 26 feature descriptors as a result.

If the results in Table 3 are compared with those ones observed in Table 2, it is easily remarkable that the feature selection process makes classification performance rates worse for all the four different classifiers analysed. Nevertheless, MLP gives the best performance rates again, with also significant differences in its favour found for those efficacy rates marked with asterisk (\*) in Table 3 (*paired T-Test*, with  $p = 0.05$ ; significant rates in favour of any of the other methods are marked with the symbol '+').





**Fig. 3.** Comparison of the ROC curves from four different supervised approach to classify healing tissue

## 4 Conclusions

A clustering-based image segmentation approach along with a standard MLP neural network have been presented to accomplish automatic tissue recognition for PU diagnosis, with images taken in environments with non-controlled illumination. Neural networks have provided high performance rates when classifying patterns composed of colour, texture, region morphology and topology features extracted from the segmented regions in a set of real PU images. Significantly higher efficacy rates have been obtained when comparing the MLP approach with other supervised strategies based on support vector machines, decision trees or Bayes classifiers. High efficacy scores are also obtained in the classification of necrotic and slough tissues, which are extremely important tissues in PU diagnosis. All these outcomes are achieved by using a standard MLP architecture with a typical parameter configuration. As future work, one may speculate on the idea that even higher performance rates could be obtained by optimizing this MLP architecture and parameter configuration (number of hidden layers, learning rate, early stopping, etc), or designing committee machines or hybrid approaches that adapt even better to this particular computer vision problem. A further systematic analysis of feature selection methods could be also done as future work to improve the results obtained.

**Acknowledgements.** This research has been partially funded by *Consejería de Salud y Bienestar Social, Servicio Andaluz de Salud, Junta de Andalucía*, projects PI-0502/2009 and PI-0027/2012. Additionally, the authors acknowledge support through grants TIN2010-16556 from MICINN-SPAIN and P08-TIC-04026 (Junta de Andalucía), all of which include FEDER funds.

## References

1. European Pressure Ulcer Advisory Panel (EPUAP): Guidelines on treatment of pressure ulcers. *EPUAP Review* 1, 31–33 (1999)
2. Tsuji, S., Ichioka, S., Sekiya, N., Nakatsuka, T.: Analysis of ischemia-reperfusion injury in a microcirculatory model of pressure ulcers. *Wound Repair and Regeneration* 13, 209–215 (2005)
3. Gawlitta, D., Li, W., Oomens, C.W.J., Baaijens, F.P.T., Bader, D.L., Bouten, C.V.C.: The relative contributions of compression and hypoxia to development of muscle tissue damage: An in vitro study. *Annals of Biomedical Engineering* 35, 273–284 (2007)
4. Stratton, R., Green, C., Elia, M.: Disease-related Malnutrition: An evidence-based approach to treatment. CABI Publishing, Wallingford, United Kingdom (2003)
5. Landi, F., Onder, G., Russo, A., Bernabei, R.: Pressure ulcer and mortality in frail elderly people living in community. *Archives of Gerontology and Geriatrics* 44, 217–223 (2007)
6. Beeckman, D., Schoonhoven, L., Fletcher, J., Furtado, K., Gunningberg, L., Heyman, H., Lindholm, C., Paquay, L., Verdu, J., Defloor, T.: EPUAP classification system for pressure ulcers: European reliability study. *Journal of Advanced Nursing* 60, 682–691 (2007)
7. Edsberg, L.E.: Pressure ulcer tissue histology: An appraisal of current knowledge. *Ostomy/Wound Management* 53, 40–49 (2007)
8. Cula, O., Dana, K., Murphy, F., Rao, B.: Skin texture modeling. *International Journal of Computer Vision* 62, 97–119 (2005)
9. Jones, T.D., Plassmann, P.: An active contour model for measuring the area of leg ulcers. *IEEE Transactions on Medical Imaging* 19, 1202–1210 (2000)
10. Karkanis, S.A., Iakovidis, D.K., Maroulis, D.E., Karras, D.A., Tzivras, M.: Computer-aided tumor detection in endoscopic video using color wavelet features. *IEEE Trans. Inf. Technol. Biomed.* 7, 141–152 (2003)
11. Kosmopoulos, D., Tzeveleku, F.: Automated pressure ulcer lesion diagnosis for telemedicine systems. *IEEE Engineering in Medicine and Biology* 26, 18–22 (2007)
12. Wannous, H., Treuillet, S., Lucas, Y.: Supervised tissue classification from color images for a complete wound assessment tool. In: *Proceedings of the 29th Annual International Conference of the IEEE EMBS, Cité Internationale, Lyon, France*, pp. 6031–6034 (2007)
13. Veredas, F., Mesa, H., Morente, L.: Binary tissue classification on wound images with neural networks and bayesian classifiers. *IEEE Transactions on Medical Imaging* 29, 410–427 (2010)
14. Veredas, F., Mesa, H., Morente, L.: Tissue recognition approach to pressure ulcer area estimation with neural networks. In: Cabestany, J., Sandoval, F., Prieto, A., Corchado, J.M. (eds.) *IWANN 2009, Part I. LNCS*, vol. 5517, pp. 1045–1052. Springer, Heidelberg (2009)

# Hierarchical Self-Organizing Networks for Multispectral Data Visualization

Esteban José Palomo, Ezequiel López-Rubio, Enrique Domínguez,  
and Rafael Marcos Luque-Baena

Department of Computer Science  
E.T.S.I.Informatica, University of Malaga  
Campus Teatinos s/n, 29071 – Malaga, Spain  
{ejpalomo,ezeqlr,enriqued,rmluque}@lcc.uma.es

**Abstract.** Image segmentation is a typical task in the field of image processing. There is a great number of image segmentation methods in the literature, but most of these methods are not suitable for multispectral images and they require a priori knowledge. In this work, a hierarchical self-organizing network is proposed for multispectral image segmentation. An advantage of the proposed neural model is due to the hierarchical architecture, which is more flexible in the adaptation process to input data. Experimental results show that the proposed approach is promising for multispectral image processing.

**Keywords:** Self-organization, multispectral data, data clustering, hierarchical self-organizing maps.

## 1 Introduction

New advances in remote sensing enable investigators to acquire larger, more complex image datasets. These images can generate data with six or more dimensions; e.g. images provided by new lasers scanning microscopy or satellites. However, the human visual system is only capable to perceive as much 3 dimensions of such data.

In many environmental assessments (agriculture, meteorology, etc.), satellite images are an important source of information. There are multispectral scanner systems that sample all available bands of the electromagnetic spectrum and exhibit an extraordinary diversity. Usually, satellites have three or more remote sensing radiometers, each of one acquire a digital image in different bands of spectra. For example, Landsat is capable to acquire multispectral images composed by eight bands: three visible bands (red, green and blue), near infrared, middle infrared, far infrared or thermal and radar band.

In addition, multispectral imaging has also assisted in many archaeological surveys. Consequently, the analysis of multispectral images is an essential issue in many research areas and management tasks. Nevertheless, it can be a daunting task to analyze these multidimensional image datasets. Such data may be so rich in information that repeated reanalysis, focusing on different systems and

hypotheses, is necessary. Even simple visualizations of the data may not be trivial. The investigator needs to be able to browse through potentially gigabytes of information, possibly arranged in a non-intuitive fashion. Moreover, some types of data may be so complex that they are not entirely represented in a three-parameter (RGB or HSV) color model on the computer screen.

In this work, a hierarchical self-organized neural network is proposed for multispectral image segmentation. In the literature, it is observed that artificial neural networks are widely used for the segmentation of remote-sensing images [1–5]. Also, the combination of the neural networks and statistical algorithms is used for the segmentation of the remote-sensing images [6, 7].

The rest of the paper is organized as follows. First the hierarchical neural network (Section 2) used in this paper for multispectral image visualization is presented. Some experimental results are shown in Section 3. Finally, Section 4 is devoted to conclusions.

## 2 GHSOM Model

The GHSOM is an artificial neural network proposed by [8] that has a hierarchical architecture arranged in layers, where each layer consists of several growing SOMs [9]. Initially, the GHSOM starts with a single SOM of 2x2 neurons. During the training, this SOM is automatically adapted according to the input patterns [10]. The SOM can grow by adding a row or a column of neurons until reach a certain level of detail in the representation of the data mapped onto the SOM. After growing, neurons that have a bad representation of the data can be expanded in a new map in the next layer of the hierarchy in order to provide a more detailed representation of the data mapped onto the neuron. The final architecture of the GHSOM mirrors the inherent hierarchical structure of the input patterns, improving the representation achieved with a single SOM. Therefore, each neuron represents a data cluster, where data belonging to one cluster are more similar than data belonging to different clusters.

Two parameters are provided by the GHSOM ( $\tau_1$  and  $\tau_2$ ) to control the growth of the maps and the hierarchical growth of the GHSOM, respectively. This adaptation depends mainly on the quantization error of the neuron ( $qe$ ). The  $qe$  is a measure of the similarity of data mapped onto each neuron, where the higher the  $qe$  is, the higher the heterogeneity of the data cluster is. The quantization error of the unit  $i$  is defined as follows

$$qe_i = \sum_{x_j \in C_i} \|w_i - x_j\|, \quad (1)$$

where  $C_i$  is the set of patterns mapped onto the neuron  $i$ ,  $x_j$  is the  $j$ th input pattern from  $C_i$ , and  $w_i$  is the weight vector of the neuron  $i$ .

When the training of the map  $m$  is finished, the growing of the map has to be checked. For that, the quantization error of each neuron ( $qe_i$ ) must be computed in order to compute the mean of the quantization error of the map ( $MQE_m$ ). If the  $MQE_m$  of the map  $m$  is smaller than a certain fraction  $\tau_1$  of the quantization

error of the corresponding parent neuron  $u$  in the upper layer, the map stops growing. This stopping for the growth of a map is defined in (2). Otherwise, the map grows to achieve a better level of representation of the data mapped onto the map, so the smaller the  $\tau_1$  parameter chosen the larger the map. The growing of a map is done by adding a row or a column of neurons between two neurons, the neuron with the highest quantization error  $e$  and its most dissimilar neighbor  $d$ .

$$MQE_m < \tau_1 \cdot qe_u. \tag{2}$$

Initially, the quantization error at layer 0 must be computed as given in (3), where  $w_0$  is the mean of the all input data  $I$ . The initial quantization error ( $qe_0$ ) measures the dissimilarity of all input data and it is used for the hierarchical growth process of the GHSOM together with the  $\tau_2$  parameter, following the condition given in (4). This condition shows that the quantization error of a neuron  $i$  ( $qe_i$ ) must be smaller than a fraction ( $\tau_2$ ) of the initial quantization error ( $qe_0$ ). Otherwise, the neuron is expanded in a new map in the next level of the hierarchy, so the smaller the  $\tau_2$  parameter the deeper the hierarchy.

$$qe_0 = \sum_{x_j \in I} \|w_0 - x_j\|. \tag{3}$$

$$qe_i < \tau_2 \cdot qe_0. \tag{4}$$

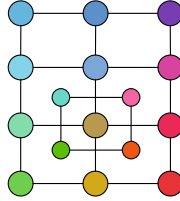
When a new map is created, a coherent initialization of the weight vectors of the neurons of the new map is used as proposed by [11]. A new map created from an expanded neuron is trained as a single SOM. During the training, the set of input patterns are those that were mapped onto the upper expanded unit. In each iteration  $t$ , an input pattern is randomly selected from this data subset. The winning neuron of the map ( $r$ ) is the neuron with the smallest Euclidean distance to the input pattern. The winner's weight vector is updated guided by a learning rate  $\alpha$ , decreasing in time (5). In addition to the winner, the neighbors of the winner are updated depending on a Gaussian neighborhood function  $h_i$  and their distances to the winner. This neighborhood function (6) reduces its neighborhood kernel  $\delta$  during training, being  $\|r_c - r_i\|^2$  the distance between neurons  $c$  and  $i$  within the output space, with  $r_i$  representing the 2-D coordinates of the neuron  $i$  within the grid.

$$w_i(t + 1) = w_i(t) + \alpha(t)h_i(t)[x(t) - w_i(t)], \tag{5}$$

$$h_i(t) = \exp\left(-\frac{\|r_c - r_i\|^2}{2 \cdot \delta(t)^2}\right). \tag{6}$$

Next we describe a method to assign a pair of coordinates to each neuron of a GHSOM network. First of all, we assign integer coordinates to the neurons of the top level map. Hence, for a top level map with  $N_1 \times N_2$  neurons we get coordinates of the form  $(i, j)$  with  $i \in \{1, 2, \dots, N_1\}$ ,  $j \in \{1, 2, \dots, N_2\}$ , so that the spacings between two neighbor neurons in each dimension are  $\zeta_1 = 1$ ,  $\zeta_2 = 1$ .

If at a level with spacings  $\zeta_1, \zeta_2$  there is a neuron with coordinates  $(a, b) \in \mathbb{R}^2$  which has a child map with  $M_1 \times M_2$  neurons, then we assign to these neurons equally spaced coordinates in the square  $\left[ a - \frac{\zeta_1}{2}, a + \frac{\zeta_1}{2} \right] \times \left[ b - \frac{\zeta_2}{2}, b + \frac{\zeta_2}{2} \right]$ , with spacings  $\zeta'_1 = \frac{\zeta_1}{M_1+2}, \zeta'_2 = \frac{\zeta_2}{M_2+2}$ . The coordinates of the child neuron at lattice position  $(h, k) \in \{1, \dots, M_1\} \times \{1, \dots, M_2\}$  are  $\left( a - \frac{\zeta_1}{2} + h\zeta'_1, b - \frac{\zeta_2}{2} + k\zeta'_2 \right)$ . An example is shown in Figure 1, with  $N_1 = 4, N_2 = 3, M_1 = M_2 = 2$ . The neurons are shown in CIELAB colors according to their positions.



**Fig. 1.** Bidimensional coordinate assignment for a GHSOM

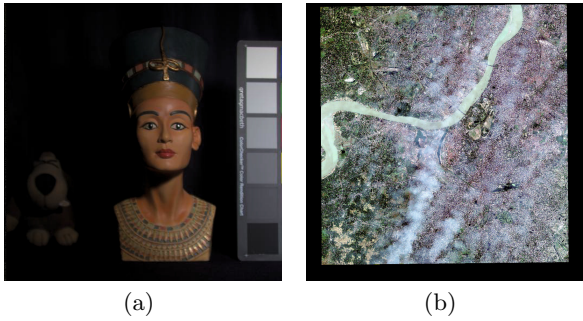
### 3 Experimental Results

In this section, the segmentation of multispectral images has been performed by using the GHSOM. Two different multispectral images were selected for our experiments: an Egyptian statue and satellite image of a reserved forest in India. The Egyptian statue image was selected from a multispectral image database of the Columbia University<sup>1</sup>. This image has a resolution of 512x512 pixels and a full spectral resolution reflectance data from 400nm to 700nm at 10nm steps (31 bands). The satellite image of a reserved forest in India was chosen from the QuickBird Imagery through the Global Land Cover Facility<sup>2</sup>. The selected image has a resolution of 4096x4096 pixels and a spectral resolution reflectance data from 450nm to 900nm dividing them into 4 bands (blue, green, red and near infrared). Note that the two selected multispectral images have different characteristics in order to compare their results. These two multispectral images are shown in RGB in Figure 2.

For both multispectral images, the GHSOM was trained during two epochs and using two different configurations of the parameters  $\tau_1$  and  $\tau_2$  to see the effects of diminishing these two parameters. We chose  $\tau_1 = 0.1$  and  $\tau_2 = 0.1$  for the first configuration; and  $\tau_1 = 0.01$  and  $\tau_2 = 0.01$  for the second. Ten folds were run and the model with minimum quantization error (see Section 2) was chosen to visualize the resulting segmentation for each configuration of the  $\tau_1$  and  $\tau_2$  parameters. The GHSOM was fed first with the multispectral data from the

<sup>1</sup> Available online: <http://www.cs.columbia.edu/CAVE/databases/multispectral/>

<sup>2</sup> Available online: <http://glcf.umiacs.umd.edu/data/quickbird/>



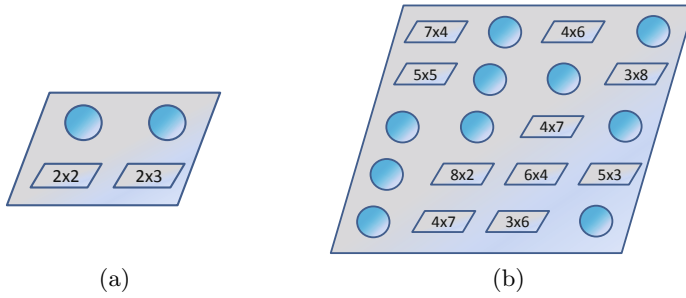
**Fig. 2.** RGB images of the two multispectral images: (a) Egyptian statue and (b) satellite image of a reserved forest in India

Egyptian statue image, from which a dataset of 262,144 input samples ( $D = 31$ ) was extracted. The obtained model for the two configurations of parameters is given in Figure 3. The first model (5(a)) has a map of 2x2 neurons at the first layer and two maps of 2x2 and 2x3 neurons at the second layer. The model for the second configuration has a 5x4 map at the first layer and ten maps of 7x4, 5x5, 8x2, 4x7, 4x6, 4x7, 6x4, 3x6, 3x8 and 5x3 neurons at the second layer.

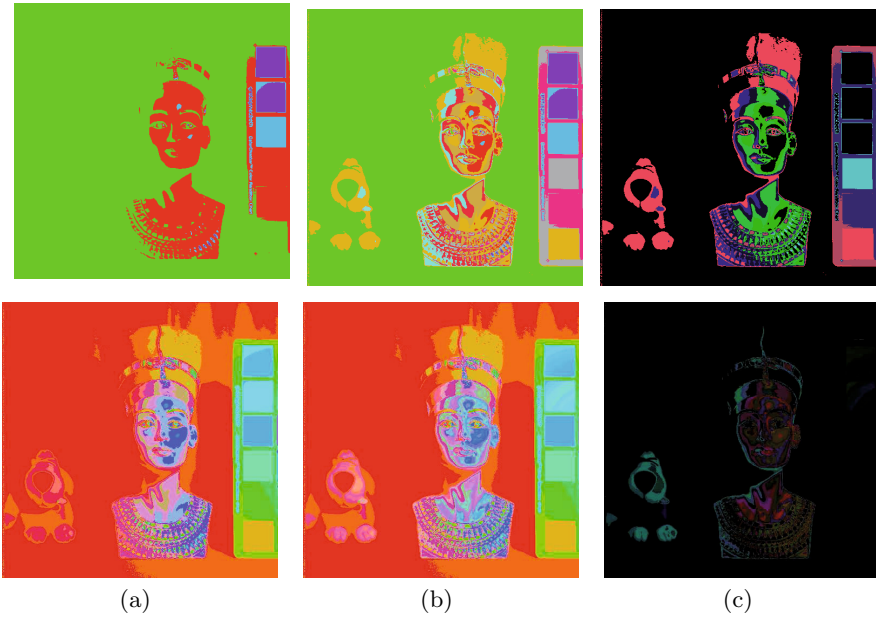
The segmentation performed for these two models is shown in Figure 4. We can see in the plots how the statue is appropriately segmented, the same as the dog doll next to the statue which almost could not be seen due to the poor contrast of the RGB image (see Figure 2(a)). Note that the deeper the layer, the better the segmentation. Thus, in the first row of Figure 4(a), the dog doll is not segmented due to the low number of neurons (4) at the first layer, whereas taking into account the second layer, this doll was segmented and the statue was represented at a higher level of detail. The difference image between the first layer and the first and second layer segmentation shows the contribution of the hierarchy to the segmentation. This contribution is lower for the second configuration (second row) since the segmentation at the first layer was performed with 20 neurons (colors).

From the second multispectral satellite image of a reserved forest in India, a dataset of 262,144 input samples ( $D = 4$ ) was designed, since the image was reduced to a resolution of 512x512 pixels. After training the GHSOM with this dataset, the obtained models for the two proposed configuration of parameters are given in Figure 5. The first model (5(a)) has a map of 2x3 neurons at the first layer, from which two neurons were expanded into two maps of 3x3 and 2x3 neurons. The second model (5(b)) presents a bigger architecture since the values of the two parameters were reduced for the training. For this configuration, a map of 5x5 neurons was generated at the first layer, whereas at the second layer ten maps of 4x2, 8x4, 4x8, 8x4, 6x6, 7x6, 9x4, 6x6, 8x4 and 6x6 neurons were obtained.

The segmentation performed by these GHSOM models is shown in Figure 6. The same analysis performed for the Egyptian statue image can be applied here.



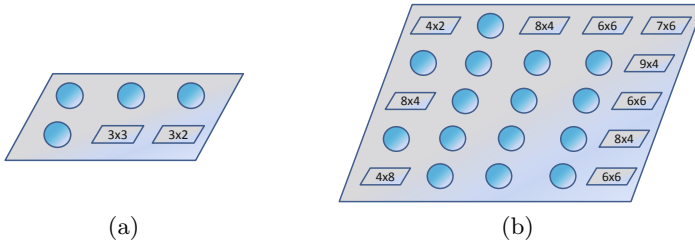
**Fig. 3.** GHSOM models in 2D of the Egyptian statue multispectral image setting: (a)  $\tau_1 = 0.1$  and  $\tau_2 = 0.1$  and (b)  $\tau_1 = 0.01$  and  $\tau_2 = 0.01$ . Neurons are represented by circles. Expanded neurons are represented by rectangles, which indicate the size of the expanded map at layer 2.



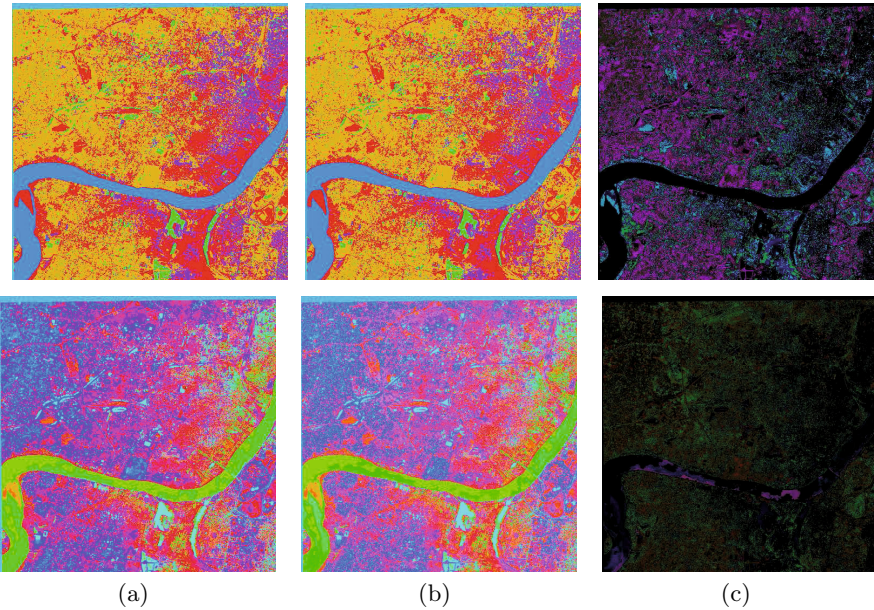
**Fig. 4.** GHSOM segmentation of the multispectral image of an Egyptian statue. The first row was obtained with  $\tau_1 = 0.1$  and  $\tau_2 = 0.1$ , whereas the second row with  $\tau_1 = 0.01$  and  $\tau_2 = 0.01$ . (a) First layer segmentation, (b) first and second layer segmentation and (c) difference image between (a) and (b) images.

Note that the river, the houses and the forest are clearly segmented in different regions. In the third column (6(c)), the differences between the segmentation achieved by the two layers of the hierarchy for both models can be noted, showing the contribution of the second layer to improve the segmentation of the first layer.





**Fig. 5.** GHSOM models in 2D of the multispectral satellite image of a reserved forest in India setting: (a)  $\tau_1 = 0.1$  and  $\tau_2 = 0.1$  and (b)  $\tau_1 = 0.01$  and  $\tau_2 = 0.01$ . Neurons are represented by circles. Expanded neurons are represented by rectangles, which indicate the size of the expanded map at layer 2.



**Fig. 6.** GHSOM segmentation of the multispectral satellite image of a reserved forest in India. The first row was obtained with  $\tau_1 = 0.1$  and  $\tau_2 = 0.1$ , whereas the second row with  $\tau_1 = 0.01$  and  $\tau_2 = 0.01$ . (a) First layer segmentation, (b) first and second layer segmentation and (c) difference image between (a) and (b) images.

As a quantitative measure, the mean quantization error of the 10 trained GHSOMs for each considered image and configuration is given in Table 1, where the standard deviations are shown in parenthesis. The mean quantization error of a GHSOM is computed recursively as the mean of the quantization errors of their leaf neurons along the hierarchy. Note that the larger the  $\tau_1$  and  $\tau_2$  parameters, the lower the mean quantization error. Also, larger values are obtained for the statue image since it is more complex ( $D = 31$ ) than the satellite image ( $D = 4$ ).

**Table 1.** Mean quantization error of the 10 trained GHSOMs for each considered image and configuration of parameters. Standard deviations are shown in parenthesis.

Image	$\tau_1 = 0.1/\tau_2 = 0.1$	$\tau_1 = 0.01/\tau_2 = 0.01$
Statue	3670.91 (299.42)	425.89 (49.88)
Satellite	2894.82 (318.12)	309.31 (30.21)

## 4 Conclusions

In this paper, a hierarchical self-organized neural network called GHSOM (Growing Hierarchical Self-Organizing Map) is used to visualize multispectral images. This neural network can be successfully applied to image segmentation tasks. Here, it is also used for segmentation and visualization of multispectral images. Two multispectral images were selected for our experiments: one with 31 bands, and the other one with 4 bands from a satellite image. Experimental results confirm the good performance of the approach.

**Acknowledgements.** This work is partially supported by the Ministry of Economy and Competitiveness of Spain under grant TIN2011-24141, project name Detection of anomalous activities in video sequences by self-organizing neural systems, and the Autonomous Government of Andalusia (Spain) under project P12-TIC-6213, project name Development of Self-Organizing Neural Networks for Information Technologies.

## References

1. Berberoglu, S., Lloyd, C., Atkinson, P., Curran, P.: The integration of spectral and textural information using neural networks for land cover mapping in the mediterranean. *Computers & Geosciences* 26(4), 385–396 (2000)
2. Jzwick, A., Serpico, S., Roli, F.: A parallel network of modified 1-nn and k-nn classifiers application to remote-sensing image classification. *Pattern Recognition Letters* 19(1), 57–62 (1998)
3. Bruzzone, L., Prieto, D.F.: An incremental-learning neural network for the classification of remote-sensing images. *Pattern Recognition Letters* 20(1113), 1241–1248 (1999)
4. Villmann, T., Mernyi, E., Hammer, B.: Neural maps in remote sensing image analysis. *Neural Networks* 16(34), 389–403 (2003)
5. Kurnaz, M.N., Dokur, Z., Lmez, T.: Segmentation of remote-sensing images by incremental neural network. *Pattern Recognition Letters* 26(8), 1096–1104 (2005)
6. Giacinto, G., Roli, F., Bruzzone, L.: Combination of neural and statistical algorithms for supervised classification of remote-sensing images. *Pattern Recognition Letters* 21(5), 385–397 (2000)
7. Serpico, S., Bruzzone, L., Roli, F.: An experimental comparison of neural and statistical non-parametric algorithms for supervised classification of remote-sensing images. *Pattern Recognition Letters* 17(13), 1331–1341 (1996)

8. Rauber, A., Merkl, D., Dittenbach, M.: The growing hierarchical self-organizing map: Exploratory analysis of high-dimensional data. *IEEE Transactions on Neural Networks* 13(6), 1331–1341 (2002)
9. Alahakoon, D., Halgamuge, S., Srinivasan, B.: Dynamic self-organizing maps with controlled growth for knowledge discovery. *IEEE Transactions on Neural Networks* 11, 601–614 (2000)
10. Kohonen, T.: Self-organized formation of topologically correct feature maps. *Biological Cybernetics* 43(1), 59–69 (1982)
11. Dittenbach, M., Rauber, A., Merkl, D.: Recent advances with the growing hierarchical self-organizing map. In: Anonymous (ed.) 3rd Workshop on Self-Organising Maps, WSOM, pp. 140–145 (2001)

# A Self-organizing Map for Traffic Flow Monitoring

Rafael Marcos Luque-Baena, Ezequiel López-Rubio, Enrique Domínguez,  
Esteban José Palomo, and José Manuel Jerez

Department of Computer Languages and Computer Science  
Bulevar Louis Pasteur, 35. 29071 Málaga, Spain,  
University of Málaga  
{rmluque, ezeqlr, enriqued, ejpalomo, jja}@lcc.uma.es

**Abstract.** Most of object detection algorithms do not yield perfect foreground segmentation masks. These errors in the initial stage of video surveillance systems could cause that the subsequent tasks like object tracking and behavior analysis, can be extremely compromised. In this paper, we propose a methodology based on self-organizing neural networks and histogram analysis, which detects unusual objects in the scene and improve the foreground mask handling occlusions between objects. Experimental results on several traffic sequences found in the literature show that the proposed methodology is promising and suitable to correct segmentation errors on crowded scenes with rigid objects.

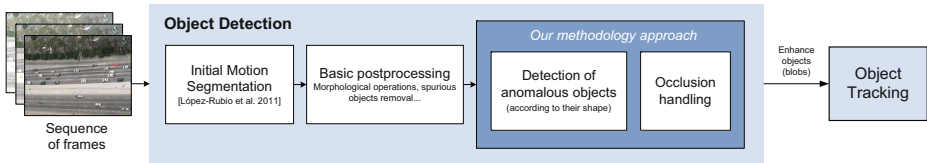
**Keywords:** self-organizing neural networks, postprocessing techniques, traffic monitoring, surveillance systems, object detection.

## 1 Introduction

Self-organizing models (SOM) have shown considerable promising in a wide variety of application areas, including hard video applications [1] like some robotic operation, visual inspection, remote sensing, autonomous vehicle driving, automated surveillance, and many others.

Several works have used self-organizing models for the representation and tracking of objects. Fritzke [2] proposed a variation of the GNG [3] to map non-stationary distributions that applies to the representation and tracking of people [4]. In [5] it is suggested the use of self-organized networks for human-machine interaction. In [6], amendments to self-organizing models for the characterization of the movement are proposed.

This paper aims to address the ability of self-organizing maps to detect poorly segmented objects in video sequences of traffic monitoring and improve the output of the segmentation mask. Standard object detection algorithms [7,8,9] do not provide a perfect foreground mask for each sequence frame, and difficulties like annoying noise, spurious blobs and occlusions among objects can arise. In this sense, we present an application of a neural architecture based on SOM that is able to adapt the topology of the network of neurons to the objects that appear in the images, and can represent the common features of the objects of interest. In traffic monitoring applications, cars are assumed to be the usual objects of interest, although other vehicles as trucks, motorcycles, etc. are unusual or anomalous objects due to the fewer occurrences of these kinds of objects in the video sequences.



**Fig. 1.** Framework of video surveillance systems in which our methodology is incorporated. It should be noticed that the results of our approach are the inputs of the following stage, object tracking.

The proposed methodology manages to detect anomalous objects, discriminate them between less frequent objects and overlapped objects generated because of segmentation errors, and correct the latter ones by analyzing their horizontal and vertical histograms. These corrections have a two-fold objective: improve the foreground mask which will benefit the subsequent object tracking algorithms, and cluster the data to determine different types of vehicles.

The rest of the paper is organized as follows: Section 2 sets out the methodology of this approach describing the self-organizing neural network adapted to this issue (Section 2.1) and the occlusion handling procedure to discriminate and correct overlapped objects (Section 2.2). Section 3 shows several experimental results over several well-known public traffic surveillance sequences and Section 4 concludes the article.

## 2 Methodology

The starting point of our proposal involves an initial segmentation of moving objects, which is achieved by separating the information corresponding to the foreground, i.e., the objects which are in movement, from the static background of the scene. Among the different alternatives, it is remarkable the model based on mixture of gaussians which uses a set of normal distributions for modeling both the background and the foreground [7]; an stochastic approximation method for representing the background and foreground with a multivariate gaussian and uniform distributions, respectively [8]; and the application of clustering techniques to group those patterns which are associated with the background to distinguish from those pixels in movement [9].

In this approach, the initial segmentation is obtained from the published work in [8]. Additionally, basic postprocessing operators such as erosion and dilatation are applied in order to filter and reduce the noise and the spurious objects of the segmentation mask.

Our approach is divided in two stages (see Figure 1), a self-organizing neural network to model the common shape objects in the scene and an occlusion handling process to deal with unusual objects, in order to detect if that anomaly is considered as a overlapped object or another kind of object with a fewer occurrence in the scene (truck, bicycle, ...). Each stage is described more thoroughly in the following sections.

### 2.1 Detection of Anomalous Objects

In order to detect anomalous objects, it is necessary to build a model of usual ones. From each object we extract a feature vector  $\mathbf{y} \in \mathbb{R}^D$ , and we aim to obtain a reduced

representation of the set of such vectors for usual objects. In a video scene, it must be taken into account that the typical features of the objects vary smoothly from one position to another. For example, approaching objects look bigger as they come closer to the camera, which means that their areas are larger. Consequently, the main task is to learn a smooth function

$$\mathcal{F} : \mathbb{R}^2 \rightarrow \mathbb{R}^D \quad (1)$$

$$\mathbf{y} = \mathcal{F}(\mathbf{x}) \quad (2)$$

In addition to this, it is also needed to record the variability among the typical data, in order to be able to spot anomalous data. This can be done by binning the typical data according to the position in the scene where they appear. Hence, we need distinct processing units spread across the scene which are able to cooperate among them. This leads to self-organizing maps, which fulfill this requirement. However, standard self-organizing maps are unsuitable for this task, since they do not output vectors.

The kind of self-organizing maps that this application requires belongs to the family of parametrized and interpolating maps, which are commonplace in robot inverse kinematics controllers [10,11,12,13]. The fundamental difference with the standard SOMs is that there are input vectors  $\mathbf{x} \in \mathbb{R}^2$  and output vectors  $\mathbf{y} \in \mathbb{R}^D$ . Each unit  $i$  has a prototype for input vectors  $\mathbf{w}_i \in \mathbb{R}^2$  and a prototype for output vectors  $\mathbf{v}_i \in \mathbb{R}^D$ . The winner unit is computed according to the input prototype, while the output prototype is used when we need to estimate the smooth function  $\mathcal{F}$ .

Let  $M$  be the number of units of the self-organizing map, which are arranged in a rectangular lattice of size  $a \times b$ , where  $M = ab$  (see Figure 2a). The topological distance between the units  $i$  and  $i'$ , located at lattice positions  $(p_1, p_2)$  and  $(p'_1, p'_2)$ , is given by:

$$d(i, i') = \sqrt{(p_1 - p'_1)^2 + (p_2 - p'_2)^2} \quad (3)$$

At time step  $n$ , a new input sample  $\mathbf{x}(n)$  and the corresponding output sample  $\mathbf{y}(n)$  are presented to the network, and a winner unit is declared:

$$Winner(\mathbf{x}(n)) = \arg \min_{j \in \{1, \dots, M\}} \|\mathbf{x}(n) - \mathbf{w}_j(n)\| \quad (4)$$

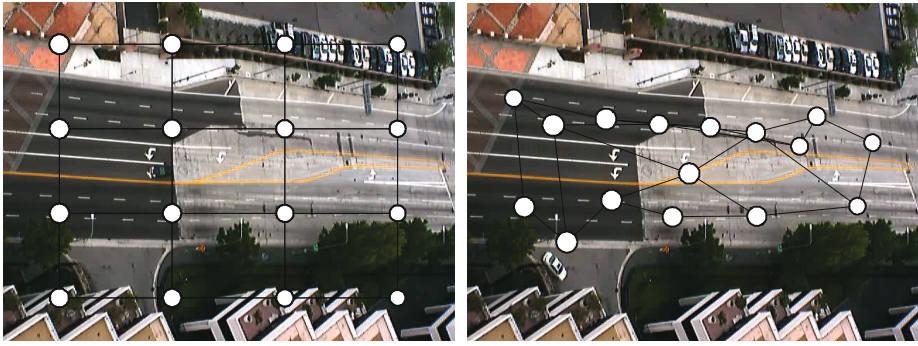
It is remarkable that only samples from one frame at each step are analyzed, since the learning strategy of the network is online. Then the input and output prototypes of all the units are adjusted, for  $i \in \{1, \dots, M\}$ :

$$\mathbf{w}_i(n+1) = \mathbf{w}_i(n) + \eta(n) \Lambda(i, Winner(\mathbf{x}(n))) (\mathbf{x}(n) - \mathbf{w}_i(n)) \quad (5)$$

$$\mathbf{v}_i(n+1) = \mathbf{v}_i(n) + \eta(n) \Lambda(i, Winner(\mathbf{x}(n))) (\mathbf{y}(n) - \mathbf{v}_i(n)) \quad (6)$$

where  $\eta(n)$  is a decaying learning rate and the neighborhood function  $\Lambda$  varies with the time step  $n$  and depends on a decaying neighborhood radius  $\Delta(n)$ :

$$\eta(n+1) \leq \eta(n) \quad (7)$$



(a) Initial topology of the self-organizing neural network (b) SOM Topology adapted to the *Lankershim* scene

**Fig. 2.** Self-organizing neural network initially distributed in the scene as a grid (a) and finally adapted to the most frequent positions of the vehicles in the scene. The size of the neurons, which represents the size of the vehicles in their corresponding zones of the scene, is also learned from the initial state.

$$A(i, j) = \exp \left( - \left( \frac{d(i, j)}{\Delta(n)} \right)^2 \right) \tag{8}$$

$$\Delta(n + 1) \leq \Delta(n) \tag{9}$$

The receptive field of unit  $i$ , i.e. the region of the input space which is represented by  $i$ , is defined as:

$$F_i = \{ \mathbf{x}(k) \mid i = \text{Winner}(\mathbf{x}(k)) \} \tag{10}$$

If we are presented a test sample  $\mathbf{x}$  and we wish to estimate  $\mathcal{F}(\mathbf{x})$ , then we compute the winning unit  $j = \text{Winner}(\mathbf{x})$  by (4) and we take

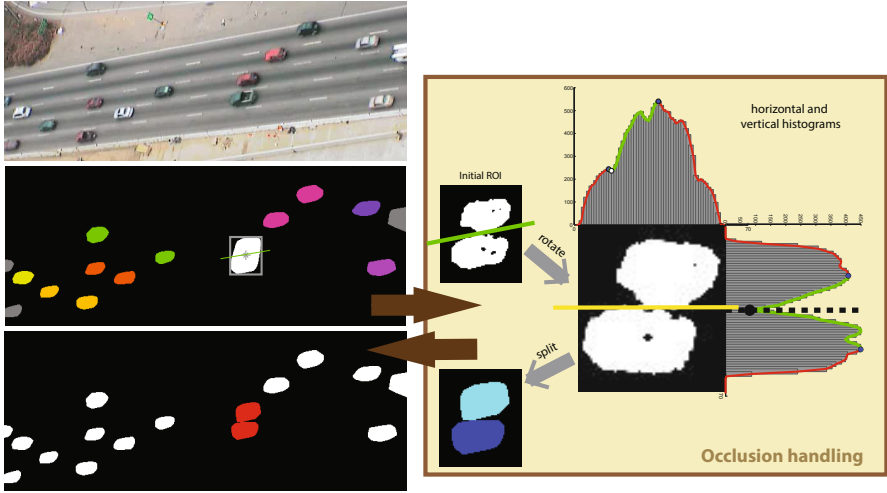
$$\mathbf{y} = \mathcal{F}(\mathbf{x}) = \mathbf{v}_j \tag{11}$$

That is, the estimated output is the output prototype of the winning unit. The topology of the SOM approach adapted to an specific scene is observed in Figure 2b. It should be noted that the size of the movement objects in the scene is also learned and represented by the size of the neurons.

Next we need a procedure to detect the anomalous samples. First of all, we keep in each unit  $i$  a log  $\mathcal{S}_i$  of the distances  $\|\hat{\mathbf{y}} - \mathbf{y}\|$  for all the anomalous test samples that belong to its receptive field  $F_i$ . This log is initialized with the inter-unit distances  $\|\mathbf{v}_i - \mathbf{v}_j\|$  for all the neighbors  $j$  of unit  $i$ . Then we decide whether an input sample belonging to  $F_i$  is anomalous as follows:

$$(\mathbf{x}, \mathbf{y}) \text{ is anomalous} \Leftrightarrow \|\hat{\mathbf{y}} - \mathbf{y}\| > \gamma P_{i,q} \tag{12}$$

where  $P_{i,q}$  stands for the  $q$ -th percentile of  $\mathcal{S}_i$ , and  $q \in \{1, \dots, 99\}$ ,  $\gamma > 0$  are suitable parameters.



**Fig. 3.** Occlusion handling process which manages the unusual objects detected in Section 2.1. From the horizontal and vertical histograms it is possible to identify the overlapped objects.

## 2.2 Occlusions Handling

The previous approach manages to model the normal shape of the objects in the scene, detecting those ones which are considered as strange or unusual. Thus, some of the abnormal objects may be due to overlapped objects caused by the segmentation algorithm. This kind of objects will be analyzed to undo the overlap and extract the individual objects. However, according to the traffic monitoring problem, our SOM approach considers as normal objects those ones whose occurrence is greater, in this case cars, while trucks, motorcycles or vehicles whose shape differs slightly normal are considered as unusual objects.

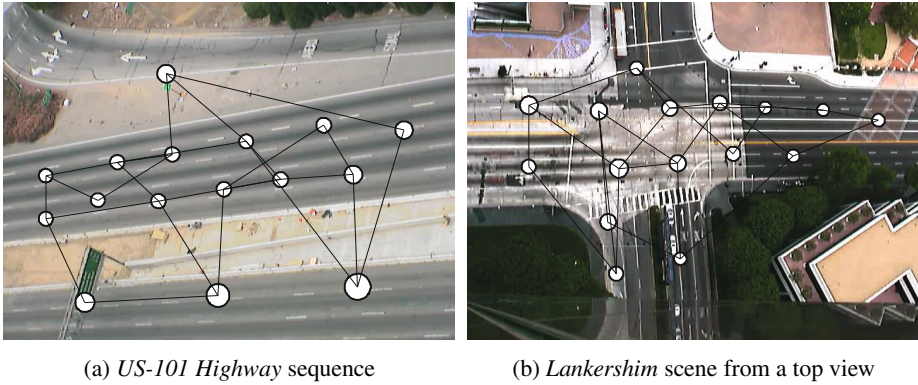
Therefore, in this section, each abnormal object is processed in order to find out if it is an overlapped object or a single object that actually differs from the normal ones (e.g. truck or motorcycle). The following steps are performed to detect and split overlapped objects:

1. From the initial image segmentation, a region of interest (ROI) of the unusual object is extracted and rotated according to the direction of movement in this particular area.
2. Computing the cast histograms over the horizontal and vertical axes.
3. For each histogram, two maximum peaks  $(x_{max_1}, y_{max_1})$  and  $(x_{max_2}, y_{max_2})$  and one minimum valley between the previous top values  $(x_{min_1}, y_{min_1})$  are obtained.
4. An overlapped object is considered if the following rule is satisfied:

$$\forall i \in \{1, 2\}, (y_{max_i} - y_{min}) \geq \alpha \max\{y_{max_i}\} \quad (13)$$

where  $\alpha \in (0, 1)$  is a factor which regulates the split process.





**Fig. 4.** Two different topologies of our SOM model which adapt automatically to the analyzed scenes. The camera perspective is also compensated.

Figure 3 shows a representation of the occlusion handling process. An unusual object is detected and colored in white (middle image on the left) because two vehicles are very close to each other (color image on the top left). Since it is considered as a overlapped object by analyzing the histograms, the final division of the objects is shown in red color in the bottom image on the left.

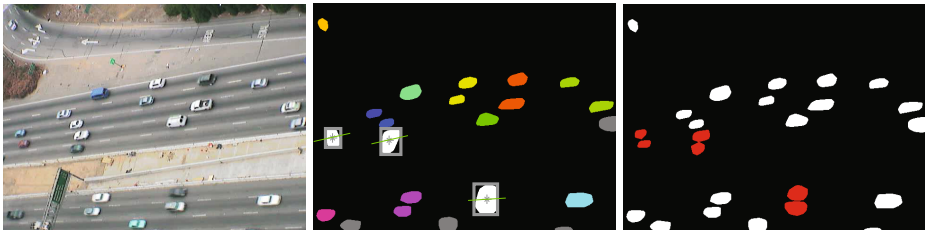
### 3 Experimental Results

In this section, our methodology has been tested over several traffic sequences provided by a video surveillance online repository, which has been generated by the Federal Highway Administration (FHWA) under the Next Generation Simulation (NGSIM) program<sup>1</sup>. The objects in these sequences are considered as rigid objects. We have used several scenes related to two key places in American vehicular traffic, *Lankershim* and *US-101* highways. Some difficulties such as occlusions, aerial perspective or overlapping objects caused by errors in the initial object segmentation phase should be handled. Additionally, it is possible to find other kind of objects like trucks or motorcycle which should not be detected as overlapped vehicles.

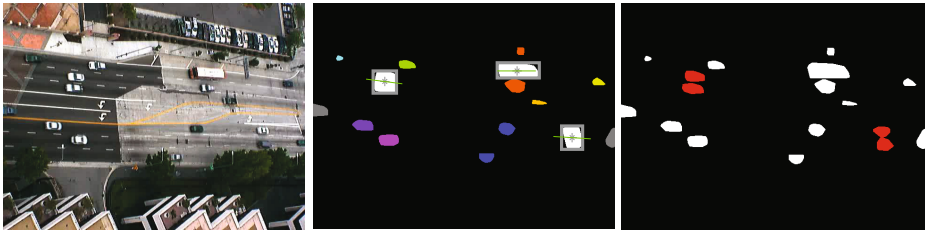
The SOM approach is adjusted with the following parameters empirically selected: a map topology of  $4 \times 4$  neurons, which can be modified without any degradation of the model; the neighborhood radius and the learning rate at the convergence point are  $\Delta = 0.5$  and  $\eta = 0.01$  respectively; finally, the factor  $\gamma$  is assigned to 2. In the occlusion handling module we have  $\alpha = 0.7$ . The map topology is flexible for any type of traffic application, taking into account that the greater the number of neurons in the SOM network, greater computation time is required. It should be emphasized that the model works in real-time, since it follows an online learning strategy.

Figure 4 shows how the neurons of the SOM approach are distributed on the *US-101 Highway* and *Lankershim* scenes. Noted that they manage to situate in areas where the

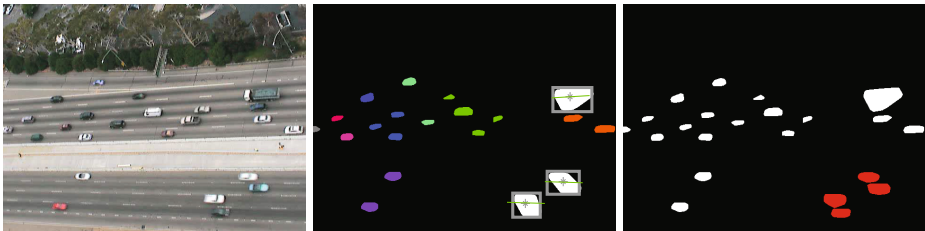
<sup>1</sup> Datasets of NGSIM are available at <http://ngsim-community.org/>



(a) *US-101 Highway* sequence from a perspective view. Three anomalous objects are corrected handled



(b) *Lankershim* scene from a top view. Both one truck and two overlapped objects are detected as unusual, and are discriminated accurately.



(c) *US-101 Highway* sequence from a top view. Two of the three overlapped objects are corrected handled.

**Fig. 5.** Several examples of anomalous objects detected

movement of the vehicles is more frequent. In addition, the perspective of the camera is captured successfully, since the area of two neurons in different zones of the scene represent the size of the objects flowing through that region. Thus, in Figure 4a vehicles in the bottom part of the image are larger than in the central part, feature which is learned by the neural model proposed. The same also occurs in Figure 4b, where the size of the objects in the left part of the scene is greater than in the right one.

Besides recognizing when objects are anomalous with respect to their shape, it is necessary to determine whether these objects correspond to occlusions caused by errors in the initial segmentation stage. In Figure 5 we can observe several frames where various possibilities are presented. In the first row it is possible to notice how the system detects multiple anomalous objects (middle image). Using the occlusion handling module the overlap is avoid and the vehicles are extracted properly (red objects in the right image). In the second row there are two unusual objects belonging to different categories; an overlapped object which integrates two cars and a truck whose shape

differs from the normal one in the analyzed scene (there is a higher frequency of light vehicles). In this case, our approach correctly detects the overlapped object and manage to split it, while the truck is not changed because it does not consider as an occlusion (right image). In some occasions (bottom row) the occlusions module fails to determine the overlap due to an object (truck) covers, to some extent, another one (vehicle).

## 4 Conclusions

In this work a methodology to improve the results of the object detection algorithms is presented. It consists of a postprocessing method based on a self-organizing neural network (SOM) to detect anomalous objects according to their shape, and an occlusion handling procedure which evaluates and identifies simple objects integrated in an overlapped one. This proposal is applied on sequences with rigid objects and high movement frequency.

Several traffic scenes have been tested to check the feasibility of the system, obtaining suitable and successful results. The SOM approach manages to adapt to the movement of objects and captures the variability of the object form in every zone of the sequence. Furthermore, the occlusion handling discriminates in most of the time between overlapped objects and other type of objects with fewer occurrence in the scene (trunks, motorcycle). This overlapping is corrected by extracting the simple objects after analyzing the horizontal and vertical histograms of the binary image.

It is remarkable that improving the segmentation of the foreground of the scene and, accordingly, detecting moving objects as accurately as possible, makes the subsequent stages, object tracking and behavior analysis, much more reliable and robust. Therefore, it is possible to infer more plausible facts on the scene.

As future work, we can study the possibility of incorporating the tracking information of the objects to determine its identity in case of anomalous situations (occlusions, disappearance). Finally some alternatives to the histogram analysis should be considered, in order to improve the detection of overlapped objects.

**Acknowledgements.** This work is partially supported by the projects TIN2011-24141 from MEC-SPAIN and P12-TIC-6213 (Junta de Andalucía). Additionally, the authors acknowledge support through grants TIN2010-16556 from MICINN-SPAIN and P08-TIC-04026 (Junta de Andalucía), all of which include FEDER funds.

## References

1. García-Rodríguez, J., Domínguez, E., Angelopoulou, A., Psarrou, A., Mora-Gimeno, F.J., Orts, S., García-Chamizo, J.M.: Video and Image Processing with Self-Organizing Neural Networks. In: Cabestany, J., Rojas, I., Joya, G. (eds.) IWANN 2011, Part II. LNCS, vol. 6692, pp. 98–104. Springer, Heidelberg (2011)
2. Fritzke, B.: A self-organizing network that can follow non-stationary distributions. In: Gerstner, W., Hasler, M., Germond, A., Nicoud, J.-D. (eds.) ICANN 1997. LNCS, vol. 1327, pp. 613–618. Springer, Heidelberg (1997)

3. Fritzke, B.: A growing neural gas network learns topologies. In: *Advances in Neural Information Processing Systems* (1995)
4. Frezza-Buet, H.: Following non-stationary distributions by controlling the vector quantization accuracy of a growing neural gas network. *Neurocomputing* 71, 1191–1202 (2008)
5. Flórez, F., García, J., García, J., Hernández, A.: Hand gesture recognition following the dynamics of a topology-preserving network. In: *Proc. of the 5th IEEE Intern. Conference on Automatic Face and Gesture Recognition*, pp. 318–323 (2002)
6. Cao, X., Suganthan, P.: Video shot motion characterization based on hierarchical overlapped growing neural gas networks. *Multimedia Systems* 9, 378–385 (2003)
7. Stauffer, C., Grimson, W.: Learning patterns of activity using real time tracking. *IEEE Trans. Pattern Anal. Mach. Intell.* 22, 747–767 (2000)
8. López-Rubio, E., Luque-Baena, R.M.: Stochastic approximation for background modelling. *Computer Vision and Image Understanding* 115, 735–749 (2011)
9. Luque, R., Dominguez, E., Palomo, E., Muñoz, J.: An art-type network approach for video object detection. In: *European Symposium on Artificial Neural Networks*, pp. 423–428 (2010)
10. de Angulo, V., Torras, C.: Learning inverse kinematics: Reduced sampling through decomposition into virtual robots. *IEEE Transactions on Systems, Man, and Cybernetics, Part B: Cybernetics* 38, 1571–1577 (2008)
11. Göppert, J., Rosenstiel, W.: The continuous interpolating self-organizing map. *Neural Processing Letters* 5, 185–192 (1997)
12. Padoan Jr., A., De, A., Barreto, G., Araújo, A.: Modeling and production of robot trajectories using the temporal parametrized self organizing maps. *International Journal of Neural Systems* 13, 119–127 (2003)
13. Walter, J., Ritter, H.: Rapid learning with parametrized self-organizing maps. *Neurocomputing* 12, 131–153 (1996)

# Image Noise Detection in Global Illumination Methods Based on Fast Relevance Vector Machine

Joseph Constantin<sup>1,2</sup>, André Bigand<sup>3</sup>, Ibtissam Constantin<sup>1,2</sup>, and Denis Hamad<sup>3</sup>

<sup>1</sup> Département des Mathématiques Appliquées, UL, Faculté des Sciences 2,  
Fanar, BP 90656, Jdeidet, Liban

<sup>2</sup> Laboratoire des Physiques Appliquées, PR2N, UL, Faculté des Sciences 2,  
Fanar, BP 90656, Jdeidet, Liban

{cjoseph, ibtissamconstantin}@ul.edu.lb

<sup>3</sup> LISIC, ULCO, 50 rue F. Buisson, BP 719, Calais Cedex, 62228, France  
{bigand, denis.hamad}@lisic.univ-littoral.fr

**Abstract.** Global illumination methods based on stochastically techniques provide photo-realistic images. However, they are prone to noise that can be reduced by increasing the number of paths as proved by Monte Carlo theory. The problem of finding the number of paths that are required in order to ensure that human observers cannot perceive any noise is still open. In this paper, a novel approach to predict which image highlights perceptual noise is proposed based on Fast Relevance Vector Machine (FRVM). This model can then be used in any progressive stochastic global illumination method in order to find the visual convergence threshold of different parts of any image. A comparative study of this model with experimental psycho-visual scores demonstrates the good consistency between these scores and the model quality measures. The proposed model has been compared also with other learning model like SVM and gives satisfactory performance.

**Keywords:** Global illumination, Human Visual System (HVS), Monte Carlo, Noise Perception, Relevance Vector Machine, Support Vector Machine, Stopping Criterion.

## 1 Introduction

The main objective of global illumination methods is to produce synthetic images with photo-realistic quality. These methods are generally based on path tracing theory in which stochastic paths are generated from the camera point of view through each pixel toward the 3D scene [1]. The Monte Carlo theory ensures that this process will converge to the correct image when the number of paths grows [2]. However, there is no information about the number of paths that are really required for the image to be visually converged.

Image quality measures are very important to characterize images visual quality. They are of great interest in image compression (JPEG models) and in image synthesis. They are classified into three models families in the literatures [3]: First

the full reference models that use the original version of the image for the quality assessment of the processed version as well known by SNR and SSIM [4], [5]. These models are the most used methods to evaluate image quality. Unfortunately, the SNR approach gives a global measure of the difference between two images without considering the perceptibility of each pixel in the image and the SSIM model needs the full original image which is not available in all cases. Second the no-reference models that evaluate the quality of the image without access to reference images [6], [7]. Some recent papers proposed no-reference quality assessment of JPEG images although the authors obtained good results, these reported quality measures have their limitations because they are based on theoretical models of noise. Finally in the reduced-reference models, the processed image is analyzed using some relevant information to calculate the quality of the result image [8], [9]. These models seem to be particularly interesting for our study as we show in this paper. However, the proposed models which are based on theoretical models of noise presents sensitivity limits in global illuminations. The HVS carries out a fascinating strategy of compression and sensitivity thresholds. In fact HVS cannot perceive equally all the components of our environment. For this system, some parts of the environment are very important while others parts are automatically ignored. As a consequence of these limits and the high computation cost of global illumination algorithms, perception approaches have been proposed in the literature. The main idea of such approaches is to replace the human observer by a vision model [10], [11]. These approaches provide interesting results but are complex and still incomplete due to the internal system complexity and its partial knowledge. They need long computation times and are often difficult to use and to parameterize.

This paper focuses on the use of a new learning model to detect and to quantify stochastic noise in an image. We propose a novel reduced image quality based on fast relevance vector machine. Relevance vector machine has been studied by Tipping [12]. Tipping introduced the principle of Bayesian inference in machine learning with a particular emphasis on the importance of marginalization for dealing with uncertainty. The RVM model conveys a number of advantages over the very popular support vector machine (SVM) because it is probabilistic and it uses a small number of kernel functions which not satisfy necessary the Mercer's condition. However, the learning algorithm is typically much slower than SVM. The fast relevance machine learning algorithm proposed also by Tipping is an accelerated version which exploits the properties of the marginal likelihood function to enable maximization via efficient sequential addition and deletion of candidate basis functions [13]. The advantages of our application are sparse Bayesian learning that makes it possible to treat complete images and to benefit of probabilistic predictions and automatic estimation of nuisance parameters [14], [15]. By mimicking the HVS, such model can provide important improvement for rendering.

The paper is structured as follows: section 2 describes the experimental we use, section 3 describes the fast relevance vector machine theory, section 4 introduces the FRVM design for image quality evaluation and section 5 shows

the experimental results obtained by the learning models. Finally the paper is summarized with some conclusions in section 6.

## 2 Data Acquisition

The model is built on data corresponding to images of globally illuminated scenes. The path tracing algorithm was used in order to reduce noise [2]. This algorithm generates stochastic paths from the camera to the 3D scene. For each intersection of a path with the surface, a direction of reflection or refraction is randomly extracted. The luminance of a pixel is evaluated recursively based on Monte Carlo. For each pixel, the final luminance is the average of the contributions of all generated paths. We can compute then several images from the same point of view by adding equally between two successive images 100 new paths for each pixel. For each scene several images were obtained, the first one being strongly noisy and the last one being the reference image (figure 1).

These images were computed at  $512 \times 512$  resolutions. The largest number of paths per pixel was set at 10100 which appeared to be sufficient for generating visually converged images. For each scene, the total number of images is equal to 101. Because we have to evaluate the noise level present in each generated image, some experiments were necessary in order to specify the threshold that is used as stopping criterion in images synthesis. However, considering the entire image for noise thresholding has two main drawbacks: first, it requires evaluation methods to work on very large data set which reduces their learning efficiency and second noise thresholds are different for each location in each image. The use of a global threshold would reduce the efficiency of the approach by requiring the same number of paths to be computed for each pixel in the image. Then, each of these images is opaque and virtually cut into non-overlapping sub-images of size  $128 \times 128$  pixels. For the used  $512 \times 512$  test image, we thus get 16 different sub-images. In order to get experimental data about noise perception, a pairs of images are presented to the observer. One of these images is called reference image that has been computed with a number of paths per pixel equal to 10100. The second image is so called the test image is chosen from a stack of images arranged from very noisy ones above to converged ones below. During the experiments, the observer is asked to modify the quality of the noisy image by pointing the areas where the differences are perceived between the current image and its reference one. Each operation then causes the selection and display of the corresponding next level sub-image by reducing visually the noise in this image's subpart. This operation is done until the observer considers that the two images are visually identical. This operation is reversible meaning that an observer is able to go down or up into the images stack. Note all the observers worked in the same conditions (same display with identical luminance tuning and same illumination conditions). The results were recorded for 33 different observers and the average number of paths that are required for each sub-images to be perceived as identical to the reference one by 95% of the observers were computed (figure 1).

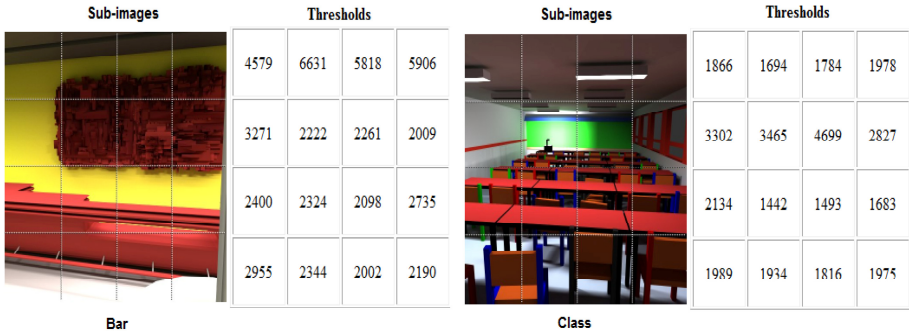


Fig. 1. The thresholds obtained for the used reference scenes

### 3 Fast Relevance Vector Machine

The major motivation of RVM implementation is to remove the limitation of SVM. Given a data set of input-target pairs  $\{x_n, t_n\}_{n=1}^N$ , we write the targets as a vector  $t = (t_1, \dots, t_N)^T$  and express it as the sum of an approximation vector  $y = (y(x_1), \dots, y(x_N))^T$  and an error vector  $\varepsilon = (\varepsilon_1, \dots, \varepsilon_N)^T$  [13]:

$$t = y + \varepsilon = \phi w + \varepsilon \tag{1}$$

Where  $w = [w_1, w_2, \dots, w_M]$  is the parameter vector,  $\phi = [\phi_1, \dots, \phi_M]$  is the  $N \times M$  matrix whose columns comprise the complete set of  $M$  basis vectors. The sparse Bayesian framework makes the conventional assumption that the errors are modeled probabilistically as independent zero-mean Gaussian with variance  $\sigma^2$ . Due to the assumption of independence of the  $t_n$ , the likelihood of the complete data set can be written as:

$$p(t | w, \sigma^2) = (2\pi)^{-N/2} \sigma^{-N} \exp\left(-\frac{\|t - y\|^2}{2\sigma^2}\right) \tag{2}$$

This likelihood function is complemented by a prior over the parameters, which takes the form:

$$p(w | \alpha) = (2\pi)^{-M/2} \prod_{m=1}^M \alpha_m^{1/2} \exp\left(-\frac{\alpha_m w_m^2}{2}\right) \tag{3}$$

Where  $\alpha = (\alpha_1, \alpha_2, \dots, \alpha_M)^T$  is a vector of  $M$  independent hyper-parameters, each one individually controlling the strength of the prior over its associated weight. Having defined the prior, Bayesian inference proceeds by computing the posterior parameter distribution from Bayes' rule:



$$p(w | t, \alpha, \sigma^2) = (2\pi)^{-(N+1)/2} |\Sigma|^{-1/2} \exp\left(-\frac{1}{2}(w-\mu)^T |\Sigma|^{-1}(w-\mu)\right) \quad (4)$$

Where the posterior covariance and mean are respectively:

$$\begin{aligned} \Sigma &= (\sigma^{-2} \phi^T \phi + A)^{-1} \\ \mu &= \sigma^{-2} \Sigma \phi^T t \end{aligned} \quad (5)$$

and  $A = \text{diag}(a_1, a_2, \dots, a_M)$ . The sparse Bayesian learning is formulated as the maximization with respect to  $\alpha$  of the marginal likelihood or equivalently its logarithm:

$$\ell(\alpha) = \log(p(t | \alpha, \sigma^2)) = -\frac{1}{2} [N \log 2\pi + \log(C) + t^T C^{-1} t] \quad (6)$$

With  $C = \sigma^2 I + \phi A^{-1} \phi^T$ . The RVM algorithm begins with all the  $M$  basis functions included in the model and updated the hyper-parameters iteratively. As a consequence of these updates, some basis functions would be pruned and the algorithm would be accelerated but nevertheless the first few iterations would still require  $O(M^3)$  computations. The FRVM algorithm begins with an empty model and adds basis functions to increase the marginal likelihood. For this purpose the term  $C$  can be decomposed as:

$$C = C_{-i} + \alpha_i^{-1} \phi_i \phi_i^T \quad (7)$$

Where  $C_{-i}$  is  $C$  with the contribution of  $i$ th basis vector removed. We can write the logarithm  $\ell(\alpha)$  as:

$$\ell(\alpha) = \ell(\alpha_{-i}) + \frac{1}{2} [\log \alpha_i - \log(\alpha_i + s_i) + \frac{q_i^2}{\alpha_i + s_i}] = \ell(\alpha_{-i}) + \eta(\alpha_i) \quad (8)$$

Where the sparsity and the quality factors are defined as:

$$\begin{aligned} s_i &= \phi_i^T C_{-i}^{-1} \phi_i \\ q_i &= \phi_i^T C_{-i}^{-1} t \end{aligned} \quad (9)$$

Analysis of  $\eta(\alpha_i)$  [16] shows that  $\ell(\alpha)$  has a unique maximum with respect to  $\alpha_i$ :

$$\begin{aligned} \alpha_i &= \frac{s_i^2}{q_i^2 - s_i} & \text{if } q_i^2 > s_i \\ \alpha_i &= \infty & \text{if } q_i^2 \leq s_i \end{aligned} \quad (10)$$

It is relatively straightforward to compute  $q_i$  and  $s_i$  for all the basis functions including those not currently utilized by the model. However, it is easier to update these values based on Woodbury quantity as follows:

$$\begin{aligned} S_m &= \phi_m^T B \phi_m - \phi_m^T B \phi \Sigma \phi^T B \phi_m \\ Q_m &= \phi_m^T B \hat{t} - \phi_m^T B \phi \Sigma \phi^T B \hat{t} \end{aligned} \quad (11)$$

Where  $B = \sigma^{-2} I$ ,  $\hat{t} = \phi_{MP} + B^{-1}(t - y)$  and  $\phi_{MP}$  is the most probable weights. It follows that in the FRVM algorithm the sparsity and the quality factors are updated as:

$$\begin{aligned} s_m &= \frac{\alpha_m S_m}{\alpha_m - S_m} \\ q_m &= \frac{\alpha_m Q_m}{\alpha_m - S_m} \end{aligned} \quad (12)$$

## 4 FRVM Design for Image Quality Evaluation

In this paper we will focus on gray-scale images, in fact 'L' component of 'Lab' color images, since noise only affects 'L' component [17]. We consider this component as input to the FRVM model. We apply to 'L' four different de-noising algorithms: Linear filtering with averaging filters of sizes  $3 \times 3$  and  $5 \times 5$ , linear filtering with Gaussian filters of same sizes and with standard deviations  $\sigma \in \{0.5, 1, 1.5\}$ , median filters and adaptive Wiener filters of same sizes. Low pass filtering using averaging or Gaussian filters helps to model the high frequency noise, non-linear median filtering addresses the salt and pepper noise and Wiener filtering can tailor noise removal to the local pixel variance. Next, the obtained image is de-noised via Wavelet analysis. After one stage 2-D wavelet decomposition, an input image is decomposed into four sub-bands namely low-low (LL), low-High (LH), high-low (HL) and high-high (HH) sub-bands (figure 2). Among these four sub-bands, the LL sub-band contains low-frequency components, while the others three are the high frequency components. In the literature, it has been observed that for a large class of images, the wavelet coefficient in the LH, HL and HH sub-bands do not follow a Gaussian distribution [18]. The final image is re-constructed by extracting noise from these components using Matlab wavelet toolbox. We are not interested in this paper in de-noising the image but rather in locating the areas where noise affects the image. So the noise feature vector given as input to the model is obtained by pixel-wise subtraction between the original image and the de-noised one. The experimental data set is then used for training the FRVM model. In the training protocol, we provided the difference of two sub-images to the model: a sub-image called reference and one of

the test sub-images. Ideally the reference sub-image should be the converged one. But during the use of the model in an iterative global illumination algorithm, the converged image is obviously not available. Thus the reference image used for learning and noise detection is a quickly ray traced image of scenes which highlights the same features of the converged one (shadows, textures, reflections, etc). The implementation of images quality evaluation based on FRVM is given by the following marginal likelihood maximization algorithm [13]:

1. Initialize  $\sigma^2$  to some sensible value and the model with a single basis vector  $\phi_i$ , setting from (10):

$$\alpha_i = \frac{\|\phi_i\|^2}{(\|\phi_i^T t\|^2 / \|\phi_i\|^2 - \sigma^2)}. \text{ All other } \alpha_m \text{ are naturally set to infinity.}$$

2. Compute  $\Sigma$  and  $\mu$  which are scalars initially along with initial values of  $s_m$  and  $q_m$  for all M bases  $\phi_m$ .
3. Select a candidate basis vector  $\phi_i$  from the set of all M.
4. Compute  $\theta_i = q_i^2 - s_i$ . If  $\theta_i > 0$  and  $\alpha_i < \infty$  then re-estimate  $\alpha_i$ . If  $\theta_i > 0$  and  $\alpha_i = \infty$  then add  $\phi_i$  to the model with updated  $\alpha_i$ . If  $\theta_i \leq 0$  and  $\alpha_i < \infty$  then delete  $\phi_i$  from the model and set  $\alpha_i = \infty$ .

5. Update  $\sigma^2 = \|t - y\|^2 / (N - M + \sum_{k=1}^M a_k \Sigma_{kk})$ .

6. Re-compute  $\Sigma, \mu$  using equation (5) and all  $s_m, q_m$  using equations (11) - (12). if converged terminate, otherwise repeat from 3.

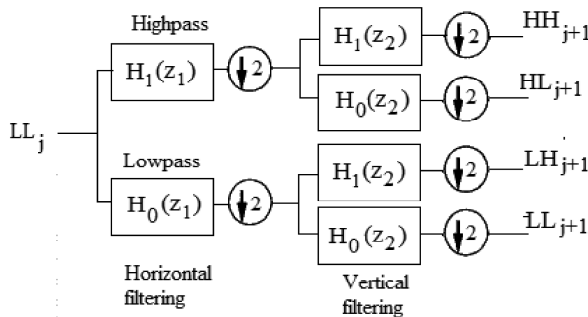
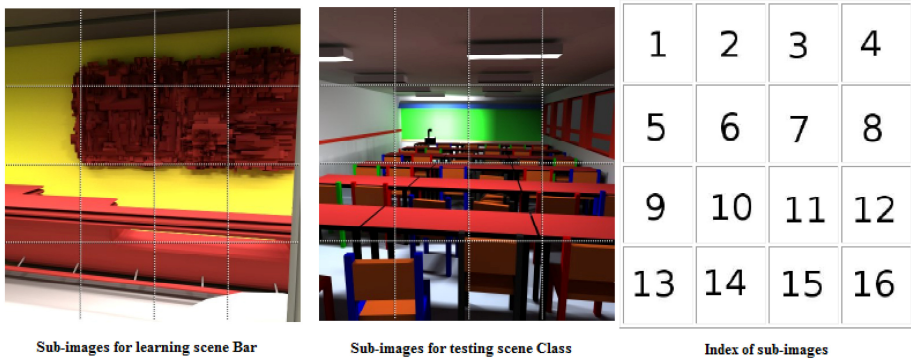


Fig. 2. One Stage of the 2D-Wavelet Transform

## 5 Experimental Results



**Fig. 3.** Learning scene "Bar" and testing scene "Class"

In the objective to test the performance of the proposed technique, the scene named "Bar" is used for learning and evaluation and the scene "Class" is used only for the testing process (figure 3). Processed sub-images (1616 different sub-images are used for learning and 1616 sub-images are used for testing) are examples obtained with different noise levels and denoise images. The input of the network is a  $128 \times 128$  vector of luminance. The output of the network is '-1' if the image is considered noisy or '+1' if the image is considered non-affected with noise. The radial basis functions used in hidden layer are defined as:

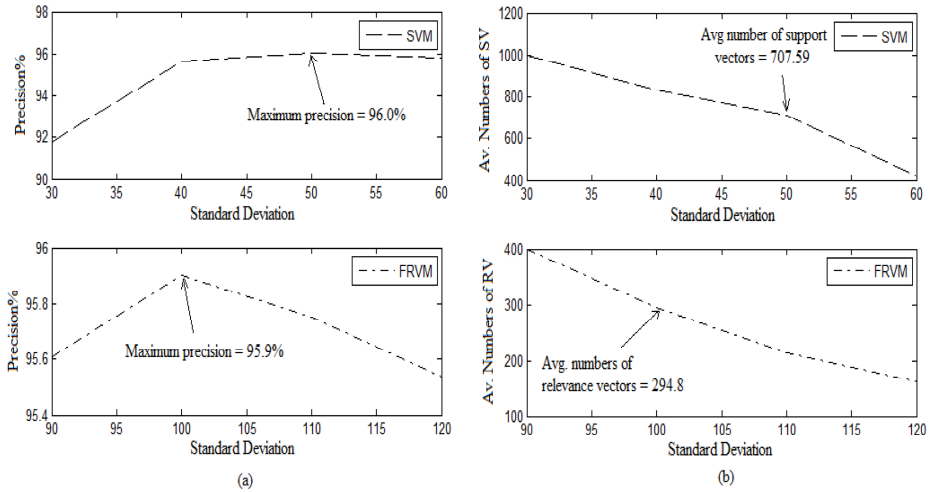
$$\phi_{nm} = k(x_n, x_m) = \exp(-\|x_n - x_m\|^2 / (\sigma^2)) \tag{13}$$

In order to obtain good precision and to minimize algorithm complexity, the network parameters are optimized using the V-times Cross-Validation technique where the learning set is decomposed into 101 groups of size 16 records each group. The method of rising exponent is used to search the proper value of the parameter C in case of SVM. Table 1 shows the average number of support vectors and the precision obtained for different values of this parameter. It is clear that the optimal value of C is equal to 16.

**Table 1.** Average numbers of support vectors and precision for different values of the parameter C

C(SVM)	Avg. Numbers of Support vectors	Precision (%)
1	724.44	95.42
2	712.18	95.54
4	708.24	96.03
8	708.13	96.03
16	707.59	96.00
32	707.59	96.03

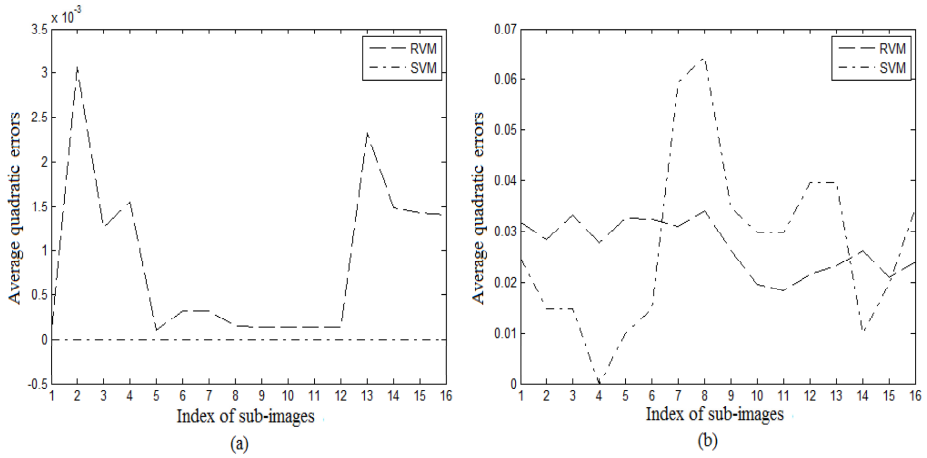
Figure 4 shows the variation of the learning precision and the average numbers of relevant vectors or support vectors with respect to the standard deviation  $\sigma$ . The optimal standard deviations for FRVM and SVM are equal respectively to 100 and 50. The maximum precision is equal to 96% for SVM and 95.9% for FRVM. The average numbers of support vectors is equal to 707.59 for SVM and the average numbers of relevance vectors is equal to 294.8 for FRVM. It is clear that the FRVM learning model assures a good precision and an optimal architecture.



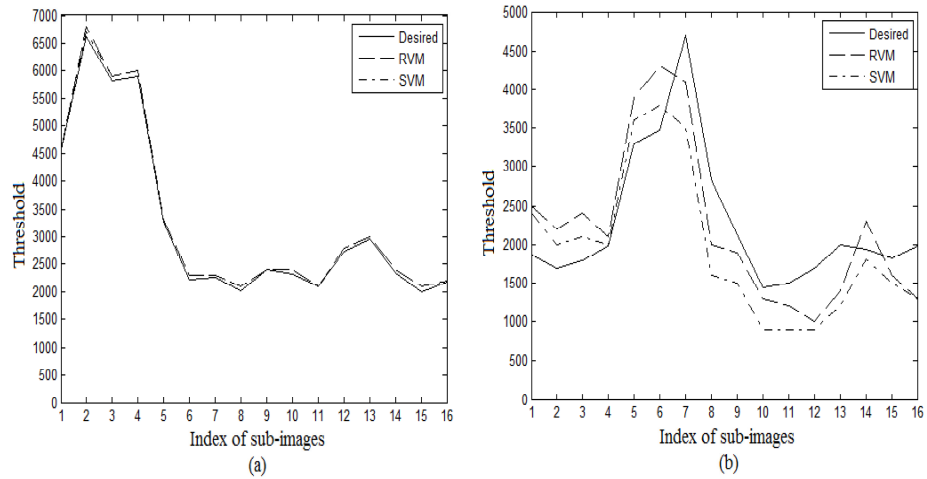
**Fig. 4.** a) Variation of the learning precision with respect to standard deviation, b) Variation of the average numbers of support vectors or relevance vectors with respect to standard deviation

Next, the FRVM and SVM learning models are evaluated on the scenes "Bar" and "Class". Figure 5 shows the variation of the average quadratic errors for the learning and the testing bases. Figure 5.a shows in case of learning base that the SVM performs slightly better than the FRVM. The average quadratic error is equal to 0 for all sub-images in case of SVM and it varies between 0 and  $3.5 \times 10^{-3}$  in case of FRVM. Figure 5.b shows in case of testing base that the SVM performs better than the FRVM for the first 6 sub-images but the FRVM model gives better result for the last 10 sub-images. The average quadratic error varies between 0 and 0.07 for SVM and it varies between 0.02 and 0.035 for FRVM.

In continuity of our experiments, comparisons in variations between the actual thresholds of the learning models and the desired ones obtained by HVS are carried out to test the performance of our approach. Figure 6.a shows that the learning models and the HVS have similar responses on the learning scene "Bar". Figure 6.b shows that the FRVM model gives a good stopping criterion for global illumination algorithm on the testing scene "Class" and assures better convergence than the SVM for the last 10 sub-images.



**Fig. 5.** a) Variation of the average quadratic errors for each sub-image on the learning scene "Bar", b) Variation of the average quadratic errors for each sub-image on the testing scene "Class"



**Fig. 6.** a) Threshold variation for each sub-image on the learning scene "Bar", b) Threshold variation for each sub-image on the testing scene "Class"

Finally, we get learning models which are expected to be able to identify whether a sub-image is noisy or not. In order to evaluate the capability of these models, we use another testing scene called "Cube" which contains different illuminations and various geometrical and textures complexities. Figure 7 shows the HVS threshold for each sub-image of this scene. We test next the efficiency of the learning models on each sub-image of the scene "Cube". Figure 8 shows the average quadratic errors and the learning threshold for each sub-image. The average quadratic error varies between 0

and 0.07 for SVM and it varies between 0.025 and 0.045 for FRVM. Moreover the comparative study of the learning models thresholds with experimental psycho-visual scores shows that the FRVM gives better consistency than the SVM. It is clear from this experimental study that the SVM performs slightly better than the FRVM only on the learning base. However the FRVM uses a small number of relevance vectors and predicts better than the SVM on the testing base.

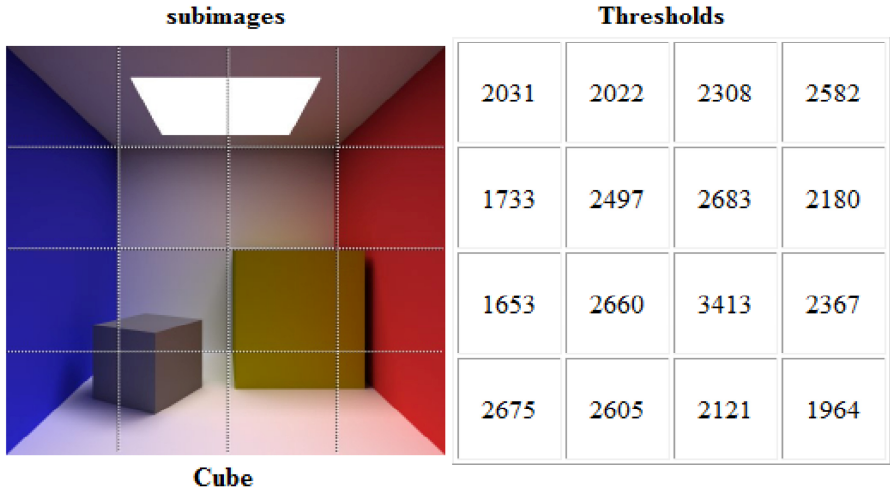


Fig. 7. The thresholds obtained by the HVS for the testing scene "Cube"

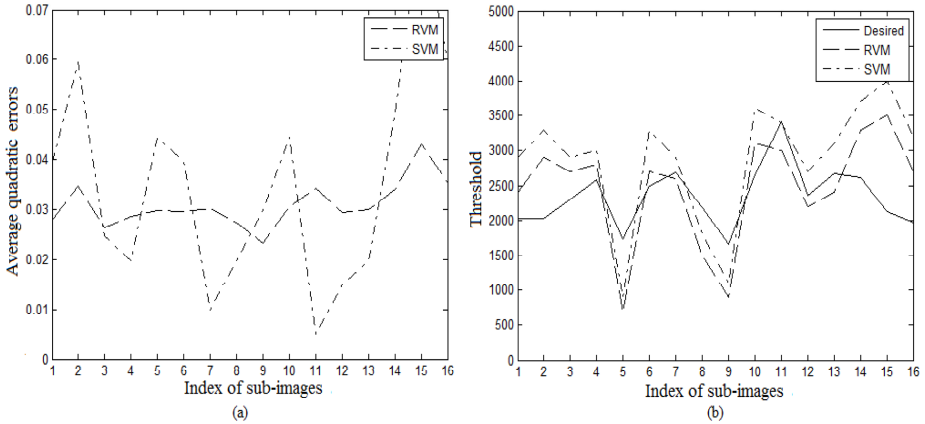


Fig. 8. a) Variation of the average quadratic errors for each sub-image on the testing scene "Cube", b) Threshold variation for each sub-image on the testing scene "Cube"

## 6 Conclusion

The central idea of this paper is to introduce the application of FRVM to take into account the uncertainty (noise) present in global illumination applications. Path tracing methods provide unbiased and realistic images but they converge slowly and highlight noise during their convergence. They should be stopped only when noise is visually not perceptible. The introduced technique uses dramatically fewer basis functions than a comparable SVM while offering a good prediction on the testing base. The biggest advantage of our application is that this model mimics the human visual system by using a sparse Bayesian learning that makes it possible to treat a huge number of images [19]. Indeed, ensuring the generalization of our approach requires establishing a more complete framework with a huge number of images which are difficult to obtain because of the time required for modeling and scene rendering.

## References

1. Kajiya, J.: The Rendering Equation. *ACM Computer Graphics* 20(4), 143–150 (1986)
2. Shirley, P., Wang, C., Zimmerman, K.: Monte Carlo Techniques for Direct Lighting Calculations. *ACM Transactions on Graphics* 15(1), 1–36 (1996)
3. Lahoudou, A., Viennet, E., Beghdadi, A.: Section Low-level Features for Image Quality Assessment by Stastical Methods. *Journal of Computing and Information Technology* 2, 183–189 (2010)
4. Gilboa, G., Sochen, N., Zeevi, Y.Y.: Estimation of Optimal PDE-Based Denoising in the SNR Sense. *IEEE Transactions on Image Processing* 15(8), 2269–2280 (2006)
5. Horé, A., Ziou, D.: Image Quality Metrics, PSNR vs. SSIM. In: 20th International Conference on Pattern Recognition, pp. 2366–2369 (2010)
6. Ferzli, R., Karam, L.: No-reference Objective Wavelet Based Immune Image Sharpness Metric. In: *International Conference on Image Processing* (2005)
7. Zhang, J., Ong, S., Thinh, M.: Kurtosis Based No-reference Quality Assessment of JPEG2000 Images. *Signal Processing: Image Communication* 26, 13–23 (2011)
8. Wang, Z., Simoncelli, E.P.: Reduced Reference Image Quality Assessment Using a Wavelet-domain Natural Image Statistic Model. In: *Proc. SPIE, Conf. on Human Vision and Electronic Imaging X*, vol. 5666, pp. 149–159 (January 2005)
9. Li, Q., Wang, Z.: Reduced-Reference Image Quality Assessment using Divisive Normalization Based Image Representation. *IEEE Journal of Selected Topics in Signal Processing* 3(2), 202–211 (2009)
10. Farrugia, J.P., Péroche, B.: A Progressive Redering Algorithm using an Adaptive Perceptually Based Image Metric. *Comput. Graph. Forum* 23(3), 605–614 (2004)
11. Longhurst, P., Debattista, K., Chalmers, A.: A GPU Based Saliency Map for High-fidelity Selective Rendering. In: *AFRIGRAPH 2006 4th International Conference on Computer Graphics, Virtual Reality, Visulisation and Interaction in Africa, ACM SIGGRAPH*, pp. 21–29 (2006)
12. Tipping, M.E.: Sparse Bayesian Learning and the Relevance Vector Machine. *Journal of Machine Learning Research* 1, 211–244 (2001)



13. Tipping, M.E.: Fast Marginal Likelihood Maximisation for Sparse Bayesian Models. In: Bishop, C.M., Frey, B.J. (eds.) *Proceedings of the Ninth International Workshop on Artificial Intelligence and Statistics*, Key West, FL, January 3-6 (2003)
14. Kim, J., Suga, Y., Won, S.: A New Approach to Fuzzy Modeling of Nonlinear Dynamic Systems With Noise: Rlevance Vector Learning Machine. *IEEE Transactions on Fuzzy Systems* 4(2) (April 2006)
15. Chen, Z., Tang, H.: Sparse Bayesian Approach to Classification. In: *IEEE Proceedings on Networking, Sensing and Control*, pp. 914–917 (2005)
16. Faul, A.C., Tipping, M.E.: Analysis of Sparse Bayesian Learning. In: *Advances in Neural Information Processing Systems*, vol. 14, pp. 383–389. MIT Press (2002)
17. Carnet, M., Callet, P.L., Barba, D.: Objective Quality Assessment of Color Images Based on a Generic Perceptual Reduced Reference. *Image Communication* 23(4), 239–256 (2008)
18. Chang, S.G., Yu, B., Vetterli, M.: Spatially Adaptive Wavelet Thresholding with Context Modeling for Image Denoising. *IEEE Trans. on Image Processing* 9(9), 1522–1531 (2000)
19. Tipping, M.E.: Bayesian Inference: An Introduction to Principles and Practice in Machine Learning. In: Bousquet, O., von Luxburg, U., Rätsch, G. (eds.) *Machine Learning 2003*. LNCS (LNAI), vol. 3176, pp. 41–62. Springer, Heidelberg (2004)

# Improving 3D Keypoint Detection from Noisy Data Using Growing Neural Gas

José Garcia-Rodríguez<sup>1</sup>, Miguel Cazorla<sup>2</sup>, Sergio Orts-Escolano<sup>1</sup>,  
and Vicente Morell<sup>2</sup>

<sup>1</sup> Department of Computing Technology at University of Alicante, Spain

<sup>2</sup> Instituto de Investigación en Informática at University of Alicante, Spain

{jgarcia, sorts}@dtic.ua.es,  
{miguel, vmorell}@dccia.ua.es

**Abstract.** 3D sensors provides valuable information for mobile robotic tasks like scene classification or object recognition, but these sensors often produce noisy data that makes impossible applying classical keypoint detection and feature extraction techniques. Therefore, noise removal and downsampling have become essential steps in 3D data processing. In this work, we propose the use of a 3D filtering and down-sampling technique based on a Growing Neural Gas (GNG) network. GNG method is able to deal with outliers presents in the input data. These features allows to represent 3D spaces, obtaining an induced Delaunay Triangulation of the input space. Experiments show how the state-of-the-art keypoint detectors improve their performance using GNG output representation as input data. Descriptors extracted on improved keypoints perform better matching in robotics applications as 3D scene registration.

**Keywords:** GNG, Noisy Point Cloud, Visual Features, Keypoint Detection, Filtering, 3D Scene Registration.

## 1 Introduction

Historically, humans have the ability to recognize an environment they had visit before based on the 3D model we unconsciously build in our heads based on the different perspectives of the scene. This 3D model is built with some extra information so that humans can extract relevant features [1] that will help in future experiences to recognize the environment and even possible objects presents there. This learning method has been transferred to mobile robotics field over the years. So, most current approaches in scene understanding and visual recognition are based on the same principle: keypoint detection and feature extraction on the perceived environment. Over the years most efforts in this area have been made towards feature extraction and keypoint detection on information obtained by traditional image sensors [2], existing a gap in feature-based approaches that use 3D sensors as input devices. However, in recent years, the number of jobs concerned with 3D data processing has increased considerably due to the emergence of cheap 3D sensors capable of providing a real time data stream and

therefore enabling feature-based computation of three dimensional environment properties like curvature, getting closer to human learning processes.

The Kinect device<sup>1</sup>, the time-of-flight camera SR4000<sup>2</sup> or the LMS-200 Sick laser<sup>3</sup> are examples of these devices. Besides, providing 3D information, some of these devices like the Kinect sensor can also provide color information of the observed scene. However, using 3D information in order to perform visual recognition and scene understanding is not an easy task. The data provided by these devices is often noisy and therefore classical approaches extended from 2D to 3D space do not work correctly. The same occurs to 3D methods applied historically on synthetic and noise-free data. Applying these methods to partial views that contains noisy data and outliers produces bad keypoint detection and hence computed features does not contain effective descriptions.

Classical filtering techniques like median or mean have been used widely to filter noisy point clouds [3] obtained from 3D sensors like the ones mentioned above. The median filter is one of the simplest and wide-spread filters that has been applied. It is simple to implement and efficient but can remove noise only if the noisy pixels occupy less than one half of the neighbourhood area. Moreover, it removes noise but at the expense of removing detail of the input data.

Another filtering technique frequently used in point cloud noise removal is the Voxel Grid method. The Voxel Grid filtering technique is based on the input space sampling using a grid of 3D voxels to reduce the number of points. This technique has been used traditionally in the area of computer graphics to subdivide the input space and reduce the number of points [4]. The Voxel Grid method presents some drawbacks: geometric information loss due to the reduction of the points inside a voxel and sensitivity to noisy input spaces.

Based on the Growing Neural Gas [5] network several authors proposed related approaches for surface reconstruction applications [6]. However, most of these contributions do not take in account noisy data obtained from RGB-D cameras using instead noise-free CAD models.

In this paper, we propose the use of a 3D filtering and down-sampling technique based on the GNG [5] network. By means of a competitive learning, it makes an adaptation of the reference vectors of the neurons as well as the inter-connection network among them; obtaining a mapping that tries to preserve the topology of an input space. Besides, GNG method is able to deal with outliers presents in the input data. These features allows to represent 3D spaces, obtaining an induced Delaunay Triangulation of the input space very useful to easily obtain features like corners, edges and so on. Filtered point cloud produced by the GNG method is used as an input of many state-of-the-art 3D keypoint detectors in order to show how the filtered and down sampled point cloud improves keypoint detection and hence feature extraction and matching in 3D registration methods.

---

<sup>1</sup> Kinect for XBox 360: <http://www.xbox.com/kinectMicrosoft>

<sup>2</sup> Time-of-Flight camera SR4000 <http://www.mesa-imaging.ch/prodview4k.php>

<sup>3</sup> LMS-200 Sick laser: [http://robots.mobilerobots.com/wiki/SICK\\_LMS-200\\_Laser\\_Rangefinder](http://robots.mobilerobots.com/wiki/SICK_LMS-200_Laser_Rangefinder)

In this work we focus on the processing of 3D information provided by the Kinect sensor. Because the Kinect is essentially a stereo camera, the expected error on its depth measurements is proportional to the squared distance to the scene.

The rest of the paper is organized as follows: first, a section describing briefly the GNG algorithm is presented. In section 3 the state-of-the-art 3D keypoint detectors are explained. In section 4 we present some experiments and discuss results obtained using our novel approach. Finally, in section 5 we give our conclusions and directions for future work.

## 2 GNG Algorithm

With Growing Neural Gas (GNG) [5] method a growth process takes place from minimal network size and new units are inserted successively using a particular type of vector quantization. To determine where to insert new units, local error measures are gathered during the adaptation process and each new unit is inserted near the unit which has the highest accumulated error. At each adaptation step a connection between the winner and the second-nearest unit is created as dictated by the competitive Hebbian learning algorithm. This is continued until an ending condition is fulfilled, as for example evaluation of the optimal network topology or fixed number of neurons. The network is specified as:

- A set  $N$  of nodes (neurons). Each neuron  $c \in N$  has its associated reference vector  $w_c \in R^d$ . The reference vectors can be regarded as positions in the input space of their corresponding neurons.
- A set of edges (connections) between pairs of neurons. These connections are not weighted and its purpose is to define the topological structure. An edge aging scheme is used to remove connections that are invalid due to the motion of the neuron during the adaptation process.

This method offers further benefits over simple noise removal and downsampling algorithms: due to the incremental adaptation of the GNG, input space denoising and filtering is performed in such a way that only concise properties of the point cloud are reflected in the output representation.

## 3 Applying Keypoint Detection Algorithms to Filtered Point Clouds

In this section, we present the state-of-the-art 3D keypoint detectors used to test and measure the improvement achieved using GNG method to filter and downsample the input data. In addition, we explain main 3D descriptors and feature correspondence matching methods that we use in our experiments.

First keypoint detector used is the widely known SIFT (Scale Invariant Feature Transform) [7] method. It performs a local pixel appearance analysis at different scales. SIFT features are designed to be invariant to image scale and

rotation. SIFT detector has been traditionally used in 2D image but it has been extended to 3D space. 3D implementation of SIFT differs from original in the use of depth as the intensity value.

Another keypoint detector used is based on a classical HARRIS 2D keypoint detector. In [8] a refined HARRIS detector is presented in order to detect keypoints invariable to affine transformations. keypoints. 3D implementations of these HARRIS detectors use surface normals of 3D points instead of 2D gradient images. Harris detector and its variants (Tomasi3D and Noble3D) have been tested in Section 4.

Once keypoints have been detected, it is necessary to extract a description over these points. In the last few years some descriptors that take advantage of 3D information have been presented. In [9] a pure 3D descriptor is presented. It is called Fast Point Feature Histograms (FPFH) and is based on a histogram of the differences of angles between the normals of the neighbour points. This method is a fast refinement of the Point Feature Histogram (PFH) that computes its own normal directions and it represents all the pair point normal differences instead of the subset of these pairs which includes the keypoint. Moreover, we used another descriptor called CSHOT [10] that is a histogram that represents the shape and the texture of the keypoint. It uses the EVD of the scattered matrix using neighborhood for each point and a spherical grid to encode spatial information.

Correspondence between features or feature matching methods are commonly based on the euclidean distances between feature descriptors. One of the most used method to find the transformation between pairs of matched correspondences is based on the RANSAC (RANdom SAMple Consensus) algorithm [11]. It is an iterative method that estimates the parameters of a mathematical model from a set of observed data which contains outliers. In our case, we have used this method to search a 3D transformation (our model) which best explain the data (matches between 3D features). At each iteration of the algorithm, a subset of data elements (matches) is randomly selected. These elements are considered as inliers; a model (3D transformation) is fitted to those elements, the rest of the data is then tested against the fitted model and included as inliers if its error is below a threshold; if the estimated model is reasonably good (its error is low enough and it has enough matches), it is considered as a good solution. This process is repeated a number of iterations and the best solution is returned.

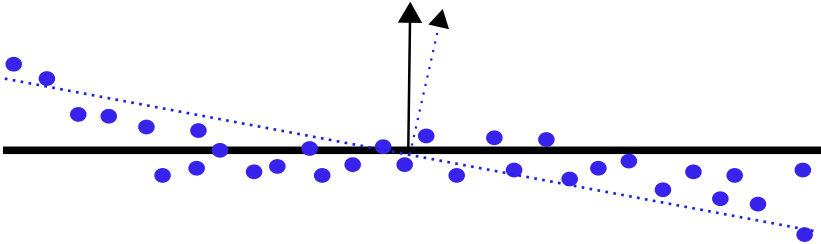
## 4 Experimentation

We performed different experiments on real data to evaluate the effectiveness and robustness of the proposed method. First, a normal estimation method is computed in order to show how estimated normals are considerably affected by noisy data. Finally, the proposed method is applied to 3D scene registration to show how keypoint detection methods are improved obtaining more accurate transformations. To validate our approach, experiments were performed on a dataset comprised of 90 overlapped partial views of a room. Partial views are

rotated 4 degrees in order to cover 360 degrees of the scene. Partial views were captured using the Kinect device mounted in a robotic arm with the aim of knowing the ground truth transformation. Experiments implementation, 3D data management (data structures) and their visualization have been done using the PCL<sup>4</sup> library.

#### 4.1 Improving Normal Estimation

In the first experiment, we computed normals on raw and filtered point clouds using the proposed method. Since normal estimation methods based on the analysis of the eigenvectors and eigenvalues of a covariance matrix created from the nearest neighbours are very sensitive to noisy data. This experiment is performed in order to show how a simple 3D feature like normal or curvature estimation can be affected by the presence of noise. In Figure 1 it is visually explained the effect caused by normal estimation on noisy data.



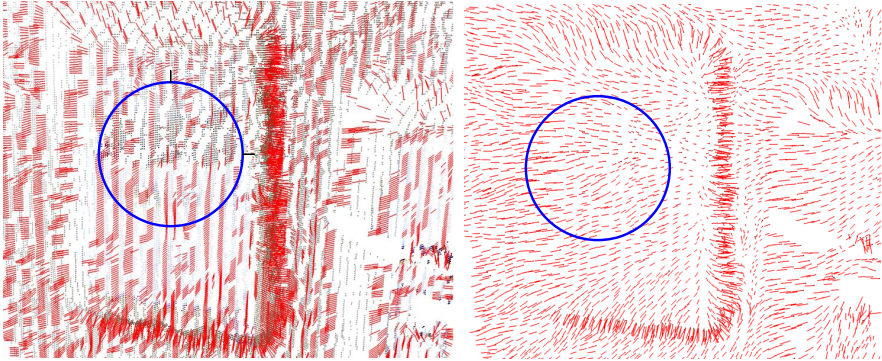
**Fig. 1.** Noise causes error in the estimated normal

Normal estimation is computed on the original and filtered point cloud using the same radius search:  $r_s = 0.1$  (meters). In Figure 2 can be observed how more stable normals are estimated using filtered point cloud produced by the GNG method. 20,000 neurons and 1,000 patterns are used as configuration parameters for the GNG method in the filtered point cloud showed in Figure 2 (Right).

#### 4.2 Improving 3D Keypoint Detectors Performance

In the second experiment, we used some keypoint detectors introduced in section 3 in order to test noise reduction capabilities of the GNG method. RMS deviation measure calculates the average difference between two affine transformations: the ground truth and the estimated one. Furthermore, we used a fixed number of neurons and patterns to obtain a downsampled and filtered representation of the input space. Different configurations have been tested, ranging from 5,000 to 30,000 neurons and 250 to 2,000 patterns per epoch. Figure 3

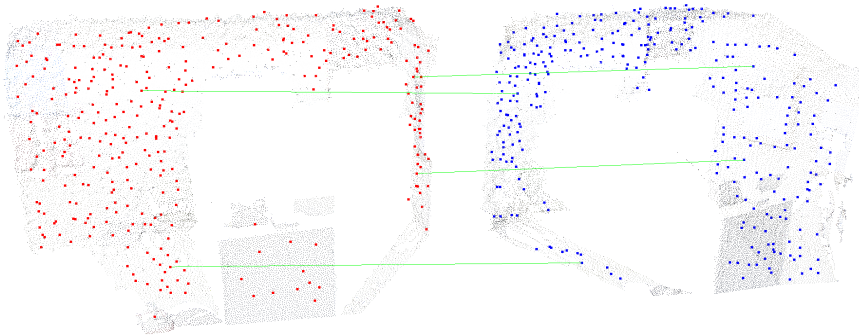
<sup>4</sup> The Point Cloud Library (or PCL) is a large scale, open project [12] for 2D/3D image and point cloud processing.



**Fig. 2.** Normal estimation comparison. Left: Normal estimation on raw point cloud. Right: Normal estimation on filtered point cloud produced by the GNG method.

shows correspondences matching calculated over filtered point clouds using the proposed method.

In Table 1 we can see how using GNG output representation as input cloud for the registration step, lower RMS errors are obtained in most detector-descriptor combinations.



**Fig. 3.** Registration example done with the HARRIS3D detector and the FPFH descriptor using a GNG representation with 20000 neurons

Experiments are performed using different search radius for keypoint detection and feature extraction methods. Search radius influences directly on the size of the extracted features, making methods more robust against occlusions. A balance between large and small values must be found depending on the size of the presents objects in the scene and the size of the features we want to extract. For the used dataset, the best estimated transformations are found

**Table 1.** RMS deviation error in meters obtained using different detector-descriptor combinations. Different combinations are computed on the original point cloud (raw), and three different filtered point clouds using the proposed method. GNG output representation produces lower RMS errors in most detector-descriptor combinations.

Keypoint detector search radius = 0.1; Feature extractor search radius = 0.2

	SIFT3D/FPFH	SIFT3D/SHOTRGB	HARRIS3D/FPFH	HARRIS3D/SHOTRGB
Raw point cloud	0.1568	0.0359	0.3074	0.0490
GNG 20000n 1000p	0.1842	<b>0.0310</b>	<b>0.1158</b>	0.0687
GNG 10000n 500p	0.1553	0.0677	0.1526	<b>0.0466</b>
GNG 5000n 250p	<b>0.0435</b>	0.0957	0.1549	0.0566
	Tomasi3D/FPFH	Tomasi3D/SHOTRGB	Noble3D/FPFH	Noble3D/SHOTRGB
Raw point cloud	0.3604	0.0764	0.3074	0.0655
GNG 20000n 1000p	2.2816	0.0416	<b>0.1095</b>	<b>0.0653</b>
GNG 10000n 500p	<b>0.1783</b>	<b>0.0349</b>	0.1526	0.0790
GNG 5000n 250p	0.1808	0.0730	0.3438	0.0925

Keypoint detector search radius = 0.05; Feature extractor search radius = 0.2

	SIFT3D/FPFH	SIFT3D/SHOTRGB	HARRIS3D/FPFH	HARRIS3D/SHOTRGB
Raw point cloud	0.1568	0.0359	0.0329	<b>0.0362</b>
GNG 20000n 1000p	0.1842	<b>0.0310</b>	0.1170	0.0415
GNG 10000n 500p	0.1553	0.0677	<b>0.0769</b>	0.0626
GNG 5000n 250p	<b>0.0435</b>	0.0957	0.1549	0.0566
	Tomasi3D/FPFH	Tomasi3D/SHOTRGB	Noble3D/FPFH	Noble3D/SHOTRGB
Raw point cloud	0.1482	0.0532	0.1059	0.0991
GNG 20000n 1000p	<b>0.0702</b>	0.0666	0.2234	0.0518
GNG 10000n 500p	0.1027	<b>0.0257</b>	<b>0.0323</b>	<b>0.0196</b>
GNG 5000n 250p	0.1110	0.0446	0.0600	0.0327

using keypoint detector search radius 0.1 and 0.05 and feature extractor search radius 0.2.

Experiments shown in Table 1 demonstrate how the proposed method achieves lower RMS deviation errors in the computed transformation between different 3D scene views. For example, the computed transformation is improved using the GNG representation as input for the Noble3D detector and SHOTRGB feature descriptor combination, obtaining a more accurate transformation. For the same combination, the proposed method obtains less than 2 centimetres error whereas original point cloud produces almost 9 centimetres error in the registration process.

## 5 Conclusions and Future Work

In this paper we have presented a method which is able to deal with noisy 3D data captured using low cost sensors like the Kinect Device. The proposed method calculates a GNG network over the raw point cloud, providing a 3D structure which has less information than the original 3D data, but keeping the 3D topology. It is shown how state-of-the-art keypoint detection algorithms perform better on filtered point clouds using the proposed method. Improved keypoint detectors are tested in a 3D scene registration process, obtaining lower RMS errors in most detector-descriptor combinations. Future work includes the integration of the proposed filtering method in a indoor mobile robot localization application.



## References

1. Anne, M.: Treisman and Garry Gelade. A feature-integration theory of attention. *Cognitive Psychology* 12(1), 97–136 (1980)
2. Szummer, M., Picard, R.W.: Indoor-outdoor image classification. In: Proceedings of the 1998 IEEE International Workshop Content-Based Access of Image and Video Database, pp. 42–51 (January 1998)
3. Nuchter, A., Surmann, H., Lingemann, K., Hertzberg, J., Thrun, S.: 6d slam with an application in autonomous mine mapping. In: Proceedings of the IEEE International Conference on Robotics and Automation, pp. 1998–2003 (2004)
4. Connolly, C.: Cumulative generation of octree models from range data. In: Proceedings of the 1984 IEEE International Conference on Robotics and Automation, vol. 1, pp. 25–32 (March 1984)
5. Fritzke, B.: *A Growing Neural Gas Network Learns Topologies*, vol. 7, pp. 625–632. MIT Press (1995)
6. Holdstein, Y., Fischer, A.: Three-dimensional surface reconstruction using meshing growing neural gas (mgng). *Vis. Comput.* 24(4), 295–302 (2008)
7. Lowe, D.G.: Distinctive image features from scale-invariant keypoints. *International Journal of Computer Vision* 60, 91–110 (2004)
8. Mikolajczyk, K., Schmid, C.: An affine invariant interest point detector. In: Heyden, A., Sparr, G., Nielsen, M., Johansen, P. (eds.) *ECCV 2002, Part I. LNCS*, vol. 2350, pp. 128–142. Springer, Heidelberg (2002)
9. Rusu, R.B., Blodow, N., Beetz, M.: Fast point feature histograms (fpfh) for 3d registration. In: *IEEE International Conference on Robotics and Automation, ICRA 2009*, pp. 3212–3217 (May 2009)
10. Tombari, F., Salti, S., Di Stefano, L.: A combined texture-shape descriptor for enhanced 3d feature matching. In: *2011 18th IEEE International Conference on Image Processing, ICIP*, pp. 809–812 (September 2011)
11. Fischler, M.A., Bolles, R.C.: Random sample consensus: a paradigm for model fitting with applications to image analysis and automated cartography. *Commun. ACM* 24(6), 381–395 (1981)
12. Rusu, R.B., Cousins, S.: 3D is here: Point Cloud Library (PCL). In: *Proceedings of the IEEE International Conference on Robotics and Automation, ICRA, Shanghai, China, May 9-13 (2011)*

# Football Video Annotation Based on Player Motion Recognition Using Enhanced Entropy

Markos Mentzelopoulos, Alexandra Psarrou,  
Anastassia Angelopoulou, and José García-Rodríguez

School of Electronics and Computer Science, University of Westminster,  
115 New Cavendish Street, W1W 6UW, United Kingdom

{mentzem,psarroa,agelopa}@wmin.ac.uk

Departamento de Tecnología Informática y Computación, Universidad de Alicante,  
Apdo. 99. 03080 Alicante, Spain  
jgarcia@dtic.ua.es

**Abstract.** This paper presents a semi-parametric Algorithm for parsing football video structures. The approach works on a two interleaved based process that closely collaborate towards a common goal. The core part of the proposed method focus perform a fast automatic football video annotation by looking at the enhance entropy variance within a series of shot frames. The entropy is extracted on the Hue parameter from the HSV color system, not as a global feature but in spatial domain to identify regions within a shot that will characterize a certain activity within the shot period. The second part of the algorithm works towards the identification of dominant color regions that could represent players and playfield for further activity recognition. Experimental Results shows that the proposed football video segmentation algorithm performs with high accuracy

## 1 Introduction

Sports Video annotation and retrieval by content are motivated by the huge amount of video daily produced within the commercial industry. Prior work has been focus in algorithms to enable to log the most relevant shots of a video stream with annotation process towards the detection of special events in football videos such as goals, penalties or corner kicks. Sports video segmentation could be categorized in two genre framework based on current research methodologies both aim to lead to a semantic classification. The first category, investigates the roles of semantic objects in the scenery and models their trajectories [8], while the second category is using structure analysis of the environment (lines in a basketball, soccer and tennis court) [1,2,5,6,7]. First approaches in sports video retrieval just added the functionality for segmentation and key-frame extraction to existing image retrieval systems. After key-frame extraction, they just apply similarity measurement on them based on low-level features [10,4]. This is not satisfactory because video is temporal media, so sequencing of individual frames creates new semantics, which may not be present in any of the

individual shots. Therefore what is needed is techniques for organizing images and videos in semantic meaning. The process of extracting the semantic content is very complex, because it requires domain knowledge or user interaction, while extraction of visual features can be often done automatically and it is usually domain independent. In this paper we present a semi-parametric method for the automatic segmentation of a football video and the extraction of its dominant regions, without *a priori* need of camera calibration or background extraction. The proposed model is using an update version of the original Entropy Difference algorithm [3] and has a double scope: 1) To provide an automatic video segmentation down to key-frames and 2) To identify the dominant colors in the shot necessary for further semantic video interpretation. The rest of the paper is organized as follows: section 2 presents the Enhanced Entropy Difference algorithm and its ability to keep track of Dominant Color Regions within a shot. Finally, section 3 presents experiments on the application to a benchmark of football videos, followed by our conclusions and future work.

## 2 Algorithm Description

The approach presented in this paper is based on the Entropy Difference Algorithm method [3], a distance metric between consecutive frames used for identifying gradually transitions between video shots. Although the algorithm showed high performance results on various video scenarios, it still had limitations when the background was dark, and if there were some fast color fluctuations, because of camera calibration or noise.

Color histogram is an important technique for color video annotation. However, the main problem with color histogram indexing is that it does not take the color spatial distribution into consideration. Previous researches have proved that the effectiveness of video retrieval increases when spatial feature of colors is included in video retrieval [10,4]. In this paper, two new descriptors, entropy distribution (ED) and Analysis of Variance in Hue Entropy (ANOVA-Hue-E), will describe the spatial information of HUE color feature in time domain.

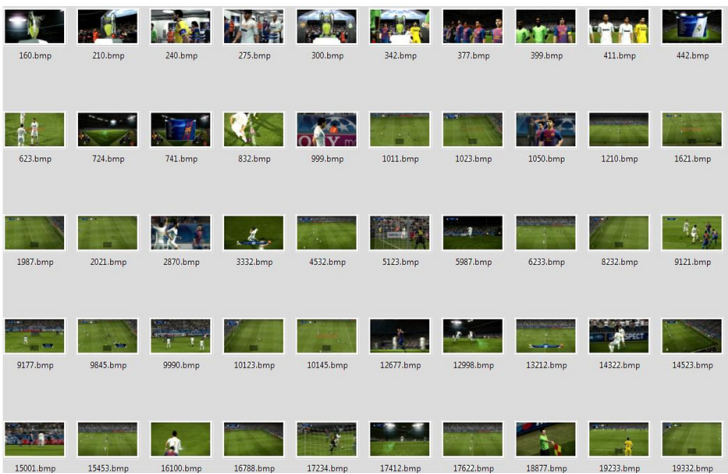
### 2.1 Entropy Difference

Entropy is a good way of representing the impurity or unpredictability of a set of data since it is dependent on the context in which the measurement is taken. In the proposed model we consider that if we distribute the entropy among the image, then the higher entropy distributions will be describing the regions containing the salient objects of a video sequence. Therefore any change in the object appearance of one of these salient regions it will affect its relevant semantic information in the entire story sequence. In order to eliminate as much as we can the possibility of the change of brightness during the frame comparison, the original RGB image has been converted to the equivalent HSV system and the HUE component has been extracted. The color gamut was further quantized down to 40 colors and then applied a median filter for region smoothing.

The reason for picking such a low color resolution is that in a football field there are not many different objects we could possibly observe. Using the algorithm from [3] we can calculate the Entropy Difference. After applying the video segmentation algorithm, for each extracted key-frame we keep a table of record (*DEC* -Dominant Entropy Color Table), that includes the key-frame ID number in the shot sequence, the HUE color bin values that include the highest entropy values, the pixel distributions and the entropy values.

Frame #16	Color Bin	Pixel	Color Bin
	12	2100	0.123
	34	127	0.34
	45	4578	0.12
	56	639	0.301
	78	8400	0.054
	.....	.....	.....
	268	124	0.09

**Fig. 1.** Dominant Entropy Color Table. Every key-frame includes the HUE color bin values with the highest entropy values, the pixel distributions and the entropy values.



**Fig. 2.** Key-frames extracted from the 10:48 min long football video [ PES 2012 ], 19440 frames at 30fps. The video has been summarized down to 55 key-frames/shots.

## 2.2 Enhanced Entropy Difference

Enhanced Entropy Difference is a post process method on the algorithm to check for color updates within the frames that can be used for:

1. Update the DEC Table for its future use on identifying Dominant objects within the Shot

2. Check whether the distance between the current selected key-frames that describe a shot is sufficient enough to describe a semantic coherent theme within the shot. This means if the variance of a dominant color within the shot is high compared to the rest of the colors, then an additional key-frame will need to be necessary within the shot boundaries.

EED is calculated based on the Variance of the Entropy that each Hue Color Bin contains over the shot time period of  $M - frames$ . Therefore if  $j$  is one of the Hue color bins from the DEC Table  $[0 \leq j \leq N]$  then in the Equation 1tab below  $A_s$  is a matrix that contains all the Entropy observations  $e_{f,j}$  for every Dominant Color  $d_j$  from the DEC table. Where  $s = Nrshot$ ,  $N = numberofcolorbins[i.e : N = 40]$  and  $f = Nrframe$ . Then:

$$A_s = \begin{matrix} e_{1,1} & e_{1,2} & \dots & \dots & e_{1,N} \\ e_{2,1} & e_{2,2} & e_{2,3} & \dots & e_{2,N} \\ e_{3,1} & e_{3,2} & e_{3,3} & \dots & e_{3,N} \\ \vdots & \vdots & \vdots & \vdots & \ddots \\ e_{1,1} & e_{1,2} & e_{1,3} & \dots & \ddots \end{matrix} \tag{1}$$

The Total Variation is comprised the sum of the squares of the differences of each mean with the grand mean. There is the between group variation and the within group variation. The whole idea behind the analysis of variance is to compare the ratio of between group variance to within group variance. If the variance caused by the interaction between the samples is much larger when compared to the variance that appears within each group, then it is because the means aren't the same. For each row in  $A_s$  we calculate the mean value of the color over the shot period  $M$  and we calculate its Total Variation Matrix  $SS_T$ . The Within Group Variation is a 1-Dimensional Vector and calculates the variation due to differences within our individual color samples, denoted  $SS_W(j)$  for Sum of Squares Within group color  $j$ .

**Table 1.** Results from the evaluation of the shots extracted from a benchmark of 6 football video sequences using the methods of: Pairwise Pixel (PP) [10], Histogram Comparison (HC) [4], Cluster (Cl)[9] and the proposed Enhanced Entropy Difference in terms of: (a) The total number of shots/key-frames retrieved/video sequence  $n_t$ , (b) the number of correct recognized shots  $n_c$ , (c)the number of false recognized shots  $n_f$  and (d) the number of missed shots  $n_m$

Video Sequence	PP				Cl				HC				EED			
	$n_t$	$n_c$	$n_f$	$n_m$	$n_t$	$n_c$	$n_f$	$n_m$	$n_t$	$n_c$	$n_f$	$n_m$	$n_t$	$n_c$	$n_f$	$n_m$
PES2012	85	57	28	0	51	51	0	6	48	48	0	9	55	55	0	2
FC Arsenal-Bluckburn Rovers	22	12	10	1	9	9	0	3	10	10	0	2	10	10	0	2
FC Liverpool-FC Real Madrid	37	34	3	2	35	35	0	0	37	33	4	4	35	33	2	0
FC Lyon-FC Zagreb	25	16	9	2	11	11	0	6	15	15	0	2	13	13	0	4
FC AEK-FC Olympiacos	115	100	15	1	92	92	0	9	88	88	0	13	93	93	0	8
FC M.United-FC Real Madrid	42	21	21	0	17	17	0	4	14	14	0	8	18	18	0	3

$$SS_W(j) = \sum_{i=1}^M (e_{i,j} - \bar{e}_j) \quad (2)$$

$$SS_T = \{SS_W[1], SS_W[2], \dots, SS_W[N]\}^T \quad (3)$$

The for each level  $j$  within the  $SS_W[j]$  if compare its value to the Mean Group Variation  $\overline{SS_T}$  we will calculate the Overall Variation  $OS_W(s)$  within the shot  $s$ .

$$OS_W(s) = \sum_{i=1}^N (SS_W[i] - \overline{SS_T}) \quad (4)$$

Finally we take the likelihood Ratio between each Group Variation  $SS_W(j)$  and the Overall Shot Variation  $OS_W(s)$ .

$$H_j = \log \frac{SS_W(j)}{OS_W(s)} < \alpha; \quad (5)$$

Using the Hypothesis that an object change within the shot is happening if the variation is more than a Threshold value  $\alpha$  [ $0 \leq \alpha \leq 1$ ], then  $H_j$  will be a binary array containing the Hypothesis for each  $j$  component. If the sum of the  $H_j$  Hypothesis is more than 40%, that means that more than 40% of the overall objects have changed within the shot, then a new Key-frame  $\mathbf{K}$  is essential to be taken within the previous key-frame boundaries.

### 3 Experimental Results

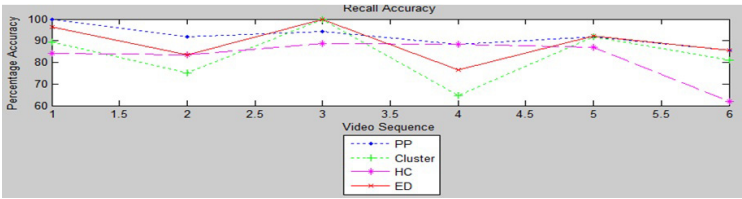
Using the proposed model, we evaluated a footage of 6 football video clips from various genres. The videos were taken from live match coverage (videos 5 & 6), game simulation (video 1- PES2012 <sup>1</sup>) and from football highlights taken from BBC(2-4). The video resolution varies on every video, that's why we applied a re-scaled process on every frame to reduce its dimensionality to a more computationally efficient size of 420 x 340 pixels /frame. The frame rate was the same for all videos at 30fps. The results are summarized over Tables 1- 3. For each video pattern we calculated Recall (R) [Figure 3 shows a Recall (R) comparison of the proposed algorithm with other models introduced in section 2] and Precision (P) to quantitatively evaluate the performance, which are defined as:

$$R = n_c / (G_t) \quad (6)$$

$$P = n_c / (n_c + n_f) \quad (7)$$

---

<sup>1</sup> Pro Evolution Soccer 2012.



**Fig. 3.** Graphical representation of the results from the key-frame extraction algorithms comparison over the 6 different sport video clips. On the X-axis are the video benchmarks 1-6) while in the Y-axis is the % Recall of the key-frames extracted compared to the Ground Truth key-frames  $G_t$ . The compared algorithms are: Pairwise Pixel (PP), Cluster, Histogram Comparison (H C) and Enhanced Entropy Difference (E D).

where for each pattern,  $n_c$  is the number of shots correctly recognized,  $n_m$  is the number of missed shots and  $n_f$  is the number of false recognized shots and  $G_t = n_c + n_m$  is the Ground Truth. Table 1 shows the comparison results from the evaluation of the 6 video patterns over the proposed method of Enhanced Entropy Difference (**EED**), Pairwise Pixel (**PP**) [10], Histogram Comparison (**HC**) [4] and Cluster (**CI**) [9]. In addition to the above characteristics we have added on the table  $n_t$  which is the total number of shots the algorithms recognized ( $n_t = n_c + n_f$ ).

**Table 2.** Performance analysis for the 6 Football Videos. The table includes the Ground Truth  $G_t$  numbered of key-frames for each video sequence and the Recall ( $R$ ), Precision ( $P$ ) calculated using the equations 6-7 for all different methods: Pairwise Pixel ( $PP$ ) [10], Histogram Comparison ( $HC$ ) [4], Cluster ( $CI$ ) [9], Enhanced Entropy Difference ( $EED$ )

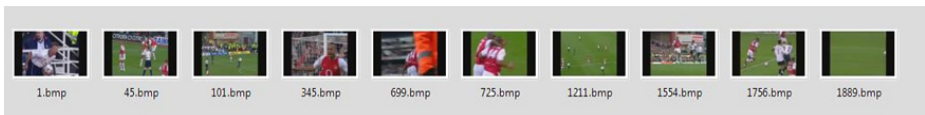
Video Sequence	$G_t$	PP		CI		HC		EED	
		R(%)	P(%)	R(%)	P(%)	R(%)	P(%)	R(%)	P(%)
PES2012	57	100.00	67.06	89.47	100.00	84.21	100.00	96.49	100.00
Arsenal-Bluckburn Rovers	12	92.30	54.55	75.00	100.00	83.33	100.00	83.33	100.00
Liverpool-Real Madrid	35	94.44	91.89	100.00	100.00	94.29	89.19	94.29	94.29
Lyon-Zagreb	17	88.88	64.00	64.71	100.00	88.24	100.00	76.47	100.00
AEK-Olympiacos	101	99.01	87.83	91.09	100.00	87.13	100.00	92.08	100.00
M.United-Real Madrid	21	100.00	51.22	80.95	100.00	66.66	100.00	85.71	100.00

All football patterns were manually annotated to extract a labeled ground truth ( $G_t$ ) number of key-frames. Although a key-frame selected to represent a shot is a semantic concept, relative agreement can be reached among different people. Table 2 shows shot Recall ( $R$ ) and Precision ( $P$ ) comparison based on the ground truth  $G_t$  number of frames for the benchmark between the 4 compared methods. Table 3 shows the comparison of the compression ratio  $CR = 1 - n_t / Total_{Frames}$  each method succeeded where  $Total_{Frames}$  are the total number of frames in the Video sequence.

**Table 3.** Compression Ratio for the 6 Football Videos. The table includes the number of frames for each video sequence and the time duration: Pairwise Pixel ( $CR_{PP}$ ) [10], Histogram Comparison ( $CR_{HC}$ ) [4], Cluster ( $CR_{Cl}$ ) [9], Enhanced Entropy Difference ( $CR_{EED}$ ).

Video Sequence	Nr Frames (min:sec)	Duration	$CR_{PP}$ (%)	$CR_{Cl}$ (%)	$CR_{HC}$ (%)	$CR_{EED}$ (%)
PES2012	19892	10:48	99.57	99.74	99.76	99.72
Arsenal-Blackburn Rovers	2070	01:09	98.94	99.56	99.52	99.52
Liverpool-Real Madrid	7350	04:05	99.50	99.52	99.49	99.50
Lyon-Zagreb	3480	01:56	99.28	99.68	99.57	99.63
AEK-Olympiacos	21150	11:45	99.45	99.56	99.58	99.56
M.United-Real Madrid	3930	02:11	98.93	99.56	99.64	99.54

It can be seen from the above tables that the results for the proposed approach are satisfactory. From Table 3 it can be seen that the proposed model shows a high compress ratio efficiency of an average above 99%. Table 1 and Figure 3 demonstrate that the EED model performs efficiently, summarizing the video sequence [99% Compression], and capturing the most salient events in the sequence. In all 6 sequences the Total number of frames returned  $n_t$  is very closed to the optimal number that have been provided from ground truth  $G_t$  while the number of redundant frames  $n_f$  is kept to a minimum. Compared to the other systems % Recall, the Enhanced Entropy Difference (EED) algorithm shows higher key-frame retrieval compared to Pairwise Pixel (PP) [10] and Histogram Comparison (HC) [4] and has very similar results to the Cluster one (Cl) [19]. Figure 3 below is the percentage Recall (R%) accuracy for the key-frames. Although it seems that PP and HC performs well over some videos, this is because these two algorithms succeed a very low compress ratio (Table 3), which means more frames are needed to represent the video shot. Examples of the retrieved key-frames can be seen in Figures [ 2, 4]. Figure 2 shows the key-frame extracted from the PES 2012 video sequence while Figure 4 are the key-frames from FC Arsenal vs. Blackburn video.



**Fig. 4.** Key-frames extracted from football Highlight video from FC Arsenal vs. Blackburn (2070 frames at 30fps). The video has been summarized down to 10 key-frames/shots.

## 4 Conclusions

Sports video segmentation is the first step for semantic game abstraction based on tactic patterns analysis and important player behaviors within the pitch.



In this paper we have presented an architecture to automatic perform Video Annotation down to Key-Frame representation/shot by adapting the original Entropy Difference algorithm [3]. The algorithm is robust to common sources of disturbance such as camera illumination changes, noise and background setup. Instead of using the Intensity color information as a metric, we extract the HUE feature from the original HSV color system and we are performing an Analysis of Variance over the scene period. The processing of the ANOVA over the HUE level allows us to identify important changes within the frame transitions in a video sequence, and check with high accuracy whether new objects have been included in the shot, or whether an entire new shot has appeared. Experimental results prove that the approach performs in high standards compare to other state-of-the-art methods. As future work we will try to model the color transitions within each extracted video shot to identify behavior of the color regions for semantic sport video annotation.

## References

1. Assfalg, J., Bertini, M., Colombo, C., Bimbo, A.D., Nunziati, W.: Semantic annotation of soccer videos: automatic highlights identification. *Computer Vision and Image Understanding* (2004)
2. Jiang, S., Ye, Q., Gao, W., Huang, T.: A new method to segment playfield and its applications in match analysis in sports videos. In: *ACM Multimedia (ACM MM 2004)*, October 10-16, pp. 292–295 (2004)
3. Mentzelopoulos, M., Psarrou, A.: Key-frame Extraction Algorithm using Entropy Difference. In: *Proc. of the 6th ACM SIGMMA International Workshop on Multimedia Information Retrieval (MIR 2004)*, pp. 39–45 (2004)
4. Nagasaka, A., Tanaka, Y.: Automatic video indexing and full-motion video search for object appearances. *Visual Database Systems II*, 113–127 (1992)
5. Pers, J., Kovačič, S.: Tracking people in sport: Making use of partially controlled environment. In: Skarbek, W. (ed.) *CAIP 2001. LNCS*, vol. 2124, p. 374. Springer, Heidelberg (2001)
6. Tong, X., Liu, Q., Duan, L., Lu, H., Xu, C., Tian, Q.: A unified framework for semantic shot representation of sports video. In: *ACM Multimedia Information Retrieval, MIR 2005*, November 10-11, pp. 127–134 (2005)
7. Xavier, D., Jean-Bernard, H., Jean-François, D., Justus, P., Benot, M.: Trictrac video dataset: Public hdtv synthetic soccer video sequences with ground truth. In: *Workshop on Computer Vision Based Analysis in Sport Environments (CVBASE)*, pp. 92–100 (2006)
8. Xie, L., Xu, P., Chang, S.-F., Divakaran, A., Sun, H.: Structure analysis of soccer video with domain knowledge and hidden markov models. *Pattern Recognition Letters* 25, 767–775 (2004)
9. Yu, X., Wang, L., Tian, Q., Xue, P.: Multilevel video representation with application to keyframe extraction. In: *10th International Multimedia Modelling Conference*, pp. 117–123 (2004)
10. Zhang, H., Kankanhalli, A., Smoliar, S.: Automatic partitioning of full-motion video. *Multimedia Systems* 3(1), 10–28 (1993)

# Model-Based Multi-view Registration for RGB-D Sensors

Marcelo Saval-Calvo, Jorge Azorín-López, and Andrés Fuster-Guilló\*

University of Alicante, Alicante, Spain  
{msaval,jazorin,fuster}@dtic.ua.es

**Abstract.** Registration is a main task in 3D objects reconstruction. Different approaches have been developed in order to solve specific problems in scenarios, objects or even the source of data. Recently, new problems have been appeared with the increasing use of low-cost RGB-D sensors. Registering small objects acquired by these cameras using traditional methods is a hard problem due to their low resolution and depth sensing error. In this paper, we propose a model-based registration method for objects composed by small planes using multi-view acquisition. It is able to deal with the problem of low resolution and noisy data. Experiments show very good promising results registering small objects acquired with low-cost RGB-D sensors compared to ICP variants.

**Keywords:** Model-based registration, 3D acquisition, multi-view, RANSAC.

## 1 Introduction

Registering different views into a common coordinated system remains an important problem to be solved in the area of 3D computer vision. This task is among the first steps in most systems that use three dimensional cameras, such as robot guidance, environment reconstruction, object modelling, etc. Currently, the use of low-cost RGB-D cameras has opened new research lines in this area. These sensors have been initially developed for gaming but they have been welcomed by computer vision researchers due to their low-cost. Despite the advantages of obtaining simultaneously color and depth information, they have low resolution and a considerable error in profundity [1–3]. For example, Microsoft Kinect depth sensor provides 320x240 matrix of real data, duplicating those values to construct a 640x480 matrix in order to match the RGB image resolution. Moreover, this device uses a structured light pattern to obtain the depth values in the scene. Then, the more focus distance, the less depth resolution, not getting data regions where the pattern is not projected.

Traditionally, well-known algorithms such as *Iterative Closest Point* (ICP [4]) or RANSAC [5] have been used to align two or more views in one coordinate

---

\* This research has been partially supported by the project GRE11-01 of the University of Alicante.

system. ICP is used for fine registration. This is, to align two views as close as possible. However, this method needs an initial transformation to avoid convergence in a local minima. On the other hand, RANSAC is used to obtain the best points that fit a model. It is used for coarse registration by obtaining the best matches between points of a view and the reference model. RANSAC is often used to extract the initial transformation for the ICP. Those methods, despite the fact that are noise-resistant, only can afford a certain signal-noise ratio (SNR). If the number of noisy data represents a big percentage of total values, then those methods cannot get a valid result. Therefore, if a sensor with low resolution is used for reconstructing small objects, the number of valid data and, in consequence, the SNR will be reduced, and making very difficult to register accurately the views.

Reconstruction of objects with low-cost RGB-D sensors is an increasing topic in computer vision applications [6, 7]. Two main problems have to be handled: low depth resolution and depth error. The first implies the non detection of thin objects due the pattern disparity. It could be solved by using multi-view techniques where a large number of views are registered. The structured light pattern is able to reach all points of an object having different views, making the whole reconstruction of an object possible even including thin parts. However, multi-view techniques require a good registration method to align perfectly the views. In this case, the second problem emerges. Traditional registration algorithms cannot be used directly due to the SNR, even with previous data filtering.

An interesting way to solve depth error related to a low SNR is the use of models calculated from the raw data. Model registration has been widely used in building or urban reconstruction [8–10] where the point cloud has a large number of data and the accuracy required is in range of centimetres. In robotics and augmented reality areas, planes registration is commonly used to estimate the position of the camera in the scenario where walls, floor and roof (apart of other possible planes detected) are used to estimate the movements along the scene [11–13]. Those planes are also extracted from a large number of points and the accuracy of registration is not highly detailed.

The problems described above become a challenging problem when intrinsic shape and very small objects have to be reconstructed. Hence, new techniques should be conceived. The motivation of this paper is to reconstruct accurately this kind of objects. In order to do this, we propose the use of 3D markers to help the reconstruction. Since the marker is known, a model-based registration could be applied reducing noise effects. The object to be reconstructed will take benefit from the marker registration accuracy. Hence, in this paper, we propose a model-based multi-view registration method for objects composed by planes to reconstruct markers with high accuracy.

## 2 Model-Based Multi-view Registration

This section will describe in detail how to obtain an object composed by planes extracted from a model, such as cubes, pyramids, triangular prisms, etc.

Moreover, we will explain the proposed method to register iteratively planes of the model until convergence. Figure 1 shows visually the process.

## 2.1 Model-Based Object Extraction

From a set of 3D points and normals, the method extracts the object of the scene by means of a sequence of steps: face estimation, planes estimation, checking constraints and planes acceptance.

The first step is to estimate parts (planes) of the object. We use the k-means algorithm to cluster the data into different areas using the information of points and normals. Due to points and normals are in a different range of values, a linear normalization is applied.

With faces estimated, a variant of RANSAC algorithm (see Algorithm 1) is proposed to extract planes that fit the points of each region. Traditionally, RANSAC pipeline first selects a subset of data, uses them to make a model and checks if the rest of data not in the first subset fit into the model. If the accepted data amount is enough, then the calculated model and the accepted group are returned. In this case, the model also should accomplish some constraints. The proposed modified RANSAC for object extraction has  $m$  separated data group incomings ( $d_1..d_m$ ), one of each region. Firstly a plane of each group is extracted as in the traditional algorithm with a subset of points ( $set_{ini}$ ). After, angles between each pair of planes are checked and they should be within certain degree range (e.g.  $90^\circ \pm threshold$  for cubes), otherwise they are rejected and new ones are calculated. Once the planes fit the angle constraint, the rest of data not in the first subset have to be checked with their correspondent plane. For this purpose, a new plane is calculated for each point joined to the initial subset and the constraint (angle) is checked. If the plane is accepted the new point is added to the accepted group.

## 2.2 Multi-view Model Registration

In this part, a novel method based on multi-view registration, where sets of  $n$  views are registered all together is described. It registers the planes extracted previously. First, the correspondence between each plane of different views has to be calculated by using the centroid and normal of each one per cube to find the

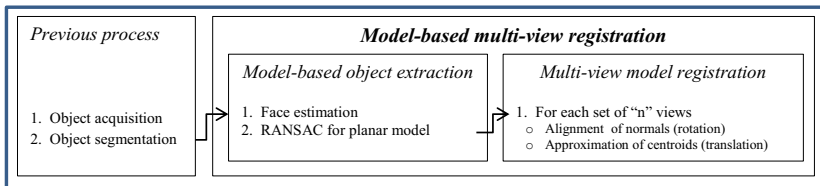


Fig. 1. Process diagram

```

Data:  $d_1 = \{x_1, y_1, z_1\} \dots d_m = \{x_m, y_m, z_m\}$ 
Result:  $\{norm_1, cent_1\}, \dots, \{norm_m, cent_m\}$ 
while not Constraint do
    |  $set_{ini1} = \text{select randomly } n \text{ points from } d_1;$ 
    |  $\{norm_1, cent_1\} = \text{extractModel}(set_{ini1});$ 
    | ... Repeat for  $d_2$  and  $d_3$ 
    | if Planes fit the constraints then
    | |  $Constraint = OK;$ 
    | end
end
for every point in  $d_1$  not in  $set_{ini1}$  do
    |  $\{norm_{aux}, cent_{aux}\} = \text{extractModel}(set_{ini1} + \text{point})$ 
    | if Planes fit the constraints then
    | | add point to  $set_{ini1};$ 
    | end
end
... Repeat for  $d_2$  until  $d_m$ 

```

**Algorithm 1.** Modified RANSAC for planar model extraction

most similar. Once these correspondences have been obtained, the multi-view algorithm is applied (Algorithm 2).

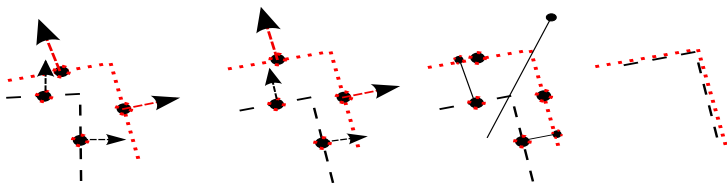
For each set of  $n$  views, we divide it into two groups of centroids and normals: Data, which is the view to be registered, and Model, which is the median value of the rest of views in the set (Algorithm 2, lines 6 and 7).

Normals alignment uses only the normals of Model and Data to align them. We use the *Singular Value Decomposition* to extract the rotation matrix to approximate the Data normals to the Model normals. Rotation matrix is applied only if the angle rotated is under a threshold (*rotTh*). Then, both normals and centroids are rotated to continue with the next step.

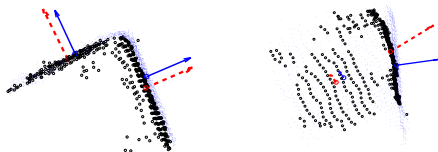
With the Data and Model aligned, the planes have to be joined. The centroids are used to find the translation that minimize the distance between each par of Model-Data planes. Due centroids position in a plane is relative to the points obtained from the sensor, their location could not be the same in two different views. Therefore, the way to register two planes is by using as Model centroids the projection of the Data centroids on the planes of the Model. Then, the translation to move Data to its projection is computed as the mean value of the distance between each Data centroid and the projection value for each axis (see Figure 2). It is computed and applied iteratively until convergence, only if the translation is under a threshold (*transTh*).

After all, the Data normals are approximated to the Model a quarter of the angle variation to avoid being hardly dependent on the first plane extraction in the previous section. With this, errors in the first plane extraction (view Figure 3) can be handled.

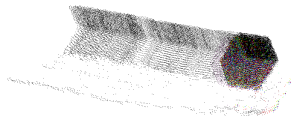
It is proposed to apply the normals alignment and centroids registration to different subsets of planes in the scene to avoid possible planes wrongly extracted previously, and then choose the best transformation found.



**Fig. 2.** Example of plane registration. Data represented by hyphens and Model by dots. First normals are aligned, and then Data centroids are projected and registered.



**Fig. 3.** Red-dotted arrows show calculated normals compared to desirable normals (blue). Left: correct 90 degrees constraint. Right: normals are wrongly extracted.



**Fig. 4.** Registration problem if only a cube is registered. If only two faces are visible some steps, the process will register across the intersection line.

If only two planes are visible, a special translation is applied. In this case, the registration could go along the edge formed by the two planes, producing situation such as in Figure 4. Then, the Data centroids are translated to the Model centroids (not the projections). In this case we assume that the cube has a face in front of the camera, so the points in the plane will be good obtained, and the centroids of Model and Data will be also well extracted.

### 3 Experimentation

The proposed Model-based Multi-view Registration method (*MBMVR*) has been validated by reconstructing a cube with 8 cm of side. Experimental setup includes a Microsoft Kinect RGB-D sensor and a turning table with the cube on, manually rotated. The distance of the camera and the object is 1 meter and the angles rotated vary approximately between 1.5 and 2 degrees.

```

Data: Views
Result: TransformedViews
for Each set of "n" views do
  while Not convergence or cont < total loops do
    for i = 1 until n do
      nData = views.normals[set(i)];
      cData = views.centroid[set(i)];
      nModel = median(views.normals[set(1..n <> i)]);
      cModel = median(views.centroids[set(1..n <> i)]);
      R = getRotation(nData,nModel);
      Apply(R,[nData cData]);
      T = getTranslation(cData,cModel);
      Apply([R T],views[set(i)];
      1/4 Alignment of normals
    end
  end
end

```

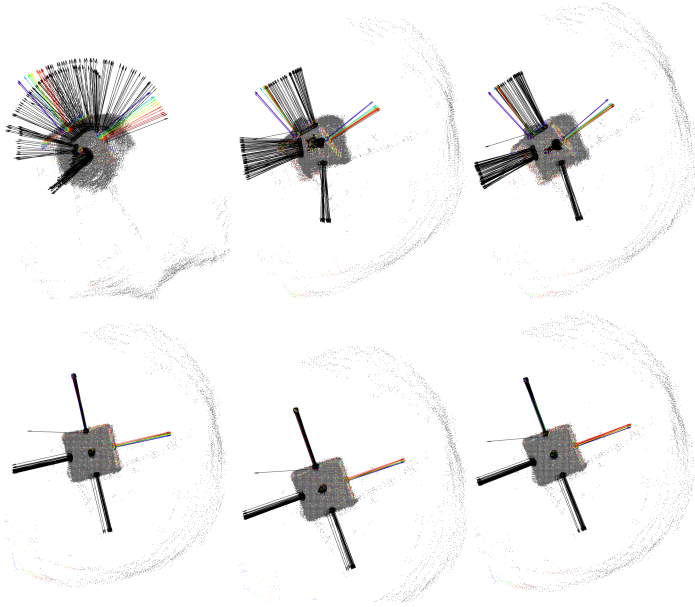
**Algorithm 2.** Multi-view registration algorithm

Registration results obtained by *MBMVR* are compared to the well-known ICP algorithm. *MBMVR* has been tested for different multi-view set sizes  $n = 5, 7$  and  $11$ . The thresholds used are:  $thrJoin = 35$ ,  $rotTh = 10$  and  $transTh = 30$ . Angle for planes acceptance is  $90 \pm 3$  in the model extraction. These parameters have been experimentally selected. On the other hand, ICP has been tested with three variants, point-to-point ( $p2p$ ), point-to-plane ( $p2pl$ ), and point-to-plane with color features ( $p2pl-c$ ), all of them with edge rejection and using 90% of best matches between views. Best matches are calculated with the distance between each point in data and its closest in the model for the  $p2p$  and  $p2pl$  variant, and also for the color difference in the  $p2pl-c$ .

Figure 5 shows registration results for visual inspection of ICP variants and *MBMVR* method for one cube. In the first row, ICP variants are shown. The second row has the *MBMVR* results for  $n=5, 7$  and  $11$  respectively. The normals are plotted in order to make easier the visual evaluation of results. The  $p2p$  ICP variant is clearly the worst. The  $p2pl$  and  $p2pl-c$  are similar, but the second is more compact due the color feature usage. The *MBMVR* method for  $n=7$ , shown at the bottom right, obtains the best result by registering accurately the cube.

Visually, the results demonstrate a better registration of our method compared to ICP variants (Figure 5). Also, a quantitative evaluation has been done, proving the enhancement of our method in registration (Table 1). This evaluation consists in providing the average distance between each centroid of each face with the closest centroid in the rest of views, the mean value of angle difference between each normal and the nearest in the registered set and, finally, the average distance of a point cloud view with the rest of views.

The table confirms previous analysis. For ICP variants,  $p2pl-c$  obtains the best results. For *MBMVR* method, the best results are achieved with  $n=7$  for centroid disparity and points dispersion, but  $n=11$  has better results for normals



**Fig. 5.** Visually illustration of algorithm results. First row: ICP variants (p2p , p2pl and p2pl-c) ; Second row: Multi-view model-based registration with  $n = 5, 7$  and  $11$ .

**Table 1.** Table of comparison results of different algorithms

Method	Variant	Centroid disparity (mm)		Normals deviation (degrees)		Points dispersion (mm)	
		<i>Mean</i>	<i>Std</i>	<i>Mean</i>	<i>Std</i>	<i>Mean</i>	<i>Std</i>
ICP	P2P	0.9526	0.3726	0.9373	0.4121	0.9526	0.3726
ICP	P2PL	0.7266	0.3327	0.4914	0.2284	0.7266	0.3327
ICP	P2PL-C	0.6953	0.3141	0.4243	0.4068	0.6953	0.3141
MBMVR	n=5	0.5449	0.3863	0.1556	0.6543	0.5449	0.3863
MBMVR	n=7	<b>0.5163</b>	<b>0.3443</b>	0.1560	0.6835	<b>0.5163</b>	<b>0.3443</b>
MBMVR	n=11	0.5179	0.3475	<b>0.1554</b>	<b>0.6626</b>	0.5179	0.3475

deviation. With  $n=11$  the normals are better registered because the alignment is easier if a view is more times iterated and with more references (bigger Model), but translation depends on the centroid position, and so, on the actual points from the camera. If the range of views is high, the probability to have differences in the centroid position for the same face is higher than for less views.

## 4 Conclusion

In this paper, the novel Model-based Multi-view registration method (MBMVR) is proposed for an accurate registering of objects composed by planes. It will be able to help in complex small object reconstruction, solving the low depth resolution and depth error of RGB-D low-cost sensors. Multi-view model registration



is proposed to reconstruct the object accurately using the models extracted. Moreover, we propose the extraction of objects composed by planes using a new variation of RANSAC, taking into account constrained group of planes. The experimental results demonstrate the improvement of the MBMVR proposed method compared to three variants of the well-known ICP algorithm. As future research lines, experiments with different kind of markers, such as pyramids or prisms, will be evaluated, as well as the comparison to more registration methods. Finally, it is proposed to validate the use of 3D markers recovered by MBMVR to reconstruct intricate shapes and small objects.

## References

1. Khoshelham, K., Elberink, S.O.: Accuracy and resolution of kinect depth data for indoor mapping applications. *Sensors* 12(2), 1437–1454 (2012)
2. Wilson, A.D.: Using a depth camera as a touch sensor. In: *ACM Intl. Conf. on Interactive Tabletops and Surfaces, ITS 2010*, pp. 69–72. ACM, NY (2010)
3. Smisek, J., Jancosek, M., Pajdla, T.: 3d with kinect. In: *IEEE Intl. Conf. on Computer Vision Workshops*, pp. 1154–1160 (November 2011)
4. Rusinkiewicz, S., Levoy, M.: Efficient variants of the icp algorithm. In: *Third Intl. Conf. on 3-D Digital Imaging and Modeling*, pp. 145–152 (2001)
5. Fischler, M.A., Bolles, R.C.: Random sample consensus: a paradigm for model fitting with applications to image analysis and automated cartography. *Commun. ACM* 24(6), 381–395 (1981)
6. Ramos, E.: Turntable scanner. In: *Arduino and Kinect Projects*, pp. 309–342. Apress (2012)
7. Kramer, J., Burrus, N., Echtler, F., Parker, M., Daniel Herrera, C.: Object Modeling and Detection. In: *Hacking the Kinect*, ch. 9, pp. 173–206. Technology in Action (2012)
8. Dold, C., Brenner, C.: Automatic matching of terrestrial scan data as a basis for the generation of detailed 3d city models. In: *International Archives of Photogrammetry and Remote Sensing*, pp. 1091–1096 (2004)
9. Dold, C., Brenner, C.: Registration of terrestrial laser scanning data using planar patches and image data. In: *International Archives of Photogrammetry and Remote Sensing*, pp. 25–27 (2006)
10. Theiler, P.W., Schindler, K.: Automatic registration of terrestrial laser scanner point clouds using natural planar surfaces. In: *22nd ISPRS Congress, Melbourne, Australia* (2012)
11. Pathak, K., Vaskevicius, N., Poppinga, J., Pflugsthor, M., et al.: Fast 3d mapping by matching planes extracted from range sensor point-clouds. In: *IEEE/RSJ Intl. Conf. on Intelligent Robots and Systems*, pp. 1150–1155 (October 2009)
12. Lee, T.-K., Lim, S., Lee, S., An, S., et al.: Indoor mapping using planes extracted from noisy rgb-d sensors. In: *2012 IEEE/RSJ Intl. Conf. on Intelligent Robots and Systems*, pp. 1727–1733 (October 2012)
13. Uematsu, Y., Saito, H.: Multiple planes based registration using 3d projective space for augmented reality. *Image and Vision Computing* 27(10), 1484–1496 (2009)

# 3D Hand Pose Estimation with Neural Networks

Jose Antonio Serra<sup>1</sup>, José Garcia-Rodriguez<sup>1</sup>, Sergio Orts-Escolano<sup>1</sup>,  
Juan Manuel Garcia-Chamizo<sup>1</sup>, Anastassia Angelopoulou<sup>2</sup>,  
Alexandra Psarrou<sup>2</sup>, Markos Mentzelopoulos<sup>2</sup>, Javier Montoyo-Bojo<sup>1</sup>,  
and Enrique Domínguez<sup>3</sup>

<sup>1</sup> Dept. of Computing Technology, University of Alicante,  
P.O. Box. 99. E03080, Alicante, Spain

{jserra, jgarcia, sorts, juanma, jmontoyo}@dtic.ua.es

<sup>2</sup> Dept. of Computer Science & Software Engineering (CSSE), University of Westminster,  
Cavendish, W1W 6UW, United Kingdom

{agelopa, psarroa, mentzem}@wmin.ac.uk

<sup>3</sup> Dept. of Computer Science, University of Malaga, Spain  
enriqued@lcc.uma.es

**Abstract.** We propose the design of a real-time system to recognize and interpret hand gestures. The acquisition devices are low cost 3D sensors. 3D hand pose will be segmented, characterized and tracked using growing neural gas (GNG) structure. The capacity of the system to obtain information with a high degree of freedom allows the encoding of many gestures and a very accurate motion capture. The use of hand pose models combined with motion information provided with GNG permits to deal with the problem of the hand motion representation. A natural interface applied to a virtual mirrorwriting system and to a system to estimate hand pose will be designed to demonstrate the validity of the system.

**Keywords:** Growing Neural Gas, 3D Sensor, Hand Pose Estimation, Hand Motion, Trajectories Description.

## 1 Introduction

The estimation of the 3D hand pose has special interest because by understanding the configuration of the hands, we will be able to build systems that can interpret human activities and understand important aspects of the interaction of a human with their physical and social environment. There are several works that address only visual data without using markers [1,2]. Existing approaches can be classified as model based and appearance based. The model based systems provide a continuum set of solutions, but are computationally expensive and dependent on the availability of a large amount of visual information (usually provided by a multi-camera system). Appearance-based systems are associated with a less computational cost and a much smaller hardware complexity, but only recognize a discrete number of hand poses that correspond generally to the training set.

Despite the large amount of work in this field [3,4], the problem is still open and has several theoretical and practical challenges, due to a number of difficulties common to most systems, among which stand out: a) High dimensionality problem: the hand is an articulated with more object than 20 DOF. b) Self-occlusions: since the hand is an articulated object, its projections generate a variety of ways with various self-occlusions which makes harder the segmentation of the various parts of the hand and the extraction of high-level features. c) Speed processing: even for a single image, a real-time computer vision system needs to process a lot of data. d) Uncontrolled Environments: for general use, many HCI systems must operate with unrestricted backgrounds and a wide range of lighting conditions. e) Rapid hand movements: hand has a very fast movement capability reaching speeds up to 5 m / s for translation and 300 m / s for the rotation of the wrist.

In this work, we propose a new model-based approach to address hands 3D tracking. The observations come from a low-cost 3D sensor (Kinect). The optimization is performed with a variant of growing neural networks GNG. We hope to achieve accurate and robust tracking with an acquisition frequency of at least 10-15Hz. Among the contributions of the proposed method is novel because (a) provides accurate solutions to the problem of 3D tracking of the hand (b) requires no complex hardware configuration (c) is based solely on visual data without using physical markers (d) is not very sensitive to lighting conditions and (e) run in real time.

The rest of the paper is organized as follows: section 2 presents the growing neural gas and describes its ability to obtain reduced representations of objects preserving the topological information. Also extend such capabilities to the representation of point cloud sequences and motion analysis. In section 3, the hand pose estimation system is described. Finally, section 4 presents experiments on the application to a virtual mirror writing system and a hand gesture recognition system, followed by our conclusions and future work.

## 2 Topological Representation with Growing Neural Gas

The approach presented in this paper is based on self-organising networks trained using the Growing Neural Gas learning method [5], an incremental training algorithm. The links between the units in the network are established through competitive hebbian learning. As a result, the algorithm can be used in cases where the topological structure of the input pattern is not known a priori and yields topology preserving maps of feature manifold.

### 2.1 Growing Neural Gas

From the Neural Gas model [6] and Growing Cell Structures [7], Fritzke developed the Growing Neural Gas model, with no predefined topology of a union between neurons. A growth process takes place from minimal network size and new units are inserted successively using a particular type of vector quantisation [8,9]. To determine where to insert new units, local error measures are gathered during the adaptation process and each new unit is inserted near the unit which has the highest accumulated error. At each adaptation step a connection between the winner and the second-nearest unit is created as dictated by the competitive hebbian learning algorithm. This is

continued until an ending condition is fulfilled, as for example evaluation of the optimal network topology based on some measure. Also the ending condition could it be the insertion of a predefined number of neurons or a temporal constrain. In addition, in GNG networks learning parameters are constant in time, in contrast to other methods whose learning is based on decaying parameters.

## 2.2 Point Cloud Data Representation with Growing Neural Gas

The ability of neural gases to preserve the input data topology will be employed in this work for the representation and tracking of objects. Identifying the points of the input data that belong to the objects allows the network to adapt its structure to this input subspace, obtaining an induced Delaunay triangulation of the object.

Learning takes place following the GNG algorithm described in previous section. So, doing this process, a representation based on the neural network structure is obtained which preserves the topology of the object  $\mathcal{O}$  from a certain feature  $\mathcal{T}$ . That is, from the visual appearance  $\mathcal{A}_V$  of the object is obtained an approximation to its geometric appearance  $\mathcal{A}_G$ . In our case the 3D hands representation.

GNG has been adapted to represent Point Cloud Sequences. The main difference with the GNG original algorithm is the omission of insertion/deletion actions after the first frame. Since no neurons are added or deleted the system keeps the correspondence during the whole sequence, solving intrinsically the problem of correspondence. This adaptive method is also able to face real-time constraints, because the number  $\lambda$  of times that the internal loop is performed can be chosen according to the time available between two successive frames that depend on the acquisition rate. The mean time to obtain a GNG on a frame is about 10ms., using the adaptive method.

GNG provides a reduction of the input data, while preserving its structure. This gives us two advantages. First, we have to process less data, so we speedup the next step of feature extraction. Second, outliers are reduced. Outliers are one of the main sources of error in this kind of applications.

## 2.3 Motion Representation and Analysis

The motion can be classified according to the way of perceiving it: common and relative, and it can be represented using the graph obtained from the neural network structure for each input data acquisition.

In the case of the common motion, it can be performed the analysis of the trajectory followed by an object by tracking the centroid of the same along the sequence. This centroid may be calculated from the positions of the nodes in the graph that represents the object in each capture (GNG structure).

To follow the relative motion, it should be calculated the changes in position of each node with respect to the centroid of the object for each capture. By following the path of each node, it can be analyzed and recognized changes in the morphology of the object.

One of the most important problems in tracking objects, the correspondence between features along the sequence, can be solved of intrinsic form [10] since the position of neurons is known at any time without the need for additional processing.

The analysis of the trajectory described by each object is used to interpret its movement. In some cases, to address the movement recognition, a trajectory parameterization is performed. In [11], it can be found some suggestions for parameterization. Also, it can be used direct measures of similarity between paths, such as the modified Hausdorff distance [12], allowing comparison of trajectories.

### 3 3D Hand Pose Estimation with Growing Neural Gas

The previous section described the ability of neural gases for the representation and tracking of data streams in several dimensions. To analyze the movement, certain characteristics will be monitored in each of the shots of each sequence, not the object itself, but its representation that is obtained with the neural network. That is, using the position of the neurons of the network (their structure) as a further feature.

The construction of a system of representation, tracking and recognition of hand gestures based on the GNG and 3D sensors capable of rendering common and relative motion is proposed (figure 1).

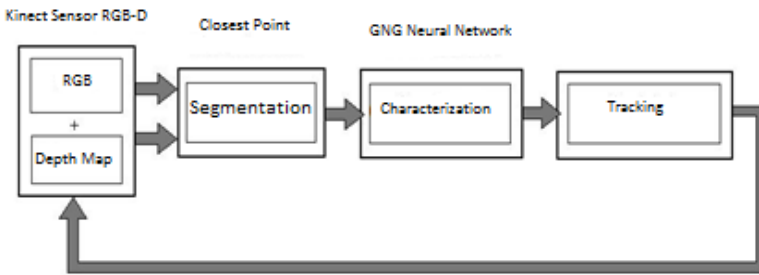


Fig. 1. Flowchart of the whole system

#### 3.1 Data Acquisition and Hands Segmentation

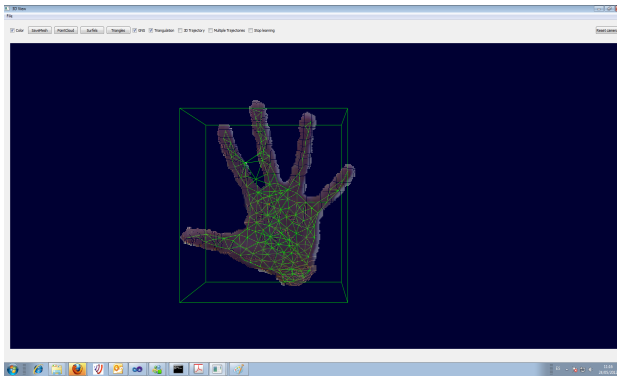
All the experimental phase is based on the use of real-world sequences obtained by a Kinect sensor. Such sensors belong to the so-called RGB-D cameras since they provide RGB format images with depth information per pixel. Specifically, Microsoft's Kinect sensor is able to get screenshots of 640x480 pixels and its corresponding depth information, based on an infrared projector combined with a CMOS sensor with a resolution of 320x240 pixels, and can reach rates of up to 30 frames per second. A first processing of sensor data enables obtaining the component in the z axis of coordinates of the points in the three dimensional space.

For the segmentation of the hands from the background, an hybrid technique based on depth information and the determination of appropriate thresholds on HSV model to filter skin color points have been developed. The system has been trained with multiple users.

### 3.2 Gesture Characterization and Recognition with Growing Neural Networks

Growing neural gas presented in section 2 is used to characterize hands allowing a reduced topological representation by a graph defining an induced Delaunay triangulation. In the experiments section, the minimum number of neurons necessary for an adequate representation of the hand is defined, which allows the subsequent tracking and recognition of gestures. Figure 2 shows an example of 3D hand characterization.

The path followed by neurons can be obtained and interpreted by processing the position information of them on the map along the sequence. This evolution can be studied at the level of the global movement, following the centroids of the map or locally, studying the deformation of the object. This is possible because the system does not restart the map for each shot, adapting the new input data to the previous map without inserting or deleting neurons. Thus, the neurons are used as stable visual markers that define the shape of objects.



**Fig. 2.** Hand pose characterization with GNG

## 4 Experimentation

Several experiments have been performed for the validation of our system. At first, it has been obtained a proper parametrization of the neural network and then a global motion experiments related to virtual mirror writing have been conducted. Finally, the system have learned and labeled various poses of the hand, performed by various users, and subsequently the same gestures, made by other users, have been presented to the system, with a high rate of correct recognition.

To carry out all the experiments we used the RGBDemo framework, a computer vision software written in C++, which allow to quickly and easily get started with Kinect-like camera and develop our own projects.

#### 4.1 Optimal Parametrization of GNG

This experiment measured the mean square error of different representations of the hand obtained with a varied number of neurons. From the graph of figure 3, it can be noticed that with approximately 200 neurons, the error is low enough and the quality provided is adequate for 3D handsrepresentation. We chose the minimum number of neurons with an acceptable quality as the computational cost is reduced and allows real-time management. The other GNG parameters used were:  $\lambda = 2000$ ,  $\varepsilon_1 = 0.1$ ,  $\varepsilon_2 = 0.01$ ,  $\alpha = 0.5$ ,  $\beta = 0.0005$ .

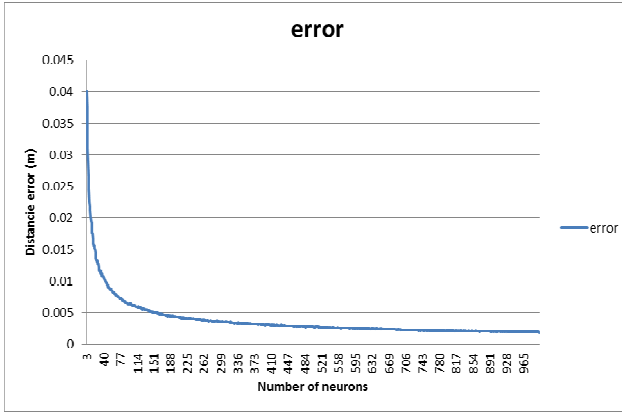


Fig. 3. Error representation based on the number of neurons in the network

#### 4.2 Virtual MirrorWriting Recognition

This section presents an application of a handwriting recognition system in a virtual mirror by tracking the trajectory of the centroid. Figure 4 shows a set of gestures.

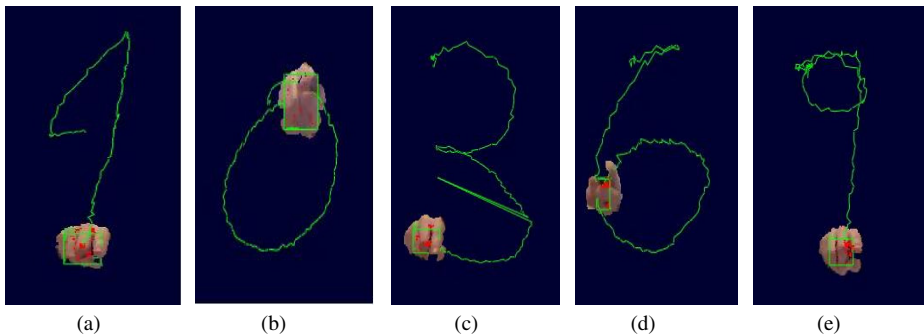


Fig. 4. Mirror writing gestures corresponding to the numbers 0, 1, 3, 6 and 9

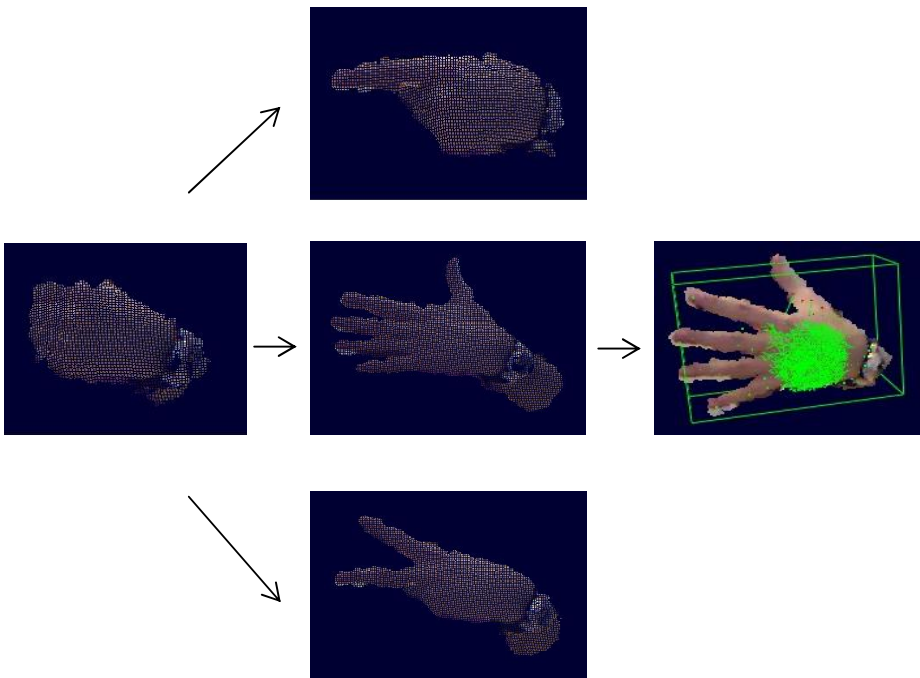
Through a training phase, the path described by the centroid of the neural network representation of different characters virtually made by different users has been tagged. Subsequently, there has been conducted a recognition phase of the symbols created by new users by comparing the paths described and labeled using the Hausdorff distance [12], with a success rate greater than 95%.

### 4.3 Recognition of Hand Poses

This section presents an application of the gesture recognition system. Figure 5 shows a set of gestures used as input to the system. Once the sequences have been learned by GNG, Hausdorff distances will be used for comparison of sets of points that define a path, in this case the ones followed by all neurons representing the gestures of the hand with respect to the centroid of the representation.

At figure 5, the pose of the left defines the start position and the center ones are different final positions for different gestures. The representation on the right shows the trajectories described by the neurons along the gesture realization.

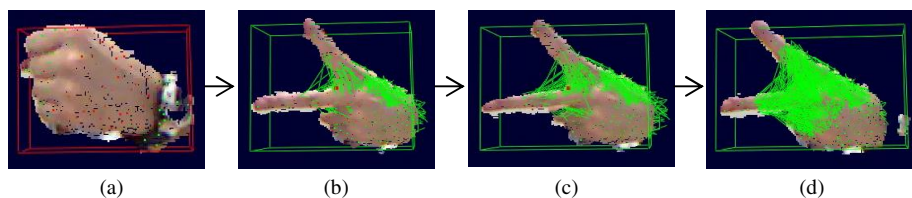
As in the previous experiment stages of training / recognition and labeling were made. The results obtained for a reduced set of gestures are promising with a success rate of 95%.



**Fig. 5.** Set of gestures used for trajectories study



In this case, it is especially important to be able to represent 3D space, as can be seen in figure 6, since some gestures present trajectories in all axes that would be impossible to perceive with a system based only on the x and y axes.



**Fig. 6.** 3D trajectories evolution during the gesture

## 5 Conclusions and Future Work

In this paper we have presented a novel architecture to represent and recognize gestures based on neural networks and 3D sensors.

It has been shown that neural gases are suitable for reduced representation of objects in three dimensions by a graph which defines the interconnection of neurons. Moreover, the processing of the position information of these neurons over time, allows us to build the hand trajectories and interpret them.

For the recognition of gestures we used the Hausdorff distance to measure the similarity between the sets of gestures that define the different trajectories global and / or local of our markers (neurons).

Finally, to validate the system it has been developed a framework that have been used to test several global and local gestures made by different users, obtaining good results in the recognition task. However, the noisy images and occlusions with the environment are two major problems.

As future work, we will improve the system performance at all stages to achieve a natural interface that allows us to interact with any object manipulation system. Likewise, it is contemplated the acceleration of the whole system on GPUs.

## References

1. Oikonomidis, I., Kyriazis, N., Argyros, A.A.: Full DOF Tracking of a Hand Interacting with an Object by Modeling Occlusions and Physical Constraints. In: ICCV (2011)
2. Oikonomidis, I., Kyriazi, N., Argyros, A.A.: Efficient Model-based 3D Tracking of Hand Articulations using Kinect. In: BMVC (2011)
3. Moeslund, T.B., Hilton, A., Kruger, V.: A survey of advances in vision-based human motion capture and analysis. *CVIU* 104, 90–126 (2006)
4. Erol, A., Bebis, G., Nicolescu, M., Boyle, R.D., Twombly, X.: Vision-based hand pose estimation: A review. *CVIU* 108, 52–73 (2007)
5. Fritzke, B.: A Growing Neural Gas Network Learns Topologies. In: Tesauro, G., Touretzky, D.S., Leen, T.K. (eds.) *Advances in Neural Information Processing Systems 7*. MIT Press, Cambridge (1995)

6. Martinetz, T., Berkovich, S.G., Schulten, K.J.: "Neural-Gas" Network for Vector Quantization and its Application to Time-Series Prediction. *IEEE Transactions on Neural Networks* 4(4), 558–569 (1993)
7. Fritzke, B.: Growing Cell Structures – A Self-organising Network for Unsupervised and Supervised Learning. Technical Report TR-93-026, International Computer Science Institute, Berkeley, California (1993)
8. Bauer, H.-U., Hermann, M., Villmann, T.: Neural Maps and Topographic Vector Quantization. *Neural Networks* 12(4-5), 659–676 (1999)
9. Martinetz, T., Schulten, K.: Topology Representing Networks. *Neural Networks* 7(3), 507–522 (1994)
10. Zhang, Z.: Le problème de la mise en correspondance: L'état de l'art. Rapport de recherche n°, Institut National de Recherche en Informatique et en Automatique (1993)
11. Cédras, C., Shah, M.: Motion-based recognition: a survey. *Image and Vision Computing* 13(2), 129–155 (1995)
12. Dubbuisson, M.P., Jain, A.K.: A Modified Hausdorff Distance for Object Matching. In: *Proceedings of the International Conference on Pattern Recognition, Jerusalem, Israel*, pp. 566–568 (1994)

# Author Index

- Abbas, Hayder Hassan II-80  
Acosta, Leopoldo I-262  
Aguiar-Pulido, Vanessa I-453  
Ahachad, Anas I-367  
Ahmad, Irfan I-592  
Aisa, Francisco II-312  
Aksakalli, Vural II-53  
Akusok, Anton I-17  
Alaíz, Carlos M. I-106  
Alcalde, Cristina II-246  
Algin, Ramazan II-53  
Aljamaan, Hamoud I-592  
Alkaya, Ali Fuat II-53  
Allende, Sira M. I-124  
Almendros-Jiménez, Jesús M. II-300  
Alonso-Betanzos, Amparo I-152  
Álvarez, Ada II-46  
AngelBello, Francisco II-46  
Angelopoulou, Anastassia II-1, II-488, II-504  
Araujo, Carmen Paz Suárez I-114  
Ariza, Alfonso I-124  
Arnay, Rafael I-262  
Arsava, K. Sarp I-169  
Atencia, Miguel II-355  
Azorín-López,, Jorge II-496  
  
Báez, Patricio García I-114  
Baños, Oresti II-208  
Bárcena-Humanes, Jose Luis I-575, I-584  
Barreto, Guilherme A. I-408, I-622  
Basawaraj, I-492  
Batista, Belén Melián II-28  
Batista, Rayco I-232  
Becerra Bonache, Leonor I-189  
Becerra García, Roberto Antonio II-115, II-135  
Behn, Carsten II-159  
Beltrán-Castro, Juan I-471  
Bermúdez, María I-445  
Bigand, André II-467  
Björk, Kaj-Mikael I-210  
Brown, John N.A. I-1  
Burusco, Ana II-246  
  
Caballero, Ricardo II-312  
Caballero-Gil, Pino I-161  
Cabestany, Joan II-142  
Cabrera, I.P. II-224  
Calazan, Rogério M. I-241  
Campbell, Colin I-427  
Cañas, Antonio II-72  
Cano, Juan Falgueras II-200  
Cano Olivares, Pedro II-334  
Caraballo, Jesús II-324  
Carpio, José II-324  
Castellanos-Domínguez, Germán I-471, II-124  
Castillo, Pedro A. II-312  
Castro, Paula M. I-144  
Castro-Bleda, María José I-376  
Català, Andreu II-142  
Cazorla, Miguel II-480  
Cerezuela-Escudero, Elena I-179  
Chaudhari, Narendra S. I-566  
Chaudhuri, Arindam I-393  
Chelbat, Noura II-200  
Chen, Fangyue I-538  
Chen, Guanrong I-538  
Cheng, Conghui II-413  
Colmenarejo, Rosa II-278  
Constantin, Ibtissam II-467  
Constantin, Joseph II-467  
Cordero, Pablo II-224, II-254  
Cordón, Oscar I-36  
Cornejo, Maria Eugenia II-266  
Corona, Francesco I-17, I-408  
Coronado, David II-439  
Costa, Tarcísio Souza II-20  
Cotta, Carlos II-324, II-346  
Craig, Tony I-152  
Cruz-Ramírez, Manuel I-270  
  
Dahl, Veronica I-189  
Damas, Miguel II-208  
Danciu, Daniela II-365  
Dapena, Adriana I-144  
de Armas, Jessica II-36  
Delachaux, Benoît II-216

- de la Hoz Correa, Eduardo I-530  
de la Hoz Franco, Emiro I-530  
del Jesus, María Jose I-331  
del-Rey-Maestre, Nerea I-575, I-584  
de Macedo Mourelle, Luiza I-241  
de Oliveira, Alexandre César  
Muniz II-20  
de Paula Barros, Ana Luiza Bessa I-622  
De Santiago, Alondra II-46  
Díaz, Juan Carlos II-246  
Díaz, Julia I-106  
Díaz Alonso, Javier II-334  
Dominguez, Enrique II-449, II-458,  
II-504  
Dominguez-Morales, Manuel  
Jesus I-179  
Dorado, Julián I-453  
Dorronsoró, José R. I-106  
Duman, Ekrem II-62
- Eirín-López, José M. I-453  
Eirola, Emil I-17  
Elikucuk, Ilker II-62  
Elish, Mahmoud O. I-592  
El-Korchi, Tahar I-169  
Enciso, Manuel II-254  
España, Miriam II-422  
España-Boquera, Salvador I-376
- Fernandes, Carlos I-604  
Fernández, Ángela I-106  
Fernández Caballero, Juan  
Carlos II-278  
Fernández-Leiva, Antonio J. II-346  
Fernandez-Lozano, Carlos I-427  
Fichera, Loris II-96  
Figueiras-Vidal, Aníbal R. I-367  
Fontenla-Romero, Óscar I-152  
Franco, Leonardo I-80, I-88, I-339  
Fuentes-González, Ramón II-246  
Fuster-Guilló, Andrés II-496
- Galea-Sevilla, N. II-422  
García-Bermúdez, Rodolfo  
Valentín II-115, II-135  
García-Chamizo, Juan Manuel II-504  
García-del-Moral, Raimundo II-72  
García-Naya, José A. I-144  
García-Pardo, F. II-224
- García-Rodríguez, José II-1, II-480,  
II-488, II-504  
García-Sánchez, Pablo II-312, II-324  
Gaunt, Tom R. I-427  
Gestal, Marcos I-427  
Gisbrecht, Andrej I-59  
Gómez-Pulido, Juan A. I-198  
González, Ana M. I-106  
Gorban, Alexander N. I-500  
Graña, Manuel II-107  
Guillén, Alberto I-604, II-72, II-422  
Gupta, Gaurav II-1  
Gutiérrez, Pedro Antonio I-270, I-613  
Gutiérrez Rivas, José Luis II-334
- Hamad, Denis II-467  
Hammer, Barbara I-59, I-347  
Hasegawa, Osamu I-321  
He, Qinbin I-538  
Hermann, Wieland I-357  
Hernández, Yadira II-355  
Herrera, Luis Javier I-604, II-72  
Hervás-Martínez, César I-270, II-278,  
I-613  
Hidano, Seira II-171  
Hoyos, Cristian Castro II-124  
Huang, Xiaotao I-633  
Huang, Xu I-280, II-430
- Izquierdo, Christopher Expósito II-28
- Ja'fari, Ahmad II-287  
Jarabo-Amores, María Pilar I-575,  
I-584  
Jaraíz-Simon, María D. I-198  
Jerez, José Manuel I-88, I-339, I-80,  
II-458  
Jiménez, Maria Jesus I-88  
Jiménez-Fernández, Angel I-179, I-299  
Jiménez-Moreno, Gabriel I-179  
Joya, Gonzalo I-124, II-355  
Joya Caparrós, Gonzalo II-115  
Julián-Iranzo, Pascual I-647, II-236  
Julián Merelo, Juan II-312, II-324  
Junior, Amauri Holanda de Souza I-408
- Karlsson, Tor Johan Mikael II-200  
Kästner, Marika I-357  
Khashman, Adnan II-80  
Kim, Deok Won II-181  
Kim, Sung Kean II-181

- Kim, Yeesock I-169  
 Kiselev, Mikhail I-510  
 Klüver, Christina I-518  
 Klüver, Jürgen I-518  
 Kodogiannis, Vassilis S. II-88  
 Korbicz, Józef I-96  
 Krueger, Lars I-253
- Laalaoui, Yacine I-547  
 Lago, Juan II-200  
 Lang, Bo II-386  
 Lara-Cabrera, Raúl II-312, II-346  
 Largo, Rogerio I-604  
 Lendasse, Amaury I-17, I-408, I-417  
 León, Coromoto I-232  
 Li I-291  
 Liang, Hong I-633  
 Linares-Barranco, Alejandro I-179,  
 I-299  
 López, Carlos Pérez II-142  
 Lopez-Coronado, Juan I-299  
 Lopez-Gordo, Miguel Angel II-404  
 López-Rubio, Ezequiel II-449, II-458  
 Luna Tedesqui, Alejandro II-300  
 Luque, Rafael Marcos I-88  
 Luque-Baena, Rafael Marcos I-339,  
 II-439, II-449, II-458
- Ma, Wanli I-280, II-430  
 Ma, Yi-De I-291  
 Madani, Kurosh I-309  
 Mann, Erwin I-133  
 Martín, Daniel Rodríguez II-142  
 Martín-de-Nicolás, Jaime I-575, I-584  
 Martínez-Abella, Fernando I-463  
 Martínez-Romero, Marcos I-435  
 Martín-Fernández, Francisco I-161  
 Massoni, Sébastien I-69  
 Mata-Moya, David I-575, I-584  
 Matsuyama, Yasuo II-171  
 Mattos, Leonardo S. II-96  
 Medina-Moreno, Jesús I-647, II-246,  
 II-266  
 Melián-Batista, Belén II-36, II-46  
 Mentzelopoulos, Markos II-1, II-488,  
 II-504  
 Mezei, József I-210  
 Miche, Yoan I-17, I-408  
 Miralles, J. Emilio I-189  
 Mirkes, Evgeny M. I-500
- Močkoř, Jiří I-385  
 Moghadam, Rasoul Hamidzadeh II-287  
 Molina, Ignacio I-80  
 Molinero, Alejandro Rodríguez II-142  
 Montoyo-Bojo, Javier II-504  
 Mora, Angel II-254  
 Mora, Antonio M. II-312, II-324, I-604  
 Morcillo, P.J. I-647  
 Morell, Vicente II-480  
 Moreno, Andrés Rodríguez II-189  
 Moreno, Ginés II-300, I-647  
 Moreno-Pérez, José A. II-36  
 Moreno-Vega, José Marcos II-28  
 Morente, Laura II-439  
 Morgado-Estevez, Arturo I-299  
 Mrugalski, Marcin I-96  
 Muñoz-Lozano, Jose Luis I-299  
 Murillo Rendón, Santiago II-124
- Najjar, Tarek I-321  
 Navas, María II-439  
 Nedjah, Nadia I-241  
 Nguyen, Phuoc I-280, II-430  
 Nóvoa, Francisco Javier I-435
- Oh, Ein II-181  
 Ojeda, Francisco Charte I-331  
 Ojeda-Aciego, Manuel I-647, II-224  
 Olteanu, Madalina I-69  
 Omari, Adil I-367  
 Orozco-Alzate, Mauricio I-471  
 Ortega Lopera, Julio I-530  
 Ortega-Zamorano, Francisco I-80, I-339  
 Ortiz García, Andrés I-530  
 Orts-Escolano, Sergio II-480, II-504  
 Ortuño, Francisco II-150  
 Öz, Dindar II-53
- Palomo, Esteban José II-449, II-458  
 Parada, Rubén I-124  
 Pardo, Diego II-96  
 Pascualvaca, José Manuel  
 Sánchez I-604  
 Pasemann, Frank I-481  
 Pastor-Pellicer, Joan I-376  
 Pazos, Alejandro I-445  
 Paz-Vicente, Rafael I-179  
 Pehlivanoglu, Y. Volkan I-218  
 Pereira, Javier I-435

- Pérez, Juan Luis I-463  
 Pérez-Godoy, María Dolores I-331  
 Pérez-Ortiz, María I-270, I-613, II-278  
 Perez-Peña, Fernando I-299  
 Perez-Uribe, Andres II-216  
 Petrounias, Ilias II-88  
 Pino Ávila, Carmen II-115  
 Polhill, Gary I-152  
 Pomares, Héctor II-150, II-208  
 Prieto Espinosa, Alberto I-530  
 Psarrou, Alexandra II-1, II-488, II-504
- Rabuñal, Juan R. I-445, I-463  
 Ramet, Daniel II-200  
 Ramík, Dominik M. I-309  
 Ramírez, Eloisa II-266  
 Răsvan, Vladimir II-375  
 Rebetez, Julien II-216  
 Riedel, Martin I-357  
 Rivas, Antonio Jesús Rivera I-331  
 Rivero, Daniel I-453  
 Rodríguez, Álvaro I-445  
 Rodríguez, Casiano I-232  
 Rodríguez, Rafael II-439  
 Rodríguez, Roberto II-135  
 Rodríguez-García, Miguel I-152  
 Rodríguez-Jiménez, José Manuel II-254  
 Rodríguez Labrada, Roberto II-115  
 Rojas, Fernando II-135  
 Rojas, Ignacio II-72, II-150, II-208, II-422  
 Romero, Yeray Álvarez I-114  
 Ron-Angevin, Ricardo II-404  
 Rosa, Agostinho C. I-604  
 Rozas-Ramallal, Ismael I-144  
 Rubio-Manzano, Clemente II-236  
 Ruiz, Eduardo Lalla II-28
- Sabourin, Christophe I-309  
 Salazar, Oswaldo Trelles II-189  
 Samà, Albert II-142  
 Sánchez, Alberto Fuentes II-346  
 Sánchez-Marroño, Noelia I-152  
 Sánchez-Monedero, Javier I-270, I-613  
 Sánchez-Pérez, Juan M. I-198  
 Sandoval, Francisco II-355  
 Satizábal Mejía, Héctor Fabio II-216  
 Saval-Calvo, Marcelo II-496  
 Savio, Alexandre II-107
- Schikuta, Erich I-133  
 Schleif, Frank-Michael I-347  
 Schmitz, Tonia II-159  
 Schulz, Alexander I-59  
 Segredo, Eduardo I-232  
 Segura, Carlos I-232  
 Seoane, Jose A. I-427  
 Serra, Jose Antonio II-504  
 Shozawa, Michitaro II-171  
 Simić, Dragan II-395  
 Simić, Svetlana II-395  
 Simula, Olli I-17, I-408, I-417  
 Sovilj, Dušan I-417  
 Starzyk, Janusz A. I-492  
 Strickert, Marc I-357  
 Suárez-Ulloa, Victoria I-453  
 Subirats, José Luis I-80, I-339  
 Szeto, Kwok Yip II-11
- Thomas, Jaya I-566  
 Tian, Le I-291  
 Tirado, Óscar Torreño II-189, II-200  
 Tran, Dat I-280, II-430  
 Travieso-González, Carlos M. II-124, I-471  
 Trawiński, Krzysztof I-36  
 Trelles, Oswaldo II-200  
 Turias, Ignacio I-88
- Urda, Daniel I-88, I-339
- Valdés, Lissette I-124  
 Valencia-Aguirre, Juliana I-471  
 Valenzuela, Olga II-150  
 van Heeswijk, Mark I-17  
 Vaz, Fermín II-324  
 Vázquez, Guillermo I-435  
 Vázquez-Naya, José Manuel I-435  
 Vega-Rodríguez, Miguel A. I-198  
 Velasco-Alvarez, Francisco II-404  
 Velázquez Pérez, Luis II-115, II-135  
 Veredas, Francisco J. II-439  
 Vieito, Ismael I-463  
 Villa-Vialaneix, Nathalie I-69  
 Villmann, Thomas I-357
- Walter, Matthias I-253  
 Wang, Fen I-633  
 Wang, Guan II-11

Wang, Guangyi I-538  
Wei, Hui II-386  
Witczak, Marcin I-96  
Witte, Hartmut II-159  
Wu, Chi-Hua II-171  
Wu, Hao I-556  
  
Xia, Bin II-413  
Xie, Changsheng I-633  
Xie, Hong II-413

Yang, Jing II-413  
Yokote, Ryota II-171  
Yoo, Tae Keun II-181  
  
Zamora-Martínez, Francisco I-376  
Zhan, Kun I-291  
Zhu, Xibin I-347  
Zimmermann, Klaus II-159  
Zinovyev, Andrei I-500  
Zuo, Qing-song II-386